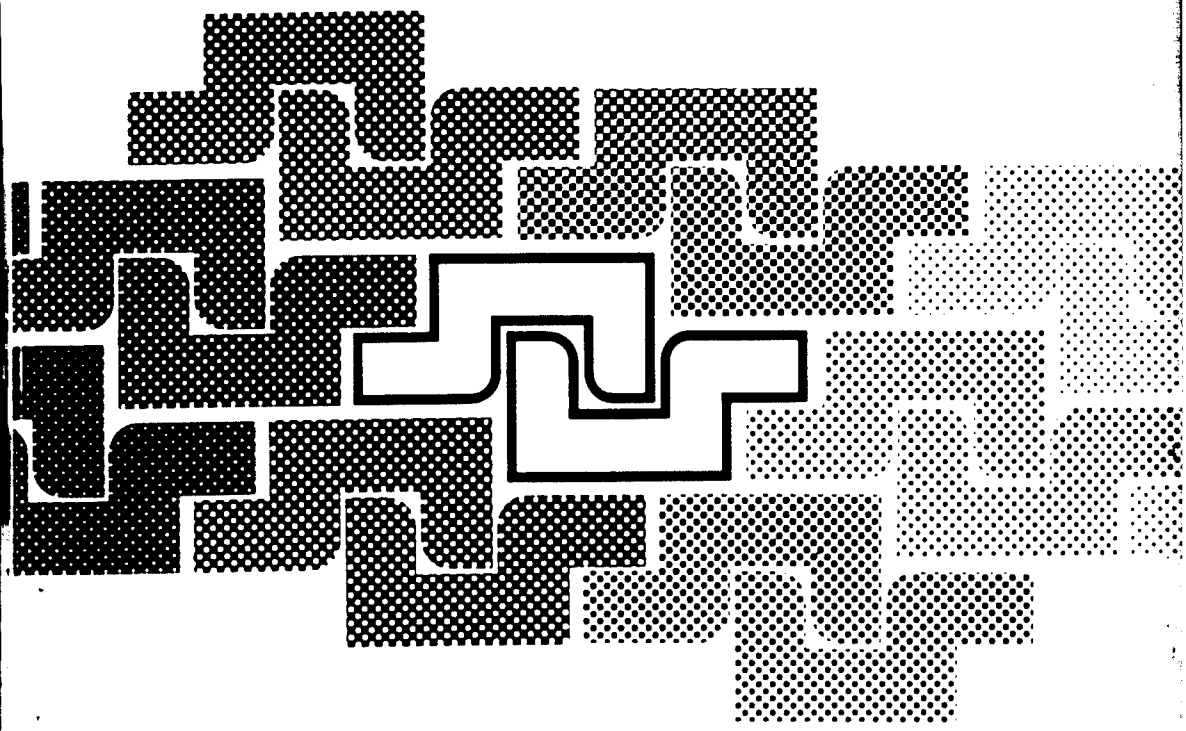


DISTRIBUTION STATEMENT A
Approved for public release
Distribution Unlimited

High Power Lasers – Science and Engineering

Edited by

Ram Kossowsky, Miroslav Jelinek
and Robert F. Walter

NATO ASI Series

High Power Lasers – Science and Engineering

NATO ASI Series

Advanced Science Institutes Series

A Series presenting the results of activities sponsored by the NATO Science Committee, which aims at the dissemination of advanced scientific and technological knowledge, with a view to strengthening links between scientific communities.

The Series is published by an international board of publishers in conjunction with the NATO Scientific Affairs Division

A Life Sciences	Plenum Publishing Corporation
B Physics	London and New York
C Mathematical and Physical Sciences	Kluwer Academic Publishers
D Behavioural and Social Sciences	Dordrecht, Boston and London
E Applied Sciences	
F Computer and Systems Sciences	Springer-Verlag
G Ecological Sciences	Berlin, Heidelberg, New York, London,
H Cell Biology	Paris and Tokyo
I Global Environmental Change	

PARTNERSHIP SUB-SERIES

1. Disarmament Technologies	Kluwer Academic Publishers
2. Environment	Springer-Verlag / Kluwer Academic Publishers
3. High Technology	Kluwer Academic Publishers
4. Science and Technology Policy	Kluwer Academic Publishers
5. Computer Networking	Kluwer Academic Publishers

The Partnership Sub-Series incorporates activities undertaken in collaboration with NATO's Cooperation Partners, the countries of the CIS and Central and Eastern Europe, in Priority Areas of concern to those countries.

NATO-PCO-DATA BASE

The electronic index to the NATO ASI Series provides full bibliographical references (with keywords and/or abstracts) to more than 50000 contributions from international scientists published in all sections of the NATO ASI Series.
Access to the NATO-PCO-DATA BASE is possible in two ways:

- via online FILE 128 (NATO-PCO-DATA BASE) hosted by ESRIN,
Via Galileo Galilei, I-00044 Frascati, Italy.

- via CD-ROM "NATO-PCO-DATA BASE" with user-friendly retrieval software in English, French and German (© WTV GmbH and DATAWARE Technologies Inc. 1989).

The CD-ROM can be ordered through any member of the Board of Publishers or through NATO-PCO, Overijse, Belgium.



Series 3: High Technology – Vol. 7

High Power Lasers – Science and Engineering

edited by

Ram Kossowsky
Emerging Technologies, Inc.,
Pittsburgh, Pennsylvania, U.S.A.

Miroslav Jelinek
Physics Institute,
Czech Academy of Science,
Prague, Czech Republic

and

Robert F. Walter
W.J. Schafer Associates, Inc.,
Alburquerque, New Mexico, U.S.A.

DISTRIBUTION STATEMENT A
Approved for public release
Distribution Unlimited

19960520 103



Kluwer Academic Publishers

Dordrecht / Boston / London

Published in cooperation with NATO Scientific Affairs Division

Proceedings of the NATO Advanced Study Institute on
High Power Lasers – Science and Engineering
Karlovy Vary, Czech Republic
July 16–29, 1995

A C.I.P. Catalogue record for this book is available from the Library of Congress

ISBN 0-7923-3959-2

Published by Kluwer Academic Publishers,
P.O. Box 17, 3300 AA Dordrecht, The Netherlands.

Kluwer Academic Publishers incorporates the publishing programmes of
D. Reidel, Martinus Nijhoff, Dr W. Junk and MTP Press.

Sold and distributed in the U.S.A. and Canada
by Kluwer Academic Publishers,
101 Philip Drive, Norwell, MA 02061, U.S.A.

In all other countries, sold and distributed
by Kluwer Academic Publishers Group,
P.O. Box 322, 3300 AH Dordrecht, The Netherlands.

Printed on acid-free paper

All Rights Reserved
© 1996 Kluwer Academic Publishers
No part of the material protected by this copyright notice may be reproduced or utilized in any form or by any means, electronic or mechanical, including photocopying, recording or by any information storage and retrieval system, without written permission from the copyright owner.

Printed in the Netherlands

LIST OF SPONSORS

North Atlantic Treaty Organization
Scientific Affairs Division

National Science Foundation, Washington, USA
European Research Office, US Army, London, UK
The Office of the Mayor of Karlovy Vary, CR.
Institute of Physics, Prague, CR.
Czech Technical University, Prague, CR.
Preciosa Crytur, Ltd., Yurnov, CR.

TABLE OF CONTENTS

LIST OF SPONSORS v

PREFACE xi

PART I: DESIGN ASPECTS 1

W. J. Witteman*
Characteristics of High Power (CO_2) Lasers 3

Ian Spalding*
Electric-Discharge Pumping 27

V. L. Moshkov*
Spatial and Temporal Scales of Active Medium Inhomogeneities in High Power Gas Lasers 47

Yu. S. Protasov
Gas Lasers with Plasmodynamic Pumping 83

V. V. Naumov, V. A. Kochelap and I. A. Izmailov
Study of Gain Media for High Power Gas Flow Lasers 95

N. D. Cherepenin, Sh. Kh. Zaripov and Yu. Ya. Usanov
On Unstable Resonators Producing Compact Output Beam 113

L. A. Kotomtseva, A. M. Samson and S. I. Turovets
Dynamics of Lasers with Passive and Active Modulation of Losses 125

P. Persephonis, A. Ioannou, J. Parthenios, C. Georgiades and V. Giannetas
The Time Evolution of the Electric Characteristics of a Laser Discharge Through Their Waveforms of the Voltage and the Current 139

G. P. Hogan*
Metal Vapour Lasers 153

T. R. Nelson, F. G. Omenetto, W. Andreas Schroeder, J. W. Longworth and C. K. Rhodes
Design and Analysis of a Deep UV Laser Based on Ce^{3+} : $LiSrAlF_6$ 177

(* Invited Lecturer)

K. A. Grozdanov and P. A. Atanasov
Simultaneous Emission in UV and IR Region in a Sliding Discharge Excited Laser 185

S. Bollanti, P. Di Lazzaro, F. Flora, G. Giordano, T. Letardi, D. Murra, C. Petrucci, G. Schina, O. Uteza and C. E. Zheng
Experimental and Theoretical Results of High Optical Quality Excimer Laser Beams 191

R. Rus, P. B. Holden, T. Mocek, M. Kalal, P. Zeitoun, A. Demir, B. Kralikova, S. Sebban, J. Skala and G. J. Tallents
A High Efficiency Soft X-Ray Laser in the 25-30 nm Spectral Region 199

H. Baumhacker*, G. Brederlow, K. Eidmann, E. Fill, A. Grabtchikov, Th. Löwer, G. Winhart and K. J. Witte
The Asterix IV Iodine Laser: Performance and Applications 217

PART II: OPTICS 239

H. J. Eichler*, A. Haase and O. Mehl
High Power Solid State Lasers with Phase Conjugation for Applications with High Beam Quality 241

S. G. Anikitchev*
Laser Resonator Concepts 255

N. Pavel, T. Dascalu, V. Lupei and H. Totia
Variable Reflectivity Mirror Unstable Resonator Thermal Lens Compensated by a Deformable Rear Mirror 283

N. Pavel, T. Dascalu, V. Lupei and M. Poterasu
Two-Rod VRM-Unstable Resonator with Deformable Mirror Thermal Compensation 293

R. Taylor*
Beam Transport Optics for High-Power Laser Systems 303

V. F. Tarasenko, M. I. Lomaev, A. N. Panchenko, V. S. Skakun and E. A. Sosnin
High-Power UV Excilamps 331

K. P. Komarov, A. S. Kuch'yanov and V. D. Ugozhayev
Reproducible Ultrashort Pulses and Multistable Monochromatic Emission from Solid-State Lasers with Saturable Absorber and Negative Feedback Loop 347

S.-A. Amarande
An Extended Characterization of Flattened Gaussian Beams 365

L. Pina, A. Inneman and R. Hudec
Optics for X-Ray Laser and Laser Plasma Soft X-Ray Radiation 373

M. Enescu, S. Amarande, I. Farcas and C. Vasilescu
Computer Simulation of the Laser Beam Intensity Distribution in Resonant Cavities 381

PART III: MEASUREMENTS 389

B. Forestier*
Laser Medium Quality Control 391

A. P. Kubyshkin
Laser Thermal-Wave Diagnostics of Stressed States in Metals 413

A. S. Kozlova
Experimental Studies of Reflection Ability of Liquid Metal Targets in Vacuum Under Conditions of Neodymium Laser Pulse Radiation 423

V. N. Shekhtman, A. Yu. Rodionov and A. G. Pel'menev
Reconstruction of a Light Beam Wave Front by Synthesis of a Shear Interferogram 433

G. Rabczuk, P. Kukiełło and G. Śliwiński
Experimental Investigations of the Output Beam Properties from a High Power CW CO_2 Laser 449

T. Bulat, S. Akyüz, T. Akyüz and J. E. Davies
The Applications of a Near-IR Laser to Raman Spectroscopy: FT-Raman Spectroscopic Studies of Adsorbed Species by Clays 455

PART IV: APPLICATIONS 461

D. M. Roessler*
High-Power Lasers in Materials Processing - an Automotive Perspective 463

B. Ivanov, C. Popov, V. Shanov and D. Filipov
LCVD with Copper Vapour and Copper Bromide Vapour Lasers - Review 505

J. Bulíř, M. Jelínek and V. Peřina
Laser Deposition and Characterization of A-C and A-C:N Films 527

Ya. V. Fattakhov, R. M. Bayazitov, I. B. Khaibullin and T. N. L'vova
Anisotropic Melting of Semiconductor at Irradiation by Powerful Light Pulses 533

C. Grivas, P. Papadopoulos and A. Klini
Excimer Laser Assisted Deposition and Characterization of Molybdenum Films - Fabrication of Molybdenum Coatings on Optical Fibres 549

M. I. Markevich and F. A. Piskunov
Pulsed Laser-Induced Synthesis of Metal Sulphides in Sulphurous Liquids Under Action of Shock Waves 561

J. Lančok, M. Jelínek, V. Trtík and L. Jastrabík
Laser Patterning of Thin Films 567

H. Jelínková, K. Hamal, V. Kubeček, J. Pašta, T. Dostálová, J. Kubelka and S. Procházka
Applications of Nd and Er:YAG Lasers in Ophthalmology and Dentistry 575

LATE SUBMISSIONS 583

A. M. Prokhorov* and A. A. Manenkov*
History, Current Status and Outlook for the Future of High Power Solid State Lasers 585

V. V. Dembovetsky and TU. N. Zavalov
Industrial Fast - Axial Flow Carbon Dioxide Lasers 603

B. Lacour*
Fundamentals and Current Status of Excimer Lasers 619

INDEX 661

LIST OF PARTICIPANTS 665

PREFACE

The year 1994 marked the thirtieth anniversary of the invention of the carbon dioxide laser. This development opened the door for the scaling of industrial lasers to the multi-kilowatt range, and military laser devices to considerably higher power levels. As a result of major investments in high-power gas laser technology in a number of countries, the principles of operation of these devices are well understood, and several distinct design approaches have evolved for achieving high power levels. The major issue for the designers of such devices has shifted from how to get to the desired power level to how to achieve reliable operation. At the same time, the opening of many laser development facilities in the former Soviet Union has enabled their achievements and design approaches to be understood and appreciated for the first time. Meanwhile, the community of users of industrial lasers has identified a number of emerging applications at higher power levels (15-20 kW) than are attainable by most commercial devices.

These trends suggest that this is an ideal time to convene an Advanced Study Institute at which the designers, developers, and users of high-power gas laser systems can meet to discuss design approaches, methods of enhancing performance, new applications, and user requirements in a setting which allows greater opportunities for interaction than the standard conference venue. Such a workshop would benefit the participants by allowing them to gain a better understanding of the current status of this technology and the directions in which it is likely to evolve. Because industrial lasers are perceived to be an important element of advanced manufacturing technology in many of the NATO countries (as indicated by the existence of several jointly sponsored laser development programs under the Eureka umbrella), the home countries of the participants will likewise gain from this exchange of knowledge. The program has been planned to provide insight into all of the perceived issues of industrial laser system performance as well as surveying the current state, of the art and the emerging applications. This enabled a unique interaction between the device development and users communities, which traditionally have their own specialist conferences.

By building a bridge between the device development and users communities, as well as between scientists from the NATO countries and the Cooperation Partners countries, specifically Russia, we hope that the Advanced Study Institute will lead to a better utilization of high power lasers in the manufacturing sector, and to a more efficient functioning of the economies which employ this technology.

The format used for the ASI is that proven to be successful in other NATO-ASIs; namely, the major portion of the time was devoted to tutorial lectures by eminent scientists, allowing sufficient time for them to develop a comprehensive treatment of their subject. The discussion period scheduled at the end of each lecture was an important part of the program. Submitted papers were assigned to poster sessions. We reserved the option to elect a few, outstanding papers for oral presentations where the paper significantly supplemented, or complemented a lecture. A balance among theory, experimental studies and engineering experiences was maintained. We have also included special panel discussions which were designed to explore and summarize major questions following a few sessions of structured lectures.

We thank all the contributors and participants for their effort. Thanks are also due to the personnel of the Scientific Affairs Division of NATO. Our daily routines were greatly facilitated by the group of Graduate Students from the Institute of Physics - Jiri Bulir, Bedrich Rus and Vitezclav Trtik, and by the attentive staff of the Grandhotel Pupp. Thanks are due to Prof. Miroslava Vrbova who undertook to expedite the reviews process, to Prof. Helena Jelinkova who spent a lot of time in her car ferrying people between Prague and Karlovy Vary, and to Dr. Hanita Kossowsky for lending a hand at registration.

Dr. Ram Kossowsky
Prof. Miroslav Jelinek
Dr. Robert Walter

November 1995

PART I: Design Aspects

CHARACTERISTICS OF HIGH POWER (CO_2) LASERS

W.J. WITTEMAN
University of Twente
Department of Applied Physics
P.O. Box 217
7500 AE Enschede
The Netherlands

1. CO_2 lasers

The CO_2 laser like any other gas laser consumes electrical power and delivers less power in its radiation at about 10 μm wavelength. The difference between input and output power is waste heat that must be consumed. To increase the output power one must increase the input power, but technical and physical constraints limit the amount of input energy. In fact, the choice of heat sink characterizes the type of laser, examples being continuous sealed-off systems, fast-flow high-power systems, and pulsed systems.

The CO_2 laser operates by exchanging energy between low-lying vibrational-rotational energy levels of the CO_2 molecule. Molecules in the higher energy state are transferred by the radiation field into a vibrational energy mode with a lower-energy state. The difference of energy of these upper and lower states is converted into infrared radiation. The upper level is excited by an electrical discharge either from the ground state or from a resonance transfer by vibrationally excited nitrogen. In both cases the input energy is at least the energy of the upper state. The maximum efficiency that is achievable is then 38%, as can be directly inferred from an energy level diagram. However, this efficiency is the theoretical limit and no actual CO_2 laser will ever achieve this quantum efficiency. Well-designed systems reach at most 20% of the electrical input energy.

The lasing process of all CO_2 lasers is sensitive to the temperature of the gas molecules in the discharge, i.e. active medium, which imposes another limit. As more power goes into the gas, its temperature rises and with this the thermal population of the lower laser level. Consequently, more radiation will be lost by the absorption of the lower-level density. In practice, therefore, one observes for increasing input energy, at first an increasing output but at a certain stage the output levels off and begins to decrease when the gas temperature rises above about 150^0C.

Knowing these principal limitations one may estimate the output capability of a system. It depends entirely on the method by which the attendant waste heat is removed from the system. There are three basic routes to dispose of this waste energy. The simplest one is to make use of the thermal conductivity of the gas. The waste heat will be conducted to the cooled walls of the vessel containing the

R. Kossowsky et al. (eds.), High Power Lasers – Science and Engineering, 3–25.
© 1996 *Kluwer Academic Publishers. Printed in the Netherlands.*

discharge. This method of diffusion cooling is always found in continuous systems with output powers in the order of 100 W or less and in compact waveguides with slab structures even up to 1 kW. A second method to get rid of the waste heat is the removal of the hot gas itself. This is the case for the so-called fast-flow systems which operate in the range of many kilowatts of output power. The third method takes advantage of the heat capacity of the active medium. This is the case for pulsed systems. The maximum input energy, again limited by the gas temperature, is for pulsed systems roughly 300 J per liter laser gas at atmospheric pressure. The output power is then about 40 J per liter active medium at one atmosphere. Both input and output energies are more or less proportional to the gas density. In the following we shall analyse the theoretical background for energy extractions from high power continuous and pulsed laser systems with emphasis on CO_2-systems.

2. Amplification of radiation

Amplification is obtained in a medium with inversion i.e. the amplification is the interaction between two levels of which the higher energy level E_m has a higher density N_m than lower energy level E_n with density N_n. If ρ denotes the photon number density one finds for the gain:

$$\frac{d\rho}{\rho dx} = \frac{A_{mn}\lambda^2}{8\pi}\left(N_m - \frac{g_m}{g_n}N_n\right)g(\nu) \tag{1}$$

Where: A_{mn} is the transition rate for spontaneous emission between the two levels; g_m and g_n are the degeneracy factors of the two levels; $g(\nu)$ is the line shape function of the transition.

Substituting for the inversion

$$\Delta N = N_m - \frac{g_m}{g_n}N_n \tag{2}$$

and for the cross section of stimulated emission

$$\sigma_s = \frac{\lambda^2}{8\pi}A_{mn}\,g(\nu) \tag{3}$$

we get for the small signal gain:

$$\frac{d\rho}{\rho dx} = \Delta N\sigma_s \tag{4}$$

For the densities of the energy states E_m and E_n we find if we are dealing with homogeneous line broadening:

$$\frac{dN_m}{dt} = P(t) - c\rho\Delta N\sigma_s - \frac{N_m}{\tau_m} \tag{5}$$

$$\frac{dN_n}{dt} = \frac{N_m}{\tau_r} + c\rho\Delta N\sigma_s - \frac{N_n}{\tau_n} \tag{6}$$

Where: τ_m and τ_n are the effective life times of the E_m and E_n states respectively. It includes the probabilities of spontaneous emission and quenching;
$1/\tau_r$ is the spontaneous emission rate from E_m to E_n;
$P(t)$ is the production rate of the upper level.

Under steady state conditions the inversion becomes:

$$\Delta N = \frac{P\tau_m\left(1 - \frac{g_m}{g_n}\frac{\tau_n}{\tau_r}\right)}{1 + \frac{c\rho h\nu}{I_s}} = \frac{\Delta N_{ss}}{1 + \frac{c\rho h\nu}{I_s}} \tag{7}$$

where

$$I_s = \frac{h\nu}{\sigma_s\tau_m\left\{1 + \frac{g_m}{g_n}\frac{\tau_n}{\tau_m}\left(1 - \frac{\tau_m}{\tau_r}\right)\right\}} \tag{8}$$

I_s is called the saturation irradiance. In the case of zero lower level lifetime ($\tau_n=0$)

$$I_s = \frac{h\nu}{\sigma_s\tau_m} \tag{9}$$

ΔN_{ss} is the steady state inversion density in the absence of an optical fluence. The quantity $c\rho h\nu$ is the irradiance I travelling in the medium. We obtain from eq. (4) for the signal gain.

$$\alpha = \frac{\alpha_0}{1 + I/I_s} = \Delta N\sigma_s \tag{10}$$

Where α_0 is the so-called small signal gain ($I<<I_s$) equal to $\Delta N_{ss}\sigma_s$

Note that the gain saturates with increasing I and that the power extraction per unit volume as derived from eq. (10) is given by:

$$\frac{dI}{dZ} = \frac{\alpha_0 I}{1 + I/I_s} \tag{11}$$

Which has the optimum value of $\alpha_0 I_s$. This means that the maximum power extraction P_{max} from an oscillator or amplifier is given by

$$P_{max} = \alpha_0 I_s V \tag{12}$$

Where V is the volume of the active medium.

3. Homogeneous line broadening

High power systems with efficient radiation production are characterized by homogeneous line broadening. The essential feature is that every atom or molecule has the same atomic line shape and frequency response so that a signal applied to a transition has exactly the same effect on all atoms in the collection.
An important consequence is that all excited particles contribute equally and that the transition will saturate uniformly. In the case of inhomogeneous broadening the center frequencies of individual particles are displaced so that the particles have different resonance frequencies on the same transition, for example owing to doppler shifts in low pressure gases (below 100 torr). An applied radiation field does not have the same effect on all particles and the gain is contributed by those particles whose resonance frequencies lie close to the radiation frequency. As a result the efficiency of an inhomogeneous medium is in general much smaller than that for homogeneous broadening.

Homogeneous broadening by collisions is caused by the fact that the radiative process is interrupted in a random manner by collisions. After a collision the radiating particle is restarted without the memory of the phase of the radiation prior to the collision. The collisions cause in fact many truncated radiative processes. Since the spectral width of a wave train is inversely proportional to the length of the train it follows that the line width increases. At high gas pressure the pressure broadening mechanism dominates the Doppler broadening.

The line shape of homogeneous broadening mechanisms leads to a Lorentzian line shape given by:

$$g(\nu) = \frac{\Delta\nu / 2\pi}{(\nu - \nu_0)^2 + (\Delta\nu / 2)^2} \tag{13}$$

Where ν_0 is the center frequency and $\Delta\nu$ the half width. The function is normalized to unity or:

$$\int_0^\infty g(\nu) d\nu = 1$$

4. Optimization of the laser in the case of non-saturable absorption of the medium

Constructing high power laser systems that have volumetric radiation losses, for example absorbing species or light scattering by inhomogeneties of the media, it is important to minimize those inherent losses. In the case those losses are propotional to the radiation intensity an analytic solution is obtained[1].

Consider a cavity having one total reflecting mirror and one outcoupling mirror. The laser oscillator contains two running waves: one to the right and one to the left with intensities I_+ and I_- respectively. Because the medium is subjected to both waves the saturation term contains the total intensity. So we can write for the I_+ wave according to eq. (11):

$$\frac{dI_+}{I_+ dZ} = \frac{\alpha_0}{1 + \frac{I_+ + I_-}{I_s}} - \gamma_0 \tag{14}$$

Where the absorption or loss coefficient γ_0 is considered constant. Similarly the I_- wave gives:

$$-\frac{dI_-}{I_- dZ} = \frac{\alpha_0}{1 + \frac{I_+ + I_-}{I_s}} - \gamma_0 \tag{15}$$

The minus sign in eq. (15) comes from the left running wave to decreasing Z.

Substituting $\frac{I_+}{I_s} = \beta_+$ and $\frac{I_-}{I_s} = \beta_-$ we have:

$$\frac{1}{\beta_+}\frac{d\beta_+}{dZ} = -\frac{1}{\beta_-}\frac{d\beta_-}{dZ} = \frac{\alpha_0}{1 + \beta_+ + \beta_-} - \gamma_0 \tag{16}$$

So that $\beta_+\beta_- = \beta_0^2 =$ constant (17)

Eliminating β_- in eq. (16) by means of eq. (17) we obtain the solution

$$\gamma_0 Z + \ln\beta_+ + \frac{\alpha_0}{\sqrt{(\alpha_0-\gamma_0)^2-(2\gamma_0\beta_0)^2}} \ln F(\beta_+) = constant \tag{18}$$

where

$$F(\beta_+) = \frac{\sqrt{(\alpha_0-\gamma_0)^2-(2\gamma_0\beta_0)^2}+(\alpha_0-\gamma_0-2\gamma_0\beta_+)}{\sqrt{(\alpha_0-\gamma_0)^2-(2\gamma_0\beta_0)^2}-(\alpha_0-\gamma_0-2\gamma_0\beta_+)} \tag{19}$$

The mirror with reflection R_1 = 1(total reflector) is at $Z=0$ and with $R_2<1$ (outcoupling) at $Z=L$. See fig. 1.

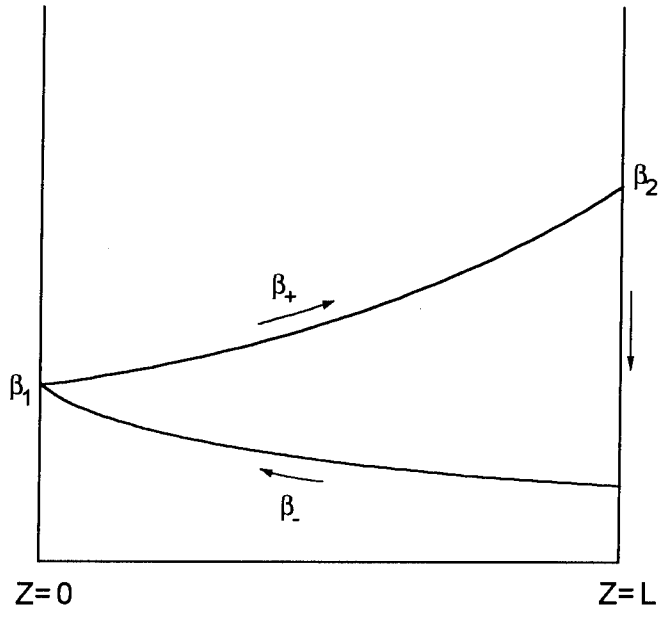


Figure 1. Schematic presentation of the running waves

The power outcoupling is then $T=1-R_2$. We assume negligible mirror losses.
The problem to be solved is to calculate R_2. If we substitute in eq. (18) $\beta_+(0) = \beta_1$ and $\beta_+(L) = \beta_2$ we obtain:

$$\gamma_0 L - ln\left(\frac{\beta_1}{\beta_2}\right) = \frac{\alpha_0}{\sqrt{(\alpha_0 - \gamma_0)^2 - (2\gamma_0\beta_0)^2}} ln\left\{\frac{F(\beta_1)}{F(\beta_2)}\right\} \qquad (20)$$

Using eq. (17) we have the following relation between β_1 and β_2

$$\beta_0 = \beta_1 = \beta_2\sqrt{R_2} \qquad (21)$$

With the last expression we eliminate β_1 and β_0 in eq. (20). We then obtain a relation between β_2 and R_2 with α_0, γ_0 and L as laser parameters. The algebra is facilitated by using the parameter λ defined as:

$$\left(\frac{2\gamma_0}{\alpha_0 - \gamma_0}\right)\beta_0 = sin\,2\lambda \qquad (22)$$

so that eq. (19) becomes:

$$F(\beta_i) = \frac{cos\,\lambda(\beta_0 cos\,\lambda - \beta_i sin\,\lambda)}{sin\,\lambda(\beta_i cos\,\lambda - \beta_0 sin\,\lambda)}, \qquad i = 1,2 \qquad (23)$$

With eq. (21) we have:

$$F(\beta_1) = cotan\,\lambda$$

and

$$\frac{F(\beta_1)}{F(\beta_2)} = \frac{1 - \sqrt{R_2}\,tan\,\lambda}{\sqrt{R_2} - tan\,\lambda}$$

Eq. (20) now becomes:

$$\gamma_0 L - \ln\sqrt{R_2} = \frac{\alpha_0}{(\alpha_0 - \gamma_0)} \frac{1}{\cos 2\lambda} \ln\left\{\frac{1 - \sqrt{R_2}\tan\lambda}{\sqrt{R_2} - \tan\lambda}\right\} \beta_1 \qquad (24)$$

The out coupled power per unit area is $(1-R_2)\ I_+(L)$ whereas the maximum available power is $\alpha_0 I_s L$. The efficiency η is therefore defined as the fraction of the maximum available power or:

$$\eta = \beta_2 \frac{1 - R_2}{\alpha_0 L}$$

Using eqs. (21) and (22) we obtain:

$$\eta = \left(\frac{\alpha_0 - \gamma_0}{2\gamma_0 \alpha_0 L}\right) \frac{1 - R_2}{\sqrt{R_2}} \sin 2\lambda \qquad (25)$$

From eqs. (22), (24) and (25) the maximum efficiency η_{max} can be determined by finding the corresponding optimum R_2 value. The results are plotted below in fig. 2 where $\gamma_0 L = \gamma$ and $\alpha_0 L = \alpha$.

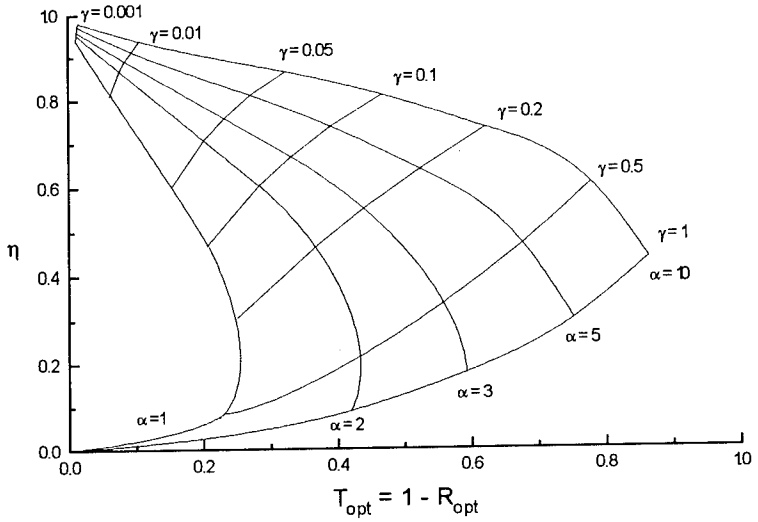


Figure 2. The maximum outcoupling efficiency

5. Pulse amplification

To obtain very high power we amplify a short pulse through an amplifier in such a way that the total inversion energy is converted into stimulated emission in a short period i.e. the pulse duration. The shorter the pulse the higher the power that can be obtained. The pumping of the active medium gives a maximum value of $N_m = P\tau_m$ so that large inversion is obtained for systems with relatively large τ_m values (Nd:YAG and CO_2 lasers). Those systems with large τ_m are therefore called storage lasers. Usually the pulse duration is much shorter than τ_m so that during the amplification we can neglect the pumping of the upper level. The dynamics of the inversion and radiation are then according to eqs. (5), (6) and (10) given by:

$$\frac{dN_m}{dt} = -c\rho\Delta N\sigma_s \tag{26}$$

$$\frac{dN_n}{dt} = c\rho\Delta N\sigma_s \tag{27}$$

$$\frac{dI}{dz} = \sigma_s I\Delta N \tag{28}$$

From (28) we obtain after integration over the length L of the amplifier

$$I_{out}^{(t)} = I_{in}^{(t)} exp(\sigma_s \Delta N_{tot}) \tag{29}$$

where $\Delta N_{tot}^{(t)} = \int_0^L \Delta N(t)dz$ is the total inversion of the amplifier.

Combining eqs. (26) and (27) we obtain:

$$\frac{d}{dt}\Delta N(t) = -c\sigma_s\rho\Delta N(t)\left(1 + \frac{g_m}{g_n}\right) = \frac{-\Delta NI(t)}{E_s^1} \tag{30}$$

where

$$E_s^1 = \frac{E_s}{1 + g_m / g_n} \quad with \quad E_s = \frac{h\nu}{\sigma_s} \tag{31}$$

The amplification $G(t)$ is defined as:

$$G(t) = \frac{I_{out}(t)}{I_{in}(t)} = exp(\sigma_s \Delta N_{tot}(t)) \tag{32}$$

Substituting eq. (28) into eq. (30) and integrating over the length L we obtain:

$$-\frac{d}{dt}\Delta N_{tot} = \frac{I_{out}(t) - I_{in}(t)}{h\nu}(1 + g_m / g_n) \tag{33}$$

The last equation expresses the energy conservation of field and inversion. The pulse energy per unit area, called fluence, is given by:

$$E_j(t) = \int_0^t I_j(t)dt \tag{34}$$

where j refers to either the input or output fluence.
Substituting eq. (32) into eq. (34) we obtain after integration:

$$G(t) = \frac{G_0}{G_0 - (G_0 - 1)exp\{-E_{in}(t) / E_s^I\}} \tag{35}$$

where G_0 is the initial amplification at the maximum inversion of the medium.

It is seen that the gain is practical constant and equal to G_0 as long as $E_{in}(t) << E_s^I$. As soon as the input energy for high gain is reaching a fraction of the saturation energy E_s^I, the gain decreases drastically and the initial pulse shape will be distorted.

As an example we plotted in fig. 3 the gain after the passage of an input beam with an energy E_{in} per unit area. The medium has a stored energy with an initial gain G_0=20, 10 and 5 and the saturation fluence E_s^I. The time behaviour of the gain for an arbitrary input beam is simply obtained from fig. 3 by substituting for E_{in} the time dependent expression (34).

It often happens that one is not primarily interested in the pulse shape but in the

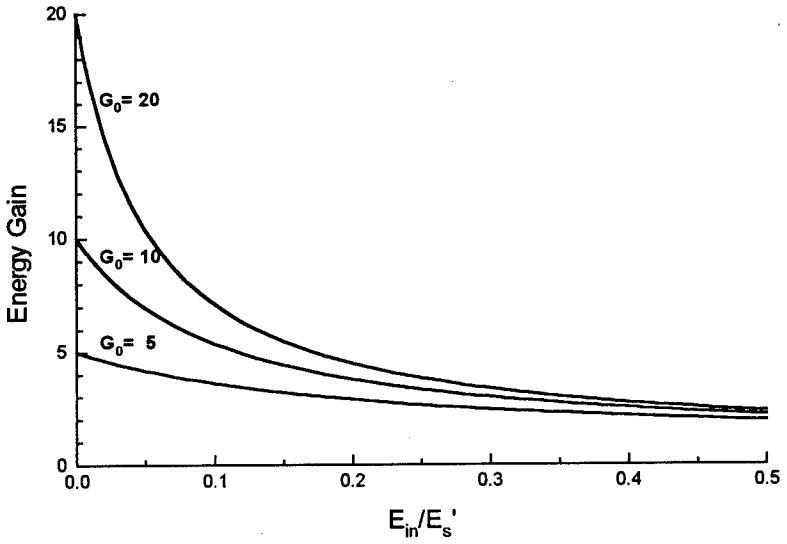


Figure 3. Residual gain after the amplified input energy

total amount of energy that is gained. This can be obtained by integrating eq. (35) over the entire pulse. We obtain then for the total gain $G = E_{out}/E_{in}$.

$$G = \frac{E_s^1}{E_{in}} ln\left[1 + G_0\left\{exp\, E_{in} / E_s^1 - 1\right\}\right] \tag{36}$$

It is seen that for $E_{in} << E_s{}^1$ the gain $G = G_0$. G is plotted in fig. 4 as a function of $E_{in}/E_s{}^1$ for several values of G_0. Saturation occurs roughly in the region for which $E_{in}/E_s{}^1 = 1/G_0$. The gain G decreases with increasing E_{in} and reaches the minimum value of 1. For large values of $E_{in}/E_s{}^1$ it is given by:

$$G_{min} = 1 + \frac{E_s^1}{E_{in}} ln\, G_0 \tag{37}$$

Subtracting the input energy from the amplified power equal to $G_{min} \cdot E_{in}$ we obtain the maximum energy fluence that can be delivered by the amplifier

$$E_{ampl} = E_s^1 \ln G_0 \tag{38}$$

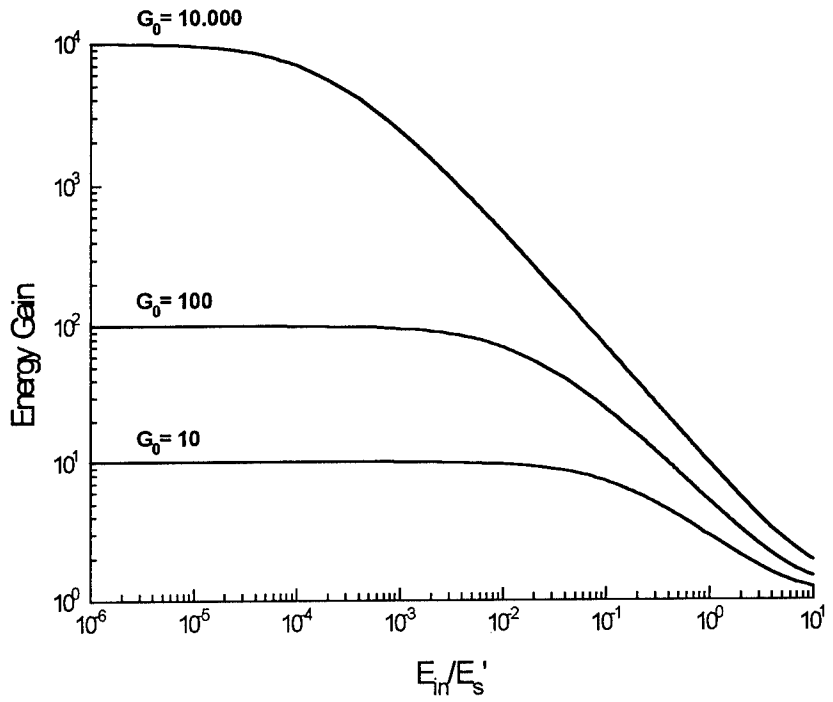


Figure 4. Total gain for the amplified input energy

6. Vibrational Excitation of the Upper CO_2 Laser Level

Laser action in CO_2 occurs on low lying vibrational levels. Several successful laser transitions are indicated in fig. 5. The most powerful is the $(00^01)\rightarrow(10^00)$ transition. Practically all efficient CO_2-laser systems use N_2 as an additional channel for energy transfer to the ν_3 vibration of CO_2. It has been observed that an electric discharge in nitrogen leads to a very effective formation of vibrationally excited N_2 molecules up to 50% of all N_2 molecules. Since the N_2 molecule has two identical nuclei, its dipole radiation is forbidden. It can only decay by collisions with the wall of the containing vessel or by collisions with other molecules. In the presence of CO_2 the vibrational energy of N_2 can be easily transfered to CO_2 because of the close resonance between the N_2 vibrations and the ν_3 vibration of CO_2. The (00^01) level of CO_2 is only $\Delta E = 18\ cm^{-1}$ higher than the vibrational level $\nu = 1$ of nitrogen.

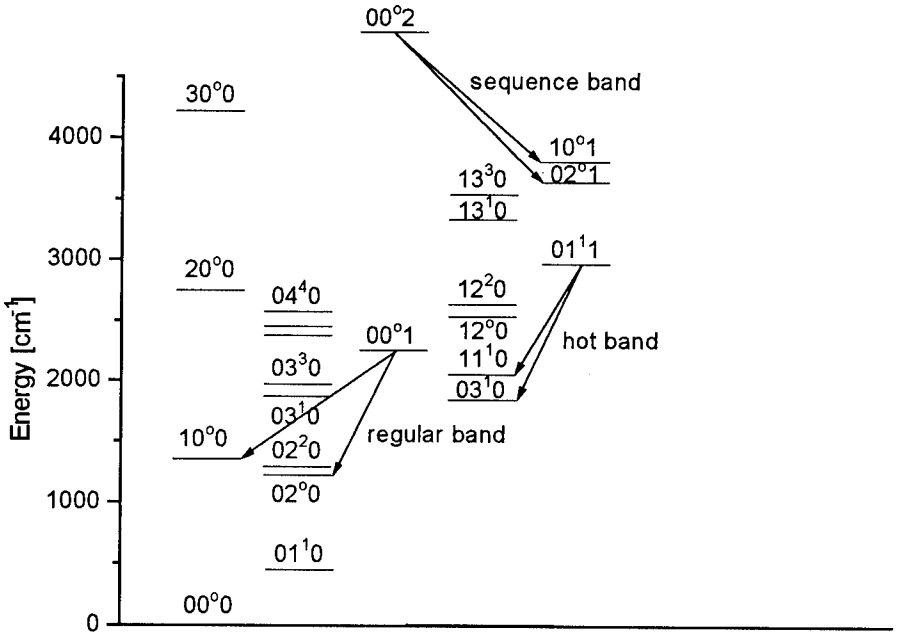


Figure 5. Some of the low-lying vibrational levels of CO_2

This energy difference is much smaller than the average kinetic energy so that during collisions the CO_2 molecules can easily draw the vibrational energy of N_2 to excite the ν_3 vibration. It should be emphasized that the efficient transfer is not limited to the first excited states of N_2 but also up to values of $\nu = 4$ in N_2 because even at this level the anharmonicity of the N_2 molecule still does not lead to quantum values differing from that of the (00^01) level by more than the average kinetic energy.

Accompanying to the energy resonance between CO_2 and N_2 there is a similar effect between CO and CO_2. During the discharge an appreciable number of CO molecules can be produced. This is especially the case in laser gas mixtures without H_2O or H_2. In these dry mixtures the dissociation of CO_2 can be as high as 50%. (The dissociation energy of CO_2 is only 2.8 eV). These CO molecules can transfer a considerable amount of energy to the ν_3 vibration, firstly because the cross section for vibrational excitation of CO is rather large, and secondly because the difference between the energies of the vibrational level of CO and the (00^01) level of CO_2 is 170 cm^{-1} which is smaller than the average kinetic energy kT. However, CO is not as effective as N_2 in exciting the ν_3 vibration of CO_2. This is understandable since the excess energy coming from the translation is for CO larger than for N_2 and furthermore since the CO molecule unlike N_2 has a dipole moment it has also spontaneous decay.

The gas mixture contains also He which has a favourable effect on the discharge and on the heat conductivity. It contributes to a considerable increase of heat transfer so that the system saturates at a higher discharge currents i.e. a higher specific output power. The gas mixture contains also a low concentration of Xe which has a favourable effect on the electron energy distribution in such a way that the excitation of N_2 and CO_2 (00^01) is more efficient. The addition of water vapour or hydrogen decreases the concentration of CO in the discharge.

7. RF-excited CO_2 waveguide systems

An effective way to increase the specific output power of a continuous CO_2 laser is to apply RF-excitation in a narrow waveguide channel between two parallel metal electrodes [2,3]. With a RF-discharge very homogeneous and stable discharges at higher gas densities are feasible. Small cross sections, for example only 2x2 mm^2 and gas pressures of about 100 torr are used. Specific output powers of more than one Watt per cm are obtained by means of RF discharges. The discharge current is perpendicular to the optical channel and is sustained between two parallel electrodes in oscillating fields of 100 to 200 MHz. A typical construction is shown in fig. 6. For a length of 37 cm output powers above 40W have been obtained [4].

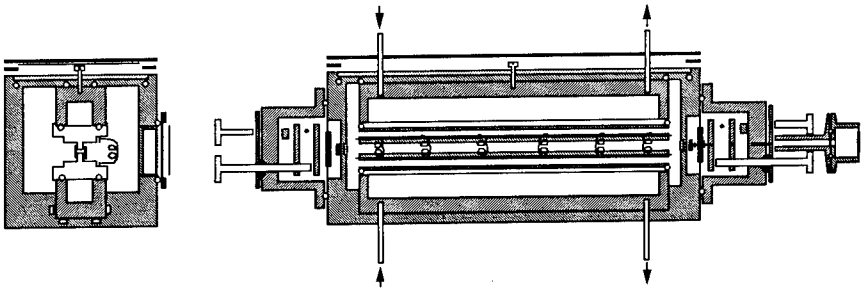


Figure 6. Waveguide laser

Output powers in the order of kW can be obtained in a so-called slab configuration using also RF excitation between parallel electrodes separated at a few millimeters but with a width of several centimeters [5]. The great advantage of these devices is the compact construction with diffusion cooling.

In a waveguide laser the high power density of the RF discharge causes severe decomposition reactions of the laser gas. The main detrimental reaction is the dissociation of CO_2 molecules, which can be as high as 50% of the initial molecules. This undesirable effect can be overcome by incorporating a CO oxidation catalyst which converts the dissociation products back into CO_2. Such a catalyst is gold at a temperature of about 60 to 70° C. The catalytic effect can then

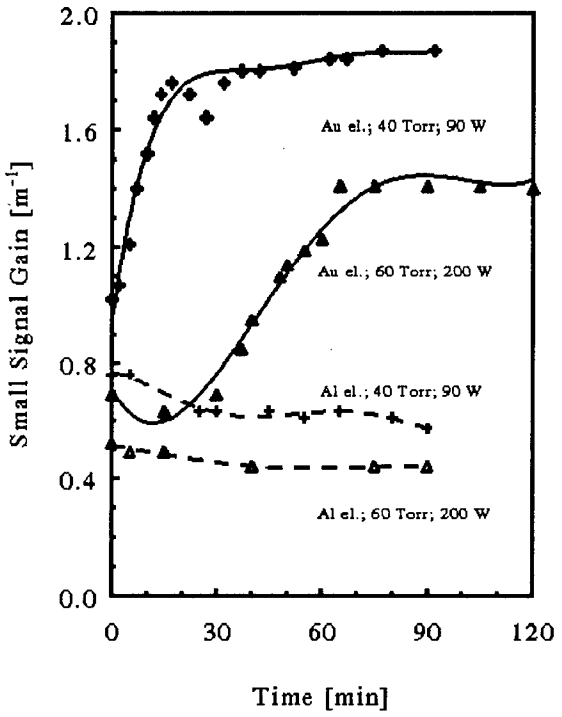


Figure 7. Small signal gain

be performed by using gold-plated electrodes of which one is not cooled [6]. The small signal gain and output enhancements are remarkable. In fig. 7 we compare the small signed gain measurements of a waveguide structure of 2.5 x 2.5 x 370 cm^3 with aluminium to those obtained with gold-plated copper electrodes. The input powers and gas densities are indicated. The gas composition is 1:1:5 + 5% (CO_2:N_2:He + Xe) and the excitation frequency 190 MHz. In fig. 8 we plotted the output powers for the same system for the used aluminium and gold-plated copper electrodes.

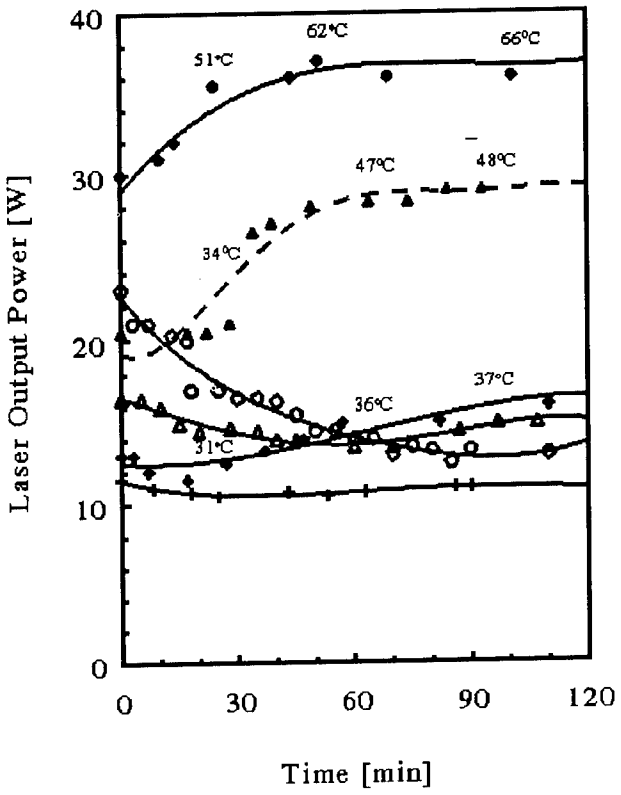


Figure 8. Laser output power as a function of time for the Au and Al electrode (el.) materials using 1:1:5+5% (CO_2:N_2:He+Xe) gas mixture composition at different gas pressures and RF input powers: (✚), Au el., 40 Torr, 120 W; (▲), Au el., 60 Torr, 200W; (●), Au el., 100 Torr, 300 W; (+), Al el., 40 Torr, 120 W; (Δ), Al el., 60 Torr, 200 W; (○), Al el., 100 Torr, 300 W. The temperature of the gold plated non-cooled top electrode is also indicated at about 30, 60 and 90 min.

8. High pressure CO_2 lasers

In low pressure CO_2 laser mixtures, even up to 5 bar, the gain spectrum of the rotational-vibrational bands shows clearly the individual rotational-vibrational transistions because of the limited bandwidth. This bandwidth is pressure broadened with about 4 GHz/bar for the usual gas mixtures. For the full overlap of

these transitions one needs about 15 bar. At these high pressures of the laser gas it is possible to obtain continuous tunability and to amplify picosecond pulses.

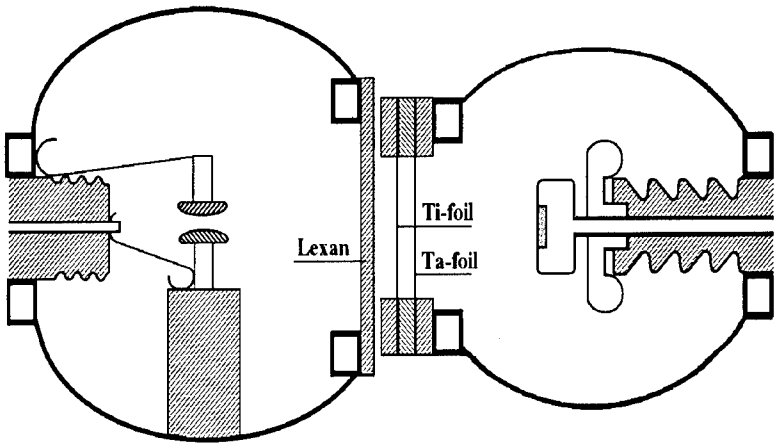


Figure 9. Schematic view of the cross section of an x-ray preionized CO_2 laser

Stable discharges at these high pressures require a proper preionisation to obtain a uniform glow discharge. The main limitation to high pressure operation with e-beam preionisation is imposed by the mechanical stength of the electron entrance window. Because the window has to be trasparent for electrons of about 200 to 300 keV thin titanium foils have to be used. These foils can not withstand the high pressure of the laser chamber. This problem can be circumvented by X-ray preionisation because of the high penetration depth of X-rays. A cross sectional view of an X-ray preionized CO_2 laser is shown schematically in fig. 9. The X-ray source consits of a cold cathode e-beam. The exit window is a 50 μm thick titanium foil which holds the vacuum. A second 10 μm tantalum foil serves as the production foil for the X-rays and as anode for the e-beam. The X-rays enter the laser chamber through a 20 μm thick lexan window. Lexan is sufficient strong to withstand the high pressure and it has very little attenuation for the incoming X-rays. In the present experiment the discharge volume between the two uniforms field electrodes is 0.8 x 0.8 x 30 cm^3. The X-ray producing electrons have an energy of 60 to 90 kV and the capacitance of the e-beam source is 20nF.

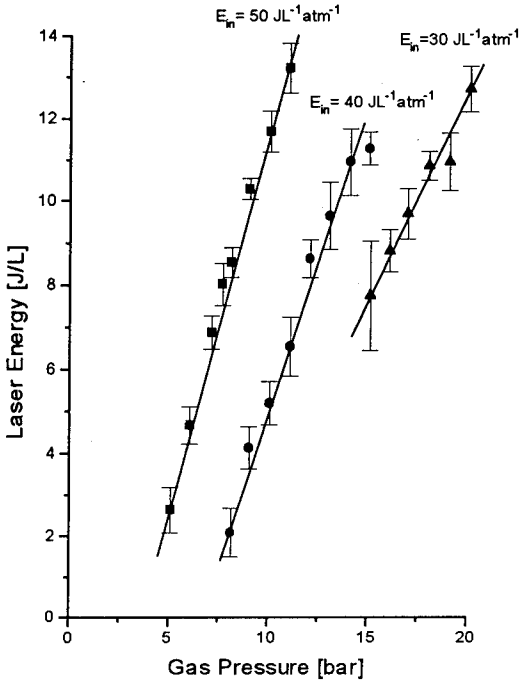


Figure 10. Output characteristics of a 1:1:10 (CO_2:N_2:He) mixture

With this device we obtain stable discharges up to 21 bar in several mixtures. The limitation in pressure is imposed by the mechanical strength of the laser chamber. The output characteristics of a 1:1:10 (CO_2:N_2:He) mixture are shown in fig. 10. It is seen that output efficiencies are in the order of 3%.

9. Picosecond pulse amplification with multi-atmosphere CO_2-lasers

High power laser development is based on the availability of large or powerful active media and the technology of generating very short pulses. Early progress in the development of short pulses was obtained by mode-locking the laser i.e. the phases of oscillating modes are correlated by imposing amplitude or frequency modulation of the laser cavity radiation. In this way high power nanosecond and sub-nanosecond pulses have been produced with multi-atmosphere CO_2-lasers. Because of the limited bandwidth of individual rotational-vibrational transitions and the short duration of the inverted medium the pulse duration could not be further reduced. For that reason the drive to generate shorter and shorter pulses by mode lock technique was much more successfully pursued with solid state lasers, as the solid state lasers have very wide continuous broadening (10^{11}-10^{14} Hz). This resulted in the development of picosecond and femtosecond solid state lasers in the near infrared. However, CO_2-lasers also have the potential of generating

picosecond pulses since the gain spectrum, although periodically modulated by the rotational structure, has a width of about 10^{12} Hz. At higher pressure the broadening effect smoothes the discrete gain spectrum.

The limitations and prospects of picosecond laser pulse amplification to high powers in CO_2 can be analyzed as follows. When a pulse propagates in an amplifying medium two characteristic time constants should be considered. First of all the time τ_l that corresponds to a frequency interval between two adjacent rotational-vibrational lines, which is for example about 16 picosecond for the P (20) and P (22) of the 10.4 μm band. The other one is the collisionally induced dephasing time τ_2 by collision broadening which is related to the Lorentzian half width $\Delta\nu$ by $T_{2=}(\pi\Delta\nu)^{-1}$. It is now instructive to consider the amplification for three cases with different initial pulse duration τ_0 relative to τ_ℓ and T_2.

a) $\tau_0 < \tau_\ell < T_2$

In this case the frequency of the original pulse obtained from slicing a small part from an oscillating line may cover several discrete rotational-vibrational lines. The smooth frequency spectrum of the incident pulse is changed into a spectrum of discrete peaks corresponding to neighbouring rotational transitions. Its Fourier transform in the time domain is a pulse train consisting of a main pulse and a few satellites separated at a distance τ_ℓ. If the original pulse is obtained from slicing a single pulse out of a multiline mode-locked laser containing, for instance, 8 rotational lines [8] then the satellite pulses are much weaker and even absent. At higher pressure the broadening effect smoothes this discrete gain spectrum of the amplified pulse. As an example the amplification of a 5 picosecond single line CO_2 laser pulse (fig. 11a) through a 10 bar amplifier results in a short train of 5 picosecond pulses, shown in fig. 11b. A further smoothening of the gain spectrum of the amplifier is obtained by using an isotopic gas mixture. If one of the oxygen atoms is replaced by an isotope the symmetry of the CO_2 molecule is lost and thus odd rotational transitions are present. The gain spectrum is then twice as dence as with a regular CO_2 mixture. Using a 10 bar mixture of $^{12}C\ ^{16}O_2$: $^{12}C\ ^{16}O\ ^{18}O$: $^{12}C\ ^{18}O_2$ = 1 : 2: 1, computer modelling shows a considerable less short-pulse distortion as is shown in fig. 11c.

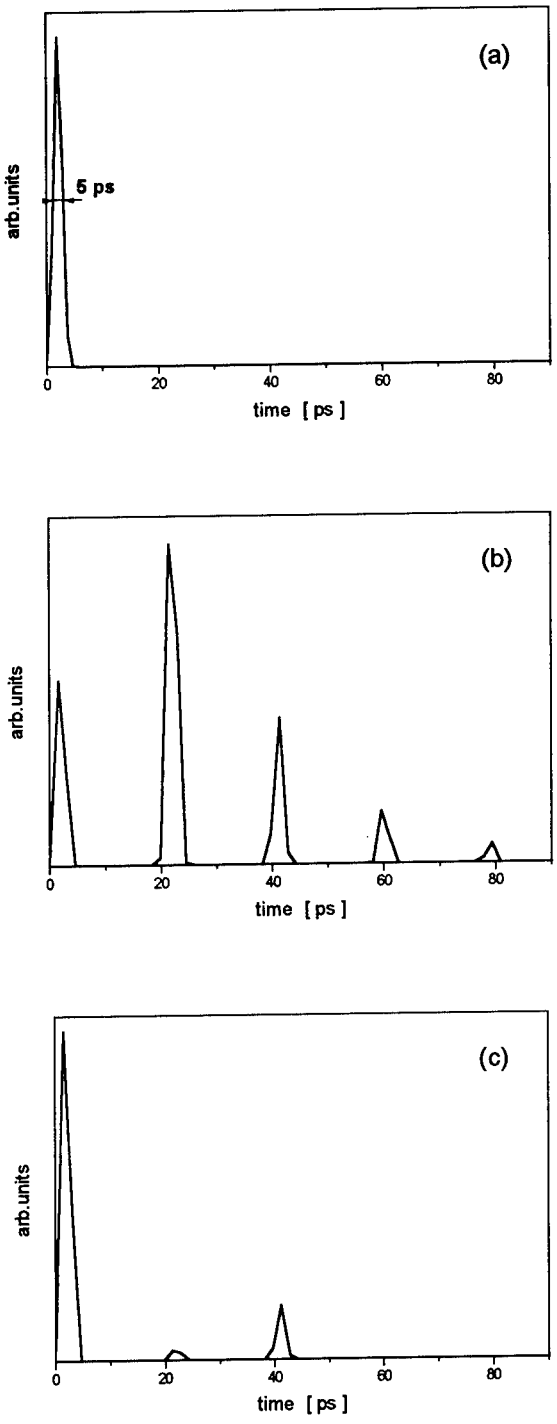


Figure 11. Amplification of a 5 picosecond pulse

b) $\tau_\ell < \tau_0 < T_2$

Since the laser pulse τ_0 is longer than τ_ℓ only one rotational line is involved in the amplification. The frequency spectrum of the pulse is larger than the gain spectrum of the transition line so that there is spectrum narrowing of the pulse and consequently the pulse duration increases.

c) $\tau_0 > T_2$

In this case the gain spectrum will not disturb the pulse spectrum and the pulse duration is unaltered. Since T_2 is inversely proportional to the gas density, it becomes about 10 picosecond at 10 bar. Computer modelling shows that pulses longer than 20 picosecond are amplified without distortion.

10. Terawatt CO_2-laser amplifier

For high power short pulse amplification pulse distortion is avoided when the frequency spectrum of the incident pulse is narrower than the line width of the particular transition. Then the saturation of the amplification depends on the pulse duration and the molecular relaxation time constants. The CO_2-laser has for the short pulses in principle two saturation energies. For the saturation energy of a P-transition with rotational number j we find according to eq. (31):

$$E_s^1 = \frac{h\upsilon}{\sigma_s\left(1+\frac{2j-1}{2j+1}\right)} \tag{39}$$

because for a P-transition in CO_2 we have $g_n = 2j + 1$ and $g_m = 2j - 1$. This saturation energy is relevant for pulse durations shorter than the rotational relation time τ_r but longer than τ_ℓ $\left(\tau_\ell < \tau_0 < \tau_r\right)$.

If τ_0 is longer than τ_r the amplification benefits also from the energy stored in other rotational transitions. The depletion of the lasing transition is then replenished by rotational relaxation. This means that the saturation energy increases with the available energy from the other transitions. This larger saturation energy E_s'' of the considered P-transition is then given by [9]:

$$E_s'' = \frac{h\upsilon}{\sigma_s\left[P(j-1)+\frac{2j-1}{2j+1}P(j)\right]} \tag{40}$$

where

$$P(j) = \left(\frac{2hcB}{kT}\right)(2j+1)\, exp\left[-Bj(j+1)\frac{hc}{kT}\right] \qquad (41)$$

where B is the rotational constant of the CO_2-molecule. Similar results can be derived for R-transitions. For short pulse high power generation high gas pressure is essential because the τ_r in inversely proportional to the pressure which makes rotational relaxation more effective and also because the saturation energy E_s'' is proportional to the pressure. Full profit of the available energy stored in the rotational transitions can also be obtained with picosecond pulses where $\tau_0 < \tau_\ell$ so that the pulse spectrum covers several rotational lines.

Output powers in the order of several terawatt peak power can be obtained in this way with a large aperture high pressure amplifier. For instance taking a 10 bar x-ray or e-beam preionized CO_2 laser discharge the energy loading may be as high as 300 J/bar liter. The stored laser energy can be as high as 30 J/bar liter. Amplifying a pulse of 20 picoseconds there is already some spectrum overlap with rotational transitions and in addition substantial rotational relaxation so that a great deal of the available energy can be extracted. The maximum saturation energy at this pressure is about 1 J/cm^2. However, the limitations to the available power from the amplifier in the picosecond regime are not set by the available stored energy but by detrimental effects as optical component damage and gas breakdown, which is roughly about 1 J/cm^2. Taking an aperture of 10 cm diameter an output energy of 100 J in 20 picosecond or multi-terawatt is feasible.

11. References

1. Schindler, G.M. (1980) Optimum output efficiency of homogeneously broadened lasers with constant loss, *IEEE J. Quantum. Electr.*, QE-**16**, 546-549.

2. He, D. and Hall, D.R. (1983) A 30W radio frequency excited waveguide CO_2 laser, *Appl. Phys. Lett.*, **66**, 801-803.

3. Hall, D.R. and Hill, C.A. (1987) *Handbook of Melecular Lasers*, edited by Cheo, P.K. Marcel Dekker, New York.

4. Heeman-Ilieva, M.B., Udalov, Yu. B., Witteman, W.J., Peters, P.J.M., and Hoen, K., (1993) R.F. excited 1.1 W/cm waveguide CO_2 laser, *J. Appl., Phys.*, **74**, 4786-4788.

5. Colley, A.D., Bakers, H.J. and Hall, D.R. (1992) Planar waveguide, 1 kW cw carbon dioxide laser excited by a single transerse rf discharge, *Appl. Phys. Lett.*, **61**, 136-138.

6. Heeman-Ilieva, M.B., Udalov, Yu. B., Hoen, K., and Witteman, W.J., (1994) Enchanced gain and output power of a sealed-off RF excited CO_2 waveguide laser with gold plated electrodes, *Appl. Phys. Lett.*, **64**, 673-675.

7. Pogorelsky, I.V., Fischer, J., Kusche, K., Babzien, M., Kurmit, N.A., Bigio, I.J., Harrison, R.F. and Shimada, T. (1995) Subnanosecond multi-gigawatt CO_2 laser, *IEEE J. Quantum Electr.*, QE-**31**, 556-566.

8. Rooth, R.A., van Goor, F.A. and Witteman, W.J. (1983) An independently adjustable multiline AM mode-locked TEA CO_2 laser, *IEEE J. Quantum Electr.*, QE-**19**,1610-1612

9. Witteman, W.J. (1987) *The CO_2 laser*, Springer Series in Optical Science volume 53, Springer - Verlag, Heidelberg.

ELECTRIC-DISCHARGE PUMPING.

DR IAN SPALDING
The Laser Centre
Abingdon, UK. (Fax: +44 1235 848296)

Abstract

This paper seeks, firstly, to view contemporary laser developments from the standpoint of industrial users. For civilian applications electric-discharge pumping is employed almost without exception: either directly by means of a gaseous or solid-state discharge, or indirectly via electrically-energized optical pumps (flash-lamps, diode-laser pumps etc.). The significance of high "wall-plug" efficiency for such systems (which typically operate with average powers in the range of 1mW to 30 kW) and of other practical factors which influence the take-up of power laser technologies are then discussed. Finally, by way of particular example, trends in discharge pumping are illustrated by considering preionization techniques used in (pulsed) excimer laser design, and DC/RF excitation techniques under investigation for (quasi-CW) CO laser research.

1. Introduction

Ten to fifteen years ago any academic meeting bearing the title "high power lasers . ." would nearly always have included topics covering developments towards 100 TW systems (for laser-fusion and related scientific experimentation), novel laser transitions, and/or very high power quasi-continuous systems for defence R&D etc. There is now increasing emphasis on "high" average power lasers for civil use - whether this be for materials-processing, medical, information technology (IT), environmental/lidar, or other measurement applications. Even these civil uses span a very wide range of the electromagnetic spectrum: potentially from the soft x-ray to IR, with average powers likely to lie in the range of <1 mW to 30 kW depending upon the application. This paper will concentrate on such systems, and more especially on those broadly capable of operating continuously for periods of some one to twelve weeks without interruption. Although this specification is characteristic of many industrial materials- processing applications, some of the conclusions will also be relevant to other systems and their applications - for reasons which will become apparent.

The "specification" just given lends itself more naturally to electrical-pumping rather than to chemical, gas-dynamic, or nuclear-pumping. Although these latter sources have all been discussed in the literature they tend to be considered for highly mobile, eg. space, applications. Now what about optical pumping? This will be included within our

R. Kossowsky et al. (eds.), High Power Lasers – Science and Engineering, 27–45.
© 1996 *Kluwer Academic Publishers. Printed in the Netherlands.*

present subject - heading (even though rather briefly) because the ultimate energy source for the (radiative) laser-pump is still most likely to be electrical, whether it be a flash-lamp, another laser, or a solid-state diode; they are also of steadily increasing industrial importance.

Apart from an all-embracing "fitness-for-purpose" what would the user-community like of this electrically-pumped laser-system?

(a) The capital (purchase) cost should be lower.
(b) It should be very reliable (ie. long period between services, with no unscheduled "outage").
(c) Its output (power, mode, polarization, pointing etc.) should be stable and reproducible.
(d) Its bulk (volume and floor space, or "foot-print") should be less.
(e) The output beam should be readily and reliably delivered to the workpiece, and suitably controlled (eg. automatically, in mass production; manually for surgery).
(f) Running-costs (for gases, flashlamps, electricity, cooling-water, other consumables, and labour) should be low.
(g) A turn-key system incorporating adequate safety-provisions etc. is usually preferred.

What factors in consequence are probably most important to the supplier, from initial concept in the research laboratory to incremental device development and value-engineering improvements?

- Laser efficiency.
- Power density in the laser medium.
- Output power-density, averaged over the laser-pumping and cooling envelope.
- Power supplies (efficiency of coupling to the discharge; and also any preionization, gas circulation, heating, cooling or ancillary pumping requirements etc.)
- Optical resonator design and beam-transport (the subject of separate lectures).

Subsequent sections will consider trends relating to the first four of these issues (for electrical discharge pumping techniques), address two of the newer systems (excimer and CO) by way of particular example and then draw some general conclusions.

2. Discharge Pumping

2.1. LASER EFFICIENCY

The overall "wall plug" efficiency of a laser (η_{WP} = output laser power/total electrical input power) is a product of many factors, in particular:

(a) The intrinsic quantum efficiency (η_Q = output photon energy/energy of pump level)
(b) The electrical pumping efficiency to that level: this is itself a product of several other factors, especially when optical-pumping is used for laser excitation

(c) The beam extraction efficiency: a combination of the time averaged optical saturation of the laser medium [1, 2] and the geometrical filling factor (ie. the percentage overlap between the optical radiation field and the volume of the electrically excited gain medium).
(d) The electrical efficiency of the power supplies, cooling systems and ancillary equipment (eg. control panels, vacuum pumps etc.)
(e) The discharge efficiency (η_e = optical output/electrical input powers) is perhaps the most commonly used figure-of-merit in the scientific literature: this is the product of all the above factors other than 2.1d.

Laser design fundamentals are treated in the standard texts, see for example references [3-6], and several specific laser types are discussed at this meeting. Table 1 lists characteristics of some of the systems most commonly encountered: the precise numbers given are not particularly important as they are sensitive to laser beam-quality, or pulse-duration etc. Additionally, engineering changes will often improve the specification year-on-year. What is not changeable of course, is the underlying physics: only systems which start with a promising quantum-efficiency and end up moderately efficient are likely to be of industrial interest. If, for example, it were possible for the same 100 kW power supply to drive a 100 W argon-ion laser, a 1 kW excimer laser, a 2 kW Nd:YAG laser or a 10 kW CO_2 (or CO) laser, there is likely to be a significant cost -advantage in principle to the more efficient system, power-for-power. (This would be particularly true when one includes the cost of removing waste heat from the less efficient systems). However, these generalizations can not be pushed too far. As one example, high voltage pulsed power supplies are usually more demanding (in cost and component lifetime) than low voltage DC systems of comparable average power. As a second example arc-welders or electron-beams are electrically more efficient heat-sources than any laser: it is some other advantage of the laser, its brightness over the former or its general convenience over the latter, which may give it a particular advantage for a specific application.

2.2. POWER DENSITY: GASEOUS LASER MEDIA

The normalized threshold pulse pump power density for laser action to commence can, for our purposes, be written as follows:

$$\eta_Q p_2/g(\upsilon) = (8\pi h\upsilon^3)(1 + \upsilon_2/A_{21})/(c^2 f(\upsilon)) \qquad (1)$$

Various simplifying approximations (eg. almost empty lower laser level) are discussed in standard texts.

p_2 is the power density used to excite the upper laser level; A_{21} is the Einstein coefficient for spontaneous emission; ν_2 is the de-excitation rate; $g(\nu)$ is the gain per unit length; and $f(\nu)$ is the spectral line profile of the lasing transition of frequency ν (normalized so that $\int f(\nu)d\nu=1$). Thus shorter wavelength lasers such as excimers require very much higher pumping powers (because of the ν^3 term), as do wide-band

TABLE 1. Characteristics of some lasers showing industrial potential.

Medium	λ (nm)	η (%)	P_{avg} (kW)	τ (ns)	F (kHz)	P_{avg} ÷ Resonator Head (kW/m^3)	P_{avg} /Total Vol. (kW/m^3)
CO_2	10600	4-15	0.01-30	-	0.1-100	1-2	0.5-0.9
CO_2	10600	6	2	2000	0.3-1		0.44
CO	≥5000	8-25(1)	0.01-4	-	-		
Nd:YAG	1060	0.2-3.0(2)	0.01-4	100-500 10-100	20-100 1-100	-	1-1.5
Nd:YAG	1060	8-15(3)	0.05-0.5				
Diode	808	30	0.1-1	200,000	1	-	50
HeNe	632.8	low	5×10^{-6}				
HeCu	5782	1	0.06	40	6	0.15	0.1
	5106						
Ar^+	5245	<0.1	0.1	-	-		
	488			-	-		
Nd:YVO_4/LBO	532		10^{-3}				
Nd:YVO_4/KTP	532	0.25(4)	10^{-4}	-	-	0.78	0.16
$XeCl^*$	308	1-2	0.1-0.5	20-200	0.1 - 0.2	0.13	
KrF^*	248						
ArF^*	193						

Notes: λ is the laser wavelength; η_{WP} an illustrative efficiency (normally higher in multimode operation); P_{avg} the average power output; τ a typical pulse duration; F the repetition/modulation frequency. The last two columns are averaged over the whole resonator enclosure and total system (including power supplies/safety cabinets etc.) respectively; they are taken from recent trade catalogues but are not necessarily state of the art for any system mentioned.

(1) Temperature-sensitive: highest η excludes liquid N_2 (energy) cost.
(2) Flash-lamp pumped.
(3) Diode-pumped.
(4) Air-cooled laser-diode-pumped monolithic "micro laser" - see ref [7].
(N.B. Last two columns refer to different device)

systems, because of the 1/f(v) dependency. The latter have an even stronger v^5 frequency dependence when the line is naturally broadened by spontaneous emissions, as in x-ray lasers.

It has therefore proved necessary to apply a very wide range of electrical discharge-excitation technologies to gas lasers, depending on the specific requirement, as will be seen from the list below, where figures in parentheses are indicative (pump) power densities:

- DC glow discharge: axial flow (AF) CO_2(15 W/cc); CO, HeNe etc
- Wall-stabilized arc: Ar^+(10 kW/cc)
- Pulsed DC: Transverse excited atmospheric (TEA) CO_2 (10kW/cc), Excimer (0.1 - 1 MW/cc).
- 10-100 kHz discharge: AF CO_2 (15 W/cc).
- 100 kHz - 200 MHz discharge: AF CO_2 or CO (25 - 35 W/cc).
- 2.45 GHz discharge: CO_2 (100 W/cc); excimer (100 kW/cc); Ar^+ (10 kW/cc).
- 0.1 - 2 Mev electron-beam (eb) excitation.

The optimum discharge conditions are sensitive to initial gas compositions (eg. the ratio of $CO_2/N_2/He$ for CO_2), to impurities resulting from leaks, and the subsequent products of volumetric and surface gas/plasma reactions. Preionization of the gas medium to ensure a uniform volumetric discharge is often achieved by external means (eg. x-rays, electron-beam, or UV) or internally. Convection of the gas within the laser is often employed to prevent overheating of the laser medium in order to reduce:

- unwanted thermal population of the lower laser levels (eg. in CW or repetitively pulsed CO_2 or CO lasers)
- discharge, eg. thermal [8] instabilities
- optical inhomogeneities, eg. thermal-lensing, and/or shocks (as in pulsed excimer operation).

However, there are also perfectly viable "no-flow" conduction-cooled slab lasers, thus the design options are enormous, even for one particular type of laser (such as CO_2).

In general, a critical parameter for glow-discharge excitation in the quasi-steady-state regime is the ratio of the applied electric field (E) to the gas number density (N), as this determines the electron velocity distribution.

To ensure efficient collisional excitation of the N_2/CO_2 gas mixture; E/N should be chosen so that the corresponding electron "temperature" in the discharge is relatively low - but a second parameter, the gas current, is also sensitive to E/N. Thus, above a critical value the field will be sufficiently high to promote avalanche ionization until a quasi-steady-state electron density is achieved: the discharge is then "self-sustained". In TEA CO_2 lasers an initial electron density of some 10^4 - 10^8/cc is required to prevent (non-volumetric) high temperature arcs, and this can be generated very conveniently by UV preionization; alternatively a 0.1 - 1 Mev electron beam (eb) preionizer can generate electron densities sufficiently high that the main discharge E/N can be sufficiently low that the discharge is "non self-sustained". Then if we turn the eb on or off the discharge

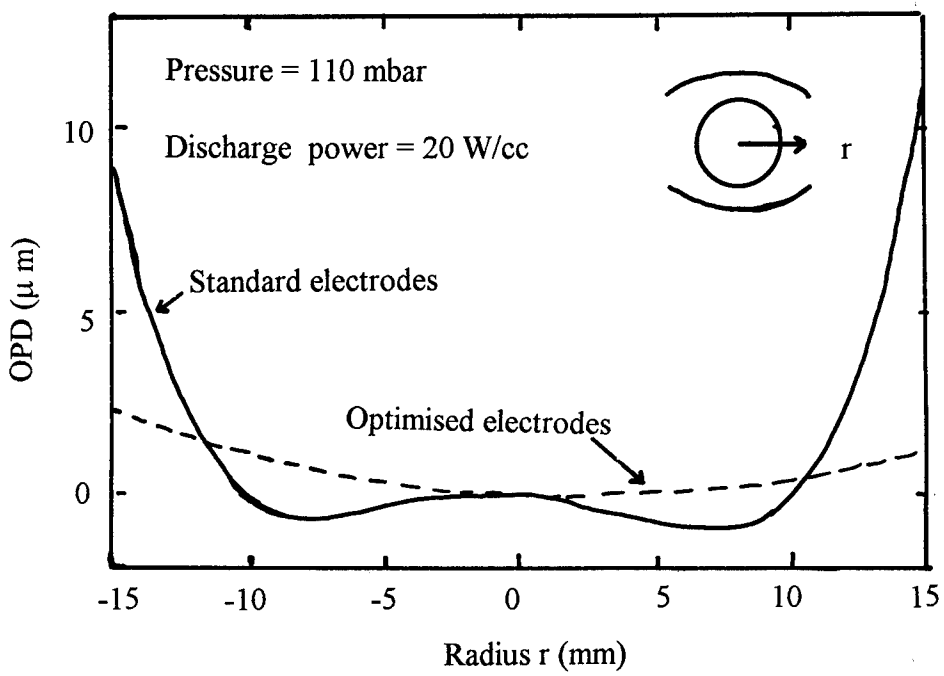
is also switched on or off.

Many would claim that capacitively-coupled RF exhibits the following advantages over DC excitation for CW CO_2, and similar, lasers:

- Improved dynamic discharge stability, and homogeneity of the discharge; for recent work see references [9,10] and Figure 1, for example.
- The ability to modulate the discharge in the industrial heating bands (eg. 13.6, or 27.1±0.16 MHz) at frequencies up to ~200 kHz (to provide a very convenient power-control facility when cutting sharp corners on work-pieces etc) , compared to modulation frequencies of ~2 kHz with DC excitation
- Reduction of sputtering, corrosion, gas-impurity, and (arguably) window-contamination problems.
- Elimination of internal structures impeding gas flow, (whether axial or transverse) and also to facilitate thin slab [11-13] or annular [9] "no flow" designs.

However RF power supplies in this frequency range are relatively expensive, require impedance-matching networks, and have efficiencies of order 65%. DC switched-mode power supplies, by comparison, can have efficiencies >95% and are compact and relatively cheap. Both types of laser therefore find a market place. Work continues to explore 2.45 GHz excitation (where the near-unity dielectric constant for CO_2 and the narrow skin-depth for excimer laser-plasmas make coupling problems more challenging), and near 1 MHz [14].

Figure 1. Variation of measured optical path difference (OPD) across tube radius for optimized RF electrodes, in a transversely-excited CO_2 laser. (Axial gas flow along optical axis; propagation length 2.5 m); see [9].



At both frequencies a potential attraction is cheaper power-sources (whether because of mass-production, or solid-state technologies, respectively).

2.3. POWER DENSITY: SOLID-STATE LASER

It is widely expected that diode-lasers will gradually displace flash lamps, because of their longer life, greater electrical efficiency and the lower thermal distortion they produce when pumping Nd glass, Nd:YAG (or other) solid state lasers[15]. At present a major holding item is their price, but bulk markets created by IT and other low-power applications may help to bring this down (as has already happened for the quartz optical-fibre delivery systems used with conventional NdYAG lasers.) However it should be noted that NdYAG flash-lamp (pump) design is still evolving. (Note also that excimer UV lamps now provide quasi-monochromatic but incoherent 172, 222 or 308 nm outputs at CW powers of up to 1.7 kW.)

Flash lamp pumped Nd:YAG lasers of up to ~4 kW average power are now standard commercial items, whereas diode-pumped solid-state (DPSS) lasers are still largely experimental. A few recent publications are therefore summarised below, to aid comparison with gas lasers (which are our primary interest).

Figure 2 illustrates a typical 72 W (multimode), low TEM_{00} mode CW DPSS (zig zag slab) Nd:YAG laser [15]. This system is uniformly (side) face-pumped and (side) face-cooled by water which helps to minimise thermal lensing and stress birefringence. For increased reliability (at some price in overall efficiency) the pump diodes were fibre-coupled into the (Teflon-coated) Nd:YAG slab. Using 25 (SDL-3450-P5) diodes of 9.5 W output, a total of 235 W pump power was delivered into a resonator assembly having dimensions of a few cms. The TEM_{00} (M^2 = 1.3) output as a function of diode power is plotted (as circles) in Figure 3. A higher power (pulsed) diode-stack generating an average pump power of 1kW and an average (slab) Nd:YAG power of 275 W has been described in reference [16]. Finally, a rod design generating Nd:YAG powers of 540 W (stable resonator, M^2 = 176) or 185 W (unstable resonator, M^2 = 3.8), with projected multimode outputs of 1 kW at higher (30%) duty-cycles for the diode arrays is discussed in reference [17]. Considerable developments in cheaper micro-optics are underway [18], and in alternative end-pumped (fibre-bundle-coupled diode bar) technologies [19]. With this short digression, to note developing competition from DPSS, let us now return to recent trends in two of the less-developed gas lasers.

Figure 2. Schematic of a 40 W CW TEM_{00} DPSS (face-pumped zigzag slab Nd:YAG) laser, after ref [15]. The thick black line represents gold coatings for confining the (fibre-coupled) diode-laser pump light.

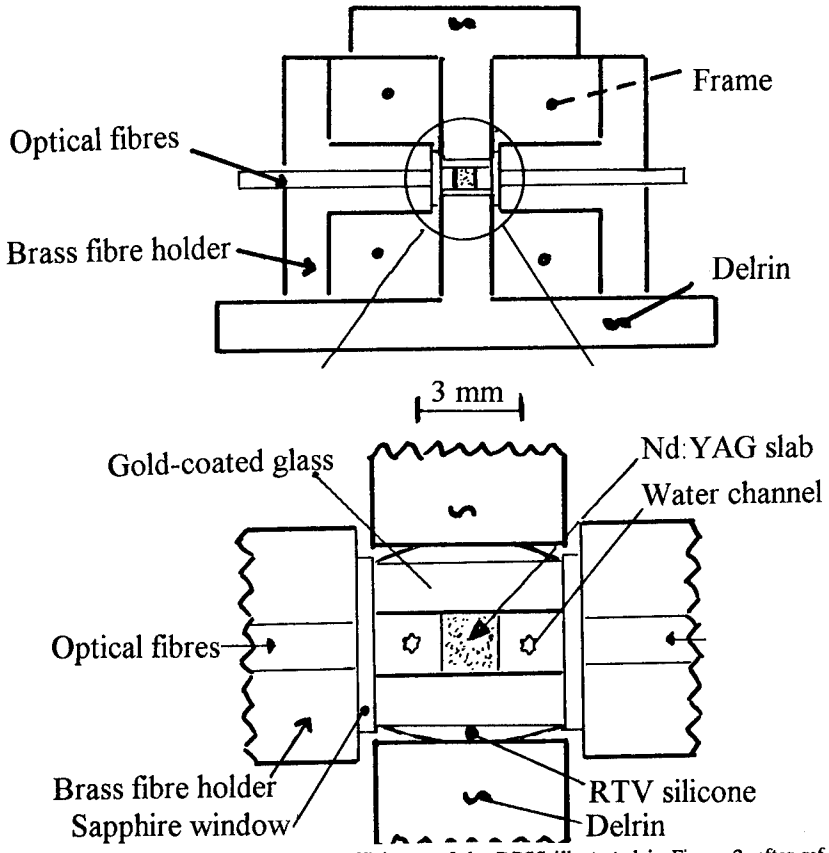
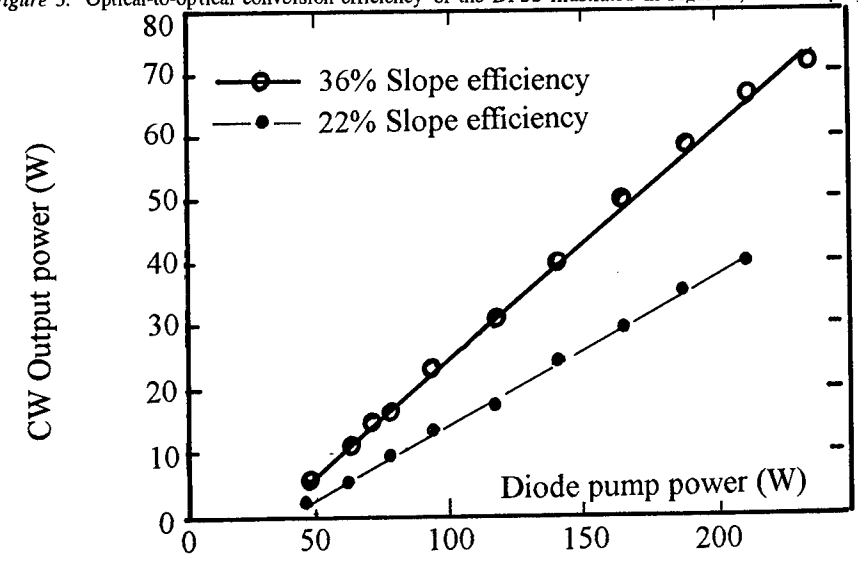


Figure 3. Optical-to-optical conversion efficiency of the DPSS illustrated in Figure 2, after ref [15].



3. Some Trends in Excimer and CO Laser Pumping

3.1. EXCIMER LASERS

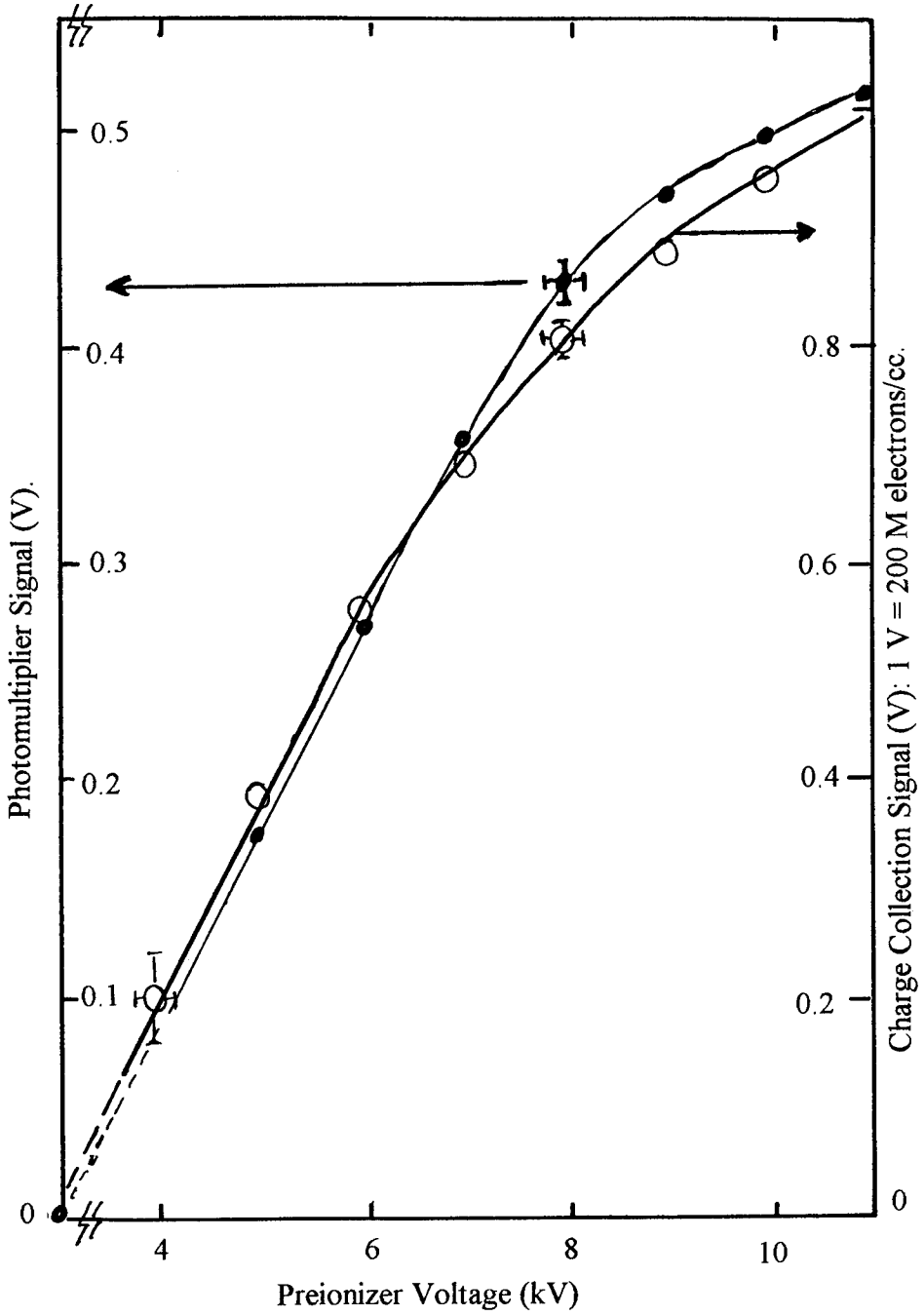
Being inherently pulsed, an important challenge for excimer laser design has been to increase the lifetime beyond ~10^9 shots for every component in the system. Specialist talks will doubtless be given on such topics during this meeting. Table 2 summarizes the status of research work by one group of laboratories two years ago [20], and reference [21] of my own laboratory at that time.

TABLE 2. Summary of some excimer (research) lasers, having target outputs in the ≤1 kW region.

Collaborator/Sub-system	ENEA	NCLR	BAe	AEA	OG
i) **Gas Flow**					
Pressure Vessel	Loop	Loop	Loop	Cylinder	Loop
Overall Dimensions					
(L x W x H) m	4.4x1.9x2.3	4.5x1.2x1.7	4.4x3.2x1.5	2.1x1.2x1.2	1x0.8x1
Max Pressure (bar,a)	4	5	10	6	5
Heat Removal (kW)	100	50	90	~ 130	~ 40
Velocity (m/s)	67	60	100	70	19
Fan Power (kW)	30	15	40	160	5
Uniformity $\Delta\rho/\rho$ (%)	0.16	0.01	1	?	0.01
ii) **Optical Configuration**	MOPA	Plane-Plane	Plane-Concave	Plane-Plane	Plane-Plane
Preionisier	x-ray	x-ray	x-ray	UV	x-ray
PRF (kHz)	1	1	2	> 10	0.135
LifeL $\log_{10}$ (shots)	7	9	9	9.6	7
iii) **Main Power Supply**					
P (kW)	60	90	300	100	40
V (kW)	22	15	30	10	30
PRF (kHz)	1	1	2	4	0.135
Voltage Rise Time (ns)	200	20	50 - 100[2]	50	100-200
Discharge Volume	100x3x3+				
(L x W x H) cm	100x2x 2	80x2x 2.5	40x2.5x2.5	60x3x3	72x4.7x4.7
iv) **Output Achieved** (XeCl)					
Pulse Duration (ns)	150	160		~ 160	
Energy (mJ)	1100 + 500	1100		424	
PRF (kHz)	0.1	0.95		1.1	
Power (W)	100	650		429	
Efficiency (%)[a]	1.6	2.3		2.3	
Efficiency (%)[b]	-	1.8		~ 1	
Beam Quality	Near Field ± 4%	Perfect Top Hat		Near Field ± 3%	

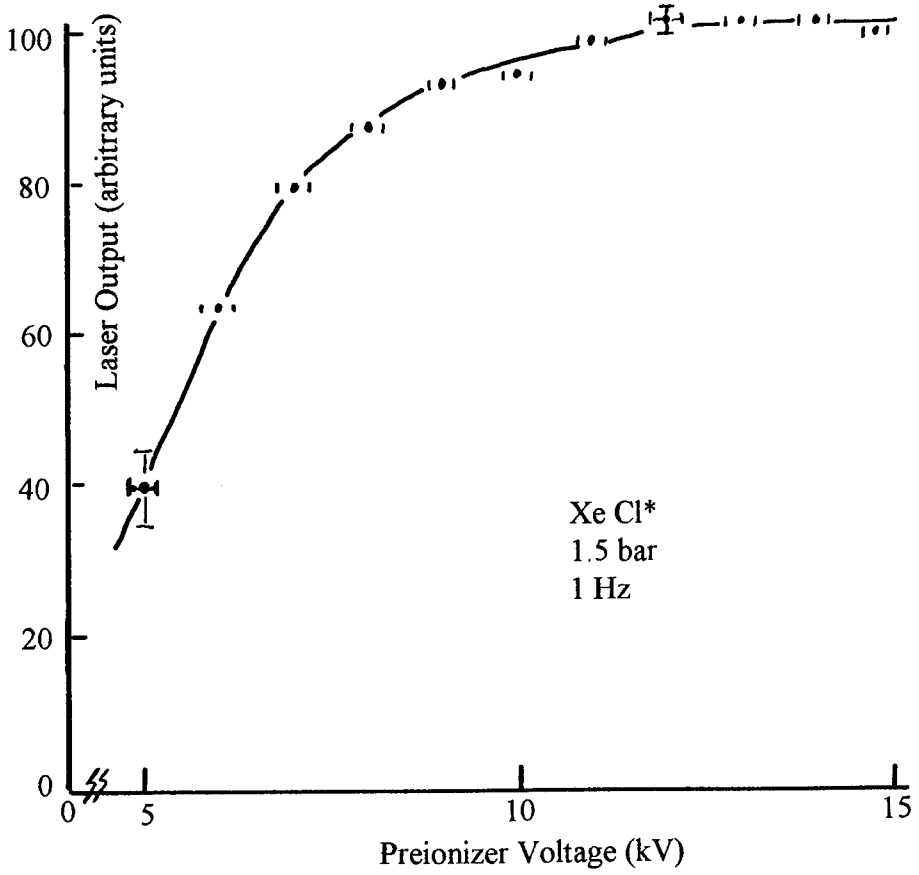
(a) Laser output/energy stored on capacitors (including preioniser)
(b) Laser output/total electrical energy stored + gas loop.

Figure 4a. Charge-collection signal as a function of preionizer voltage for an ultra-violet corona-preionizer, working in a standard XeCl gas mixture. Courtesy of AEA Technology, see ref [21]. (The photomultiplier signal measures visible fluorescence from the corona discharge, and is seen to provide a good diagnostic of its relative performance.)



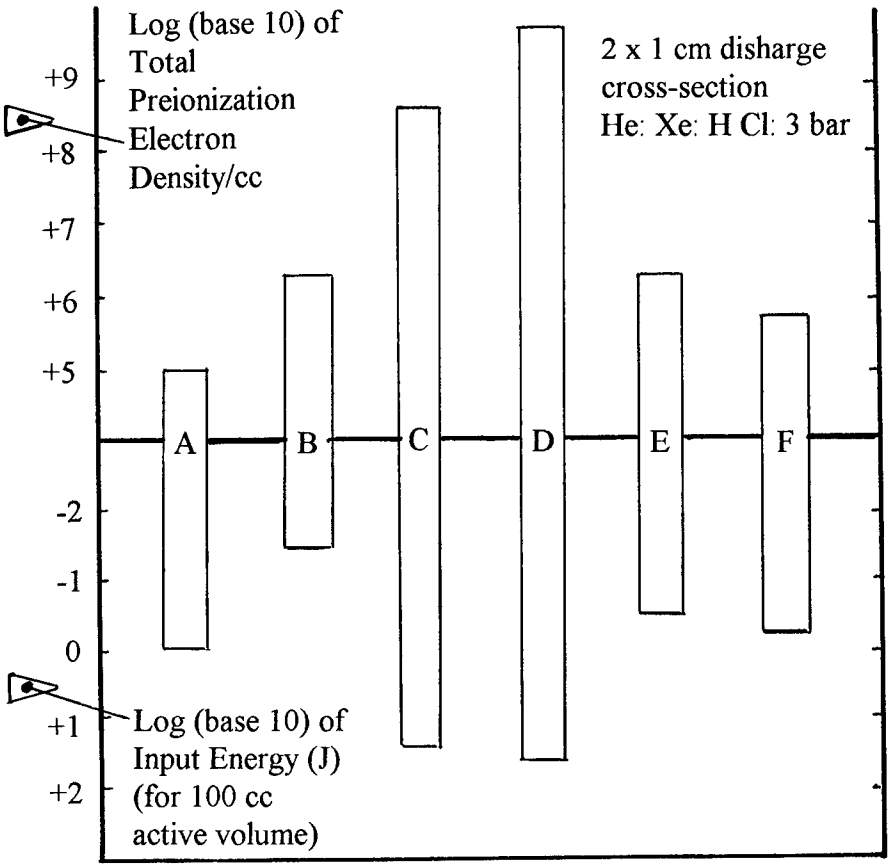
Perhaps of particular interest is the CHIRP UV preionizer system, which proved capable of operating at a pulse repetition frequency (PRF) of up to 4 kHz. At lower PRF and higher electrical-input pulse energies (~150 mJ) it has successfully operated for almost 10^{10} shots (without failure), generating preionization densities of ~2 x 10^8/cc (Figure 4). This was sufficient to permit a uniform 36 x 36(mm)^2 output from a XeCl laser [21], when operating at a pressure of ~ 4 bar(g).

Figure 4b. Relative XeCl laser output as a function of the UV preionizer voltage [21], when operating as in Figure 4(a).



An alternative preionizer for use in such systems is discussed in reference [22]. Here a fast (20 ns) rise-time pulsed 100keV x-ray source, has been developed, using a corona plasma-cathode (Figure 5). This is capable of operating at a PRF of ≤2 kHz for a demonstrated life-time of 2.5 x 10^8 shots (with an estimated life of 10^9 shots). Developments reported elsewhere, for fully-commercialized devices, have included careful attention to gas life-time and purity and magnetic switching techniques [23].

Figure 4c. Comparison of preionization techniques available in 1989 (courtesy of AEA Technology).



KEY.

A= Semiconductor- ballasted sparks.
B= Corona, capacitative.
C= Spark, some energy recoverable.
D= X-Ray, cold cathode - (readily scalable).
E= U. V. Laser (Ar F*, assuming 1% efficient).
F= U.V. Laser (Xe Cl* , assuming 1% efficient)

Figure 5a. Schematic of a corona plasma-cathode, used for the (XeCl) X-ray preionizer discussed in ref [22].

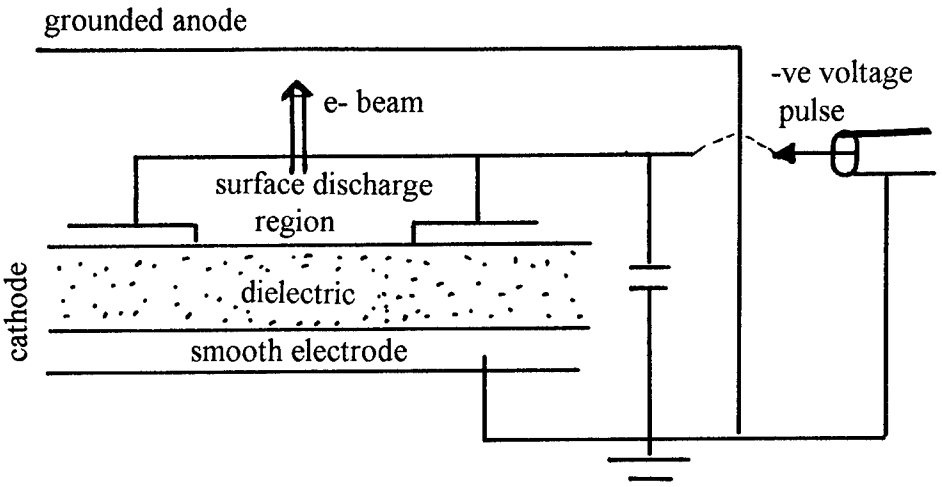


Figure 5b. Longlife 2 kHz X-ray preionizer: transmitting anode target consists of 50 mm x 50 mm x 1mm thick Al squares, flame-sprayed with a 20 μm tungsten surface layer, supported by cooled stiffening ribs [22].

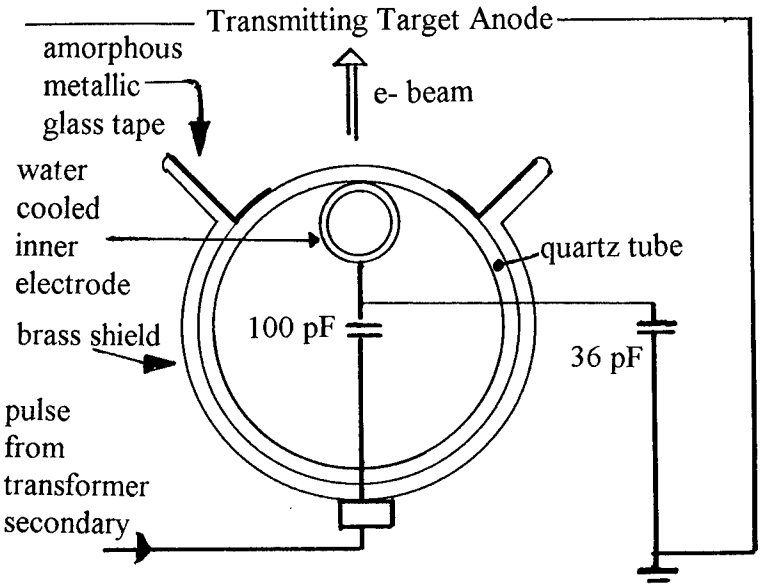
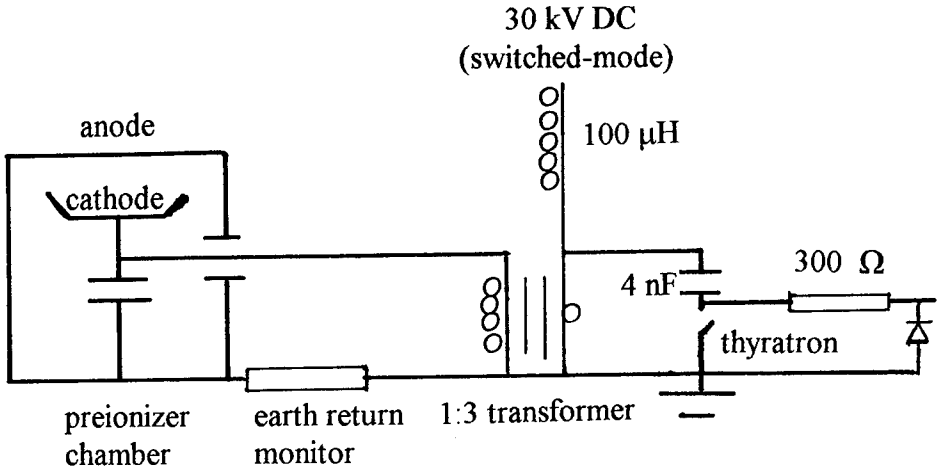


Figure 5c. Cooled, oil-immersed, electrical driving circuitry used on test-bed trials for system of 5(b). (3:1 step-up pulse transformer command-charged to 30 kV by switch-mode power supply.)



3.2. CO LASER

In strong contrast to the short-pulse electric-discharge technologies which must be used in the efficient excitation of excimer lasers, for CO lasers the interest is currently in quasi-CW pumping techniques. Table 3 summarizes the characteristics of some systems which have recently received attention in the scientific literature and/or technical press [24-30]. Although one or two of these devices may already be economically capable of single-shift operation (ie. running ~ 8 hours per day) and all closed gas-loop systems might eventually prove their capacity to do so, there is at present more emphasis on investigating the practical potential of such systems eg. for materials-processing, medical applications etc. etc. [28, 31-33]. Indeed, as recent deep-penetration CO laser welding investigations [32] and earlier CO_2 work have shown, it is perfectly possible to get interesting surfacing, cutting or welding applications-data from pulses lasting just a few seconds, as long as the beam quality and power are both reproducible and fit-for-purpose. ($M^2 \rightarrow 1$ makes a useful start!).

It is apparent from Table 3 that the electrical excitation technologies appropriate to the CO molecular-gas laser are those which have already been widely employed on CO_2.

In a bid for cheaper electrical excitation-sources for molecular-gas lasers a wide range of other discharge technologies have been used, and discussed in the literature. These include direct excitation at microwave frequencies and various preionization schemes which seek to avoid the complexities of electron-beam preionization: for example, RF assisted DC glow-discharges [28] and 3 kHz pulse-preionizer DC systems [34]. In order to keep this brief review to manageable proportions these options are not tabulated here.

Note that laser action in CO was first demonstrated in the same year as CO_2 [35]. The CO laser is interesting because $\eta_Q \sim 100\%$ and its multiplicity of anharmonic v-r lasing levels are very effectively collisionally coupled. It has been almost traditional to cool the CO lasing medium to ~150 K in a search for high efficiency. These low

TABLE 3. Comparison of some recent CO lasers

REFERENCE (and Organisation)	24 HWU	25 HWU	26 LE	27 ISL	28 MHI	29 LOK	30 IHI
PARAMETER (UNIT)							
OUTPUT POWER (kW)	0.13	1.1	3-4	4 → 7	15	200	0.99
MODE: (M^2) if known	[a]	[b]	Good	9 → ?	MM	MM	MM
η_e (%)	17	28	-	9 → 14	17	>40	15
Excitation(MHz)	125	27	DC	13.6	DC	DC (+eb)	13.6
Gas Inlet Temp. (K)	243	145	275	105	150	80	286
Gas Pressure (Torr)	100	105	-	296	40	[c]	61
Gas Flow	No	AF	AF	TF	TF	TF	TF
Closed Loop	Sealed	✓	✓ (or sealed)	Semi-closed	✓	Not yet	✓
Typical O/P duration	?	1 - 2hrs	8hrs	8s every 15 mins	-	≤1s	5-30m
Coolant	-30C	$l.N_2$	-	SS	$l.N_2$	SS	H_2O
Cavity length (m)	0.39	1.4	-	1.8	8.4	-	-
Stable (s) or Unstable (u/s) Resonator?	s	s	s	us or s	s	s	s
Beam diameter (mm)	2 x 20	<40	-	28	57	140 x 140	28
Full angle beam-divergence (mrad.)	-	[b]	-	2.5 or 8	-	-	7.5

NOTES:

[a] EH [11] for 2 mm x 2 mm cross-section: multimode at larger cross-sections/power

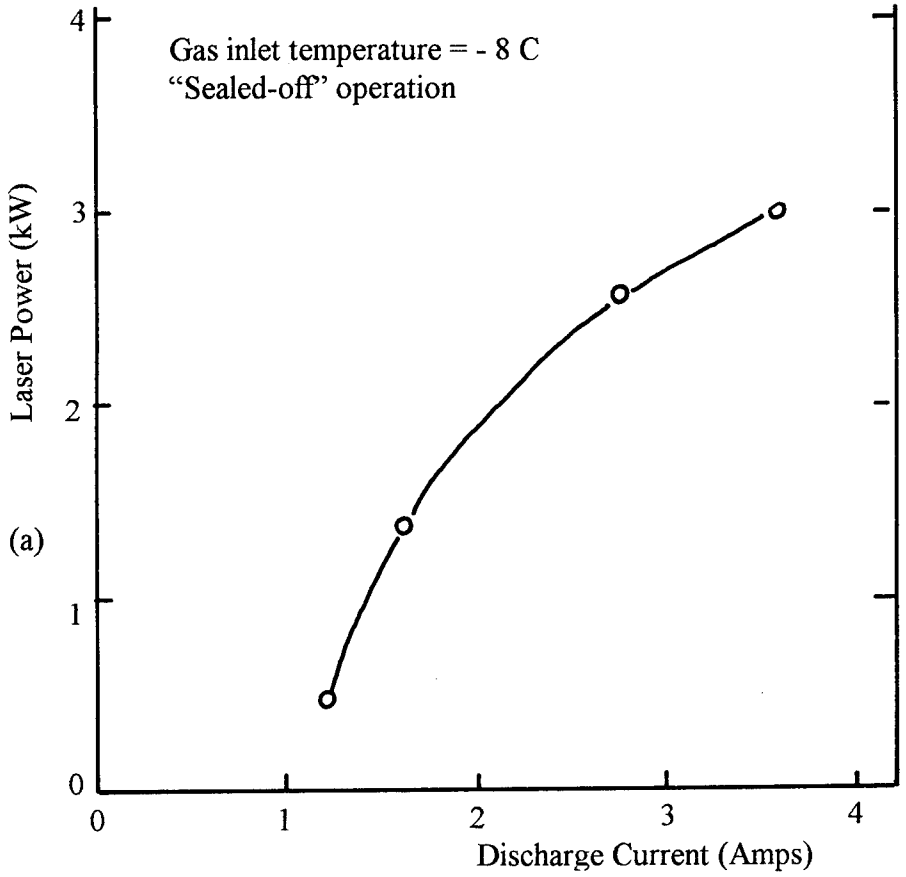
[b] Ref [25] discusses a two-tube system: using a folded four-tube system, a plane-polarized 950 W beam having M^2 = 2.5-2.7 has been obtained: D.R Hall (private communication)

[c] ρ_1=0.2 Amagat in discharge zone.

ABBREVIATIONS: MM = multimode; $l.N_2$ = liquid nitrogen; AF and TF = axial and transverse gas flow relative to optical axis: hyphen (-) indicates data not available to author; SS = supersonic cooling.

temperatures have been achieved either by using cryogenic heat-exchangers (cooled by bulk supplies of liquid nitrogen), or by super-sonic expansion from ambient temperature (usually with the gas flow transverse to the optical axis). Their output tends to be in the wavelength range 5.0-5.3 μm. The most convenient atmospheric window is <5.2 μm. However there is also growing interest in near-room-temperature lasers [36] (although they generate their output at slightly larger wavelengths, primarily in the range 5.3-5.7 μm), and in "no-flow" conduction-cooled systems [24]. In the UK a 3-4kW (good mode-quality) "room-temperature" industrial-prototype device, developed by Laser Ecosse Limited, has been available for laser and applications experiments for the past eighteen months, see Fig 6. Some of the first applications work with this, and also work with the 950 W (M^2 = 2.5-2.7) axial-flow system located at Heriot-Watt University, have been summarized in reference [33]. It is my personal view that though there remain some engineering challenges (to refine electrical-discharge aspects of CO laser designs), it is probably more important to take an integrated (systems) approach to well-identified

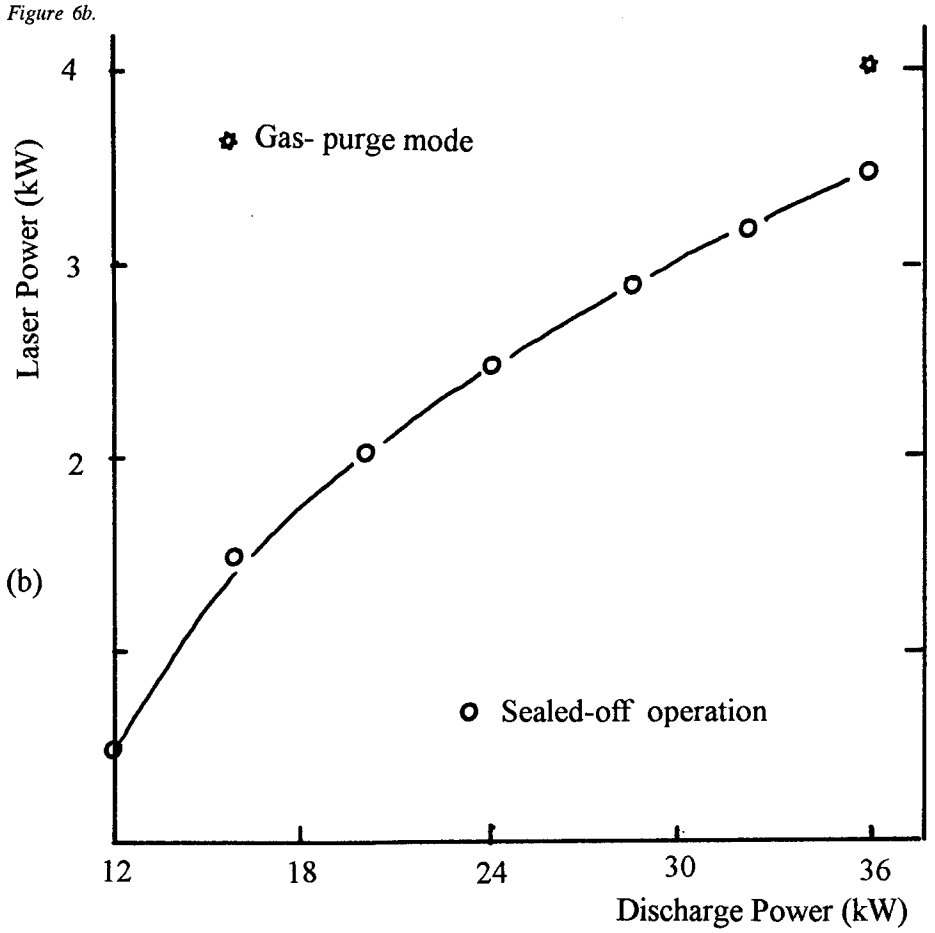
Figure 6. Unpolarized output of 3-4kW DC-excited "room-temperature" CO continuous laser, as a function of (a) discharge current and (b) power input to discharge: courtesy of Laser Ecosse Limited, Dundee, Scotland. Using a (Farnell-Hi volt) switched-mode DC power-supply, the ratio of power-input (to the discharge) to mains-supply (to excitation circuit) exceeds 95%.



applications-requirements. This implies not only clear specifications for optical power,

but also incident intensity, beam-delivery, safety etc. etc. This development has already occurred, of course, for CO_2 and Nd:YAG through the provision of "turn-key" systems.

Figure 6b.



4. Conclusion

"Electric-discharge-pumping" is rarely a "stand-alone" design requirement for any high-power industrial laser-system. Often the laser designer will start with a specification which includes the desired power and beam-quality (together with current window capabilities, if they are a potential "weak link") and will proceed from there to assess possible geometries, and cooling implications. Somewhere along the line the electrical pump-specification (and any pre-ionization needs) will emerge! As an illustration of the iteration which may be required the reader is referred back to Table 2, where the (deliberately conservative) fan-power requirements quoted are a consequence of the high pulse-rate envisaged for some of these 1 kW nominal-output (research) lasers. If the highest possible "wall-plug" efficiency were an over-riding factor of the specification, other design-options might be adopted.

By illustrating some current engineering trends in industrially rated laser design, it is

hoped to compliment other topics scheduled for discussion at this meeting. It should be noted that although capital cost, reliability, compactness etc are also relevant to many lower power (eg. medical or IT) applications, other over-riding considerations (eg. ease of beam delivery under sterile conditions) may then prove more important than factors such as wall-plug efficiency and related consumable (gas or flash lamp, cooling etc.) and servicing costs.

5. Acknowledgements

Although all sources have been referenced, the author would like to acknowledge specifically the contributions made to some of the CO and excimer work material here by EUROLASER EU113 and EU213 partners, respectively. A full listing of the 34 organisations involved in one or other of the two projects is to be found in references [37] and [20].

6. References

(1) Rigrod W.W., (1978), *"Homogeneously broadened CW lasers with uniformly distributed loss"*, IEEE J.Q.E.**14**, pp.377-381.

(2) Schindler G.M., (1980), *"Optimum output efficiency of homogeneously broadened lasers with constant loss"*, IEEE J.Q.E. **16**, pp.546-549

(3) Maitland A. & Dunn A.H., (1969), *"Laser Physics"*, North Holland, Amsterdam.

(4) Svelto O., (1982), *"Principles of Lasers"*, Plenum, New York, (2nd Edition).

(5) Siegman A.E., (1986), *"Lasers"*, University Science Books, Mill Valley, California.

(6) Witteman W.J., (1987), *"The CO_2 Laser"*, Springer Series in Optical Sciences Vol. **53**, Springer-Verlag, Berlin.

(7) Mitchard E. and Bergman T., (May 1995), *"Introducing Microlasers"*, Photonics Spectra pp.136-142.

(8) Nighan W.L. et al. (1973), *"Ionization instability in CO_2 laser discharge"*, Appl. Phys Lett. **22**, pp.579-582.

(9) Loosen P., (1992), *"Recent developments of lasers for materials processing"*, in A. Matsunawa & S. Katayama (eds), *"Proceedings of LAMP'92"* Vol.**1**, Nagaoka (ISSN 0918-2993), pp.61-66.

(10) Pfeiffer W. et al, (1994), *"Scalability of RF gas discharges for high power CO_2 lasers"*, in *Bohrer et al, (eds), "High Power Gas & Solid State Lasers"*, Proc.SPIE **2206**, pp.80-90.

(11) Abramski K.M. et al. (1989), *"Power scaling of large area transverse RF discharge CO_2 lasers"* Appl. Phys. Lett **54** pp.1833-1836.

(12) Abramski K.M. et al. (1992) *"Compact diffusion-cooled array and slab CO_2 lasers at the 1kW level"*, in Reference 9, pp.73-77.

(13) Macken J., (1992) *"DC slab CO_2 lasers"*, in Reference 9, pp.67-72.

(14) Terai K. et al. (1992), *"Laser pulsing characteristics of RF excited high power CO_2 laser at a frequency of 1MHz"*, in Reference 9 pp.79-83.

(15) Shine R.J. et al. (1995), *"40W CW, TEM_{00}, DP Nd:YAG miniature slab laser"*, Opt. Lett. **20**, pp.459-461.

(16) Comaskey B.J. et al. (1992), *"High average power diode-pumped slab laser"*, IEEE J. Quantum Electron **28**, pp.992-996.

(17) Burnham R. et al. (1994), *"Diode-pumped solid-state lasers with kilowatt average power"*, in Reference 10 pp.489-498.

(18) Snyder J.L. et al. (1991), *"Fast diffraction limited cylindrical micro lenses"*, Appl. Opt. **30**, pp.2743-2747.

(19) Nighan W.L., (May 1995), *"Diode bars pump solid state laser crystals to high powers"*, Laser Focus World, pp.97-106.

(20) Spalding I.J. (20 June 1993), *"EU 213: Hipulse excimer laser project"*, BRITE/EUREKA European

Industrial Laser Forum, Munich.

(21) Osborne M.R. et al. (1994), *"High power operation of the Chirp II excimer laser"*, in Reference 10, pp.4-15.

(22) Scott S.J., (1994), *"Long-life 2KHz x-ray preionizer"*, in Reference 10, pp.16-24.

(23) Rebhan U. et al. (1994), *"Nova Tube: first excimer laser design for quasi-sealed-off operation"*, in Proceedings of GCL 10, Friedrichshafen, Germany, SPIE (Bellingham) Vol. **2502**, pp.426-432.

(24) Hall D.R. et al. (1992) *"New technology for industrial CO lasers"*, in Reference 9, pp.55-60.

(25) Yu G. et al. (1994) *"Compact high-efficiency CO laser at 1kW"* Appl. Phys. Lett. **65**, pp.2904-2906.

(26) Freeman G., (Dec 1993) Laser Ecosse Limited, private communication.

(27) Schellhorn M. & Bülow H.v, (1994) *"High power gas-dynamically cooled CO laser with unstable resonator"*, in Reference 23, pp.63-68.

(28) Kuribayashi S. et al. (1992) *"Current status of the high power CO laser program"*, in Reference 9, pp.51-54.

(29) Dymshits B.M. et al. (1994), *"CW 200kW supersonic CO laser"*, in Reference 10, pp.109-120. (Note, also, Golovin A.S. et al. (1995), *"eb sustained CW Cryogenic CO laser with subsonic gas flow"*, in the present proceedings.)

(30) Uehara M. et al. (1994) *"Recent studies of high power CO laser in room-temperature operation"*, in Reference 23, pp.38-43.

(31) Spalding I.J. et al. (July 1993) *"Industrial laser developments in the UK"*, AIAA Paper 93-3152, pp.1-8, Orlando, FL, USA.

(32) Schellhorn M. & Bülow H.v., (1994), *"CO laser deep-penetration welding - a comparative study to CO_2"*, in Reference 23, pp.664-669.

(33) Spalding I.J. et al. (1995), *"EUROLASER activities and EU113 achievements in particular"*, paper submitted to SPIE Proceedings of ILLA'95, Shatura, Moscow.

(34) Generalov N.A. et al. (1995) *"Industrial CO_2 lasers with high beam quality for cutting non-ferrous metals"*, submitted to SPIE Proceedings of ILLA'95, Shatura, Moscow Region. (See also Generalov N.A. et al. (1994), Pure. Appl. Opt. 3, pp.533-540.)

(35) Patel C.N.K. & Kerl R.J., (1964), *"Laser oscillation on $X^1 \sum^+$ vibration rotation and transitions of CO"* Appl. Phys. Lett. **5**, pp.81-83.

(36) Sato S. et al. (1994) *"Efficient room-temperature CO laser with high specific output"*, Optics. Lett. **19** pp.719.

(37) Spalding I.J. (1993) *"EU113: Industrial CO laser systems and their applications"*, European Industrial Laser Forum, Munich.

SPATIAL AND TEMPORAL SCALES OF ACTIVE MEDIUM INHOMOGENEITIES IN HIGH POWER GAS LASERS

V.L.MOSHKOV

Baltic State Technical University
St.Petersburg, Russia

Nomenclature

x,y,z,ξ,η	-coordinates
l	-geometrical path length
S	-area
v	-velosity
d	-diameter
τ	-time
ρ	-density
k	-specific heats ratio
N_e	-electron density
μ	-dynamic viscosity
G	-gas rate
α	-fuel aboundance coefficient
I	-intensity
W	-energy
k_0	-small signal gain
n	-refraction index
K	-Gladstone-Dale constant
L	-optical path length
n_e	-electron gas refraction index
λ	-wave legth
φ	-phase of the light wave
D	-phase dispersion
D_φ	-structural function of phasc distribution
Λ	-integral scale of the inhomogeneity
u	-wave function
A	-amplitude of the wave function
$B_\perp$	-transverse correlation function
γ	-coherence index
ρ_c	-coherence radius

R. Kossowsky et al. (eds.), High Power Lasers – Science and Engineering, 47–82.
© 1996 *Kluwer Academic Publishers. Printed in the Netherlands.*

Γ	-aberration factor
M	-magnification coefficient
δ	-interferention fringe displacement
e_0	-interferention fringe width
V	-contrast of the interferention pattern
ω	-spatial frequency
θ	-divergence angle
ε	-observation axis angle
St	-Strehl tatio
Re	-Reynolds number

1. Theoretical foundation

High spatial coherense and small angular divergence are the main properties of laser beam wich determine the possibility of focusing on a small target or energy transmission at great distances. The performance of high-power lasers in wich large active medium volumes or flow rates are used depends to a large extent upon the medium optical homogeneity and hence upon its gasdynamic uniformity.

Refraction of the gas laser active medium is less by several orders than any other. This fact decreases for a first look the pressing of problem to provide its high optical quality giving the possibility to concentrate efforts on looking for the ways to increase the output energy of systems. Nevertheless the gas laser as a thermal machine has rather low efficiency (no more than 10%) and a major portion of pumping energy releases as a heat in the cavity.

Therefore pumping power increase as an intensive way gives rise as a rule to nonuniformity of main gasdynamic parameters distribution (temperature, density and others) and in finally to phase aberrations of the laser beam. It is not so complicated to show the aberrations to reach the value of several wavelengths on very modest (no more than 1 meter) resonator pathlength, and strong exponential dependence of far field intensity upon laser beam wavefront deformations makes further pumping power growth senseless. Later it will be shown that the same reasons put the limit on development of the most attractive - extensive way i.e. resonator length increase or use of several power amplifiers in a sequence.

Way out of this situation is either organizing of the excitation process with minimal gas disturbances or application of effective output wavefront correction methods. It is evident that in both cases the more information about active medium disturbances, causes of their appearance, their spatial and temporal structure, dependence of their value on operational parameters and laser media composition are available the better the result will be.

In gas laser as in any other active medium is limited by plates that are parallel to resonator mirrors or output windows in case of amplifier.

Therefore optical path length variation proportional to phasevariation called phase inhomogeneity appears as a result of variation only refractive index:

$$\Delta L=\Delta(n\cdot l)=l\cdot\Delta n+n\cdot\Delta l=l\cdot\Delta n$$

Main dependences of refractive index on gasdynamic parameters in finally determine causes of active medium disturbances that is their gasdynamic subjects. Indeed the simple Gladstone-Dale low determines a number of gasdynamic phenomena being at the basis of inversion population creation in the gas lasers and at the same time giving rise to the active medium inhomogeneities. For instance: the fuel and oxidizer mixing process in the supersonic flow of CW Chemical Laser can lead to the following phasevariation:

$$\frac{\Delta L}{\lambda}=\frac{l}{\lambda}(n_{fuel}-n_{oxid})=\frac{l}{\lambda}(K_{fuel}\rho_{fuel}-K_{oxid}\rho_{oxid})=0.8$$

for $l=1m$, $\lambda=3\,\mu m$.

Shock wave due to 20 degrees angle interaction of neighbor oxidizer jets in this system gives:

$$\frac{\Delta L}{\lambda}=\frac{l}{\lambda}K\rho_1\left(\frac{\rho_2}{\rho_1}-1\right)=\frac{lK\rho_1}{\lambda}\left(\frac{\frac{k+1}{2}M^2Sin^2\beta}{1+\frac{k-1}{2}M^2Sin^2\beta}\right)=0.15$$

It is obvious that the same processes take place in GDL too.

For instance boundary layer appearance on the nozzle blade gives the phasevariation:

$$\frac{\Delta L}{\lambda}=\frac{l}{\lambda}K\rho_e\left(1-\frac{\rho}{\rho_e}\right)=0.35$$

for $l=1m$, $\lambda=10.6\,\mu m$,

The processes of inversion population creation in gas lasers are frequently accompanied by free electrons appearance in the medium.

According literature data [1]:

electric discharge excitation	$N_e\sim10^{10}\div10^{13}$ cm^{-3}
unequilibrum thermal ionization	$N_e\sim10^{8}\div10^{9}$ cm^{-3}
chemical ionization	$N_e\sim10^{12}\div10^{14}$ cm^{-3}
electron beam pumping	$N_e\sim10^{16}$ cm^{-3}

It is evident that the nonuniformity of electron density distribution in the cavity will inevitably lead to laser beam aberration if we take into account the following dependence:

$$n_e\text{-}1 = -\,4.46\ 10^{-14}\ N_e\ \lambda^2$$

The contribution of the free electron component into the active medium refraction in the e-beam pumped excimer laser gives:

$$\frac{\Delta L}{\lambda} = \frac{l}{\lambda}(n_e - 1) \approx 1$$

for l=1 m, λ=248 nm

Note that the role of free electron gas refraction in IR range increases and should be estimated each time.

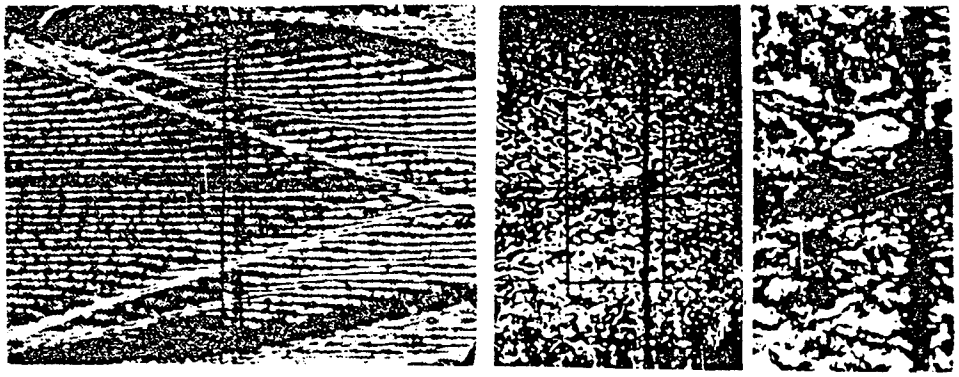
Let's further talk about inhomogeneities pattern, their spatial and temporal scales and about optical quality criteria. Inhomogeneities described above can be called "ordered". Flat chock waves, laminar boundary and mixing layers and so on are causes of them. In this case phasevariation is in direct proportion with geometrical pathlength of the beam. As a rule the dimensions of ordered inhomogeneities are comparable with an aperture size so that they are inhomogeneities of large scale. Light propagation through them is governed by scalar theory of diffraction.

However besides the disturbances determined (located) in the space and in general case in time in active medium of gas lasers random inhomogeneities may appear. Light propagation through them can be described by statistical lows. Sutton has shown phase aberrations to be in proportion with square root of the product of the geometrical path length and the characteristic scale length. For a first look with the laser size increase random inhomogeneities have a weak influence on the laser beam quality comparing with ordered ones because Λ is usually much less than l. However it is not always true as the random nonuniformities have a small scale unsteady pattern and are very difficult to correct. As a rule the spatial scale of random inhomogeneities is comparable with Frenehl's zone size.

Gas flow turbulence is one of the main gasdynamic processes leading to random inhomogeneities. Reynolds number $Re=\rho vl/\mu$ is the main criterion of their appearance:

Gasdynamic laser	$Re \sim 1.5\ 10^5$
Excimer laser	$Re \sim 10^6$
CO_2 TEA laser	$Re \sim 1.5\ 10^5$

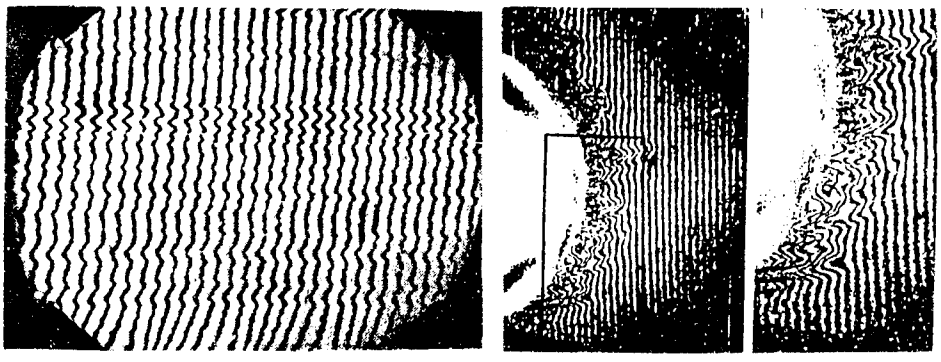
The example of GDL active medium interferograms at laminar and turbulent flow conditions are shown in the Figure1.



a *b*

Figure 1. GDL active medium interferograms without (a) and with (b) turbulence in the flow.

Mode medium interaction process (or stimulated enthalpian scattering in Russian publications [2,3]) is the other important cause of the random inhomogeneities appearance in high power gas lasers active media. This effect is founded on the dependence of main kinetic processes rate (for instance rate of V-T relaxation in CO_2-laser or chemical reaction rate in Photodissotiated Iodine laser) upon local value of the stimulated radiation intensity in the cavity. This phenomenon can be met in pulsed lasers having a high power density level (Figure2).



a *b*

Figure 2. Interferograms of the MMI process in the CO_2 TEA (a) and PDIL (b) lasers.

To compare different laser systems active media complex criteria of its homogeneity are worked out. Maximal phase defect on the output aperture is the first and simplest of them:

$$\Delta\varphi_{max}=\varphi_{max}-\varphi_{min},$$

The following values are directly connected with him:

$$\Delta L_{max},\ \frac{\Delta\rho_{\max}}{\rho},\ \frac{\Delta n_{\max}}{n-1}$$

Extreme ease of estimation necessary for express analysis is the main positive feature of this criterion, the fact that spatial structure of the disturbances is not taken into account at all - is negative one.

The appearance of root-mean-square phase variation was first attempt to account spatial distribution of the active medium nonuniformities:

$$\Delta\varphi_{rms}=\sqrt{\sum_{i=1}^{n}\frac{(\varphi_i-\bar{\varphi})^2}{n}},\ \text{where}\ \bar{\varphi}=\sum_{i=1}^{n}\frac{\varphi_i}{n}$$

Phase dispersion is directly connected with this value:

$$D=\Delta\varphi^2{}_{rms}$$

Sutton has shown [4] clear connection between $\Delta\varphi_{rms}$ and gasdynamic characteristics of medium for both ordered and random cases:

$$\Delta\varphi_{rms}=\frac{2\pi}{\lambda}lK\frac{\rho}{\rho_0}\left(\frac{\Delta\rho}{\rho}\right)_{rms}\ -\text{for ordered,}$$

$$\Delta\varphi_{rms}=\frac{2\pi}{\lambda}K\sqrt{l\Lambda}\frac{\rho}{\rho_0}\left(\frac{\Delta\rho}{\rho}\right)_{rms}\ -\text{for random,}$$

but it is very difficult to find the physical meaning of these values. Nevertheless these criteria are in wide use. For example in terms of root-mean-square values the criterion of GDL optical homogeneity was figured out [5] (ordered pattern of disturbances is assumed):

$$\Delta\rho_{rms}l\ \le 3.5\cdot10^{-4}\,g/cm^2\ .$$

So frequent use of *rms* phase variation can be explained by existence of simple approximation formula connecting $\Delta\varphi_{rms}$ with other important optical

criterion - Strehl ratio wich has clear physical sense. It expresses a maximum relative far field intensity of wavefront disturbed by medium inhomogeneities and difracted on the outcoupling aperture[6]

$$St = \max_{\{x,y\}} \left\{ \frac{I(x,y)}{I_0} \right\}$$

Strehl ratio is always less than unity as flat wavefront intensity is chosen as a norm. Scalar theory of diffraction gives the following expression if the light wave amplitude is assumed to be constant:

$$St = \max_{\{x,y\}} \left\{ \frac{1}{S^2} \left| \int_S \int exp\left[-i(\varphi(\xi,\eta) + \frac{2\pi}{\lambda z}(x\xi + y\eta)) \right] d\xi \cdot d\eta \right|^2 \right\}$$

Simple relationship between *rms* phase variation or dispersion can be written as:

$$St \approx exp(-\Delta\varphi^2{}_{rms}) = exp(-D)$$

The estimation error of last formula is about 15% when $\Delta\varphi_{rms}$ exceeds 1 rad. In several publications more complicated formula can be found giving better results (less than 5%) [7]:

$$St \approx \frac{1 + cos(1.75\Delta\varphi_{rms})}{2} - \frac{sin^2(1.75\Delta\varphi_{rms})}{12}.$$

Consider an example of Strehl ratio application [8]. Assume that one cascade of laser amplifier has following parameters: k, l, D_1. The near field intensity of incident beam I_0 after one pass amplification becomes

$$I_1 = I_0 exp(k_0 l)$$

and far field intensity is proportional to Strehl ratio:

$$I_{far\,field\,1} \sim I_1 Sh_1 = I_0 exp(k_0 l - D_1)$$

Try to increase the far field intensity with use of n similar cascades in a sequence. The efficiency of amplification can be characterized by function of relative intensity

$$\bar{I} = \frac{I_{farfield\,n}}{I_{farfield\,1}}$$

It's no so complicated to show this function to depend on inhomogeneities pattern and to have a maximum in case of ordered one. Indeed :

$$I_n = I_0 \exp(n\, l\, k_0)$$

$$I_{far\ field\ n} = I_n\, Sh_n = I_0 \exp(k_0 ln - D_n)$$

$$\left.\begin{array}{l} D_n = n^2 D_1 \text{ - for ordered} \\ D_n = nD_1 \text{ - for random} \end{array}\right\}$$

$$\text{then } \bar{I} = \exp\left[(n-1)(k_0 l - D_1(n+1)\right],\ n_{opt} = \frac{k_0}{2\left\{\frac{D_1}{l}\right\}} \text{ - for ordered}$$

In other case extremum doesn't exist and random inhomogeneities only decrease the effective value of gain k_0.

$$\bar{I} = \exp\left[(n-1)(k_0 l - D_1)\right]$$

These conclusions are correct for linear amplification governed by Bouguer's low. In case of active medium saturation the exponential part is relatively short and linear growth of the near field intensity with an amplifier length can be accepted. The same reasons give following relations for efficiency.

$$\bar{I} = n \cdot \exp(-D_1(n^2 - 1)),\ n_{opt} = \frac{1}{\sqrt{2D_1}} \text{ - ordered}$$

$$\bar{I} = n \cdot \exp(-D_1(n - 1)),\ n_{opt} = \frac{1}{D_1} \text{ - random}$$

It is interesting that in case of saturation the optimal number of cascades doesn't depend on gain properties of active medium but only on its optical uniformity [Figure3].

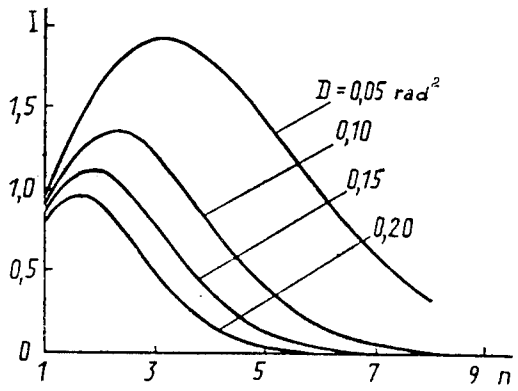


Figure3. Dependence of relative farfield intensity upon number of power amplifiers.
(regular disturbances , saturated amplification)

A lot of authors connect other important characteristic of the laser beam with Strehl ratio - relative focal spot size [9]:

$$\frac{\theta}{\theta_{dif}} \approx \sqrt{\frac{I_0}{I}} = St^{-1/2}$$

However precise calculations according scalar diffraction theory formula give significantly different results (Figure4).

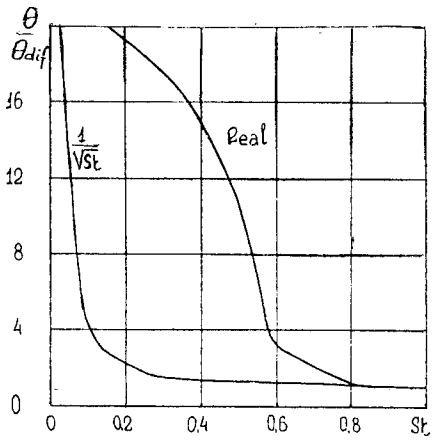


Figure 4. Focal spot size versus Strehl ratio.

The Strehl ratio is widespread, popular and useful criterion, but by definition it doesn't take into account the amplitude of light wave. This fact is some limitation for use the Strehl ratio to characterize strongly inhomogeneious active media.

Proposed by Anan'ev [14] aberration factor is free of last disadvantage.

$$\Gamma = \frac{|\bar{u}|^2}{|\overline{u^2}|} = \left|\frac{1}{S}\int\limits_S \int u(\xi,\eta)\,d\xi\,d\eta\right|^2 \times \left[\frac{1}{S}\int\limits_S \int [u(\xi,\eta)]^2\,d\xi\,d\eta\right]^{-1}$$

The symbol "—" means the averaging around the aperture. This value has a clear physical meaning - this is axial luminous intensity of real source of light normalized to the axial luminous intensity of ideal one having constant amplitude and phase distribution (or constant wavefunction). Obviously aberration factor characterizes both phase and amplitude aberrations. Besides this aberration factor is defined as not maximal but axial luminous intensity. If the aberration takes place these values may uncoincide with each other. The estimation shows the following: if wave function has constant phase but amplitude distribution is equally probable from minimal to maximal value aberration factor is 0.89. In opposite case of constant amplitude when wavefront deformation as low as one wavelength Γ croutially drops (until 0.08). This reason strongly supports the fact that amplitude aberrations weakly affect the luminous intensity. It means that Strehl ratio may be applied without serious limitations.

Optical homogeneity criteria discussed above are used as a rule to describe the light propagation through the large scale inhomogeneities appearance of wich in the active medium results in decreasing of centerline intensity and increasing of second diffraction orders. Small scale random disturbance lead to the wide angle scattering that can be described by "plato" on the far field intensity distribution diagram [10]. Small scale random inhomogeneities became serious limitation in obtaining of high intensities for visible and UV lasers. They can lead to saturation or even decay of intensity with wavelength decreasing instead of theoretically predicted growth [10]. Such kind of disturbances has a negative influence on the laser lightwave propagation making whorse one of main its parameters - spatial coherence.

Define a transverse correlation function of electromagnetic field as:

$$B_\perp(\bar{r}_1,\bar{r}_2,z,t) = \langle u(\bar{r}_1,z,t)\,u^*(\bar{r}_2,z,t)\rangle$$

where $\langle\ \rangle$ mean averaging with account of distribution function [11]. Then coherence index can be expressed as

$$\gamma(\bar{r}_1,\bar{r}_2,z,t)=\frac{B_\perp(\bar{r}_1,\bar{r}_2,z,t)}{\sqrt{I(\bar{r}_1,z,t)I(\bar{r}_2,z,t)}}$$

It is not difficult to see the index to always be less than unity. As a characteristic scale of length it is useful to choose coherence radius according the relations:

$$\bar{s}=\bar{r}_1-\bar{r}_2=\bar{\rho}_c:$$
$$\left|\gamma(\bar{\rho}_c)\right|=e^{-1}$$

Having supposed the phase aberration to mainly affect the laser radiation structure it is easy to show the following [12]:

$$\left|\gamma(s)\right|=exp\left[-\frac{2\pi^2}{\lambda}D_\varphi(s)\right],$$

where D_φ is spatial structural function of random phase distribution. Last values have a clear physical meaning - the scattered part of beam energy and random phase distribution dispersion:

$$1-\left|\gamma(s)\right|\xrightarrow[s\gg\rho_c]{}\frac{W_{scat}}{W},$$
$$\frac{2\pi^2}{\lambda}D_\varphi(s)\xrightarrow[s\gg\rho_c]{}\Delta\varphi_{rms}^2$$

After comparison with Strehl ratio formula the connection between refraction and light scattering becomes evident. Coherence index and Strehl ratio have the same properties and dependences.

The simple instance [13] clearly shows the importance of keeping of high laser beam coherence value. Assume the absolutely coherent wavefront to be focused by positive lens with aperture d. As the field is concentrated coherently we have following value of the intensity:

$$u\sim Ad^2,\ I_0\sim u^2\sim A^2d^4$$

Note that last is true only when coherence radius is sufficiently large: $\rho_c > d$. In case of small scale random disturbances appearance spatial coherence decays so that coherence radius becomes less than lens diameter d. This means that aperture is divided into coherent parts having an areas proportional to ρ_c^2. In the limits of these parts coherent concentration of

energy takes place but they aren`t coherent between each other and only energetically additive:

$$I \sim I_c \frac{d^2}{\rho_c^2} \sim A^2 \rho_c^2 d^2 = I_0 \left[\frac{\rho_c}{d}\right]^2$$

This means that focal spot intensity grows or drops as a square of coherence radius. For example if d=100 mm, ρ_c=10 mm, then I=0.01I_0, when I_0 is maximally possible value.

It is obvious that described variants of light wave interaction with disturbances having different scales are correct for the laser amplifier. Light propagation through the inhomogeneous medium in the resonator cavity is a separate complicated problem. In case of large scale inhomogeneities method of aberration coefficients proposed by Anan`ev [14] is very useful. Their values show in how many times definite aberration order manifests itself in the resonator stronger than in the one pass amplifier:

$\varphi(x) = \sum_{k=0}^{\infty} \varphi_k x^k$ –one pass wave front aberrations.

$\Phi(x) = \frac{2\pi}{\lambda} l \sum_{k=1}^{\infty} \varphi_k \left[1 + \frac{1}{k+1} \frac{M^{k+1} - 1}{(M-1)M^k}\right] x^k = \frac{2\pi}{\lambda} l \sum_{k=1}^{\infty} \varphi_k \alpha_k x^k$ - wave front aberrations behind the outcoupling mirror of telescopic unstable resonator,

α_k - aberration coeffitients.

By the way unstable telescopic resonator was shown to have a minimal sensitivity to the active medium inhomogeneities essentially with magnification coefficient increasing (Figure 5).

With appearance of small scale disturbances the problem may be solved taking into account that the part of the laser beam energy gone at each pass to the scattered component is equal to the random phase dispersion [15]. The part of energy remaining in the diffraction limited component can be estimated according the relation:

$$\delta_{dif} = \frac{W_{dif}}{W} \approx exp\left[-\Delta\varphi_{rms}^2 \ln\frac{\theta_{scat}}{\theta_{dif}} / \ln M\right] =$$

$$exp\left[-\Delta\varphi_{rms}^2 \ln\frac{d}{\Lambda} / \ln M\right]$$

Remember that for one pass amplifier this value is equal to coherence index magnitude:

$$\delta_{dif}^{1} = \frac{W_{dif}^{1}}{W} \approx |\gamma| = exp(-\Delta\varphi_{rms}^{2})$$

For the conditions of CWCL:

$$\Delta\varphi_{rms}^{2} = 0.2 rad^{2}, M = 2, d/\Lambda = 40, l = 1m$$

$$\delta_{dif}^{1} = 0.82 \quad \text{meanwhile} \quad \delta_{dif} = 0.34$$

that shows a significant role of small scale inhomogeneities in increasing of angular divergence. After last reasons it becomes evident that in case of both large scale disturbances and small scale ones for estimation of the laser beam angular divergence the information about one pass beam phase distribution is necessary.

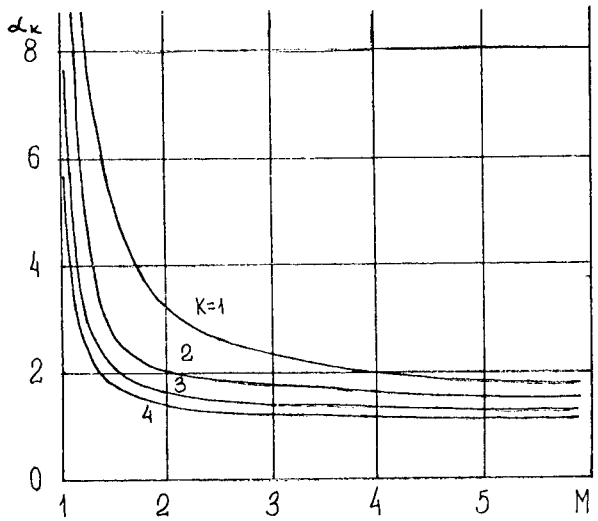


Figure 5. Dependence of the aberration coefficients upon resonator magnification.

Consider the temporal scales of the disturbances after discussion two important details.

First is concerned with the results of work of Sutton, Knight and others [16] who have investigated the dependence of diffraction limited part of the light beam energy upon turbulent medium parameters (intensity and scale of the turbulence). Karman's spectrum of turbulence was assumed. Significant

scattering was shown to take place even at modest d to Λ relations (from 10 to 100) that is more than Fresnel's zone size.

Second remark touches on appearance of the transverse periodic inhomogeneities in the active medium. The problem of monochromatic wave propagation through such medium is solved analytically in [17] and angular divergence of the beam passed through it is shown to have inmonotonous periodic dependence on pathlength (Figure 6).

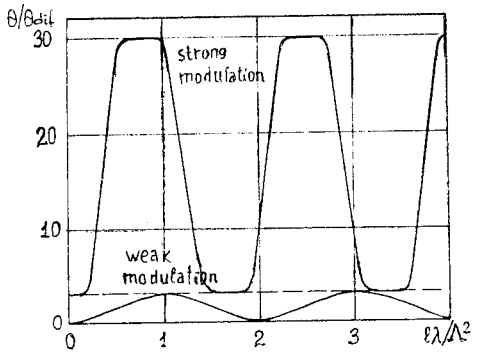


Figure 6. Dependence of the angular divergence of the beam passed through the transverse periodic inhomogeneities on the geometrical pathlength.

This effect of selfcompesation must be taken into account when carrying out the wavefront diagnostics by means of testing beam. Periodic disturbances for wich pathlength l exceeds the value Λ^2/λ can manifest itself weaker or cannot be found out at all.

The wavefront behavior in time is not less important than in the space because every laser beam interaction (or investigation) has a finite duration. Therefore it is naturally to find out the temporal scales of active medium inhomogeneities. Time of existence and time of changing seem to be the main characteristics.

Time of existence is the period during wich some fixed value of wavefront disturbance takes place in the aperture. Time of changing is the period during wich the disturbance increases (or decreases) by prescribed value from its average one. It is evident that τ_{ex} and τ_{ch} tends to infinity for steady state inhomogeneities.

When unsteady pattern is a result of inhomogeneity movement along the medium or with the medium following relations are correct:

$$\tau_{ex} \sim \frac{d}{v}, \tau_{ch} \sim \frac{\Lambda}{v}$$

where v is an absolute velocity of disturbance. It is not so difficult to find out that in this case the relation:

$$\frac{\tau_{ch}}{\tau_{pulse}} = \frac{\Lambda}{v\tau_{pulse}}$$

expresses well-known similarity criterion of unsteady gasdynamic processes - Strouchal's number:

$$Sh = \frac{l}{v\tau}$$

In general case the value τ_{ch}/τ_{pulse} is a profound generalization of later that is measure of relative unsteadiness of two physical processes - development of the laser generation and rise of the disturbances in active medium.

Comparison of the existence and changing times with others important characteristics of laser processes allows to lay down physically - founded temporal scales.

Inhomogeneities for wich the relation $\tau_{ch}/\tau_{pulse} >> 1$ is true are typical for pulse-periodic lasers having a short pulse duration (less than 1 microsecond) - for instance - excimer lasers. High energy and short pumping time gives rise to intensive gasdynamic discontinuities in the active medium that move with a gas and a reflect at the cavity walls. The values of existence and changing times are relatively high. For example, for excimer mixture of KrF laser the existence time of acoustic wave at three times reflection is about 3 milliseconds. Thanks to low value of pulse duration time (τ_{pulse} - several nanoseconds) and finite rate of energy transmission into the transitional degrees of freedom the first pulse divergence angle rising is impossible. However the time till the moment of second pulse beginning has a time of inhomogeneity existence as a lower limit. Violence of the condition that

$$T_{rep} > \tau_{ex}$$

will inevitably lead to the divergence angle increase of second pulse. So that the inhomogeneities for wich the relation is true limit the pulse repetition rate. Note the paradoxal fact that inhomogeneities of such kind cannot be strictly defined as unsteady ones because during the pulse time no changes take place.

With increasing of pulse duration and at the same time decreasing of existence and changing times there comes a point described by relationship

$\tau_{ch}/\tau_{pulse}<1$. Formally the appearance of unsteady disturbances in CW lasers can be assigned to this case. For pulsed laser last unequality means that the inhomogeneities have a time to appear and to change their distribution during generation pulse. It is obvious that the angular divergence is a function of time and becomes as a rule worse. Therefore it is reasonable to set up the question about the pulse duration determination when keeping the Strehl ratio on the prescribed level (not less 0.8) (Figure7).

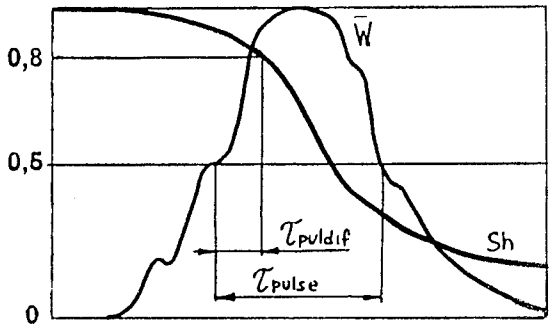


Figure 7. Limitation of the effective pulse duration due to decreasing of the medium optical quality.

The MMI process in the PDIL and TEA CO_2 EDL is typical example of such kind inhomogeneities.

It is nessesary to note that the information about spatial and temporal scales of active media inhomogeneities is very important to choose the adequate low cost method of output wavefront correction. Causes of inhomogeneities spatial and temporal scales considered above can form the basis of their classification. One of such attempts is shown in the Table 1.

2. Application to gasdynamics

Part two is concerned to the only purpose - to practically prove the classification i.e. to find out different kind disturbances of in real high power gas lasers.

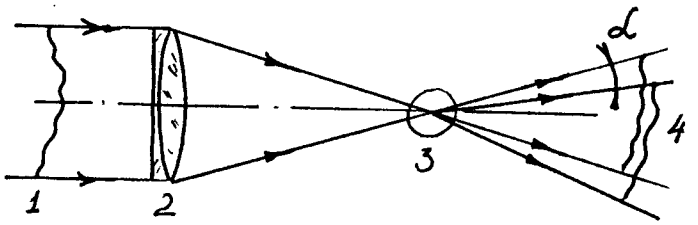
Firstly it is necessary to discuss the methods of diagnostics.

Shear interferometry is especially designed to investigate the large scale phase nonuniformities and is successfully applied in the gasdynamic experiments. The fact that wavefronts shifted to some distance keep the spatial coherence and can be in mutual interference is in the basis of this

TABLE 1

Active medium inhomogeneities of the high power gas lasers					
steady - state $\tau_{exist},\ \tau_{change} \to \infty$		unsteady $\tau_{change} < \tau_{exist} < \infty$			
Large scale $\Lambda \sim d$	Small scale $\Lambda \sim \sqrt{(d\lambda)} << d$	Large scale $\Lambda \sim d$		Small scale $\Lambda \sim \sqrt{(d\lambda)} << d$	
		$\tau_{ex}/\tau_{puls} > \tau_{ch}/\tau_{puls} >> 1$	$\tau_{ch}/\tau_{puls} < 1$	$\tau_{ex}/\tau_{puls} > \tau_{ch}/\tau_{puls} >> 1$	$\tau_{ch}/\tau_{puls} < 1$
Causes					
Shock waves, laminar boundary layers, mixing layers in CWCL, EDL, GDL.	Jets interaction in screen-nozzles of GDL, fuel injection through discreet holes in CWCL, cathode plates splitting in EDL.	Shock waves due to pulse pumping in Excimer lasers, pulse EDL.	Photodissotiation wave in PDIL	Turbulence in TEA EDL, Excimer lasers	Turbulence in CW-lasers, MMI process in TEA CO_2, PDIL
Consequences					
Shifting of the far field intensity maximum. Decreasing of the Strehl ratio due to refraction	Strehl ratio decreasing due to scattering.	Strehl ratio decreasing due to refraction. Repetition rate limiting.	Maximum of the far field intensity jitter. Strehl ratio decreasing due to refraction.	Strehl ratio decreasing due to refraction. Spatial coherence decreasing	Strehl decreasing due to scattering. Spatial coherence decreasing. Effective pulse duration decreasing.
Correction					
Adaptive optics, retromirrors, predicted resonator disalignment	Resonator axis angle optimisation, retromirrors, Fourier-correctors.	Application of the accoustic moufflers Geometry of pumping optimisation. Laser medium composition optimisation.	Wave front conjugation	Gas dynamic duct optimisation. Wave-front conjugation.	Wave front conjugation. Gas dynamic duct optimisation. Laser medium composition optimisation.

method. The wavefronts are obtained as a rule from that to be measured by means of angular rotation nearby the focal point (Figure8).



1- wavefront under test 3 - shear interferometer
2 - lens 4 - interferention pattern

Figure8. Principle of shear interferention pattern obtaining.

All details of the method are described in the literature, for instance "Optical shop testing" by Malacara [18] and especially in the articles of V.Shechtman [19] that became classical in our country. Small dimensions and weight of shear interferometer, possibility of investigation of large fields limited only by main objective size and extreme vibrostability are beneficial advantages of the method making it very competitive among others.

Principle of shear interferention pattern obtaining determines main relationships of treatment:

$$\varphi(x+s) = \varphi(x) + 2\pi \frac{\delta(x+s)}{e_0(x+s)}$$

$$\varphi(n \cdot s) = 2\pi \sum_{i=1}^{n} \frac{\delta(i \cdot s)}{e_o(i \cdot s)}$$

In addition to this shear interferention gives an opportunity to find Fourier components without wavefront reconstruction [20]:

$$\text{if} \quad \phi(\omega) = \frac{1}{2\pi} \int_{-\infty}^{+\infty} \varphi(x) e^{-i\omega x} dx$$

$$\Delta(\omega) = \frac{1}{2\pi} \int_{-\infty}^{+\infty} \delta(x) e^{-i\omega x} dx \quad \text{then}$$

$$\Delta(\omega) = \phi(\omega)\left[1 - e^{-i\omega s}\right] \quad \text{where} \quad \omega = \frac{2\pi}{\Lambda}$$

At last the shear interferention fringe contrast is directly equal to coherence index [21]

$$V = \frac{I_{max} - I_{min}}{I_{max} + I_{min}} = |\gamma(s)|$$

The fact allows to use the method for investigation of random inhomogeneities.

The optical quality diagnostics of large scale gas lasers are of definite interest because the structure of active media disturbances in them may differ in comparison with that occurring in small installations. But the active medium of the high power gas laser is very difficult object for experimental study and in each particular case the careful adaptation of well- known diagnostic method is necessary. For example if the active medium under test has a high level of population inversion the optical elements must be protected against superluminescence radiation by spectrally selective filters and aperture diafragms or else thermal stresses due to its absorbtion leads to aberrations wich amount to approximately 10 times the values being measured (Figure9).

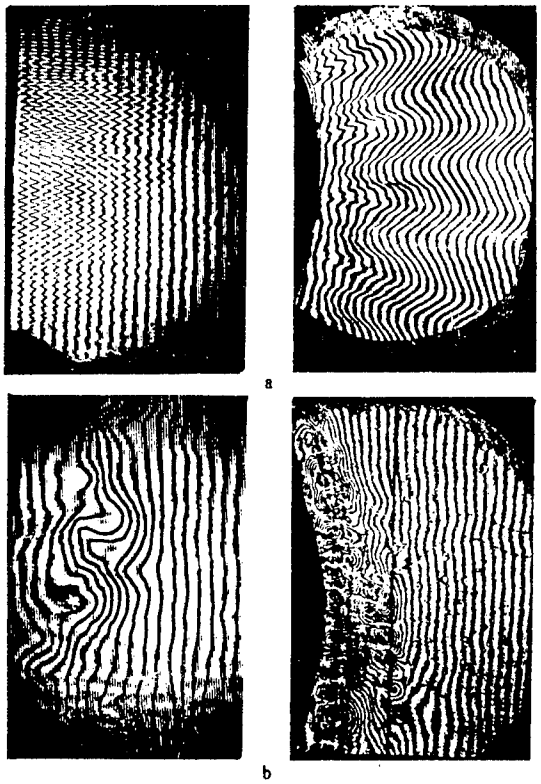


Figure9. Comparison of CWCL flowfield interferograms recorded with (a) and without (b) the application of spectrally selective optics.

This picture shows the comparison of CW Chemical laser flowfield interferograms with and without the taking a special care of optics protection.

The focal spot method [22] is designed for direct measurement of scattered part of probe beam energy that has passed through turbulent flow (Figure10).

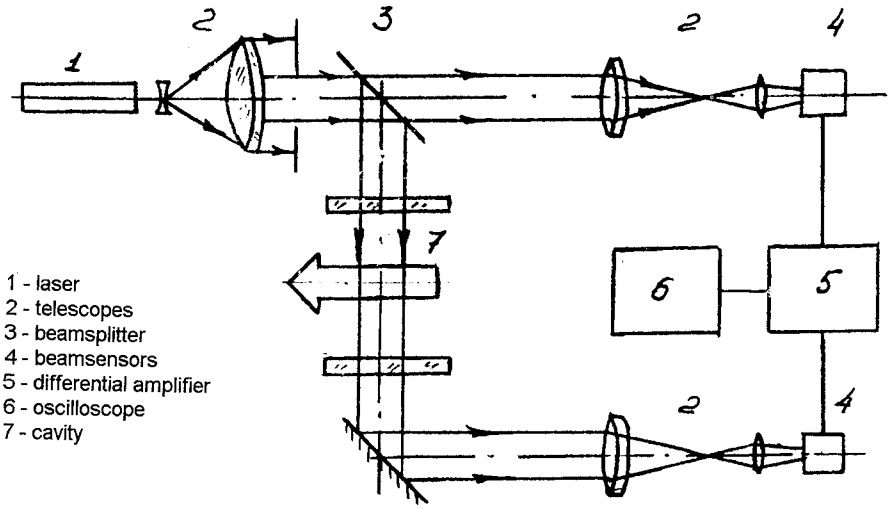


Figure10. Optical layout of the focal spot method.

Usually in such a case broad aperture beam is used that is probe beam has the same dimension as the aperture of the laser being studied. This gives the possibility to answer questions about the influence of the magnitude of the total sum density inhomogeneity in a cavity on laser output radiation quality. The detailed study of the gas flow structure demands a certain spatial resolution in the measurements. Therefore small size probe beams were used. Their diameter must simultaneously be larger than the characteristic scale of turbulence to provide representative data smoothing and smaller than scale size required for change of averaged parameters.

In this case the results obtained will reflect correctly the phase change by internal turbulent flow structure development.

Gasdynamic lasers.

Active medium optical quality of GDL depends to a large extent upon the way of supersonic flow organizing hence upon nozzle bank design. To understand the peculiarities of supersonic flow of active medium produced by both blade nozzle banks and screen nozzles was the main goal of the

investigation. The interferometric measurements shown the homogeneity of GDL media behind screen nozzles to depend upon observation axis angle. The curve of Strehl ratio versus angle in Figure11 has a maximum near 5 degrees for the hexagonal screen nozzle structure.

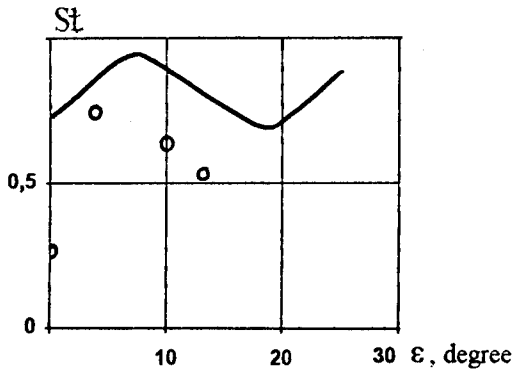


Figure11 Dependenece of the optical homogeneity of the GDL active medium behind screen nozzles on the observation axis angle.

This experimentally obtained fact is in close agreement with results of numerical simulation of the spatial structure of shock waves and wakes downstream of the nozzle bank exit plane [23]. Using this integral compensation of transverse periodic aberration by means of optimal nozzle block orientation allowed us to increase the Strehl ratio number by more than a factor 3.

Positive features of screen nozzles such as small scale mixing, regular structure and absence of vibration make them able to provide high optical homogeneity in the laser medium. Moreover the turbulent scales of turbulent flow that develop at small distances downstream of the screen nozzle banks are appreciably less than the turbulent scale in freely developing wakes behind blade nozzle banks. This fact shown by the focal spot measurements may be one of the most important advantages of the screen nozzles. Indeed the dependence of scattered part of probe beam ΔI has a decreasing pattern that may be explained by decrease of intensity of turbulent density pulses. (Figure 12) Quite different dependencies for ΔI have been obtained for blade nozzle banks. The growth of ΔI with increasing the distance x takes place due to turbulent scale size Λ growth while the turbulent pulse density keeps the constant value in this case.

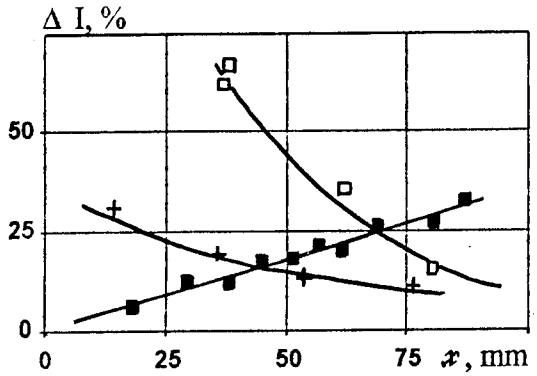


Figure12 Dependence of scattered part of probe beam on the distance behind a blade nozzle bank (■-P_0=2.4Mpa) and a screen nozzles (□-ε = 0^0, +-ε=13^0, P_0=2.4Mpa)

An increase in nozzle blade height must also increase the static and dynamical deformations of the blades hence causing turbulent pulsations to appear in the gas flow especially since the Reynolds' numbers are close to critical value (*Re* - 10^5). The random unsteady character can be revealed using ultrashort exposures (Figure13).

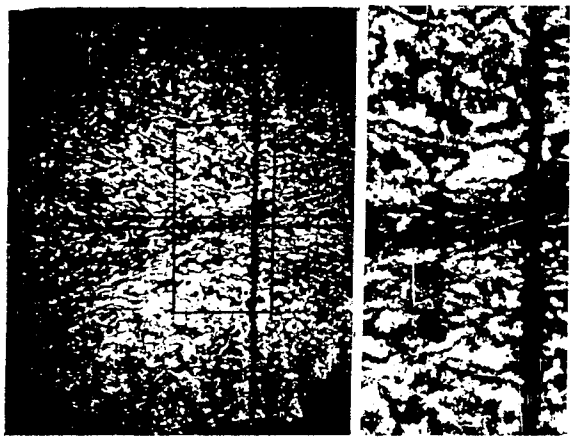


Figure13 Large scale GDL flow field interferogram recorded with 3 10^{-8} sec exposure.

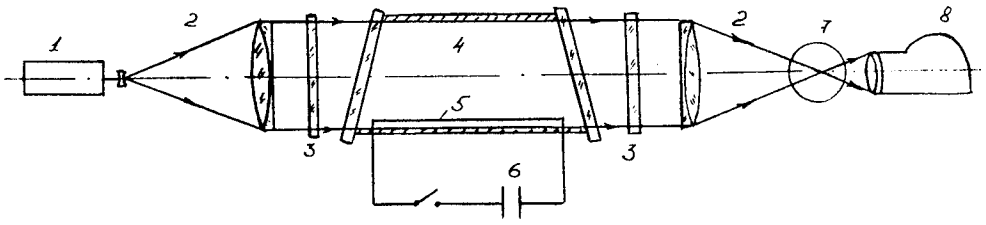
This picture shows the large scale GDL flow field interferogram recorded with thirty nanoseconds exposure time allowing to "freeze" the turbulent structure of supersonic flow having a Mach number 6.

Pulsed lasers.

Physical processes underlying the creation of a population inversion in a pulsed photodissotiated iodine laser and KrF excimer laser pumped by high energy electron beam specify an unstable pattern of active medium inhomogeneities.

But the PDIL is a very difficult object for optical investigations because of extremely high level of pumping light intensity, short pulse duration and necessity of carrying out the measurements through the resonator during the laser generation. The wave length =1.315 microns being in the transmittance range of glass optics and generation energy reaching several hundred joules should be also taken into account.

Experimental installation (Figure14) involves the cylindrical cuvette 700 millimeters length and 100 millimeter light diameter filled with the working gas mixture.



1. laser
2. telescopes
3. resonator mirrors
4. cavity
5. explosive wire
6. capacity 20μF, 50 kV
7. shear interferometer
8. fast speed rotating mirror camera

Conditions

λ=1.314 μm

$T_{equiv.bl.body}$=30,000° K

τ_{ex}~15÷25 μs

τ_{ch}~1÷2 μs

Λ~0.2÷0.5 mm

$\frac{\tau_{ch}}{\tau_{pulse}} < 1$

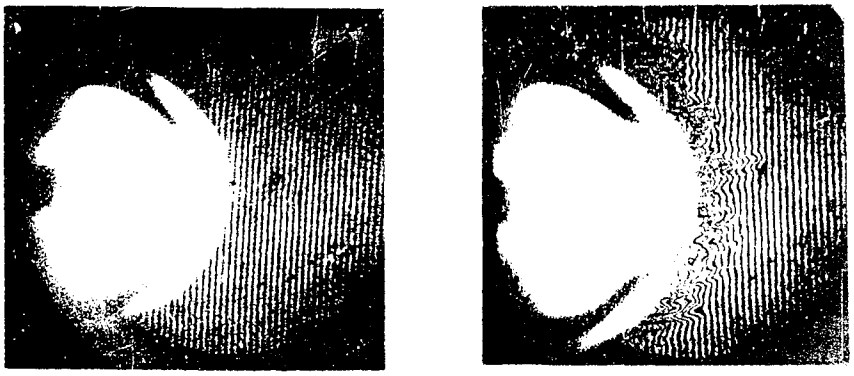
Figure14. PDIL Experimental installation layout and conditions of the tests.

The pumping is performed by the light of open discharge that is obtained by means of explosive tungsten wire located near the cuvette wall.

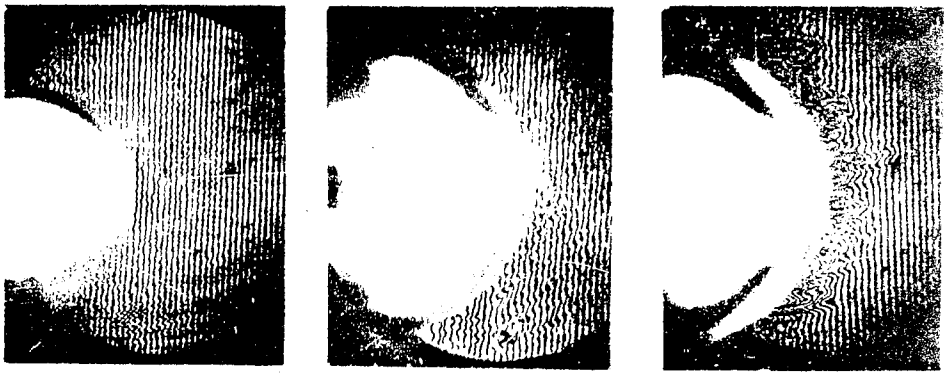
The active area has a shape of semimoon and is separated from the expanding plasma by cylindrical shock wave. The duration of the process is about 30-40 microseconds. Argon laser is used as a testing beam source. The recording of Shear interferograms obtained with four mirror Zabelin's device is performed with high speed rotating mirror camera, providing 75000 turns per a minute. Time resolution is 2 microseconds per a frame. The example of the sequence of interferograms is shown in the Figure15



Development of active medium nonuniformities



Laser resonator is not aligned (a), is aligned (b)



R_1-I R_2-I R_3-I

Dependence on working medium composition

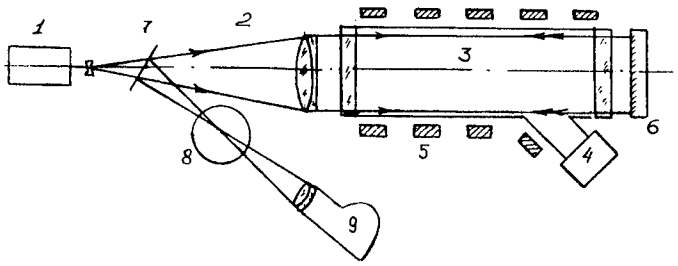
Figure15 Interferograms of MMI process in the PDIL.

Comparison of active medium interferograms recorded with and without the resonator alignment proves the fact that MMI process is a cause of inhomogeneities observed.

Data obtained in these experiments allow to make a conclusion about value of spatial and temporal scales of disturbances. Characteristic spatial scale Λ is in the range 0.2-0.5 millimeter, maximal phase defect 0.1-0.15 λ, existence time no more than 25 microseconds. Changing time about 2 microseconds. So that the inhomogeneities of such kind are essentially unsteady and the relation $\tau_{ch}/\tau_{pulse}<1$ is true in this case. This means that these disturbances are formed and their distribution is changed during the pulse generation.

The dependence of the disturbances magnitude found out in the tests allows to hope for choose of the optimal mixture composition for wich the MMI effect will manifest yourself as weakly as possible.

Completely different gasdynamic situation takes place in the Excimer laser pumped by high energy electron beam. The experimental installation with λ-shaped configuration of e-beam injection and magnetic orientation system is shown in the Figure16.



1. laser
2. telescope
3. cavity
4. e-beam source
5. magnetic orientation system
6. back mirror
7. beam splitter
8. shear interferometer
9. rotating mirror camera

Conditions
λ=248 nm
$E_{el.\ beam}$ = 0.5 MeV
τ_{pulse}~50 ns
τ_{exist}~500 μs > D/a = 100μs

Figure16. EL-experimental installation and conditions of the tests.

Optical registration part is the same as in previous case; e-beam duration is no more than 50 nanoseconds. Interferogram of the inhomogeneities development process in the excimer mixture at the pressure one atmosphere and in its separate components at the corresponding partial pressures are presented in Figure17 and show the appearance of significant disturbances as a result of e -beam interaction with the gas under test.

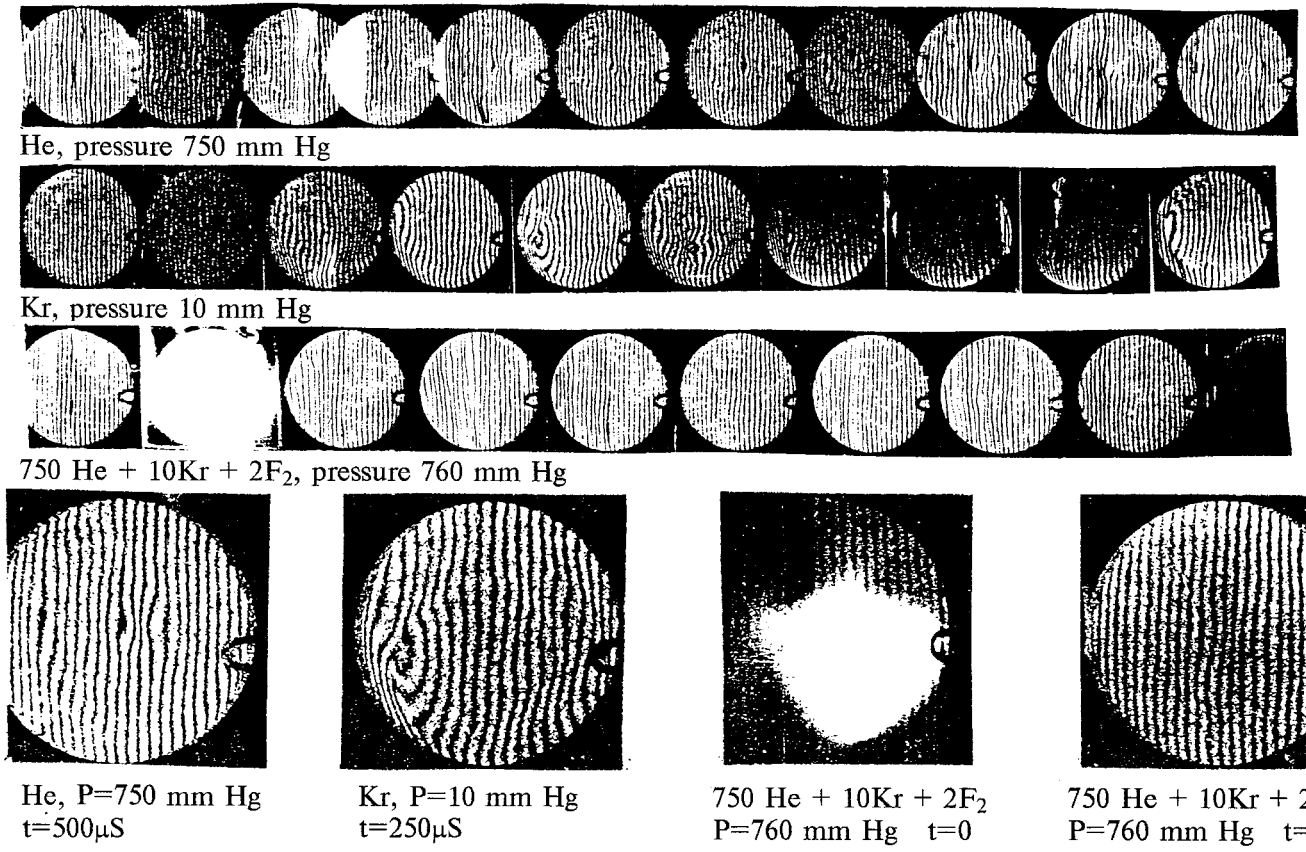


Figure 17. Gasdynamic disturbances appearing in the excimere mixture and its components due to interaction with electron beam.

Dependence of Strehl ratio as an integral optical quality criterion of the medium upon the time elapsed after e-beam injection in the case of full excimer mixture (Figure 18) means that the medium has low homogeneity even after 0.5 milliseconds after the action.Note that existence time is much more than characteristic gasdynamic time $d/a \sim 0.1$ milliseconds that is a consequence of repeated reflections.

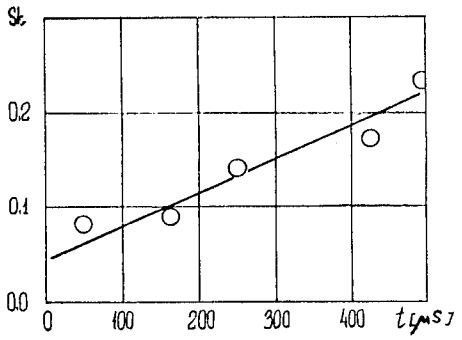


Figure 18. Dependence of Srehl ratio upon time after e-beam pulse.

A marked decreasing of disturbances value in full excimer mixture comparing with that in its separate components requires the further investigation and may be explained by presence of very complicated physico-chemical processes at electron beam interaction with a gas.

CW Chemical lasers

The gas flow in CW Chemical lasers is characterized by a modest Reynolds' numbers ($Re \sim 10^3$) and contains all the features typical for supersonic motion of a viscous gas - shock waves due to jet interactions, large boundary layers and others. The flowfield structure is also complicated by both the mixing process of fuel and oxidizer that have different thermodynamic and optical properties and by abundant heat generation as a result of chemical reaction. These are the phenomena that determine the optical homogeneity of the CWCL active medium.

The structure of disturbances depends on the organization of the mixing process, and the search for an optimal hydrogen injection method is one of the important technical problems. Therefore the flows formed by different kinds of mixing schemes have been investigated. The major configurations will be discussed.

Figure 19 shows the "classical" configuration called nozzle-nozzle being made up of alternatively situated flat blades for fuel and oxidizer gases.

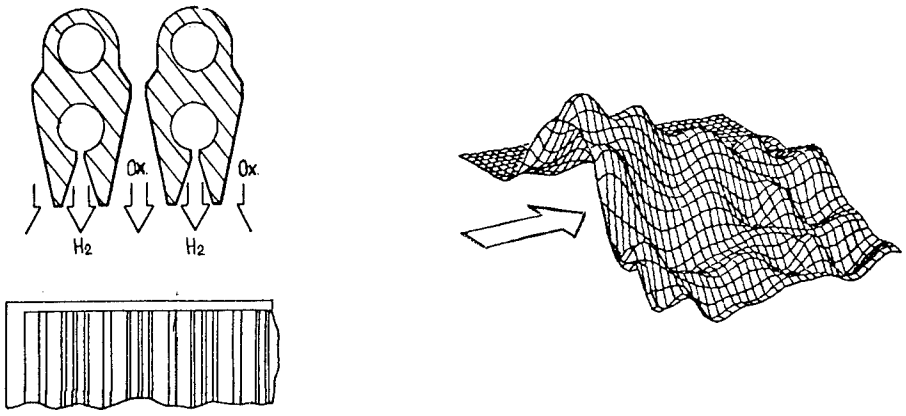


Figure 19. Classical CWCL "nozzle-nozzle" mixing scheme and wavefront aberrations.

The 7.5 millimeter distance between the symmetry axes determines the mixing step. The fact that this mixing distance is not related to the spatial scales of active medium disturbances is the main beneficial feature of this configuration. However there are serious difficulties with production of large scale construction involving the maintenance of constant nozzle throat dimensions.

The fact that the nozzle-nozzle mixing scheme produces quasi-two-dimentional flow makes the experimental results of aberrations measurement very useful for verification of different kind numerical simulations. The comparison of active medium refractive index value obtained with isenthropic estimation or by means of boundary layer and Navier-Stokes equations solution is presented in the Figure 20.

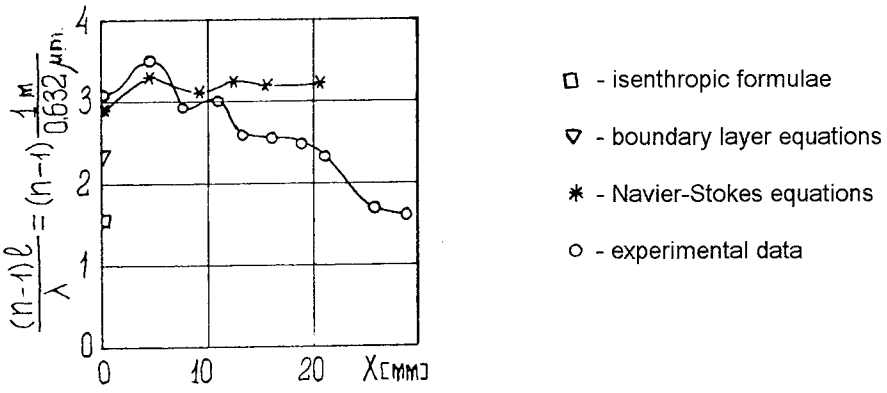


Figure 20. Comparison of experimental and numerical data.

It is clear the Navier-Stokes simulation taking into account all details of multicomponent chemically reacting viscous gas movement gives the best results [24].

The magnitude of Chemical Laser active medium disturbances depends on two main factors: the transverse injection nonuniformity of the cold and strongly refracting hydrogen and the change of gasdynamic characteristics of the supersonic flow caused by the chemical reactions. By adequately choosing regime parameters we have managed to "switch off" the combustion without changing the average refractive index level in the gas. Strehl ratio was raised by 25% in this manner, that characterizes the contribution of chemical reaction to active medium homogeneity loss (Figure 21). These results have been applied to the design and study of advanced nozzle block construction using three-jet mixing.

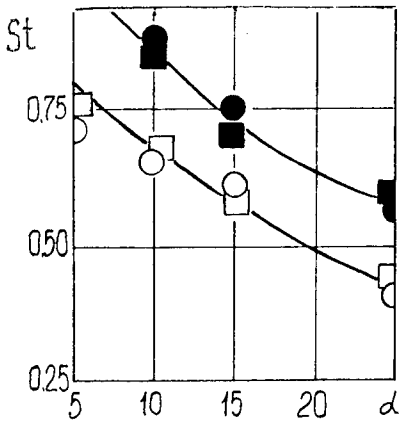


Figure 21. Dependence of Strehl ratio on fuel abundance coeficient (o -with and • -without chemical reaction in the supersonic flow)

There is a direct connection between the phase aberration value and the operational parameters of the laser installation. Apparently as the intensity of main processes leading to output power growth is increased (that is gas rate G or fuel abundance coeficient α) the active medium optical quality is decreased. This fact allows the possibility to determine complex criteria taking into account both active medium gain performance and its optical homogeneity. These criteria are useful for determining the optimal parameters of system operation. For instance for the "nozzle-nozzle" mixing scheme these values are - relative gas rate is 0.5, Fuel aboundance coefficient - 7.5 meanwhile maximal output power was obtained at G=1 and α=15 (Figure 22).

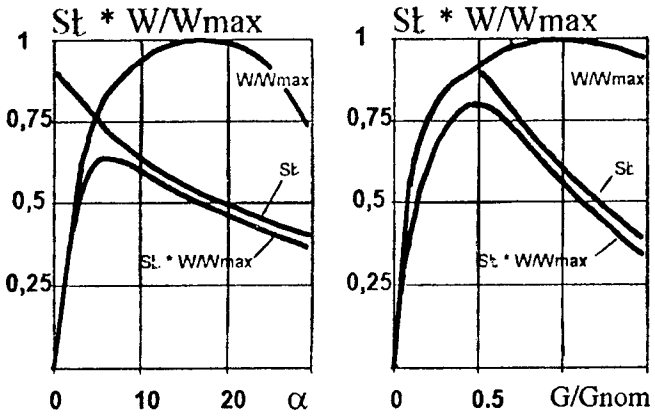


Figure 22. Complex criterion $St \times (W/W_{max})$ behavior versus main operational parameters.

A bank with discrete hydrogen injection through pyramidal shaped nozzles placed with a step 2.6 millimeters in the wertical direction is a further development of CWCL mixing schemes (Figure 23).

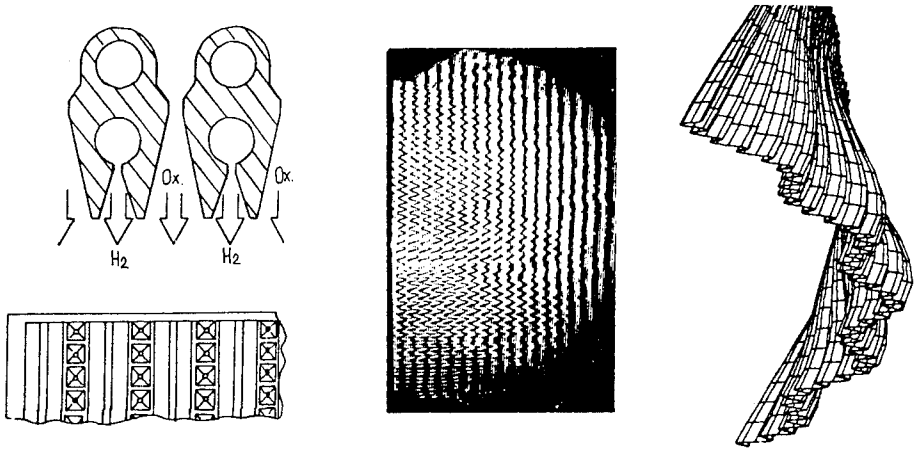


Figure 23. Mixing scheme with discrete hydrogen injection through pyramidal nozzles and wavefront aberrations.

The output power grows due to mixing step decrease and the rigidity of construction increases as well. However the regular location of fuel injection holes gives rise to small scale transverse periodic wavefront modulations that can lead to the light scattering and must be corrected. Besides these

disturbances gasflow organized by this mixing scheme contains nonuniformities of intermediate scale appearing due to baffles installed in the oxidizer nozzles to keep a constant throat dimension.

Screen nozzles may also be applied to produce the active medium in Chemical laser. The construction of nozzle bank and flowfield interferograms are shown in the Figure 24. The absence of intermediate scale of disturbances is the main difference with previous case and seems to be a positive features of screen nozzles concept that will be discussed later.

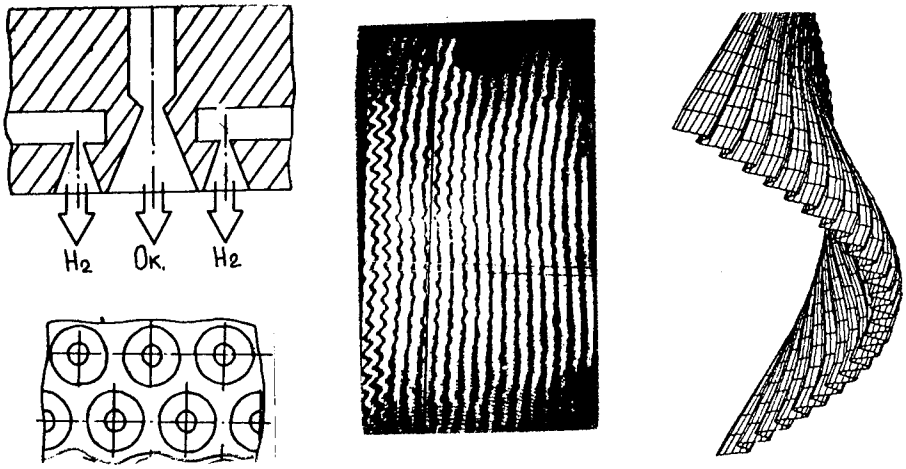


Figure 24. CWCL screen nozzles concept and wavefront aberrations.

The radial expansion nozzle bank shown in the Figure 25 represents another type of CWCL mixing scheme development.

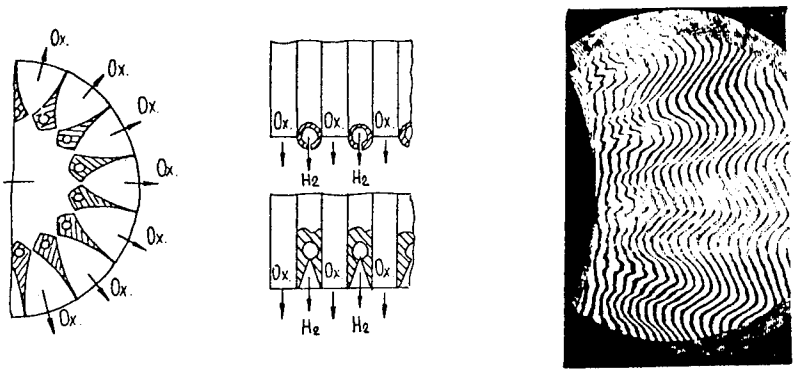


Figure 25. Radial expansion concept nozzle bank and flowfield interferogram.

Here the direction of oxidizer gas expansion and mixing process are mutually perpendicular to one another while the fuel is supplied through the small holes randomly placed in the tube collectors situated at nozzle exits. Shock waves due to the interaction of the fluorine carrying jets were found to be the main cause of the appearance of gas flow nonuniformities. Active medium interferogram allowed to reconstruct the flowfield pattern and oxidizer gas jet Mach number was experimentally estimated from shock wave location and geometry of the nozzle. This value was only 4 meanwhile isenthropically predicted value was 5. This disagreement may be explained by extremely viscous character of gas movement.

Thus, flowfields produce by nozzle bank with discrete hydrogen injection and by screen nozzles have a transverse periodic inhomogeneity wich may be corrected with selfcompensation method. This method involves the searching for an optimal observation axis angle. The positive experience obtained from investigation of GDL's screen nozzles allows to hope for the good results in the case of CWCL.

The experiments shown the possibility of decreasing of periodic phase modulation magnitude by a factor of 5 for both mixing schemes (Figure 26).

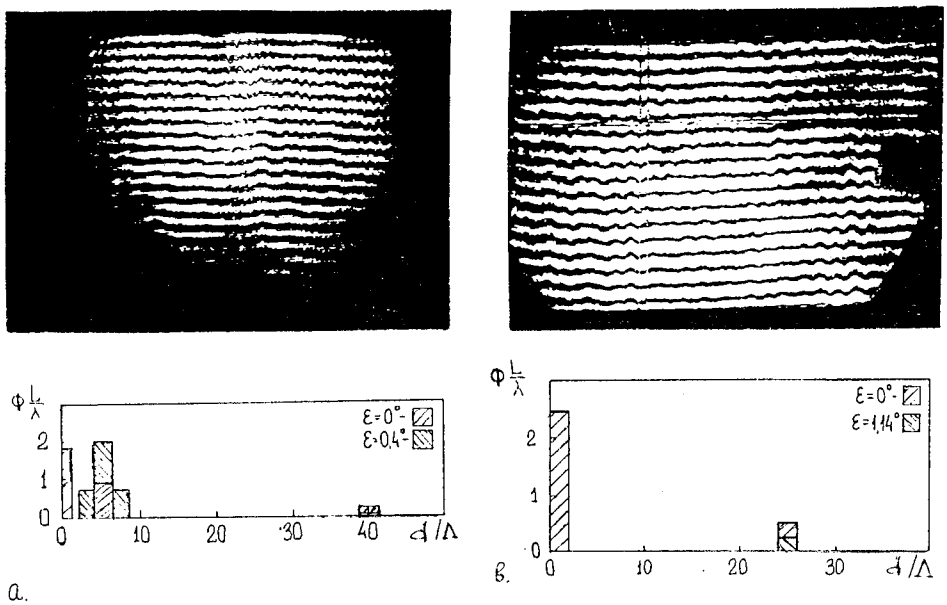
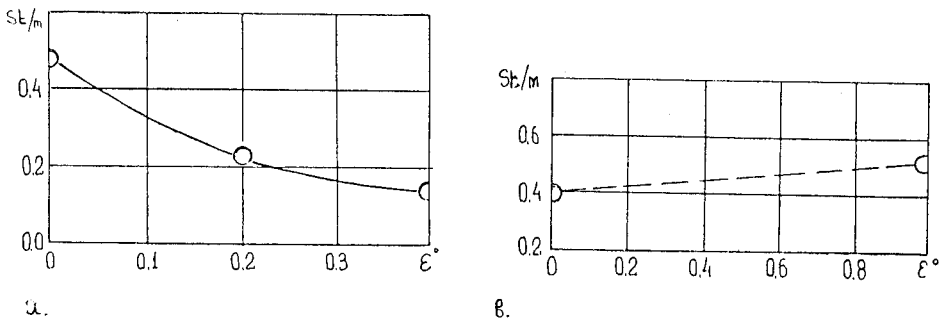


Figure 26. Flowfield interferograms and changing of the main spatial frequencies versus observation axis angle for nozzle bank with discrete fuel injection (a) and screen nozzle bank (b).

However in the first case this did not lead to the improvement of general optical quality of active medium. The drop of Strehl ratio for nozzle bank with discrete fuel injection may be explained by increasing of role of intermediate scale disturbances (Figure 27).



Fugure 27. Strehl ratio versus angle for nozzle bank with discrete fuel injection (a) and screen nozzle bank (b).

For screen nozzles the inhomogenieties of such scale do not exist. This fact gives an opportunity to suppose that monoscaling of active medium inhomogeneities is required for successful application of the self-compensation method.

The positive experience obtained from the investigations discussed above allowed to propose some technical details that improve optical quality of CWCL active medium. For example the replacement of discrete pyramidal fuel nozzles by ones having discrete throats and a common diffuser region has provided a successful resolution of the problem with small-scale disturbances (Figure 28).

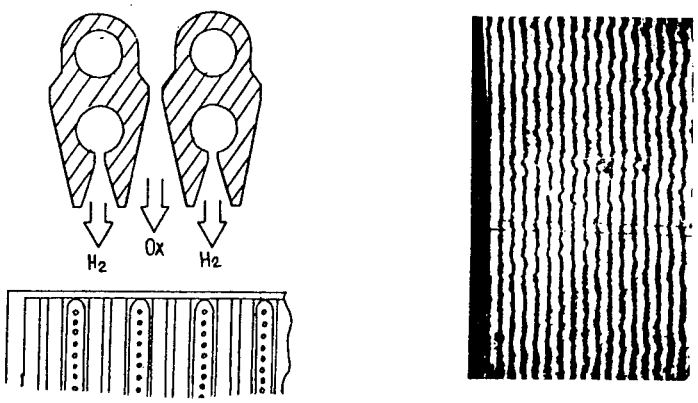


Figure 28. CWCL mixing scheme with fuel injection through the nozzles having discrete throats and common diffuser region and gasflow interferogram.

A random pattern of hole location combined with a flattened diffuser section practically eliminates small-scale nonuniformities.

The development of an idea involving the injection of neutral gas between the fuel and oxidizer also appears to be very fruitful since experiments showed the active medium homogeneity to increase.

At least the analysis of CWCL active media interferograms allows to conclude that the gas flow has a laminar character in all cases. The pictures have a high contrast wich indicates that the medium do not contain random unsteady density disturbances caused by turbulent pulsations in the flow.

Conclusions

1. The active medium creation for laser leads to the appearance of various kinds of inhomogeneities in the medium itself. Regardless of their different nature and history all of them may exert important influence on the laser performance.

For majority of laser systems the higher level of the pumping the higher active medium inhomogeneity magnitude takes place. Thus the optimal operational parameters from the point of view of maximal far field intensity may significantly differ from these wich give maximal output power. This fact strictly proved for CWCL is apparently typical for the wide range of laser systems.

2. Measurements that we have performed allowed to obtain data that characterize the active medium optical homogeneity in different types of gas lasers. Using the Strehl ratio as a criterion gave us the opportunity to consider verification of active medium optical quality for many different laser configurations on a common basis.

3. Different kind of disturbances that were found out in real large scale laser installation have their place in the classification discussed in the Part One (See Table 1). Last fact proves the reality of this approach.

References.

1. Eletsky, A.V., Smirnov, B.M. (1985) *Physical Processes in the Gas Lasers,* Moskow, Energoizdat.

2. Dimakov, S.A., Malakhov, L.M., Sherstobitov, V.E. (1983) Investigation of the optical homogeneity of TEA CO_2 laser active medium during the beam generation, *J. of Quant. Electr.* **10** N2, pp.397-401.

3. Borovich, B.L., Zuev, V.S., Katulin, V.A. (1983) Small scale nonuniformities appearance in the photodissotiated Jodine lasers during the beam generation, *J. of Quant. Electr.,* **2** N5, pp.1282-1290.

4. Sutton, G.W. (1969) Influence of the turbulent pulsation of the optical active medium on the light beam, *RTC* 7 N9, pp. 94-103.

5. Novoselov, A.G., Pustogarov, A.A., Sharkov, V.F. (1985) About some physical criteria of the active media supersonic flows attestation, *Physical Gasdynamic,* LCWP, Minsk, ITMO BSSR, pp.134-147.

6. Born, M., Wolf, E. (1964), Principles of Optics, Edited by Pergamon Press, New York,

7. Quinnell, R.D., (1981), Limitation on the Root-mean-Square *(rms)* Phase to Describe Beam Quality Charachteristics, *SPIE* **293** pp. 12-19

8. Lobachev,V.V.,Moshkov,V.L. (1993) Limitation on the multicascade laser amplifiers realization *IFJ* N1, **63**, pp.83-87

9. Glessner,J.W.,Tannen,P.D.,Walter,R.F.(1990) Review of oscillator performance for electric discharge lasers. *Proc. conf.SPIE.*, **24**.

10. Hogge,Ch.B. (1981) Aberrations in high power laser systems. *SPIE.*. **293**, pp.20-26.

11. Achmanov,S.A.,Dyakov,U.E.,Chirkin,A.S. (1981) *Introduction into statistical radiophysics and optics* Moskow Nauka.

12. Klyatskin,V.I. (1980) *Stochastical equations and waves in the randomly in homogeneious media.*Moscow;Nauka.

13. Kon,A.I. (1990) Qualitive linear theory of the light beam propagation in the turbulent athmosfhere, *Lasers and Athmosphere.* Obninsk .pp.96-99.

14. Ananyev, Y.A.(1979) *Optical Resonators and the problem of the laser radiation divergence.*Moskow;Nauka

15. Ananyev, Y.A.(1993) *Optical Resonators and laser beams.*Moskow; Nauka

16. Knight,C.I. Sutton,G.W., Berggen,R. (1981) Phase aberrations and laser output beam guality *SPIE.* **293** pp.2-11.

17. Gorbachev, B.U.(1990) Investigation of the energetical characteristics and farfield energy distribution of the lasers with unstable telescopic resonator. Ph.D.thesis.Moscow Ph.I AN

18. Malacara,D(1984). *Optical Shop Testing* .Edited by John Wiley and Sons. New York.

19. Shekhtman,V.N.(1982) Reconstruction of the light wavefront from the side-shearing interferogram *OMP.* .N6.pp.2-6.

20. Shekhtman,V.N. Rodionov,A.Y. Pelmenev,A.G (1994), Reconstruction of the light beam wavefront by means of shearing interferogram synthesis. *Journ.of Optics and Spectr.* **76**,N6,pp.884-888.

21. Kromin,S.M. Lubimov,B.B. Shekhtman,V.N. (1986) Measurements of the light wave scattered component *.J.Quant.Electr.* **13**.N5,pp. 962-966.

22. Ktalcherman,M.G.,Malkov,V.M. (1993) Aerooptics of GDL Nozzle Banks. *Journ. of Appl.Mathem. and Techn.Phys.* **5**.

23. Boreisho,A.S. Lobachev,V.V. (1989) Flow Optical Quality Formed by Screen Nozzles, *.J.of Appl.Math.and Techn.Phys.* N4 pp. 94-98.

24. Rotinian,M.A. Strelets,M.Ch. Shur,M.L, (1991) Navier-Stokes simulation of the supersonic combustion in CW-chemical laser,.*Proc.of 7-th conf in Stanford,USA,July 8-12,* .7,part.2, pp.1132-1148.

GAS LASERS WITH PLASMODYNAMIC PUMPING

YU.S. PROTASOV
Moscow Bauman State Technical University
107005, Moscow, Russian Federation

Abstract

It is a brief review of studies of lasing and energy-spectral characteristics of gas lasers utilizing - the excimer-like mercury halide vapor HgX_2 (X=Cl, Br, I), inert gas halogenides - XeF (B-X), (C-A) and molecules of the stable halogens (I_2, Br_2), optically pumped by wide-band UV-VUV radiation of high-current radiative discharges.

1.Introduction

Advances of radiative-plasmodynamic processes of short-wavelength radiation laser-matter interaction research, aimed at solving some problems of applied physics and high technology - stimulate R&D of gas-phase visible and ultraviolet lasers featuring high lasing energy and average power ratings. A wide range of attractive laser-active mediums in such lasers includes dihalogenides of the metal $MeÃ_2$ (Me=Hg, Cd, Zn,..., Ã=Cl, Br, I), homonuclear molecules of halogens (e.g. I_2, Br_2, Cl_2,), exiplex compounds of oxides and halogenides of noble gases (XeO, XeF, KrF,...); they make it possible to produce high power lasing over the entire spectral band.

In contrast to electronic (electron-beam, electrical-discharge) excitation, the method of wide-band optical pumping of gas lasers is rather perspective - physically and technologically [1]. Inspite of the methods of formation of population inversion differences for these gas laser-active mediums, wide-band noncoherent pumping source requirements which govern efficient lasing are very similar - and are aimed mainly at providing a powerful UV-VUV (in the spectral range $h\nu$~4-20 eV) radiation continuum with brightness temperatures 25-40 kK.

When high-power short-wave pumping sources are designed a number of principle problems shall be tackled: a)input of energy into the large volumes of sufficiently dense (n_e~10^{10} ---10^{20} cm^{-3}) plasma having temperatures of several (3-10) eV and plasma heating; b)escape of plasma short-wave radiation; c)controlling emission spectrum variation.

2. High-power UV-VUV plasma sources for optically pumped gas lasers

R. Kossowsky et al. (eds.), High Power Lasers – Science and Engineering, 83–93.
© 1996 *Kluwer Academic Publishers. Printed in the Netherlands.*

2.1 PLASMA RADIATION SOURCES WITH OHMIC HEATING

Among the short wavelength (open-type) radiative discharges with ohmic heating - high current surface discharges with different methods of ignitions (sliding, barrier, laser spark) - are powerful pulse-periodic sources of high brightness UV-VUV radiation for gas lasers optical excitation. We proposed and studied a new type of high current surface discharge, namely, surface discharge with linear stabilized streamer (spark) channel [2] having (in typical scheme) an additional system of distributed electrode-capacitor elements in the gap for initiation of extended spark discharges over the dielectric surface. This type of surface discharges does not require the use of "hard" electrical circuits (i.e. circuits having a high value of U_0/L_0) and makes it possible to form long discharge channels (>0.5 m) with relatively low operating (5-25 kV) and ignition (~25 kV) voltage; simultaneously, the conditions are satisfied for the spatial stabilization of streamer channel and this makes it possible to obtain radiating (with T_{Br}^{VUV}~ 40 kK) plasmas of an any given geometry and, in particular, strictly linear plasma columns.

2.2 PLASMODYNAMIC SOURCES OF HIGH-POWER UV-VUV RADIATION

High-current plasmodynamic discharges of various type [3] differ from discharges characterized by ohmic heat evolution because plasma is heated by shock-wave thermalization of the kinetic energy of high-velocity plasma flow decelerated in a dense gas, plasma, solids, or magnetic field (as at a target).

So, (in particular, one can eliminate the main constraint in ohmic heating):

- the plasma resistance is not depend explicitly on the temperature of the heated (radiating) plasma;
- the plasma heated generally outside the circuit part, so the heating rate can differ substantially from the energy input rate to the discharge which is used in generation of high-power light pulses with short pulse lengths and steep leading edges.

We suggest and examine the physical and technical aspects of using plasmodynamic methods to generate high-power UV-VUV radiation in vacuum [4] and gases [5] implemented by means of an erosion-type magnetoplasma compressor [6] (MPC) as a generator of hypersonic dense plasma flows. A plasma flow traveling at velocities v_{pl}~ 40-60 km/s is formed in MPCs by electromagnetic forces generated as a result of interaction of discharge currents with intrinsic magnetic fields. Chemical composition of the electric-discharge plasma is governed by the products of erosion of the electrodes and insulators separating them in MPCs. From the technical point of view, MPCs as a directed kinetic energy generators with high specific energy content ($v^2/2 \geq$ MJ/g) of the generated plasma hypersonic flow and high kinetic efficiency (η_{kin}~ 0.6-0.8) are fairly simple and reliable devices which can operate in a wide range of compositions and initial pressures of the gases ($p \sim 10^{-2}$-10^2 atm) and are capable of high output energies (10^4-10^7 J); they can be also used in the pulse-periodic regime at high repetition frequencies (f ≥ 1-100 Hz) governed primarily by the power and operational characteristics of the power sources and current switches (low induction

capacitor banks, explosive magnetocumulative [7] and magnetohydrodinamic [8] generators).

Experimental investigation and numerical analysis of high-current plasmodynamic MPC-discharge (plasma focus-type [9] in vacuum and gases, R-constricted [10], discharges with axis constriction [11], localized [12] and cumulative [13]), their spectral-brightness and energy characteristics showed the feasibility of constructing high-brightness ($T_{Br}^{UV} \geq$ 40 kK) sources of wide-band VUV radiation (open or lamp type) for optical pumping. The main radiating MPC configurations and their spectral-energy characteristics are been described in [3].

So, the powerful VUV light sources open type design on the basis of MPC discharges:

in vacuum - have the brightness temperatures $T_{Br} \geq 5$ eV in the spectral range $h\nu \geq 25$ eV and radiation power $P_{rad}^{VUV} \geq 0.1$ GW/cm^2. Emitting surface area ($S \geq 10^2$ cm^2) can be increased for required by using multichannel MPC discharged geometry;

in gases - required spectral and brightness characteristics ($T_{Br}^{UV} \geq$ 40 kK) in range λ ~100 nm, spatial and geometric parameters are achieved by the choosing gasdynamics structure when take into account the effect of the turbulent modification [14] the thermodynamics and optical properties of the transition region between the plasma flow and the unperturbed gas facilitating the escape of UV and VUV photons from the hot discharge zone into the unperturbated gas, (of necessary chemical composition and pressure level).

The plasmodynamic high-power UV-VUV light sources of flashlamp-type on the basis of cumulative MPC-discharges (when broad-band UV-VUV radiation is generated by means of cumulation of hypersonic counterdirected plasma flows formed by opposite MPCs in vacuum (or dense gas) in an optical tube) have the high brightness temperature of 30 kK in the UV and VUV spectral regions and a luminous body isolated by transparent walls [15] (providing under conditions of formation of a gas layer optically dense for the hard VUV radiation).

In the case of localized MPC discharges a new scheme of a flashlamp-type emitter was suggested in which heating of an electric discharge plasma is implemented as a result of shock-wave thermalization of the directional kinetic energy of a high speed plasma flow upon its deceleration in the dense gaseous mediums (before optical target) which simultaneously plays the part of an gas filter for the hard component of the emission spectrum of the emitting plasma flow. Radiation flux densities in the hard component of the emission spectrum of the emitting plasma flow. Radiation flux densities in the short-wave UV region (180-250 nm), which correspond to the black body radiation with the temperature of the level of 40 kK have been achieved for the first time for the quartz light sources [16].

3. Gas laser modules with high current sources of UV-VUV radiation

The above-mentioned features of high current light sources for optical pumping have been utilized in design of gas laser modules; structurally, the laser module is a

cylindrical thermostatic (50-350 °C) chamber measuring 300 to 1500 mm in length and 120 to 500 mm in diameter, having set of optical pumping sources installed in its diameter plane (or along its axis), quartz windows and resonators, connected to a systems of differential pumping and mixing.

3.1 EXIMER-LIKE OPTICALLY PUMPED MERCURY DIHALIDE LASERS

Generation of stimulated radiation in mercury halide vapors due to an allowed ionic-covalent B-X transition in molecules (radicals) of mercury monohalides HgX formed from the original molecules of HgX_2 dihalides as a result of dissociation (here, X=Cl, Br, I). Minimal of the potential curves of the $B^2\Sigma^+_{1/2}$ and $X^2\Sigma^+_{1/2}$ states of the HgX molecules are shifted by 0.04-0.06 nm, so that in accordance with the Franck-Condon principle the transition occur preferentially from lower vibrational (v'=0-3) levels of the B states to upper levels (v"=15-25) of the X state.

The lower active levels are emptied by vibrational relaxation occurring at a high rate, which is responsible for the quasi-cw nature of lasing ($\tau_{las} >> \tau_{spont} \sim 20$ nsec) subsystems.

Main features of mercury halogenides, by which they compare favorably with other blue-green laser-active mediums are based on large cross-sections of induced transitions ($\sigma_i \sim 10^{-16} cm^2$) and regeneration of active molecules which makes it possible to develop high gains ($\alpha > 10^{-2} cm^2$) and allows closed-circuit high frequency pulse-periodic operation.

3.1.1 *Blue-green molecular HgBr/HgBr$_2$ laser*

Lasing was observed when HgX vapor was pumped with radiation from an open linearly stabilized surface discharge acting directly in the active mixtures. Experiments have been carried on installation [17] with discharge parameters: $W_0=(0.95\text{-}2.85)\cdot 10^3$ J, U_0=25 kV, $\tau/2 \sim 11$ μs. The gases (SF_6, CF_4, N_2) mixed with inert gases have been as buffer gases with $p_\Sigma \sim 0.5\text{-}4$ atm.

As regards output energy (~3 J), the optimum composition is a mixture $(Ar:N_2) \sim 1:1.5$, p_Σ= 2.5 atm and vaporous at a concentration of $(0.8 \text{ to } 2)\cdot 10^{17} cm^{-3}$. Under these conditions detectable are 6 or 7 lines grouped near the wavelength λ~502 nm and 504 nm. The maximum unsaturated gain and internal loss index have been ~0.04 cm^{-1} and 0.002 cm^{-1} respectively. The total efficiency HgBr laser is $\eta_L \sim 0.3\%$, which is a present-day maximum value for optically pumped visible gas lasers. According to measurements the total laser efficiency can be 1.2 to 2%, which corresponds to instantaneous values of lasing efficiency, determined in the experiments.

The specific laser energy output ~15 J/L, long pulse lasing $\sim 4\cdot 10^{-6}$s - are the best present-day characteristic for optical pumped visible gas lasers of this type.

3.1.2 *Green-emitting mercury chloride laser*

Interest to the laser is based on possibilities of attaining high energy/power characteristics and a high efficiency and frequency of lasing in the green region of the spectrum on a wide lasing wavelength tuning from 533 to 565 nm. Under mentioned conditions the lasing of HgCl laser was in the from of two lines λ=558/559 nm which

are in the green region of the spectrum and corresponded to allowed bound-bound transitions between the lower (v'=0 and 1) levels of the electronically excited state $B^2\Sigma^+_{1/2}$ and the upper vibrational (v"=22 and 23) level of the ground state $X^2\Sigma^+_{1/2}$ of the $HgCl_2$ molecules; lasing line width (~1 nm) is determined by unresolved vibrational structure.

The laser energy output is optimal at an active medium absorbtion factor of 1.2 m^{-1} (i.e. a repetition frequency f ~ 0.1 Hz, $W_0 = 8.5 \cdot 10^2$ J).

The output energy and the specific values of this energy (~2.1 J and ~7.6 J/L) were much higher than the values obtained for electric discharge HgCl lasers or for lasers optically pumped with narrow-band radiation [18], the laser efficiency is respect to the stored energy was as high as ~0.1%.

3.1.3 *Blue-violet HgI/HgI_2 laser*

Under our conditions (p_{HgI}~1 torr+N_2:Ar=1.5:1, p_Σ~2.5 atm) the lasing was observed when the concentration of HgI_2 active molecules exceeded $1.2 \cdot 10^{16}$ cm^{-3}. The maximum laser radiation energy recorded at this way was Eout~ 0.5 J ($W = 2.85 \cdot 10^3$ J) which was much higher than the values obtained in electric discharge HgI laser [19]. The optimum value of the concentration of the active molecules was in the range (7-8)$\cdot 10^{16}$ cm^{-3} and corresponded to a depth of penetration of the pump photons (λ~225 nm) in the active medium amounting to l~0.3 cm - i.e., HgI laser operated in the photodissotiation wave regime (v~10 km/s, τ_L~3.5 μs).

The spectrum of the stimulated radiation obtained from mercury iodide photodissotiation laser corresponded to the electronic B-X transition in the HgI molecule with the vibrational numbers v-v"=1-17 (λ=444 nm), 0-15 (λ=443 nm); the bulk of the radiation was concentrated in the group of lines at λ=443 and 444 nm.

3.1.4 *Multicolor visible radiation emitted by mercury halides vapor laser*

The HgX_2 molecules have several absorbtion bands in the ultraviolet range and this correspond to their dissociation channel responsible for deformation of radicals in various electronic states. These electronically excited radicals form in the $B^2\Sigma^+_{1/2}$ state only when the HgX_2 molecules absorbed radiation in the so-cold b-bands with maxima located at the wavelengths of λ=183,198 and 225 nm for $HgCl_2$, $HgBr_2$, HgI_2 respectively. The half-widths of this bands are $5 \cdot 10^{-3} cm^{-1}$. Irradiation with longer wavelength ultraviolet radiation creates HgX molecules in the ground $X^2\Sigma^+_{1/2}$ state. The wavelengths dependencies of the absorbtion cross-sections of molecules of the various mercury halides demonstrate that the active laser medium composed of the three mercury dihalides mentioned early cave have fairly wide absorbtion region of λ~175-240 nm when the concentration of molecules are suitably selected. This facilitates a more efficient utilization of the emission spectrum of a wide-band optical pumped source.

An active mixture consisted of mercury dihalide vapors at pressure of $p_{\Sigma HgX}$=1-10 torr and it contained buffer gases (N_2:Ar=1.5:1), p_Σ=2.5 Amagat.

Simultaneous lasing was observed for all the binary mixtures ($HgCl_2$-$HgBr_2$, $HgCl_2$-HgI_2 and $HgCl_2$-HgI_2) as well as for a ternary $HgCl_2$-$HgBr_2$-HgI_2 mixture.

The space and time structures of the laser radiation field were completely identical for different mercury halide mixtures.

Analysis of emission spectrum of three-color laser utilizing a mixture with equal energy yields of the radiation in the individual spectral components shows that in case of the HgCl molecules emitted two lines at λ=558 and 559 nm in the green part of the spectrum, corresponding to transitions with the vibrational numbers v'-v" in the range 1-23 and 0-22, whereas the HgBr molecules emitted four lines in the blue-violet part of the spectrum with maxima at λ=444.0 and 443.2 nm (1-17 and 0-15 transitions). The laser emission lines coincided with the strongest lines in the spontaneous emission spectra of the HgX molecules.

When the partial composition of a mixture of mercury dihalides was altered, there was a change in the energy distribution of the output radiation between the various spectral components, i.e., the "chromatisity" of the emission spectrum changed.

The energy measurements indicated that the total output energy E_n obtained from lasers, utilizing HgX was less then the maximum energy E_i of the lasers utilizing, any one of the halides - $E_n \sim n^{-2}\Sigma E_1$, where n is a number of halides in the mixture.

The reduction of the output energy in the case of mercury dihalide mixtures was clearly due to enhancement of the role of the quenching of the B state of the monohalides ($k_q > 10^{-10} cm^3/sec$) when the total concentration of the HgX_2 molecules in the active mixture was increased.

The total radiation energy of the lasers with binary mixtures of mercury dihalides was 0.5±0.1 J (depending on the mixture) and the maximum output energy obtained for a three-color HgCl-HgBr-HgI laser was~0.31 J, so that the efficiency of transformation of the lasing time was~0.1% and ~0.07%, respectively.

So, a combination of vapors of different halides could be used as the active medium and this provides a new opportunity for constructing a high-power photodissotiation laser emitting "white" light [20].

3.1.5 *Low-temperature lasing of mercury monohalides*

Mercury dihalides HgX_2 have a low vapor pressure at room temperature. The medium must be heated to ~200 °C for efficient operation of Hg lasers and this creates some tehnological and operational difficulties that limit appreciably the scope for whitespread application of this lasers.

In order to reduce the operating temperature of HgX lasers (<100 °C) one can replace dihalides with more volatile organically substituted mercury halides RHgX, where R is organic radical. Trifluoromethil mercury bromide, chloride, iodine - CF_3HgBr, CF_3HgCl, CF_3HgI - are potentially useful for this purpose.

In the laser cell a vapor of trifluoromethil mercury halides was dilated with buffer gas (N_2:Ar=1.5:1) at a total pressure p_Σ~2.5 atm.

High-power stimulated emission from media utilizing CF_3HgBr was observed at temperatures of the laser cell and the vaporizer above 88 °C. In this case, the coefficient of absorbtion of the active medium at λ=257 nm varied in the range ~0.95-1.75 m^{-1}. Radiation was only amplified in one (λ=502 nm) of the two known lasing bands of the HgBr radical, for which up to four vibrational-rotational components were distinguished in the spectral substructure.

Lasing of the HgCl molecule, formed from CF_3HgCl, was obtained at a cell temperature T_C~95 °C. The coefficient of absorbtion in the medium at λ=247 nm was ~1 m^{-1} and the laser pulse energy was ~6 mJ. Two groups of lines, near λ=558 and 552 nm, where recorded in the stimulated emission spectrum [21]. For comparison, we note that, in the case of an $HgCl/HgCl_2$ photodissociation laser, lasing is generally observed near λ=558 and 559 nm.

3.2 VISIBLE AND UV XeF LASER WITH WIDE-BAND OPTICAL PUMPING

XeF lasing is one of the best illustration of efficiency application wide-band optical pumping concepts for gas lasers technique. VUV optically pumped photodissotiation XeF (B-X) lasers ensure smooth lasing wave turning from 345 to 353 nm by changing buffer gas pressure and demonstrate the maximum output energy in the blue-green spectrum range at the (C-A) transition.

An investigation have been performed of a XeF laser with an active length 1.7 m and an exit aperture of 0.12×0.2 m. The built-in resonator L_S~2.8 m, T_1= T_2=30 % (λ=350 nm, B-X; T_1= T_2=11 %, λ=480 nm, C-A) was employed. The optical pumping source was a single channel sectionalized surface low voltage discharge with the input power density averaged over the half period dP/dx~41.6 MW/cm, τ/2=6 μs, and brightness temperature in VUV T~30 kK.

The maximum output energy due to B-X transition was E=70 J and it was obtained from a mixture of the $Ar:N_2$=3:1 composition containing an XeF_2 vapor at p=2 torr and the total pressure of the mixture p_Σ=1.4 atm. The specific output energy averaged over the lasing region (zone) was 4.2 J/l. The lasing energy at the (C-A) transitions it was as high as 98 J with the average output energy from the active volume releasing 90 % of the total energy was 5.5 J/l, the technical efficiency reached 0.17% [22,23]

3.3 OPTICALLY PUMPED UV MOLECULAR (I_2,Br_2) DIMER LASERS

Homonuclear halogen molecules are promising candidates for high-power lasing in UV-VUV (λ=157-344 nm).

3.3.1 *I_2 - laser*

To optically excite molecular iodine (λ=200±10 nm) it's possible to use flashlamp-type light sources in the microsecond range. A cumulative type plasmodynamic source [24] was used to investigate the lasing characteristics. The mechanism of population inversion in the case of I_2 laser is well known. The necessary I_2 vapor pressure was ensured in the thermostabilized laser cell at 70-80 °C. Under this conditions lasing occurs at two wavelength λ~342.0 and 324 nm corresponding to transition with the vibrational numbers 1-14 and 2-15. The maximum energy generation (E_L~J) has been obtained using a buffer gas (perfluoromethan) at a pressure of 1.5 atm and of I_2 molecules p_I=3 torr with lasing duration being τ~16 μs corresponding to the pumping pulse.

3.3.2 *Br_2 laser*

The first achievement of lasing in optically pumped molecular bromide has been given recently [25].

A possible mechanism of photoexitation and lasing of bromide vapor in the presence of a buffer gas consist in the following. Absorbtion of pump radiation in the VUV spectral range ($\Delta\lambda_{pump}$~150-170 nm) leads to the Br_2 molecule being exited from the $X^1\Sigma^+_g$ ground covalent state to the $D^1\Sigma^+_g$ Coulomb state. The exited bromide molecules relax to the lower $D'^3\Pi_{2g}$ ionic state when they collide with the buffer gas particles and emit in the λ_L~292 nm region due to the allowed $D'^3\Pi_{2g}$ - > $A'^3\Pi_{2u}$ bound-bound electronic transition (the laser transition). Rapid depopulation of the lower active level (a weakly bound state) is due to electron-vibrational relaxation and, possibly, to dissociation during collisions with atoms of the buffer gas.

In our experiments the Br_2 vapor was optically by thermal VUV radiation from multichannel (10) plasmodynamic discharges of magnetoplasma compressors formed directly in the laser active medium.

The maximum brightness temperature T_{br} of a discharge in argon, at a pressure of p_{Ar}~2-4 atm, reached 35-38 kK in the ultraviolet spectral range for light pulse duration of $\tau/2$=6-8 μs, (W_0~$6\cdot10^3$ J), the expansion velocity of the plasma in this range of argon pressure was 3.6-2.8 km/s.

The active medium consisted of Br_2 vapor (p~3-20 torr) strongly diluted with the argon buffer gas (p_{Ar}~1-4 atm), and was prepared by mixing the gases directly in the laser cell, which was passivated before gases were admitted.

As a rule, the stimulated spectrum consisted of a large number (~20) of partially overlapping lines, grouped near three basic wavelength: 291.5, 292.9, and 292.5 nm. Lasing occurred due to transitions which had the maximum intensity in the spontaneous emission spectra of the bromide molecule. The relative intensities of the lasing spectral components varied as a function of the composition of the medium and the resonator parameters.

The laser output energy increased monotonically with the pressure of the argon buffer gas up to its maximum value, for the present apparatus, of p~4 atm. The range of optimal partial pressures of the active molecules was p_{Br}^{opt}~3-10 torr. Outside this range reductions were observed in both the laser output power and the duration of lasing. The maximum laser output energy of E_L~1.1 J recorded in the experiments, for all overall laser pulse duration of τ_L~5 μs, was obtained using an active mixture Br_2:Ar=$2.4\cdot10^{17}$:$1.1\cdot10^{20}$ cm^{-3} and a resonator with R_1R_2~0.93.

Despite the fact that there is quite a substantial reserve evidently for raising the output parameters of the investigated lasers, the results obtained serve to provide evidence that the energy possibilities of all mentioned laser active media are similar. From the technical point of view, the use of molecular bromide as the working component of the active mixture of an optically pumped ultraviolet laser is preferable, since Br_2 is more stable (it is replenished) and is also a less chemically aggressive and toxic substance then xenon difluoride and has quite a high saturated vapor pressure at room temperatures (p_{Br}^{sat}=200 torr).

Finally, we have to add that high potential possibilities of the radiative plasmodynamic discharges as a powerful optic pumping sources with universal energy-spectral characteristics have been stressed in a wide spectral-energy range:

- in deep VUV band - by design, theoretical and experimental research of the first photoionization-recombination atomic xenon laser excited by ionizing VUV radiation of the multichannel plasmodynamic MPC-discharge (open-type VUV source, T≥40 kK in the spectral range ≤ 100 nm), acting in the active medium of the laser [26];
- in UV band - by design and successful experiments on wide-band optical excitation of new laser with bleaching wave (utilizing an enter solution of coumarine-6 with 1,4-diphenylbutadiene) excited by UV radiation of flashlamp type source based on cumulative MPC-discharge [27].
- by design and investigation of high-power pulse-periodic iodine (in C_4F_3I-C_6F_4I mixture) lasers with high (500-1000 J) output energies, pumped by non-magnetic plasmodynamic flashlamps (τ~35-40 μs, the angular divergence ~0.5 mrad, the efficiency in terms of the electrical energy deposited in the pumping system ~1% [29]).

4.Conclusion

Our lasing experiments in a wide spectral range, using new class of high-power radiative discharges proved high potential, universal possibilities and efficiency of the optical pumping concepts for development of gas laser techniques.

5. References

1.Kamrukov, A.S., Kozlov, N.P., Protasov, Yu.S (1984) *Plasma Accelerators and Ion Injectors [in Russian]*, Nauka, Moscow.

2.Bugrimov, S.N., Kamrukov, A.S., Kozlov, N.P. et al. (1986) High Brightness pulse-periodic ultraviolet radiation source utilising a lineary stailized surface discharge, *Sov.J.Quantum Electron.* **16**, 44-56.

3.Protasov, Yu.S. ed. by (1991) *The Radiative Plasmodynamics [in Russian]* **1**, Energoatomizdat, Moscow.

4.Kamrukov, A.S., Kozlov, N.P., Protasov, Yu.S. (1982) Dynamics and radiation of the open (vacuum) plasmodynamic disgharges "plasma focus" type, *Teplofiz.Vys.Temp. (Sov.J.High Temp)* **20**, 359-382.

5.Kamrukov, A.S., Kozlov, N.P., Protasov, Yu.S., Shushkovskii, S.G. (1989) Bright thermal VUV sources based on plasmodynamic discharges in gases, *Ibid.* **27**, 152-170.

6.Kozlov,N.P., Protasov,Yu.S. (1978) On the mechanism of the plasma focus formation in magnetoplasma compressor, *Phys. Lett.* **67A**, 191-195.

7.Divnov, I.I., Kamrukov, A.S., Kozlov, N.P. et al. (1979) Magnetoplasma compressor with expolsive MC-generator, *Zh.Tehn.Fiz .(Sov.Phys.Tech.Phys.)* **49**, 2415-2430,.

8.Kamrukov, A.S., Kozlov, N.P., Protasov, Yu.S. (1984) Experimental investigation of the efficiency of the magnetoplasma compressor with explosive-type magnetohydrodynamic generator, *Teplofiz.Vys.Temp. (Sov.J.High Temp.)* **22**, 225-235.

9.Kamrukov, A.S., Kozlov, N.P., Protasov, Yu.S. (1982) Experimental research of plasma focus in erosion type plasma accelerators, *Zh.Tehn.Fiz. (Sov.J.High Temp.)* **49**, 164-180; (1979) **52**, 1115-1129.

10.Kamrukov, A.S., Kozlov, N.P., Protasov, Yu.S. (1978) Plasmodynamic discharges with radial constriction of the plasma flow research, *Teplofiz.Vys.Tempr. (Sov.J.High Temp.)* **16**, 268-280.

11.Kamrukov, A.S., Kozlov, N.P., Protasov, Yu.S. (1978) Research of blast-wave deceleration processes of magnetoplasma compressors hypersonic dence plasma flows, *Ibid.* **16**, 1235-1249.

12.Kamrukov, A.S., Kozlov, N.P., Protasov, Yu.S. (1978) Plasmodynamic sources of continuouse radiation, *Dokl.Akad.Nauk SSSR (Soviet Physics-Doklady)* **239**, 831-837; Ardelyan, N.V., Kamrukov, A.S., Kozlov, N.P. et al., (1987) *Ibid.* **292**, 78-85; *(Soviet Physics-Doklady)* (1987) **292**, 590-595.

13.Kamrukov, A.S., Kozlov, N.P., Protasov, Yu.S. (1982) A high-brigtness UV radiation source utilizing cumulative plasmodynamic discharge, *Sov.J.QuantumElectron* **19**, 1429-1442; (1979) Dynamics and radiation of the cumulative plasmodynamic discharges, *Fiz.Plasmy* **5**, 368-382; (1981) *Fiz.Plasmy* 7, 1234-1244.

14.Kamrukov, A.S., Kozlov, N.P., Protasov, Yu.S. et al. (1987) About hydrodynamic instabilities influence on the spectral-brightness characteristics of open-type radiative discharges. Effect of turbulent modification, *Sov.Phys.Tech.Phys.* **32**, 839-850.

15.Kamrukov, A.S, Kashnikov, A.S., Kozlov, N.P. et al. (1984) Experimental imvestigation of radiation-gasdynamic interaction of high-power vacuum ultraviolet radiation fluxes with transparent condensed media, *Sov.J.Quantum Electron.* **14**, 655-670.

16.Kamrukov, A.S., Kozlov, N.P., Protasov, Yu.S. et al. (1984) High-power quartz plasmodynamic source of short-wavelength and vacuum ultraviolet radiation with a brightness temperature ~ 40 kK, *Sow.J.Quantum Electron.* **14**, 1094-1111.

17.Bazhulin, S.P., Basov, N.G., Kamrukov, A.S. et al. (1986) Photodissociation molecular blue-green laser with generation energy ~3J, *Pis'ma Zh.Tehn.Fiz. (Sov.Tech.Phys.Lett.)* **12**, 1423-1428.

18.Bazhulin, S.P., Basov, N.G., Kamrukov, A.S. et al. (1986) Blue-violet HgI/HgI_2 laser with wide-band optical pumping by a linearly stabilized surface discharge, *Sov.J.Quantum Electron.* **16**, 836-842.

19.Bazhulin, S.P., Basov, N.G., Kamrukov, A.S. et al. (1986) Green-emitting mercury chloride laser pumped by wide-band optical radiation, *Sov.J.Quantum Electron.* **16**, 663-671.

20.Bazhulin, S.P., Basov, N.G., Kamrukov, A.S. et al. (1986) Mercury halide vapor molecular laser pumped by a wide-band optical radiation and emitting three-color visible radiation, *Sov.J.Quantum Electron.* **16**, 990-999.

21.Kamrukov, A.S., Kozlov, N.P., Lacoba, I.S. et al. (1988) Low-temperature lasing of mercury monohalides, *Sov.J.Quantum Electron.* **18**, 972-982.
22.Zuev, V.S., Kashnikov, G.N., Kozlov, N.P. et al. (1986) Photodissotiation XeF laser emitting visible and ultraviolet radiation when pumped with radiation from a sectioned surface discharge, *Sov.J.Quantum Electron.* **16**, p.1665-1679.
23.Zuev, V.S., Kashnikov, G.N., Kirilenko, V.V. et al. (1989) Characteristiks of an XeF (C-A) laser emitting visible light as a result of optical pumping by surface-discharge radiation, *Sov.J.Quantum Electron.* **19**, 748-758.
24.Kamrukov, A.S., Kashnikov, G.N., Kozlov, N.P. et al. (1983) Cumulative plasmodynamic reactor for laser and photochemical studies, *Sov.J.Quantum Electron.* **13**, 1183-1193.
25.Kamrukov, A.S., Kozlov, N.P., Protasov, Yu.S. et al. (1989) Optically pumped ultraviolet Br_2-laser, *Sov.J.Quantum Electron.* **19**, 1551-1570.
26.Kamrukov, A.S., Kozlov, N.P., Opekan, A.G., et al. (1989) Atomic xenon recombination laser excited by thermal ionising radiation from a magnetoplasma compressor and discharge, *Sov.J.Quantum Electron.* **19**, 859-875.
27.Kamrukov, A.S., Logunov, O.A., Ovchinnikov, P.A. et al. (1989) A laser with bleaching wave excited by the light of magnetoplasma compressors, *Sov.J.Quantum Electron.* **16**, 686-698.
28.Protasov, Yu.S. et al. (1992) *Thermodynamic and Optical Properties of Ionised Gases*, Hemisphere Publ. Co., New-York.
29.Abashev, A.S., Kamrukov, A.S., Protasov, Yu.S. et al. (1991) Pulse-periodic iodine photodissociation lasers with a high output energy, *Sov.J.Quantum Electron* **21**, 438-508.

STUDY OF NEW GAIN MEDIA FOR HIGH POWER GAS FLOW LASERS

V.V. NAUMOV, V.A. KOCHELAP AND I.A. IZMAILOV
Institute of Physics, Ukrainian Academy of Sciences
45 Prospect Nauki, 252650 Kiev, Ukraine

Abstract. To look forward to new trends in modern gas lasers and their applications, the current theoretical and experimental studies (*state-of-art*) on search of new active media for high-power short-wavelength gasdynamic and chemical lasers are reviewed.

The basic physical aspects (optical, kinetical, thermal and fluid dynamical) in operation of gas flow lasers on electronic transitions are discussed. The perspective electronically excited diatomic molecules (halogens, halkogens and other possible candidates from the elements of Group VI and VII) as the potential lasants, and exoenergic gas-phase reactions of radiative recombination of atoms ($S + S$, $Cl + Cl$, $Br + Br$ and others) as the promising way to pump a high energy gain media in the gas flow are considered. The key spectral and kinetic characteristics (recombination efficiency, its branching ratio, quantum yield, rates of E-V-T energy relaxation, radiative lifetime, etc.) important for excitation of the $(B - X)$ band systems of S_2, Cl_2, Br_2 and other molecules are analyzed. The initial thermodynamic parameters, gas mixture composition, pressure and temperature regimes and other conditions necessary for the population inversion and the light amplification sufficient for laser generation in recombining supersonic flows are searched and optimized. The complex strategy of research which includes the pre-laser gasdynamic modeling by 'shock tube' technique and photochemical modeling by 'flash tube' technique to understand a behavior of generator/amplifier laser system are proposed and tested.

As a result of conducted pre-laser studies, the principal possibilities to develop the new powerful laser sources for the wide range of wavelengths in visible and near-IR spectrum are found. Expected performance and advanced applications are discussed also.

R. Kossowsky et al. (eds.), High Power Lasers – Science and Engineering, 95–111.
© 1996 *Kluwer Academic Publishers. Printed in the Netherlands.*

1. Introduction

Since the discovery of the first laser by Basov, Prokhorov, Townes and Schawlow and the first laser demonstrations by Maiman and Javan, there has been considerable progress in the development of industrial lasers and their applications. Due to unique physical properties of the laser beam (high coherence, monochromatic radiation and high power density), the modern laser technologies offer us such important advantages as the high productivity, precision accuracy, high quality, economy of material and energy resources, possibility of automatic processing and clean environment. The further progress of laser technology depends both on the improvement of existing industrial lasers (in order to increase the output, stability, efficiency, reliability, simplicity in use and in service) and on the research and development of perspective technological lasers of new capabilities (in terms of energy and spectral ranges).

Near-IR and visible high power gas lasers on electronic transitions (ET) might be extremely attractive for science and engineering. But all existing now ET gas lasers operate only in pulsed regimes (rare-gas and halide excimers, halogen dimers, etc), commonly initiated by the electron impact or by optical pumping [1]. As is known, a convective flow technique can be used to improve the performance of pulsed lasers and to provide more efficient continuous-wave (CW) laser action. However, there is only the one practical CW chemical oxygen-iodine laser (COIL) operating on the atomic ET of the iodine in the near-IR spectrum at $1.315\mu m$ [2], and this is a most promising type of technological gas flow lasers nowadays [3, 4]. CW gas flow and chemical lasers on molecular ET in visible spectrum have not been demonstrated yet [5, 6, 7]. But in case of success, a discovery of new generation of powerful and efficient short-wavelength gasdynamic lasers on ET (ET GDL) is expected [8, 9, 10].

2. Fundamentals

In principle, from an operational viewpoint, the ET GDL is analogous to well-developed CO_2-, $CO-$ GDL or chemical HF/DF lasers operating on vibrational-rotational transitions (VRT) in the mid-IR spectrum because the key elements of laser technique are similar: gaseous active medium, thermo- and gasdynamic pumping, optical resonant oscillation (for illustration, a typical scheme of ET GDL design is shown in Fig. 1). But to extend an idea of GDL to the near-IR and visible spectral region is not easy, a lot of physical and technical nontrivial problems should be overcome [9].

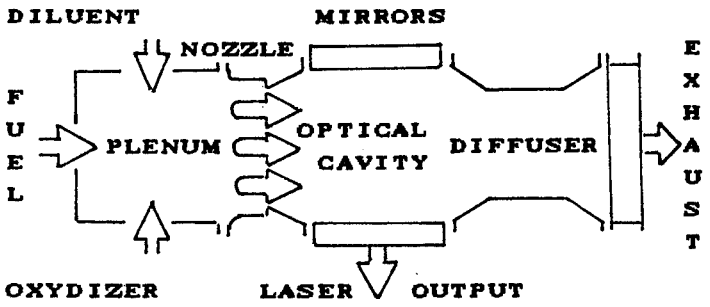


Figure 1. Scheme of gasdynamic laser on electronic transitions (ET GDL). Main units: 1) heat chamber, 2) supersonic nozzle, 3) optical cavity and 4) exhaust system

2.1. BASIC CONCEPTIONS OF ELECTRONIC TRANSITION LASERS

The *basic conceptions* about the specificity of ET GDL can be given without going into particulars of the laser action and above of concrete laser devices [10]. Actually, one of the main difficulties is to produce the intensive excitation of electronically excited states (EES), another is to provide the conditions for the population inversion during the EES relaxation in the gas flow. The integration of these hard-combined requirements imposes the strong limitations on the properties and parameters of laser medium and dictates a choice of methods and regimes of laser generation.

TABLE 1. Typical characteristics of gas laser transitions

Value	Molecular VRT	Atomic ET (line)	Molecular ET (bound)
$\lambda, \mu m$	2.7–2.9	0.5	0.5
$\tau_{rad}, \mu s$	10^4	0.1	10
$R^*, cm^{-3}s^{-1}$	10^{16}	10^{17}	10^{21}
$W_{sp}, W/cm^3$	10^{-5}	10^3	5
σ_{st}, cm^2	10^{-15}	10^{-14}	10^{-17}

For classification, in Table 1 the comparative characteristics of basic types of gas laser transitions are given: the pumping rate R^* required for achieving a threshold gain coefficient of $\alpha \simeq 10^{-3}cm^{-1}$, specific power of spontaneous emission W_{sp}, and cross-section of stimulated emission σ_{st}.

It is known the Einstein's relation that the probability for spontaneous emission varies as factor of ν^3 from the probability for stimulated emission, and the drain of population inversion due to spontaneous emission increases dramatically at short wavelengths. Thus, we can see that for the changeover

from IR to visible region (from VRT to ET) a rate of laser pumping should be increased by factor of 10^3 or more, and it takes a very high pump energy. On the other hand, the molecular ET, due to its close-spaced manifold of vibrational and rotational energy levels, have a broad bandwidth that leads to low gain cross-section (in comparison with the atomic ET), thus a large value of EES population is necessitated for achieving the reasonable light amplification and steady laser oscillation.

In practice, these conclusions results in a high density of active particles and low temperatures of the gas medium necessary to use in ET GDL. To assist in inversion formation and in thermalization, the working mixture must contain a certain gases at a certain pressure. Therefore, a commonly used low-pressure reactive flow mixing technique could not be useful for pumping since it might bring problems. In addition, quite a number of further important points should be borne in mind (the reactive stability, optical homogeneity and waste heat in the gas flow as well as the design of the gasdynamic tract and optical cavity) for providing the efficient laser action. That is why more easy to initiate ET laser in pulsed regime, since its operational time is much shorter that associated with the flow mixing and relaxation in CW mode. Still one difficulty is the lack of reliable kinetical and spectral data (EES excitation and deactivation rates, radiative lifetimes, absorption cross-sections etc.) which are crucial to the selection of suitable laser species and chemical reactions. All this gains the impression that the demonstration of visible ET GDL would take much more efforts than for the conventional IR GDL.

2.2. METHOD OF LASER EXCITATION

Radiative recombination of atoms and free radicals in molecular gases represents an important class of rapid and highly exoenergic chemiluminescent reactions [11]. It attracts our attention potentially as one of the most perspective way to create the thermally pumped and chemically driven ET GDL - a so-called recombination GDL (RGDL).

Unlike the usual IR GDL on VRT, the RGDL can use EES with the excitation energy up to 4 eV. An exemplary energy distribution in the diatomic gas AB for different degrees of freedom as a function of temperature is shown in Fig. 2.

As it seen, in contrast with a relatively small fraction of the vibrational energy, a thermal energy which can be stored in breaking chemical bonds under the molecular dissociation and partitioned into the EES under the atomic recombination amounts to 60%.

The typical potential energy diagram for the diatomic AB lasant with possible electronic-vibrational transitions is shown in Fig. 3. If to produce

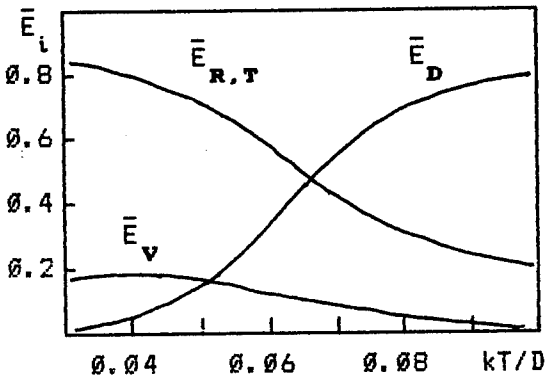


Figure 2. Distribution of the total molecular energy stored in the internal degrees of freedom of the diatomic gas AB versus temperature. $\bar{E}_{R,T}$ - translational and rotational, $\bar{E}_V$ - vibrational, $\bar{E}_D$ - chemical (dissociational) energy fractions.

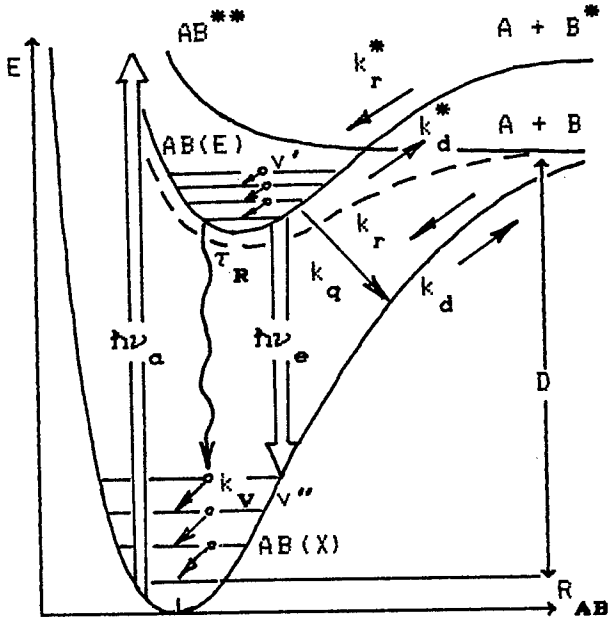


Figure 3. Schematic potential-energy curves (rotationless) and possible electronic-vibrational transitions in the diatomic lasant AB

a net ET inversion with the quantum efficiency of 50%, one could create a laser with the efficiency of conversion up to 10-30%, depending on the laser medium and its mode of operation. Hence, RGDL may be regarded as a

powerful and efficient laser sources.

2.3. KINETICS AND MECHANISM OF LASER PUMPING

The internal kinetics of RGDL can be complicated, but the basic scheme of the *pumping mechanism* is simple enough:

$$
\begin{array}{lllllllll}
A & + & B & + & (M) & \Leftrightarrow & AB(X) & + & (M) \quad (1) \\
A & + & B & + & (M) & \Leftrightarrow & AB(E) & + & (M) \quad (2) \\
 & & AB(E) & + & (M) & \Rightarrow & AB(X) & + & (M) \quad (3) \\
 & & AB(V) & + & (M) & \Rightarrow & AB(v \pm \Delta v) & + & (M) \quad (4) \\
 & & & & AB(E) & \Rightarrow & AB(X) & + & \hbar\nu \quad (5)
\end{array}
$$

Here, A and B are recombining atoms, process (1) is recombination into the ground ES of product molecules $AB(X)$ and its dissociation, (2) is recombination into EES $AB(E)$, (3) is collisional quenching of EES, (4) is vibrational relaxation of ES, (5) is emission of radiation or lasing; processes (1) and (3) compose a "dark" channel, (2) and (5) determine a "light" channel of recombination.

This kinetic mechanism can provide a high rate of molecular EES production and a large quantum yield. In steady-state conditions, the concentration of $AB(E)$ molecules can be found as follows

$$
[AB(E)] = \frac{\eta R}{k_d[M] + k_q[M] + \tau_R^{-1}}, \quad \text{were } R = k_r[A][B][M].
$$

A usual order of magnitude for the atomic recombination rate constant is $k_r = 1 \times 10^{-33}\ cm^6 s^{-1}$ (at room temperatures) and its branching ratio into the EES is $\eta \sim 0.1$. Therefore, to reach the required value of pumping rate $R^* \simeq 10^{21}\ cm^{-3}s^{-1}$ in quasi-equilibrium conditions, the concentration of atoms must be as high as $[A] = [B] \simeq 10^{18}\ cm^{-3}$ (at the mixture dilution of $[AB] : [M] = 1 : 5$). It means the chemical process should be proceed at strong nonequilibrium to shift one toward to the EES production. To do it, a characteristic gasdynamic time, $\tau_g = 1/(dlnT/dt)$, should be much less than a characteristic recombination time, $\tau_r = 1/k_r[A][B]$, which in its turn, should be less than the times of EES collisional quenching $\tau_q = 1/k_q[M]$ and radiative decay τ_R.

Considering terms in the equation for $[AB(E)]$, it is useful to draw the *limit regions* of pressure and temperature parameters that to classify the different cases of EES recombinative population. Appropriate status diagram is shown schematically in Fig. 4.

In $\mathcal{A}$ region, only the equilibrium radiative recombination/dissociation process is realized. The nonequilibrium one occurs in $\mathcal{B}, \mathcal{C}$ and $\mathcal{D}$ regions.

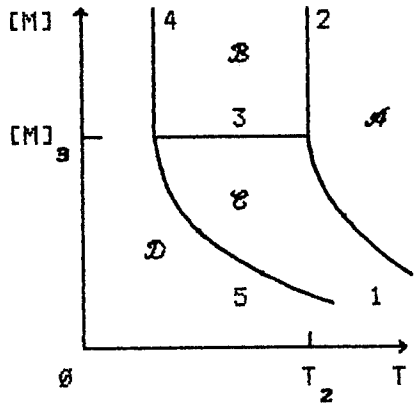


Figure 4. Status diagram for AB EES population formation

In $\mathcal{B}$ region, the quenching predominates to the emission, so the EES population and radiation have an "apparent" two-body character. In $\mathcal{C}$ region, the emission dominates, so the chemiluminescence has a three-body character. In $\mathcal{D}$ region, the EES decay is in excess of VT-relaxation, and the vibrational distribution is substantially nonequilibrium. The maximum of $AB(E)$ population is achieved in $\mathcal{B}$ region with increasing of gas density $[M]$ and decreasing of gas temperature T. The lines 1–5 in Fig. 4 are determined by a set of following relationships:

$$[M] = f_1(T) = 1/\tau_R k_d^*; \qquad T_2 \Leftarrow k_d^*(T_2) = k_q;$$
$$[M] = f_2(T) = 1/\tau_R k_q; \qquad T_4 \Leftarrow k_{VT}(T_4) = k_q;$$
$$[M] = f_5(T) = 1/\tau_R k_{VT}.$$

2.4. CRITERIA OF INVERSION AND LASER AMPLIFICATION

A case of achieving the *population inversion and light amplification*:

$$\alpha^{(+)} = \sigma_E[AB(E)] > \alpha^{(-)} = \sigma_X[AB(X)]$$

varies with the parameters of working molecules (molecular constants, energy-level structure, transition probabilities, etc) and presents a complex quantum "trade-off" between gain and loss mechanisms (Fig. 3).

A simplest criteria of net inversion under atomic recombination is

$$[A][B] \geq [AB] \times K_P(T)\ exp(\hbar c/\lambda kT),$$

where $K_P(T)$ is the thermodynamic constant of $A + B \Leftrightarrow AB$ equilibrium.

Putting $[A] = [B] = [AB]$, one can define a top limit of operational temperatures in which the inversion and gain occurs:

$$T^* = (D - \hbar c/\lambda)/k\ ln(K_P/[AB]).$$

For most appropriate molecular lasants, due to a shift of the EES potential energy curves relatively to the ground ES and because of favorable Frank-Condon factors, a partial population inversion should be created between the low v'-levels of the laser EES and the high v''-levels of the ground ES, essentially unpopulated at low operational temperatures. This occurs necessarily when VT-relaxation is more rapid than EES-deactivation (due to presence of chemically active atoms and relatively small vibrational quants). The condition of $k_{VT}[M]) < \tau_R$ determines a bottom limit of the gas densities [M] needed.

The criterion for evaluation of partial population inversion is as follows:

$$\frac{\eta R\ exp(-v'\hbar\omega'/kT)}{k_{VT}[M] + \tau_R^{-1}} > \frac{\omega''\ exp(-v''\hbar\omega''/kT)}{\omega' K_P(T)\ exp(\hbar\omega''/kT)} + \frac{R}{k_{VT}[M]v''\hbar\omega''/kT}.$$

A bandwidth of radiative ET depends on the electronic structure of the emitting EES and ground ES, as well as the function of distribution among rovibronic energy levels. Normally, laser EES have the short radiative lifetimes (microseconds). But many molecules have a long-lived metastable EES also that lie close and sometimes below the upper laser level. These EES act as the energy storage reservoirs for electronic excitation that channeling via radiative EES due to numerous curve crossings and overlappings. The role of such metastables should not be ignored.

2.5. BACKGROUND FOR LASER DEVELOPMENT

To summarize our knowledge, we have a sufficient *background* for RGDL:

a) there are specific diatomic molecules as the potential lasants and radiative gas-phase recombination processes going by the scheme (1)-(5), for which the spectral, kinetical and other properties are favorable and well-known (halogens, halkogens and other possible candidates from the elements of Group VI and VII);

b) high degree of dissociation of this molecules is reached at the practicable temperatures of plenum gas: for Br_2 (dissociation energy $D \simeq 2eV$) the corresponding temperature is $T_d \simeq 2000K$, for Cl_2 ($D \simeq 2,5eV$) - $T_d \simeq 3000K$, for S_2 ($D \simeq 4eV$) - $T_d \simeq 4000K$. This allows to produce the high densities of atoms in the plenum chamber under thermal heating by electrical arc, shock waves, explosion or combustion;

c) hot dissociated gas can be gasdynamically cooled ("chemically frozen") to temperatures below $T \leq 500K$ fast enough under the supersonic expansion (Mach number $M_e \geq 3$) in the small-scale Laval nozzles (throat height $h_* \leq 1\ mm$) during the times $\tau_g \leq 10^{-5}s$ that to initiate the recombinative pumping followed by the inversion formation and light amplification. Laser output is gained by stimulated emission in the optical resonator.

d) In addition to the gas pressure and temperature regulation, the supersonic flow provides also to rapid remove the waste species and heat release following the laser action in the cavity. Presence of the buffer component in the gas mixture promotes to extend the length of inversion zone in the flow up to a few tens (10-50) *cm*.

f) RGDL can operate under a wide range of intracavity paramenters to provide a steady beam at moderate pressures ($\sim$ 0.1 *atm*) normally, or very powerful pulses at high pressures ($\sim$ 1.0 *atm*). It allows recovery to the atmospheric pressure by the simple supersonic diffuser, thus eliminating the need for mechanical pumps or ejectors.

g) There are some fuels can contain all necessary species and supply the temperature and pressure regimes required, so the pure chemical RGDL can operate continuosly as long as the gas flows through the laser cavity (like a rocket jet engine).

TABLE 2. Operational parameters of recombination gasdynamic laser (RGDL)

Gas composition	Laser electronic transitions	λ μm	T_0 K	P_0 atm	M -
Br_2:Ar=1:5	$B^3\Pi_{1u}(v'=0) \rightarrow X^1\Sigma_g^+(v''=14-20)$	1.0-1.3	2200	20	5
Cl_2:Ar=1:5	$B^3\Pi_{0u}^+(v'=0) \rightarrow X^1\Sigma_g^+(v''=12-18)$	0.9-1.2	3000	25	4
S_2:Ar=1:5	$B^3\Sigma_u^-(v'=0) \rightarrow X^3\Sigma_g^-(v''=10-15)$	0.4-0.5	4000	30	3

Table 2 represents the optional operational conditions selected within the framework of the RGDL theory predictions [10].

3. Results and Discussions

Because of a complexity of the RGDL development, it takes the special 'step-by-step' strategy of research: first of all, to carry out the *pre-laser* gasdynamic, photochemical and optical studies and only then to work out a practical RGDL device. The elements of such strategy have been tested by the RGDL Group in Kiev.

3.1. GASDYNAMIC PRE-LASER EXPERIMENTS

The method of thermal heating - fast cooling of the gas medium and the recombination pumping scheme (1)-(5) were realized under the supersonic flow conditions for the $Cl_2(B-X)$ system in the gasdynamic pre-laser experiments [12, 13]. This technique consists of the shock-wave dissociation of molecular gas in the shock tube followed by recombination of atoms in the supersonic nozzle.

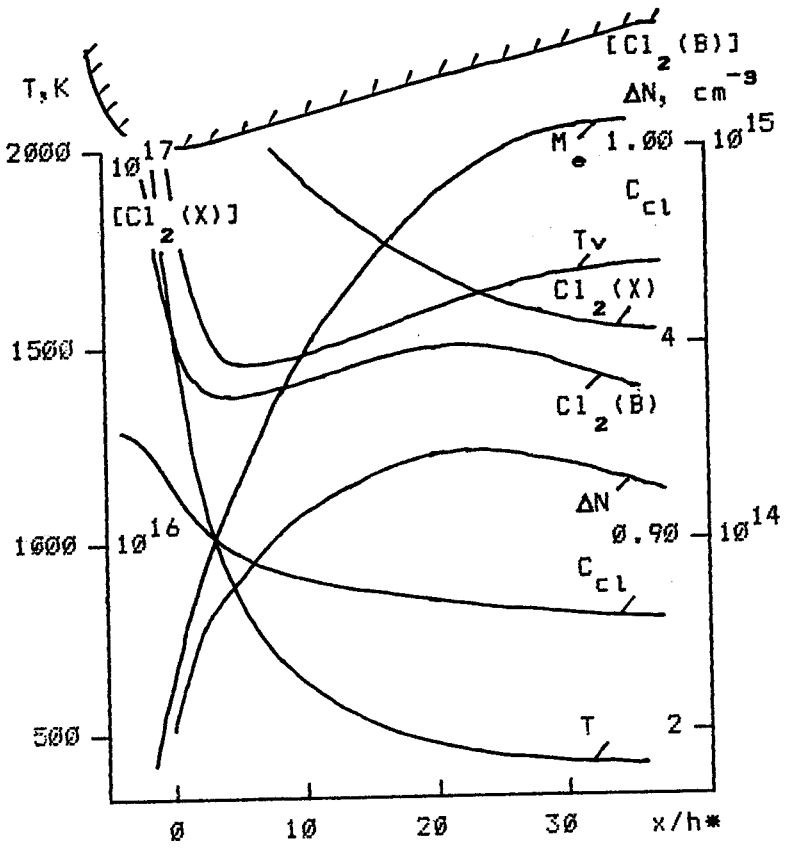


Figure 5. Results of pre-laser studies of $Cl_2(B-X)$ RGDL. Evaluation of the gas flow parameters and population inversion formation versus distance x/h_* in the nozzle $h_* = 0.18\ mm, \theta^0 = 30^0$ for the plenum conditions T_0=3530 K, P_0=17 atm, pure Cl_2. Lines - simulation, I - observation.

The pure chlorine and diluted mixture with argon were used. The optical (shadow and interferometric) visualization and spectroscopic (emissive and absorptive) flow diagnostics in complex with the two-dimensional flowfield numerical simulation were performed. The population of the ground ES $[Cl_2(X)]$ and vibrational temperature T_V were defined from the measured values of gas absorptivities A_λ, and the population of the radiative EES $[Cl_2(B)]$ - from the measured gas emissivity I_λ. The absorption coefficients ε_λ and radiative lifetimes τ_R were found on the basis of analogous measurements behind the shock waves in the shock tube and respective spectroscopic calculations. Solving an inverse kinetical problem, the recombination efficiency $k_r(M)$, excitation branching ratio k_r^*/k_r, rates of EES quenching $k_q(M)$, vibrational relaxation $k_{VT}(M)$, and other characteristics of Cl_2 kinetics were determined (see for details [13]).

As a result, the high nonequilibrium concentration of atoms $[Cl] \geq 10^{17} cm^{-3}$ in the supercooled gas flow was produced, and the extremely intensive recombinative radiation, $I_R = \int I_\lambda d\lambda \simeq 10^{18} phot\ cm^{-3} s^{-1}$ was achieved (equivalent specific power of emission W_{sp} is evaluated to be up to 0.1 W/cm^3). The effects of "chemiluminescence ignition" in downstream, "red" shift and narrowing of the emission spectra also was observed.

TABLE 3. Conditions of pre-laser studies of $Cl_2(B-X)$ RGDL

h^* mm	T_0 kK	P_0 atm	Cl_2 : Ar	I_λ $cm^{-4}s^{-1}$	T K	T_V K	$[Cl_2(X)]$ cm^{-3}	ΔN cm^{-3}	α cm^{-1}
0.11	3.3	20	1:0	1×10^{23}	365	1230	6×10^{16}	2×10^{14}	0.003
0.11	2.6	19	1:2	2×10^{22}	252	1120	8×10^{16}	4×10^{14}	0.002
0.18	3.4	41	1:0	8×10^{22}	620	980	2×10^{17}	8×10^{13}	0.001

It was found that in the supersonic gas flow (Mach number $M_e > 3$) due to the high rate of recombination pumping into the radiative B-state ($R^* \geq 10^{20}\ cm^{-3}s^{-1}$), slow quenching of metastable $^3\Pi$-states as a whole ($k_q \leq 10^{13}\ cm^3 s^{-1}$) and rapid VT-relaxation in the absorbing X-state ($p\tau_{VT} \leq 5 \times 10^{-8}\ atm\ s$, and T_V is not for much more than T), the partial population inversion on ET $Cl_2(B, v' = 0,1 \rightarrow X, v'' = 12-18)$ in near-IR spectrum ($\lambda = 0.9 - 1.2 \mu m$) with the density of $\Delta N \geq 10^{14}\ cm^3$ is formed.

Experimental varying of the initial thermodynamic parameters over the range of T_o=2000-4000 K, P_o=10-50 atm, Cl_2 : Ar=1:0-1:8 showed that a value of optical gain $\alpha \sim 10^{-3} cm^{-1}$ in the nozzle flow obtained agrees well with the theoretical predictions and seems to be a sufficient for laser generation. The gasdynamic quality of the recombining flow in the designed part of supersonic micronozzles is found also to be a good enough.

The typical conditions and results of pre-laser studies of $Cl_2(B-X)$ system are shown in Fig. 5 and summarized in Table 3.

3.2. PHOTOLYTIC PRE-LASER EXPERIMENTS

The recombination pumping scheme (1) - (5) at the regime of laser amplification was realized under the flashlamp photolysis conditions for the $Br_2(B-X)$ system in the *photochemical pre-laser experiments* [14]. This technique consists of the pulse photodissociation of molecular gas followed by recombination of photofragments in the flash tube.

In the pure bromine gas at the pressure of 100 Torr, the optical gain up to $5 \times 10^{-4} cm^{-1}$ at $\lambda = 1.06 \mu m$ and the specific laser energy up to 7 J/l in the pulse duration of 100 ms was achieved without any optimization. We estimate that the specific laser energy can be increased by order of

magnitude, and the efficiency up to 5-10% can be obtained potentially. We have succeed in analogous photolytical pumping for the $Cl_2(B-X)$ system in high-pressure Cl_2/Ar mixture also.

3.3. CRITICAL REVIEW OF EARLY EXPERIMENTS

It should be mentioned some early attempts to realize the RGDL when the preliminary phase of laser studies was ignored [15, 16].

The first experiments were done in the FIAN in Moscow [15]. Unfortunately, the $O_2(B-X)$ system was wrongly selected as a lasant, and the direct driving of the dissociating-recombining gas through the supersonic nozzle and resonator with high quality mirrors have not been resulted in the laser action neither in visible nor in near-IR spectrum. In accordance with our estimating, under these conditions the optical gain was not more than of $10^{-6}cm^{-1}$. The point is that the low-lying EES of O_2 molecules, populating under the $O+O$ atomic recombination, have a strongly forbidden ET, thus the RGDL could not be possible.

The researchers from the IFM in Marseille [16] failed to demonstrate RGDL directly taken the experimental set-up as for the heat pumped CO_2-GDL. They ran experiments simply using various dissociated molecular gases: SO_2, NO_2 and others, but did not obtain any laser effect under the atomic recombination $SO+O, NO+O$, etc. Moreover, they have not been able to do any conclusions since they have not got necessary instruments to measure parameters in the recombining gas flow. Such a way without detailed spectral and kinetical investigations could not be successful.

More reliable pre-laser gasdynamic studies have been carried out recently for the $Cl_2(B-X)$, $S_2(B-X)$ and $NF(B-X)$ systems by the LASERDOT Group in Paris [17]. Although the conditions of the standard HF/DF laser set-up used in experiments were unsufficient for laser generation (due to a low pressure mixing technique selected), they have realized the partial inversion under the recombination pumping scheme (1)-(5) and observed the superluminescent emission in the supersonic flow. It seems to be a promising way to obtain a pure chemical RGDL in principle.

3.4. ALTERNATIVE APPROACH

Besides the direct recombination pumping scheme, it is known an alternative way to create the powerful visible GDL on ET using a *donor-accepter* pumping scheme based on the resonant molecular E-E energy transfer.

Actually, there are quite a number of fast chemical reactions (atomic recombination reactions are among these) which have a high yield into the metastable excited states of molecules. In this way, one can obtain a high density of product metastables (up to $10^{16}cm^{-3}$) carrying a great electronic

excitation energy (from 1 to 6 eV). Unfortunately, it is difficult to transform the metastables' energy into the laser radiation directly because ET into ground ES are forbidden by Vigner-Witmer rules on spin and orbital symmetry correlations (cross-section of ET is very small $\sigma_* < 10^{-20} cm^2$). Such a situation may be a case with products of recombination for the oxygen $O_2(a^1\Delta_g)$, nitrogen $N_2(A)$, etc. But using these metastables as the EES energy donors, one can find the suitable near resonant EES energy accepters. The criteria for choice of the donor-accepter pares are the EES excitation efficiency and radiative property of lasants. Halogens and halkogens are also appropriate candidates here due to a good combination of spectral and kinetical characteristics, so the partial population inversion arises between low v'-levels of the radiative EES and high v''-levels of the ground ES.

To contrast with the above mentioned COIL on the molecular-atomic EE, the molecular-molecular EE laser system has not been demonstrated yet [18], although efforts to develop chemically driven EE lasers for the green $NB(b-X)$ and blue $BiF(A-X)$ systems were attempted too [19].

3.5. OPTIMISTIC REMARKS

It is important to highlight that all molecular candidates selected for the RGDL has been approbated in the practical dimer ET $(B-X)$ and/or $(D'-A')$ lasers with the direct optical and photolytical pumping [20, 21]. If to consider the laser operation as a complex of three sequential stages: 1) high laser levels population, 2) broad band stimulated radiative ET, and 3) low laser levels depopulation, experimentally two last processes have been successfully demonstrated, and the mechanism of V-T relaxation proved to be able "over-work" the molecular rate of radiative ET in CW lasing comparable to analogous in the RGDL. This fact inspires the optimism.

4. Perspectives

Although presently the ET GDL (RGDL) is under research and development and is not demonstrated yet, we have to see and discuss what can be expected in progress.

4.1. EXPECTED PERFORMANCE

The RGDL on ET will differ from the usual GDL on VRT by the following important advantages:
- short wavelengths of laser radiation ($\lambda = 0.4 - 1.2\mu m$);
- wide tuning of laser spectrum ($\Delta\lambda/\lambda = \pm\ 15\%$);
- high specific laser energy (up to 500 J per gram of the mass flow rate and

up to 10 kW per cm^2 of the cross-section of the flow in the cavity);
- high laser efficiency (up to 5-10%);
- high beam quality (divergence less then 1 mrad);
- wide range of operation (CW or pulsed, multi-wavelength or single mode)

As the RGDL is a low-gain laser system ($\alpha \sim 1\%/cm$), it can be scaled to a very powerful device (tens of kilowatts) without losses of efficiency. For example, compact RGDL with a cross-section of $5 \times 50\ cm^2$ would produce of 50 kW in a steady beam. In a pulsed mode, for the laser pulse duration of 10 ms and repetition rate of 10 Hz, the RGDL may have pulse energy up to 1 kJ and average power about 10 kW.

Again, all optically pumped recombination (photodissociation) lasers on ET have confirmed their high performance in terms of specific energy, efficiency and tunability as well [21].

4.2. ADVANCED APPLICATIONS

Due to its unusual energetic and spectral characteristics, RGDL will have potential for all high-power laser applications in science and engineering.

As the RGDL will have no physical limitation in output power and the beam quality can be good enough, an efficient application for high-speed *material processing* (cutting, welding, drilling, etc) should be expected.

In fact, for industrial laser technologies the gas flow CO_2 and solid state $Nd:YAG$ lasers are most widely used now: the users of CO_2 lasers take advantage of its high power output capability, and the users of $Nd:YAG$ lasers focus on its high fiber-optic transmission capability. The RGDL will possess both important advantages simultaneously being able to operate in CW and multi-pulsed regimes. While a power level of the RGDL (scaling up to 10- 100 kW) is superior to that of CO_2 lasers at the same conditions, its operating wavelength lies in the range of minimum optical loss of silica fibers as for $Nd:YAG$ lasers. Therefore, it is feasible to produce and deliver high-power laser output through a multi-users fiber-optic network system with the RGDL as a central power station and combined it with a robot X-Y processing for precision *microtechnology* (semiconductor scribing, photolitography, etc.) also. Decrease of the beam divergence (up to 2-3 diffraction limits) in the RGDL, associated with the shorter wavelength, results in the better focusability ($\sim \lambda^2$) which allows to increase the energy concentration on the target for 100 times higher than in the CO_2 laser of the same power. Combining this effect with the lesser reflectivity and greater absorptivity of metals ($\sim \lambda^{-3/2}$), the RGDL may be expected to give more high quality of material processing.

The wide-range tunability of RGDL (like for dye lasers) will open the new possibilities for high-power *photochemistry* (laser-induced catalysis, isotope separation, etc.), *biotechnology* and *medicine.*

The RGDL can be multifunctional ground-based, transport-mounted or space-based laser *module* system. For special *laser energy production* and direct (wireless) long-distance beam *transmission* and *communication*, the RGDL would operate in an autonomous regime and without using an electric input energy sources. A powerful *lidar* (laser radar) for *remote sensing*, *environmental control* and *atmospheric monitoring* will be possible as well.

At last, due to the favorable characteristics of short-wavelength operation and high-energy storage, the efficient repetitively-pulsed (up to $10^4 Hz$) *generator-amplifier* system can be expected to construct as an alternative laser driver for the *nuclear fusion* research.

5. Conclusions

Despite these fascinating possibilities nobody has tried really to develop the ET GDL (RGDL) probably because of some difficulties mentioned above. It motives us to take part in this challenge because it will be a discovery of unusual and interesting laser sources which will have a significant impact in the advanced laser technology for the next century.

6. Acknowledgements

The authors would like to acknowledge the support of Directors of the NATO Advanced Study Institute "High Power Lasers - Science and Engineering", Dr. Ram Kossowsky and Dr. Robert Walter, without which this paper would not have been possible.

References

1. (a) *Electronic Transition Lasers* (1977) Eds. L.E.Wilson, S.N.Suchard and J.I.Steinfeld, MIT Press, Cambridge;
   (b) *Excimer lasers* (1979) Ed. Ch.K.Rhodes, Topics in Applied Physics: Vol.30, Springer-Verlag, Berlin;
   (c) *Gas Lasers* (1982) Eds. E.M.McDaniel and W.L.Nighan, Academic Press, N.Y.
2. McDermot, W.E., Pchelkin, N.R., Benard, D.J. and Bousek, R.R. (1978) An electronic transition chemical laser, *Appl. Phys. Lett.* **32** No.8, 469–470.
3. (a) Fujii, H., Yoshida, S., Iizuka, M. and Atsuta, T. (1990) Development of high-power chemical oxygen-iodine laser for industrial applications *J. Appl. Phys.* **67** No.9, 3948–3952;
   (b) Yoshida, S. and Shimizu, K. (1990) High power chemical oxygen iodine laser for industrial applications, in *Proc.Intern.Conf.on High-Power Gas Lasers*, SPIE Vol.1225, 478–481.
4. (a) Avizonis, P.V. (1984) Chemically pumped electronic transition lasers, in *Gas Flow and Chemical Lasers*, Plenum Press, N.Y.;

(b) Avizonis, P.V. and Truesdell, K.A. (1994) The chemical oxygen-iodine laser (COIL), in *Proc.10th Intern.Symp. on Gas Flow and Chemical Lasers, Friedrichshafen*, 180–203.

5. Report of the APS Study Group (1987) *Rev. Mod. Phys.* **59** No.3, S33–S68.
6. (a) Gavrikov, V.F., Dvoryankin, A.N., Stepanov, A.A., Shmelev, A.K. and Shcheglov, V.A. (1989) Chemical lasers of visible and near IR spectral ranges, in N.G.Basov (ed.), *Investigation of Chemical Lasers*, Proc.Lebedev Phys.Inst., Moscow, 171–211 *(in Russian)*;
(b) Dvoryankin, A.N. (1990) Continuous wave chemical lasers of visible region, in *Proc.8th Intern.Symp. on Gas Flow and Chemical Lasers, Madrid*, 145–152.
7. Rosenwaks, S. (1992) The search for short-wavelength chemical lasers - an overwiew, in *Proc.9th Intern.Symp. on Gas and Flow Chemical Lasers, Heraklion*, 232–239.
8. (a) Bashkin, A.S., Igoshin, V.I., Nikitin, A.I., Oraevskii, A.N. (1975) *Chemical Lasers*, VINITI Publ., Moscow *(in Russian)*;
(b) Losev, S.A. (1977) *Gasdynamic Lasers*, Nauka Publ., Moscow *(in Russian)*.
9. Eletskii, A.V. and Smirnov, B.M. (1985) *Physical Processes in Gas Lasers*, Energoatom Publ., Moscow *(in Russian)*.
10. Kochelap, V.A. and Pekar, S.I. (1986) *Theory of Spontaneous and Stimulated Chemiluminescence of Gases*, Naukova dumka, Kiev *(in Russian)*.
11. Izmailov, I.A. and Mel'nikov, L.Yu. (1989) *Mechanisms of Electronic Chemiluminescence in Gases*, VINITI Publ., Moscow *(in Russian)*.
12. Belokrinitskii, N.S., Kochelap, V.A., Kernazhitskii, L.A. and Shpak, M.T. (1982) Pre-laser studies of the recombination of chlorine atoms, *Quant. Electron.* **9** No.2, 298–308 *(in Russian)*.
13. (a) Kernazhitskii, L.A., Nosenko, V.E., Naumov, V.V., Kochelap, V.A. and Izmailov, I.A. (1985) Kinetics of the intense chlorine chemiluminescence in a supersonic nozzle, *Chem. Phys. Lett.* **116** No.2/3, 197–201;
(b) Izmailov, I.A., Kernazhitskii, L.A., Kochelap, V.A., Naumov, V.V. and Shpak, M.T. (1988) Dynamics of radiative recombination of chlorine atoms in supersonic flows, *Arch. Combust.* **8** No.3/4, 277–286;
(c) Izmailov, I.A., Kernazhitskii, L.A., Kochelap, V.A., Naumov, V.V. and Shvarchuk, E.A. (1990) Gasdynamic recombination pumping of $Cl_2(B-X)$ inverse system: theory and experiments, in *Proc.8th Intern.Symp. on Gas Flow and Chemical Lasers, Madrid*;
(d) Kochelap, V.A., Izmailov, I.A., Kernazhitskii, L.A. and Naumov, V.V. (1991) Study of recombination gasdynamic lasers on electronic transitions, *J. de Physique IV* **C7-1**, 637–642;
(e) Naumov, V.V., Kochelap, V.A. and Izmailov, I.A. (1993) Analysis of new active media for high power gas flow lasers in visible and near IR spectrum, *LAMP Series Report*, ICTP Preprint No.93/2, Trieste.
14. Antipenko, V.M., Privalova, T.A. and Tarasenko, V.V. (1985) Recombination Br_2–laser with optical excitation, *Opt.& Spectrosc.* **59** No.5, 947–950 *(in Russian)*.
15. Volkov, A.Yu., Demin, A.I., Kudryavtsev, E.M. and Sobolev, N.N. (1976) On the possibility of designing a recombination gasdynamic O_2-laser, *JETP* **70** No.2, 503–510 *(in Russian)*.
16. Fontaine, B. and Forestier, B. (1976) On potentiality of three body recombination processes for the high power continuous wave visible laser generation, *Quant. Electron.* **3** No.4, 897–905 *(in Russian)*.
17. (a) Prigent, P., Giraud, X., and Brunet, H. (1988) Study of the production of $Cl_2(B)$ from the recombination of chlorine atoms, in *Proc.7th Intern.Symp. on Gas Flow and Chemical Lasers, Vienna*, 408–413;
(b) Prigent, P., and Brunet, H. (1990) Study of the production of $S_2(B)$ from the recombination of sulfur atoms, in *Proc.8th Intern.Symp. on Gas Flow and Chemical Lasers, Madrid*, 197–201;
(c) Voignier, F., and Leporcq, B. (1992) Experimental study of the production of

electronically excited $IF(B)$ in a supersonic flow, in *Proc.9th Intern.Symp. on Gas Flow and Chemical Lasers, Heraklion*, 265–268.

18. Gole, J.L., Woodward, J.R., Cobb, S.H., Shen, K.K. and Doughty, J.R. (1990) Chemically driven pulsed and continuous visible laser amplifiers and oscillators, in *Proc.8th Intern.Symp. on Gas Flow and Chemical Lasers, Madrid*, 125–135;
19. (a) Herbelin, J.M. (1986) Prospects of a visible (green) NF chemical laser, *Appl. Opt.* **25** No.13, 2138–2141;
    (b) Herbelin, J.M. (1990) Progress toward the demonstration of a visible (blue) BiF chemical laser, in *Proc.8th Intern.Symp. on Gas Flow and Chemical Lasers, Madrid*, 161–167;
    (c) Benard, D.J. and Winker, B.K. (1991) Chemical generation of optical gain in BiF at 471 nm, *J. Appl. Phys.* **69** No.5, 2805–2809.
20. Wellegehausen, B. (1979) Optically Pumped CW Dimer Lasers, *IEEE J. Quantum Electron.* **15** No.10, 1107–1130.
21. (a) Kamrukov, A.S., Kozlov, N.P. and Protasov, Yu.S. (1990) Visible and UV gas lasers with high current radiative discharge excitation, in *Proc.8th Intern.Symp. on Gas Flow and Chemical Lasers, Madrid*, 137–144;
    (b) Protasov, Yu.S., Kamrukov, A.S. and Kozlov, N.P. (1992) Near IR and visible lasers with wide-band UV-VUV pumping for technological application, in *Proc.LAMP'92 Conf., Nagaoka.*

ON UNSTABLE RESONATORS PRODUCING COMPACT OUTPUT BEAM

N.D. CHEREPENIN AND SH.KH. ZARIPOV
Kazan State University
Kazan, Tatarstan, Russia

AND

YU.YA. USANOV
Blaster Ltd
Kazan, Tatarstan, Russia

Abstract. A class of unstable laser resonators producing output beams with a continuous compact aperture by a simple manner, without involving special optical components is described. These resonators are composed of spherical mirrors and belong to unstable optical ones both for positive and negative branches. Space distributions of the cavity lasing modes and output characteristics of such resonators for a fast-flow discharge CO_2 laser are investigated numerically. The results demonstrate very favourable prospects for using this type of resonators.

1. Formulation of the problem

Obtaining the beam with a compact aperture (i.e. a continuous beam's cross section possessing as minimal as possible sizes under a fixed area) on output of an unstable optical resonator (UOR), provides, as a rule, considerable advantages in angular divergence of laser radiation in comparison with beams of usual UOR. It is of particular importance for lasers with weakly amplifying media (such as gas CW lasers used for industrial applications) [1]. The known techniques of shaping such beams [1-3] have some defects, in avoidance of which a simple design of the UOR with beam inversion between the mirrors was presented in the previous work of the authors of this paper [4]. Main part of the output aperture of this resonator has a

R. Kossowsky et al. (eds.), High Power Lasers – Science and Engineering, 113–123.
© 1996 *Kluwer Academic Publishers. Printed in the Netherlands.*

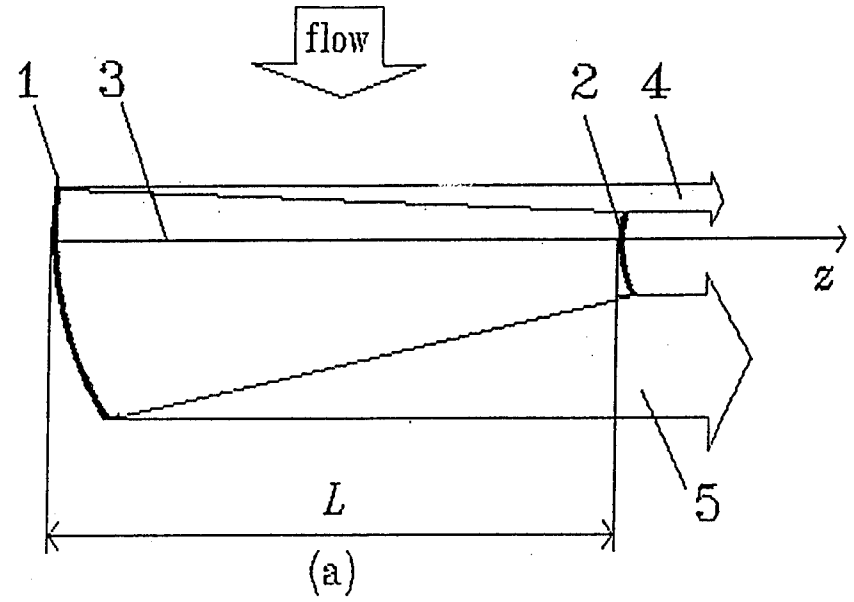
continuous rectangular shape and the cross section of two separated near-axial parts of the output beam has an insignificant area, the ratio of which to the area of the main aperture can be made as small as is wished.

Here, in development of this proposal, the unstable resonators are considered in which obtaining a compact aperture of the output beam is based on a general idea, that permits us to integrate them into one class of compact beam resonators (CBR). The proposed resonators are composed of spherical mirrors and shape the output beams with compact apertures by a simple manner, without involving special and/or external optical components. These resonators belong to the UOR's type for positive as well as for negative branches.

Two characteristic schemes of these CBR are presented in Figures 1 and 2. First of them is constructed on the base of the telescopic resonator and second is based on the unstable confocal one with inversion of the beam between concave mirrors. In the both cases the specific features that provide the compactness of the main part of the laser beam aperture are as follows. First, there is a comparatively small-sized near-axial generation region of the beam (with dimensions $a \times b$) along the edge of which an insignificant part of radiation has to be removed (screened). Second, the output mirror is placed with certain asymmetry with respect to the optical axis. Here M is the resonator magnification modulus, L is the distance between mirrors, and n is the number of amplification cavity round trips, starting from the generation region.

A small protrusion δ of the left-hand edge of the output mirror beyond the optical axis is added for suppressing possible strong diffraction effects (see Figure 1). It is chosen from the condition $\delta > r_1$, where radius of the first Fresnel zone r_1 is determined by the equation $F_{eq}(r_1)$=0.5 (see, for example, [5]). For a telescopic resonator we have $r_1 = \sqrt{\frac{L\lambda}{M-1}}$ (λ is the radiation wavelength).

The schemes in Figure 2 correspond to odd n; whereas, in the case of an even n, the near-axial and principal output beams are to be located on the same side (downstream) with respect to the optical axis. Thus, the geometrical cross sections of the laser beam on the both mirrors consist of n adjoined rectangles obtained via consecutive transformations of the generation region within the resonator. The last-named rectangle in this sequence is as big as $(M^n - M^{n-1})a \times M^n b$ (Figure 1) or $(M^n - M^{n-2})a \times M^n b$ (Figure 2). It is located downstream from the right-hand edge of the output mirror and determines the shape of the principal output beam.



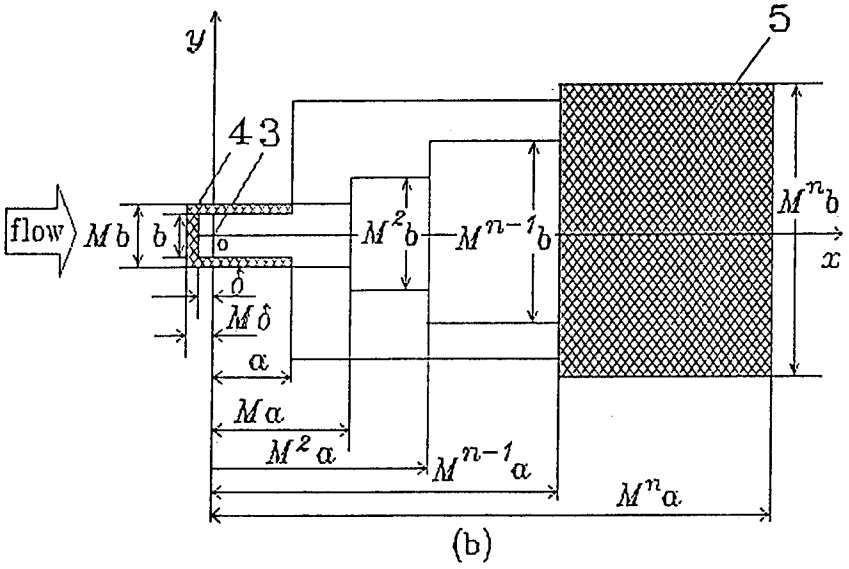
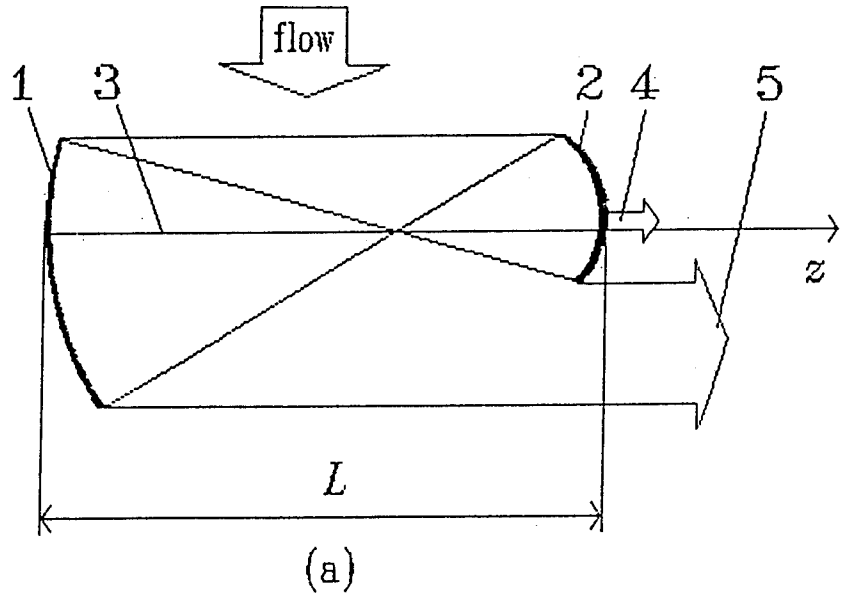


Figure 1. Schemes of the positive branch CBR (a) and beam in the output cross section (b): 1 and 2 are the mirrors; 3 is the optical axis; 4 and 5 are the near-axial and principal output beams, respectively.



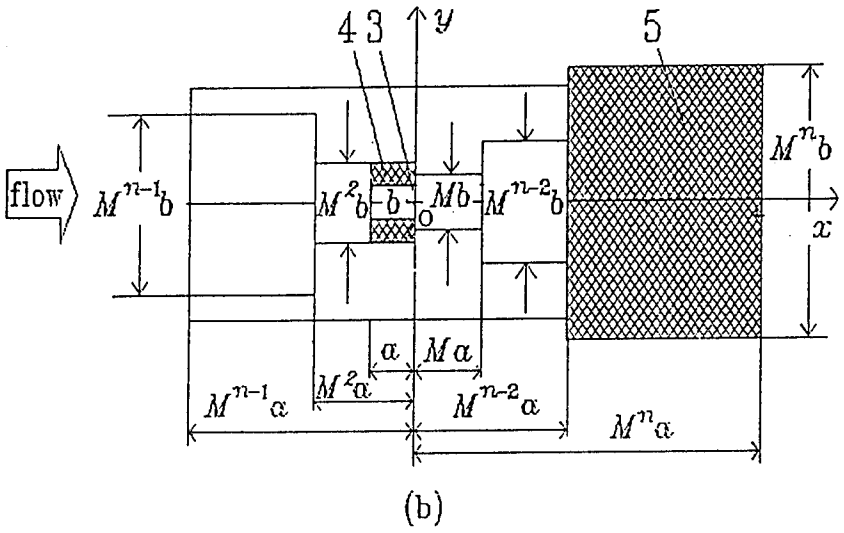


Figure 2. Same as Figure 1, but for the negative branch CBR.

2. Mathematical simulation

The mathematical model of such discharge laser cavities was developed for a fast-flow industrial CW laser with the transverse pump of the mixture CO_2-N_2-He excited by a self-sustained discharge. This 3-D model for the case of the negative branche CBR is described in [4]. It is based on solving the quasi-optical or geometric-optical equations for the radiation field simultaneously with a set of the equations of nonequilibrium gas dynamics and vibrational kinetics for the laser medium [6]. This medium is taken into account in discrete amplitude-phase cross sheets z=const in which the distributions of the gain and the refraction index are determined from the solution of the gas-kinetic equations under given radiation intensity $I(x, y, z)$.

The resonator lasing mode is interpreted as the eigen-function of a complex nonlinear operator describing the transformation of the light waves during the complete round trip pass within the resonator; this operator is defined by successive solving the equations mentioned above. The self-consistent solution for the entire problem is obtained numerically by the steady-state method implying separating into two parts an operator of transition between the mentioned cross sheets. One of the parts describes the propagation (and diffraction) of the light waves in a free space, and the other describes the amplification (or absorption) and the refraction within the laser medium and on the mirrors. The diffraction step of this operator is performed by the spectral method in discrete form via the fast Fourier transform [7,8]. After finishing the iterations of the steady-state method, the far-field intensity distribution and the corresponding values of radiation divergence are to be computed via the Fourier transform of the output wave's field.

Notice that the developed mathematical model includes all the principal design features of one or other species of the considered cavities. Both the telescopic and confocal negative branch designs of the CBR with rectangular apertures are studied.

3. Numerical results

Below we present some results of calculations. Notice that in choosing principal initial parameters we assume the conditions which are typical of the actual industrial CO_2 laser. Figure 3 shows the intensity distributions of the output beam in the near- and far-field zones for the empty positive branch CBR at M=1.5, n=2, and b/a=0.84; the collimated Fresnel number [7] $F_c = \frac{M^{2n}b^2}{4(M+1)L\lambda}$=80. As well as in the case of the negative branch CBR [4], the output wave's field indicates that the effect of intracavity

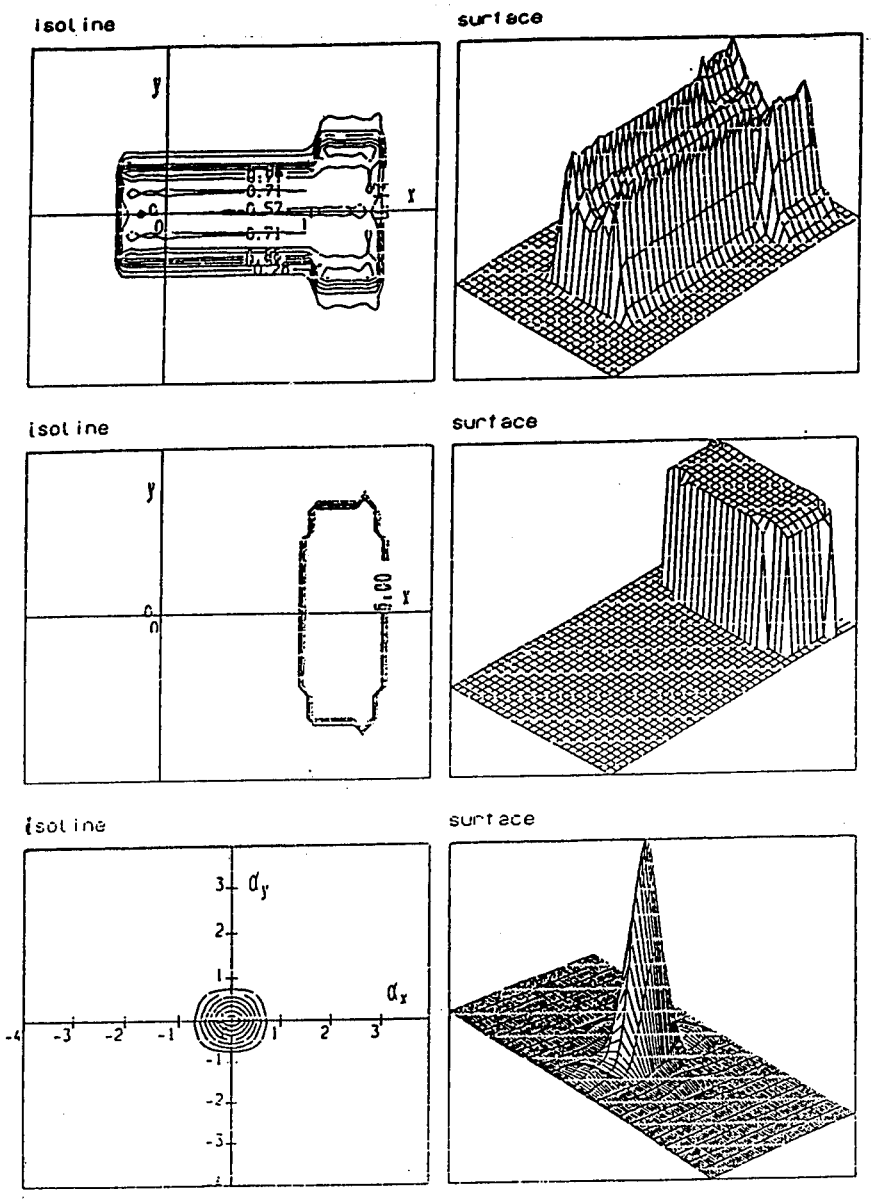


Figure 3. The radiation intensity in the output cross section, the output beam phase, and the far-field intensity for the empty positive branch CBR; angular coordinates α_x and α_y are expressed in terms of diffraction scales λ/c and λ/d, respectively (c and d are geometrical dimensions of the output beam).

diffraction is negligible, whereas the far-field intensity distribution is close to the corresponding one for an ideal rectangular source of radiation [1].

Numerical simulation shows that in many cases of practical importance the problem can be considered within the framework of geometrical optics, i.e., the simplest mathematical model is acceptable, in which the mentioned diffraction step of the operator of transition between the amplitude-phase sheets proves to be unnecessary. The results presented below were obtained without taking into account the diffraction and under the following initial parameters. At the inlet, the flow velocity, pressure and temperature were assumed to be as follows: v=120 m/s, p=50 Torr, and T=290 K, respectively. Composition of the mixture CO_2-N_2-He=1:10:10; the intensity of gas discharge w=10.8 W/cm^3; the specific strength of the electric field $E/N = 3.5 \times 10^{-16}$ V×cm^2; L=150 cm; M=1.5 or 2, and the distance between the left-hand edge of the discharge and the optical axis l_0=6.5 cm. For the parametric study the dimensions of the generation region a and b along the axis x and y were chosen so that the length and the width of the geometric beam within the resonators were constant, l_x=16 cm and l_y=5.5 cm, respectively. For the positive branch CBR $l_x = M^n a + M\delta$ and for the negative branch $l_x = (M^n + M^{n-1})a$; in the both cases $l_y = M^n b$ (see Figures 1,2).

Figures 4 and 5 illustrate the radiation fields which are generated in the positive branch CBR for different numbers of amplification cavity round trips n=1 (Figure 4) and n=3 (Figure 5) at M=1.5. The analogous distributions for the negative branch CBR are presented in [4]. The diagrams in Figure 6 illustrate the dependences of some laser output parameters on n at M=1.5 and M=2. Here η is the electricity-to-light efficiency; St is the Strehl number.

We note qualitative similarity of dependences on n for principal output parameters of the considered resonators. So, in the both cases there are optimum values of n such that the magnitudes of η reach their maxima, and the angular divergence as well as the output beam deviation from the optical axis grow as n increases. The explanation for this behaviour of mentioned dependences is identical for the both resonators and presented in [4] for the negative branch CBR.

At the same time, the energetic efficiency for the telescopic CBR is distinctly higher than for the confocal negative branch CBR. This difference may be attributed to that the volume of laser medium interacting with radiation in the former case is greater than in the latter case (providing the both resonators are of the same over-all dimensions). On the other hand, the angular divergence and the output beam deviation in the latter case are less than in the former case, because the confocal resonator with beam inversion is less sensitive to the presence of aberrations than the telescopic one (see, for example, [1]) .

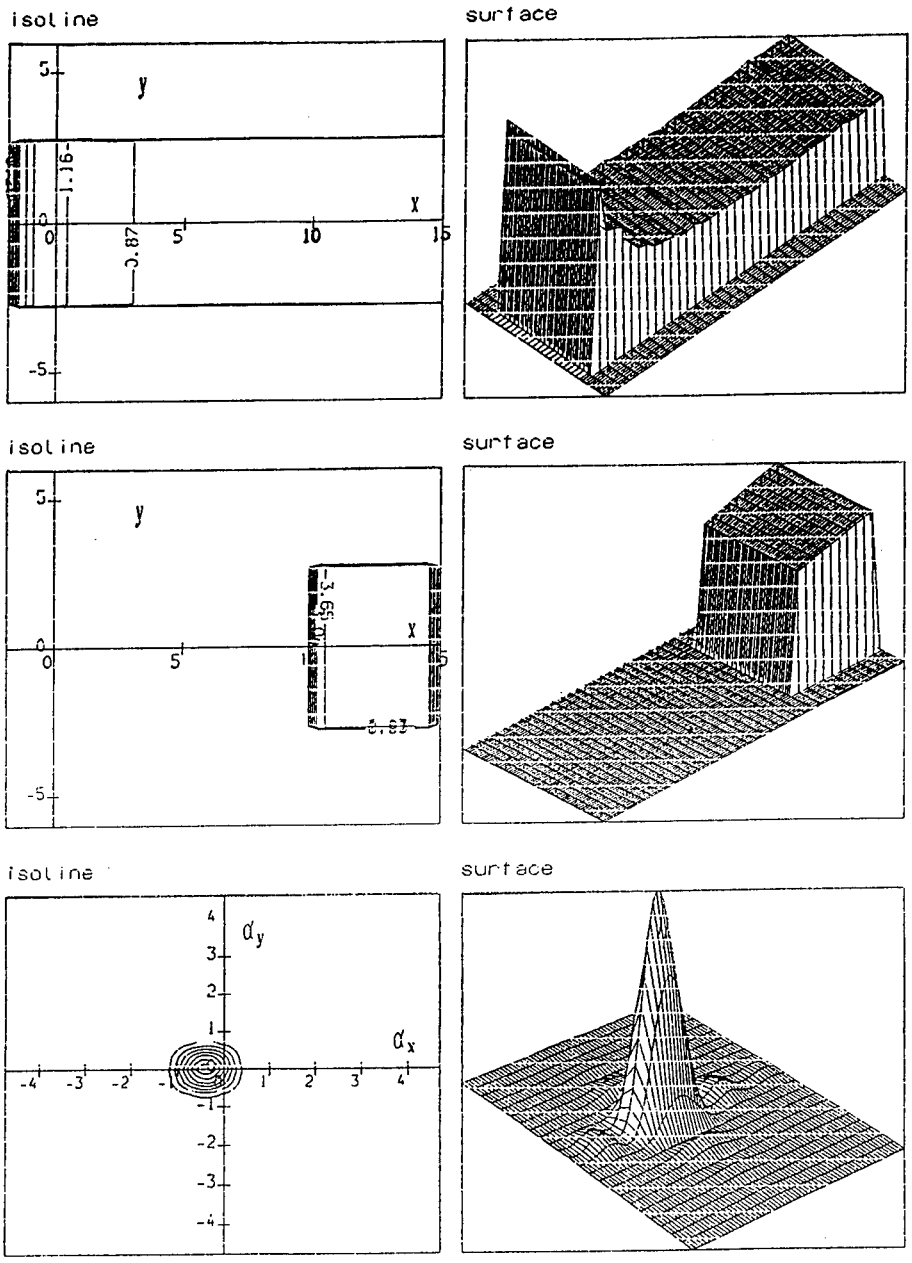


Figure 4. The radiation intensity in the output cross section, the output beam phase, and the far-field intensity at $n=1$ for the laser positive branch CBR.

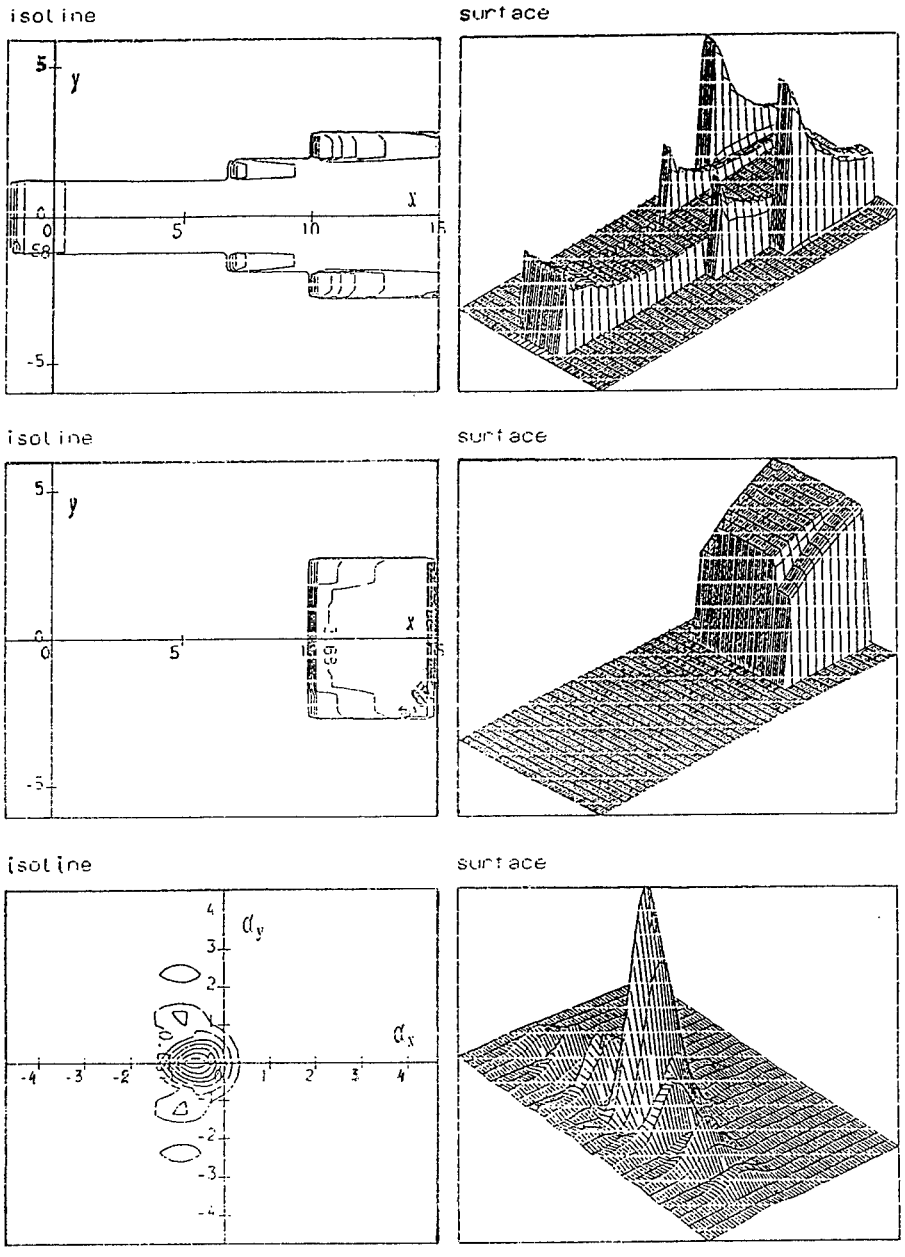


Figure 5. Same as Figure 4, but for the case $n=3$.

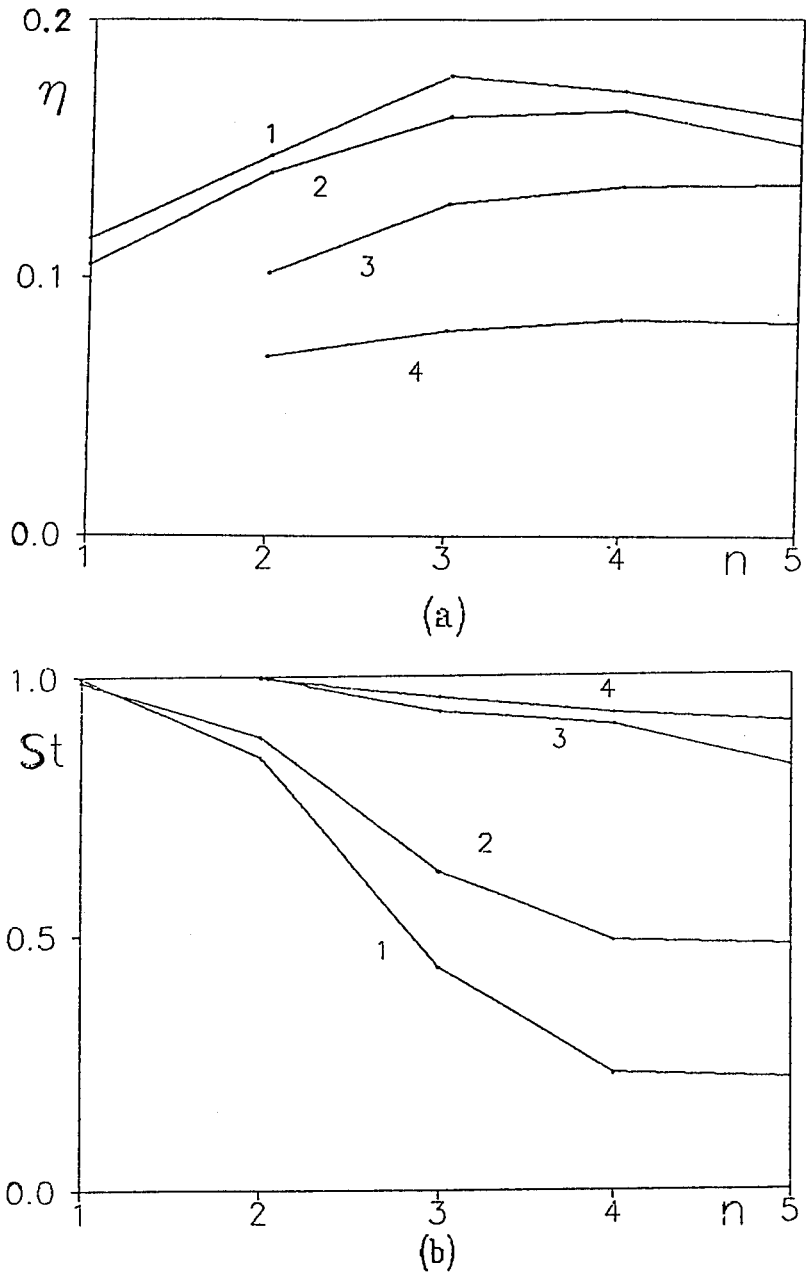


Figure 6. Electricity-to-light efficiency η (a) and Strehl number St (b), respectively, given in dependence on the number of amplification round trips n (lines 1 and 2 corresponds the values M=1.5 and $M = 2$ for the positive branch CBR, lines 3 and 4 are the same as 1 and 2, but for the negative branch one).

4. Conclusions

Numerical simulation allows us to make the following conclusions. In actual operation practice of an industrial CO_2 laser with the resonators considered here, the electricity-to-light efficiency can be rather high, the divergence of output radiation being close to the diffraction limit, which is extremely low and corresponds to an ideal rectangular source of radiation [1]. In addition, a part of the output radiation power corresponding to side lobes of its angular distribution proves to be insignificant. This indicates that the proposed resonators with a compact cross section of the output beam promise better prospects, particularly for high power industrial lasers. The results of numerical simulation allow optimum design parameters to be chosen for laser devices with resonators of such a type.

References

1. Anan'ev, Yu.A. (1990) *Optical Resonators and Laser Beams.* Nauka Publishers, Moscow (in Russ.).
2. Anan'ev, Yu.A., Kuprenyuk, V.I., and Sherstobitov, V.E. (1979) Properties of unstable resonators with field rotation. I. Elements of theory, *Kvantovaya Elektronika* **6**, 1871-1879 (in Russ.).
3. Zavgorodneva, S.I., Kuprenyuk, V.I., Sergeev, V.V., and Sherstobitov, V.E. (1980) On the conversion of the unstable-resonator laser radiation by means of the conical optics, *Kvantovaya Elektronika* **7**, 142-146 (in Russ.).
4. Cherepenin, N.D., Usanov, Yu.Ya., and Zaripov, Sh.Kh. (1993) Unstable laser cavity with compact output aperture, *Laser Physics* **3**, 826-830.
5. Akhmedyanova, F.A., Zaripov, Sh.Kh., and Cherepenin, N.D. (1985) On the influence of asymmetry on output characteristics of an unstable optical resonator, in O.M. Kiselev (ed.), *Mathematical Simulation in Physical Gas Dynamics*, Kazan University Publishers, Kazan, pp. 84-102 (in Russ.).
6. Zaripov, Sh.Kh. and Cherepenin, N.D. (1989) Calculation of radiation performance data for a gas discharge flow CO_2 laser with an unstable resonator, in O.M. Kiselev (ed.), *Calculation Methods in Physical Gas Dynamics*, Kazan University Publishers, Kazan, pp. 61-73 (in Russ.).
7. Sziklas, E.A. and Siegman, A.E. (1975) Mode calculations in unstable resonators with flowing saturable gain. 2: Fast Fourier transform method, *Applied Optics* **14**, 1874-1889.
8. Elkin, N.N. and Napartovich, A.P. (1988) *Applied Optics of Lasers*, TsNII Atominform Publishers, Moscow (in Russ.).

DYNAMICS OF LASERS WITH PASSIVE AND ACTIVE MODULATION OF LOSSES

L.A.KOTOMTSEVA, A.M.SAMSON and S.I.TUROVETS
B.I.Stepanov Institute of Physics of the Academy of Sciences of Belarus
70 F.Skaryna ave.Minsk 220072 Belarus

1.Introduction

Lasers with active and passive modulation of losses are widely used as sources of high power pulses of light. There is a lot of experimental publications on the passive mode-locking in solid state and dye lasers with a saturable absorber (LSA)and on passive modulation of losses in CO2 LSA. Various regular and chaotic pulsations have been observed and theoretical models for their interpretation have been proposed and explain many features of experiment [1-15]. For CO2 lasers with active modulation of losses (LAML) experimental results with different successions of high power pulses have found good confirmation in theoretical description [16-25]. For a ring He-Ne laser theoretical verification of some original experiments has been got [26-29]. Below brief review of the last results for some models of such lasers is proposed.

2. Models of a laser with a saturable absorber

Solid state and dye LSA in passive mode-locking behavior give rise to ultrashort intensive pulses of light . Under conditions of passive modulation of losses such and gas LSA produce intensive pulsations of microsecond period. To explain their mechanisms the system of semiclassical equations for a LSA with detuning of the frequency of radiation w from the resonant frequencies of the cavity wc, an active medium w1 and absorber w2 has been considered both for extended and concentrated models. The steady states and some examples of dynamics have been got [8,9] and compared with results of [30-32]. For a LSA with common active medium in two crossed cavities and saturable absorber in each beam multistability has been got and action of additional optical feedback between cavities on the number of the steady states has been shown [10,11]. For the model of CO_2 LSA regimes of intensive pulsations and some roads to chaos have been got due to the presence of the second longitudinal mode over the threshold [12-15]. Possibility of the observation of unstable orbits in such laser due to fast switching off of losses of the cavity is shown, which has been got experimentally [14].

R. Kossowsky et al. (eds.), High Power Lasers – Science and Engineering, 125–137.
© 1996 *Kluwer Academic Publishers. Printed in the Netherlands.*

2.1. DETUNED LASER WITH A SATURABLE ABSORBER

The basic system of semiclassical equations for a ring LSA with light propagating along coordinate x looks in such way

$$\frac{\partial e_i}{\partial t}+\frac{\partial e_i}{\partial x}=a_i p_i \sin F_i - b_i e_i,$$

$$\frac{\partial f_i}{\partial t}e_i+\frac{\partial f_i}{\partial x}e_i=-a_i p_i \cos F_i - \delta_c e_i,$$

$$\begin{aligned}
&\frac{\partial p_i}{\partial t}+g_i p_i = g_i k_i e_i \sin F_i,\\
&\frac{\partial h_i}{\partial t}p_i = g_i k_i e_i \cos F_i - \delta_i p_i,\\
&\frac{\partial k_i}{\partial t}=d_i(k_{0i}-k_i - p_i e_i \sin F_i).
\end{aligned} \qquad (1)$$

Equations are written for e_i and f_i - the amplitude and phase of electric field, p_i and h_i - amplitudes and phases of polarization, $F_i=h_i-f_i$, k_i - the relative inversion of populations [7,9] and k_{0i} is it's nonsaturated value, b_i are the distributed losses, a_i are the polarization - field coupling constants,. d_i and g_i are the rates of relaxation of populations and polarization of an active (i=1) and passive (i=2) medium. Equations are written for sizeless variables, for time in units of the time of relaxation of polarization of an active medium and space coordinate x in units of the distance which light passes during the time of relaxation of polarization of an active medium. Values of detunings $\delta_c=w-w_c$ $\delta_i=w-w_i$.

Boundary conditions for the ring LSA of the running wave look in the next way:

$$\begin{aligned}
&e_1(0,t)\exp[if_1(0,t)]=\frac{R}{s}e_2(l_b,t-t_1),\exp[if_2(l_b,t-t_1)-i\delta_c t_1 - ikL],\\
&e_2(l_a,t)\exp[if_2(l_a,t)]=se_1(l_1,t-t_2)\exp[if_1(l_1,t-t_1)-i\delta_c t_2]
\end{aligned} \qquad (2)$$

There is written that light enters into an active medium to x=0 after reflection on mirrors with reflectivity R through the time interval t1 of the time of passage of light from an absorber at x=lb to the active medium, and light enters into absorber at x=la after the air space trip time t2 from exit out of an active medium at x=l1.These conditions take into account for the solution of the field equation in the air space

leading to phase changes $\delta_c t_1$ and $\delta_c t_2$ in exponent. Value s is the square root from the ratio of the intensities of saturation of an active medium and absorber. The optical length of the cavity in our normalization is equal to the round trip time of the cavity: L=l1+t1+l2+t2, where l2=lb-la is a length of an absorber.

The steady states of the system (1) corresponding to the constant intensity of light with frequency w+dfi/dt can be determined from the next correlations

$$
\begin{aligned}
&k_{01}\sin^2 F_1(1+s^2e_1^2\sin^2 F_2)+k_{02}\sin^2 F_2(1+e_1^2\sin^2 F_1)=(1+e_1^2\sin^2 F_1)(1+s^2e_1^2\sin^2 F_2),\\
&(g_1 ctgF_1+\delta_c-\delta_1+2\pi j/L)(1+e_1^2\sin^2 F_1)(1+s^2e_1^2\sin^2 F_2)+\\
&+k_{01}\sin F_1\cos F_1(1+s^2e_1^2\sin^2 F_2)/2L+k_{02}\sin^2 F_2(\delta_2-\delta_1+g_1 ctgF_1)(1+e_1^2\sin^2 F_1)/2L=0.
\end{aligned}
\tag{3}
$$

and give a set of longitudinal modes with number $j=0,\pm 1,\pm 2,..$ in the cavity. Results of numerical experiment. for a passive mode-locking show chirp of the laser frequency during oscillations of regular pulsations with period close to L [9] and the sign of the frequency shift depends on the sign of the detuning as of an active medium so of an absorber. Illustration of it is given in Fig.1.

For a single mode detuned LSA possible steady states have been considered in [30-31] for the real and imaginary parts of the field and polarization in both media. We propose results of consideration of the system of ordinary differential equations for amplitudes and phases of the field and polarization of both media, which have been derived from the system (1) in the same way as for a laser without an absorber in [7]

$$
\begin{aligned}
&\dot{e}=a_1 p_1\sin F_1+a_2 p_2\sin F_2-be,\\
&\dot{p}_i=g_i e k_i\sin F_i-g_i p_i,\\
&\dot{k}_i=d_i(k_{0i}-k_i)-ep_i\sin F_i,\\
&\dot{f}=-\delta_c-(a_1 p_1\cos F_1+a_2 p_2\cos F_2)/e,\\
&\dot{h}_i=-\delta_i+g_i k_i e\cos F_i/p_i.
\end{aligned}
\tag{4}
$$

Here amplitude e and phase f of the field are common for both media and other variables are the same as in the system (1), only in field equations coefficients are normalized to the round trip time in the cavity L. Amplitudes and phases for three types of the steady states and dynamics are got [8] and compared with results of [30-33]. We show changes in phase and amplitude similar to those in a laser without an

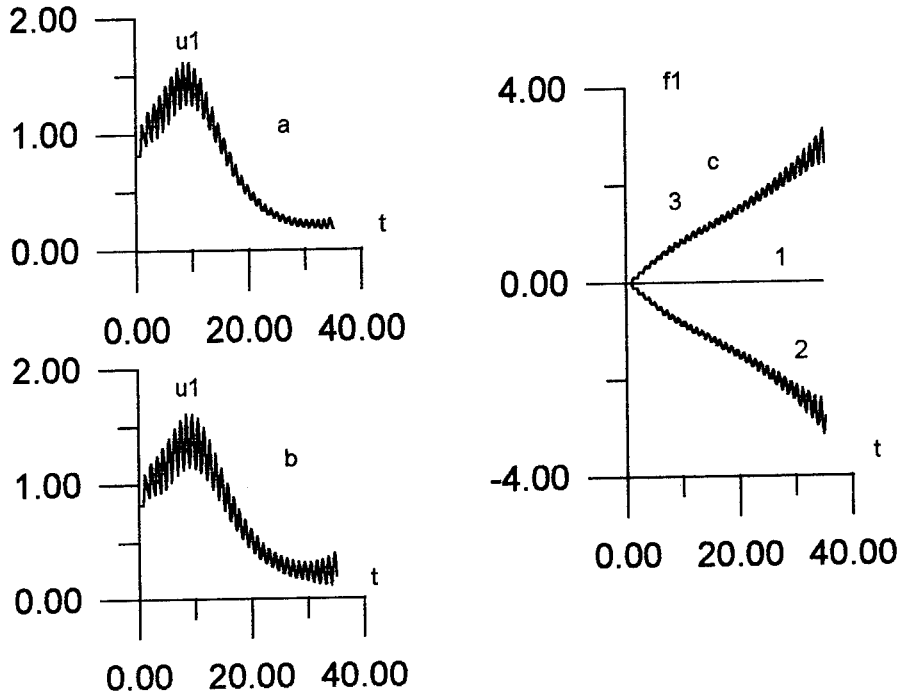


Figure 1. Intensity u1=|e1|*|e1| (a,b) and phase f1 (c) vs time t (normalized to the round trip time L), for w-w1=0 (a, c - curve 1), 0.1 (b, c - curve 2), - 0.1 (b, c - curve 3), w-w2=w-wc=0,, g=0.1, d1=d2=0.003, k01=0.32, k02=- 0.2, L=10

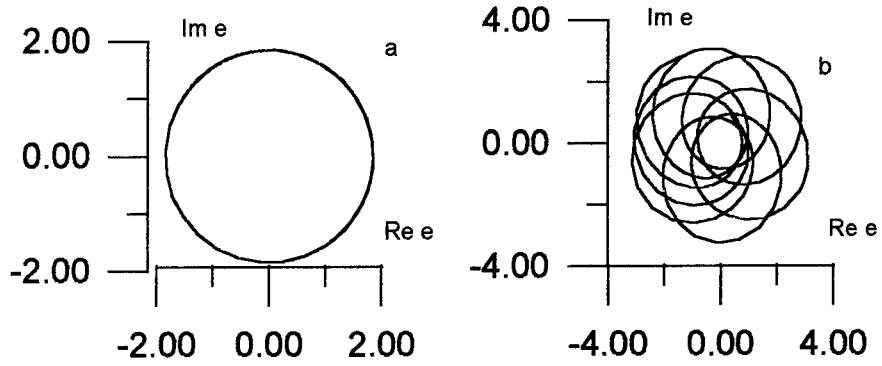


Figure 2. Phase portrait in the plane (Re e, Im e) for w-w1=w-w2=0.3, w-wc=0, d1=0.05(a),0.0003(b), d2=0.01, g=0.1, s=2, k01=5, k02=-3.

an absorber [34,35] when constant intensity is observed at rotating phase of the field and the rate of rotation depends on the detuning. At some other parameters pulsations of light develop, the phase of field rotates as in Fig.2.

2.2. TWO-BEAM LSA AND ACTION OF ADDITIONAL OPTICAL FEEDBACK

On the basis of the rate equations for the laser with one active medium inside two cavities with a saturable absorbers in each of them the next system for the intensities of light in each beam u_1 and u_2 and inversion of populations y is considered:

$$\begin{aligned} \dot{u}_1 &= v_1(y - 1 - \frac{b_1}{1+a_1u_1})u_1 + g_1u_2 + e_1, \\ \dot{u}_2 &= v_2(y - b - \frac{b_2}{1+a_2u_2})u_2 + g_2u_1 + e_2, \\ \dot{y} &= y_0 - y - y(u_1 + u_2). \end{aligned} \tag{5}$$

Their dependences on y0 - the unsaturated gain in active medium, b1 and b2 - unsaturated absorptions of absorbers , a1 and a2 - their parameters of saturation, b - the ratio of losses in both cavities, v1 and v2 - the ratios of the time of relaxation of populations in active medium to the time of life of photons in the cavity are determined. The action of the additional optical feedback due to mirrors, reflecting light from one cavity to the other with coupling coefficients g1 and g2, and it's influence on the number of steady states and their stability is studied. The items e1 and e2 are added as possible noise sources suitable for numerical experiment. It is shown, that four steady states can exist and their number depends on the parameters. Additional feedback leads to appearance of new types of changes of intensities of steady states .upon unsaturated gain y0 as it is seen in Fig.3. Boundaries of stability of each state can be found analitically as for the bifurcations saddle - focus so for saddle - knot bifurcation. Results of numerical simulations in accordiance with analytical description permit to get bifurcation diagrams for the definite set of parameters..

2.3. TARGETTING TO UNSTABLE ORBITS IN LSA WITH SWITCHED OFF LOSSES

For a model of CO_2 LSA when the rate of relaxation of population of the lower working level in an active medium is important and two longitudinal modes can be under the conditions over the laser threshold the next system of equations has been considered:[12-15]:

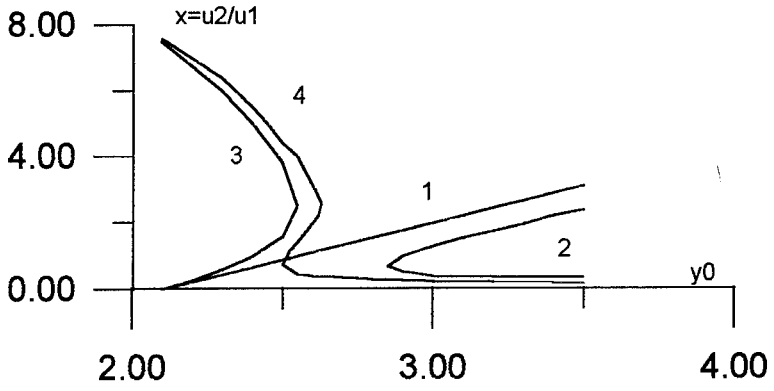


Figure 3. Dependence of the ratio of intemsities of the steady state x=u2/u1 on y0 for a1=5, b=1.5, b1=1.5, b2=0, g1=0 (1,2), 0.1 (3,4), g2=0 (1,3), 0.1 (2,4).

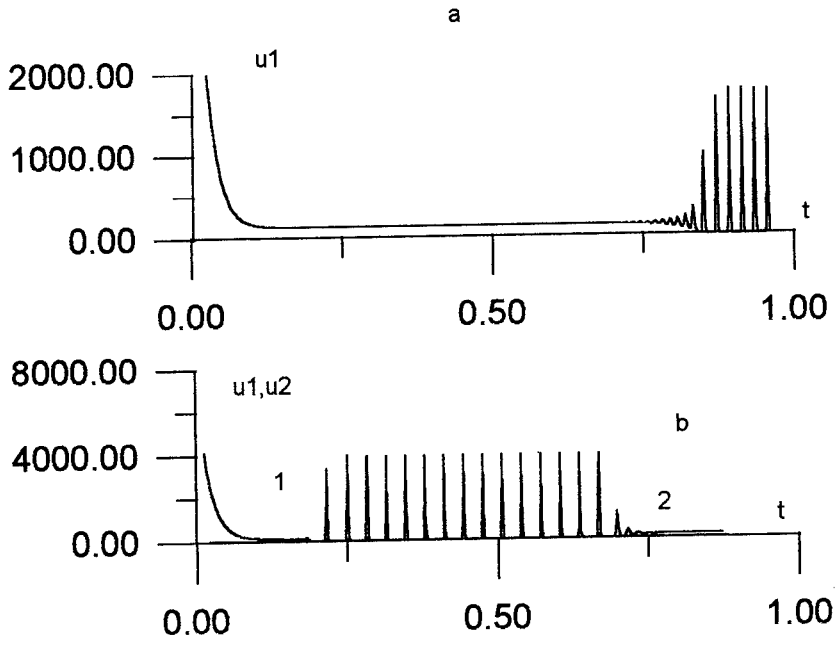


Figure 4. Intensities of the first mode u1 (a,b - curve 1) and of the second mode u2 (b - curve 2) vs time t for fast switching off of losses for parameters of CO2 LSA [12-14], q2=3.3(a),6.6(b).

$$\dot{u}_1 = v[f_1 y - f_3 q_2/(1 + s(f_3 u_1 + f_4 u_2)) - 1]u_1 + e_1,$$

$$\dot{u}_2 = v[f_2 y - f_4 q_2/(1 + s(f_3 u_1 + f_4 u_2)) - 1]u_2 + e_2, \qquad (6)$$

$$\dot{y} = a_1 - a_2 y + a_3 y_3 - (f_1 u_1 + f_2 u_2)y,$$

$$\dot{y}_3 = b_2 y - b_3 y_3 + (f_1 u_1 + f_2 u_2)y/2..$$

Intensities of both modes u1 and u2, inversion of populations y of the active medium and population of the lower working level y3 depend on the rates of relaxation of the levels of an active medium through ai and bi, the spectral properties of an active and passive media f1,f2,f3,f4, unsaturated absorption of an absorber q2 and parameter of saturation s for the noninertial absorber and value v - the ratio of the time of relaxation of populations in an active medium to the time of life of photons in the cavity.. Possible four steady states of this system and their stability have been considered and the roads to chaos through period doubling and through the regular pulsations of the complicated form have been got for bimodal behavior [12,13] and compared with a single mode case. For high power pulses some dependences on parameters have been got in accordance with experiment [14]. Under the conditions of fast switching off of losses of the cavity unstable steady states with constant intensity or regular pulsations are seen in Fig.4.[15]. Their coincidence with oscillograms of experiment [14] permits us to speak that unstable states are observed experimentally..

3.Some new effects in dynamics of modulated lasers

The theoretical consideration and experimental observation in the modulated CO2 laser and the ring He-Ne laser gyro with an alternating bias of temporal instabilities and chaos, including such new effects as deterministic phase diffusion, amplification and squeezing near bifurcation points, noncritical slowing down, internal bifurcations of strange attractors, targetting to unstable orbits at definite phases of modulation are reported. Because of their high stability and relative simplicity, lasers with actively modulated parameters are the most convenient choises for experimental studies on fundamental aspects of nonlinear dynamics in quantum optics. For a LAML rich dynamics has been described in [7,15-17] and further detailed consideration of it in the vicinity of the bifurcation points is obtained [18-24].

The kinetics of single-mode lasers with a wide variety of active media, including most solid state lasers, semiconductor lasers, and certain molecular lasers (e.g., CO2), obeys two rate equations for the field and population inversion of the gain medium. The response of such lasers to a short and small perturbation is a train of

damped relaxation oscillations. It suggests an analogy with the behavior of a weakly damped oscillator and has been used in experimental studies to determine the constants of the rate equations. In order to observe dynamic chaos and accompanying effects, it is necessary to increase the dimensionality of the phase space of the system from two by at least one. This can be done easily through an active modulation of one parameter of the laser. The rate equations can be rewritten in a form which is the same as that equation of motion of a nonlinear oscillator with a Toda potential, in which the time-dependent part of the modulated parameter serves as a periodic external force. There would necessarily be additional resonances in the system at subharmonics and ultraharmonics of it. The threshold effect was established for the generation of subgarmonics in the early theoretical papers on laser dynamics.. The nonlinear oscillator model along with the familiar Lorenz model presently occupy central positions in the theory of dynamic chaos. The circumstance that both these models have analogs in laser theory has recently intensified interest in laser dynamics.

3.1. LASERS WITH MODULATED LOSSES

One of the first experimental results on observation of dynamical chaos in lasers was reported by Arecchi et al., who used a CO2 laser with electrooptic Q switching (for review of the early studies of laser chaos see [7,16]). Further theoretical analysis, numerical simulations [16-18] and experiments [19,20] have drawn a more detailed picture of nonlinear resonances and regions in which various regimes overlap (multistability), of collisions of periodic attractors, and of crises of strange attractors.

The effect of small signal amplification near period-doubling bifurcations had been predicted and studied theoretically some years ago [7,16], and was observed experimentally in a radio-frequency quantum oscillator on NMR Only recently small signal amplification and phase properties of the laser response signals near period-doubling bifurcations were got in modulated CO2 lasers [19-21]. Owing to the parametric character of period doubling the laser "strengthens" the spectral components of perturbation near half the modulation frequency, which can be used for increasing the sensitivity in laser intracavity measurements [21].

The rate equations of a LAML can be written in the dimensionless form [7,16-18]:

$$\ddot{x}+(\varepsilon_1+\varepsilon_2 e^x)\dot{x}+(1+q\cos mt)e^x-1=q(m\sin mt-\varepsilon_1\cos mt)/\varepsilon_2. \qquad (7)$$

where x is the laser intensity on a logarithmic scale, q is the relative loss modulation depth, m is the modulation frequency, ε_1 and ε_2 depend on a kind of laser .

For a combined modulation of laser cavity losses consisting of a harmonic part and a short-time pulsed action at the instant of time t equation (7) is modified and for a small departure of x(t) from the steady periodic solution $x_0(t)$ we have

$$\ddot{x}+[\varepsilon_1+\varepsilon_2\exp(x_0)]x+[1+q\cos mt+\varepsilon_2 x_0]\exp(x_0)x= \qquad (8)$$
$$= -(q_0/\varepsilon_2)\delta(t-t_0)-(q_0/\varepsilon_2)\{\varepsilon_1+\varepsilon_2\exp[x_0(t_0)]\}\delta(t-t_0),$$

where $\delta(t-t_0)$ - is the Dirac δ -function. Note that the function x(t) is "right-hand-sided", i.e. it is other than zero only for $t>t_0$ and represents a response of a linear system with time periodic coefficients to the δ (t)-action. The system given by (8) represents a parametric amplifier with the self-pumping period $2\pi/w$ equal to the period of the function x(t). From the continuous spectrum of the δ -function the parametric amplifier selectively transmits only frequencies near lw/2, l=1,3,5,... The non-autonomous equation (8) is equivalent to the autonomous equation with appropriate initial conditions. According to the Flokuet theory , it's general solution is

$$x=C_1\exp[-a(1-m/a)t]v(t,s_1)+ C_2\exp[-a(1+m/a)t]v(t,s_2), \quad a=(\varepsilon_1+\varepsilon_2)/2, \qquad (9)$$

where the constants C_1 and C_2 are determined by the initial conditions. The function v(t,s) has the period $4\pi/w$, with the components at frequencies multiple of w being absent from its spectrum. Like the increment m and parameters s, it can be calculated analytically in the form of converging series if the coefficients of expansion of the function x (t) into a Fourier series are known. In this case, equation (8) is reducible to the canonical form of the well-known generalized Hill equation [17]. Near the bifurcation point the first of the partial solutions x (t) predominates. At the same time the short-lived solution x (t) decays even faster by a factor of almost 2 than in the case of the absence of modulation (m=0). Sensititvity of laser to a pulsed perturbation in dependence on the approach to period-doubling threshold has been shown in [20-22].

On the other hand, this effect depends on the phase, i.e. on the moment t_0 of switching on of the δ -pulsed perturbation. There exist such t_0' and t_0'' , determined by the relations $\dot{v}(0,s_2)=(a+m)v(0,s_2)$, $\dot{v}(0,s_1)=(a-m)v(0,s_1)$ at which, respectively, $C_1\equiv 0$ or $C_2\equiv 0$. In other words, in the phase space there exist t -dependent directions of "fast" and "slow" relaxation of perturbations to a given periodic regime. At $t=t_0''$ ($C_2=0$) the deviation with the amplitude q_0/ε_2 wholly lies on the slow central manifold and amplification is maximum, at $t=t_0'$ ($C_1=0$) the perturbation acts across the central manifold and the laser response quickly decays. Naturally, under the action of noise on the system the fluctuations will be stretched along one direction and squeezed along the other. Obviously, the feature of squeezing under an action of a single δ -pulsed perturbation will be the faster decay of the laser response compared with an unmodulated case.The effect of small signal amplification and squeezing near the period doubling bifurcation can be considered as a manifestation of the more

general phenomenon of critical slowing down which is well known in the theory of bifurcations and, in particular, in optical bistability. It consists in an abnormally large increase in the time of system relaxation to a steady state near critical (bifurcations) points. This is attributed to the fact that at a bifurcation point the real part of one or several characteristic exponents passes through the zero value and, correspondingly, the partial solutions of linearized problem associated with them are retarded. Since the sum of all the Lyapunov exponents is equal to the dissipation coefficient (in our case it is equal to $(\varepsilon_1+\varepsilon_2)$) and remains, as a rule, unaltered, a decrease in one of the exponents automatically leads to an increase in the others and, thus, to an increase of the phase space anisotropy. The results of the experiments with combined sinusoidal and pulsed modulation of the CO2 laser cavity have confirmed it [19-21,24,25].

Another interesting effect in modulated lasers is noncritical slowing down [15,19,20, 22,23]. Usually, the presence of several attractors for a given set of parameter values was demonstrated by slowly sweeping the control parameter in a sawtooth fashion. The application of a short pulsed perturbation to the system can cause a rapid switching from one attractor to another during the pulse itself. Furthermore, by choosing the appropriate amplitude and duration of the pulse, one can prepare a system in one of the unstable states. If there is a good signal-to-noise ratio, the system can stay in this state for a fairly long time. The unstable laser limit cycles and various regimes of optically induced amplitude and phase switching have been observed experimentally in [19,22]. Now this procedure is called by "targetting to unstable orbits". For the fast switching on/off of losses of the cavity in LAML we show possibility to observe unstable orbits [15]. Similar effects in the optical bistability field received the name "noncritical slowing down" or frustrated switching.

3.2. LASER GYRO WITH AN ALTERNATING BIAS

The gas ring laser as a sensitive element of measuring instruments can find itself in the conditions of narrow-band noise, e.g., vibrations of electromagnetic fields. Such periodic perturbations of the parameters lead to induced locking of the beat frequency of counterpropagating waves and to the appearance of insensitivity "shelves" on the output characteristic of the laser. In [23,26-29] it was shown that alongside the locking effect in such lasers dynamical chaos must be observed. The dynamics of a single-mode ring gas laser obeys the well-known system of the Lamb amplitude-phase equations. If external perturbations only lead to periodic oscillations of the frequency bias then, in the approximation of a weak coupling through backscattering for the phase difference of counterpropagating waves v we obtain

$$\ddot{v}+\dot{v}/b+\sin v=n_0+n_1\sin wt/\sqrt{n_3}G, \qquad (10)$$

where the dimensionless quantities $t=\sqrt{Gn_3}t'$, $b=\sqrt{n_3/G}$, $n_0=W_0/n_3$, $n_2=W_1/n_3$ and n_3 is the "dead band" half-width, G is the coefficient of phase relaxation,

W0+W1sinwt corresponds to the cavity frequency difference for counterrunning waves. The dynamics of the phase difference is analogous to the dynamics of the rf-biased Josephson junction with the hysteresis parameter b for which the dynamic chaos has been got [26 and references therein]. We have found zones with the highest probability of detecting chaos: $b>0.5$, $w\leq\sqrt{Gn_3}$, $n_0\leq 1$, $n_1\approx 1-10$.. A number of ring gas lasers can be described with help of model (10). Our numerical simulations indicate at least two types of chaos in the system: "period-doubling" and "intermittency". In the first case, the phase difference oscillations are irregular but amplitude-limited, while in the second case the phase difference experiences diffusive motion. Experiments [27-29] were performed on a monoblock four-mirror He-Ne laser with a wavelength of 0.63 mkm and a dual isotope mixture of Ne. Near the generation line center the half-width of the dead band n3 was 700-800 Hz at the hysteresis magnitude 40-50%, which corresponds to b~ 2.45.. At scanning of one of the control parameters (perturbation amplitude, constant bias, detuning from the center of the line) the transition from the time-periodic beat signal to chaos was observed. The phase portrait of the system took on a "smeared" form of a strange attractor, and the noise level in the signal spectrum rose jumplike by 30 dB. The boundaries of chaos are in good agreement with the results of numerical modeling. We have also directly proved by experiment the dynamic nature of irregular pulsations by means of determining the correlation dimension D and entropy K on the basis of the Grassberger-Procaccia algorithm. Irregular oscillations of the beat signal are dynamic (K is positive and finite), motion occurs on the low- dimensional strange attractor with D =2.6. The dynamics of such lasers can be described by a system of no more than three autonomous first-order differential equations (D <3). Thus, the transition from the Lamb equations to the simpler model (10) is reasonable. Within error, the experimental value of D coincides with the value obtained in the phenomenological model which permits classifying the observable chaotic regimes as intermittency or chaos with diffusion in the phase space.

4. Conclusion

Results of consideration of some models of high power lasers with passive and active modulation of losses show us rich variety of steady and unstable states. We get multistable states and can change their number. Some roads to dynamical chaos. are shown for such systems. Possibility of observation of unstable orbits is demonstrated due to the fast switching on of the quality of the cavity both in LSA and LAML.

Acknowledgments

The research described in this publication was made possible in part by Grant MX5000 from the International Science Foundation and by Grant F15-006 of the Foundation of Fundamental Researches of the Republic of Belarus..

References

1. Arimondo, E., Casagrande, F., Lugiato, L., and Glorieux, P. (1983) Repetitive passive Q-switching and bistability in lasers with saturable absorber, *Appl.Phys.B* **30**, 57-77.

2. Tanii, K., Tachikawa, M., Kajita, M., and Shimizu, T. (1988) Sinusoidal self-modulation in the output of a CO2 laser with an intracavity saturable absorber, *J.Opt.Soc.Am.B* **5**, 24-28.

3. Weiss, C.O., and Vilaseca, R. (1991) *Dynamics of Lasers*. VCH Publishers New York.

4. Hennequin, D., deTomasi ,F., .Zambon, B., and Arimondo,.E. (1988) Homoclinic orbits and cycles in the instabilities of a laser with a saturable absorber, *Phys. Rev. A* **37**, 2243-2246.

5.Zambon B. (1991) Theoretical investigations of models for the laser with a saturable absorber: A case of homoclinic tangency to a periodic orbit, *Phys. Rev. A* **44**, 688-702.

6. Lefranc, M., Hennequin, D.,and Dangoisse, D.. Homoclinic chaos in a laser containing saturable absorber, *JOSA B* .**8**, 239-249.

7. Samson, A.M., Kotomseva, L.A., and Loiko, .N.A. (1990) *Selfpulsings in lasers,* Nauka i Tekhnika, Minsk.

8. Kotomtseva, L.A., and Samson, A.M. (1995) Steady states and their instability in a laser with a saturable absorber, *Zhurnal Prikladnoi Spektroskopii (Journ. Appl. Spectr.)* **62,** No 1.

9. Kotomtseva, L.A., and Samson, A.M. (1994) Instabilities and tunable oscillations in a detuned laser with a saturable absorber, *Abstracts of Intern. Conf. on Tunable Solid State Lasers,* Minsk, *p.33..*

10. Kotomtseva, L.A, and Samson, A.M. (1994) .Dynamics of a two-beam laser with a saturable absorber and additional optical feedback, *Bulletin of Russ.Acad. Sc. Physics Suppl* **58,** 196-201 .

11. Kotomtseva, L.A., and Samson, A.M. (1994) Dynamics of a two-channel laser with a saturable absorber and additional optical feedback, in L.A.Melnikov (ed.) *Nonlinear Dynamics in Lasers and Optical Systems* SPIE Proceedings **2099**, pp.141-149.

12.Gaiko, O.L.,Grigoryeva, E.V., Kotomtseva, L.A., Nevdakh, V.V., Orlov, L.N., Samson, A.M., and Startseva, T.Yu. (1992) Nonlinear dynamics of CO2 laser with a saturable absorber, *Reprint N 657, Institute of Physics Academy of Sciences of Belarus*, Minsk

13. Gaiko, O.L., Kotomtseva, L.A., Nevdakh, V.V., Orlov, L.N., and. Samson, A.M. (1993) Dynamical chaos in a CO2 laser with a saturable absorber, *Zhurn. Prikl.Spektr. (Journ. Appl.Spectr.)* **58**, 287-293

14..Gaiko, O.L., Kotomtseva, L.A., Nevdakh, V.V., Orlov, L.N., and,. Samson A.M.(1994) Dynamics of operation of a CO2 laser with a saturable absorber, *Quantum Electronics.* .**24(7)**, 603 -607.

15. Kotomtseva, L.A., Naumenko, A.V., Samson, A.M., and Turovets, S.I. (1994) On observability of unstable orbits in lasers with a step-wise Q-switching, *Techn. Digest 5th Europ.Quant.Electr.Conf.,* Amsterdam, p. 227 .

16. Samson, A.M., and Turovets, S.I. (1986) Instabilities in lasers with periodical modulation of parameters, *Preprint No. 438, Institute of Physics,* Minsk.

17. Samson, A.M., and Turovets, S.I. (1987) Hierarchy of bifurcations in a laser with periodical modulation of losses, *Dokl. Acad. Nauk BSSR,* **31,** 888-890.

18. Samson, A.M,.and Turovets, S.I. (1988) Topological and statistical properties of atrange attractors in lasers with periodically modulated parameters, *Zhurn.Prikl.Spektr.(J. Appl. Spectr).* **48**, 258-263.

19. Samson, A.M., Turovets, S.I., Chizhevsky, V.N., and Churakov, V.V. (1991) Nonlinear dynamics of CO2 laser with acustooptical modulator of parameters, *Preprint No.648, Institute of Physics*, Minsk.

20. Samson, A.M., Turovets, S.I., Chizhevsky, V.N., and Churakov, V.V. (1992) Nonlinear dynamics of loss - switched CO2 laser, *Sov. Phys. JETP,* **74**, 628-639.

21.. Chizhevsky, V.N., and Turovets, S.I. (1993) Small signal amplification and classical squeezing near period-doubling bifurcations in a modulated CO2 laser, *Opt. Commun.* **102**, 175-182.

22. Chizhevsky, V.N., and Turovets, S.I. (1994) Periodically loss-modulated CO2 laser as an optical amplitude and phase multitrigger, *Phys. Rev. A* **50**, 1840-1843.

23. Samson, A.M., Turovets, S.I., Zuikov, I.E., and Krivitsky, P.G. (1991) Deterministic phase diffusion in the modulated He-Ne ring laser gyro, *in 14- Intern. Conf.Lasers 91* Techn. Digest, San Diego (USA), p.6

24. Turovets, S.I., and Chizhevsky, V.N. (1991) Spatio-temporal dynamics in a modulated CO2 laser, *Ibidem,* p.20.

25. Chizhevsky, V.N, Churakov, V.V., Samson, A.M.,, and Turovets, S.I. (1992) Nonlinear dynamics in a CO2 laser with combined modulation technique, *In Intern. Conf. Quant. Electr.* Techn. Digest, Vienna , p.43.

26. Samson, A.M., and Turovets, S.I. (1992) Deterministic diffusion and chaos in a ring gas laser with periodical frequency substitution, in P.A. Apanasevich and A.S. Rubanov (eds.) ***Lasers and optical nonlinearities*** . Minsk, p. 36-40.

27. Zuikov, I.E., Krivitsky, P.G., Samson, A.M., and Turovets, S.I. (1991) Deterministic phase diffusion, dimensions and entropies of chaotic lasing in the He-Ne ring laser gyro, In R. Vilaseca and R. Corbalan (eds.), *Nonlinear dynamics and quantum phenomena in optical systems*, Springer Proc. in Physics, **55**,Berlin-Heidelberg, Springer-Verlag, p. 218-221.

28. Zuikov, I.E., Krivitsky, P.G., Samson , A.M., and Turovets, S.I. (1990) Chaotical behavior in a ring He-Ne laser with modulation of frequency substitution, *Sov.Tech. Phys. Lett.* **16,** 34-38.

29. Zuikov, I.E., Krivitsky, P.G., Samson, A.M., and Turovets, S.I. (1991) Dynamical chaos in a ring He-Ne laser with a periodical substitution, *Dokl. Acad. Nauk BSSR* **35,** 36-39.

30. Erneux, T., and Mandel, P. (1981) Bifurcation phenomena in a laser with saturable absorber, *Z. Phys. B* **44,** 353-363, 365-374; Erneux,T., and Mandel, P. (1984) Stationary, harmonic and pulsed operations of an optically bistable laser with saturable absorber, *Phys. Rev. A* **30,** 1893-1901; 1902-1909.

31. Chyba, D.E., Abraham, N.B., and Albano, A.M. (1987) Semiclassical analysis of a detuned ring laser with a saturable absorber: New results for the steady states, *Phys. Rev. A* .**35,** 2936-2950.

32. Tatarkova ,S.A., and Tuchin, V.V. (1992) Pulse shape and transition to chaos in the laser with a saturable absorber, *Kvantovaja Elektronika.* .**19,** 757-761.

33. Dembinski, S.T., Kossakowski, A., Peplowski, P., Lugiato, L.A.,. and Mandel, P. (1978) Laser instability below threshold, *Phys.Lett. A* **68,** 20-22.

34. Ning, C.Z., and Haken, H. (1990) Detuned lasers and the complex Lorenz equations: Subcritical and supercritical Hopf bifurcations, *Phys. Rev. A* **41**, 3826-3837.

35. Roldan, E., de Valcarcel,G.J., Vilaseca, E., and Mandel, P. (1993) Single-mode-laser phase dynamics, *Phys.Rev. A* **48,** 591-598.

The time evolution of the electric characteristics of a laser discharge through their waveforms of the voltage and the current

P. Persephonis, A. Ioannou, J. Parthenios, C. Georgiades and V. Giannetas
University of Patras, Physics Department
26500 Parta, Greece

Abstract :

The time behavior of the electric characteristics resistances and inductances in the discharges in pulsed gas lasers is revealed through a procedure which exploits only the voltages or the currents waveforms. This can be achieved combining step by step the waveforms with the equations governing the performance of the system. This method is described analytically in the text. Its application showed that the resistances drop rapidly (first 10nsec) from very high values to low values, while the inductances increase to high values and subsequently decrease, forming an abrupt high peak (first 40nsec). The steep drop of the resistances is due to the electron avalanche multiplication, while the peak of the inductances is due to the centripetal magnetic forces (Laplace forces), which cause a temporary constriction of the plasma. In the "main phase" of the discharge the resistances present a damping oscillation with the same frequency as the voltages, while the inductances present light fluctuations around constant values. The time varied resistances and inductances strongly influence the electrical and optical behavior of the laser system.

1. Introduction

Pulsed gas lasers (N_2, CO_2, excimer, etc.) have been studied extensively from the Sixties to date and the interest in them continuously increases because of the plethora of their applications. Their optical output is based on the combination of the properties of the gases used and on the ability of the electric circuit to deposit in the laser chamber maximum electric energy in the proper time as well. This type of laser has been dealt with as a highly integrated electrooptical system. This system comprises two electric discharges which are influenced by and influence the behavior of the driving circuit [1,2]. The plasma of the discharges varies in time and this complicates an understanding of the performance of the entire laser system. One electric discharge takes place in the switch system (spark-gap, thyratron etc.) and the other in the laser chamber. The latter constitutes the connective link between electrical and optical elements of the system. Electrically, each of the

R. Kossowsky et al. (eds.), High Power Lasers – Science and Engineering, 139–152.
© 1996 *Kluwer Academic Publishers. Printed in the Netherlands.*

discharges represents a time dependent resistance and inductance in series combination which constitute elements of the driving circuit. Unfortunately, there was no way of finding the time histories of these elements to date. The lack of the knowledge of these time dependent parameters has created obstacles and serious problems for the consideration of this particular laser system compelling the authors to turn to assumptions. Thus, chronologically we can say that, up to the middle of the Seventies in all the theoretical studies the resistances and inductances of the discharges, in pulsed gas lasers, had been considered constant [3-6]. Afterwards, during the next decade up to the middle of the Eighties many authors calculated in their considerations the resistance through electron avalanche multiplication using the Townsend equation [7,8]

$$\frac{dn_e}{dt} = \alpha U_d n_e \qquad (1)$$

(α is the first Townsend coefficient and U_d is the drift velocity). This calculation showed a sharp drop of the resistance during the initial stage of the discharge and introduced the time dependent resistance in the consideration of this type of laser system. Finally, from the middle of the Eighties to date the predominant procedure was for the resistance to be parametrized through an exponential drop during the initial stage of the discharge [9]

$$R = R_0 + R_1 e^{-\frac{t}{\tau}} \qquad (2)$$

The determination of the constant characteristics R_0, R_1 and τ was realized through the best fitting of the experimental and theoretical waveforms of the voltages [10]. It is worth mentioning that the inductances of the discharges have not been considered as time dependent quantities to date.

In this work a method of finding the time dependent resistance and inductance of the discharges in pulsed gas lasers is presented, utilizing step by step the voltage waveforms through the differential equations governing the performance of the electric circuit.

Afterwards, a comprehensive experimental and theoretical consideration of a pulsed gas laser through the known time dependent parameters of the discharges of the laser system is carried out. To the best of our knowledge this is the first analysis of the laser system to date with real time dependent resistances and inductances of the discharges.

2. Description of the method

Although this method can be applied to any circuit, the electric circuit which is widely in use in pulsed gas lasers is the "Charge Transfer Circuit" ("C-to-C") shown in fig. 1. In this figure R_1, L_1 is the resistance and inductance of the switch system (thyratron or spark-gap), while R_2, L_2 is the resistance and inductance of the laser channel.

The performance of the laser system is realized in two stages.

In the first stage the high voltage V_0 is applied across the storage capacitor C_1,

charging it, while the peaking capacitor C_2 remains uncharged. When the switch is turned on, charges are transferred through it to the peaking capacitor, building up the voltage difference across the laser electrodes V_{el}. This V_{el} stops increasing, reaching a peak value V_b (Breakdown voltage) at a time t_b. During this initial stage (from t=0 to $t=t_b$), the laser channel is ineffective and only loop I of the circuit shown in fig 1 performs. For this loop of the circuit Kirchhof's Law gives

$$V_1=I_1R_1+\frac{d(L_1I_1)}{dt}+V_2 \qquad (3)$$

Also we have

$$I_1=C_2\frac{dV_2}{dt}=-C_1\frac{dV_1}{dt} \qquad (4)$$

Replacing eqs (4) into eq. (3) we have the following differential equation which governs the behavior of the voltage V_2 across the peaking capacitor C_2 in loop I of this circuit

$$L_1C_2\frac{d^2V_2}{dt^2}+C_2(R_1+\frac{dL_1}{dt})\frac{dV_2}{dt}+(1+\frac{C_2}{C_1})V_2-V_0=0 \qquad (5)$$

In the second stage (after t_b) the discharge in the laser tube develops producing a highly conducting plasma. The voltage falls rapidly and finally the entire laser system oscillates. The Kirchoff's Law in the loops I and II in the circuit gives

$$V_1=I_1R_1+\frac{d(L_1I_1)}{dt}+V_2 \qquad (6)$$

and

$$V_2=I_2R_2+\frac{d(L_2I_2)}{dt} \qquad (7)$$

Also we have

$$I_1=-C_1\frac{dV_1}{dt} \quad , \quad I_2=-C_1\frac{dV_1}{dt}-C_2\frac{dV_2}{dt} \qquad (8)$$

Replacing eqs (8) into eqs (6) and (7) we have the following differential equations which

govern the behavior of all the system,
for loop I of the circuit

$$L_1C_1\frac{d^2V_1}{dt^2}+C_1(R_1+\frac{dL_1}{dt})\frac{dV_1}{dt}=V_2-V_1 \qquad (9)$$

and for loop II of the circuit

$$L_2(C_1\frac{d^2V_1}{dt^2}+C_2\frac{d^2V_2}{dt^2})+(R_2+\frac{dL_2}{dt})(C_1\frac{dV_1}{dt}+C_2\frac{dV_2}{dt})=-V_2 \qquad (10)$$

where V_1 and V_2 are the voltages across the storage and peaking capacitors respectively.

Nevertheless, voltage waveforms can be easily obtained in pulsed gas lasers through suitable and very fast high voltage probes. These waveforms can be digitized and after being filtered for noise elimination, the first and second derivatives can be taken through a computer. Substituting their values into equations (5) for the first stage and (9), (10) for the second one, relationships among resistances and inductances can be obtained for every time instant during the discharge. Thus equations (9) and (10) give relationships between R_1, L_1 in the switch system before and after the breakdown in the laser chamber respectively, while equation (10) gives relationships between R_2, L_2 in the laser chamber after the breakdown.

However, if we consider that for a sequence of four extremely close adjacent time instants the resistances and inductances are varied linearly, then the four relationships which correspond to these time instants can be written. Because of the linear variation of L_1 and L_2 we can have $dL_1/dt=\Delta L_1/\Delta t$ and $dL_2/dt=\Delta L_2/\Delta t$. For the first stage these originate from equation (5) and are the follow :
for the time instant t-Δt

$$(L_1-\Delta L_1)\frac{d^2V_2}{dt^2}\Big|_{t-\Delta t}+(R_1-\Delta R_1+\frac{\Delta L_1}{\Delta t})\frac{dV_2}{dt}\Big|_{t-\Delta t}+\frac{C_1+C_2}{C_1C_2}V_2|_{t-\Delta t}=\frac{V_0}{C_2} \qquad (11)$$

for the time instant t

$$L_1\frac{d^2V_2}{dt^2}\Big|_t+(R_1+\frac{\Delta L_1}{\Delta t})\frac{dV_2}{dt}\Big|_t+\frac{C_1+C_2}{C_1C_2}V_2|_t=\frac{V_0}{C_2} \qquad (12)$$

for the time instant t+Δt

$$(L_1+\Delta L_1)\frac{d^2V_2}{dt^2}\Big|_{t+\Delta t}+(R_1+\Delta R_1+\frac{\Delta L_1}{\Delta t})\frac{dV_2}{dt}\Big|_{t+\Delta t}+\frac{C_1+C_2}{C_1C_2}V_2|_{t+\Delta t}=\frac{V_0}{C_2} \qquad (13)$$

and for the time instant t+2Δt

$$(L_1+2\Delta L_1)\frac{d^2V_2}{dt^2}\bigg|_{t+2\Delta t}+(R_1+2\Delta R_1+\frac{\Delta L_1}{\Delta t})\frac{dV_2}{dt}\bigg|_{t+2\Delta t}+ +\frac{C_1+C_2}{C_1C_2}V_2\big|_{t+2\Delta t}=\frac{V_0}{C_2} \quad (14)$$

where R_1, L_1 is the resistance and inductance at the time instant t (t is a certain time in the time region of the first stage). Solving the system of the above equations, the values of R_1, L_1 can be obtained for the time t. Scanning the time region in the first stage with the same procedure, the values of R_1, L_1 for every time instant can be found.

Similarly in the second stage, considering again that for four extremely close adjacent time instants the linearity of the variation of the quantities R_1, L_1 is valid, we can write again the four relationships for these time instants. These originate from equation (9) and are :

for the time instant t-Δt

$$(L_1-\Delta L_1)\frac{d^2V_1}{dt^2}\bigg|_{t-\Delta t}+(R_1-\Delta R_1+\frac{\Delta L_1}{\Delta t})\frac{dV_1}{dt}\bigg|_{t-\Delta t}=\frac{V_2|_{t-\Delta t}-V_1|_{t-\Delta t}}{C_1} \quad (15)$$

for the time instant t

$$L_1\frac{d^2V_1}{dt^2}\bigg|_{t}+(R_1+\frac{\Delta L_1}{\Delta t})\frac{dV_1}{dt}\bigg|_{t}=\frac{V_2|_{t}-V_1|_{t}}{C_1} \quad (16)$$

for time instant t+Δt

$$(L_1+\Delta L_1)\frac{d^2V_1}{dt^2}\bigg|_{t+\Delta t}+(R_1+\Delta R_1+\frac{\Delta L_1}{\Delta t})\frac{dV_1}{dt}\bigg|_{t+\Delta t}=\frac{V_2|_{t+\Delta t}-V_1|_{t+\Delta t}}{C_1} \quad (17)$$

and for the time instant t+2Δt

$$(L_1+2\Delta L_1)\frac{d^2V_1}{dt^2}\bigg|_{t+2\Delta t}+(R_1+2\Delta R_1+\frac{\Delta L_1}{\Delta t})\frac{dV_1}{dt}\bigg|_{t+2\Delta t}= \\ =\frac{V_2|_{t+2\Delta t}-V_1|_{t+2\Delta t}}{C_1} \tag{18}$$

where in this case, t is a certain time in the time region of the second stage. Solving the system of the above equations, the values of R_1, L_1 can be obtained for the time t. Scanning the time region in the second stage, the values of R_1, L_1 for every time instant can be found. Having found the time histories of R_1, L_1 in both stages, the time histories of R_2, L_2 can be found repeating the same procedure during the time period of the second stage. The assumption of the linear variation of the quantities R_2, L_2 for four extremely close adjacent time instants is taken again.

The four relationships used for this case originate from equation (10) and are: for the time instant t-Δt

$$(L_2-\Delta L_2)(C_1\frac{d^2V_1}{dt^2}\bigg|_{t-\Delta t}+C_2\frac{d^2V_2}{dt^2}\bigg|_{t-\Delta t})+ \\ +(R_2-\Delta R_2+\frac{\Delta L_2}{\Delta t})(C_1\frac{dV_1}{dt}\bigg|_{t-\Delta t}+C_2\frac{dV_2}{dt}\bigg|_{t-\Delta t})=-V_2|_{t-\Delta t} \tag{19}$$

for the time instant t

$$L_2(C_1\frac{d^2V_1}{dt^2}\bigg|_t+C_2\frac{d^2V_2}{dt^2}\bigg|_t)+(R_2+\frac{\Delta L_2}{\Delta t})(C_1\frac{dV_1}{dt}\bigg|_t+C_2\frac{dV_2}{dt}\bigg|_t)=-V_2|_t \tag{20}$$

for the time instant t+Δt

$$(L_2+\Delta L_2)(C_1\frac{d^2V_1}{dt^2}\bigg|_{t+\Delta t}+C_2\frac{d^2V_2}{dt^2}\bigg|_{t+\Delta t})+ \\ +(R_2+\Delta R_2+\frac{\Delta L_2}{\Delta t})(C_1\frac{dV_1}{dt}\bigg|_{t+\Delta t}+C_2\frac{dV_2}{dt}\bigg|_{t+\Delta t})=-V_2|_{t+\Delta t} \tag{21}$$

and for the time instant t+2Δt

$$(L_2+2\Delta L_2)\left(C_1\frac{d^2V_1}{dt^2}\Big|_{t+2\Delta t}+C_2\frac{d^2V_2}{dt^2}\Big|_{t+2\Delta t}\right)+$$
$$+\left(R_2+2\Delta R_2+\frac{\Delta L_2}{\Delta t}\right)\left(C_1\frac{dV_1}{dt}\Big|_{t+2\Delta t}+C_2\frac{dV_2}{dt}\Big|_{t+2\Delta t}\right)=-V_2|_{t+2\Delta t} \quad (22)$$

where t is a certain time instant in the second stage. Solving the system of the above equations and scanning the time region of the second stage, as previously described, the time histories of R_2, L_2 can be found. Thus, the time histories of the resistances and inductances for both discharges in a pulsed gas laser can be revealed in the entire time region of the discharges (in both stages). An application of this method took place in a N_2 Laser system. The voltage waveforms are shown in fig.2. Elaborating the voltage waveforms the time histories of the resistances and inductances of the two discharges were found. The resistance R_1 and inductance L_1 of the spark-gap are shown in fig. 3 while the resistance R_2 and inductance L_2 of the laser chamber are shown in fig. 4. Details on this method are in refs [11,12].

3. Time dependent resistances and inductances.

The time evolution of the resistances and inductances (figs 6,7) shows clearly that these quantities present strong variations in the "formation phase" of the discharges (first 50nsec) while after this unstable phase, in the following "main phase" of the discharges, their configuration presents fluctuations around constant values. Concretely, in the "formation phase" the resistances present the expected drop, caused by the electron avalanche multiplication while the inductances present an abrupt high peak. It is worth mentioning again that the inductance is always taken as constant quantity to date. Although a comprehensive examination of the behavior of these electric quantities is beyond of the scope of this work, a qualitative interpretation will be attempted. Thus, the high peak of the inductance in the formation phase of the discharge can be explained only through the generalization of Lenz' Law referring that not only the current but also the inductance (if it is possible) oppose the oncoming sudden variation of the magnetic flux. In our case, because the discharge develops freely, not only the current but the inductance can also be varied. Thus, we can say that the reaction of the system to the oncoming variation is manifested through both the current and inductance behavior. The case of the electric discharges is one of the rare cases where the inductance is variable, as this is verified in the present work. Faraday's Law must be generalized for the discharges as follows

$$E=-\frac{d(LI)}{dt} \quad (23)$$

This relationship has been taken into account for the formation of the differential equations

(5), (9) and (10) which describe the behavior of the circuit in the two stages.

However, as it is known, the inductance of an element depends mainly on its dimensions. This means that the inductances depend on the dimensions of the discharges [1,2]. The freely varied dimensions of the two discharges namely the diameter in the discharge of the spark-gap and the thickness in the discharge of the laser chamber determine eventually the variations in their inductances. The lower these dimensions the higher the inductances and vice versa [1,2,13]. Consequently, the abrupt peak in the inductances during the formation phase is attributed to a shortening of the freely varied dimensions of the discharges and a consecutive broadening, obtaining their final almost constant values.

A plausible explanation for this phenomenon is that the electrons originating from a large area of the cathode experience a centripetal electromagnetic force (Laplace force) because of their motion. This force is initially dominant over the electrostatic one causing a constriction of the plasma through the freely varied dimensions. Afterwards, the capacitors continue to feed the plasma, the electron density increases and the electrostatic repulsive force begins to dominate causing the broadening of the plasma. This procedure stops at the end of the formation phase when the plasma has been formed with a final critical electron density securing the equalization of the two forces. Subsequently, the discharge has almost constant dimensions and the inductance remain quite constant determining the "main phase" of the discharges (figs 3,4).

On the other hand the resistances in the "main phase" present a damping oscillation with the same frequency as the current and voltage. Our opinion is that this oscillation is due to the fact that the light electrons can follow the current oscillation while the heavy ions cannot. Thus, at a half period, both electrons and ions travel in parallel, while at the other half period they travel antiparallel. This latter motion appears as "difficulty" of the current flow and finally creates an additional resistance which oscillates with the same frequency and phase as the current ones.

4. Consideration of the laser system

In this section an analysis of the laser system will be attempted through the known time dependent resistances and inductances of the discharges (figs 3 and 4). These influence the performance of the electric circuit which, in its turn determines the optical output. Consequently, this analysis will take place in two steps examining first the behavior of the electric circuit and then the optical behavior of the laser system.

4.1 THE BEHAVIOR OF THE ELECTRIC CIRCUIT.

The performance of the electric circuit has been described in section 3. During the first stage the differential equation governing the performance of loop I of the circuit for the voltage V_2 is

$$L_1C_2\frac{d^2V_2}{dt^2}+C_2(R_1+\frac{dL_1}{dt})\frac{dV_2}{dt}+(1+\frac{C_2}{C_1})V_2-V_0=0 \qquad (24)$$

which is the same with eq (5).

During the second stage the differential equation governing the performance of the entire circuit shown in fig. 1 for the voltage V_2 is

$$\frac{d^4V_2}{dt^4}+K\frac{d^3V_2}{dt^3}+\Lambda\frac{d^2V_2}{dt^2}+M\frac{dV_2}{dt}+NV_2=0 \qquad (25)$$

where K, Λ, M, N are known functions of the time varied R_1, L_1, R_2, L_2. This equation derives from the system of eqs (9) and (10) deleting voltage V_1. Solutions of these equations have an approximate coincidence with the experimental waveforms shown in fig.2

4.2 THE OPTICAL BEHAVIOR OF THE LASER SYSTEM

The optical behavior of the laser system is studied through the laser rate equations. These are

$$\frac{dN_C}{dt}=\frac{N_eN_{gass}}{V}\int_0^T g(T_e,u)\sigma_{Cv=0}(u)4\pi u^3du-\frac{\sigma_{stim}n_{ph}c(N_C-N_B)}{V}-\frac{N_C}{\tau_C} \qquad (26)$$

$$\frac{dN_B}{dt}=\frac{N_eN_{gass}}{V}\int_0^T g(T_e,u)\sigma_{Bv=0}(u)4\pi u^3du+\frac{\sigma_{stim}n_{ph}c(N_C-N_B)}{V}+\frac{N_B}{\tau_B}-\frac{N_C}{\tau_C} \qquad (27)$$

and

$$\frac{dn_{ph}}{dt}=\frac{\sigma_{stim}n_{ph}c(N_C-N_B)}{V}-\frac{n_{ph}}{\tau_{ph}}+\gamma\frac{N_C}{\tau_C} \qquad (28)$$

where N_{gass}, N_C, N_B and n_{ph} are the total number of the gass, the C(u=0), the B(u=0) state and the photons respectively. The spontaneous lifetimes of the two levels are τ_C and τ_B are 40nsec and 6μsec respectively. The photon lifetime τ_{ph} represents the mean time a photon stays in the cavity. The quantity γ is a geomentrical factor for spontaneous photons emitted in the forward direction and V is the discharge volume. The quantities σ_C and σ_B are the cross sections for the C(u=0) and B(u=0) state. Finally σ_{stim} is the cross section for the stimulated emission. These equations have been given elsewhere [7,8] and the symbols

have the accustomed meaning. Assuming a Maxwellian electron distribution function for $g(T_e,u)$ the only quantity that needs to be known is the electron temperature T_e. This can be easily related to the applied electric field through the relationship [7]

$$kT_e=0.11\left(\frac{E}{P}\right)^{0.8} \quad eV \tag{29}$$

where k is the Boltzman constant, E is the electric field and P is the pressure in the laser channel. This equation is the connection link between eqs. (5)-(25) and eqs (26)-(30).

Finally, solving the system of the laser rate equations (26)-(28) the number density of the upper and lower laser state as well as the photon density are known in time. Then, the optical laser power was calculated through the relationship [14]

$$P(t)=\frac{\gamma_1 c}{2L}h\nu n_{ph} \tag{30}$$

where γ_1 is the logarithmic loss per pass due to transmission through the exit window of the laser chamber and c is the speed of light. In fig 5 the voltage V_2 waveform as well as the optical power of the laser pulse are shown together. The observed and calculated curves have an approximate coincidence. In fig 6 the population inversion as well as the optical power of the laser pulse are shown together.

5. Discussion

The knowledge of the time dependent resistances and inductances of the discharges in the laser system is the key for accurate analyses of the pulsed gas lasers. However, the time behavior of the resistances was expected bearing in mind the avalanche multiplication of the electrons during the "formation phase" of the discharges. On the other hand, the behavior of the inductances was unexpected, bearing in mind that this quantity was considered constant in the literature to date. The main feature of its time behavior is undoubtedly the created high peak in the formation phase of the discharges. This influences the electrical and optical behavior of the system. An investigation of this influence can be carried out comparing electrical and optical quantities taken with varied inductances and constant ones. Thus we can assume the inductances L_1, L_2 constant by eliminating the high peaks and taking their values to be as the average values of the time dependent inductances during the "main phase" of the discharges. The previous procedure of solving equations (24), (25) of the circuit and the laser rate equations (26)-(28) was repeated and the results are shown in figs 5 and 6. As it can be seen the high peak of the inductances influences the electrical and optical quantities of the laser system. Concretely, the laser optical output decreases about 40% in comparison with the optical output with constant inductances. The time duration of the optical pulse remained the same while the light pulse appeared 2nsec earlier. The conclusion of this comparison is that if in a somehow technological way the high peaks of the inductances were eliminated an increment of the energy output would

be expected in pulsed gas lasers.

6. Conclusion.

In the present work a method of finding the time dependent resistance and inductance in the discharges in pulsed gas lasers has been described. According to this method, an utilization step by step of the voltage waveforms through the circuit differential equations leads finally to the revelation of the time histories of the inductance and resistance of the discharge in the laser channel as well as in the switch system. These time dependent quantities show strong variations in the formation phase of the discharge while in the main phase their values present fluctuations. The knowledge of the time dependent resistances and inductances of the discharges in a pulsed gas laser constitute an advantage for the authors who attempt a circuit and optical analysis of their system. The circuit equations and the laser rate ones give accurate solutions and the theoretical results are in excellent agreement with the experimental ones. The annihilation of the high peak of the inductances in the formation phase of the discharges will increase the energy of the optical output about 40%.

ACKNOWLEDGEMENT

The authors wish to thank Mr. S. Koutsouvelis for his invaluable technical assistance.

REFERENCES :

[1]. P. Persephonis, V. Giannetas, C. Georgiades, J. Parthenios and A. Ioannou (1995) "The influence of the external circuit on arc-discharge of a spark-gap : Its application to a pulsed gas laser". *IEEE J. Quantum Electron.* **31**, 567-572

[2]. P. Persephonis, V. Giannetas, C. Georgiades, J. Parthenios and A. Ioannou (1995) "The inductance and resistance of the laser discharge in a pulsed gas laser". *IEEE J. Quantum Electron.* **31**, 573-581

[3]. Edward T. Gerry (1965) "Pulsed Molecular Nitrogen Laser Theory" *Appl. Phys Lett* **7**, 6-8

[4]. A. W. Ali., A. C. Kolb and A. D. Anderson (1967) "Theory of the Pulsed Molecular Nitrogen Laser" *Appl. Opt* **6**, 2115-2119

[5]. A. W. Ali. "A study of the Nitrogen laser power density and some design considerations" (1974) *Appl. Opt* **8**, 993-998.

[6]. H. E. B.. Anderson, S. A. Borgstrom. (1974) "Time-resolved analysis of a transvely excited nitrogen laser" *Opto-electronics*, 6, 225-234

[7] W. A. Fitzsimmons, L. W. Anderson, C. E. Riedhauser and Jan M. Vrtilek (1976) "Experimental and Theoretical Investigation of the Nitrogen Laser" *IEEE J. Quantum .Electron* **QE-12**, 624-633

[8]. N. Spyrou, P. Leprince et H. Milleon. (1980) "Description d' une discharge implulsionelle transverse. Application au laser N_2 " *Rev. Phys. Appl.* **15**, 1459-1467.

[9]. A. Dipace and E. Sabia, (1987) "An analytical approach to discharge circuits in Gas Lasers" *Il Nuovo Cimento* **9**, 1477-1484.
[10]. T. Letardi, S. Bollanti, A. De Angelis, P. Di Lazzaro, I. Giabbai, G. Giordano and E. Sabia (1987). "Characterization of a High - Uniformly, X-Ray Preionized XeCl laser". *Il Nuovo Cimento.* **9**, 873-891.
[11]. P. Persephonis, V. Giannetas, A. Ioannou, J. Parthenios and C. Georgiades. (1995) "The time dependent resistance and inductance of the electric discharges in pulsed gas lasers." *IEEE J. Quantum Electron.* **31 (10),** in press.
[12]. P. Persephonis, V. Giannetas, A. Ioannou, J. Parthenios and C. Georgiades (1995) "Time history of the resistance and inductance in a pulsed electric discharge" *Jpn. J. Appl. Phys* (Part I), **34 (11)**, in press.
[13]. P. Persephonis, K. Vlachos, C. Georgiades, and J. Parthenios. (1992) "The inductance of the discharge in a spark-gap". *J. Appl. Phys.* **71(10)**, 4755-4762.
[14]. A.E. Siegman (1986) *"Lasers"*. University Science Books, Mill Valley, California.

Fig. 1 The electric circuit of a C-to-C pulsed gas laser

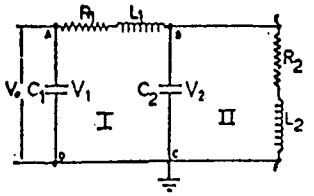


Fig. 2 Voltage V_1 and V_2 waveforms

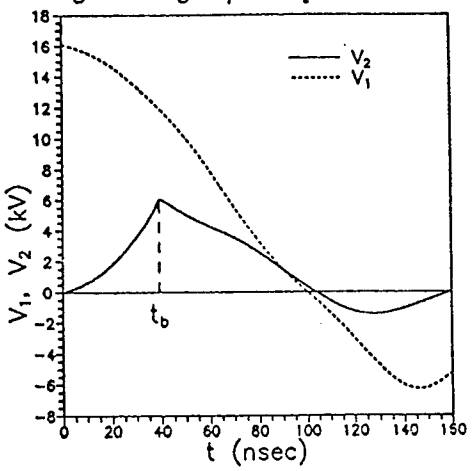


Fig. 3 The time dependent resistance R_1 and inductance L_1 of the spark-gap.

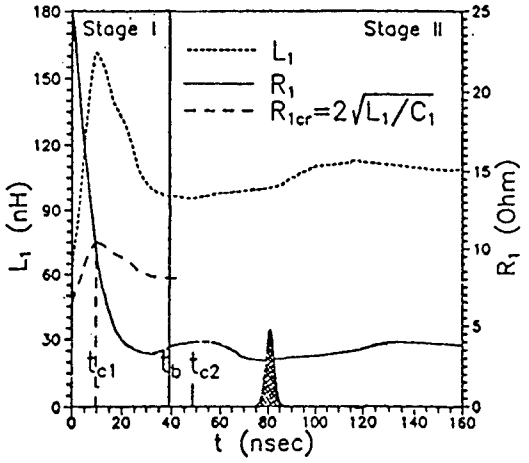


Fig. 4 The time history of the resistance R_2 and inductance L_2 of the laser chamber.

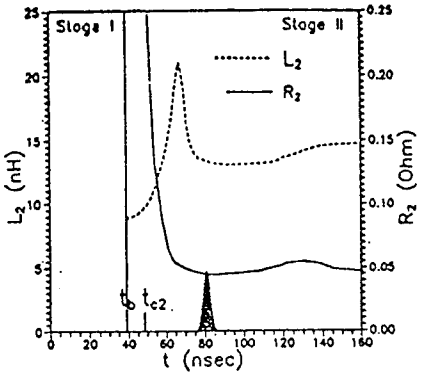


Fig. 5 Voltage V_2 waveform and laser light pulse
a) with L_1, L_2 time varied and b) with L_1, L_2 constant

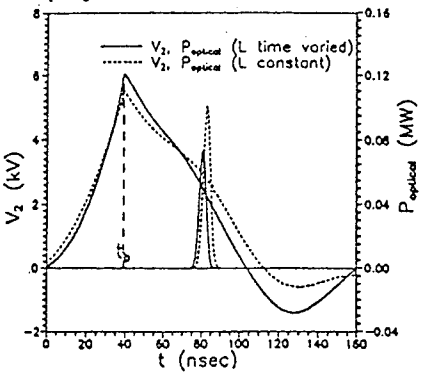
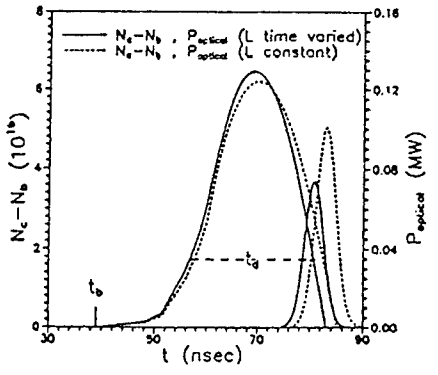


Fig. 6 Population inversion and laser light pulse
a) with L_1, L_2 time varied and b) with L_1, L_2 constant



METAL VAPOUR LASERS

Fundamentals and current status

G.P. HOGAN
Laser Group, Clarendon Laboratory,
University of Oxford, Parks Road, Oxford OX1 3PU, UK

1. Introduction

The class of laser to be considered in this paper is that of the neutral, self-terminating, or cyclic, metal vapour lasers (MVLs) that operate between a resonance upper and metastable lower level, excited by direct electron bombardment. Many other lasers employ the vapour of a metal as the active medium, many with laser transitions of the ion, and with a variety of excitation mechanisms including charge transfer, Penning ionisation and recombination routes, however the mechanisms involved, and the characteristics of these lasers render separate consideration of these devices appropriate.

There is, however, a group of metals with sufficiently similar term diagrams that they may form the active medium of lasers with many operating characteristics in common, that may be considered to form a family. Many physics and engineering considerations are relevant to the whole family and it is therefore appropriate to discuss them together.

These lasers are intrinsically pulsed, typically operating in the 1 – 20 kHz region, although pulse repetition frequency (prf) up to 100 kHz has been achieved, with pulse lengths of typically 10 – 100 ns. Output wavelengths range from the near UV to the IR, with most members of the family offering total efficiency between 0.1% and 3% and output powers measured in watts.

The best known, and head of the family, is undoubtedly the copper vapour laser (CVL). First reported in 1966 [1], operating simultaneously on two laser transitions, at 510.6 nm, in the green, and 578.2 nm, in the yellow, commercial devices are available offering 120 W average power (total of both lines) while laboratory devices with outputs up to 750 W have been built. Conventional CVLs typically exhibit wall plug efficiencies of the order of 1%, although recent variants on the system have shown 3.2%.

The other members of the family currently available commercially are the gold and barium vapour lasers. Laser output from gold is predominantly in the red at 627.8 nm with commercial devices offering 9 W, and lab ones up to 16 W. Laser output is also available in the near UV at 312.2 nm, analogous to the copper green line, but output is generally well below 1 W.

R. Kossowsky et al. (eds.), High Power Lasers – Science and Engineering, 153–175.
© 1996 *Kluwer Academic Publishers. Printed in the Netherlands.*

Commercial barium vapour lasers typically yield 10 W at 1.50 μm, with lab devices giving 12 W at 1.50 μm, 1.5 W at 2.55 μm and 1 W at 1.13 μm, with efficiencies up to 0.72% reported.

Lead (406.2 nm and 722.9 nm) was the first of the family to exhibit gain, in 1965 [2], with manganese (a number of lines: 534.1 – 553.8 nm and 1.29 – 1.40 μm) a few months later [3], a few watts of laser output can currently be obtained from each. Output from iron (452.9 nm) and bismuth (472.2 nm) has been observed.

2. Elementary MVL kinetics

2.1. THE TERM DIAGRAM

Figure 1 is part of the term diagram of copper. From this can be seen a number of the factors, common to all members of the family of cyclic MVLs, that determines their characteristics.

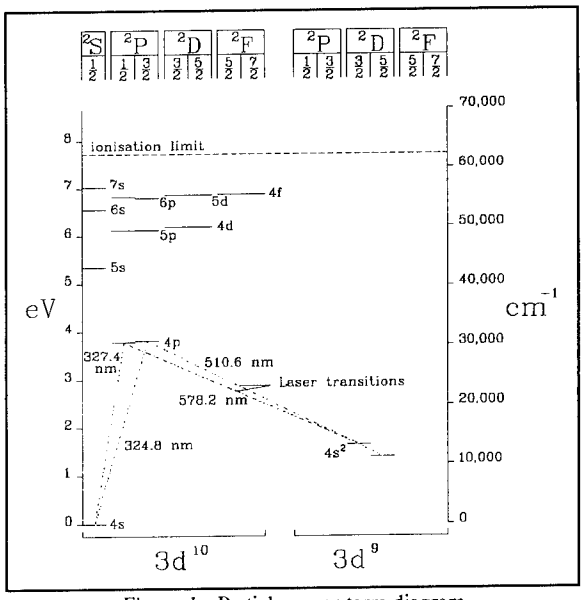


Figure 1. Partial copper term diagram

The ground state consists of a fully populated electron shell with one additional electron: in the case of copper the designation is $3d^{10}$ 4s. The upper laser levels are the resonance levels in which the 4s electron has been promoted to 4p via fully allowed, strong transitions. The lower laser levels, however, are of a different core configuration ($3d^9$), in which one of the inner shell electrons has been excited to 4s. Transition between this levels and the ground state is optically forbidden by parity selection rules, in addition to requiring the excitation of an inner shell electron, and is consequently of very low probability, rendering these levels metastable.

The difference between the probabilities for the transitions between the ground state and the upper and lower levels allows temporary population inversion to be generated.

The laser transitions themselves, although allowed by parity selection, are relatively forbidden as they require the simultaneous rearrangement of two electrons, however configuration mixing gives small but appreciable transition probabilities.

Provided that there is a sufficiently high ground state density, decay from the upper laser levels can be restricted to the laser transitions by resonance trapping.

Finally, it can be seen from the energies of the laser levels that the ratio of the energy contained in the laser photon to that of the excitation transition is relatively high, giving a high quantum efficiency for the laser process.

Even with the resonance transition fully trapped, the lifetime ratio between the upper and lower laser levels is such that inversion cannot be maintained indefinitely, and the laser is intrinsically pulsed, self-terminating or cyclic.

2.2. DISCHARGE EXCITATION

Having established that transient population inversion is potentially realisable, a suitable excitation scheme is required. Pulsed discharge through the metal vapour, in a low pressure (10 – 100 mbar), inert buffer gas provides such a mechanism. Neon, or occasionally helium, are usually used. The buffer gas performs a number of functions. In a laser with insufficient vapour pressure of metal at room temperature, and no external heater mechanism, the discharge runs in the buffer gas until a sufficient vapour pressure of metal has been generated, whereupon its lower ionization energy ensures that this takes over, except in the cooler end regions. In lasers that are not sealed off the slow flow of buffer gas helps to minimise any build up of impurities outgassed from thermal insulation or other sources. Finally, the thermal conductivity of the buffer gas helps to establish the thermal environment within the plasma and minimise cataphoretic effects.

The pulsed discharge provides the pump mechanism for the laser by direct electron collision, but also provides a mechanism for de-excitation from the metastable levels by collisions of the second kind (super-elastic collisions) towards the end of the discharge, to allow them to be returned to thermal equilibrium. In addition the discharge generates the heat necessary to raise the temperature of the plasma tube to the correct operating temperature, sufficient to generate a suitable vapour pressure of the metal lasant. In most of today's MVLs this is the only heating mechanism for the plasma tube, however some incorporate a supplementary, electrical heater element to allow the temperature to be raised quickly from cold to allow faster warm up times.

A number of devices have been built employing a transverse discharge. This geometry allows much greater ratio of electric field strength to vapour number density (E/N, and hence electron temperature) for a given voltage, and better discharge stability for low pre-pulse electron density, however it entails significant engineering difficulties. Maintaining electrodes at high temperatures for extended periods leads them to denature to powder as a result of decrepitation along grain boundaries. Also low inductance, low (electrical) resistance feeds through to the electrodes also exhibit low thermal resistance, which requires additional power input. There are also problems with differential expansion at metal-ceramic or -glass junctions. It has, however, been employed on a copper iodide laser [4], and there is still research in elemental devices.

Electron beam and microwave pumping of MVLs have also been undertaken, though the vast majority of MVLs are longitudinal discharge pumped devices.

If pumping efficiency is to be maximised, the electron temperature must be optimised. In the case of copper an electron temperature greater than about 2 eV is

required for excitation from the ground state to the resonance levels to dominate over that to the metastables. Once there is significant population in the upper laser levels, stepwise excitation from them to higher lying levels also become important as competing processes.

The active medium is a true plasma, with zero space charge, equivalent to the positive column of the low pressure dc discharge. The concept of temperature in this pulsed, non-equilibrium context is not strictly relevant, however it can still be used to convey some information. The electron density is not sufficiently high to ensure that Coulomb relaxation between electrons is rapid enough for a simple Maxwellian energy distribution function, characterised by a single electron temperature, to be maintained in the presence of many inelastic loss processes depleting the high energy tail. For much of the pulse cycle, too, the electrons are not in equilibrium with the heavy bodies, giving rise to different "temperatures" for the electrons and gas.

3. MVL engineering

3.1. BASIC LASER HEAD DESIGN

The essential features of a simple, elemental MVL laser head are illustrated in Figure 2.

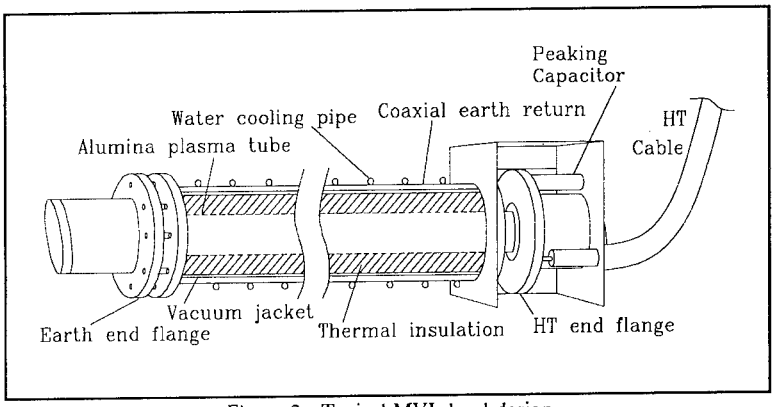


Figure 2. Typical MVL head design

The heart of the system is the alumina plasma tube which contains the high temperature environment of the MVL plasma. In an elemental CVL this tube runs at a temperature of around 1500°C. Surrounding the plasma tube is a layer of ceramic fibre thermal insulation. In a discharge heated MVL the balance between the power deposited into the plasm by the discharge, and the heat flow through the thermal insulation sets the plasma tube wall temperature and, in most MVLs, the vapour pressure of lasant. The exception is the HyBrID lasers which will be dealt with in a later section. As the vapour pressure of metal, and hence the wall temperature, for optimum laser action is fairly precisely determined, in practice the level of thermal insulation determines the input power density required to reach it.

The vacuum jacket allows containment of the low pressure buffer gas, and keeps out

impurities. Outside the vacuum jacket is a coaxial metal cylinder that acts as both earth return connection for the discharge circuit, and water cooling jacket, allowing heat generated to be managed conveniently.

Not shown are the discharge electrodes which vary in sophistication from the very simple to the exotic. These will be discussed in slightly more depth below.

In addition to these, there are the gas and water handling components and electronic components that form part of the discharge circuitry.

Finally there is the optical cavity, if the device is to be used as an oscillator. Again, this will be discussed in greater depth in a subsequent section.

3.2. BASIC DISCHARGE CIRCUITRY

A typical, fairly basic, first generation circuit of the capacitor transfer, resonant charging design is shown in Figure 3.

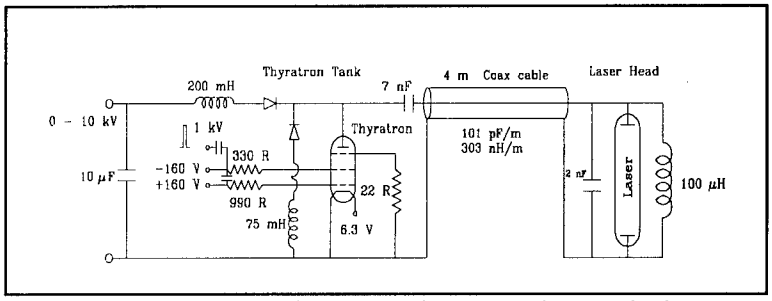


Figure 3. Typical basic MVL capacitor transfer discharge circuit

High voltage ac is taken from the HT transformer, via a Variac to allow control of voltage, smoothed on smoothing capacitor and applied to the resonant charging circuit. This consists of a charging inductor, charging diode and storage capacitor. The bypass inductor behaves as a short circuit on this slow time scale, completing the circuit, bypassing the laser and peaking capacitor. At the operating pulse frequency of the laser (ie kHz) the charging inductor and storage capacitor form a series tuned circuit allowing the voltage across the storage capacitor to be effectively doubled from that on the smoothing capacitor.

On discharge, a trigger pulse applied to the grids of the thyratron allows it to conduct, acting as a fast switch, grounding one plate of the storage capacitor. Twice the supply voltage now appear across the peaking capacitor and laser tube because the bypass inductor appears as an open circuit on this time scale. Current initially flows into the (relatively small and therefore fast) peaking capacitor until the voltages are approximately equalised. The voltage then appears across the laser tube. During the initial stages of the discharge, charge can be drawn fast out of the low value peaking capacitor, giving a fast rising edge, whilst the storage capacitor contains the rest of the charge. The ratio of capacitances is typically around 2:1 to give optimum circuit matching. On this simple circuit the HT coaxial connection from the storage capacitor to the laser head (including the peaking capacitors and bypass inductor) becomes part of the peaking capacitance.

This circuit accomplishes the task of providing a relatively fast discharge at the laser head, however it is not particularly well optimised. Up to 50% of the total energy can be dissipated in the thyratron, while the rising edge of the voltage pulse is significantly slower than would be desirable.

3.3. DISCHARGE CIRCUITRY MODIFICATIONS

Figure 4 shows a modification of the circuit incorporating a single stage of magnetic pulse compression (MPC). First proposed in 1983 [5], and in a fuller form in 1989 [6], this typically allows the pulse to be shortened by a factor of around 3 per stage. When a number of stages are combined it can be configured in a number of ways depending upon the requirements. It can be used to provide the fastest possible discharge pulse to the laser, to give more efficient pumping, or to give the slowest pulse through the switching circuitry to reduce dissipation in the thyratron, increasing efficiency and prolonging its lifetime. It can even allow its replacement by cascaded, fast, sold state switches, with their considerably longer operating lifetime. In addition, minor alteration of the circuit allows a further doubling of the supply voltage.

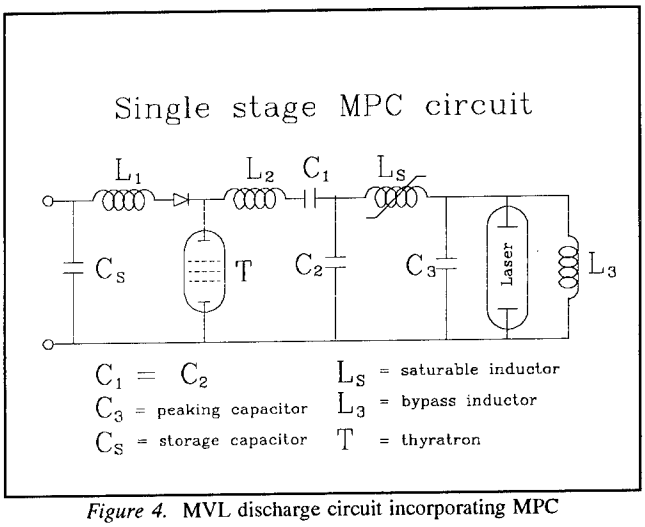


Figure 4. MVL discharge circuit incorporating MPC

Other work has been concerned with reducing the inductance of the discharge circuit, and optimising matching. The thyratron and storage capacitors can be mounted within, or close to the head, and multiple thyratrons can be used to minimise inductance and prolong lifetime, especially on larger devices.

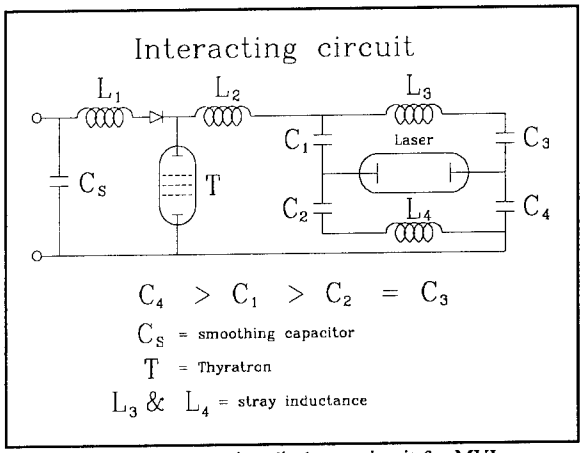


Figure 5. Interacting discharge circuit for MVLs

Another modification of the discharge circuit that appears to be giving promising results in application to copper halide, and HyBrID lasers, is that of the interacting circuit (Figure 5) [7]. It has been suggested that it reduces the low current through the plasma during the afterglow period, increasing the rate of fall of electron temperature, and hence recombination rate.

Switch mode power supplies can be used to improve efficiency and reduce the need for heavy, bulky HT transformers.

Overall, major improvements have been made in output power, overall efficiency, reliability and component lifetime.

3.4. LASER HEAD MODIFICATIONS

As was mentioned above, the plasma tube wall temperature, or the lasant reservoir temperature in the case of side-arm devices, is the primary determinant of the vapour pressure of lasant in the majority of MVLs. This is not the case in the family of HyBrID lasers, which will be dealt with in depth later.

All MVLs display an optimum tube (reservoir) temperature. For all metals this gives rise to an approximately equal vapour pressure of metal, regardless of the element, and the temperature at which it is attained. This corresponds to a vapour pressure of around 0.2 – 0.4 mbar, or a number density of $0.5 - 1 \times 10^{15}$ cm^{-3}. Even copper halide lasers, which typically exhibit an optimum number density of halide molecules of around 10^{17} cm^{-3}, only have about 1% dissociation, and so a similar free copper density. In view of the metals involved, and including all the compounds that have been employed in order to reduce the temperatures required, this observation represents a very wide range of temperatures.

The reason for this is the balance between two competing effects. At low metal density the rate of excitation to the upper laser levels is roughly proportional to the ground state density. As the density rises, however, the ratio of E/N (electric field strength to number density of colliders) that determines the electron temperature attained, falls. In this situation the relevant N is that of the inelastic collision partners, ie the metal. This reduction in peak electron temperature with increasing ground state density causes a gradual reduction in pumping efficiency to the upper lasers levels, relative to the lower levels.

The roll off of laser output power occurs at different ground state densities (and therefore wall temperatures) for different laser lines within a multiple line system. In the case of copper this roll off occurs at lower temperature for the green line than for the yellow as a result of the different relative pump rates to the upper and lower levels of the two transitions with falling electron temperature, as well as the increased pre-pulse thermal populations in the lower laser levels.

It was this precise requirement on tube temperature, and the high values leading from it for many of the elemental metals, that led to the search for metal compounds that could give a suitable vapour pressure at much lower temperatures, and yield ground state lasant by dissociation in the discharge. In 1973 gain was observed from CuI at

600°C [8], later that year CuCl at 400°C [9], and in 1975 CuBr at 450°C [10]. In 1977 an organic compound of copper, copper acetyl acetonate was observed to lase at 20°C [11], although in this case the problem became how to keep the temperature down!

Another very hopeful approach is that of the metal HyBrID lasers, to which reference has already been made, in which a charge of elemental metal is combined with an admixture of HBr in the buffer gas, such that metal bromide is formed at the surface of the metal, and transported into the discharge. Further discussion on HyBrID lasers will follow in a separate section on this topic.

Although the density of metal in proximity with the plasma tube wall is set by its local temperature, away from the wall, into the plasma, the density is primarily set by the local gas temperature (subject to a certain amount of modification as a result of ambipolar diffusion of any ions present). For this reason, not only is the plasma tube wall temperature important, but so is the radial gas temperature profile.

Having established the critical importance of plasma tube wall temperature, it can be seen that uniformity of temperature along the length of the tube is also important (Figure 6).

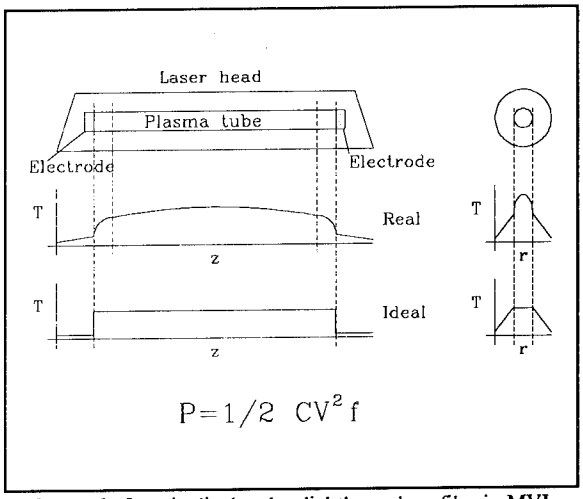


Figure 6. Longitudinal and radial thermal profiles in MVL

Longitudinally a high degree of homogeneity is desirable, and it is therefore necessary to optimise the thermal insulation accordingly. In the absence of any precautions to the contrary, the longitudinal temperature profile will assume a maximum at the centre, falling slowly towards the ends, with a region of rapid fall over the last few centimetres as longitudinal radiation and conduction losses become more significant. Over this end region the tube temperature will typically fall from around 1500°C to only a few hundred degrees adjacent to the (usually water) cooled end flange. If the thermal insulation is "profiled" such that the amount is not constant along the length, it is possible to minimise the length of the "dead" region at the two ends where the wall temperature is too low for there to be significant metal vapour, and maximise the uniformity of temperature along the remaining length. Different schemes exist to accomplish this, however most are proprietary, and significant increases in output power and efficiency can be accomplished in this way.

With the thermal insulation optimised for longitudinal homogeneity, it is necessary to optimise the overall level of insulation, thus determining the input power density

required to provide the optimum metal vapour pressure. If the efficiency remained constant this would directly determine output power, however it also determines the gas temperature radial profile, which leads to a significantly lower ground state density on axis, which reduces efficiency and also beam homogeneity. For these reasons the optimisation of thermal insulation for a given device, and operating criteria is a complex process and depends upon the relative importance placed on output power, efficiency and beam homogeneity.

MVLs display relatively efficient volumetric scaling. In the CVL the optimum prf scales inversely with tube radius whilst, at this prf, the specific pulse energy is approximately constant for a wide range of tube sizes. This leads to output power scaling linearly with tube radius, rather than with cross-sectional area (r^2).

There are currently two schools of thought concerning the mechanism leading to the fall off in efficiency at prfs above the optimum. One says that it is the build up of metastable population density that reduces the gain available, whilst the other ascribes it to an increasing pre-pulse electron density giving rise to a lower quality discharge and lower peak electron temperature. Analogy with the red line of the gold vapour laser, the upper and lower levels of which lie much higher than those in the copper, and which shows a flat laser efficiency curve with prf, suggests that metastable density is responsible, while comparison with the copper HyBrID laser, which exhibits very low pre-pulse conductivity, and considerably higher optimum prf, and also the results of computer modelling, suggest that it is the electron density that is important. Both of these theories have their adherents, with experiments claimed to prove the matter. In a system with as many interrelated, interdependent processes, and that is so strongly affected by relatively minor modifications to the physical construction, it is very difficult to perform an experiment which probes the relevant parameter in isolation from other effects. It is also entirely conceivable that the relative importance of these effects is different on devices of different sizes, or with different physical or electrical constructional details.

As plasma tube diameter increases two factors rapidly become more significant. Firstly the skin depth. If a high frequency signal, or high speed pulse, are applied to a conductor the current density is greatest near the surface of the conductor, falling off with a depth constant (skin depth) δ, which is given by:

$$\delta = \left(\frac{2}{\omega \mu_0 \sigma} \right)^{1/2} \qquad (1)$$

where ω is the angular frequency and σ the conductivity. This has the effect of delaying the propagation of the electric field into the axis of the plasma. Excitation from the ground state to the upper laser levels in the CVL is typically delayed by around 10 ns in a 42 mm diameter tube, or by 20 – 30 ns in a 60 mm bore device. The field, by the time it has propagated into the core of the plasma, is also reduced, giving less efficient excitation, however this may be ameliorated by a lower ground state density because of the higher gas temperature.

The radial gas temperature profile caused by power deposition into the plasma, combined with radial heat flow outwards through the thermal insulation layer, is the

second effect exacerbated by increasing bore size. It has already been mentioned how a higher input power density, as a result of reduced thermal insulation, leads to a higher axial gas temperature, and lower ground state density. As tube diameter is increased this effect becomes more significant still. It is found that the ground state population density on axis is even lower than that predicted from the gas temperature profile as a result of the accelerated radial diffusion of the (significant population of) residual ions as a result of ambipolar diffusion relative to the return diffusion of recombined ions from the wall. In addition, although in relatively small bore tubes the electron coupling is sufficiently great that there is relatively little radial variation in electron temperature, as bore increases some maximum on axis may be observed. The pre-pulse metastable population density is determined by the local electron temperature and ground state density. The relationship between the electron temperature and the gas temperature in the late afterglow is still not thoroughly understood. The electron temperature also exerts a very strong influence on three body electron recombination rate, and hence the pre-pulse conductivity of the plasma.

An innovation from the group at the Lawrence Livermore National Laboratory (LLNL) succeeds in effectively reducing the axial gas temperature in their 80 mm bore CVL amplifiers. Short lengths of refractory metal plate, placed vertically within the plasma tube, parallel to the axis, effectively absorb heat from the plasma and radiate (and conduct) heat to the walls [12], giving rise to improved output power, efficiency and beam uniformity.

Absorption of IR black body emission from the plasma tube by the windows gives rise to distortion of the beam by thermal lensing. Where beam quality and stability is of primary importance this can be unacceptable. The use of window materials exhibiting low IR absorption, such as MgF_2 significantly ameliorates this effect.

Much development over the years has been concerned with the optimisation of electrode design to give maximum discharge stability, maximum electrode lifetime and minimum window contamination, especially at higher buffer gas pressure. A number of designs have attempted to exploit the hollow cathode effect by using slots cut in the cathode of width approximately twice the cathode fall region. The LLNL group has designed a copper electrode incorporating this design, with a profile to maximise field uniformity [13], from which they report excellent results.

3.5. OPTICAL CAVITY

The simplest optical cavity for use with MVLs is a plane–plane cavity with a 100% rear reflector and a silica output coupler with either 4% or 8% Fresnel reflection from one or two uncoated surfaces. Because of the very high gain, and short gain period of the MVL the cavity has a very low Q allowing maximum coupling of the photon flux to the outside world before the gain medium goes into strong absorption. This allows time for a very few round trips of the cavity, even for the very tail of the pulse, which, combined with the relatively large bore of typical MVL plasma tubes, yields a low effective aspect ratio, and therefore a highly divergent beam. During the early stages of the laser output pulse, consisting of only 2 or 4 passes of the cavity, the beam

divergence is even worse giving rise to improving beam quality through the length of the pulse. In a typical MVL output pulse, as a result of the manner of formation of the intra-cavity photon flux [14], successive round trips can be seen as a series of humps from which a beam of successively decreasing divergence may be measured.

Even by the end of the pulse, however, the divergence obtainable from a plane-plane cavity may be around 100 times diffraction limited, typically having improved from around 10 mrad to around 2 mrad. In order to improve the output beam quality there have been a number of improvements to the optical cavity and seeding techniques.

The first was proposed in 1974 [15] in which a high magnification, unstable cavity was used on a CVL. There are a number of potential variants of this technique, but by using amplified spontaneous emission (ASE) falling into a very small angular range to seed the cavity, the effective aspect ratio of the laser is increased by the magnification of the cavity, and the divergence improved accordingly. Typically a small feedback mirror is employed as an output coupler, either converging or diverging depending on precise design, and either directly, or in a side branch via a small, 45° pick-off mirror, with a large concave mirror as the 100% reflector. By positioning the output feedback pick-off such that it collects light originating from the proximity of the plasma tube wall rather than on axis, use can be made of the fact that gain rises earlier in the discharge pulse close to the wall. The greater the degree of magnification the lower the divergence, and the lower the total output power in comparison with a plane-plane cavity. In this way, typically 75-80% of the power available from a plane-plane cavity can be obtained within 400 μrad.

This still represents around ten times the diffraction limit for a typical MVL, and the beam quality still improves with successive round trips of the optical cavity. In order to improve this further the Injection Controlled Oscillator (ICO) configuration was proposed independently, at the same meeting (CLEO '86) by both Naylor [16] and Warner [17]. This arrangement consists of two lasers with coupled, unstable cavities: a small master oscillator and a larger, controlled oscillator. The master oscillator is triggered first to allow good beam quality to develop, with the controlled laser triggered after a precise delay. This allows the controlled oscillator to be seeded with very low divergence light from the extreme tail of the master laser pulse, which is then present in the cavity from the onset of gain giving rise to very high quality light throughout the output pulse. A spatial filter between the two lasers

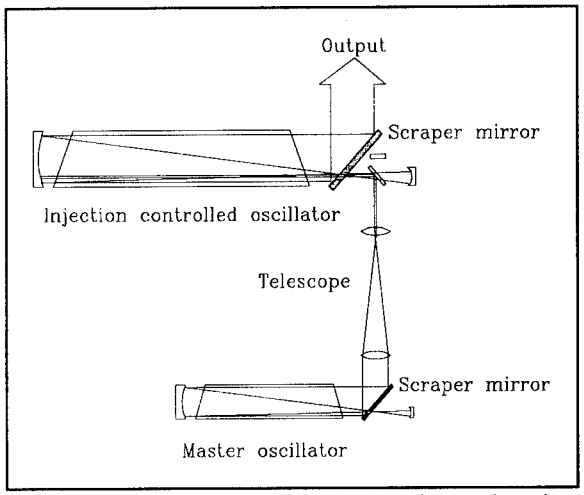


Figure 7. Adjoint-coupled self-filtering injection configuration

removes residual ASE from the injected beam.

A recent, further refinement of the technique [18] termed adjoint-coupled self-filtering injection (Figure 7) uses negative branch (self-imaging) unstable optics to remove the hard aperture of the scraper or feedback mirror, preventing it giving rise to diffraction. This is combined with telescoping down the master oscillator beam to a diameter (1.3 mm) at which value the combined diffraction and focusing from the concave rear mirror of the controlled oscillator, and a small (2.7 mm) adjoint coupling scraper mirror effectively form a large spot spatial filter (self-filtering). In this way output beam quality within twice the diffraction limit can be achieved with output powers of 40 W or so.

3.6 AMPLIFIER CHAINS

One of the great strengths of the MVLs is that they can be used very effectively in an amplifier, rather than an oscillator configuration. A device that yields 60 W as an oscillator can be expected to add around 60 W to a suitable (in terms of timing and diameter) beam passing through it, in an amplifier configuration. This is known as the Master Oscillator, Power Amplifier (MOPA) configuration [19]. Better still, the output beam quality is dictated by that of the input beam, and consequently a high quality input beam from an ICO arrangement can be input to a chain of high power amplifier units to yield many kilowatts average power of low divergence, pulsed, visible light. Since the gain medium is a gas, with a refractive index ≈ 1, even in the presence of strong thermal gradients such phenomena as thermal lensing, which can cause significant problems in high power solid state lasers, have negligible effect.

4. MVL diagnostics

4.1 RELEVANCE

Much recent work on MVLs has been concerned with improving our level of understanding of the kinetics involved. This has involved two distinct, but complementary approaches. Firstly there has been the empirical measurement of laser parameters eg [20] and secondly there has been computer modelling eg [21].

Measurement of laser parameters can cover everything from merely recording the output power from a device of given dimensions and input power to a full parameter map. This could involve time and radially resolved measurements of population densities in a wide range of energy levels in both the metal lasant, the buffer gas and any additives, electron density, discharge parameters such as current and voltage as a function of time, as well as the output parameters of average power, pulse length and shape and efficiency. The results of these measurements can then be given to those developing computer models to allow them to confirm the accuracy of their predictions, thus confirming the values of cross-sections, and any assumptions that have been used. It is very important that if the results of measurements are to be used together to draw

a conclusion, or compared, that they must have been made on the same device under identical operating conditions. A number of erroneous deductions concerning MVL kinetics have been made as a result of the unjustified assumption that sets of measurements made on different devices represent identical kinetics. In order to confirm the validity of a given computer model, too, it is necessary to have a set of measurements that represent the same set of operating conditions in order that the model may predict them all simultaneously. The greater the number of parameters accurately fitted, the more confidence that can be placed in the model.

The measurements included in a full parameter mapping can fall into a number of categories. Firstly there are the "off-line" measurements of parameters not directly related to a specific system, but required in order to make or interpret the more direct measurements. These can include such parameters as transition oscillator strengths, electron collision cross-sections and vapour pressure curves. Secondly there are the "passive" measurements that can be made non-invasively of the external parameters of the laser. These can include output power, efficiency, voltage and current traces (at different points in the circuitry), and pulse energy, length and timing (total or spectrally and radially resolved). These may also be measured as a function of input power, prf, plasma tube dimensions, voltage on storage capacitance, capacitance values, circuit design, head design, introduction of additives and many other conditions. Finally there are the "active" measurements. These are the direct radially and time resolved measurements of population densities and electron density within the MVL plasma.

In addition to their value in providing corroboration of computer models of MVL kinetics, they can also give interesting insight into the relative importance of processes and parameters directly. It is important, however, always to be aware of the highly complex and interdependent nature of the processes involved. For this reason the conclusions that can be drawn by considering the results of only a few measurements, or a limited subset of the data must always be viewed with caution.

From the pre-pulse values can be obtained information on the equilibrium thermal and electronic environment within the laser medium. From the pre-pulse radial profile of vapour density can be calculated an approximate radial gas temperature profile, as in Figure 8, although if there is a high pre-pulse ion density this can be modified by the effects of ambipolar diffusion. Where the metal vapour

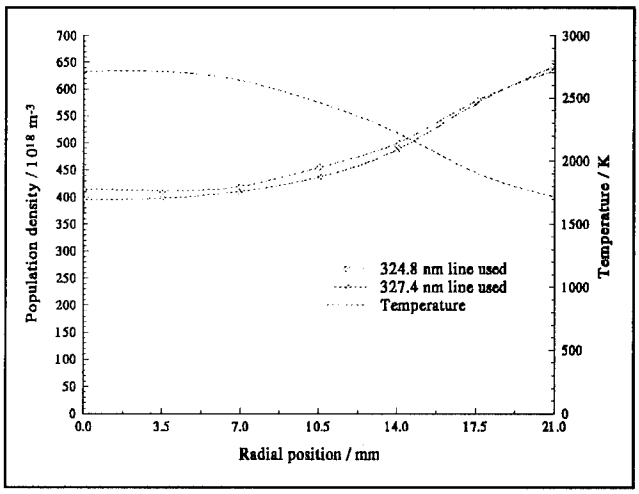


Figure 8. Copper ground state, pre-pulse radial profile: 42 mm bore CVL

pressure is determined purely by the temperature of metal blobs in contact with the plasma tube the measured metal vapour number density immediately adjacent with the plasma tube wall can be combined with a vapour pressure curve for the metal to calculate the wall temperature. If the latter can be measured independently, such as by a calibrated optical pyrometer then this can give a useful independent corroboration of the validity of the measured results.

From the measured electron density the likely importance of ambipolar diffusion in modifying the metal radial profile, and hence the calculated radial gas temperature profile, can be assessed. More importantly however, it gives a measure of the pre-pulse conductivity of the plasma, which has a profound effect on the nature and quality of the discharge, and through this, the increase in electron temperature and hence the relative efficiency of excitation of ground state metal to the different excited states, including the upper laser levels. In addition, the plasma conductivity σ is important in determining the skin depth (Equation (1)), and hence, in large bore devices, the attenuation and delay in propagation of the discharge to the axis of the plasma.

During the discharge, comparison of magnitudes and time courses of population densities in the various excited states, and their relationships with the voltage and current traces can give information on excitation efficiency, electron temperature, the relative importance of competing or undesired transitions, and the timescales of the different excitation and de-excitation processes in relation to the laser pulse duration.

Over the course of the inter-pulse period, the relaxation of populations in the afterglow, and particularly the recovery of the ground state density and the decay of electron density can yield significant information on the development of the thermal environment leading to the creation of the pre-pulse conditions.

It is also possible to compare such results obtained on different devices to allow tentative conclusions to be drawn concerning observed differences in efficiency, specific power density or other performance parameters, to investigate the effects of scaling, different excitation circuitry, thermal insulation design, buffer gas additives and other modifications. Once again, however, it is important to stress that assumptions based on incomplete analysis of a restricted data set is liable to lead to inaccurate or incomplete conclusions, or those with a limited applicability. The complexity and interdependence of the processes and parameters within the plasma of a typical MVL is such that, in order to be able to draw categorical conclusions on the relative importance of different processes, make predictions of the outcome of a given modification, or suggest modifications that should prove beneficial, with a high degree of confidence, a computer model is required. In order to be able to take the predictions of that as accurate, it must first have been able to prove itself by comparison with highly comprehensive data sets covering a wide range of operating conditions and constructional parameters.

4.2 DIAGNOSTIC TECHNIQUES

In order to be able to measure the parameters of interest it is necessary to have a suite of diagnostic techniques allowing access to them, without introducing any significant

perturbation either in the parameter to be measured, or in the environment that helps to determine its value. In addition it is desirable that the minimum of assumptions are required to derive results from the measurements.

The most popular technique currently employed in the measurement of population densities in MVLs is that of the hook method [22, 23]. In its modern implementation (the "fast" hook technique) a degree of both time and spatial resolution can be obtained by using a short pulse dye laser as the probe beam source.

In the hook method the test cell of interest (such as the laser tube) is placed in one arm of an interferometer, with a spectrograph at its output. A pseudo broad-band light source is used to generate interference fringes in the vicinity of an absorption line, such that the refractive index excursions of the anomalous dispersion curve are generated in the interferogram. By careful alignment of the interferometer, and choice of interference order, these can be converted to distinctive hooks and the effective population difference between the upper and lower levels can be calculated from the hook spacings, in conjunction with a number of calibration constants including the oscillator strength of the transition. Few other parameters are required that cannot be measured directly from the interference patterns making this technique very free of assumptions. In particular, as the hooks are generated in the extreme wings of the absorption line, no knowledge of line broadening mechanisms or magnitude are required. As the information required can be contained within a single frame very high time resolution (of the order of nanoseconds) can be obtained by the use of a short pulse laser source, with radial resolution determined by probe beam diameter.

The hook method is, however, relatively insensitive, requiring a large Nfl product, where N is the number density, f is the oscillator strength and l is the length over which the population is measured. In order to measure lower population densities (or use weaker lines) other techniques must be employed, such as absorption.

In order to measure electron density two main techniques have been employed. The measurement of linewidth of a number of hydrogen lines (usually present as an impurity) in an attempt to deconvolute the relative contributions of Stark broadening (as a result of the electric field due to the electrons), Doppler broadening (as a result of, and thus potentially yielding, gas temperature), hyperfine structure, and other components [24]. Owing to the low intensity of the emission on these lines, obtaining time and radial resolution using this technique can be extremely difficult, and interpretation of results ambiguous.

The alternative technique is that of measuring the change in refractive index as the electron density changes, in the mid infra-red (IR), where the refractive index is dominated by the free, rather than the bound electrons. First proposed in this application in 1977 in Russia [25] using a wavelength of 10.6 μm and relatively slow detectors, it has recently been reapplied by the author, using more modern equipment [26]. The use of a low power, CW CO_2 laser, a fast, liquid nitrogen cooled, HgCdTe detector, a fast, digital oscilloscope and the laser, with appropriate, 10.6 μm transmitting optics, mounted in an IR interferometer, allows the change of electron density to be observed as a change in interference fringe intensity. By ceasing the discharge trigger pulses to the laser for a very brief period to allow full recombination

of all electrons back to the Saha value, the change in electron density to this value too can be measured, allowing absolute values to be calculated.

5. Metal HyBrID lasers

One of the most exciting developments in the field of MVL technology in recent years concerns the discovery of the class of metal Hydrogen Bromide In Discharge (HyBrID) lasers [27] at St Andrews University, Scotland. Consisting of, in effect, a hybrid of conventional, elemental MVL technology, and the metal halide lasers, it employs an elemental metal lasant charge which is converted to the bromide at the wall, and carried into the discharge by an additional component of HBr in the buffer gas mixture (about 10%) in a manner similar to a tungsten halogen lamp.

HyBrID lasers are characterised by high efficiency (up to 3.2% based on stored energy having been reported [28]), high specific power (up to 2 Wcm^{-3} [29]), with a fast warm up time in comparison to an elemental MVL, and an insensitivity to plasma tube wall temperature. In addition, the radial beam profile more nearly approximates a Gaussian, rather than the top hat of a conventional CVL, they optimise at higher prf, for a given tube diameter and the pulse lengths are generally found to be longer. Although most development in this field has been on copper HyBrID lasers, including the results quoted above, the technology is applicable to, and results have been obtained with, a range of other metals from the MVL family.

Analysis of the kinetics of the copper HyBrID in a back-to-back study with a conventional CVL has yielded interesting insight into the possible interpretation of the observed differences in performance and operating parameters [30]. When comparing specific pulse energy, it is found that there is no significant difference between the two devices, however the ability of the HyBrID to maintain this at an optimum prf roughly three times that of the conventional device accounts for its much greater specific output power.

When the measured ground state densities (an axis) are compared (Figure 9) it can be seen that, although the pre-pulse ground state is considerably greater in the HyBrID, the quality of discharge has been maintained (see Section 3.4 above) as the degree of ground state depletion during the discharge testifies.

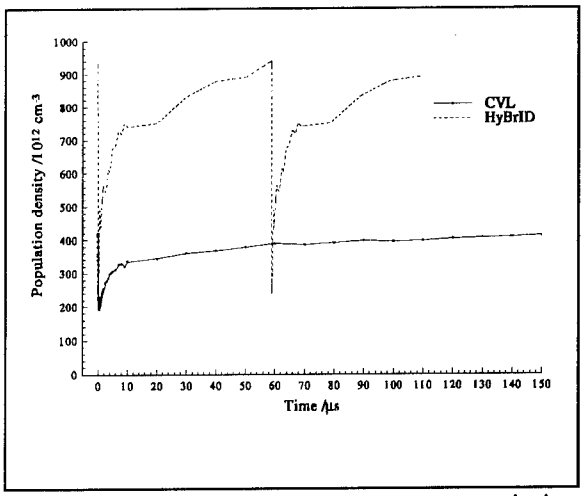


Figure 9. Depletion of the copper ground state, on axis, in a conventional CVL and a HyBrID

By direct measurement of the electron density the reason for this retained discharge quality in the presence of a high ground state density, that would have an extremely deleterious effect in a conventional CVL, can be seen.

In Figure 10 the electron density in the two devices, on axis, has been compared, and two, very striking, observations may be made.

The peak electron density in the HyBrID can be seen to be considerably higher, although as this device had a smaller plasma tube bore diameters (25 mm, as opposed to 42 mm for the CVL) this is, to an extent, to be expected and the importance should not be overstated. Of considerably greater significance, however, is the fact that the pre-pulse electron density is more or less negligible in the HyBrID, but is around 25% of the peak value in the conventional CVL.

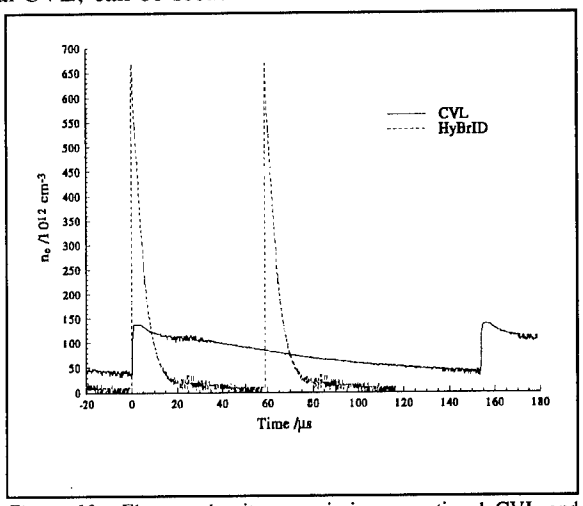


Figure 10. Electron density on axis is conventional CVL and copper HyBrID

The significance of the relatively high pre-pulse electron density in the CVL is observed in a phenomenon known as the Phantom Current [31]. This is a time during the early part of the discharge, of typically 60 – 100 ns duration, during which current can be measured, but no excitation or spontaneous emission can be detected. This consists purely of an ohmic type conduction current carried by the high density of electrons already present prior to the discharge and which persists until the current demanded is sufficient to raise the electron temperature high enough to reach threshold for inelastic collisions with the copper. In the HyBrID a very much reduced phantom current is observed as a vestigial hump on the leading edge of the current trace [32] as a result of this very much reduced pre-pulse electron density.

This absence of a classical breakdown event as a result of the high pre-pulse conductivity of the plasma in the CVL gives rise to a very much reduced peak electron temperature, and decreased efficiency. It is now thought that the much higher observed efficiency of the HyBrID, higher optimum prf and higher acceptable pre-pulse copper ground state density are all resultant from the very much lower pre-pulse conductivity and the consequent higher quality breakdown.

There is currently still a degree of uncertainty of the precise mechanism of the very fast decay of electron density observed during the first 15 μs or so of the afterglow in the HyBrID laser. This has generally been attributed to electron attachment by the strongly electronegative monatomic bromine present in the plasma, followed by two body recombination of the copper ions with bromide ions [33], however recent

calculations of observed recombination rates [34] suggest that the strong dependence of electron stabilised three body recombination upon electron density allows this to be a considerably more rapid process at the densities observed in the HyBrID than in the CVL, even at relatively high electron temperatures. Without an independent mechanism to measure or calculate the electron temperature accurately throughout the afterglow it will be very difficult to determine the relative importance of the two process until a full computer model is available. With the considerably greater complexity of such a model over one for a conventional CVL as a result of the many more processes available because of the addition of hydrogen and bromine species, it may be some time before one is available.

An extension of this work has been to attempt to isolate the relative importance of contributions from hydrogen and bromine by a separate study on the effects of adding hydrogen to the buffer gas of a conventional CVL. This has suggested a relatively minor role for hydrogen, being primarily concerned with the flattening of radial gas temperature profile and possibly enhanced rate of reduction of electron temperature in the early stages of the afterglow.

Lasers based on metal HyBrID technology are not yet available commercially. It seems likely that in time commercial exploitation of their attractive characteristics will occur, however the requirement for highly corrosive, toxic HBr gas is currently acting as something of a disincentive!

6. MVL applications

Metal vapour lasers as a class have found their way into a very wide range of applications. Of these by far the greatest number exploit the capabilities of the CVL, however a number of other members of the family do have their niches. In most applications it is the combination of high prf, short pulse length, relatively high average power and the visible wavelength that is currently uniquely available from this class of lasers.

6.1 MATERIALS PROCESSING

Currently one of the biggest development fields in MVL applications is that of materials processing. Most metals are highly reflecting at the relatively long, IR wavelengths of most current commercial materials processing lasers such as CO_2 and Nd:YAG. Once molten, however, they do absorb more efficiently. The mechanism of interaction for cutting, therefore, is thermal, followed by oxidation, or blowing away with an assist gas. This is inefficient and incurs a high heat loading for the job. This leaves a relatively wide heat affected zone around the cut edge and is not good enough for very high precision cutting. At the short wavelengths of excimer lasers metals are highly absorbing, giving a very shallow interaction depth (typically 80% of the incident energy absorbed in <0.5 μm). Excimers typically exhibit high pulse energy, low prf and poor beam quality. They are therefore good for shallow, large surface area work, especially

that employing a mask, where the short wavelength assist precision.

Wavelengths in the mid visible range, like that obtained from MVLs such as the CVL, can be seen to offer many advantages, coupled with the other characteristics of short, high peak power pulses. As the pulse lengths are much shorter than the thermal diffusion time of the substrate material, this is vaporized and ejected at extremely high velocities (eg 10^3 ms^{-1}) by the increase in pressure, in a process of direct ablation. This yields minimal heat damage, with a heat affected zone typically less than 1 μm thick. The visible wavelength allows a depth of around 10 μm to be removed per pulse, which, together with the high prf, allows for good cutting speed. High beam quality and a relatively short wavelength allows a small focused spot size allowing high precision micro-machining. Volumetric scaling and MOPA chains allow high power facilities.

Cutting rates of 1 m per min can be obtained in thin metal foils (<150 μm) with over 25 mm per min in 0.5 mm samples. Slots and holes can be produced with very high aspect ratio, and a wide variety of materials can currently be machined in this way, including metals, ceramics, plastics, refractories and composites with glass and carbon fibre.

To extend the high prf, high beam quality attributes into the UV, for even higher precision and stronger absorption especially in some material such as polymers, work has been concerned with frequency doubling CVL output, with very high efficiencies, up to 40%, achieved [35].

6.2 AVLIS

Much of the materials processing work, and in fact a great deal of the development work on CVL technology, has been derived from the world Atomic Vapour Laser Isotope Separation (AVLIS) programmes for the enrichment of nuclear fuel.

Tuned, narrow bandwidth laser light is used to photoionize a vapour phase material via a number of intermediate steps. The isotope shift in the wavelength of absorption lines allows the selective ionization of only one isotope which can then be collected on a charged plate. In order to maximise throughput it is necessary that the pulsed laser light operate at high prf to match to the sonic flow rates of vapour. High power dye lasers pumped by CVL MOPA chains are the technology currently employed around the world. Such chains currently yield many hundreds of watts, to kilowatts of average power each, typically running 24 hours a day, with a planned programme of maintenance with additional, spare lasers in the maintenance bay for immediate replacement of devices in the main chains, thus allowing extremely high availability of power.

6.3 HIGH SPEED PHOTOGRAPHY

Currently a large market for low power CVLs is that of use as a high speed stroboscopic light source for photography. The short pulse length, high prf visible light source allows very high speed action and processes to be stopped with minimal blurring,

even at sonic velocities, with potentially multi frame sequential photographs. Ancillary advantages include minimised sample heating by a low duty cycle and minimal radiation lying outside the visible band, and the flexibility of the CVL in responding to external trigger pulses. With all the radiation lying within a very narrow bandwidth it is possible to take pictures in high levels of ambient lighting by the appropriate use of filters and laser light can be easily coupled into fibre optics for convenient delivery to inaccessible locations.

As a direct result of the relatively high efficiency of CVLs, small, compact air cooled devices can be built requiring only a single 13 A, single phase power socket to operate. CVL laser strobes have been used in fluid flow analysis, textile spinning analysis (monitoring the behaviour of 10 μm threads moving at extremely high speeds) and ballistics (it is relatively easy to take a sequence of photographs of a bullet in flight at sonic velocity).

6.4 ADAPTIVE OPTICS

Almost all large astronomical telescopes currently being constructed today have been designed to incorporate an adaptive optics (AO) capability. If a telescope on earth is used to observe an object then the image it obtains is degraded by the effect of turbulence in the atmosphere. For telescopes of diameter greater than a few inches this determines the limiting resolution, rather than the diffraction limit of the telescope aperture. As the degradation to the incoming wavefront is one of phase rather than amplitude, as a result of variations of refractive index within the atmosphere, this degradation can be corrected by use of an adaptive element which can introduce relative phase retardations or advancements to different regions of the wavefront. This can be done using a deformable mirror, or a liquid crystal screen, however a reference wavefront is required to allow the extent of perturbation to be measured. A very bright natural star can be used, however this only allows observation in close proximity to that star. The alternative is to make use of the back scatter from a laser beam which then can be directed in any arbitrary direction. This is called a laser guide star (LGS) or laser beacon.

There are two ways in which CVLs can be used in this application. In first generation LGS systems the Rayleigh scattering of the beam from air molecules at altitudes up to around 25 km was used, in combination with range gating in the time domain, to generate the laser beacon. Recent research in this field has centred around the construction of tunable lasers to generate resonance scattering from the natural sodium layer at 90 km, and CVLs represent one potential pump technology for dye lasers, currently under investigation [36].

6.5 PHOTODYNAMIC THERAPY

Although MVLs are not appropriate for use in surgery directly for cutting or cautery (although the CVL yellow line is used in dermatology), they find there way into hospitals in the field of photodynamic therapy (PDT) in oncology. In order to minimise

the undesirable side effects of chemotherapy in the treatment of cancers it is desirable to be able to administer the cytotoxic agent in an inactive form, allow it to be concentrated in the tumour(s) before being activated at will. This is essentially the principal behind PDT in which the inactive therapeutic agent, such as an haematoporphyrin derivative (HPD) is administered and allowed to permeate the body for a few days, during which it is selectively cleared out of healthy tissues, whilst being accumulated in tumour cells. This must then be photo activated using a laser. Red is the ideal colour, and currently both gold vapour, and CVL pumped dye lasers are used to generate this. Use of fibre optics facilitates delivery of light to inaccessible locations and can aid even illumination.

The use of a pulsed pump source allows a very robust, simple dye laser to be built (if the output is not intrinsically red) in comparison with a CW dye laser system. Again a compact, air cooled, single phase laser provides a suitable source for use in a non-laboratory environment.

6.6 OTHER APPLICATIONS

Resonance Ionization Mass Spectrometry (RIMS) works in a similar way to AVLIS to use a number of narrow bandwidth, tuned beams to provide highly specific ionization of a species. In combination with a time of flight mass spectrometer this can give extremely high selectivity, of the order of 1 part in 10^{12}.

Again in combination with a dye laser the high prf of the CVL allows very high rates of analysis in OH radical detection for atmosphere analysis.

In entertainment MVLs, in particular CVLs, are used to provide light shows, both directly and in combination with dye lasers, to provide a wide range of colours, as for example in the recent Pink Floyd tour. They can be used in high brightness, high definition, large screen projection television and public address, where the ability to synchronise with TV raster scan rates (requiring 15.6 kHz) is vital. Currently this is practically restricted to monochrome. however the combination of gold (red), copper (green) and another to yield the blue is likely to give full colour performance in the relatively near future.

The high gain of the MVL, particularly the CVL, leads to its use as an optical brightness amplifier in such applications as laser projection microscopy. The combination of high magnification optics with a CVL gain tube (without a cavity) allows high optical magnification to be realized without requiring unacceptably high levels of illumination upon the subject. Magnification of several thousand can be realized, with the image projected upon a screen. In a modification of this technique a small feedback element in the image plane can be used to provide high precision laser damage in the object plane. Either a movable small mirror, or a combination of a mirror and mask can be used in this way to allow modification or trimming of microchips or other electronic components, or marking of very small objects.

7. Conclusions

The last 30 years has not only seen the increasing use of MVLs in laboratories, but also emerge from the laboratory into the marketplace in a wide variety of applications. The advances in understanding, and the consequent improvements in specific output power, efficiency and beam quality have led to their increased deployment in laboratory and research environments, however it is the increased convenience, reliability and user friendliness that has principally led to their increased acceptance in the wider community in the prevalence in which we see them today.

High prf, frequency doubled solid state lasers, such as Nd:YAG, are currently encroaching on the ground traditionally held by CVLs, particularly in the low to medium power range, but are still unable to match them in a number of aspects. CW pumped Q-switched Nd:YAG lasers are not yet available commercially that can combine high prf with the short pulse lengths needed for high efficiency dye (and Ti:Sapphire) pumping. Current laser diode pumped devices, too, are unable to generate more than relatively low power with an acceptable level of reliability. In addition, the thermal problems of thermal lensing, thermal birefringence and heat management, as well as the problems of frequency doubling to reach visible wavelengths, make the output stability of current high power solid state devices problematical and the beam quality poor.

Where high average power visible laser light is required at high prf, and with good beam quality, therefore, MVLs, and in particular CVLs, represent a unique solution, offering a desirable combination of attributes. It many lower power applications, too, MVLs still represent a relatively low cost, reliable, convenient source of visible laser light.

8. References

1. Walter, W.T., Piltch, M., Solimene, N. and Gould, G. (1966) Pulsed-laser action in atomic copper vapour, *Bull. Am. Phys. Soc.* **11** 113
2. Fowles, G.R. and Silfvast, W.T., (1965) High-gain laser transition in lead vapor, *Appl. Phys. Lett.* **6** (12) 236-237
3. Piltch, M., Walter, W.T., Solimene, N., Gould, G. and Bennett, W.T. Jr. (1965) Pulsed laser transitions in manganese vapor, *Appl. Phys, Lett.* **7** (11) 309-310
4. Piper, J.A., (1975) A copper iodide laser excited by transverse discharge, *Opt. Commun.* **14** (3) 296-299
5. Petr, R.A., Zumdieck, J.F., Dembski, J., Smilanski, I., Ewing, J.J. and Centre R.E., (1983) Magnetic pulse-compression for copper vapor lasers, *4th IEEE Pulsed Power Conf.* 236-241
6. Nehmadi, M., Kramer, Z., Ifrah, Y. and Miron, E., (1989) Magnetic pulse compression for a copper vapour laser, *J. Phys. D* **22** 29-34
7. Vuchkov, N.K., Astadjov, D.N. and Sabotinov, D.N., (1988) High-efficiency CuBr laser with interacting peaking circuits, *Opt. and Quantum Electron.* **20** 433-438
8. Lieu, C.S., Sucov, E.W. and Weaver, L.A., (1973) Copper superradient emission from pulsed discharges in copper iodide vapor, *Appl. Phys. Lett.* **23** (2) 92-93
9. Chen, C.L., Nerheim, N.M. and Russel, G.R., (1973) Double-discharge copper vapor laser with copper chloride as a lasant, *Appl. Phys. Lett.* **23** (9) 514-515
10. Akirtava, O.S., Dzhikiya, V.L. and Oleinik, Y.M. (1975) Laser utilizing Cu I transitions in copper halide vapors, *Sov. J. Quantum Electron.* **5** (8) 1001-1002
11. Andrews, A.J., Webb, C.E., Tobin, R.C. and Denning, R.G., (1977) A copper vapour laser

operating at room temperature, *Opt. Commun.* **22** (3) 272-274
12. Warner, B.E. and Weber, P.D., (1993) High-power copper vapor lasers and their application to precision drilling and cutting, *LEOS '93 Conference Proceedings* 782-783
13. Chang, J.J., Alger, T.W., Anderson, A.T. and Arnold, P.A., (1994) New hollow-cathode electrode for high power copper lasers, *CLEO '94 Technical Digest* 402
14. Carman, R.J., (1995) Modelling of the intracavity optical fields in a copper vapour laser, *Opt. Commun.* **119** 415-423
15. Zemskov, K.I., Isaev, A.A., Kazaryan, M.A., Petrash, G.G. and Rautian, S.G., (1974) Use of unstable resonators in achieving the diffraction divergence of the radiation from high gain pulsed gas lasers, *Sov. J. Quantum Electron.* **4** (4) 474-477
16. Naylor, G.A., Kearsley, A.J. and Shaw, H., (1986) High-power low-divergence injection-locked copper vapor laser, *CLEO '86 Technical Digest* 160-161
17. Warner, B.E., (1986) Injection locking of a copper laser oscillator, *CLEO '86 Technical Digest* 160-161
18. Chang, J.J., (1995) Copper-laser oscillator with adjoint-coupled self-filtering injection, *Opt. Lett.* **20** (6) 575-577
19. Anderson, R.S., Bricks, B.G., Springer, L.W. and Karras, T.W., (1975) A discharge heated copper vapor master oscillator power amplifier, *IEEE/OSA CLEA '75 Digest of Technical Papers* 56-57
20. Hogan, G.P., (1993) A study of the kinetics of copper vapour lasers, *D.Phil Thesis, Oxford University*
21. Carman, R.J., Brown, D.J.W. and Piper, J.A., (1994) A self-consistent model for the discharge kinetics in a high-repetition-rate copper-vapor laser, *J. Quantum Electron.* **30** (8) 1876-1895
22. Rozhdestvenskii, D.S., (1912) Anomale dispersion im Natriumdampf, *Ann. Physik.* **39** 307-345
23. Marlow, W.C., (1967) Hakenmethode, *Appl. Optics* **6** (10) 1715-1724
24. Blau, P., Smilanski, I. and Rosenwaks, S., (1992) Simultaneous time-averaged measurements of gas temperature and electron density in a copper-vapor laser using hydrogen emission spectroscopy, *J. Appl. Phys.* **72** (3) 849-854
25. Batenin, V.M., Burmakin, V.A., Vokhmin, P.A., Evtyunin, A.I., Klimovskii, I.I., Lesnoi, M.A. and Selezneva, L.A., (1977) Time dependence of the electron density in a copper vapor laser, *Sov. J. Quantum Electron.* **7** (7) 891-895
26. Hogan, G.P. and Webb, C.E., (1993) Radially and time resolved measurements of electron density in a copper vapour laser, *LEOS '93 Conference Proceedings* 738-739
27. Livingstone, E.S. and Maitland, A., (1989) A low temperature, segmented metal, copper vapour laser, *J. Phys. E* **22** 63
28. Jones, D.R., Maitland, A. and Little, C.E., (1994) A high-efficiency 200 W average power copper HyBrID laser, *J. Quantum Electron.* **30** (10) 2385-2390
29. Sabotinov, N.V., Jones, D.R., Maitland, A. and Little, C.E., (1995) A copper HyBrID laser with 2 W/cm^3 specific average output power, *J. Quantum Electron.* **31** 747-753
30. Hogan, G.P. and Webb, C.E., (1995) Experimental studies of CVL kinetics, *NATO ARW, Pulsed Metal Vapour Lasers Conference Proceedings* (in press)
31. Hogan, G.P. and Webb, C.E., (1994) Pre-ionization and discharge breakdown in the copper vapour laser: the phantom current, *Opt. Commun.* **117** 570-579
32. Jones, D.R., Halliwell, S.N. and Little, C.E., (1994) Influence of remanent electron density on the performance of copper HyBrID lasers, *Opt. Commun.* **111** 394-402
33. Jones, D.R. and Little, C.E., (1995) Kinetics of copper HyBrID lasers, *International Conference "Pulsed Lasers on Atomic and Molecular Transitions" (PLAMT '95)*
34. Whyte, C.E., (1995) Private communication
35. Coutts, D.W. and Piper, J.A., (1992) One watt average power by second harmonic and sum frequency generation from a single medium scale copper vapor laser, *J. Quantum Electron.* **28** (8) 1761-1764
36. Hogan, G.P. and Webb, C.E., (1995) Proposed design for a scalable dye laser for use in sodium laser guide star generation, *OSA/ESO Topical Meeting on Adaptive Optics Conference Proceedings* (in press)

Design and Analysis of a Deep UV Laser based on Ce^{3+}: $LiSrAlF_6$

T. R. Nelson, F. G. Omenetto*, W. Andreas Schroeder,
J. W. Longworth**, and C. K. Rhodes
Laboratory for Atomic, Molecular and Radiation Physics,
Department of Physics, University of Illinois at Chicago,
845 W. Taylor St., Chicago, Il. 60607

Abstract

Ce^{3+}:$LiSrAlF_6$ (Ce:LiSAF) has been demonstrated to amplify light between the wavelengths of 285 and 297 nm by several groups. A source in this region of the ultraviolet is attractive for biophysics, physical chemistry, and ultra-strong-field physics, particularly if femtosecond operation can be achieved. Motivated by the successful operation of Kerr-Lens mode-locked (KLM) Cr^{3+}:LiSAF oscillators in the red and near infrared, we have undertaken the analysis and design of a KLM oscillator and amplifier system based on Ce:LiSAF. Since Ce:LiSAF has an absorption band centered near 260 nm, a limited selection of pump sources is available. A comparison of those sources is presented. The two-photon absorption band edge of the colquiriite host can be estimated to be in the region of 105 - 130 nm, a range based on the absorption properties of its constituents. This suggests minimal two-photon absorption of the UV radiation by the host. As a result, the second order index of refraction (n_2) should be positive so that conventional KLM operation of a laser cavity will be possible. In addition, since the bandwidth is capable of supporting sub-100 femtosecond pulses, the material is a promising gain medium for amplification to high peak powers. Accordingly, an outline of the development of a terawatt class 290 nm, sub 100 fs laser system is given.

1. Introduction

Recent developments in rare-earth doped colquiriites have yielded significant advances in UV laser generation and amplification. Interesting solid-state media for laser action in the ultraviolet utilize a $d \rightarrow f$ transition of the active rare-earth dopants inside wide bandgap dielectric hosts [1]. Until now, the laser performance of these materials has been inhibited by solarization and excited state absorption (ESA). However, these limitations do not seem to apply to Ce^{3+}-doped $LiSrAlF_6$ (Ce:LiSAF). Laser action in this material based on a $5d^1 \rightarrow 4f^1$ transition producing amplification ranging from 285 - 297 nm has been demonstrated, with the peak performance occurring at 290 nm

R. Kossowsky et al. (eds.), High Power Lasers – Science and Engineering, 177–184.
© 1996 *Kluwer Academic Publishers. Printed in the Netherlands.*

[2,10]. For this material, although excited state absorption exists for both polarizations, the ESA cross section for π-polarization is roughly a factor of 3 lower than the stimulated emission cross section for the laser transition (see Table 1). Given that the stimulated emission bandwidth of this material is theoretically capable of supporting optical pulses with durations as short as 10 femtoseconds (Fig. 1), the material appears to be extremely promising as the basis for an ultrafast, high power UV laser/amplifier system. This work is devoted to a discussion of the design for such a system.

Polarization	Emission Cross-Section (x 10^{-18} cm^2)	ESA Cross-Section (x 10^{-18} cm^2)	Gain Cross- Section (x 10^{-18} cm^2) (σ_{EM} - σ_{ESA})
π-pol	9.5	2.7	6.8
σ-pol	6.1	4.6	1.5

Table 1. Ce:LiSAF Emission Properties.

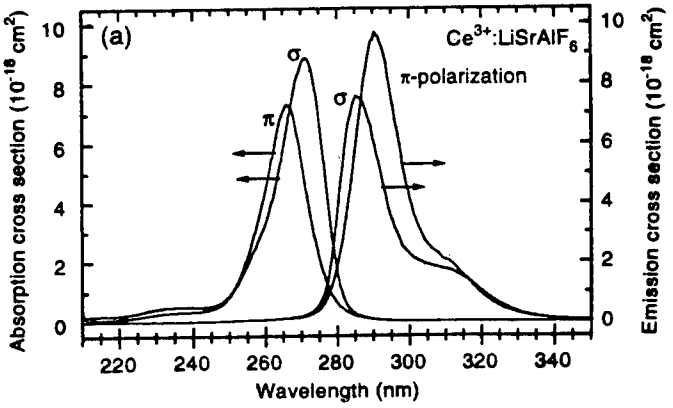


Figure 1. Absorption and Emission Spectra for Ce:LiSAF.
(Figure adapted from Ref. [2] and used with permission.)

2. Short Pulse Generation

The front end of the laser system would necessarily be a laser oscillator capable of producing ultrashort pulses. The mode-locking of an oscillator to produce such short optical pulses can be accomplished by any number of well established techniques. The most attractive of these methods for solid state gain media like Ce:LiSAF is Kerr-lens mode-locking (KLM), a technique which is a widely used [3] with infrared ultrafast gain media [e.g. Ti^{3+}:Al_2O_3].

With Kerr-lens mode-locking, the configuration of the oscillator takes advantage of the nonlinear index of refraction in the gain medium,

$$n = n_0 + n_2 I \tag{1}$$

in which n is the total index of refraction, n_0 is the linear refractive index, n_2 is the second order nonlinear index of refraction, and I is the intensity of the light in the medium. This leads to a critical power for self-focusing which is given by

$$P_c = \frac{a\lambda^2}{8\pi n_0 n_2} \tag{2}$$

where a is an empirical constant and λ is the wavelength of the light. In an oscillator cavity at sufficiently high intracavity powers ($P \gtrsim 0.2P_c$), the beam experiences self-focusing in the gain medium. This produces a change in the waist of the oscillating mode that differs from that of the normal cavity mode. The cavity can then be configured in such a way that a high power beam (pulsed) experiences a significantly lower loss than a low power (cw) beam. The oscillator then favors mode-locked performance.

However, in order to apply conventional KLM methods to a specific laser oscillator, there are strict requirements that must be met by the gain medium. First, the material must have a positive second order index of refraction (n_2) at the oscillating wavelength. Second, the material must have negligible nonlinear absorption (specifically two-photon absorption) at the oscillating wavelength, so that there are no significant nonlinear losses introduced under mode-locked operation. These two equally important criteria are, in fact, related to the position of the two-photon absorption edge (band gap) of the material [4].

Information about the band gap for LiSAF may be obtained by examining the absorption properties of the various compounds fluorine makes with the other elements in the host. It should be noted that the influence of the dopant on the two-photon absorption edge is negligible. Upon examination, we see that the relevant fluorine compounds to consider are LiF, SrF_2, and AlF_3, materials which all have two-photon absorption edges falling in the region from 105 to 130 nm. Based on this, a conservative estimate of the two-photon absorption edge for LiSAF is approximately 125 nm, or 9.9 eV. Since the energy of the oscillating photon is 4.3 eV, we see that the energy of two photons fails to bridge the gap and the conclusion that there will be no significant two-photon absorption follows. Furthermore, from our estimate of the band gap, we can obtain an estimate of n_2 for LiSAF at 290 nm by using the theoretical method developed by M. Sheik-Bahae et. al. [4]. This yields a value of n_2 of $\sim 1.4 \times 10^{-20}$ m^2/W (positive), which is of the same order of magnitude as that of Ti:Sapphire at 800 nm ($\sim 3 \times 10^{-20}$ m^2/W) [5]. Therefore, on the basis of the successful KLM operation of Ti:Sapphire, Ce:LiSAF seems to be a very promising candidate for the construction of a KLM UV oscillator.

2.1. PUMP SOURCES

As shown in Figure 1, Ce:LiSAF has an absorption peak near 260 nm, a property that limits the alternatives for pump sources. The short upper state lifetime (28 ns) of the material eliminates the possibility of flashlamp pumping. The two sources which seem to be most promising as candidates for pumping the oscillator are examined in Table 2. The first of these is a frequency-doubled, single-line Ar-ion laser operating at 514 nm. In order to obtain enough power at 257 nm, a fairly high doubling efficiency is required. This may be achieved in one of two ways: (*i.*) doubling the radiation inside the laser cavity, where the power is significantly higher than externally, or (*ii.*) doubling the radiation in an external cavity that is doubly resonant at 514 nm and 257 nm. The latter method would be preferable, since there are several adjustable parameters in the design of the resonant cavity which would allow control over the doubling efficiency and output. This design also allows the use of a standard commercially available Ar-ion laser, without the need to modify the laser cavity.

The other possibility for the oscillator pump source would be the frequency-quadrupled output of a cw mode-locked Nd:YLF laser system, which delivers the 263 nm output in a picosecond pulse train. This source embodies two significant advantages. First, 263 nm is closer to the absorption peak (266 nm) than 257 nm. This would yield a higher efficiency for pumping. Second, the mode-locked output could be used to synchronously pump the Ce:LiSAF oscillator, which would help to initiate the KLM operation. This technique has already been applied in Ti:Sapphire oscillators [6], and is expected to be more efficient in Ce:LiSAF due to this materials short upper state lifetime. It should be noted, however, that although the beam pointing stability of the frequency-quadrupled Nd:YLF is not as good as that of the frequency-doubled output of the Ar-ion laser, it can easily be stabilized with a PZT feedback loop.

With these considerations in mind, the design of the cavity for KLM operation of Ce:LiSAF can be based on the conventional z-fold dispersion-compensated configuration commonly employed in the infrared (i.e. Ti:Sapphire oscillators). For Ce:LiSAF, second order dispersion compensation can be achieved by using fused silica, as opposed to dense flint glass prisms, so that detrimental UV absorption can be avoided. By compensating the dispersion to second order, the production of optical pulses ranging between 50 and 100 femtoseconds in duration is a realistic expectation. The generation of 10 fs pulses is theoretically possible, based on the 12 nm bandwidth of Ce:LiSAF, but would most likely require third order dispersion compensation.

Characteristic	Ar^+	Nd:YLF
Wavelength	257 nm	263 nm
Power	~ 2 W	~ 2 W
Power Stability	good	two doubling processes...
Pulse Duration	cw	~ 50 ps
Beam Pointing	good	good (better than Nd:YAG)

Table 2. Comparison of Pump Sources.

2.2. ESTIMATE OF POWER OUTPUT

Using the expected pulse duration, it is possible to estimate the output power of the oscillator. This can be achieved by comparing the parameters we have estimated for Ce:LiSAF with those parameters for a canonical Ti:Sapphire laser. The critical power (P_c) for Ti:Sapphire is approximately 2 MW [7]. However, we see from Eq. (2) that P_c is proportional to λ^2/n_2. Given that our estimate for n_2 for LiSAF differs from that of Ti:Sapphire by a factor of 2, and the wavelength difference introduces a factor of approximately 9, we estimate that P_c for LiSAF at 290 nm should be roughly 0.4 MW. Since a typical KLM oscillator requires a minimum intracavity power at least 20% of the critical power to operate, the minimum intracavity power required for KLM operation using Ce:LiSAF can be estimated to be ~ 90 kW. If we then assume a 100 fs pulse duration (a conservative estimate), this yields ~ 9 nJ/pulse inside the laser cavity. If a 5% output coupler is employed and a repetition rate of 76 MHz is assumed (2 meter laser cavity), this yields an average power output of ~30 mW for KLM operation with ~ 0.5 nJ/pulse.

3. Amplification

Once these pulses have been generated, amplification would be possible by the application of standard Chirped Pulse Amplification (CPA) techniques [8] in order to avoid nonlinear effects and possible damage in the amplification process. It is important to note that all the optics and gratings necessary to accommodate the ultraviolet radiation are presently commercially available.

3.1. REGENERATIVE AMPLIFICATION

The first stage amplifier in our scheme is a regenerative amplifier. There are two important considerations in this design. First, the fact that the upper state lifetime is only 28 ns enforces the restriction that the regenerative amplifier cavity must be kept short in order to allow a significant number of round trips during that lifetime. For a

cavity length of 0.5 meters, a maximum of 8 round trips would be theoretically possible. This equates to 16 trips through the gain medium. A single pass gain of 2 would prove sufficient to yield several microjoules of energy per pulse. As of this point, the beam could be recompressed for UV pulse powers on the order of $\sim$ 0.1 GW. Due to the upper state lifetime, a relatively long pulse would be required to pump this amplifier. A frequency-quadrupled Q-switched Nd:YAG laser would provide 266 nm radiation in a several-nanosecond pulse. These lasers are commercially available with UV energies of up to 1 mJ at kHz repetition rates. This suggests that the amplifier could be run at 1 kHz. The second consideration is the fact that the radiation to be amplified is in the ultraviolet region of the spectrum. A Pockels cell is required to allow switching of the pulse into and out of the amplifier cavity. These devices normally require high voltage and would need extremely fast electronics to be effective as optical switches for such a short cavity. However, the voltage required by the Pockels cell is proportional to the optical wavelength. Therefore, in our case, considerably less voltage would be required, which would allow for faster rise times and lessen the need for special electronics. In addition, a Faraday rotator which could transmit the UV, would be necessary to isolate effectively the amplifier from the rest of the system. Such a device is currently under independent development.

3.2 MULTIPASS AMPLIFIERS

The last stage of this amplifier system would be comprised of one or more Ce:LiSAF crystals configured as simple multipass amplifiers. In order to extract sufficient pump energy from a frequency-quadrupled Nd:YAG source, a lower repetition rate would be required. However, a repetition rate of 10 Hz appears possible. The only limitations to amplification would appear to be those imposed by the Ce:LiSAF gain medium itself, i.e. the saturation fluence of the material and the thermal effects. The gain cross sections for Ce:LiSAF [2] suggest a maximum saturation fluence of $\sim$220 mJ/cm^2. This, along with possible thermal limits, establishes the requirement of a large beam aperture in this last stage. Crystals of appropriate sizes (2 cm diameter) to accommodate this requirement are available. Given this, an overall energy output of 100 mJ after compression seems to be a realistic goal. This would yield roughly 1 TW of power in a 100 fs optical pulse at 290 nm.

4. Conclusions

In conclusion, it should be pointed out that the pulses generated by this laser system would have a myriad of applications. The mode-locked Ce:LiSAF oscillator could produce coherent, tunable UV pulses that are ideal for fluorescence spectroscopy of proteins and nucleic acids. The system as a whole provides a high powered UV source which could be used for many other applications such as specialized forms of lithography or microfabrication. Applications to photocatalysis-related research and the manufacture of pharmaceuticals are well suited to ultrafast optical pulses in the ultraviolet. Scientific uses would include physical and biological applications such as the generation of X-rays from atomic rare gas clusters [9]. Such X-rays could be used

for a number of applications including ultrafast time-resolved X-ray diffraction. In short, the output of every stage of this system is readily applicable to numerous areas of scientific activity.

5. Acknowledgements

Support for this research was provided under contracts with SDI/NRL (N00014-93-K-2004), ARO (DAAH-04-94-G-0089) and the University of California/Lawrence Livermore National Laboratory (W-7405-Eng-48). The authors wish to acknowledge useful conversations with C. D. Marshall (Lawrence Livermore National Laboratory) and G. J. Quarles (Lightning Optical Corporation).

* F. G. Omenetto is visiting from the Dept. of Electrical Engineering, University of Pavia, Italy.
** J. W. Longworth is a faculty member of the Dept. of Physics, Illinois Institute of Technology, Chicago Il., 60616.

6. References

1. Yang, K. H. and Deluca, J. A. (1977) UV Fluorescence of Cerium doped Lutetium and Lanthanum trifluorides, potential tunable coherent sources for 2710 to 3220 Å, *Appl. Phys. Lett* **31**, 594-596.
2. Marshall, C. D., Speth, J. A., Payne, S. A., Krupke, W. F., Quarles, G. J., Castillo, V., and Chai, B. H. T. (1994) Ultraviolet laser emission properties of Ce^{3+} - doped $LiSrAlF_6$ and $LiCaAlF_6$., *J. Opt. Soc. Am. B* **11**, 2054-2065.
3. Spence, D. E., Kean, P. N., and Sibbett, W. (1991) 60-fs Pulse generation from a self-mode-locked Ti:Sapphire laser., *Opt. Lett.* **16**, 42-44.
4. Sheik-Bahae, M., Hutchings, D. C., Hagan, David J., and Van Stryland, E. (1991) Dispersion of bound electronic nonlinear refraction in solids., *IEEE J. Quant. Elect.* **QE-27**, 1296-1309.
5. Salin, F., Squier, J., and Piche', M. (1991) Mode locking of Ti:Al_2O_3 lasers and self-focusing: a Gaussian approximation., *Opt. Lett.* **16** 1674-1676.
6. Spielmann, Ch., Krausz, F., Brabec, T., Wintner, E., and Schmidt, A. J. (1991) Femtosecond pulse generation from a snchronously pumped Ti:Sapphire laser., *Opt. Lett.* **16**, 1180-1182.
7. Brabec, T., Curley, P. F., Spielmann, Ch., Wintner, E., and Schmidt, A. J. (1993) Hard aperture Kerr-lens mode-locking., *J. Opt. Soc. Am. B* **10**, 1029-1034.
8. Maine, P., Strickland, D., Bado, P., Pessot, M., and Mourou, G. (1988) Generation of ultrahigh peak power by chirped pulse amplification., *IEEE J. Quant. Elect.* **QE-24**, 398-403.
9. McPherson, A., Thompson, B. D., Borisov, A. B., Boyer, K., and Rhodes,

C. K. (1994) Multiphoton-induced X-ray emission at 4-5 keV from Xe atoms with multiple core vacancies., *Nature* **370**, 631-634.

10. Rambaldi, P., Douard, M., and Wolf, J. P. (1995), New UV tunable solid state lasers for Lidar applications, *Appl. Phys. B* **61**, 117-120.

SIMULTANEOUS EMISSION IN UV AND IR REGION IN A SLIDING DISCHARGE EXCITED LASER

K.A. GROZDANOV AND P.A. ATANASOV

Institute of Electronics, Bulgarian Academy of Sciences
72 Tzarigradsko Shose, Sofia 1784, Bulgaria

Abstract

Simultaneous laser action in UV (337.1 nm and 357.7 nm) and IR (2.6 - 3.1 μm) spectral ranges are obtained in SF_6/N_2/propane-butane mixture directly excited by a sliding discharge. Output energies of 1.1 mJ in the ultraviolet and 12 mJ in the infrared are obtained, respectively. Some performance parameters are presented.

1. Introduction.

Discharge sliding along the surface of a dielectric has many applications in TE gas lasers as preionizer, plasma electrode, and direct excitation source [1 - 4]. The application of the sliding discharge as a direct excitation source is limited by the small transverse to the discharge size of the excited region (less than 1 mm [2]). However, this property of the discharge can be an advantage in laser with high gain of the laser medium (such as N_2 HF lasers, etc.) resulting in low divergence in this direction [2]. The low divergence and the small size would also provide narrow bandwidth in the tuneable HF lasers. Another advantage of the sliding discharge is its ability to work at higher repetition rates than these for the volumetric discharge [2]. A benefit of the sliding discharge as direct excitation source is also the simplicity of obtaining homogeneous discharge at high pressure or in electronegative gas mixtures (such as SF_6\propane-butane mixture for the HF laser), avoiding in this way the usage of preionization techniques [5 - 7], resistive electrodes[8], etc.

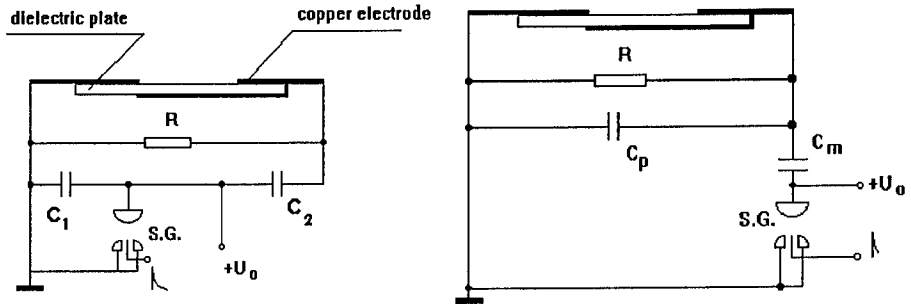
In our previous investigations [3,4], we demonstrated that it is possible to add large amount of SF_6 to the nitrogen in N_2 laser exited by sliding discharge (up to 3:1 SF_6:N_2) associated with a significant increase (up to 4 times) of the output energy. Since the pressure of the propane-butane in our preliminary experiments of HF laser excited by sliding discharge was small (about 5 mbar propane-butane compared to more than 60 mbar SF_6) we supposed that its addition to the N_2/SF_6 mixture would not have significant influence on the UV generation. However the presence of nitrogen in the HF laser medium would have greater effect on the IR generation.

R. Kossowsky et al. (eds.), High Power Lasers – Science and Engineering, 185–190.
© 1996 *Kluwer Academic Publishers. Printed in the Netherlands.*

In this paper we report, for the first time to the best of our knowledge, on a study of simple laser with sliding discharge used simultaneously as direct excitation source for N_2 molecule and as an initiating source in HF chemical laser. Simultaneous lasing in the UV and IR spectral region is obtained and some of the parameters of the laser are investigated.

2. Experimental set-up.

The cross section of the laser channel and the discharge circuits (doubling circuit and charge transfer circuit) are presented on Figure 1 (a,b) respectively. The value of the capacitors C_1 and C_2 in Figure 1 (a) is 9 nF. The values of the main capacitor C_m and the peak capacitor C_p in Figure 1 (b) are 18 nF and 6 nF, respectively. The charging voltage U_0 was 30 kV. The channel is made from 1.5 mm thick Fibreglass textolite plate ($\varepsilon = 5$) with copper electrodes 2.6 cm apart forming an active area of (2.6x26) cm^2. The channel is placed in vacuum tight Plexiglas chamber having two CaF_2 windows at Brewster angle for $\lambda = 3$ μm. The optical cavity has 55 cm length and it consists of flat



(a) (b)

Figure 1. Cross section of the laser channel and electrical excitation circuits.
(a) - doubling circuit; (b) charge transfer circuit.

silver coated rear mirror and BaF_2 output coupler.

The output energy is monitored by means of PRJ-D (GenTec) energy meter with ED-200 and ED-100 pyroelectric probes. The UV laser pulses are observed with a fast avalanche photodiode (LFD-2A/USSR) and Tektronics 406 storage oscilloscope. The voltage pulses are observed by means of H.V. 100 voltage probe (GenTec), and the current pulses are monitored by 10 mΩ shunt. The experiments are performed in a single pulse regime.

3. Results and discussion.

Figure 2 presents the dependence of the laser output energy in the IR and UV region as a function of the N_2 pressure (the SF_6 and propane-butane pressures are optimum for the IR output without nitrogen). The maximum output energy for the UV

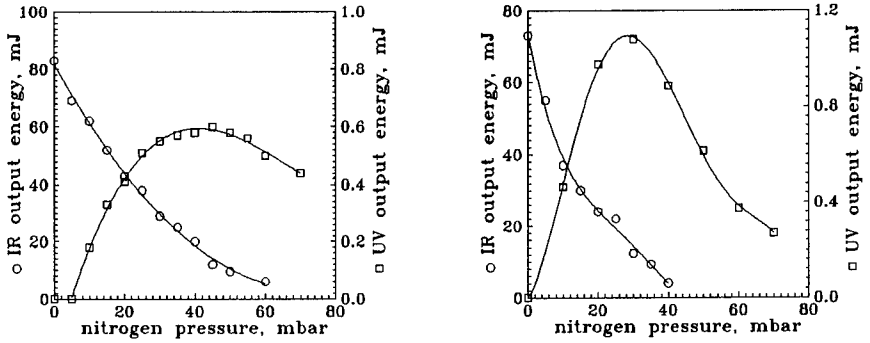


Figure 2. IR (o) and UV (□) output energy as a function of N_2 pressure.
(a) - doubling circuit, 100 mbar SF_6, 5 mbar propane-butane;
(b) -charge transfer circuit, 65 mbar SF_6, 5 mbar propane-butane.

radiation is 1,1 mJ in the case of charge transfer circuit, and 0.6 mJ for the doubling circuit. The IR pulse energy decreases with the increase of the N_2 pressure (from about 80 mJ without nitrogen to less than 20 mJ at optimum for the UV generation conditions). This behaviour is logical since the optimum average electron energy in the discharge for the HF laser is about 3.1 eV [9] (the dissociation energy for the SF_6 molecule) and the excitation energy of the $C^3\Pi_u$ state of the N_2 molecule is about 11 eV, i.e. the optimum discharge conditions for the N_2 generation are not optimum for the HF generation. Taking into account the current pulse shapes (Figure 3 (b,d)) and the

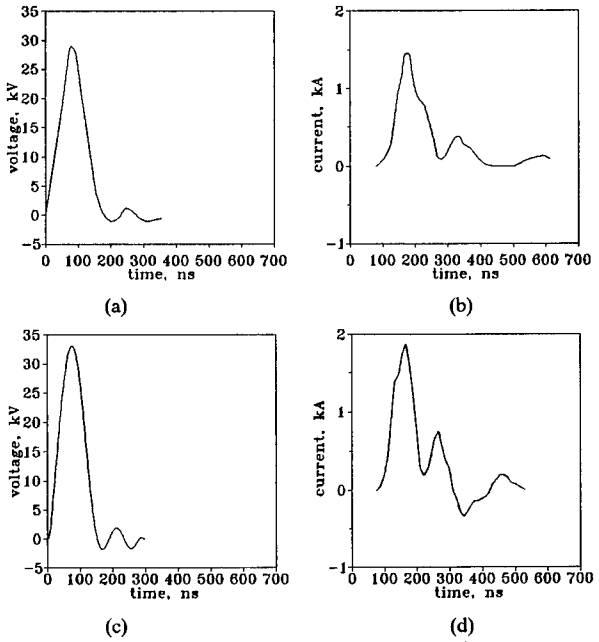


Figure 3. Voltage (a,c) and current (b,d) pulses.
doubling circuit, 100 mbar SF_6, 5 mbar propane-butane;
(a,b) - without nitrogen; (c,d) - 40 mbar nitrogen.

oscillations in the pulse of Figure 3 (d), we can also conclude that another purpose for the decrease of the IR output energy can be the presence of some mismatching between the discharge and the discharge circuit when N_2 is added. The last is result of the lower discharge resistance. Moreover, we would like to point out that the charge transfer circuit is more efficient for the UV generation. On the contrary the doubling circuit is more efficient for the IR generation. This is consistent with the fact that faster electrical circuits are needed for the N_2 laser generation.

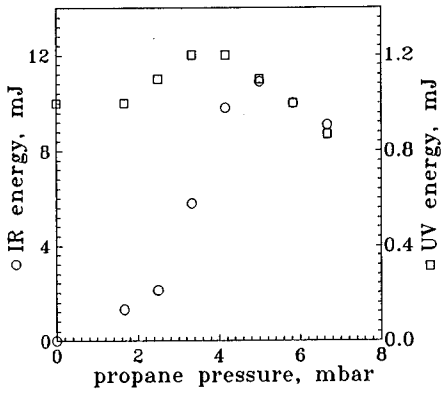


Figure 4. IR (o) and UV (□) output energy as a function of propane-butane pressure. charge transfer circuit, 65 mbar SF_6, 35 mbar N_2.

Figure 4 presents the dependence of the IR and UV pulse energy from the propane-butane pressure. It can be seen that the UV energy increases slightly when small amount of propane-butane is added. However the addition of propane-butane to pure nitrogen did not cause any positive effect on the laser generation. We consider that such behaviour is related to better uniformity of the discharge when propane-butane is added to the SF_6/N_2 mixture. Taking into account the UV laser pulses (Figure 5) we can see that addition of propane-butane causes a decrease of the pulse width (from 20 ns FWHM to 10 ns FWHM). Therefore the peak power increases more than twice for this case. This effect can not be explained only by the improved uniformity of the discharge.

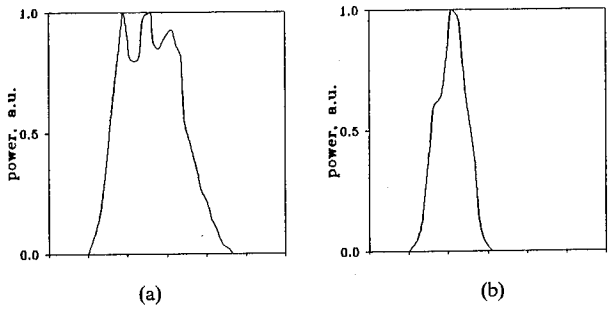


Figure 5. UV laser pulses.
charge transfer circuit, 65 mbar SF_6, 30 mbar N_2; time scale: 10 ns/div.
(a) - without propane - butane, (b) - 5 mbar propane - butane.

Taking into account the data in [6 - 9] we can estimate that the delay between the UV and IR generation would be in the range of 20 - 100 ns. More detailed analysis of the time behaviour of the laser pulses will be an object of future investigation.

Figure 6 presents the spectrum of the HF laser generation, without nitrogen. We used SPM-2 prism monochromator (Carl Zeiss Jena) with NaCl prism and ED-100 pyroelectric probe connected to the amplifier of the oscilloscope. However, the resolution of the apparatus is not sufficient to separate the different HF laser lines.

Nevertheless some information about the spectrum can be obtained. The wavelengths of the laser lines are between 2.6 and 3.1 μm and the strongest line is at 2.7 μm. The spectrum of the HF laser depends on the pressure and the discharge conditions, therefore the addition of N_2 will probably change its shape. In the UV laser spectrum

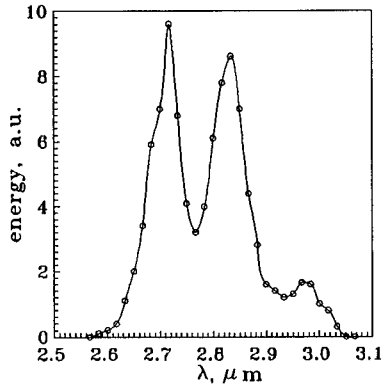


Figure 6. Spectrum of the HF laser generation.
doubling circuit, 100 mbar SF_6, 5 mbar propane-butane.

we observed generation at $\lambda = 357.7$ nm with more than an order of magnitude less intensity than the common 337.1 nm line.

4. Conclusion.

In conclusion, we obtained UV and IR laser generation in SF_6/N_2/propane-butane mixture, using sliding discharge simultaneously as direct excitation source for N_2 laser and as initiating source for HF chemical laser for the first time. The performance parameters of the laser are studied. This novel gas laser will be an object of future investigations and the main efforts will be concentrated on a study of its temporal, spectral and spatial characteristics as well as on the development of simultaneously tuneable gas laser in the UV and IR region.

Acknowledgement.

This work is partially supported by Contract No. F-434 with the Ministry of Science and Education, Bulgaria.

References:

1. Atanasov, P. and Serafetinides, A. (1989) TEA gas lasers excited by a sliding discharge along the surface of a dielectric, *Opt.Commun.* 72, 356 - 360.
2. Branzalov, P.P. (1989) *Sliding discharge in pulsed gas laser*, dissertation, Institute of General Physics, Russian Academy of Sciences, Moscow.
3. Tzolov, V.P., Grozdanov, K.A., and Atanasov P.A. (1994) Nitrogen laser employing twin sliding discharges, *Journal of Applied Physics* 75, 1210 - 1212.
4. Grozdanov, K.A. and Atanasov P.A. (1994) Investigation of a Nitrogen Laser Excited by Sliding Discharges, CTuK94, CLEO, Europe, Amsterdam, The Netherlands.
5. Wlodarczyk, G. (1978) A photo - preionized atmospheric pressure HF laser, *IEEE J. of Quantum Electr.* QE-14, 768 - 771.
6. Serafetinides, A.A., Rickwood, K.R., and Papadopoulos, A.D. (1991) Performance studies of a novel design atmospheric pressure pulsed HF/DF laser, *Appl.Phys.B* 52, 46 - 54.
7. Brink, D.J. and Hasson, V. (1980) Compact megawatt helium free TEA HF/DF laser *J. Phys E: Sci. Instrum.* 13, 553 - 556.
8. Gibson, A.F. Hall, T.A., and Hatch, C.B. (1977) Discharge stabilisation in HF lasers using resistive electrodes, *IEEE J. of Quantum Electr.* QE-13, 801 - 803.
9. Deka, B.K. and Dyer, P.E. (1978) Mode control and performance studies of a pulsed unstable resonator HF/DF laser, *IEEE J. of Quantum Electr.* QE-14, 661 - 673.

EXPERIMENTAL AND THEORETICAL RESULTS OF HIGH OPTICAL QUALITY EXCIMER LASER BEAMS

S. BOLLANTI, P. DI LAZZARO, F. FLORA, G. GIORDANO,
T. LETARDI, D. MURRA[a], C. PETRUCCI[b], G. SCHINA,
O. UTEZA[b], C.E. ZHENG[c]
ENEA, Dip. Innovazione, Settore Fisica Applicata,
Centro Ricerche Frascati,
C.P. 65, 00044 Frascati, Rome (Italy)
[a] *ENEA, Dip. Innovazione, Settore Fisica Applicata,*
Centro Ricerche Trisaia,
C.P. 1, 75025 Policoro (Italy)
[b] *ENEA Guest*
[c] *EL.EN. Firenze*

1. Introduction

High optical quality and high brightness excimer lasers beams are required in many applications. In the frame of the excimer lasers development program at the ENEA Frascati Centre, several x-ray preionised, discharge pumped XeCl laser systems have been realised [1,2]. In particular, two of them have been used to achieve a near diffraction-limited ultraviolet (λ=308 nm) laser beams.

The characteristics of these two lasers are quite different from each other: Hercules is a photo-triggered discharge pumped, large aperture (5x8x100 cm^3) system, with a high energy per pulse and a low repetition rate (<10 Hz) [3,4]. Ianus has a double discharge head (cell 1: 1.5x2x90 cm^3; cell 2: 2x3x90 cm^3), pumped by a spiker-sustainer circuit, with a lower energy per pulse and a higher repetition rate (<100 Hz) [5].

In order to generate high optical quality beams, both of them have been equipped with an unstable resonator (UR). A confocal positive branch UR (CPBUR) was chosen for Hercules, in order to fill all the large section active medium, and a negative branch, generalised self-filtering UR (GSFUR) [6] was mounted on Ianus cell 1, the choice being suggested by the smaller active medium size and shorter gain time duration. The small fundamental mode volume of the GSFUR lead to a low extraction efficiency, but the beam energy was recovered through a single pass amplification in cell 2.

The beam quality was assessed through near- and far-field time-integrated intensity distribution measurements. From now on, we will omit the attribute "time-integrated", to be more fluent in writing. The experimental results were analysed following a new suggestion for the definition of the "times diffraction limit" (TDL) of a laser beam [7].

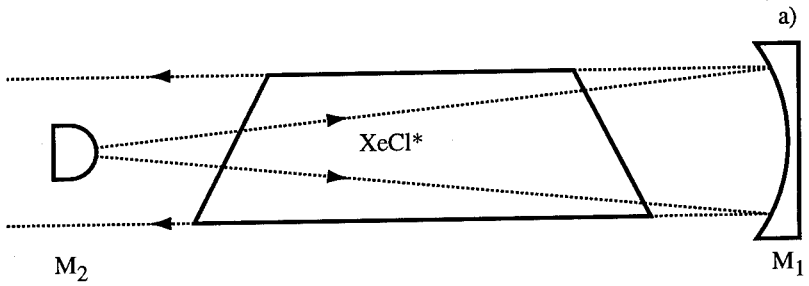
R. Kossowsky et al. (eds.), High Power Lasers – Science and Engineering, 191–198.
© 1996 *Kluwer Academic Publishers. Printed in the Netherlands.*

2. Experimental results

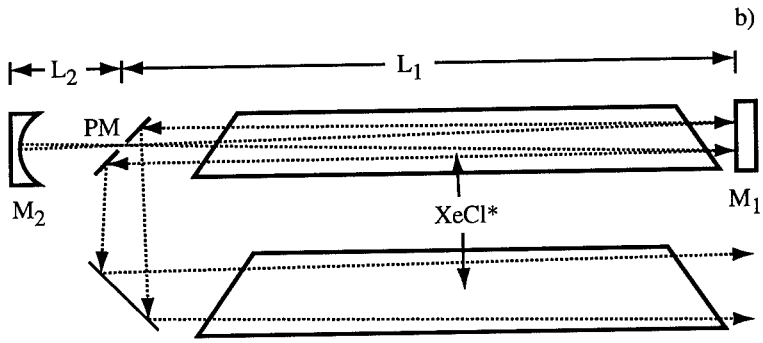
Both Hercules and Ianus have been extensively characterised in the past with flat-flat cavities [3,5]. The main results, obtained with a 36% reflectivity output coupler and a Ne/He/Xe/HCl=2200/40/13/1 gas mixture at an absolute pressure of 3 bar, are reported in Table 1.

TABLE 1. Main experimental results from Ianus and Hercules laser systems using flat-flat resonators

Laser System		Output Energy E [J]	Pulse FWHM [ns]	Near-field spot-size @ .865xE (wxh)[cm^2]	Divergence @ .865xE [mrad]	Brightness [W $cm^{-2}ster^{-1}$]	TDL
Ianus	cell 1	0.35	160	1.7x2	4x3	$4.5x10^{10}$	170x153
	cell 2	0.65	170	2x3	5x2	$5.5x10^{10}$	255x153
Hercules		8	160	4.5x7.4	4x6	$5.3x10^{10}$	460x1100



Confocal positive branch unstable resonator (CPBUR). Magnification $M=-f_1/f_2=5$.



Generalised self-filtering unstable resonator (GSFUR). Magnification $|M|\sim|-2\ L_1/f_2|=8$

Figure1. a) Schematic layout of the CPBUR mounted on Hercules. M=magnification, M_1=totally reflecting mirror with f_1 =3.5 m focal length, M_2=totally reflecting mirror with f_2=-0.7 m. b) Schematic layout of the GSFUR mounted on cell 1 in Ianus and of the single passage amplification in cell 2. M_1=totally reflecting flat mirror, M_2=totally reflecting mirror with focal length f_2=50 cm, PM=totally reflecting mirror with a circular hole (at 45°) 0.06 cm diameter.

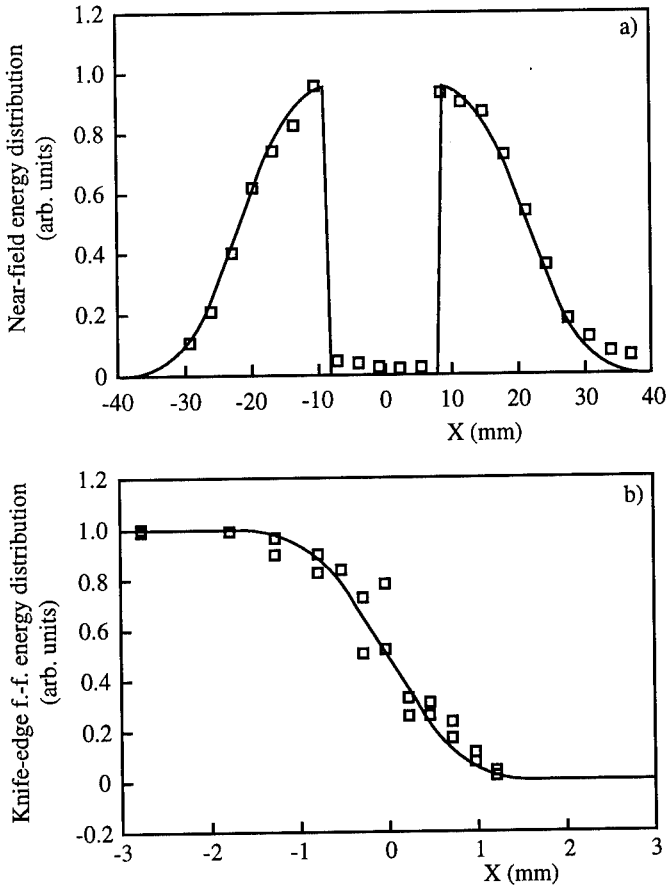


Figure 2. a) Hercules near-field time-integrated intensity profile along the x-axis (squares); b) knife-edge beam scan in the far-field along the x-axis (squares). For details on fit functions, see Sect.3.

When Hercules was equipped with a CPBUR with magnification M=5 (see Fig. 1a), the output laser energy was 5 J in a FWHM of 120 ns. The output laser beam had a rectangular cross section with dimensions (discharge height [x] x electrode gap [y])=(5x7.5) cm^2, with a square hole (1.6 cm side) in the middle, corresponding to the shadow of the output coupler mirror. Near-field measurements have been performed by converting the u.v. laser radiation to visible through an alumina target, and collecting the 2-D image with a tv camera. In order to measure the beam far-field properties, the beam was focused by putting the cavity mirrors at a little longer distance than the confocal one, obtaining the far-field waist at 26 m from the output coupler mirror. Then, the intensity distribution was measured in that plane using the knife-edge (KE) technique in the two orthogonal direction x and y. The results of both series of measurements are reported in Figs. 2a and 2b, respectively. Here, the near-field intensity profile along the

horizontal direction is shown (a) together with the results of the KE beam scan in the far-field along the same axis (b).

The GSFUR mounted on Ianus-cell 1 (see Fig.1b) had a magnification |M|=8, allowing the extraction of 10 mJ output energy, in a pulse with a FWHM time duration of 75 ns. The output beam had a circular symmetry and a slightly curved wavefront (due to the non-confocal cavity geometry), with a geometrical full divergence angle θ_g=1.8 mrad. In order to measure the near-field intensity distribution the same setup was used as in the case of Hercules. On the other side, for the far-field distribution we had to use in this case a focusing element (a concave mirror with focal length of 200 cm, put where the near-field was measured), performing the measurements in the resulting focal plane, moving the KE alternatively along the x and the y axes. In Fig. 3a the beam profile is

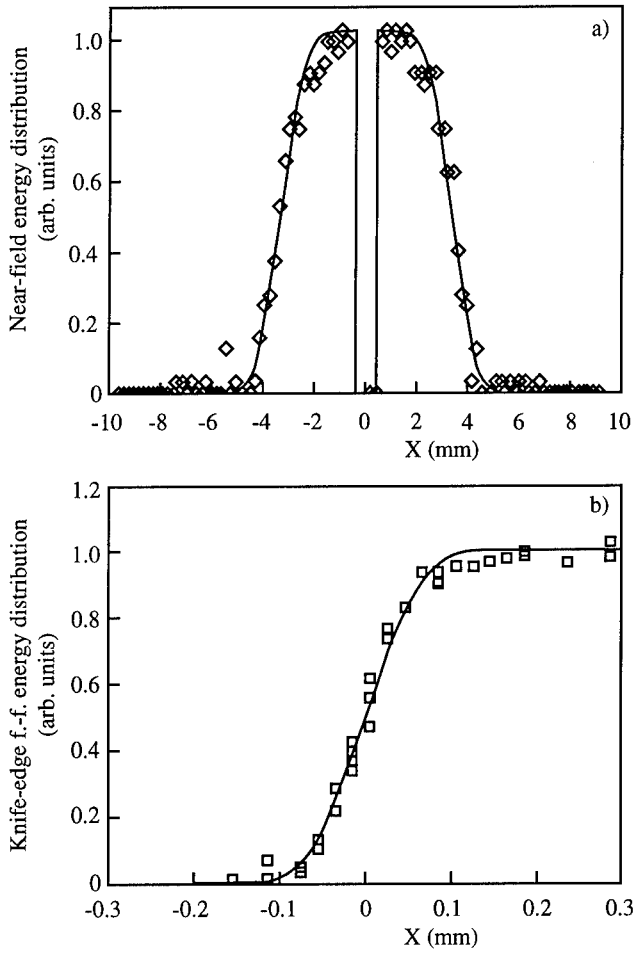


Figure 3. a) Ianus GSFUR near-field time-integrated intensity profile along x-axis (diamonds); b) knife-edge beam scan in the far-field along the x-axis (squares). For details about fit functions, see Sect.3.

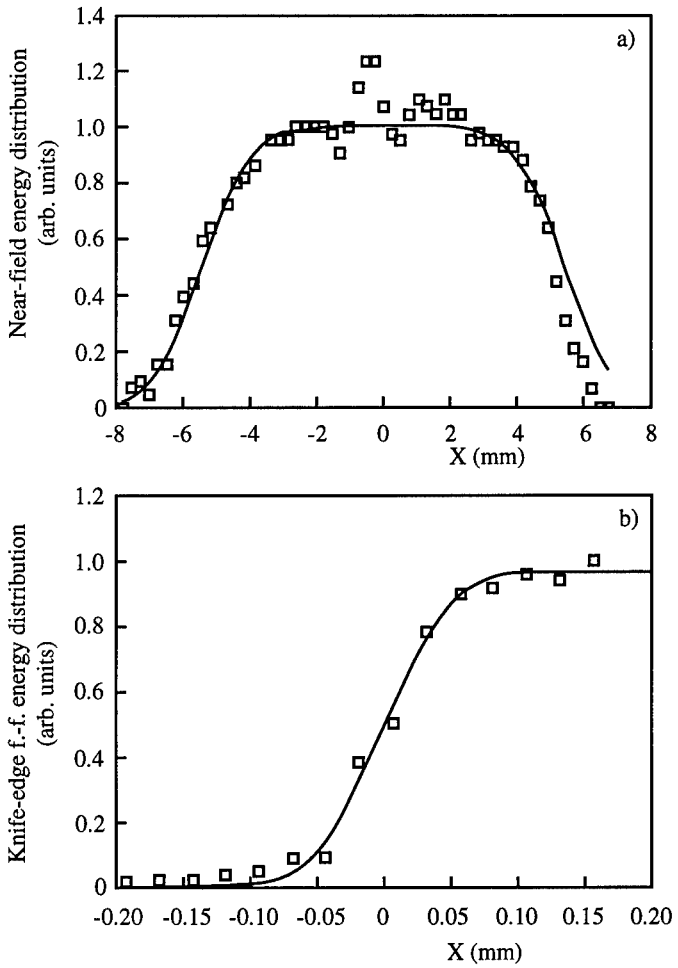


Figure 4. a) Ianus GSFUR amplified beam near-field time-integrated intensity profile along x-axis (squares); b) knife-edge beam scan in the far-field along the x-axis (squares). For details about fit functions, see Sect.3.

shown in the near-field along the x direction, while in Fig. 3b the KE-integrated intensity distribution in the far-field is reported along the same axis.

The output beam from Ianus-cell 1 was injected in cell 2 by a 45° totally reflecting flat mirror (see Fig. 1b). In this way, the time interval between the pulse formation in the oscillator and the amplification in cell 2 is minimised (we remind that the cell 1 and 2 are simultaneously discharged), and the geometrical divergence of the GSFUR beam allows an acceptable filling of the amplifier active medium. After the single passage amplification, the beam energy was 90 mJ, with a FWHM pulse duration of 85 ns. The features of the amplified beam were measured using the same techniques as for the GSFUR oscillator beam. The horizontal beam profile in the near-field (that is, just at the amplifier output) is reported in Fig.4a, where the recombination of the secondary

wavelets around the central hole is already visible. Figure 4b shows the integrated distribution measured with the knife-edge in the far-field along the x direction.

3. Data analysis

The beam divergence can be deduced from the analysis of the experimental far-field intensity distribution, once the divergence has been defined either at a given intensity level, or at a fixed energy content, or through the distribution variance. Anyway, the most significant parameter of a beam is its "optical quality", that can be easily identified with its TDL, the "times diffraction limit" number, which tells how many times the divergence of a laser beam is far from its own diffraction-limited value. As diffraction-limited beam to which refer the real beam measurements, we have used the beam whose amplitude profile in the near-field is the same of the experimental one, but which has a constant-phase wavefront, i.e. it is "diffraction-limited".

Then, in order to calculate the TDL of our laser beams, we carried out the following steps, which are extensively discussed in [7]: a) interpolation of the experimental near-field intensity distribution with a suitable function; b) calculation of the squared Fourier Transform of the corresponding field amplitude, supposed to be spatially coherent, in order to obtain the diffraction limited far-field distribution (TID); c) interpolation of the experimental far-field intensity distribution with the "KE-simulating" integral of a properly widened TID-like function. Finally, the TDL is given by the horizontal scale factor which is needed to widen the TID until it fits the experimental data.

The fit functions reported in Figs. 2b, 3b and 4b are the KE-integrated, enlarged TID-like functions, whose derivation started from the near-field fit functions of Figs. 2a, 3a and 4a, respectively, as explained before. Fig. 5 shows the calculated diffraction-limited far-field intensity distribution (TID) for the Hercules CPBUR beam together with widened TID-like function which fits the experimental points of Fig. 2b when KE-

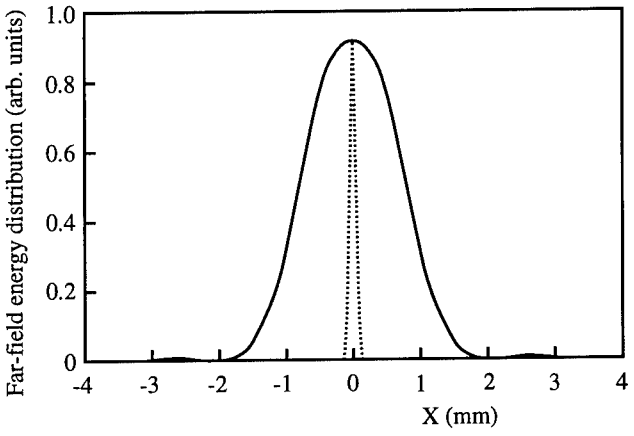


Figure 5. Hercules diffraction-limited calculated far-field distribution (TID) (dotted line) and widened TID-like function which fits experimental data (solid line) for the horizontal direction

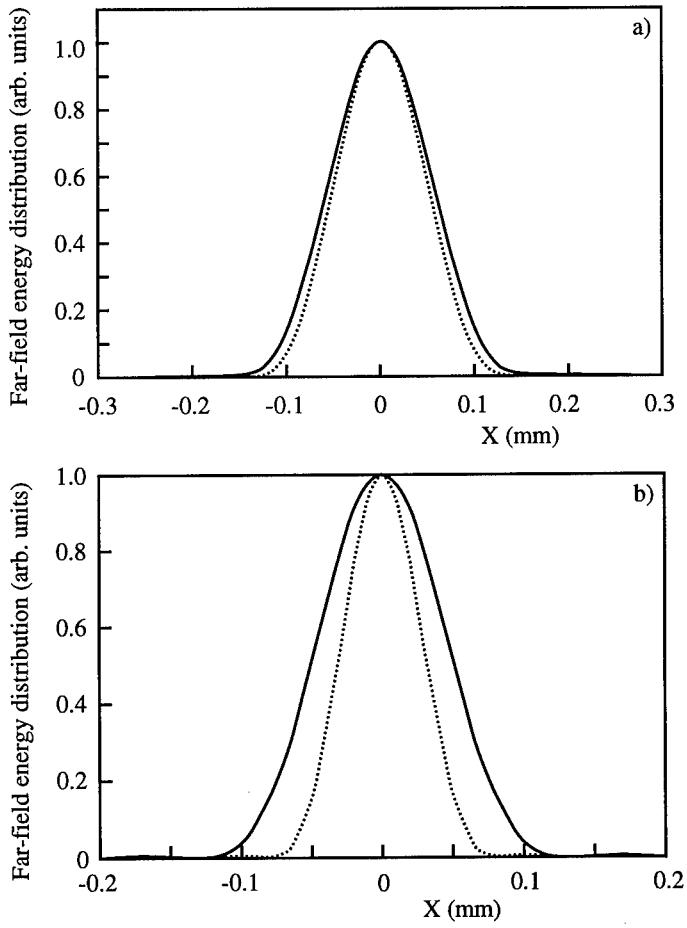


Figure 6. a) Diffraction-limited calculated far-field distribution (TID) for the Ianus GSFUR output beam (dotted line) and widened TID-like function which fits experimental data (solid line) for the horizontal direction; b) the same for the amplified GSFUR beam.

integrated. The same is shown in Figs. 6a and 6b for the Ianus GSFUR and Ianus amplified beams, respectively. From these figures it is possible to see that the horizontal TDL of Hercules is equal to 13.4. An analogous procedure along the vertical direction gave a TDL=17.4. For the circularly symmetric Ianus beams we obtained TDL values of 1.12 from the GSFUR and 1.6 after amplification. These significant results permitted the achievement of a brightness as high as $\approx 10^{14}$ W/(cm^2 ster) from both laser systems.

A schematic summary of the main results obtained from the Hercules and Ianus lasers when operated with UR is reported in Table 2, where also the M^2 parameter is calculated for the three beams.

TABLE 2. Main experimental results from Ianus and Hercules laser system using unstable resonators

Laser System	Optical Cavity	Output Energy E [J]	Pulse FWHM [ns]	Near-field spot-size @ .84*E (wxh)[cm^2]	Divergence @ .84 * E [mrad]	Brightness [W cm^{-2} $ster^{-1}$]	TDL	M^2
Hercules	PBUR	5	120	4.7x7.5	.102x.169	$6.2x10^{13}$	13.4x17.4	13.3x19.1
Ianus	GSFUR	0.01	75	$\pi(0.39)^2$	0.062	$7.5 \cdot 10^{13}$	1.12	1.27
	GSFUR+ amplif.	0.09	85	$\pi(0.58)^2$	0.060	$3 \cdot 10^{14}$	1.6	2.26

4. Conclusions

Two unconventional XeCl laser systems developed at the ENEA Frascati Research Centre, named Hercules and Ianus, have been operated with unstable resonators in order to generate high optical quality, high brightness ultraviolet laser beams. The CPBUR mounted on the large aperture Hercules system allowed to obtain TDL values of 13x17 on a rectangle-shaped beam, with a brightness of $6.2 \cdot 10^{13}$ W/(cm^2 ster). The beam generated by the GSFUR on the double-head Ianus-cell 1 had a TDL value equal to 1.12, with a corresponding brightness of $7.5 \cdot 10^{13}$ W/(cm^2 ster). Finally, the amplified GSFUR beam reached a brightness of $3 \cdot 10^{14}$ W/(cm^2 ster), with a TDL number of 1.6.

5. References

1. Bollanti, S., Di Lazzaro, P., Flora, F., Fu, S., Gerardino, A., Giordano, G., Letardi, T., Lisi, N., Schina, G., and Zheng, C.E. (1990) Excimer laser development at ENEA in frascati under the eurolaser program, in Proc. of 13th Int. Conf. on Lasers and Applications, San Diego.
2. Letardi, T., Bollanti, S., Di Lazzaro, P., Fang, H., Flora, F., Fu, S., Gerardino, A., Giordano, G., Lisi, N., Mezi, L., Schina, G., Torre, A., and Zheng, C.E. (1992) Excimer laser development and applications at the ENEA frascati centre, Proc. 9th Int. Symp. on GFCL, Heraklion, Crete, Sept. 21-25.
3. Bollanti, S., Di Lazzaro, P., Flora, F., Giordano, G., Hermsen, T., Letardi, T., and Zheng, C.E. (1990) Performance of a ten-liter electron avalanche-discharge XeCl laser device, *Appl. Phys. B* **50**, 415-423.
4. Bollanti, S., Di Lazzaro, P., Giordano, G., Flora, F., Letardi, T., Schina, G., Portaccio, M., Torre, A., and Zheng, C.E. (1991) High brightness large aperture excimer laser radiation, in Proc. of 14th Int. Conf. on Lasers and Applications, San Diego.
5. Bollanti, S., Di Lazzaro, P., Flora, F., Giordano, G., Letardi, T., Petrucci, C., Schina, G., and Zheng, C.E. (1994) Compact three-electrode excimer laser IANUS for a POPA optical system, in M. Bohrer, T. Letardi, D. Schuocker, and H. Weber (eds.), *High-Power Gas and Solid State Lasers*, SPIE vol. 2206, pp. 144-153.
6. Di Lazzaro, P., Hermsen, T., and Zheng, C.E. (1988) A generalization of the self-filtering unstable resonator, *IEEE J. Quantum Electron.* **24**, 1543-1547.
7. Bollanti, S., Di Lazzaro, P., and Murra, D. (1995) How many times is a laser beam diffraction-limited?, ENEA Report RT/INN/95/, submitted for publication to *IEEE J. Quantum Electron.*

A HIGH EFFICIENCY SOFT X-RAY LASER IN THE 25-30 NM SPECTRAL REGION

B. RUS[(*)], P.B. HOLDEN[(*)], T. MOCEK[(*)], M. KALAL[(@)], P. ZEITOUN[(†,¶)], A. DEMIR[(†)], B. KRALIKOVA[(*)], S. SEBBAN[(¶)], J. SKALA[(*)], G.J. TALLENTS[(†)]

[(*)] *Gas Lasers Department, Institute of Physics, 18040 Prague 8, Czech Republic*

[(@)] *Faculty of Nuclear Science and Physical Engineering, Czech Technical University, 11519 Prague 1, Czech Republic*

[(¶)] *Laboratoire de Spectroscopie Atomique et Ionique, Université Paris-Sud, 91405 Orsay Cedex, France*

[(†)] *Department of Physics, University of Essex, Colchester CO4 3SQ, U.K.*

This paper outlines a strategy to obtain a soft X-ray laser providing saturated output in the wavelength region 25-30 nm, pumped by a small-scale subnanosecond driver of energy below 50 J. We will briefly review the basic principles of collisional excitation pumping in neonlike plasmas and discuss the application of prepulse driving in low-Z element slab targets. We summarise the conclusions of detailed computer modelling performed for neonlike iron (Z=26, dominant lasing line at 25.5 nm). This modelling predicts a gain coefficient of ~7 cm^{-1} using driving energies of ≈15 Jcm^{-1} (assuming a 400 ps pulse, line focused to 100 μm) and thus saturated output should be achievable by double passing a 2 cm long plasma. Preliminary results of an experiment aimed at obtaining a detailed understanding of the parameters of prepulse-created plasma are presented. These data reveal that the nature of the prepulse plasma strongly depends on the target material and their detailed analysis is expected to indicate not only the optimal pumping regime but also the preferred target characteristics.

1. Introduction

Since the invention of the first laser 35 years ago, there has been considerable and steady effort to achieve lasing action at progressively shorter wavelengths. Following the first conclusive demonstration of a soft X-ray laser in 1984 (based on the electron collisional excitation of neonlike Se ions) at wavelengths 20.64 and 20.97 nm [1] both the experimental and theoretical development of these devices have been outstanding. Generation of strongly amplified soft X-ray radiation has now become routine in many laboratories world-wide. Although basic research in this field is continuing, the

R. Kossowsky et al. (eds.), High Power Lasers – Science and Engineering, 199–215.
© 1996 *Kluwer Academic Publishers. Printed in the Netherlands.*

emphasis of the current effort is progressively moving towards applications. The X-ray laser is expected to offer numerous new research opportunities in atomic physics, microbiology, chemistry, material sciences and applications [2].

Current soft X-ray lasers are driven by terawatt-class optical lasers operated as large facilities. The development of X-ray lasers as a tool available to the scientific community would benefit greatly from the development of a small-scale system, even operating at "moderate" wavelengths around 20-50 nm. The purpose of this paper is to investigate one possible route to this goal.

The paper is structured as follows. In Section 2 we outline some of the basic physics of plasma-based, collisionally-pumped Ne-like X-ray lasers. In Section 3 we briefly discuss the use of low-level prepulses as a means to greatly enhance the intensity of the J=0-1 lasing line. This is illustrated through the example of the zinc laser which provides ~0.4 mJ at 21.2 nm and is pumped relatively efficiently by 350 J of net energy. In Section 4 we consider the Z scaling of the lasing wavelength and required pump intensity. This simple scaling is corroborated by the detailed numerical modelling of lasing in Ne-like Fe, presented in Section 5. Sections 6 and 7 describe the experimental configuration and results of a recent experiment we performed to investigate the prepulse plasma. Section 8 concludes.

2. Basic principles of collisional-excitation X-ray lasers

Among the numerous soft X-ray laser schemes investigated, pumping of highly charged ions by electron impact has hitherto proven to be far the most successful approach. At present, the ion species practically used are Ne- and Ni-like, supplying lasing lines through 9.94 to 46.9 and 3.56 to 7.36 nm spectral ranges, respectively [3], [4]. Here we will discuss the X-ray lasers using Ne-like ions and exploiting plasma created by the impact of a high-power optical laser pulse onto a slab target as the active medium.

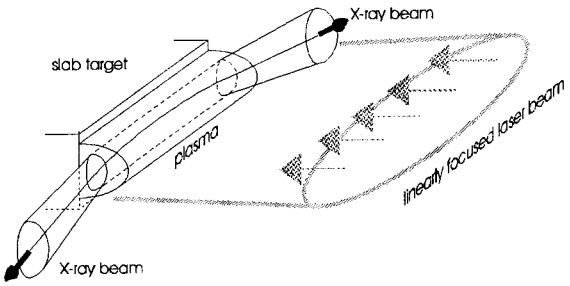


Figure 1. X-ray laser amplifier produced by the impact of a cylindrically focused high-power optical laser pulse onto a slab target. Under saturation conditions the energy stored in the population inversion is fully extracted in the form of a beam emerging from the ends of the plasma.

The collisional-excitation scheme employs an atomic system in which the upper lasing level is metastable with respect to the ground state, whilst the lower level is radiatively coupled to the ground by dipole decay. This is illustrated in Figure 2 on the level diagram of Ne-like Fe (Z=26) which is of particular interest in this paper. The excited levels of the Ne-like structure are populated through collisions of free plasma electrons with ions in the ground state $(1s^2 2s^2 2p^6)_{J=0}$, with the strongest rate corresponding to the $1s^2 2s^2 2p^5 3p\ (1/2,1/2)_{J=0}$ level. Whereas 3p levels are metastable due to $\Delta l=\pm 1$ selection rule forbidding dipole deexcitation into the ground, the 3s levels $(3/2,1/2)_{J=1}$ and $(1/2,1/2)_{J=1}$ are strongly depleted by radiative decay and maintain the inversion. The collisional excitation is assisted in creating population inversion between 3p and 3s levels by dielectronic, three-body and radiative recombination from F-like ions (the importance of this pumping channel increases with Z and favours lasing transitions with upper levels of high statistical weight).

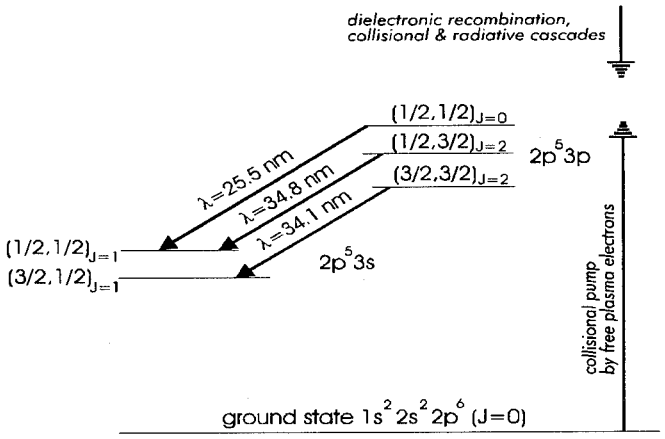


Figure 2. Simplified Grotrian diagram of Ne-like Fe (Fe XVII), with main pumping channels indicated. The levels are labelled by j-j notation, J being the total orbital and spin angular momentum, wavelengths of the lasing transitions are in nm. Among the monopole excitations into 3p levels the strongest is to $(1/2,1/2)_{J=0}$ level.

Although simulations predict the largest gain for the $(1/2,1/2)_{J=0}$ to $(1/2,1/2)_{J=1}$ ("J=0-1") transition independently of Z, the observed spectrum is especially for the high Z dominated by the $(3/2,3/2)_{J=2}$ to $(3/2,1/2)_{J=1}$ and $(1/2,3/2)_{J=2}$ to $(1/2,1/2)_{J=1}$ ("J=2-1") transitions. A detailed discussion on this point is beyond the scope of this paper but it should be noted that the discrepancy tends to be smaller for low Z systems.

Regarding the features of plasma produced from a slab target (these features are essential for the functioning of low Z systems, see Section 5), the X-ray amplification occurs in a medium with a transverse gradient of refraction index η ($\eta(x)=\sqrt{(1-n_e(x)/n_c)}$ where $n_e(x)$ is the transverse profile of the electron density and n_c the critical electron density for the X-ray radiation, equal to $\sim 1.7\times10^{24}$ cm^{-3} at 25.5 nm). In consequence, the X-rays propagating along the amplifier are refracted outwards the target, as

outlined in Figure 1. The key condition for the efficient functioning of the laser is that the X-rays receiving amplification must be able to propagate the full plasma length without being refracted out of the gain region; the refraction thus strongly limits the range of working conditions.

X-ray lasers become saturated when the gain-length product exceeds a typical value of 15, which is few dependent on the particular lasing system. The saturation is highly desirable as the laser produces almost the maximum power possible for the given plasma conditions. As a convenient means of achieving saturation a half cavity, using a multilayer mirror to reinject the beam emerging from one plasma end for second-pass amplification, may be exploited [5]. In addition to significant improvement of efficiency, the double pass operation may relax the constraints imposed by refraction.

3. Pumping regime using a low-level prepulse

Since the demonstration of the first neonlike X-ray laser, it has been observed that its output is dominated by the J=2-1 lasing lines, in contrast to numerical modelling predicting the strongest amplification for the J=0-1 ($^1S_0$-$^1P_1$) transition, as a consequence of the high collisional pumping rate to the upper J=0 level. It is likely that the cause of this disagreement lies with the difficulties in the treatment of the $(1/2,1/2)_{J=0}$ level in atomic physics calculations, resulting in an inaccurate determination of the wavefunction of this level and consequently in the collisional rate from the ground state (see for example [6]). Another difficulty in accurate theoretical reproducibility of the observed magnitudes of J=0-1 amplification may reside in the morphology of the gain region, situated in dense plasma near the critical surface. The amplitude of local gain, Ne-like abundance and conditions for radiation propagation along the plasma being very sensitive on the actual density profile, even a small difference between calculated values of these parameters and those experimentally achieved may result in a notable disagreement in effective gain and output intensity of this lasing line. The problems concerning reproducibility of the experimental results may also be due to those experimental conditions not covered by the modelling, such as small-scale non-uniformities in the pump intensity.

Re-examining an early work on neonlike Ti [7], experiments performed during approximately the last three years (e.g. [8] - [10]) have provided evidence that using a small prepulse preceding by several ns, the main driving pulse may dramatically (by more than one order) enhance propagated gain and output intensity of the J=0-1 lasing line of moderate- and low-Z systems. Although the *qualitative* nature of influence of the prepulse on the lasing plasma is understood (smaller density gradient, more uniform plasma - preplasma may act like a tamper in which the laser energy is redistributed more smoothly, better coupling laser-plasma) and is supposed to predominantly consist of alleviating refraction effects, the modelling thus far fails to *quantitatively* reproduce the dependence of the J=0-1 output as a function of prepulse

intensity. At any rate, the "prepulse effect" makes the experimental gains closer to those calculated by "free prepulse" simulations [11].

A spectrum emitted by zinc (Z=30) laser as a good example of prepulsed pumping is displayed in Figure 3 [5]. Saturation was achieved at the J=0-1 lasing line (21.2 nm) using ~350 J of net pumping energy (~600 ps pulses, 1.06 μm) and employing half cavity. The dependence of the J=0-1 output with respect to the prepulse fraction (the prepulse arrives 4.5 ns before the main pulse) is shown in Figure 4.

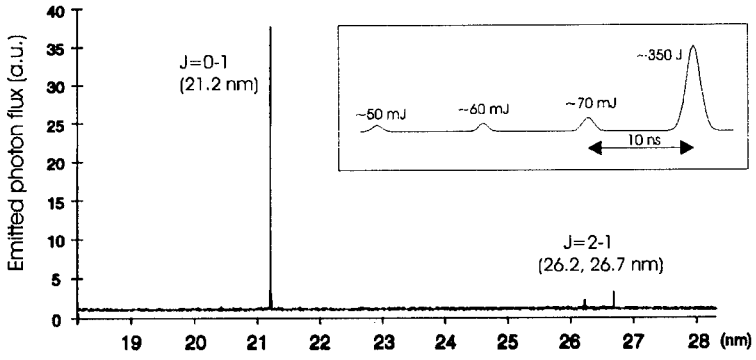


Figure 3. Illustration of performance of moderate-Z neonlike systems employing a prepulsed pumping regime: time-integrated spectrum emitted by a 2 cm long Zn plasma (a result obtained at LULI, Ecole Polytechnique, France [5], [12]).The pumping sequence is shown in inset.

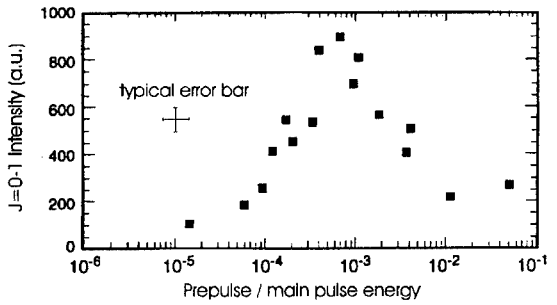


Figure 4. Intensity of the J=0-1 emission in Zn laser with respect to prepulse fraction [12].

4. Scaling laws of neonlike X-ray lasers

The question of practical importance is whether the above results can be scaled to a system being pumped by a "tabletop" driver (E<50 J). The first important feature of Ne-like scheme is the strong dependence of the pump intensity on the atomic number. If we take [12] (other papers, e.g. [13], assume even stronger dependence)

$$I \propto Z^8 \qquad (1)$$

and consider the pumping intensity for the zinc laser ~1.4×10^{13} Wcm^{-2}, the intensity

required to create analogous plasma conditions for Fe (Z=26) may be assessed as ~4.5×10^{12} Wcm^{-2}. This suggests that with a focus 2.5 cm x 100 μm and pulse duration ~400 ps a laser delivering ~45 J would be sufficient as a pumping device.

The J=0-1 wavelength scales relatively slowly with Z, compared to the J=2-1 lines, see Figure 5a. The corresponding dependencies may be approximated as [13]:

$$\lambda_{0\text{-}1} \propto Z^{-3/2} \qquad (2)$$

$$\lambda_{2\text{-}1} \propto Z^{-2} \qquad (3)$$

It is obvious that the J=0-1 lasing systems scale favourably when going to low-Z: whilst by decreasing the atomic number the required pump intensity becomes quickly reduced, the increase of the J=0-1 wavelength is acceptably small.

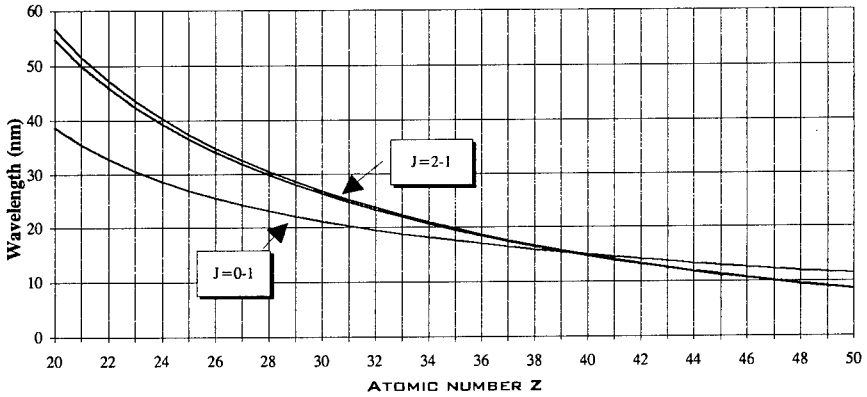


Figure 5a. Wavelengths of three main lasing lines in neonlike lasers, as a function of Z.

Another scaling feature is the emission oscillator strength (Fig. 5b), directly intervening in the gain coefficient (the emission cross section is proportional to the oscillator

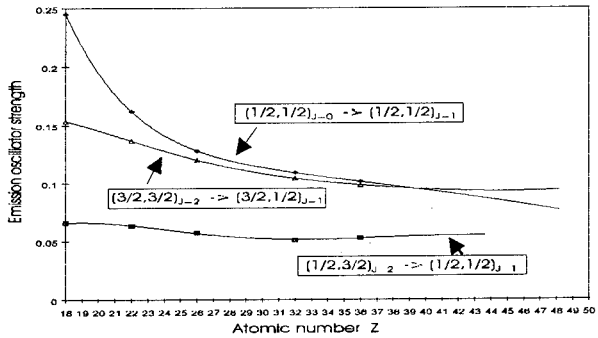


Figure 5b. Emission oscillator strengths of three main lasing lines as a function of Z (according to the data in [14]).

strength). Provided the inversion density is constant, the J=0-1 gain should increase as Z decreases. The strategy to achieve an efficient soft X-ray laser in 25-30 nm wavelength region is thus obvious: using the J=0-1 transition in elements such as Fe and optimising the prepulse conditions to make it analogously beneficial as in the case of zinc.

5. Computer modelling of neonlike Fe X-ray laser

To understand the underlying hydrodynamics and excited level kinetics of the low-Z neonlike systems, we recently carried out a detailed simulation of iron X-ray laser. Here we merely summarise the most significant results - for details and discussion see a specialised paper [13]. The modelling was performed using the quasi-2D code EHYBRID [15], self-consistently solving the plasma hydrodynamics with the atomic physics. The population kinetics is treated in a collisional-radiative model, in which Ne-like excited levels belonging to configurations with n=3 are described in full detail (36 levels) and those belonging to n=4 manifolds are grouped into two aggregate levels. Other ions species are treated by a simplified manner (for details see [16]). The code is post-processed by a 2D raytracing, examining propagation of the X-ray emission through the plasma and thereby solving for the emergent beam characteristics.

A very essential result of the modelling to be emphasised first is that iron plasma is capable of supporting appreciable population inversions *only when its ionisation balance is far below the steady state value*. The reason is that under steady state the plasma conditions requisite for maximising the abundance of Ne-like ions are very different from those producing large electron collisional pumping yield, i.e. those creating large population inversion density. This arises from the feature of the Ne-like structure whose ionisation energy is typically only ~60% higher than energy of the $(1/2,1/2)_{J=0}$ level above the ground state (in Fe these energies are 1262 and 787 eV, respectively), and from Z-scaling of the processes involved in creating the ionisation balance: whilst the total rate of dielectronic and radiative recombination decreases with decreasing Z, the collisional ionisation rate rises. Thus if the temperature in steady state conditions is sufficient to collisionally drive the inversion in low-Z ions, the plasma becomes largely overionised beyond Ne-like: for instance, in Fe plasma with ion density $\sim 10^{19}$ cm^{-3} and electron temperature 400 eV only a small percentage of Ne-like ions is present.

To make low-Z Ne-like systems lase it is consequently necessary to create a plasma far from steady state, in which ionisation balance is "frozen" on Ne-like and the temperature is comparable to the energy of the 3p levels. This may be accomplished using slab targets, and, as the modelling [13] reveals, can be promoted by using a 1.315 μm iodine laser as a driver instead of 1.06 μm Nd:glass. Taking into account the pulse characteristics of the PERUN iodine laser system (see Section 6), the simulations were performed with a 400 ps FWHM flat-top symmetrical pulse of 100 ps rise time.

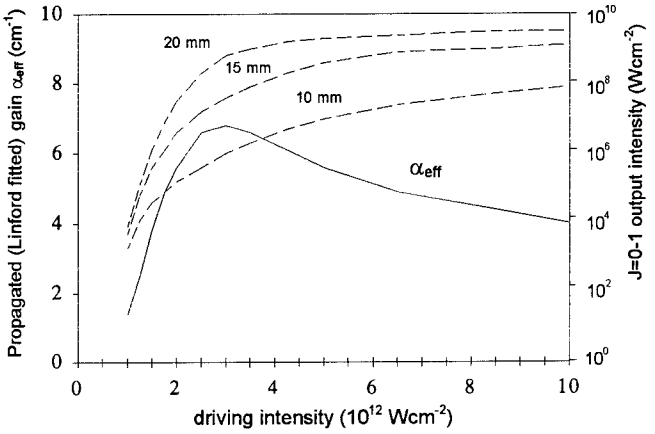


Figure 6. Calculated time-integrated efficient (propagated) gain of the J=0-1 lasing line (25.5 nm) in neonlike iron as a function of net driving intensity (1.315 μm laser). The dotted lines represent output intensity produced by 10, 15 and 20 mm long plasmas.

The driving intensity optimising the performance of the J=0-1 line of an iron X-ray laser is calculated as ~$3x10^{12}$ Wcm^{-2}. This is illustrated in Figure 6 - the time integrated propagated gain for this intensity is ~7 cm^{-1}. It can be seen that in the range ≈$2\div4x10^{12}$ Wcm^{-2} the line exhibits a near exponential growth with respect to the plasma length, which indicates good conditions for the X-ray beam propagation. The simulations further indicate that the J=0-1 output signal maximises near 400 ps with respect to the drive pulse. The spatial profiles of the plasma parameters and the local gains for J=0-1 (25.5 nm) and J=2-1 (34.8 nm) lasing lines at this instant are shown in Figure 7 and illustrate basic features of the hydrodynamics and ionisation kinetics of the laser. The Ne-like ions are predominantly produced in the dense and relatively cold plasma (T_e<150 eV) beyond the critical surface, where ionisation relaxation times are very short. As the plasma expands from the target, these ions are blown through the corona where density rapidly falls. Whilst electron temperature in the corona is high enough (≈360 eV) to ensure significant collisional excitation, only little additional ionisation beyond Ne-like occurs as the lowered density makes the ionisation relaxation times too long (of order ns) - the Ne-like abundance is "frozen" in excess of 50%. Maximum J=0-1 amplification results when refractive properties allow the X-ray beam to propagate along the plasma (350÷400ps), i.e. when the electron density gradient is sufficiently relaxed. Although we do not show results for J=2-1 lines here, we note that their intensity is calculated to be much weaker than the intensity of the J=0-1 line (more than 100 times for a 2 cm long plasma) and to emerge ≈100 ps later than the J=0-1 output.

The calculated optimal driving intensity ~$3x10^{12}$ Wcm^{-2} results from the requirement that the high Ne-like abundance, the high electron temperature (to collisionally drive the inversion) and the density gradient below ~$3x10^{20}$ cm^{-4} be

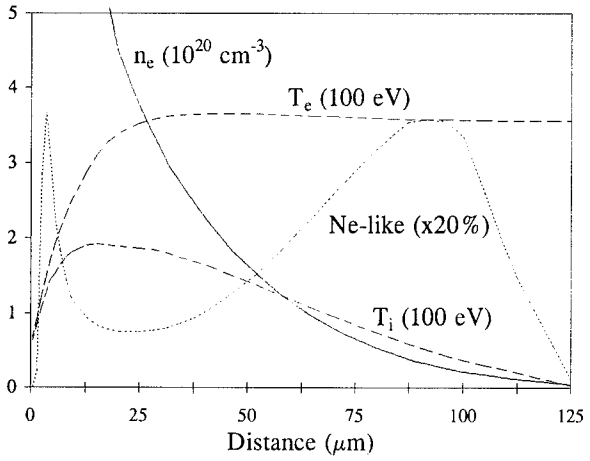


Figure 7a. Electron density (solid line), electron and ion temperatures (broken lines) and Ne-like fraction (dot line) versus distance from the target, in time 400 ps. The outer Ne-like abundance peak is remnant from the early plasma times, having expanded from dense plasma close to the target to hotter corona where low density prevents its additional ionisation.

optimally matched to one another. For a too low intensity (~10^{12} Wcm^{-2}) appreciable local gains are generated, but due to slow expansion rate the "frozen" Ne-like ions reach the density region where the X-ray beam may propagate too late, when the drive laser is already being switched off. In the opposite case of high intensity (~10^{13} Wcm^{-2}), the expansion rate is too fast and the Ne-like ions reach the appropriate density region too early when large gradients are present - as a result, amplification along the plasma is hindered by refraction.

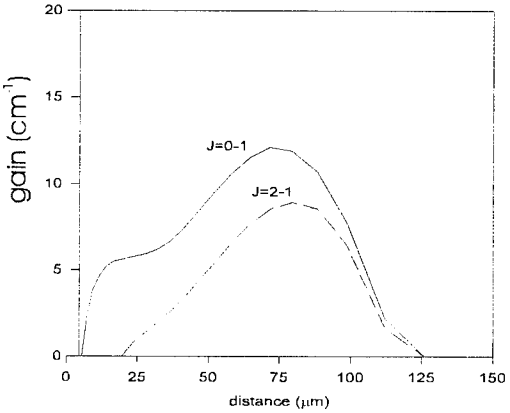


Figure 7b. Gain profiles of the $(1/2,1/2)_{J=0} \rightarrow (1/2,1/2)_{J=1}$ and $(1/2,3/2)_{J=2} \rightarrow (1/2,1/2)_{J=1}$ lasing lines versus distance from the target, in time 400 ps.

Figure 8 displays the time history of the numerical cell of maximum gain (one of those cells acquiring high Ne-like abundance in early times near the target surface and

then blown into the corona) for 1.315 and 1.06 μm drivers. The comparison reveals that higher corona temperature produced in the 1.315 μm case is not accompanied by significant overionisation and as the collisional pumping rate is a much stronger function of the electron temperature (roughly exponential) than of the Ne-like density (linear), the calculated local gain is ≈20% larger compared to the case of 1.06 μm driver. In addition, as longer driving wavelength implies longer density scalelength, the refraction in the 1.315 μm case is smaller and the calculated J=0-1 output intensity for a 2 cm plasma is one order of magnitude higher than for a 1.06 μm driver [13].

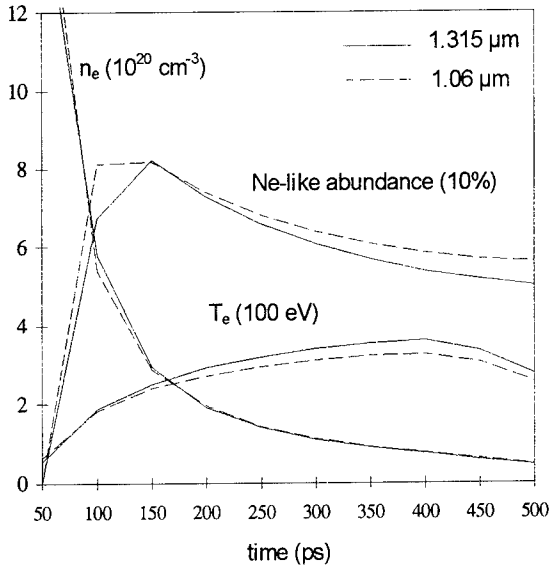


Figure 8. The temporal evolution of the plasma parameters in the cell of maximum local gain, for 1.315 μm (full lines) and 1.06 μm (dot lines) driving lasers, both of net intensity $3x10^{12}$ Wcm^{-2}.

6. Experimental arrangement for the investigation of prepulse plasma

As has been pointed out, the most likely cause of the qualitative discord between the theory and experiments concerning the low-level prepulse effect resides in the incorrect modelling of the "preplasma" itself. This spells out the imperative need to experimentally characterise the plasma produced by intensities corresponding to those applied in the prepulse, i.e. ranging typically from 10^9 to 10^{11} Wcm^{-2}. Ideally, such an experiment should provide information about electron and ion density and temperature spatial profiles resolved in time, and its benefit would thus be two-fold. First, it should provide data directly comparable to those provided by the modelling of the "preplasma" and thereby serve as a testing ground to spot eventual problems. Secondly, it could be used to supply a set of initial conditions, at a given time corresponding to the arrival of

the main drive pulse, for a hydrodynamic/atomic physics code thus allowing for the modelling interaction of the drive pulse coupled into the preplasma with measured parameters. By avoiding the necessity of modelling the preplasma itself, this approach, while not explaining the nature of effects involved in preplasma formation, could be hoped to provide a realistic description of the prepulse on the J=0-1 lasing.

The experiment we have recently performed addresses some of these issues. In particular, we have investigated the following parameters of a plasma produced by a linearly focused laser beam:

- electron density profile in the plane perpendicular to the plasma axis, at times 4 and 10 ns subsequent to the laser pulse
- time-integrated electron temperature and degree of ionisation
- time-integrated lateral extent of the plasma

The experiment was carried out at the iodine laser system PERUN at the Institute of Physics in Prague. This laser supplies up to 50 J over ~400 ps full width at half maximum pulses, at the fundamental wavelength of 1.315 μm. The output 84 mm diameter beam may be frequency doubled or tripled using DKDP crystals with 80 and 60% efficiency, respectively, to provide emission at 658 (red) or 438 nm (blue) wavelengths. The mutual ratio of the three harmonics may be adjusted over a wide range and any combination can be used for a front- or side-illumination of the target.

The irradiation geometry employed in this experiment is shown in Figure 9. The laser was fired at ~20 J level to ensure in the given configuration a reproducible conversion rate to second and third harmonics. 50% of the energy of the 1.315 μm beam is first extracted with the help of a splitter-dielectric mirror M1 and is sent via reflection by another mirror M2 towards the target to create the investigated plasma. The remaining ~10 J of energy is sent through the DKDP crystals to produce the third harmonics, which is then employed as a probe. The conversion efficiency to 438 nm was ~20% and ~30% to 658 nm. Appropriate wavelength-selective filtering at different stages is used to eliminate the 1.315 μm and 658 nm radiation. The mirror M3 extracts the red light from the beam which is then sent via two reflections on dielectric mirrors M4 and M5 and via a spatial filter to side-illuminate the target and to thus to act as interferometry beam. The mirrors M4 and M5 also function as a delay line, allowing to properly retard the interferometric beam with respect to the drive beam. The purpose of the spatial filter was on the one hand to improve the beam quality and on the other hand to reduce the beam diameter.

The inset in Figure 9 outlines the target geometry. The targets were slabs 1 mm in length so as to minimise the deflection of the probe beam in the density gradient of the investigated plasma (this effect would otherwise greatly complicate the interpretation of the interferograms); the length 1 mm was chosen as a suitable compromise from the point of view of minimising the refraction effects on the one hand and the boundary effects at the plasma ends on the other hand. The 1.315 μm beam creating the plasma was vertically line-focused down to 100 μm wide spot of length equal to the beam

diameter - most of the laser energy was thus deliberately dumped by largely overfilling the target. Using a set of mirrors M2 of different reflectivities, the net nominal irradiances on the target were equal to $4.8\text{x}10^{9}$, $1.2\text{x}10^{10}$, $2.4\text{x}10^{10}$, $6.6\text{x}10^{10}$ and $1.2\text{x}10^{11}$ Wcm^{-2}, with an uncertainty smaller than 20%.

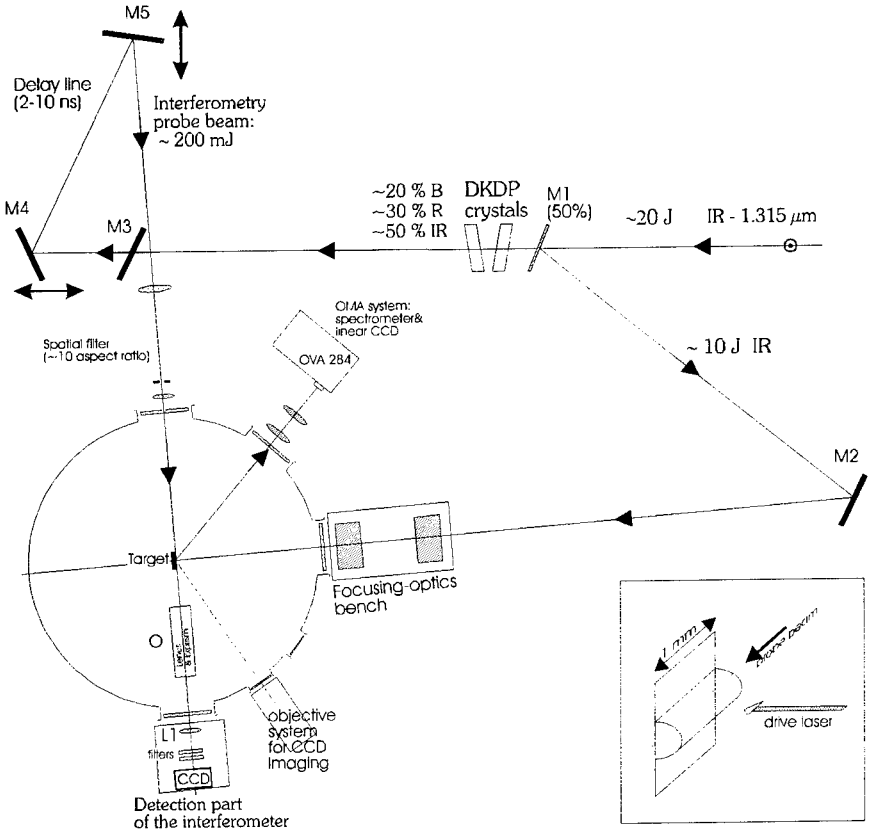


Figure 9. Experimental setup for investigation of line plasma produced by 1.315 μm beam of nominal intensities 4.8×10^{9}, $1.2\text{x}10^{10}$, 2.4×10^{10}, 6.6×10^{10} and 1.2×10^{11} Wcm^{-2}. The target setup for the down-the-axis probing of the plasma by the delayed 438 nm beam is provided as an inset.

The interferometry probe beam was injected "down the plasma column axis"; care was taken to ensure that this beam was parallel to the target surface. Assuming the refraction effects are negligible, the electron density n_e along the ray trajectory in the plasma of length l is constant; the relative phase of the probe emission is then

$$\Phi(x,y) = \frac{2\pi}{\lambda} l \sqrt{1-\frac{n_e(x,y)}{n_c}} - \frac{2\pi}{\lambda} l \cong -\frac{\pi}{\lambda}\frac{n_e(x,y)}{n_c} l \qquad (4)$$

where n_c is the critical electron density for the 438 nm light, $n_c \cong 6\text{x}10^{21}$ cm^{-3}, and (x,y) denote the coordinates in the plane perpendicular to the plasma axis. The

interference fringes are produced by using a Fresnel biprism causing convergence, under an angle α, the part of the probe beam having passed through the plasma and the part having passed in free space in front of the target. The microscope objective O and the lens L1 ensure imaging and magnification of the plasma output plane onto the detector. Using (4) we may express the relative fringe shift at the plane of detector

$$\Delta\Phi = \frac{1}{2\pi}\left|\Phi(x,y)\right| = \frac{n_e(x,y)}{2n_c}\frac{l}{\lambda} \qquad (5)$$

so that $n_e(x,y)$ may be easily determined (details of mathematical processing of the interferograms have been described in detail elsewhere [18]).

The interference patterns were detected by a high-dynamic range CCD camera StarTrek ST6 (375×242 pixels 23×27 μm, cooled down to -15°C, 12-bit output data), protected from stray light by a narrow-bandpass filter. The intensity of the fringe-containing beam was properly attenuated by a combination of two crossed polarisers and neutral density filters so as to fall within the camera dynamic range.

The plasma produced bound-bound emission in the spectral region ≈300-800 nm was investigated by using an optical spectrometer (OVA 284) incorporating a blazed lithographic grating of 280 nm period and two spherical mirrors. The plasma was imaged onto the 300 μm wide entrance slit by two lenses. A 512-pixels linear CCD device was used as a detector. The absolute spectral resolution of this device was ~0.5 nm in the given configuration.

The diagnostic suite is completed by a telescope with a magnification of ~3, coupled to a CCD camera StarTrek ST4 (192×165 pixels 13.75×16 μm). This device was employed to obtain time-integrated images of the visible light emitted by the plasma.

7. Experimental results

The scope of our investigation were zinc (Z=30) and copper (Z=29), regarding recent comparative studies of the J=0-1 lasing [17], together with Fe (Z=26). The targets employed were of a purity of at least 99.5%. Whilst copper was chemically treated by acid mixture to remove the surface oxide layer, zinc and iron were used untreated, i.e. with a thin layer of natural oxide present. Created plasmas were probed in times 4 and 10 ps after the peak of the drive pulse and for both of these delays the five illumination intensities were employed. For each set of experimental conditions, two or more shots were carried out to establish the reproducibility of the data.

In this paper we present only a few raw experimental results obtained by the interferometry measurements. The full account of the obtained data as well as their detailed analysis which are currently underway will appear later [19].

The results of the interferometric probing of the three elements, irradiated at ~1.2×10^{10} and ~6.6×10^{10} Wcm^{-2}, are displayed in Figures 10 and 11. The interferograms in Figure 10 were obtained for probing time 4 ns and those in Figure 11 for 10 ns with respect to the peak of the 1.315 μm creating pulse. It is worth reminding that the

intensity $1.2x10^{10}$ Wcm^{-2} roughly corresponds to prepulse conditions optimising performance of the zinc laser at 21.2 nm (prepulse to main pulse ratio $\approx 10^{-3}$).

It is apparent from Figure 10 that in time 4 ns and for the illumination intensity $\sim 1.2x10^{10}$ Wcm^{-2} the investigated elements behave very differently. Whilst well developed plasma is present in the case of zinc, virtually unperturbed fringes are observed for copper, which indicates that the intensity $1.2x10^{10}$ Wcm^{-2} is only on the brink of producing plasma on this element. Under the same conditions plasma is created on iron, although it is notably less voluminous than that on zinc.

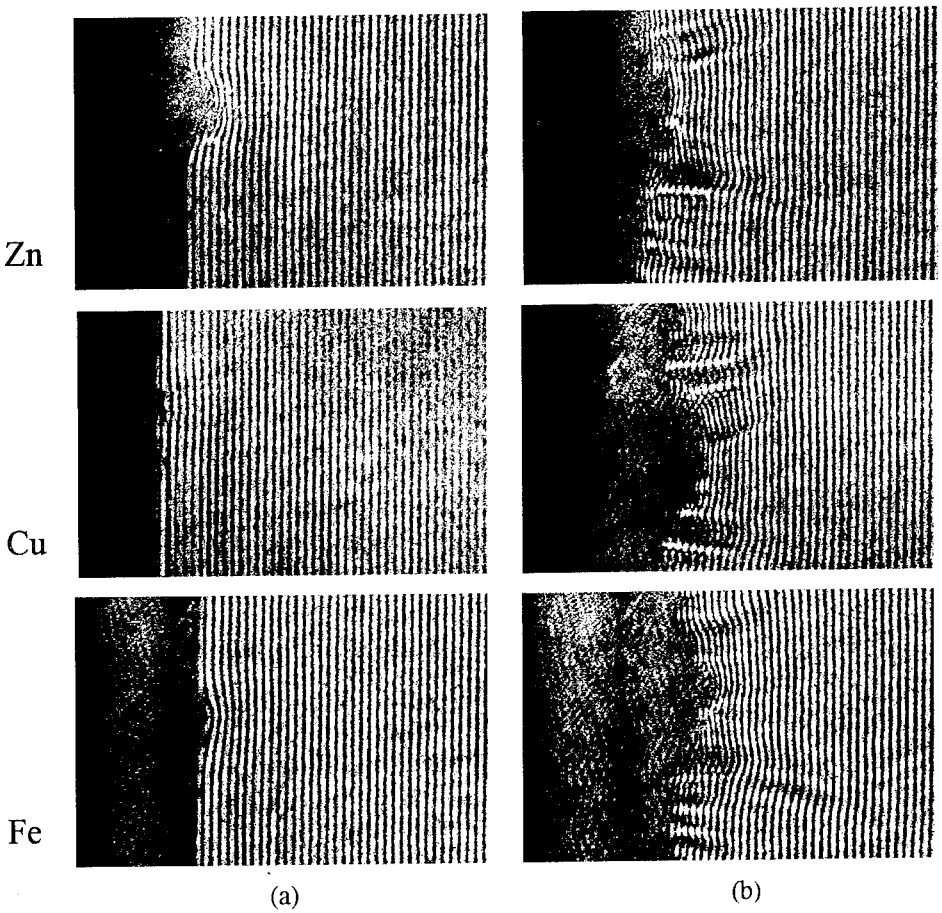


Figure 10. Interferometric records of plasmas created at the surface of Zn, Cu and Fe targets by intensity of (a) 1.2×10^{10} Wcm^{-2} and (b) 6.6×10^{10} Wcm^{-2}, at time t=4 ns.

For the intensity $\sim 6.6x10^{10}$ Wcm^{-2} differences between the investigated elements are less apparent. The plasma in all three cases reveals quite a complex structure, which was originally unexpected. Although little changes in structure of these images occur on a shot-to shot basis, the overall features of the interferograms are well reproducible under the same illumination conditions, which rules out small target imperfections as

being responsible for these observations and strongly suggests that the observed patterns reflect the real nature of the interaction. Besides two major "jets" outlining the impact region of the laser, there are other smaller "jets" outside the impact region, "streaming out" from the target. Whilst interpretation of these observations is not straightforward, it is obvious that theoretical modelling aspiring to reproduce them must fully account for 2D-effects.

The interferograms in Figure 11, obtained for time 10 ns subsequent to the laser pulse are less complex in shape. For the illumination ~$1.2x10^{10}$ Wcm^{-2} we again see the outstanding behaviour of zinc, where a plasma layer of ~100 μm thickness is present. This contrast to the cases of copper and iron, where the fringe patterns reveal only a marginally thin plasma layer on the target surface. The interferograms for intensity ~$6.6x10^{10}$ Wcm^{-2} show in all the three cases a plasma in the form of a "nozzle" whose lateral extent is smallest for zinc and largest for copper. The reason for these differences might consist in different expansion rate in each case, being larger for the

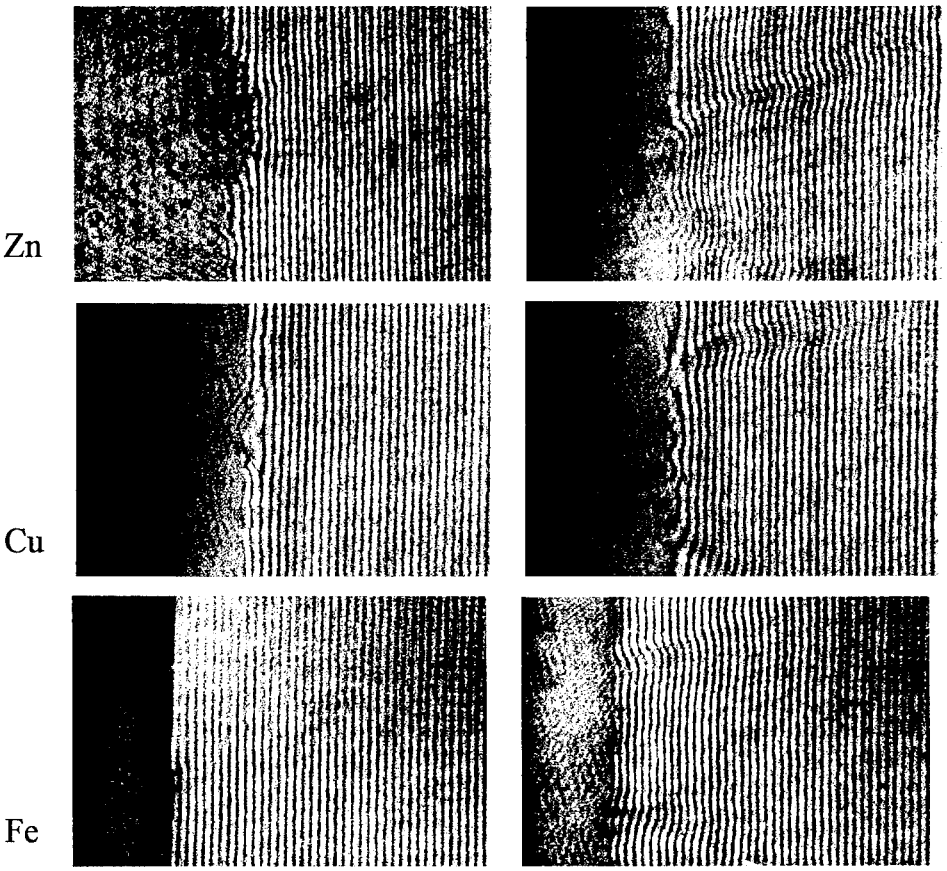


Figure 11. Interferometric records of plasmas created at the surface of Zn, Cu and Fe targets by intensity of (a) 1.2×10^{10} Wcm^{-2} and (b) 6.6×10^{10} Wcm^{-2}, at time t=10 ns.

copper than for the zinc plasma. This would imply higher plasma temperature in the case of copper than of zinc, which seems to be corroborated by the spectroscopic data: whereas lines belonging to twice ionised copper can be identified in the spectra, only singly ionised zinc spectral lines are present.

8. Conclusions

Whilst analysis of the obtained data is still in progress, it is evident that plasma produced by the prepulse of a given intensity is considerably different for the targets investigated. It turns out that even the lowest intensity employed in this experiment ($\sim 5 \times 10^9$ Wcm^{-2}, the data not shown here) creates well developed plasma on the zinc target, whereas only marginally observable or none plasma in the case of copper is detected. The iron target presents an intermediate case between zinc and copper, although it is rather closer to copper. The observed difference between zinc and copper corresponds to the differences of the solid state properties of these elements - the low thermal conductivity of zinc together with its low latent heat of fusion and temperature of evaporation make it easy for a low intensity laser pulse to create a plasma, contrary to copper which has large thermal conductivity and high temperature of evaporation.

The data make it obvious that if density profiles similar to that of a zinc target are to be created for copper and iron, both the delay and the intensity of the prepulse must be varied. Should other quantities such as ablated mass or electron temperature intervene in the prepulse effect, no combination of prepulse intensity and delay would be possible to attain all the desired plasma parameters and a special target design (e.g. a sandwiched structure) would be necessary.

Taking as a reference the preplasma parameters in zinc under which performance of this laser is optimised, the design of prepulse conditions for the proposed iron soft X-ray laser will be established after quantitative analysis of the experimental data, i.e. after unfolding the electron density profiles, temperature and perhaps the ablated mass.

Acknowledgements

The authors are extremely grateful to Ladislav Pina from the Faculty of Nuclear Sciences and Physical Engineering, Czech Technical University, for the loan of the ST4 and ST6 CCD cameras and for the assistance during their implementation. We further thank M. Hudecek, M. Soukup, J. Zeman and J. Macha for providing excellent technical support without which this project would have been impossible. Finally our thanks go to Libor Juha for help in preparation of the targets.

9. References

1. D.L. Matthews, P.L. Hagelstein, M.D. Rosen, M.J. Eckart, N.M. Ceglio, A.U. Hazi, H. Medecki, B.J. MacGowan, J.E.Trebes, B.L.Whitten, E.M.Campbell, C.W.Hatcher, J.H.Scofield, G.Stone, T.A.Weaver, Phys.Rev.Lett. 54, 110 (1985)

2. Applications of X-ray Lasers (San Francisco, 1992), R. London, D. Matthews, S. Suckewer, Eds., National Technical Information Service, Doc. No. LLNL-CONF-9206170
3. B.J. MacGowan, L.B. DaSilva, D.J. Fields, C.J. Keane, J.A. Koch, R.A. London, D.L. Matthews, S. Maxon, S. Mrowka, A.L. Osterheld, J.H. Scofield, G. Shimkaveg, R.S. Walling, Phys.Fluids B 4, 2326 (1992)
4. "X-Ray Lasers 1994", Fourth International Colloquium, Williamsburg, VA, D.C. Eder, D.L. Matthews, Eds., AIP Conference Proceedings 332 (1995)
5. P. Jaeglé, A. Carillon, P. Dhez, P. Goedtkindt, G. Jamelot, A. Klisnick, B. Rus, P. Zeitoun, S. Jacquemot, D. Mazataud, A. Mens, J.P. Chauvineau, "X-Ray Lasers 1994", D.Eder, D.Matthews, Eds., 4th International Colloquium on X-ray Lasers, Williamsburg, VA, AIP Conference Proceedings 332 (1995)
6. P.B. Holden, M. Nantel, B. Rus, A.Sureau, J. Phys. B: At. Mol. Opt. Phys. 28, 1369-1380 (1995)
7. T. Boehly, M. Russotto, R.S. Craxton, R. Epstein, B. Yaakobi, L.B. DaSilva, J. Nilsen, E.A. Chandler, D.J. Fields, B.J. MacGowan, D.L. Matthews, J.H. Scofield, G. Shimkaveg, Phys. Rev. A 42, 6962-6965 (1990)
8. J.Nilsen, J.C.Moreno, B.J.MacGowan, J.A.Koch, Appl.Phys.B 57, 309-311 (1993)
9. G.F. Cairns, M.J. Lamb, C.L.S. Lewis, A.G. MacPhee, D. Neely, P. Norreys, M.H. Key, C. Smith, S.B. Healy, P.B. Holden, G. Pert, J.A.Plowes, "X-Ray Lasers 1994", D.Eder, D.Matthews, Eds., 4th International Colloquium on X-ray Lasers Williamsburg, VA, AIP Conference Proceedings 332 (1995)
10. B. Rus, A. Carillon, P. Dhez, B. Gauthé, P. Goedtkindt, P. Jaeglé, G. Jamelot, A. Klisnick, M. Nantel, A. Sureau, P. Zeitoun, "X-Ray Lasers 1994", D.Eder, D. Matthews, Eds., 4th International Colloquium on X-ray Lasers Williamsburg, VA, AIP Conference Proceedings 332 (1995)
11. S. Jacquemot, "X-Ray Lasers 1994", D.Eder, D.Matthews, Eds., 4th Int.Coll. on X-ray Lasers Williamsburg, VA, AIP Conference Proceedings 332 (1995)
12. B. Rus, PhD Thesis, Université Paris-Sud, 1995 (in French)
13. P.B. Holden, B. Rus, G. Pert, Phys. Rev. A, in press (1995)
14. A.K. Bhatia, U. Feldman, J.F. Seely, At. Data and Nucl. Data Tables 32, 435 (1985)
15. G.J. Pert, J.Fluid. Mech. 131, 401 (1983)
16. S.B. Healy, A. Djaoui, P.B. Holden, G.J. Pert, S.J. Rose, J. Phys. B: At. Mol. Opt. Phys. in press (1995)
17. J. Warwick, C.L.S. Lewis, A. MacPhee, M. Holden, J. Krishnan, G. Tallents, P. Jaeglé, G. Jamelot, A. Klisnick, M. Nantel, P.Zeitoun, Rutherford Appleton Laboratory Report 1995
18. M.Kalal, K.A. Nugent, B. Luther-Davies, Appl.Optics 26, 1674 (1987)
19. B. Rus, T. Mocek, M. Kalal, P. Zeitoun, A. Demir, B. Kralikova, J. Krasa, S. Sebban, J. Skala, G. Tallents, in preparation

The Asterix IV Iodine Laser: Performance and Applications

H. Baumhacker, G. Brederlow, K. Eidmann, E. Fill, A. Grabtchikov*, Th. Löwer, G. Winhart, K.J. Witte

Max-Planck-Institut für Quantenoptik, D - 85740 Garching, Germany

* Institute of Physics of the Academy of Sciences, F. Scaryna Prospect 70, Minsk 220602, Belarus

Abstract

The layout and performance of the single beam Asterix IV high-power iodine laser operating either at the fundamental wavelength at 1315 nm or the second or third harmonic at 658 nm and 438 nm, respectively, are described. Every 20 minutes Asterix IV can provide output pulses with durations ranging from 0.4 ns to several ns with pulse energies of up to 2.1 kJ and pulse powers reaching 3 TW. Preliminary experiments and calculations revealed that by pumping Ti:S disks with the 3ω-radiation of Asterix IV much higher powers in the multi-100 TW region can be attained. Since 1988 the laser fired 6500 target shots as a reliable tool. As a selection among numerous experiments three highlights will be dealt with: (i) uniform megabar shock waves in solids, (ii) XUV opacities in hot dense Al, Fe, and Ho, and (iii) lasing on the J = 0 - 1 line of neon-like ions using the prepulse technique.

1. Asterix IV

Asterix IV is a single beam atomic iodine laser. Its medium is a mixture of the perfluoroalkyl-iodide, C_3F_7I, at low pressure and a buffer gas, usually argon, at high pressure. The buffer gas is needed to control the induced emission cross section and thereby the small-signal amplification. The C_3F_7I is photodissotiated by UV pump light emitted from flashlamps in the wavelength region between 240 and 320 nm. The laser transition in atomic iodine between the upper level $^2P_{1/2}$ and the ground state $^2P_{3/2}$ is of the magnetic dipole type and occurs at $\lambda = 1315$ nm. Asterix IV provides output pulses with lengths flexible between 0.4 ns and 5 ns and pulse energies of up to 2.1 kJ and laser powers reaching 3 TW. Besides the fundamental wavelength the laser can also be operated at either the second or third harmonic at 658 nm and 438 nm, respectively.

R. Kossowsky et al. (eds.), High Power Lasers – Science and Engineering, 217–237.
© 1996 *Kluwer Academic Publishers. Printed in the Netherlands.*

For prepulse or diagnostic purposes a synchronized second beam with energies of up to 100 J is split off behind the fourth amplifier. It can be time shifted and also converted into the second and third harmonic.

1.1 Layout of the laser facility

Asterix IV was described in detail in previous reports [1]. Hence in this paper only a short survey emphasizing the latest improvements is presented.

1.1.1 Overall system

The scheme of Asterix IV is shown in Fig. 1.

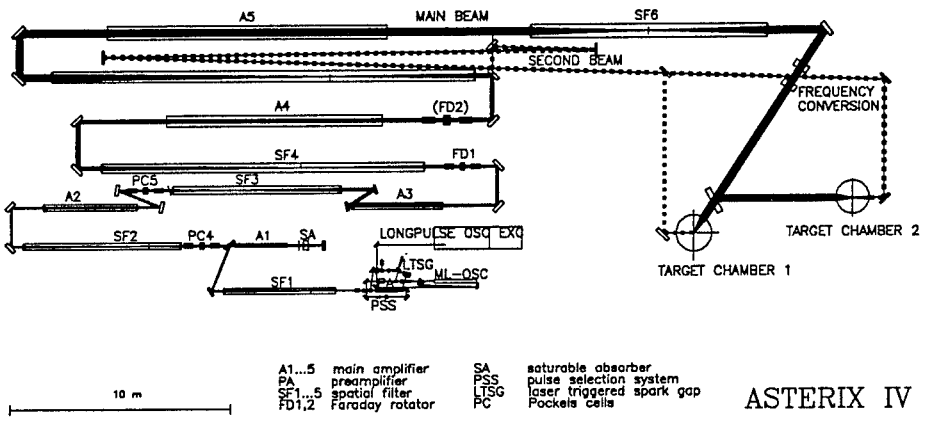


Figure 1: Scheme of Asterix IV laser.

An acousto-optically mode-locked oscillator in conjunction with a high-extinction ratio ($1 : 10^9$) pulse selection system [2] and a long-pulse oscillator [3] provides single pulses with lengths variable between 0.4 and 15 ns.

The selected pulse is fed into an amplifier chain consisting of a preamplifier and five consecutive main amplifiers of increasing diameter and length, the last one being 13 m long and allowing a beam diameter of 290 mm. The layout of these amplifiers is such that the input energy density is in the region of the saturation energy density of about 1 J/cm^2 and that the output energy density does not exceed 3 J/cm^2, thus giving an extraction efficiency for the stored inversion energy between 50 and 55 %.

Six telescopes are placed between adjacent amplifiers and are used for beam expansion, spatial filtering, and - in order to maintain an optimal filling factor - image relaying a rectangular and smooth intensity profile through the amplifier system. The spatial filtering is performed by apertures with 10 times diffraction limited diameters thus removing the high spatial frequency components from the angular beam spectrum, which may arise from inhomogeinities in the pumped medium, diffraction- and self-focusing effects.

A saturable absorber and several Pockels cells serve for prepulse reduction and for amplifier decoupling. Even at 1-ω only one Faraday rotator is neccessary to protect the laser system from light retro-reflected from the target. This is due to the small bandwidth of the iodine transition of less than 1 cm^{-1} and a frequency shift of the backreflected light.

The laser pulse can be frequency doubled and tripled using two KD*P type II crystals mounted in the polarization mismatch scheme as suggested by Craxton [4]. Their thicknesses are optimized for a power density of 3 GW/cm^2.

The laser system with a multiply folded beam path length of 175 m is mounted on a 70 cm thick concrete plate mechanically decoupled from the building in a temperature stabilized class 1000 clean room.

Alignment of the laser is performed semi-automatically using a cw YAG laser at λ = 1319 nm and infrared sensitive vidicons.

1.1.2 Laser medium handling and replacement

The active component of the laser medium, C_3F_7I, is stored as a liquid in a closed loop laser medium regeneration system at such temperatures that its vapour pressure corresponds to the pressure p required in the amplifier. This partial pressure determines the radial inversion density profile in the amplifier with diameter d. In order to obtain a rectangular profile the relation $p \cdot d = 200$ mbar $\cdot$ cm must be satisfied. The actual value of p is monitored by an UV-light absorption method and can be kept stable within ±3%.

After a shot the photo-dissociated C_3F_7I molecules do not completely recombine and strongly quenching products like I_2 appear. Whilst the latter condensate in the laser medium regeneration system during circulation the used-up portion of the C_3F_7I is replaced by an equivalent amount of freshly vaporized C_3F_7I.

The shot rate of the laser system depends mainly on the replacement time of the used-up alcyliodide and also on the recovery time of the original laser beam direction, which is due to a downward deflection induced by a temperature gradient in the laser gas. By applying a locally and temporally varying heating of the stored liquid C_3F_7I the required partial pressure can be restored within 10 minutes. In the same time the laser beam direction can be reestablished by using as new flow-guiding system, by which the laser medium is forced to pass the amplifier in a helicoidal manner. With these

improvements the shot rate was raised from one shot per hour to now one shot per 20 minutes.

1.1.3 Flashlamps

Asterix IV is pumped by 172 flashlamps of different size and loading, the maximum loading being 8 kJ. They were developed at MPQ and allow an exchange of the used-up Xe-gas and of molecular impurities, forming during the discharge.

About 70 % of the flashlamp radiation is focused into the laser gas via elliptic reflectors, which originally served as current return pass, too. This simple construction comprise the disadvantage that the current always flows on that wall side of the flashlamp which is closest to the reflector, due to the fact that at the beginning of ignition the electric field strength is highest in the gap between the high voltage electrode (anode) and the grounded reflector. Therefore the electric breakdown and the discharge channel occur in this direction along the reflector wall side, and cracks will develop which lead to a weakening of the wall structure. Hence the flashlamps had to be exchanged after about 350 shots. If, however, the electric field is axially symmetric before ignition breakdown will take place along the flashlamp axis. This situation is realized in the so-called cage solution (see Fig. 2), where the current flows in four wires surrounding the lamp symmetrically. With this arrangement which has been installed in the last 3 amplifiers one year ago the lifetime of the flashlamps increased by almost a factor of 3; the lamps now withstand mechanically about 1000 shots. However, due to a decreasing efficiency of the lamps their actual life time is only ~ 500 shots. This degradation in performance is caused by a thin layer of dusty quartz and electrode material deposited on the inner lamp wall and slowly increasing in thickness from shot to shot.

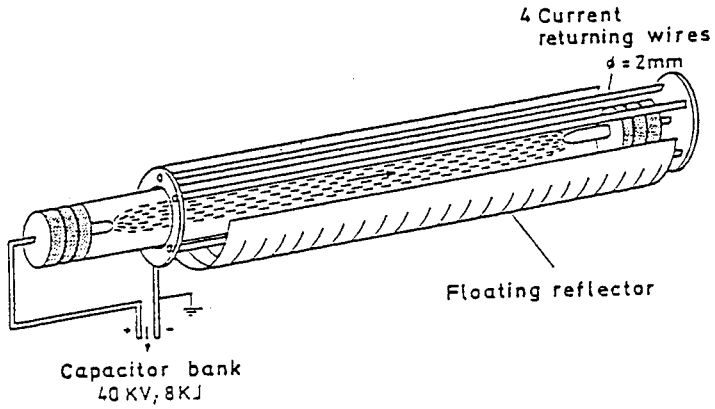


Figure 2. Current circuit of an Asterix IV flashlamp.

1.1.4 Damage threshold enhancement of optical components

Thin film polarizers and anti-reflective coatings are the optical components most sensitive to laser-induced damage. Given the system output energy their damage thresholds determine the beam diameter and the size of the optical components. The failure of coated transmission optics has several causes, the most serious may be absorption of laser energy in particles trapped in the glass/coating interface or in pre-existing defects in the glass surface. Besides this the choice of the high-refractive component and the deposition method of quarter-qave layers play a significant role [5].

The **anti-reflective (AR)** layers on highly-loaded Asterix IV components, like amplifier windows, spatial filter lenses, and target chamber optics were produced both applying the Neutral Solution Process (NSP) and the SOL GEL technique.

The NSP [6] uses controlled corrosion in nearly neutral salt solutions to produce a porous silicon-rich surface of low refractive index, but it is restricted to borosilicate glasses like BK7, a glass which is exclusively used in the Asterix IV facility. In the MPQ we applied the NSP very successfully to a lot of BK7 components of up to 400 mm diameter at the fundamental wavelength at 1315 nm and simultaneously to the third harmonic at 438 nm. A typically transmission spectrum of a 7 mm thick sample treated by NSP is shown in Fig. 3. From that it can be concluded that the reflection per surface can be lowered to ≤0.25% at 1315 nm and to 0.8% at 438 nm.

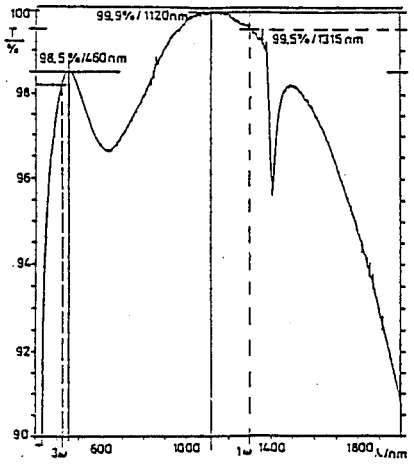


Figure 5. Transmission of a NSP treated sample of 7 mm thickness produced as hybrid to be used at 1ω (1315 nm) and 3ω (438 nm).

The damage threshold of NSP treated samples was found to be D_T = 25 J/cm^2 for both 1 shot on 1 site (1-on-1) and for many shots of equal energy on 1 site (s-on-1) for pulse durations of τ = 0.5 ns at λ = 1315 nm. These values are comparable to those of bare substrates.

With the SOL GEL technique [7] uniform layers of oxide based colloidal suspensions can be deposited on a variety of substrates such as glass, quartz glass, or frequency conversion crystals at room temperature. Not only AR-coatings but in principle also high-reflectivity and polarizing coatings can be fabricated. The layer deposition is achieved either by the well-known dipping or spinning process or by the laminar flow coating process, which is a relatively new method recently developed at Centre d'Etudes de Limeil-Valenton (CEA - CEL-V).

For Asterix IV a variety of windows and aspheric lenses with diameters of up to 360 mm were SOL GEL AR coated by CEL/V. The deposited standard AR-layers are monolayers and they consist of spherical particles of amorphous SiO_2 about 20 nm in diameter packed in a roughly 50 % porous structure yielding a refractive index of 1.22 to 1.25. The spectral transmission is similar to that of NSP layers (see Fig. 4). Values as high as 99.6 % at 1315 nm and 98.8 % at 438 nm could be measured simultaneously.

According to our measurements the damage threshold of this SOL GEL AR-coatings reaches values of $D_T = 19$ J/cm^2 (1-on-1) for 0.6 ns / 1315 nm pulses and 29 J/cm^2 after laser conditioning; this means the same site is exposed to multiple shots with large increments in the fluences from shot to shot (n-on-1).

The first **polarizers** which we used in Asterix IV were stacks of multilayer TiO_2/SiO_2 films. Their original damage threshold (1-on-1) was 8 J/cm^2, but it decreased from shot to shot and finally stabilized at about 1 J/cm^2, thus limiting the output energy of Asterix IV to below 1 kJ. As was originally found in Nd-glass lasers HfO_2/SiO_2 films provide a much higher s-on-1 damage threshold in iodine lasers, too, by applying the method of laser conditioning [8]. With this technique the damage threshold for Asterix IV polarizers could be raised significantly from original 4 J/cm^2 to 8 J/cm^2 for 1315 nm pulses of 0.6 ns duration. This high value is now standing for more than 2 years.

A second attempt to overcome the "polarizer limit" was made by replacing the multilayer polarizers by stacked low-cost two-layer polarizers [9]. These layers are either ZrO_2/SiO_2 or HfO_2/SiO_2 films simultaneously applied on both sides of a BK7-substrate by the forementioned SOL GEL technique. In order to achieve a contrast ratio of about 250 : 1 calculations show that these polarizers have to be inclined at an angle of incidence of 70 to 72° in a stack of 3 plates [10]. First tests with ZrO_2/SiO_2 polarizers produced at CEL/V agree with these predictions and show D_T values of ~ 9 J/cm^2 at 0.5ns/1315nm.

1.2 Laser performance

Since November 1988 the Asterix IV laser is in use for laser-plasma and X-ray laser experiments. According to the experimental needs 6500 target shots have been delivered so far, corresponding to about 1000 shots per year. The laser achieves a maximum output energy of 2.1 kJ at a pulse length of 5 ns, presently generated by the long-pulse oscillator. The maximum power is 3 TW obtained at $t_p = 0.4$ ns, the shortest pulse length till now employed for target experiments. Thus, the projected performance

concerning output energy and power was achieved. For long pulses ($t_p > 1$ ns) the laser performance is limited by the available pump energy, for pulses of medium duration ($t_p = 0.3 - 1$ ns) by optical damage and for short pulses ($t_p < 0.3$ ns) by small-scale self-focusing.

The obtained pulse data are in good agreement with the values computed by our 1-D and 3-D pulse propagation codes and also correspond to the projected overall efficiency of $\eta = 0.16$ %. The laser light has been converted into the second harmonic with an efficiency of over 60 % and into the third harmonic with an efficiency of 56 % (with the inclusion of all losses). Behind the 5th amplifier the focusability was measured to be better than 4 times diffraction limited at both 1-ω and 3-ω. The 1-ω energy density distribution recorded in a plane equivalent to that of the frequency conversion crystals shows a smooth and nearly rectangular profile with a relative maximum deviation from the mean value of at most ±6 % (see Fig. 5). The profiles at 3ω are of the same quality.

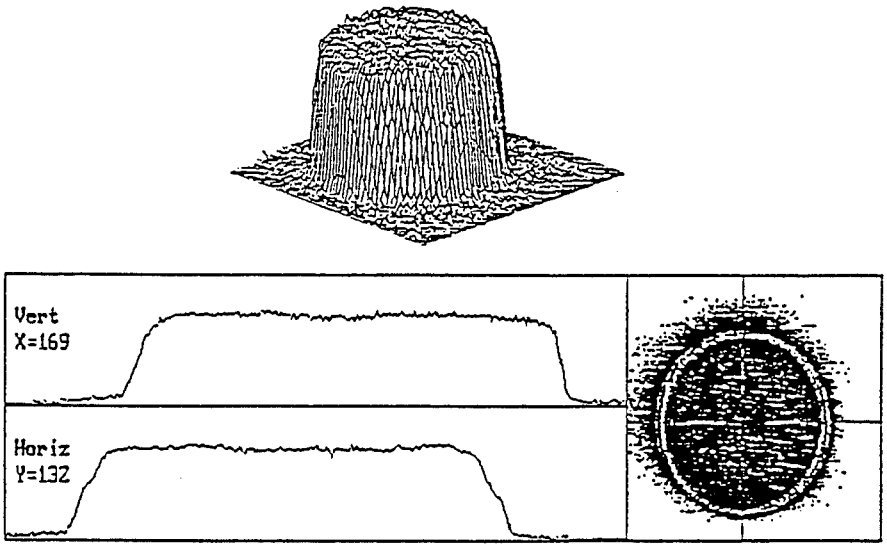


Figure 5. Vidicon record of a typical 1-ω energy density distribution in a plane equivalent to that of the frequency conversion crystals

The laser shows a very dependable and stable performance. Its reliability - defined as perfect shots over delivered shots - has been found to be better than 95 % for a typical period of 400 shots. The output energy is very constant during this period, too. Its

relative standard deviation from the mean value is ±4 % and can be kept to ±1.3 % in short term use (12 shots). The pointing stability of the laser beam during a shot sequence is < ±50 μrad and thus satisfies all requirements. The laser also does not need any beam realignment within months. Because of these facts, its moderate maintenance effort, and the high shot rate of 1 shot per 20 minutes the Asterix IV laser has been proven to be a very valuable tool for laser-plasma and X-ray laser experiments.

1.3 Scalability and prospects

Flashlamp pumped iodine lasers have the potential to be scaled up to still higher output energies and powers than those achieved in Asterix IV. Amplifiers with diameters in the 1m range can be realized. Calculations based on the experience gained with the Asterix IV laser predict an output energy of 10 kJ for an end amplifier with an aperture of 70 cm.

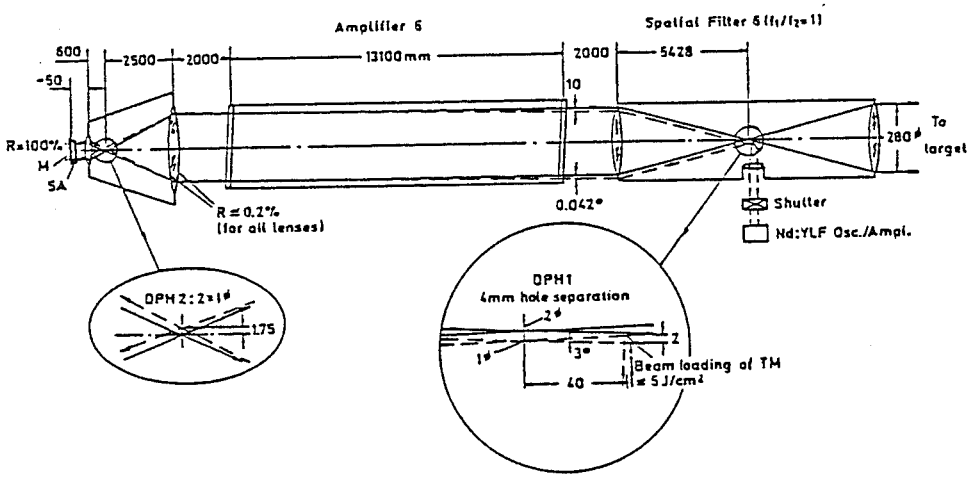


Figure 6. Double passed Asterix IV amplifier A5. M, plane mirror with 100 % reflectivity. SA, saturable absorber JUL II with small signal transmission, T_{SS}=2%, and large signal transmission, T_{LS}=0.75. The shutter decouples the front-end driver, a Nd:YLF osc./amplifier system, from the amplifier A5. DPH1 and DPH2, double pinholes. TM, turning mirror.

An iodine laser system can be considerably simplified if the final high-power amplifier is double passed using a one-way small signal amplification of A_{SS} = 200...1000. Under these conditions only a rather low input energy is needed to get access to a fraction of the stored energy which is not as high as that obtainable with the system described above, but still has a reasonable value. This and the strongly reduced system complexity makes the "lean configuration" an attractive option. The basic reason for the favorable energy extraction behaviour is the low value of the saturation energy density of only ≈ 0.9 J/cm^2 in the iodine laser medium.

To avoid parasitic oscillations in the amplifier the two passes must be optically decoupled. One possibility is to use a phase conjugating mirror, as successfully tested by Bessarab et al. [11]. For Asterix we propose a somewhat different design schematically sketched in Fig. 6, where - in conjunction with the last amplifier - an ordinary mirror together with a saturable absorber having a small-signal transmission of 2 % is used.

The overall reflectivity of the combination mirror/saturable absorber is 50 %. The direction of the backreflected pulse is slightly different from that of the incoming pulse so that the former does not fire back into the front-end driver. Instead, on its way to the target it passes through a second pinhole adjacent to the first pinhole which is thus only used by the incoming pulse. The shutter necessary to decouple the front-end driver from the amplifier only needs a contrast ration of 10^6:1 which is not difficult to achieve.

Calculations revealed that at accessible A_{SS} values of 200 to 300 output energies in excess of 1 kJ can be obtained with input energies of $\geq$ 200 mJ. An attractive choice for the front-end driver which can provide these input energies at low effort is a state-of-the-art Q-switched Nd:YLF oscillator/amplifier system tuned to the iodine transition and capable of delivering pulses with durations of a few ns up to about 20 ns. Saturation effects in the iodine amplifier and in the absorber shorten the output pulse duration to values ranging from about 1 ns to several ns. Due to its repetition rate of 1 Hz or more the Nd:YLF laser is also very advantageous for system and target alignment.

2. Asterix IV as a pump source for a multi-100 TW Ti:S system

For many plasma and X-ray laser experiments extremely high powers at short pulse durations are desirable. Increasing the power and energy of commercially available fs-Ti:S laser systems to the 100 TW / 10 J level or beyond requires strong pump lasers. As can be seen in Fig. 7 besides the second harmonic of Nd-glass lasers at 532 nm the third harmonic of atomic iodine lasers at 438 nm is also within the absorption spectrum. Asterix IV with its energies of up to 500 J at 3ω is thus well-suited for this purpose.

Whereas a lot of information concerning pumping at 532 nm has been accumulated in the past - to the best of the authors' knowledge - no material of pumping at 438 nm has been published so far. Therefore experiments at 438 nm have been carried out since October 1993 to confirm the absorption data which gives the optimum Ti^{3+} dopant concentration and to obtain the dependence of small-signal gain coefficients as a function of the pump energy density. This data allows us to scale the 1.7 TW Ti:S laser system of CONTINUUM [12] running in our group since the beginning of 1995 to the 100-TW region using Asterix IV as the pump source.

The Ti:S pulses to be amplified are generated in a COHERENT MIRA oscillator with a repetition rate of 76 Mhz: The pulse duration is t_p = 100 fs, time-bandwidth product is

about 0.5, center wavelength 790 nm, pulse energy E_p = 6 nJ, linearly polarized, TEM_{00} mode.

As pump sources we used 3ω of Asterix IV and Plasterix iodine lasers at 438 nm and pulse durations of 0.5 or 5 ns. In addition and in order to check the reliability of our measuring method we also used 2ω of Nd-glass or -YAG lasers at 532 nm with t_p = 3 - 5 ns and selected wavelengths of 438, 465, 488, 500, 520 and 532 nm from an OPO.

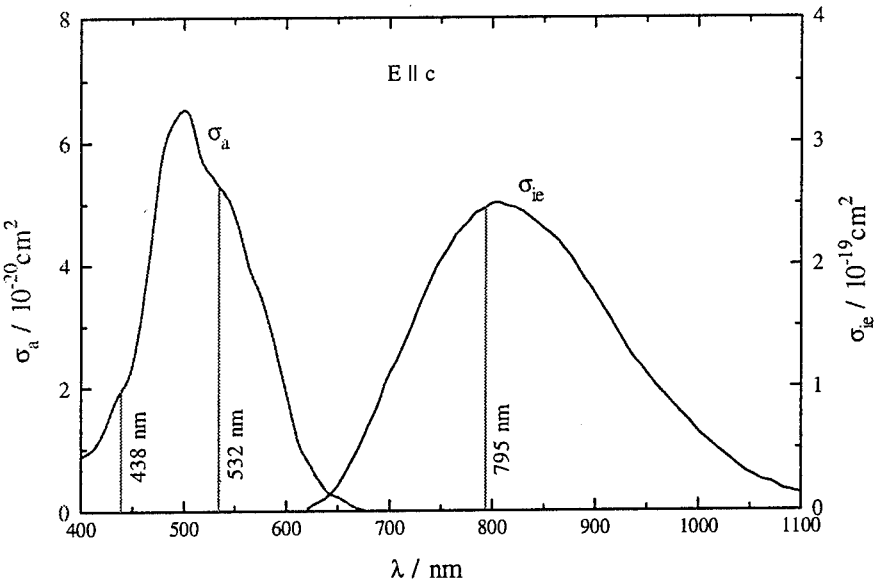


Figure 7. Ti:S cross sections for absorption and stimulated emission

The experimental setup for the amplification measurements is shown in Fig. 8. The Ti:S pulses to be amplified are generated in a COHERENT MIRA oscillator with a repetition rate of 76 MHz: The pulse duration is t_p = 100 fs, time-bandwidth product is about 0.5, center wavelength 790 nm, pulse energy $E_p \approx$ 10 nJ, linearly polarized, TEM_{00} mode.

As pump source we used 3ω of Asterix IV and Plasterix iodine lasers at 438 nm and pulse durations of 0.5 or 5 ns. In addition and in order to check the reliability of our measuring method we also used 2ω of Nd-glass or -YAG lasers at 532 nm with t_p = 3 - 5 ns and selected wavelengths of 438, 465, 500, 520 and 532 nm from an OPO.

Four Ti:S crystals with different specifications regarding the geometry, Ti doping between 0.1 and 0.25 weight % and FOM better than 150 and 300, respectively, were used.

During the measurements the pump pulse energy and - by monitoring the beam profile - the energy density profile at the entrance of the Ti:S crystals are monitored carefully at each shot. The energy amplification ratio of the MIRA pulses is measured with a photodiode / fast oscilloscope combination and is taken to be equal to the ratio of the largest abscissa after pumping to the mean value of the abscissas prior to pumping (see Fig. 8).

Our measurements revealed that for all measured Ti:S crystals and pump sources at 438 and 532 nm the dependence of the small signal gain gl = ln G_0 on the pump energy density is linear up to 3 J/cm^2 corresponding to an stimulated emission cross

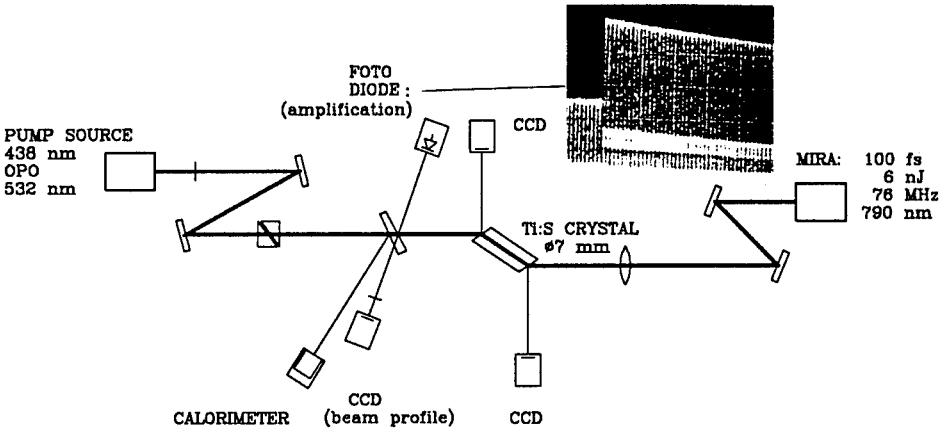


Figure 8. Experimental setup for amplification measurements in Ti:S crystals.

section of $\sigma = 3.\ 10^{-19}$ cm^2 at 790 nm. But above 3 J/cm^2 the gain surprisingly rises less than linearly (Fig. 9) and eventually saturates. The mechanism for this behaviour is not quite clear, but we have indications that among the various possible causes the onset of self-oscillations by zig-zag modes is highly probable.

Supported by these findings and by additional experiences made when - in good agreement with Frantz-Nodvik calculations - we achieved gains of up to 10 in a Ti:S amplifier of ∅ 30 mm pumped with a Nd-YAG laser at 2 J/cm^2 from two sides and the Ti:S beam traversing the crystal twice we designed the chain of 2 Ti:S booster amplifiers pumped by Asterix IV. The layout can be seen schematically in Fig. 10.

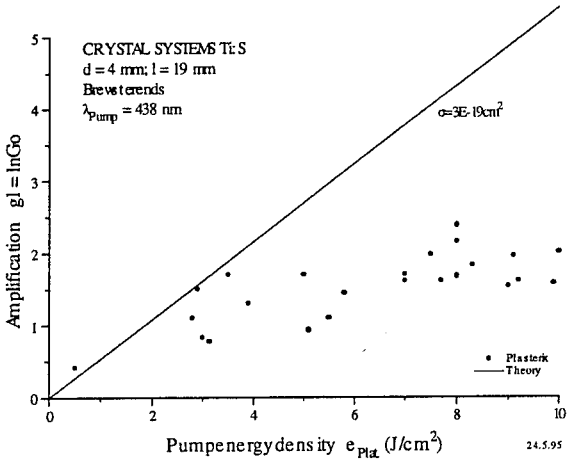


Figure 9. Small signal amplification as function of pumpenergy density

Two Ti:S crystals with 30 mm and 80 mm diameters are pumped from two sides. In order to avoid parasitic self oscillation, esp. perpendicular to the laser propagation axis the pump energy density must not exceed 3 J/cm^2 in each side and the Ti:S crystals must be surrounded by an absorbing index matching fluid like 1-bromonaphthalene (n = 1.66) and the larger Ti:S crystal should be a composition of 2 pieces with 40 mm width each separated by the absorbing index matching fluid.

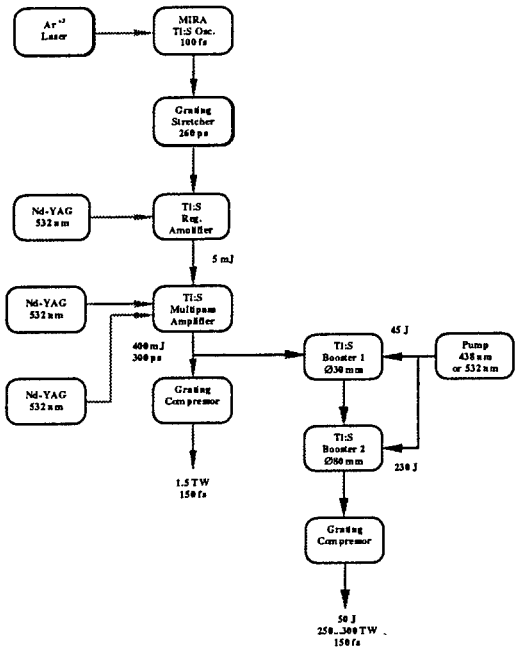


Figure 10. Asterix IV pumped Ti:S booster

Taking into account a 50 % efficiency of the compressor a total pump pulse energy of about 300 J at 438 nm is needed to achieve an output energy of 50 J at 790 nm and 150 fs duration, which corresponds to a power of 330 TW. Focused to a diameter of 30 µm (~ 3 · $\varnothing_{\text{diffr. limit}}$) this gives a power density of $4.6 \cdot 10^{19}$ W/cm^2, a value which is highly interesting for a variety of experiments like relativistic self focusing.

3. Asterix IV for laser plasma and X-ray laser experiments

As a selection among numerous experiments three highlights will be dealt with. These are uniform megabar shock waves in solids, XUV opacities in hot dense Al, Fe, and Ho, and lasing on the J = 0 - 1 line of neon-like ions using the prepulse technique.

3.1 Uniform multimegabar shock waves in solids driven by laser-generated thermal radiation

The generation of extremely high pressures in the laboratory by focusing a high-power laser beam onto a thin layer of a solid material thus creating an intense shock wave is of considerable interest. In particular, it is hoped to study the equation of state of dense matter and up to now not achieved phase transitions of matter at very high pressures. Shock waves with pressures in the 100-Mbar region have been demonstrated [13] when solid samples were irradiated directly by pulsed laser light. However, it turned out that these shock waves could not achieve adequate uniformity due to spatial intensity modulations of the laser beam which arises from the coherent nature of the laser light. As for quantitative evaluations the shock waves must be spatially uniform, of constant velocity, and free of preheating we have demonstrated the generation of planar shock waves of very high uniformity with pressures of up to 14 Mbar in solid samples, using the incoherent thermal radiation from a cavity which was irradiated by the Asterix IV 3-ω beam.

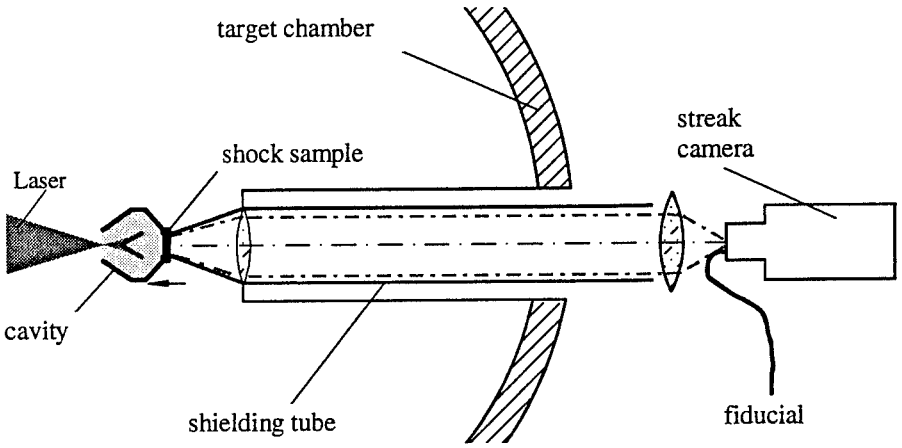


Figure 11. Experimental setup for shockfront velocity measurement.

The principle of our experiments (Fig.11) is to heat a mm size cavity by pulsed laser light and to generate in this way intense thermal soft X-rays [14]. The radiation temperature depends on the cavity size and the available laser energy and is in the range of 90 - 150 eV. The intense thermal radiation ablates material from the shock

sample and generates a shock wave in it. The flash of light emitted by the shock-heated material during shock breakout at the outer surface is registered by an optical streak camera. The velocity of the shock wave is determined from the time delay of shock arrival between areas of the sample with different thicknesses.

Experiments were performed using the 3-ω radiation of Asterix IV with energies of 250 J at τ_{pulse}= 450 ps. An advanced labyrinth cavity (see Fig. 12) was made of gold with 1 to 3 mm inner diameter and a wall thickness of 15 μm.The shock samples were fabricated as flat, single- and double-step and wetched from gold or aluminum.

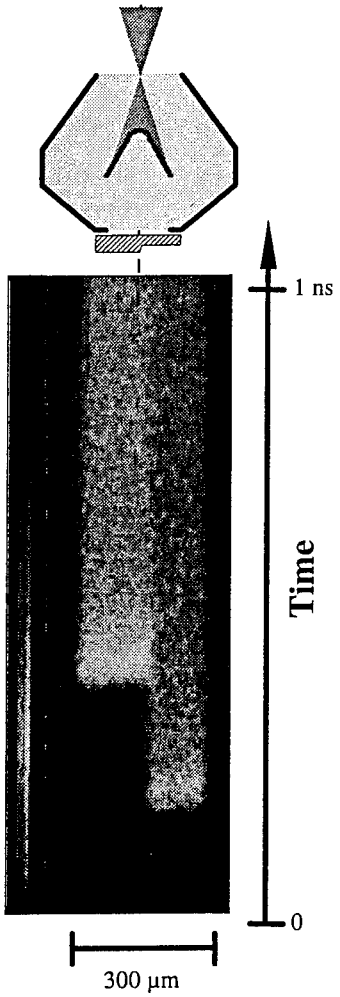


Figure 12. Streak camera record of the shock induced light emission.

A shock wave signal obtained from the cavity just described is shown in Fig.12. From that the shock wave velocity can be determined and with the help of Hugoniot curves calculated from SESAME equation-of-state data this leads to shock wave pressures of up to 14 Mbar, which is in good agreement with the theoretically predicted pressures. The shock wave velocity in all experiments is uniform to better than ±0.6 % and the total error of the pressure can be determined to ±1.6 %.

Our experiments showed that not only small scale modulations of the shock front can be eliminated, but also that a high degree of uniformity may be achieved on macroscopic samples and that radiative preheating effects may be minimized by proper cavity design and irradiation conditions.

With the achieved high-quality shock signals we are now able to carry out quantitative measurements to verify theoretically predicted equations of state.

3.2 Measurements of XUV opacities in hot dense Al, Fe, and Ho

An essential contribution to the energy transport in hot dense plasma is caused by radiation. This is of importance, for example, in astrophysical models of stars or in indirect drive inertial confinement fusion targets. Modeling of such plasmas strongly relies on radiative opacities. Theoretical calculations of opacities are very complex and need numerous approximations. Therefore it is not surprising that different opacity models often differ in their results. To check opacity models clear measurements at a well defined temperature and density are strongly needed [15].

Opacity measurements were performed with the Asterix IV iodine laser at $T \approx 22$ eV and $\rho \approx 0.01$ g/cm^3 in the spectral range $70 \text{ eV} \leq h\nu \leq 280$ eV at a low level of self-emission. As sample materials aluminum (Z = 13), iron (Z = 26), and holmium (Z = 67) were used. These elements are considered as being representative for low, medium, and high Z.

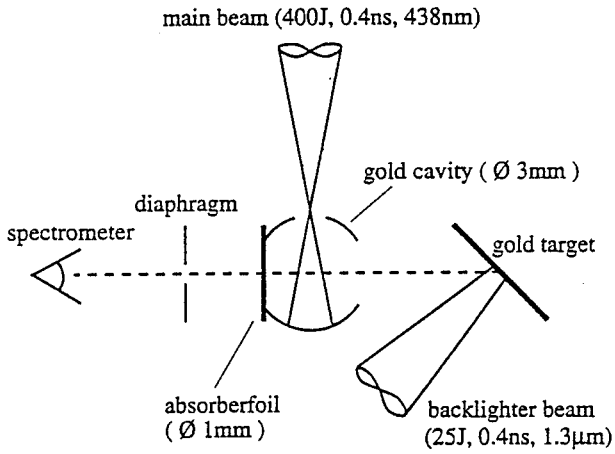


Figure 13. Experimental setup for XUV opacity measurements.

The scheme of the experimental setup is seen in Fig. 13. The main beam of Asterix IV (400J, 0.4 ns, 438 nm) is focused into gold cavities with 3 mm diameter thus heating the absorber foils which were glued on one of the two diagnostic holes with a diameter of 1 mm. The sample layer was either 1075 Å (30 μg/cm^2) thick aluminum or 191 Å (15 μg/cm^2) thick iron or 170 Å (15 μg/cm^2) thick holmium, embedded in 560 Å (15 μg/cm^2) carbon foils on each side to reduce axial density gradients due to expansion.

A backlighter source was generated by a second Asterix IV laser beam (25 J, 0.4 ns, 1.3 μm), which was focused on a planar gold target with a delay of 800 ps to the main beam. The transmission of the backlighter probe beam through the sample was measured spectrally and temporally resolved by a XUV spectrometer.

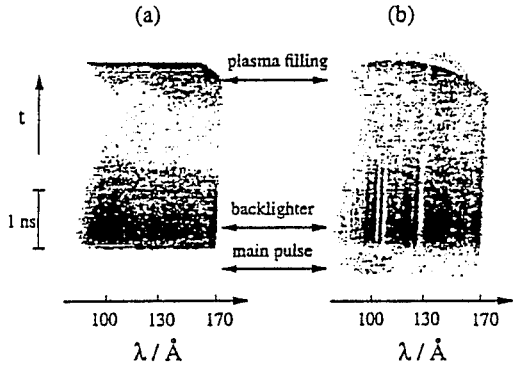
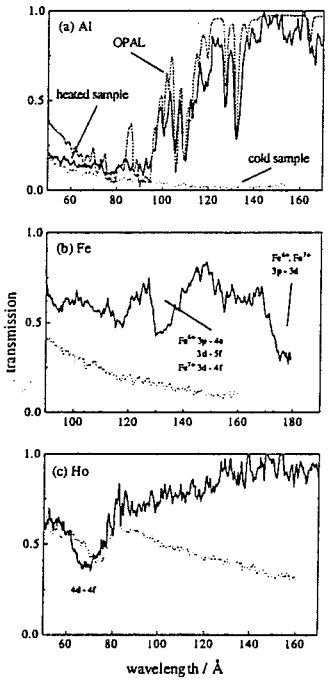


Figure 14. Streak camera signals of the backlighter through a heated cavity a) without a sample and b) with an aluminum sample.

Fig. 14 shows two streak camera records, a) is a record of the backlighter spectrum observed through a heated cavity without a sample, and b) is the signal with an aluminum absorber foil on the cavity. The tranmission was obtained by normalizing the absorption spectrum to the backlighter spectrum.



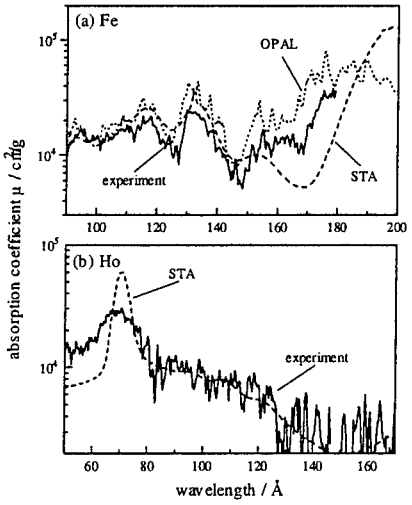


Fig. 15. Measured transmission spectra of a) Al, b) Fe, and c) Ho for heated or cold sample. For Al (a) also a comparison also a comparison with OPAL code is shown.

Fig. 16. Measured and calculated mass absorption coefficient for Fe (a) and Ho (b).

The measured transmission spectra of the heated and cold samples are given in Fig. 15. For a comparison with opacity codes the temperature and density of the samples are needed. In aluminum the sample temperature was determined spectroscopically from the measurement of the ratio of the two most prominent absorption lines in Al^{4+} and Al^{3+} assuming LTE. This temperature is believed to also hold for iron and holmium. From hydrodynamic simulations with the MULTI [16] hydrocode it can then be concluded that the pertaining density is about 0.01 g/cm^3 in all cases.

A comparison of the experimantal results with the codes OPAL [17] and STA [18] is shown in Figs. 15 and 16. It can be seen that there is a good agreement between theory and experiment.

3.3 Investigation of lasing on the J = 0 - 1 line of neon-like ions using the prepulse technique

The successful demonstration of collisional X-ray lasers was puzzled by the observation that lasing occured at transitions not expected to have significant gain, e.g., on two J = 2 - 1 transitions whereas the J = 0 - 1 transition originally predicted to have the highest gain only showed very small gain, if at all.

However, a few years ago significant progress was achieved, when it was observed that the application of a weak pulse several ns ahead of the main pulse was mandatory for the generation of J = 0 - 1 lasing in many neon-like ions. Smoothing of the steep electron density distribution by the prepulse plasma was made responsible for the effect.

We report on a systematic investigation of the prepulse effect on the lasing properties of low-Z neon-like X-ray lasers, by comparing a variety of materials and observing the laser emission spatially and temporally resolved [19]. This study was intended to provide information for an improved understanding of the role of the prepulse in generating gain on the J = 0 - 1 transition.

The experimental setup is shown in Fig. 17. To generate a well-defined prepulse a part from the Asterix IV laser beam (450 - 800 J, 450 ps, 1.315 μm) is coupled out by the mirror M1 and is - in a shortened way via the mirror M2 - directed to the focusing optic. A specially designed cylindrical lens array produced a line focus about 130 μm wide and 30 mm long.

The targets used in the experiments consisted of flat slabs with lengths of up to about 25 mm. For some materials (manganese, scandium, and vanadium) the 100-μm thick target material was glued onto flat Al substrates.

Time-integrated and time-resolved spectra were recorded by using the axial emission from the two sides of the line focus. For the time-integrated spectra a transmission grating spectrometer was coupled to a backside illuminated CCD, and for the time-

resolved data a transmission grating was coupled to a X-ray streak camera with a temporal resolution of 30 ps.

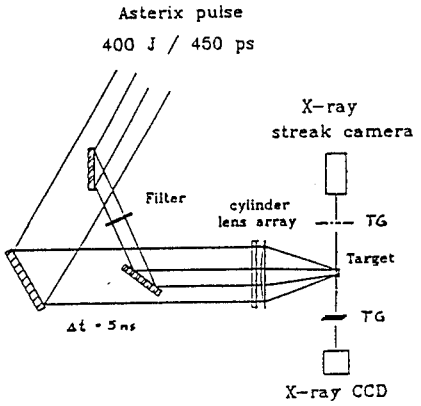


Figure 17. Arrangement to generate a well-defined prepulse.

We observed lasing in the X-ray and XUV region of the spectrum for materials ranging from chlorine to germanium (Fig. 18). Of all materials investigated only germanium lased strongly without a prepulse, e.g., on the well-known J = 2 - 1 lines at 23.2 and 23.6 nm.

The application of the prepulse changed the spectrum dramatically, with the intensity on the J = 0 -1 line (λ = 19.6 nm) by far exceeding the ones on the J = 2 - 1 lines. In all other materials the J = 2 - 1 lines lased only weekly or not at all without the prepulse. With the prepulse the J = 2 - 1 lines were enhanced but the J = 0 - 1 line again dominated the emission. In vanadium an anomalously strong laser emission on a second J = 0 - 1 line was observed.

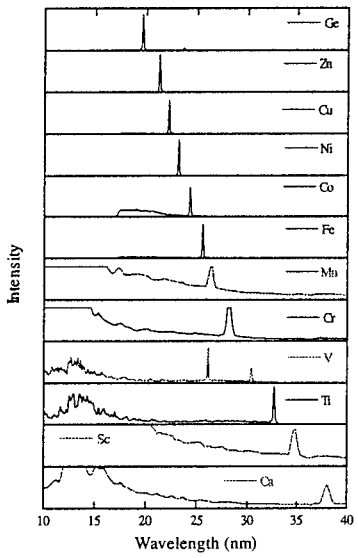


Figure 18. Prepulse induced Neon-like X-ray lasers using Asterix IV.

For zinc the emission on the J = 0 - 1 line at 21.2 nm was measured as a function of the prepulse energy. It was found that the emission was optimized around a prepulse of about 2 % of the main pulse energy. Time-resolved investigation of the laser emission shows that the laser emission is considerably shorter than the duration of the pump pulse.

All of these observations corroborate the simple explanation for prepulse lasing, i.e. that the prepulse generates a plasma with a large scale length and a low density gradient, which is heated to the required electron temperatures

by the main pulse. The J = 0 - 1 gain line requires a higher electron density than the J = 2 - 1 line and is therefore considerably more affected by beam deflection due to an electron density gradient.

This work was supported in part by the Commission of the European Communities in the framework of the Association Euratom / Max-Planck-Institut für Plasmaphysik.

4. References

1. Baumhacker, H., Brederlow, G., Fill. E., Volk, R., Witkowski, S., and Witte, K.J. (1995) Layout and performance of the Asterix IV iodine laser at MPQ, Garching, accepted for publication in *Applied Physics B.*

2. Volk, R. and Stähler, S. (1989) *Proceedings of the Workshop on Iodine Laser and Applications, Liblice,* 44-47.

3. Fill, E., Skrlac, W., and Witte, K.J (1981) *Optics Comm.* **37**, 123.

4. Craxton, R.S. (1980) *Optics Comm.* **34**, 474.

5. Kozlowski, M.R., Wolfe, C.R., Staggs, M.C., and Campbell, J.H. (1990) Large area laser conditioning of dielectric thin film mirrors, *Laser Induced Damage in Optical Materials: 1989, SPIE* **1438**, 376-390.

6. Hagedorn, Ch. and Baumhacker, H. (1993) Neutral solution antireflective treatment of optical glass surfaces, *MPQ-Report* **170**, MPI für Quantenoptik, D-85740 Garching.

7. Floch, H.G. and Belleville, P.F. (1994) Damage-resistant SOL-GEL optical coatings for advanced lasers at CEL-V, to appear in *Journal of SOL-GEL Science and Technology.*

8. Wolfe, C.R., Kozlowski, M.R., Campbell, J.H., Rainer, F., Morgan, A.J., and Gonzales, R.P. (1990) Laser conditioning of optical thin films, *Laser Induced Damage in Optical Materials: 1989, SPIE* **1438,** 360-374.

9. Baumhacker, H., Fill, E., and Schrödter, Ch. (1992) *Private commun.,* MPI für Quantenoptik, D-85740 Garching.

10. Floch, H.G. (1993) *Private commun.,* CEA - Centre d'Études de Limeil-Valenton, 94195 Villeneuve Saint Georges Cedex, France.

11. Bessarab, A.V., Dolgopolov, Y.V., Zhidkov, N.V., Kirillov, G.A., Kochemasov, G.G., and Kulikov, S.M. (1988) *Izwestia Akad. Nauk SSSR, Ser. Fisich.* **52**, 333.

12. Continuum GmbH, (1993) Ti:Sapphire Terawatt Laser Proposal, Continuum GmbH, Boschstr. 12, D-82178 Puchheim.

13. Hammel, B.A., Griswold, D., Landen, O.L., Perry, T.S., Remington, B.A., Miller, P.L., Peyser, T.A., and Kilkenny, J.D. (1993) *Phys. Fluids B* **5**, 2259.

14. Löwer, Th. (1994) Production of multimegabar shock waves in solids by laser-generated thermal radiation, *PhD dissertation,* Universität Frankfurt, Germany, (in German).

15. Winhart, G. (1995) Messung der Absorption von XUV-Strahlung in heißer, dichter Materie, *PhD dissertation,* Techn. Universität, München, (in German).

16. Ramis, R., Schmalz, R.F., and Meyer-ter-Vehn, J. (1988) *Computer Physics Comm.* **49**, 475.

17. Rogers, F.J., Iglesias, C.A., and Wilson, B.G. (1992) *Ap. J.* **397**, 717.

18. Bar-Shalom, A., Oreg, J., and Goldstein, W.H. (1994) *JQSRT* **51**, 27.

19. Fill, E.E., Li, Yuelin, Pretzler, G., Schlögl, D., Steingruber, J., and Nilson, J. (1995) Investigation of lasing on the J = 0 - 1 line of neon-like ions using the prepulse technique, *Proc. SPIE Confer. "Soft X-rayLasers and Applications"*, San Diego.

PART II: Optics

HIGH POWER SOLID STATE LASERS WITH PHASE CONJUGATION FOR APPLICATIONS WITH HIGH BEAM QUALITY

H.J. EICHLER, A. HAASE, O. MEHL
Technische Universität Berlin, Optisches Institut / Sekr. P11,
Straße des 17. Juni 135, D-10623 Berlin, Germany

Abstract

A lot of important laser applications in industry and science require high average output power in conjunction with high beam quality. To increase the beam quality of high power solid state lasers up to the diffraction limit phase conjugation by SBS (stimulated Brillouin scattering) is promising. Oscillators and different master oscillator power amplifier systems (MOPA) with Nd:YALO as active medium and phaseconjugating mirrors were realised. Using simple SBS-cells as phase conjugating mirrors results in an average output power up to 210 Watts at 1.08 μm in a near diffraction limited beam. Applications in material processing were tested with these systems.

1. Introduction

For laser applications like material processing, frequency conversion and plasma generation the brightness of a laser is an important parameter. The brightness depends quadratically on the beam quality, whereas the power has a linear influence. The lowest possible beam parameter product leads to micrometer structures in material processing. In conjunction with high average output power the required time for the process and the material losses during the cutting process decrease. The Rayleigh length of the laser beam increases, so that deep and narrow cuts with a high aspect ratio can be realised. Also the large focal length for a given beam waist results in an increased distance between the target and the focusing optics.

Figure 1 shows the beam quality of industrial laser systems for a given average output power. The CO_2 laser delivers a high beam quality up to powers

R. Kossowsky et al. (eds.), High Power Lasers – Science and Engineering, 241–253.
© 1996 *Kluwer Academic Publishers. Printed in the Netherlands.*

of several thousand Watts, but the solid state laser shows a lower beam parameter product because of the shorter wavelength. However, solid-state laser systems usually show a rapid decrease of the beam quality for higher average output power. The beam distortions are generated by thermally induced lensing and stress birefringence in the active material.

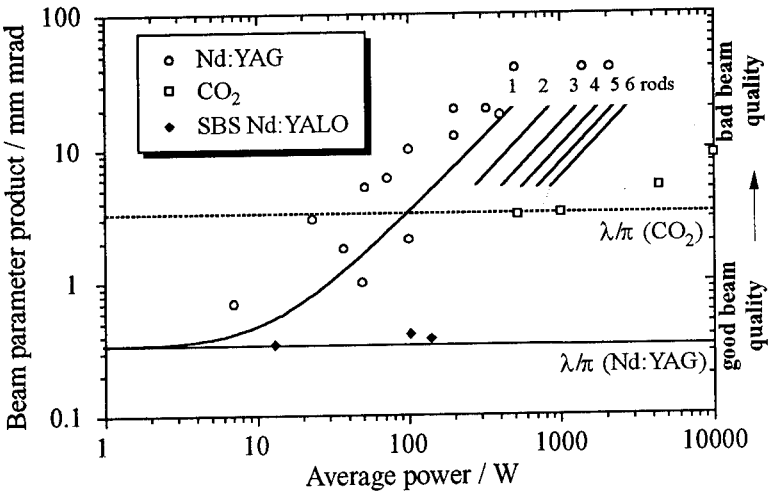


Figure 1. Achieved beam quality for industrial laser systems [1].

Using phase conjugating mirrors, based on stimulated Brillouin scattering (SBS), phase distortions can be compensated resulting in a near diffraction limited beam quality. We have applied this technique to realise solid state laser systems based on Nd:YAG and Nd:YALO as active material in oscillator and master-oscillator power amplifier systems (MOPA).

2. Phase conjugation by stimulated Brillouin scattering

SBS is the major process used for the realisation of self-pumped phase conjugating devices. Liquid and gaseous media of high purity as well as solid materials like glass fibres can be used with high efficiency. SBS means interaction between the incident laser beam with hypersonic sound waves. This process can be described in the following steps:

1. A pump beam is scattered spontaneously in all directions from sound waves of thermal noise.

2. A backscattered, slightly frequency-shifted wave interferes with the incident wave.
3. Electrostriction leads to strong density variations with the period of the interference structure.
4. The induced density variations have the frequency of the initial sound wave, which is amplified therefore.
5. The amplified sound wave reinforces the backscattering, leading to an exponential rise of the reflected signal.

Acoustic waves are pressure and density changes, they are correlated with a refractive index modulation. Therefore backscattering from sound waves can be assumed as reflection from a multi-layer system, comparable to a dielectric mirror. The most important feature of SBS mirrors is that they are light-induced and any disturbance of the incident wavefront will result in a self-adapted mirror curvature with response times in the ns range. As a result the reflected signal is phase conjugated and will be completely corrected after a second pass through phase aberrations. Furthermore, SBS mirrors are self-adjusting and this property is very useful e.g. for resonator mirror applications.

For the construction of SBS mirrors the properties of the used laser have to be considered carefully. In most cases the mirror consists of a cell filled with liquids of gases and a focusing lens to increase the intensity. Focal length and scattering material have to be chosen suitable to achieve a high SBS reflectivity and a good reproduction of the wave front. Unwanted side-effects in the material like absorption, optical breakdown or other scattering processes have to be avoided.

3. Oscillators with SBS-mirrors

Laser oscillators with SBS phase conjugating mirrors have perspective to generate diffraction-limited beam quality up to 100 Watt average output power in a simple way. The highly reflecting mirror in a linear resonator can be substituted by an SBS-mirror to increase the beam quality and to compensate thermal lensing of the pumped laser rod. The SBS-process leads to a simple Q-switch generating short and intensive pulses.

The intensity needed to build up the SBS-mirror has to be provided during the initial stages of the laser process. Therefore, to reach the SBS-threshold an auxiliary resonator L_{Aux} can be used (see Figure 2).

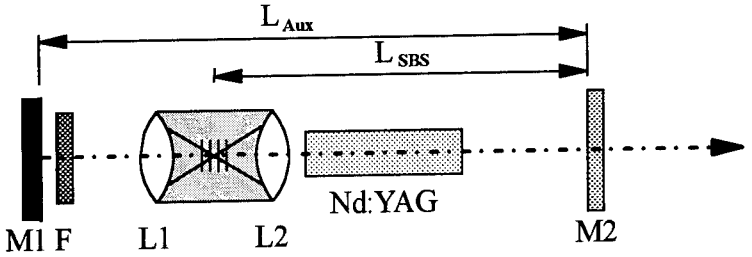


Figure 2. SBS resonator set-up.

The power to build up the SBS-mirror is provided by initial laser oscillation between the mirrors M1 and M2. The two lenses L1 and L2 form a telescope to generate a focal point inside the SBS cell. When the SBS-reflectivity is sufficient, the laser oscillates between M2 and the SBS-mirror, leading to a Q-switch. The longitudinal and transversal mode structures of the two coupled resonators have to be matched in this scheme to achieve a stable laser operation [2,3]. The time to generate the Q-switch is determined by an attenuation filter F, so that the number of pulses in a shot can be adjusted as shown in Figure 3.

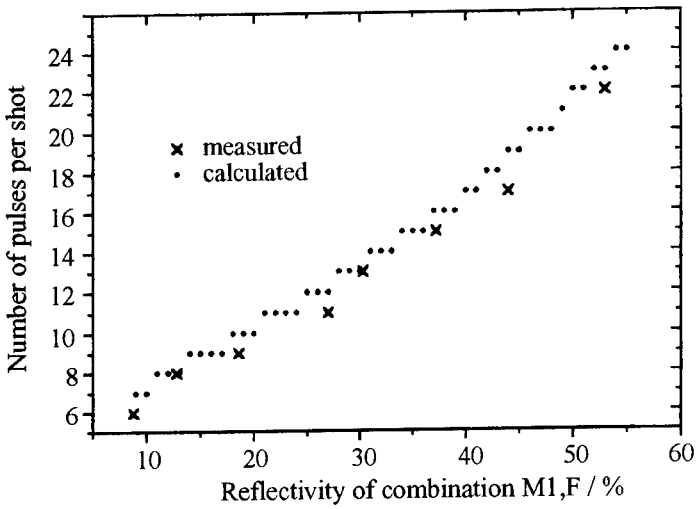


Figure 3. Number of pulses per shot vs. the reflectivity of the combination mirror M1 and attenuation filter F [4].

Experimentally, a system with a single Nd:YAG rod and an average output power up to 17 Watts (Figure 4) has been realised with a nearly diffraction-limited beam. As SBS-material SF_6 at 20 bar was used.

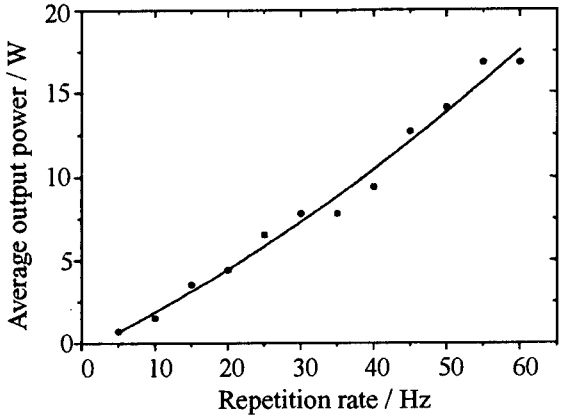


Figure 4. Average output power vs. frequency of a Nd:YAG-SBS-oscillator [4].

Because thermal lensing is compensated, the laser power can be tuned from 3 to 17 Watts with no remarkable changes in the transversal beam profile. Figure 5 shows the transversal beam profiles measured in a distance of 1 m from the outcoupling mirror.

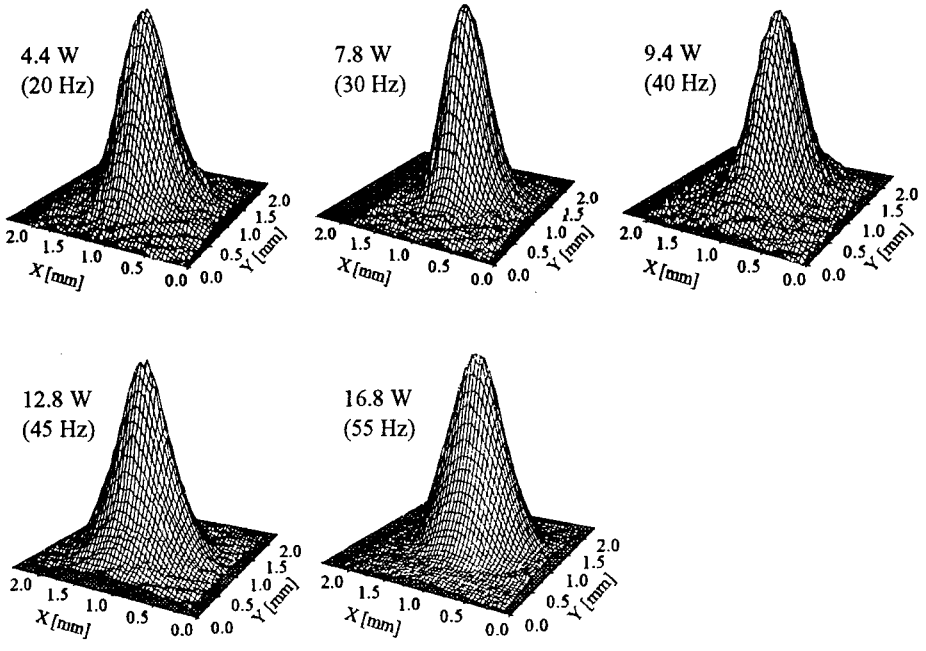


Figure 5. Transversal beam profile for different average output powér [4].

In this set-up the temporal emission of the oscillator consists of a train of 10 Q-switched pulses per shot with an FWHM of 30 ns.

To reduce the complexity of such a system shown in Figure 2 the lens L1 and the mirror M1 can be integrated into the SBS-cell [5].

4. Oscillator amplifier systems

Master oscillators with power amplifiers (MOPAs) are effective to achieve high average power. Phase distortions in highly pumped amplifiers like thermal lensing can be compensated using SBS mirrors.

4.1. One amplifier system

To avoid the complexity of existing SBS-systems with Nd:YAG [6,7] based on diode pumping and slab laser technology we developed a flashlamp pumped double-pass MOPA with a single Nd:YALO rod amplifier [8,9]. Carbon disulfide (CS_2) is used as the SBS medium because of its low threshold (20 kW) to reduce the peak power for applications like material processing. The used active material shows a higher efficiency than Nd:YAG (see Figure 6) probably because of more active ions per volume.

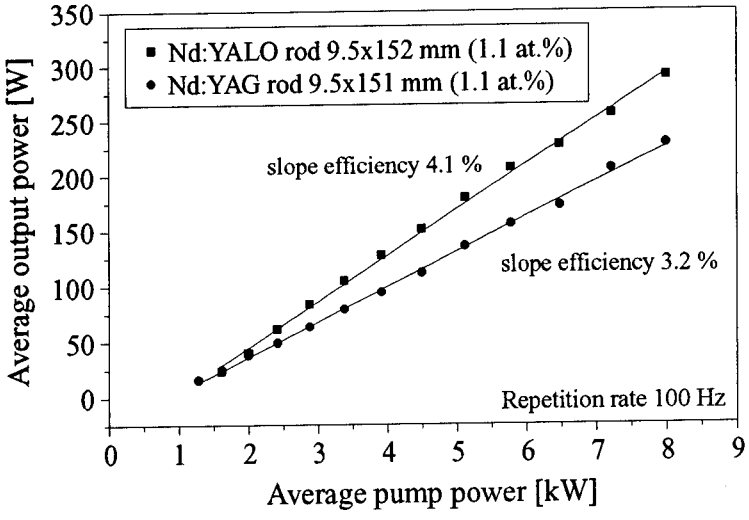


Figure 6. Average output power of a free running oscillator for different active material.

Figure 7 shows the used set-up. The oscillator delivers an average output power up to 6 Watt with diffraction-limited beam quality. The system works with a repetition rate of 100 Hz and emits per shot a burst of Q-switched pulses generated by a Cr^{4+}-doped YAG crystal [10]. Additional etalons increase the coherence length to achieve a high SBS reflectivity.

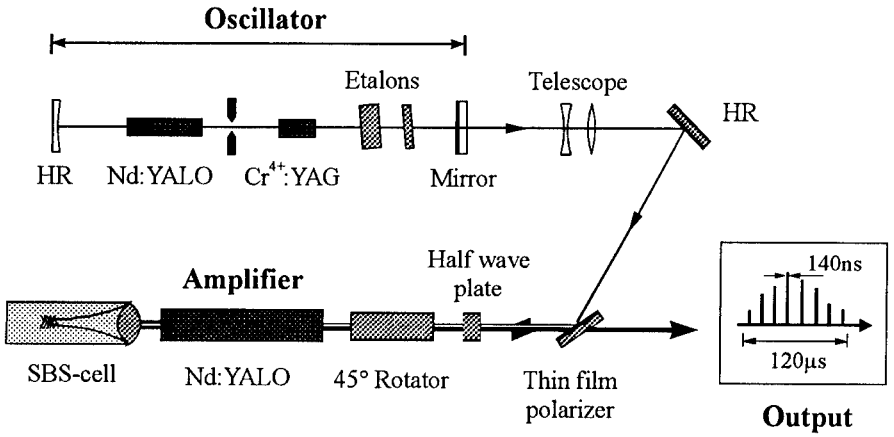


Figure 7. Single rod Nd:YALO double-pass amplifier with an SBS-mirror.

The beam of the oscillator is coupled into the amplifier rod by a thin film polariser. After the first pass, the transversal beam profile is changed severely by phase distortions and focused by thermal lensing. After the second pass, thermal lensing and other phase distortions are compensated due to effective SBS-phase conjugation, so that the transversal beam profile is reproduced (see Figure 8) and a 1.1 times diffraction-limited beam quality is obtained.

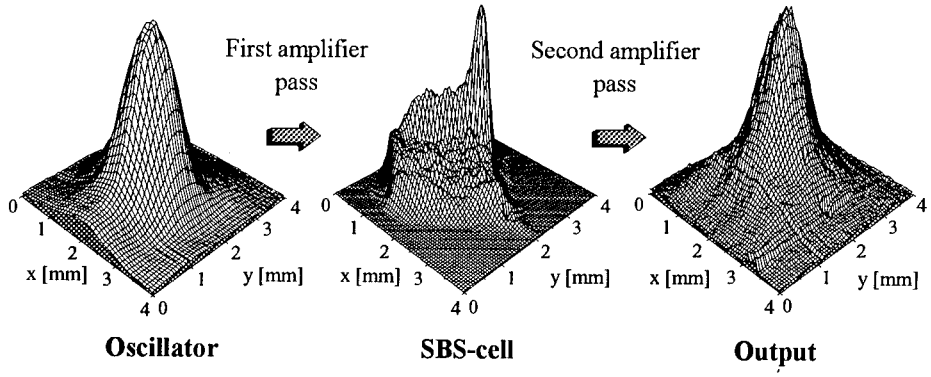


Figure 8. Reproduction of the transverse beam profile.

Because thermal lensing is compensated, the output power can be tuned from 4 W to 140 Watts without changes of the beam profile and the beam quality. In contrast to commonly used Nd:YAG, the Nd:YALO-crystals are optically anisotropic and show no remarkable stress birefringence. Therefore, depolarisation losses in the pumped laser crystals are negligible. Losses in the output power and a decrease of the beam quality due to depolarisation can be avoided. To tune the polarisation of the incident beam for maximum amplification in the YALO crystal we used a half-wave plate.

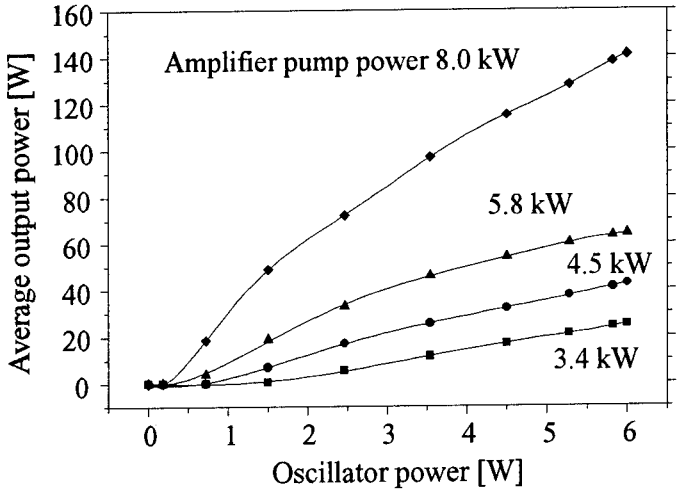


Figure 9. Average output power vs. the used oscillator power for different amplifier pump power.

4.2. Two amplifiers in a serial arrangement

To achieve an average output power in the range of several 100 Watts, serial arrangements of amplifiers are under development [11]. Figure 10 shows the used set-up. As master oscillator a ring laser was developed to achieve a high coherence length with only one etalon. The two rod amplifiers are flash lamp pumped with a total average pump power up to 18 kW at a repetition rate of 100 Hz. An optical system between the amplifiers permits to vary the average pump power of both amplifiers without damage of optical components. The two lens system matches also the beam diameters to the laser rod diameters to achieve a good extraction of both amplifiers despite of thermal lensing.

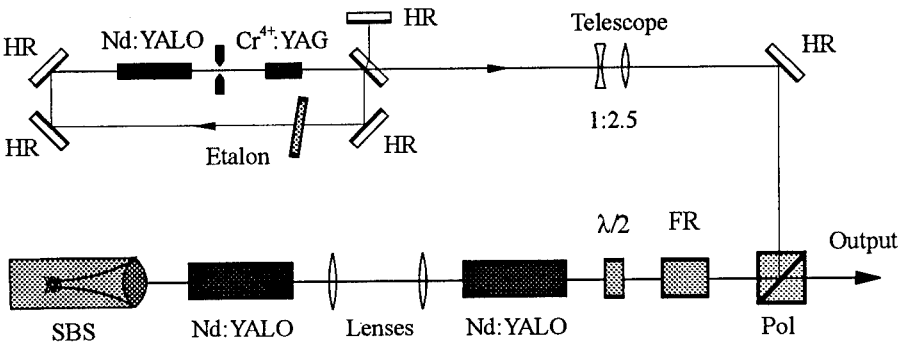


Figure 10. Nd:YALO system with two amplifiers in a serial arrangement.

As a first result the output power is tuneable from 1 up to 210 Watts in a near diffraction limited beam (Figure 11). An optimised version of this system is under development to increase the average output power up to 300 Watt.

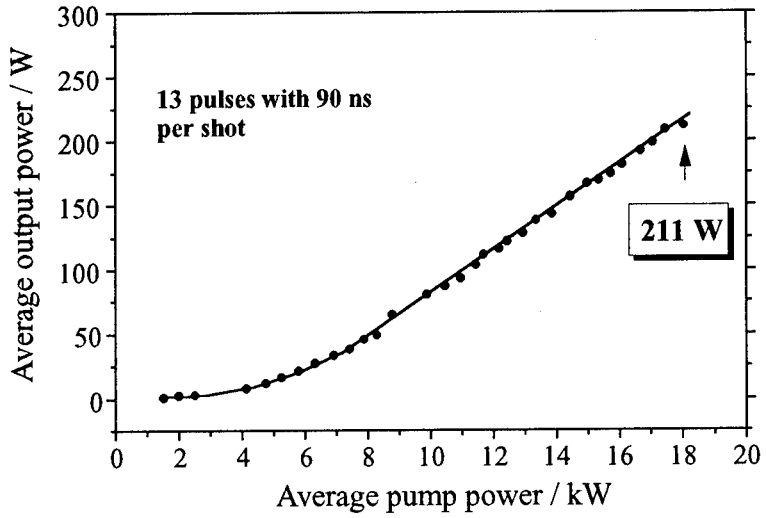


Figure. 11. Average output power vs. average pump power for the serial arrangement.

5. Precision drilling and cutting

Drilling was investigated at high average power in metals, glasses and ceramics with different thickness from 50 μm up to 1 cm, using focusing lenses with focal lengths from 500 mm down to 100 mm. Due to the high beam quality small

holes can be produced, e.g. bore diameters below 4 μm in aluminium were realised (Figure 12).

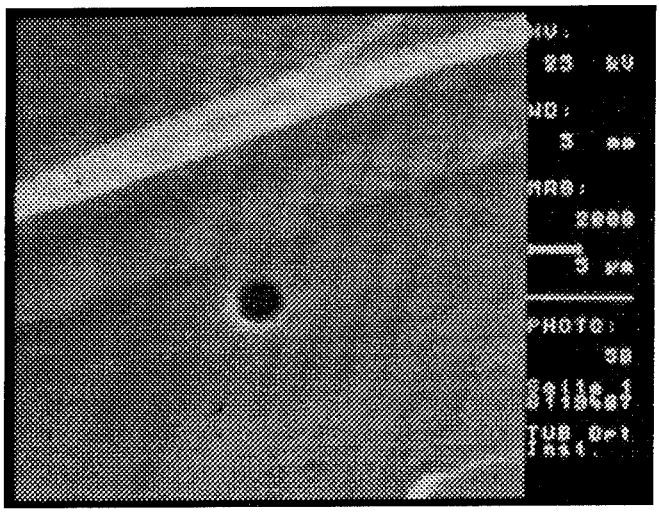


Figure 12. Precise hole in aluminium (thickness 100 μm, bore diameter 4 μm).

The used laser repetition rate of 100 Hz allows fast drilling of hole arrays (one hole can be drilled with one shot). Figure 13 shows a photograph of a hole array in aluminium. The holes have a diameter of 20 μm and are separated by 45 μm. The translation stage was moved with a speed of about 0.45 cm/s. The drilling time per hole is in the range of 100 μs, so that the geometry of the holes cannot be deformed by the used translation speed. The different diameters are due to material inhomogeneities.

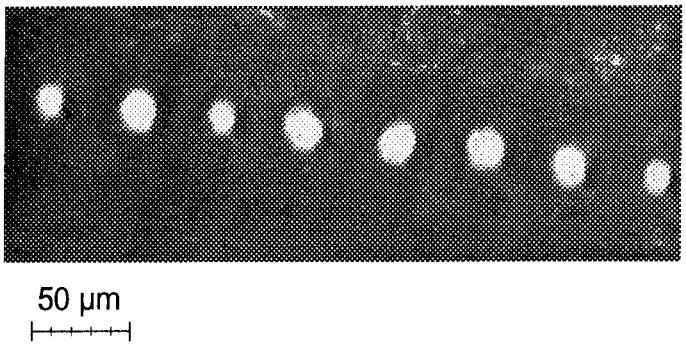


Figure 13. Array of holes in aluminium (bore diameter 20 μm, bore distance 45 μm)

Because of the high Rayleigh length, cuts and holes can be realised with a high aspect ratio and dimensions in the μm-range. Figure 14 shows a cutting kerf in ceramics for different positions of the focal point relative to the target. For the best configuration a kerf width of 30 μm was realised with an aspect ratio of 1:37. At high average output power, holes with high aspect ratio in thick material are possible, e.g. hole diameters of 60 μm in aluminium with a thickness of 0.5 cm and a drilling time of 0.4 seconds were demonstrated. These results show the advantages of the used high beam quality.

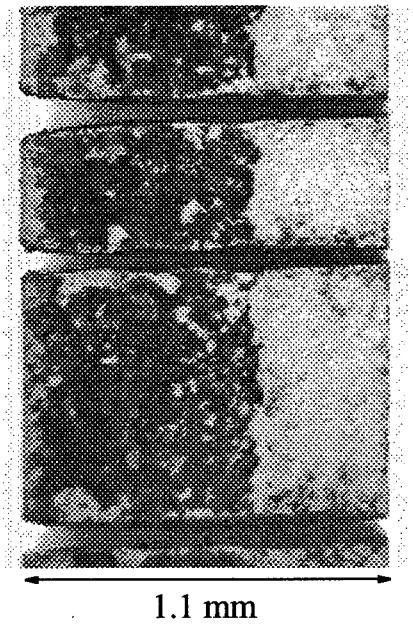


Figure 14. Cutting kerf in ceramics.

6. Summary

Phase conjugation by SBS is a powerful tool to increase the beam quality of high power solid state lasers up to the diffraction limit. Oscillators based on Nd:YAG and master oscillator power amplifier systems with Nd:YALO as active medium were realised. An oscillator was realised with an average output power tuneable from 3 up to 17 Watt in a near diffraction limited beam. A simple single rod amplifier system was optimised to produce an average output power tuneable from 4 up to 140 Watt with a beam quality of 1.1 times the diffraction limit. With a serial arrangement of two amplifier rods as a first result

an output power from 1 up to 210 Watt was obtained. Thermal lensing was compensated resulting in a constant beam diameter independent of the output power. With these systems material processing experiments were carried out. Due to the high beam quality structures of 4 μm in aluminium and cuts in ceramics with a kerf width of 30 μm and an aspect ratio of 1:37 are demonstrated.

7. Acknowledgements

The authors wish to thank the following co-workers for experimental help and stimulating discussions: E. Geinitz, S. Jobst and R. Menzel. Financial support from the Bundesministerium für Bildung, Wissenschaft, Forschung und Technologie (BMBF) and the Verein Deutscher Ingenieure (VDI) is greatfully acknowledged.

8. References

1. N. Hodgson and H. Weber (1994) Optische Resonatoren, Springer-Verlag.
2. A. Kummrow, R. Menzel, D. Schumann, H.J. Eichler (1993) Length tuning effect in SBS-lasers, Int. J. of Nonl. Opt. Phys. **2** , 261-266.
3. H.J. Eichler, Chen Jun, A. Kummrow, R. Menzel, D. Schumann, (1993) Nd-YAG-Laser with SBS-Q-switching mirror and repetition rate up to 50 Hz, Int. J. of Nonl. Opt. Phys. **2** , 187-204.
4. E. Geinitz: Diploma thesis, Optisches Institut, TU Berlin, 1994.
5. R. Scherrer: Diploma thesis, Optisches Institut, TU Berlin, 1994.
6. M. Hermann, J. Honig, L. Hackel (1995) High-average-power diode-pumped solid-state laser for industrial applications, Technical Digest: Conference on Lasers and Electro-optics '95 **15**, 61.
7. TRW Space and Electronics Group (1995) Diode array-pumped kilowatt laser (DAPKL) Program, CLEO '95 post deadline paper CPD30
8. H.J. Eichler, A. Haase and R. Menzel (1995) 100-Watt Average Output Power 1.2 Diffraction Limited Beam from Pulsed Neodymium Single-Rod Amplifier with SBS Phase Conjugation, IEEE J. Quantum Electron. **31**, 1265-1269.
9. H.J. Eichler, A. Haase, R. Menzel, High Beam Quality by SBS Phase Conjugation of a Single Rod Nd-Amplifier up to 140 Watts Average Output Power, Opt. Lett. (submitted).
10. H.J. Eichler, A. Haase, M.R. Kokta, R. Menzel (1994) Cr^{4+}:YAG as Passive Q-Switch for a Nd:YALO Oscillator with an Average Repetition Rate of 2.7 kHz, TEM_{00} Mode and 13W Output, Appl. Phys. B **58**, 409-411.

11. H.J. Eichler, A. Haase and R. Menzel (1995) Power enhancement and application of a Nd:YALO rod amplifier with a phase conjugating mirror, Technical Digest: Conference on Lasers and Electro-optics '95 **15**, 61-62.

LASER RESONATOR CONCEPTS

Described some new resonator arrangements and their employment in powerful lasers.

S. G. ANIKITCHEV

1. Introduction

The theory of laser resonators is now in an advanced stage of development. Most prominent in the investigation of resonators are schools of Prof. Yu. A. Anan'ev [1] from Russia and Prof. A. E. Siegman [2] from USA. By now calculational techniques of open resonators have basically been developed. The basic types of resonators (stable and unstable resonators) have been devised. The new resonator arrangements arise rather seldom. The line of investigations is currently directed towards an application of existing knowledge in different areas of laser industry.

Our principal concern will be with the area of powerful CO_2 lasers for industrial applications and chemical lasers. All laser resonators may be classified under three chief groups:

- open resonators for lasers with usual form of its cross section (circular or right-angled);
- open resonators for lasers with annular form of active medium and
- wave-guide resonators.

2. Open Resonators, Usual Form of Active Medium

Open resonators are used in most types of lasers. We shall restrict our consideration to the case of standing-wave resonators that are in use in powerful lasers. Stable, plane and unstable open resonators show different characteristics in operation, but at the same time have certain features in common with each other.

General properties of open resonators are understood by diffraction theory.

2.1. MATHEMATICAL DESCRIPTION

To a good approximation the electromagnetic field in open laser resonators is transversal and can be described in the framework of scalar theory. The eigen oscillations of the resonator (quasi modes) are described by the functions of the form

$$U(x,y,z,t) = u(x,y) \cdot \exp[-i(\omega t - kz)], \quad (1)$$

R. Kossowsky et al. (eds.), High Power Lasers – Science and Engineering, 255–282.
© 1996 *Kluwer Academic Publishers. Printed in the Netherlands.*

where $\omega = \omega' - i\,\omega''$; ω', $\omega'' \in \mathbb{R}$, $\frac{\partial u}{\partial z} << \frac{\partial u}{\partial x}, \frac{\partial u}{\partial z} << \frac{\partial u}{\partial y}$. The imaginary part ω'' of the frequency describes attenuation of the field with time in empty open resonators, whereas the distribution of the complex field amplitude does not depend on time: $u(x,y,z) = const(t)$. It is usual to produce an equation that describes function $u(x,y,z)$ by using Huygen's integral operator [3]. From the fact $\omega \in \mathbb{C}$ it follows that propagation constant $\beta = \omega/c$ is also complex:

$$\beta = \beta' - i\beta'', \tag{2}$$

where $\beta' = \omega'/c$, $\beta'' = \omega''/c$. That is to say that we have to consider waves from a damping source; the greater is a distance from the source, the greater is an amplitude of the wave at given time. The relationship between distributions at two reference planes separated by distance L (in empty space) can be described, in view of (2), as follows:

$$u(x_2, y_2, z+L) = exp(i\beta' L + \beta'' L) \cdot \int_A \mathbb{K}(x_1, y_1, x_2, y_2, L) u(x_1, y_1, z) dx_1 dy_1 \tag{3}$$

where $K(x_1,y_1,x_2,y_2,L) = (i\lambda L)^{-1} exp[i\,\beta\,\Delta L(x_1,y_1,x_2,y_2,L)]$ is a Huygen's propagation kernel; function $\Delta L(x_1,y_1,x_2,y_2,L) = \rho(\{x_1,y_1\}, \{x_2,y_2\}) - L$ gives the added optical path variation over the basic distance L between reference planes, this variation is usually calculated within paraxial approximation (correct to second order of $x_{1,2}$ and $y_{1,2}$); differential $dx_1 dy_1$ is integrated over the full cross section A of an input aperture. Equation (3) gives us an opportunity to compile an equation that describes the field distribution in open resonator or periodic optical structure:

$$\begin{aligned} u(x,y,z) &= exp(2i\beta L) \cdot \int_A \mathbb{K}(x,y,x_0,y_0,z) \cdot u(x_0,y_0,z) dx_0 dy_0 \equiv \\ &\equiv exp(2i\beta L) \cdot \hat{\mathbb{P}}\big(u(x_0,y_0,z)\big), \end{aligned} \tag{4}$$

where propagation kernel $\mathbb{K}(...)$ includes any finite mirrors, apertures and intracavity optics in the resonator. The integral (4) corresponds to one round trip through the resonator, the reference plane z is arbitrary chosen inside the cavity. The operator $\hat{\mathbb{P}}$ (depending on z) is referred to as an operator of round trip. By assuming that the set of eigen functions (or "transverse eigen modes" or "Fox and Li modes") $\{u_n(x,y,z)\}_{n=0,1,...}$ and the set of eigen values $\{\gamma_n\}_{n=0,1,...}$ (we write only one transverse index "n" for simplicity) of operator $\hat{\mathbb{P}}$ are known, i.e.

$$\hat{\mathbb{P}}\, u_n = \gamma_n u_n \equiv exp(-i\,\delta_n' - \delta_n'')\, u_n\,, \tag{5}$$

one obtains with regard to Eq. (4) an equation $exp\,(2i\beta L - i\delta_n' - \delta_n'') = 1$, whence it follows that

$$\omega'_{n,q} = \frac{c}{2L}(2\pi q + \delta_n'), \tag{6}$$

$$\omega''_{n,q} = \frac{c}{2L}\delta_n''. \tag{7}$$

Eq. (6), Eq. (7) define the complex frequency of quasi modes that are given by Eq. (1). From Eq. (7) it follows that the power loss for the nth mode in one round trip due to diffraction is $\Delta_n \equiv 1 - exp(-2\,\delta_n'') = 1 - |\gamma_n|^2 = const(q)$; δ_n' gives the phase variation caused by terminal size of the beam in transversal direction for the same mode ($\delta_n' = 0$ corresponds to a plane wave of an infinite extend). Operator $\hat{\mathbb{P}}$ depends on position z of the reference plane, consequently Eq. (4), or Eq.(5) provides the transverse

eigen modes only at that plane. The mode variation with z can be determined by propagation of the mode from reference plane with a help of Huygen's operator, Eq. (3). Unlike transverse eigen modes, the eigen values γ_n (together with power losses Δ_n and phase variations δ_n') are entirely independent of the choice of z. This fact is simpler to understand physically, though the rigorous mathematical treatment may become complicated.

2.1.1. *Some general properties of eigen modes*

All necessary information about field in open resonator can result from Fredholm integral equation (5). For an empty open resonator Eq. (5) is a conventional eigen value problem for the linear integral operator $\hat{P}$. This operator falls to a thoroughly studied category of compact or completely continuous linear operators, see, for example [4].

It is well known that eigen values (and eigen functions) of compact operator form at most a countable set. Generally the eigen values $\gamma_n \in \mathbb{C}$ and therefore $u_n(x,y,z)$ are complex-valued. Because we consider the open systems, operator $\hat{P}$ is not Hermitian. The theory of operators can not rigorously guarantee an existence of eigen elements in that case. But in resonator theory it is agreed by analogy with quantum-mechanics operators that for every resonator operator a set of eigen functions (and eigen values) with an infinity of members exists, i.e. one can use the set $\{u_n(x,y,z)\}$ and the set $\{\gamma_n\}$ where $0 \le n < \infty$. This agreement is based on a fact that it is comparatively easy to calculate several first modes for each open resonator or lens guide configuration.

It should be noted that by proper chose of reference plane z (at one of the mirrors) the operator $\hat{P}$ of round trip can be done symmetrical, that is to say that for an arbitrary chosen couple of functions f and g one can write

$$\int_A f\hat{P}(g)\,dS = \int_A g\hat{P}(f)\,dS\,, \tag{8}$$

where A - surface of the mirror, $dS = dx\,dy$ or $dS = r\,dr\,d\theta$. Substitution of nondegenerate eigen modes u_n and u_m ($n \neq m \Rightarrow \gamma_n \neq \gamma_m$) for f and g in Eq. (8) gives

$$\int_A u_n u_m\,dS = 0, \quad n \neq m. \tag{9}$$

Eq. (9) shows that eigen modes of open resonators are not "normal modes", i.e. they are not power orthogonal, though Eq. (9) and property of power orthogonality are similar in appearance. This superficial analogy in properties of complex symmetrical and Hermitian operators suggests the authors of [5,6] to use the set of "Fox and Li" modes for expansion of arbitrary functions into series of the form

$$f = \sum_{n=0}^{\infty} c_n u_n \tag{10}$$

where $c_n = \int_A f u_n\,dS \Big/ \int_A u_n^2\,dS$. Such an approach is not correct. There are examples [7], in which expansion (10) not only does not converge on initial function f but does not even give the result with finite power. By this is meant that generally a set of eigen functions $\{u_n\}$ of resonator operator $\hat{P}$ does not form a complete system. It is well known [8] that a set of eigen transverse modes $\{u_n^0\}$ of a confocal resonator (or confocal lens guide) operator $\hat{P}_0$ is a basis set; in addition,

$\forall n \; u_n^0 \in \Re$ and from Eq. (9) it follows that they are power orthogonal with the result that $\left\langle u_n^0, u_m^0 \right\rangle \equiv \int_A u_n^0 u_m^0 dS = \int_A u_n^0 u_m^0 dS \equiv \left(u_n^0, u_m^0\right) = \delta_{mn}$.

It is easy to show (see App. 1) that the confocal resonator is the only resonator among that with hard-edged finite mirrors which has transverse modes forming a basic set.

The second (and the last) example of resonator with the basic set of eigen functions is a hypothetical stable resonator with infinite mirrors. Such a resonator has no losses for every eigen mode. So eigen modes are real functions and they are orthogonal in usual Hermitian sense. The completeness of this set in the space of square-integrable functions defined at two-dimensional subspace is evident from an explicit form of eigen modes. It is common knowledge (see, for example [1,2]) that these transversal modes are described by the functions of the form

$$\varphi_{mn}(x,y,z) \sim u_{m,n}(x,y,z) = \frac{w_0}{w(z)} H_m\left(\frac{x}{w(z)}\sqrt{2}\right) H_n\left(\frac{y}{w(z)}\sqrt{2}\right) exp\left(-\frac{x^2+y^2}{(w(z))^2}\right)$$

if we use Cartesian coordinate system and

$$\varphi_{pl}(\rho,\phi,z) \sim \left(\frac{\rho}{w(z)}\sqrt{2}\right)^l L_p^l\left(\frac{\rho^2}{(w(z))^2}2\right)\begin{Bmatrix} sin(l\phi) \\ cos(l\phi) \end{Bmatrix} \cdot exp\left(-\frac{\rho^2}{w(z))^2}\right)$$

if one uses the polar system; H_n is a designation of well known in quantum theory Hermitian polynomials; L_p^l is a designation of Laguerre polynomials; $\rho \equiv \sqrt{x^2+y^2}$; $w(z)$ - mode parameter depending on a length of resonator L and curvature of resonator mirrors R_1, R_2.

The lack of convenient (complete and orthogonal) set of eigen functions makes the analytical calculations of most if not all of the resonators too difficult even in a case of empty cavities. This is just the reason of appearance of some specialized methods for numerical resonator computations. We shall take a quick look at two methods in most common use for all types of open resonators under the next heading.

2.1.2. *Numerical techniques.*

- Fox and Li method [3]

It is an iterative method [9] of solving of the linear eigen value problem (Eq. 5) for the fundamental $(n = 0 \Leftrightarrow (m,l) = (0,0))$ mode for an arbitrary resonator : $\hat{P} u_0 = \gamma_0 u_0$ or, for simplicity, $\hat{P} u = \gamma u$. They started with the uniform initial distribution of the wave amplitude. Formally the iterative process can be written in a form: $u^{(i+1)} = \hat{P} u^{(i)}$. The process is over when $\gamma = \dfrac{u^{(i+1)}(x,y)}{u^{(i)}(x,y)} = const(x,y,i)$, where "$i$" is a current number of an iteration; the reference plane is chosen at one of the mirrors. Although this approach was initially applied for the empty plane (or Fabri-Perot) resonator, it was later successfully used for calculations of open resonators of all types and for the first numerical investigations of the mode competition in presence of a saturable active medium [10]. The success of applying of this approach depends on the problem to be solved.

A very important dimensionless parameter in the resonator theory is the Fresnel number $N_{Fr} = a^2/\lambda L$, where a is a half of resonator aperture, λ is a wavelength, L is a distance

between resonator mirrors. The Fox and Li algorithm is effective only if $N_{Fr} < 5$. The first reason is that the necessary number N_t of operations to calculate field in the resonator is proportional to the second power of N_{Fr} ($N_t > 16^*[N_{Fr}]^2$) and becomes too great if $N_{Fr} > 5$. The second reason is that the requisite number of iterations for resonators with great apertures (N_{Fr}) is growing up to hundreds.

- Fourier transform method [11]

The author of [11] avoided the difficulties associated with the huge volume of Fox and Li computations by Fourier transform of the Cartesian resonator integral equation. The requisite number of grid points at the chosen cross-section would remain as before. A considerable gain in computation time can be obtained by using a technique of Fast Fourier Transform (**FFT**). In this case N_t is proportional to $N_{Fr} \cdot ln(N_{Fr})$. A related technique of Fast Hankel Transform (**FHT**) is in use [12] for the calculation of the resonators with circular mirrors. The difficulties associated with calculations of high order eigen modes (and eigen values) are common to both numerical techniques. One way around this problem is to use some semianalytical method of mode calculations described under the next heading.

2.1.3 *Semianalytical techniques.*

These methods are in use for the stable resonators.

- The approach using expansion of kernel [13]

The essence of the method is in the 2-dimensional expansion of the kernel, Eq. (14), in series with the use of basic set of the confocal resonator modes $\{u_n^0\}$. Such an approach is properly changing Eq. (14) to the equation with finite-dimensional degenerate kernel. The last equation may be rearranged to give the eigen value problem for a system of linear equations. The system can be numerically solved for the unknown eigen values and eigen vectors with the use of perturbation methods. The eigen values as usually give the phase shifts and losses for the several lowest modes, the eigen vectors enable the field distributions to be found at any point. In consequence of the use of a confocal resonator as a referent system, this method gives a good accuracy only for resonators that are close to confocal one.

- The approach using expansion of desired modes [14]

As already noted, the second example of resonator with the basic set of eigen functions is a stable resonator with infinite mirrors. To have an opportunity to use this basic set $\{\varphi_n\}$ for the expansion of desired functions into series we looked for coming to the mirror instead of reflected from the mirror wave. By this is meant that required functions are defined in the interval $\{[-\infty, +\infty] \times [-\infty, +\infty]\}$. Detailed consideration concerning this method of calculations one can find in App. 2. Some results of such calculations allowed to argue against the "geometrical" point of view [15] that for the resonators not so close to the plane (or concentric) one power loss of n-th mode may be approximately calculated in a form

$$\Delta \approx \int_{-\infty}^{\infty} h(x) \cdot (\varphi_0)^2 dx = 1 - \int_{-\sqrt{c}}^{\sqrt{c}} (\varphi_0)^2 dx. \qquad (11)$$

The diffraction approach [14] gives another result:

$$\Delta \approx \int_{-\infty}^{\infty} h(x)\cdot(\varphi_n)^2 dx = 1 - \int_{-\sqrt{c}}^{\sqrt{c}} (\varphi_n)^2 dx. \qquad (12)$$

The distinction between Eq. 11 and Eq. 12 is caused by the fact that one portion of power p_{nn} is passing by the resonator mirrors (the geometrical part of loss), the other portion p_{nn} is scattering to high order modes (the diffracting part of power loss). Eq. 12 gives a simple recipe for the loss estimations; it works well if $g_1 g_2 < 0.9$. The distinguishing features of this approach from the previous one are:

- the initial resonator system has the same configuration (the length L of resonator and curvatures $R_{1,2}$ of mirrors or $g_{1,2}$ - factors), as a system to analyze;
- the complex amplitude of incident wave is always more smooth then that of reflected one, therefore it is easiest to treat;
- the calculations with the set $\{\varphi_n\}$ is more simple then that with the set of eigen functions of confocal resonator.

These features allow to calculate eigen modes and eigen values of stable resonators throughout the entire range of configuration parameters $0 < g_1 g_2 < 1$.

2.2 STABLE RESONATORS

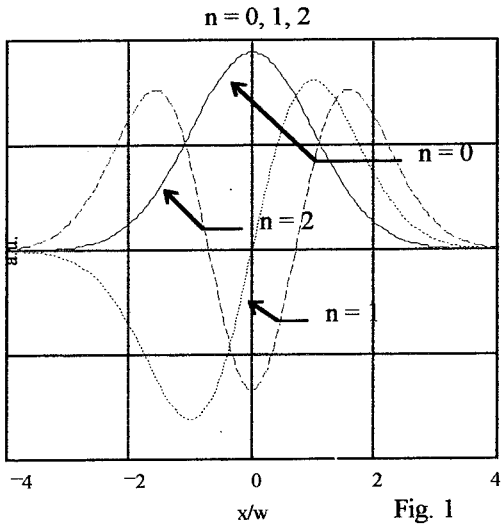


Fig. 1

In the field of powerful industrial lasers (up to several kW) the stable resonators are of great utility. Let us consider first of all some properties of their modes.

2.2.1. *Modes of stable resonators.*

We shall consider the field distribution over the resonator cross section and neglect the field structure over the resonator axis. It is a common knowledge that modes of hard edged stable resonators are very close to ideal modes of stable resonators with infinite mirrors. Three first two-dimensional ideal modes are shown in the picture. One can see from the Fig. 1 that all modes are of different volume inside the gain volume. It is evident that efficient laser with the stable resonator has to work in a multimode regime. The multimode oscillation originates from an inhomogeneity in the inverse population distribution induced by the fields of individual oscillating modes, see Fig. 2.

2.2.2. *Criterion of single-mode oscillation*

Single transverse mode oscillation is usually achieved by restricting the gain volume (the use of resonator with small Fresnel numbers, the use of intracavity apertures and telescopes). The conditions of single-mode operation, whose far field distribution is favorable for most applications, are traditionally determined experimentally. Some years ago we undertook the investigation to describe the mode competition in active stable resonators and to derive the analytical criterion of single mode oscillation [16].

The mathematical model of the process includes:

extensionality of gain medium (undertaking numerical calculations we can only consider a gain medium as some infinitely thin layers);

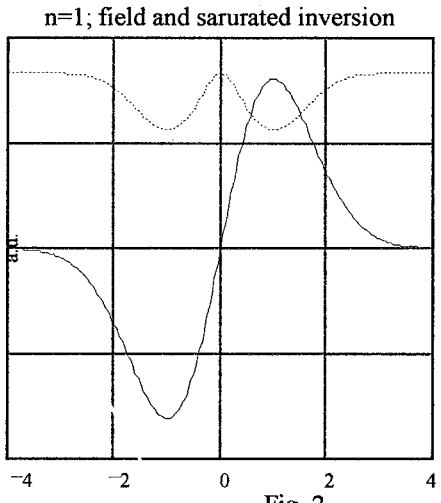


Fig. 2

the cases of weak and strong saturation of inversion;

the case of the nonuniform initial distribution of inversion.

Let us consider the state of laser with a homogeniously excited active medium which has stable resonator oscillating in one fundamental mode u_{00} . In the case of weak saturation (small excess of the threshold, when $u_{mn}(x,y,z) \approx \varphi_{mn}(x,y,z)$ or $u_{mn}(\rho,\phi,z) \approx \varphi_{mn}(\rho,\phi,z)$) the shape of the gain coefficient over the cross section takes the form [17]: $k(x,y,z) = k_0 - \eta(z) exp[-2(x^2+y^2)/w^2(z)]$, where k_0 is the value of an amplitude unsaturated gain, $\eta(z)$ is a function depending on lasing power and the parameters of active medium. As is shown in [17] the effective gain coefficient ξ_{mn} for the given mode u_{mn} under these conditions is given by the equation

$\xi_{mn} = k_0 - \eta(z) \iint_{R^2} exp\left[-2\frac{x^2+y^2}{w^2(z)}\right] \cdot |u_{mn}|^2 dxdy \equiv k_0 - \eta(z) \cdot q_{mn}$. It can easily be shown that $q_{mn} = const(z)$; $q_{00} = 1/2$; $q_{01} = q_{10} = 1/4$. Therefore, the summarized gain coefficient over the resonator length L can be described by the equation

$\int_{z=0}^{z=L} \xi_{mn}(z)dz = k_0 L - q_{mn} J$, where $J = \int_{z=0}^{z=L} \eta(z)dz$. Taking into account the power loss due to reflection and due to diffraction we can find the equation for the round trip eigen value Γ_{mn} of the resonator with active medium:

$\Gamma_{mn} = \sqrt{R}\gamma_{mn} exp[2(k_0 L - q_{mn} J)]$, where γ_{mn} is an eigen value of the empty resonator, R is a reflection coefficient of the output mirror. Now the condition of single mode oscillation is following:

$$|\Gamma_{00}| = 1 \tag{13}$$

$$\text{and } |\Gamma_{mn}| < 1 \ \forall m,n: \ m+n \geq 1. \tag{14}$$

As shown in [17] it is only necessary to check inequality (14) for the modes with $m+n = 1$. Having solved Eq. (13), (14), we obtain the desired criterion of single mode oscillation:

$$ln\left(\frac{1}{R(1-\Delta_{00})}\right) \leq 4k_0 L \leq ln\left(\frac{1-\Delta_{00}}{R(1-\Delta_{01})^2}\right), \tag{15}$$

where Δ_{mn} is a power loss for 'mn' mode of an empty resonator. When inequality (15) is valid one can find from the Eq. (13) the value of J and the power of single mode oscillation. The criterion under the conditions when the saturation is strong or the initial distribution of inversion is not constant over the cross section of resonator one can find in [17]. As it was shown there, the range of single-mode oscillation may be expanded by the use of lasers with nonuniform (its maximum is on the optical axis) initial distribution of inversion or by the use of resonators with variable reflectivity mirrors. This fact can be very important with recent achievements in laser technology: diode pumping of solid-state lasers with cylindrical active medium and development of high reflecting mirrors with nonuniform distribution of the reflection coefficient [17].

An important conclusion can be drawn from the inequality (15): the possibility of single mode operation is determined by the difference of mode losses instead of their ratio. This means that single-mode oscillation may be stable only if the loss for fundamental mode Δ_{00} is high (the difference Δ_{01} - Δ_{00} reaches reasonably large value only if both Δ_{00} and Δ_{01} are high). It is evident that this conclusion is valid not only for stable but also for plane and unstable resonators.

2.2.3. *Multimode lasing in stable cavities with spherical mirrors*

In a quantity of applications, for instance in cutting and welding, it is important to know the power ratio of different oscillating modes (in a case if the condition of single-mode lasing can not be fulfilled). Let us consider some results of [18] to understand how to determine the laser power and powers of individual oscillating modes.

As is well known, the transverse distributions of the fields of individual modes in hard edged stable resonators can be approximately described as modes of stable cavity with infinite mirrors: $u_{pl}(r,\varphi) \propto f_{pl}(r/w)exp(\pm il\varphi)$. We shall assume f_{pl} to be normalized, based on the condition $2\pi\int_0^\infty \left(f_{pl}(t)\right)^2 tdt = 1$ in each cross section inside the cavity. Since the modes with $l \neq 0$, which differ only in the sign of $il\varphi$, are degenerate, to the modes of an ideal cavity (without azimuthal perturbations) there also correspond the fields

$$u_{pl} \propto f_{pl}(r/w)\left[a_{pl}\,exp(il\varphi) + b_{pl}\,exp(-il\varphi)\right] \tag{16}$$

with arbitrary complex a_{pl} and b_{pl}. To the functions (16), normalized on each cross section of the cavity, correspond the intensity distributions $\left|u_{pl}\right|^2 = w^{-2}(f_{pl})^2(r/w)[1+\beta_{pl}\cos(2l\varphi+\varphi_{pl})]$, where $\beta_{pl} \geq 0$ and φ_{pl} are real parameters, easily represented in terms of a_{pl} and b_{pl} The value of β determines the azimuthal modulation depth. As was shown in [19], only sets of modes with azimuthally

uniform distribution of total intensity can have the property of stability in stable cavities with spherical mirrors on the condition that active medium is saturable. This fact makes it possible to propose a fairly simple analytical method of calculation of a multimode operation allowing for the volumicity of the medium for arbitrary excesses over the threshold (problems of this kind previously could not be solved even with the aid of the time consuming Fox-Li procedure). We shall assume that a wide spectrum or other causes make it possible to disregard the fine structure (with a scale $\sim \lambda/2$) of the field along the axis and at the same time, the axial mode index. Then the distributions of the radiation intensities of the individual modes can be written in the form $P_{pl}\left|u_{pl}(r,z)\right|^2 = P_{pl}w^{-2}(z)\left[f_{pl}(r/w(z))\right]^2$; here P_{pl} is the sum of the two counterpropagating flows, pertaining to a given mode. The total intensity I of the lasing field is obviously

$$I(r,z) = w^{-2}(z)\sum_{pl} P_{pl}\cdot f_{pl}^2(r/w(z)). \tag{17}$$

We now write the steady-state condition for each lasing mode

$$\int_0^l\int_0^{2\pi}\int_0^{\infty} k(r,z)\cdot\left|u_{pl}\right|^2 r dr d\varphi dz = \frac{1}{2}ln\left(\frac{1}{R\left|\gamma_{lp}\right|}\right), \tag{18}$$

where, as usually, R is the reflectance of the output mirror, k is the gain, γ_{pl} is the hollow cavity eigen value. For the gain we shall use the same standard relation $k=k_0/(1+\alpha I)$ as in Ref. [17] (k_0 is the unsaturated gain, α is the nonlinearity coefficient). Using (17), we transform the expression for k as in the example of Ref. [17] to

$$k(r,z) = k_0 - k_0\frac{\alpha I}{1+\alpha I} \cong k_0 - k_0\frac{\alpha I}{1+\alpha I_{max}(z)} = k_0 - k_0\frac{\alpha}{w^2(z)+\alpha P}\sum_{pl} P_{pl}f_{pl}^2\left(\frac{r}{w(z)}\right), \tag{19}$$

where $I_{max}(z)$ is the maximum value of the intensity in the cross section with the z coordinate, $P=I_{max}(z)w^2(z)$; it can easily be shown that $P = const$. As is shown in Ref. [19], Equation. (19) provides for a high degree of accuracy of the calculation of k for any excess over the lasing threshold during the multimode operation. Supplementing Eq. (18) with operating stability conditions which reduce to the fact that for modes do not participate in the lasing, the gain should not exceed the loss we arrive the equations

$$k_0 L - \sum_{m,n} c_{mn}^{pl} A_{mn} - \frac{1}{2}ln\left(\frac{1}{R\left|\gamma_{pl}\right|}\right)\begin{cases} = 0, & A_{pl} \neq 0, \\ \leq 0, & A_{pl} = 0, \end{cases} \quad \text{where } A_{pl} = \eta P_{pl},$$

$$\eta = \int_0^l \frac{K_0\alpha}{w^2(Z)+\alpha P}dz, \tag{20}$$

$c_{mn}^{pl} = 2\pi\int_0^{\infty} f_{pl}^2(t)f_{mn}^2(t)tdt$ being coefficients easily calculated analytically. Eq. (20) pertaining to lasing modes are combined into a linear system whose solution makes it possible to find the values of A_{pl} proportional to the powers of these modes (they must be positive). After substitution of the A_{pl} obtained, all the remaining conditions (20) must be also satisfied. As a result of the necessity of simultaneously satisfying the indicated requirements, the set of lasing modes turns out to be completely defined. Thus, even for high saturation of gain, to find the lasing modes and the distribution of intensity among

them, it is sufficiently analyze a comparatively simple system of linear equations. Inclusion of the nonlinear character of the dependence of k on I is necessary only for calculating the absolute values of the powers (for more details, see [19]). The method of calculation can be modified without any particular difficulty to the case in which k_0 is dependent on r.

2.2.4. *Some conclusions*

- As can be readily appreciated, the scope of possible applications of stable resonators in powerful lasers is restricted by the output beam quality. The criterion of single-mode lasing and numerous experimental data show that single-mode operation along with low divergence of the beam can be achieved only by considerable decreasing of the Fresnel number resulting in lowering of laser efficiency.
- Successful implementations of stable resonators is possible if the Fresnel number of active medium falls in the range between 1 and 1.5 (example - CO_2 lasers with axial flow of gas mixture and output power of the order of 1 kW).
- Stable resonators will be again taken up in powerful solid-state lasers if methods of shaping of nonuniform (with a maximum at the optical axis) unsaturated distribution of inversion appear.
- In lasers operating under pulsed excitation, stable resonators are used very rarely, since the mode selection process in stable cavities takes up too much time (the rate of this process is proportional to $\Delta_{01} - \Delta_{00}$).

2.3. UNSTABLE RESONATORS

2.3.1. *General information*

It is the practice to consider unstable resonators within the simplest geometrical optics approximation [1,2]. The matter is that almost all details of its operation can be understood in the frameworks of the geometrical approach.

We shall restrict our consideration to the case of linear resonators with circular symmetry which is of major interest for industrial applications.

The analysis of geometrical solutions reduces to a search for a light beams whose transverse structure would not change in a round trip through the resonator. For the spherical waves centered on the resonator axis one can obtain the expression $\rho_{\pm} = \pm (AB/CD)^{1/2}$, where $\rho_{\pm}$ are the radii of curvature satisfying the conditions for reconstruction, A, B, C, D are the elements of $ABCD$ resonator ray matrix (see, for example Ref. [1]). For unstable resonators $ABCD > 0$, so we have two real values of ρ differing in sign but coinciding in absolute magnitude.

If the cross section of one of the waves grows in passing around the resonator, that of the other decreases by the same factor. The transverse dimensions of the regions encompassed by these waves vary in the ratio $\mu_{\pm} = AD + BC \pm 2 (ABCD)^{1/2}$, with $\mu_+ \mu_- = (AD-BC)^2=1$. The value of μ which is larger is called the coefficient of magnification of the resonator and denoted by M, $|M| > 1$.

The cross section of the wave with $\mu = 1/M$ decreases with each resonator round trip and in the long run contracts into a point. It is clear that this wave cannot form a basis for a selfconsistent solution. The matter is that radius of curvature for converging wave

is self-reproducing only within the geometrical optics approximation. Diffraction does not allow a beam to contract into a point and transforms the converging wave to diverging one (this process has been detailed in Ref. [1]).

The cross section of the other wave expands $|M|$ times after each round trip and the excess part of the beam cross section passes past mirrors (or mirror, because most of the unstable resonators of practical significance are designed for one-sided beam extraction) of finite size. This entails substantial losses which, in geometrical approximation are $1-1/M^2$. Because of the large losses such resonators were called unstable.

Within the geometrical optics approximation the fundamental mode of unstable resonator is spherical wave with a uniform distribution of its amplitude $u(r) = const$; with the eigen value $\gamma_0=1/|M|$. The total mode spectrum of unstable resonators cannot be determined within the framework of geometrical optics. The spectrum along with condition of single mode lasing can be derived only within diffraction approximation.

After that we are ready to discuss applications of the unstable resonators.

If the total gain along the resonator is high enough to permit radiative losses of tens of percent, one can use unstable resonators capable of supporting single-mode oscillation in intermediate ($N > 1$) and wide-aperture ($N >> 1$) lasers (as we now from **2.1, B**, the stability of single-mode regime depends on the loss value for the fundamental mode).

The very important characteristic for the resonator implementation is sensitivity to misalignments. The information about this characteristic can be derived from geometrical consideration. Without going into detail we shall simply note that the sensitivity is proportional to $B/(1-1/M)$ where B is "effective length" of resonator. This restricts employment of unstable resonators in lasers with moderate values of gain, for example, in industrial CO_2 lasers (allowable magnification coefficient in this case increases only moderately from unity). Another shortcoming for the use of unstable resonators of "small" M is a cross section of output beam. In this case the diffraction output coupling of an annular beam becomes unreasonable from the standpoint of the divergence [1].

Unstable resonators are in considerable use in pulsed lasers in which gain is sufficient to use resonators with relatively high values of M. In the case of pulsed lasers the oscillation onset time should be taken into account [1, 19, 20]. Even if the decision to use unstable resonator is taken the choice of the parameters of unstable resonator is a non-trivial problem. For example, the choice of magnitude of radiation loss is already not an easy step because of the variation of M affects not only efficiency of lasing (as it is in the case of the use of stable or plane resonators) but also the spatial structure of the output radiation.

2.3.2. *New type of multiple-pass unstable resonator* [21, 22]

Choosing the type of resonator for multiple-pass systems used in many fast-flow lasers remains an acute problem. While lasing in a single transverse mode at large cross sections of the active medium can be achieved only in unstable resonators, their standard arrangements have a number of undesirable properties.

The so-called telescopic resonators with magnification $M>1$ are highly sensitive to misalignment, particularly under the conditions typical of many cw lasers, where the allowable radiation losses are low and M only slightly exceeds unity [1]. Apart from this, multiple-pass resonators commonly have large total length and, hence, modest Fresnel numbers. The radiation distribution in this case exhibits considerable diffraction-induced wings leading to useless radiation losses and low quality of output beam. Confocal resonator of the negative branch with $M < -1$ have a much lower sensitivity to misalignment and larger Fresnel numbers for the same overall dimensions and radiation losses [1]. However, one of the two beams inside a cavity has a long waist, resulting in too high radiation loads at some intermediate mirrors. Because of this negative-branch resonators are never used in multiple-pass arrangements.

At the same time if the number of intermediate mirrors is even, one can not only eliminate the above mentioned shortcoming of the negative-branch resonators but achieve a still lower sensitivity to misalignment and a larger Fresnel number as well [22]. The corresponding arrangement is illustrated by Fig. 3(a) showing an unfolded three-

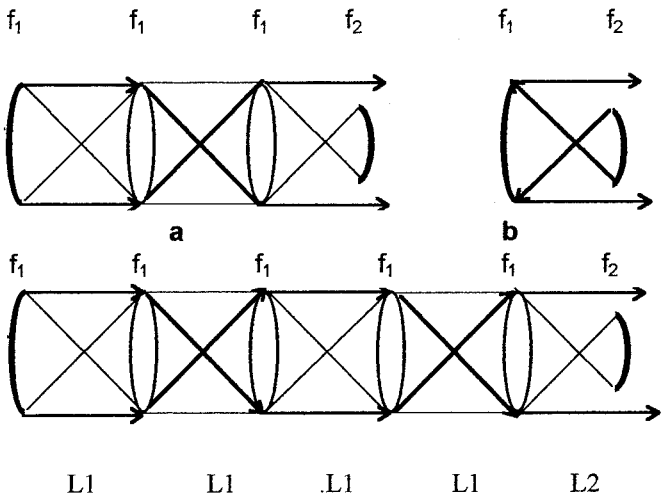


Fig. 3

pass resonator with two concave rather than plane intermediate mirrors, where $L_1=2f_1$, $L_2=f_1+f_2$ magnification of the resonator is $M=-f_1/f_2$.

The ray trajectories in Fig. 3 show beams uniformly filling the working cross section of all optical components; everywhere along the resonator one of the beam completely fills the cross section of active medium. Taking into account the properties of optical repeater one can easily see that resonator shown in Fig. 3(a) is totally equivalent to that shown in Fig. 3(b) with the same end mirrors spaced f_1+f_2 apart.

The length of the equivalent resonator being small, the Fresnel number will exceed a few times the N value of a resonator with plane intermediate mirrors and the same M, and the mirror curvature will also be substantially larger. The higher Fresnel number brings the intensity distribution over the cross section closer to the rectangular shape given by

geometrical approximation, thus reducing the parasitic losses from the diffraction-produced wings.

The larger mirror curvature along with lesser value of effective length greatly reduce the sensitivity to the aberration, including those caused by misalignments.

A simple analysis (one can find the details in Ref.[23]) shows that the resonator with repeaters possesses considerable advantages with respect to misalignments compared with the telescopic arrangement of the same length and with the same radiation losses, (i.e. with the same value of $|M|$). For the five-pass resonator (see Fig. 3(c)) a tilt of the left-hand end mirror produces here a shift of the optical axis at the output mirror smaller by a factor $(9|M|+1)(|M|+1)/(|M|-1)^2$ than in a telescopic resonator, and a tilt of output mirror, smaller by a factor $(9|M|+1)(|M|+1)^2(|M|-1)^3$. Accepting a value $|M|=1.5$ typical of industrial transverse-flow CO_2 lasers, these rations become 145 and 725 respectively. Axial tilts are likewise five time smaller.

The still more impressive gain is achieved with respect to small turns of the two resonator units facing one another in gas-flow lasers, one of them containing the left-hand end and even-numbered intermediate, and the other, the remaining mirrors. One can readily check that, with $|M| = 1.5$, axis shifts caused by such turns in a five-pass resonator with repeaters are about *three orders* of magnitude, and axial tilts, *two orders* smaller than those in a similar telescopic arrangement.

There is nothing remarkable in the properties of the resonator with repeaters as far as second-order aberrations are concerned. The effect of small curvature changes in the end mirrors on the output beam wave front is the same as that in a similar telescopic resonator, and for the intermediate mirrors it is even somewhat greater.

This resonator is not devoid of shortcomings. One of them, typical of all systems with repeaters, is connected with the high energy density in the waists. One should evidently operate below the optical-breakdown threshold, which limits the range of intracavity repeater use primarily to cw lasers not too large cross section of the active medium.

2.3.3. *Unstable resonator with semi-transparent output mirror* [23, 24, 25, 1]

As we know from 2.2 A., when using the unstable resonators of "small" M the diffraction output coupling of an annular beam becomes unreasonable from the standpoint of the divergence. To remedy this, unstable resonators with semi-transparent mirrors were designed. It was an old idea of Prof. Anan'ev, but the most important experimental results were obtained by Japanese researchers [24,25,26]. The idea of this resonator is very simple and well-known for opticians [1] (see also the drawing of output coupler for usual telescopic resonator of discussing type at Fig. 4). The output mirror for such a resonator is a transparent plate with a semitransparent coating deposited on its central part, and an antireflection film of a properly matched optical thickness on the mirror periphery. The transition from diffraction to mixed output coupling permits one to increase the energy contained in the central maximum of the angular distribution close to the level of 84% (this level for the ideal circular source). We consider this type of resonator here only because of a possibility to combine this efficient and simple approach with the idea of multiple-pass resonator with repeaters.

This combination eliminates the two main shortcomings for implementation of resonator with "small" M in cw lasers: high sensitivity to misalignments and strong wings in far-field output distribution.
The other possible way to achieve similar results is to use the technology of variable reflectivity mirrors - VRM in multiple-pass resonators with repeaters. It should be pointed out, however, that VRM technology is too costly as compared with the

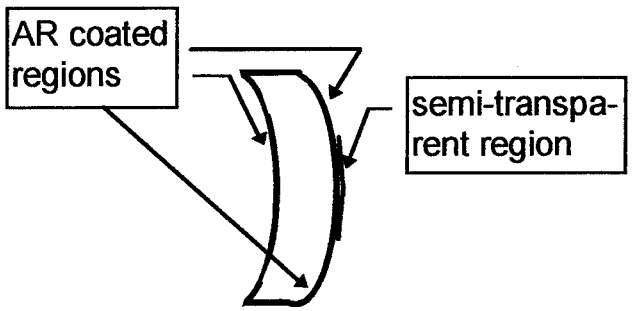


Fig.4

technology designed by Japanese researchers.

2.4 SIMPLE RESONATOR WITH SPATIAL FILTERING [26, 27, 28]

It is well known that spatial filtering unstable resonators (SFUR), Fig. 5(a), proposed in [29, 30] combine the attractive characteristics of stable and unstable resonators. Magnification of this resonator is $M = - f_1/f_2$, where f_1 and f_2 are the focal lengths of the mirrors. As in any unstable resonator radiation here flows out from the near-axial region resulting in the low sensitivity of resonator to inhomogeneties of the medium [1].

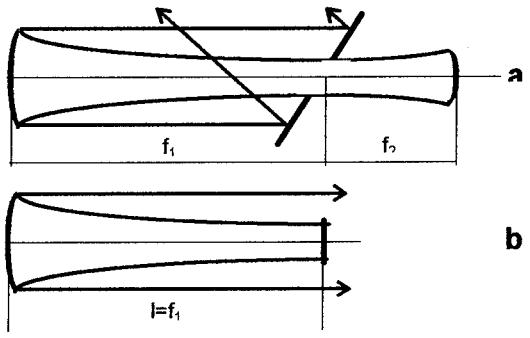


Fig. 5

The presence of a diaphragm with radius $a = (0.6\lambda f_2)^{1/2}$ at the common focus of the mirrors leads on account of spatial filtering to a smooth distribution of the field of the fundamental mode, which is usually inherent in the basic mode of stable resonators [30]. The presence of the comparatively wide distribution of the intensity over the cross section guarantees high efficiency of the single mode regime in such resonators for moderate Fresnel numbers and considerable gains in the medium [31]. However, it can be assumed that the simpler and more convenient semi-confocal resonator (SCR) with diffraction output of

radiation[27, 28] depicted in Fig. 5(b) has similar properties. Similar treatments in favour of such a resonator confirmed by appropriate experiments were published in Ref. [32] a year later.

Resonator shown in Fig 5(a) is formally unstable and exhibits some properties of stable resonators. By contrast, SCR is formally stable but exhibits some properties of unstable resonators.

Since the plane mirror of SCR is located in the focal plane of the spherical mirror the distributions of the field incident and reflected from the plane mirror are connected by a Fourier transform: $U_{in}(x) = \Im[U_{ref}(\xi)]$(this is true for rectangular form of resonator mirrors; the case of circular mirrors has been detailed in [29]). Therefore, the product of the characteristic sizes of the distributions is bounded below $w_{in} \cdot w_{ref} \leq (w_b)^2$. Considering that $w_{ref} = a_{scr}$, where a_{scr} is the size of the plane mirror, the smallness of

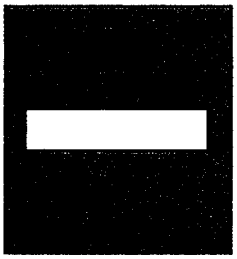


Fig. 6

the plane mirror size leads to a considerable width w_{in} of the beam incident. Therefore, the efficient dispersion of the radiation exists in SCR, i.e. the radiation flows out from the near-axial region as in unstable resonators. On the other hand, since the plane mirror limits the width of angular (Fourier) spectrum of output beam, the property of spatial filtering of the radiation also holds here. From this qualitative analysis it follows that at least for considerable diffraction losses, these resonators must have similar characteristics. We undertook numerical testing using the Fox and Li method. In a comparison we considered both resonators as intended for one and the same active element, therefore $f_1 = l$ and the radius a_{scr} of the plane mirror is equal to the radius a of diaphragm. The both resonators can be characterized by the single parameter $|M|=0.6\ \lambda l / a^2 > 1$. The results of the calculations lived up to our expectations. The basic part of the output beam cross section has a smooth distribution of an intensity and the plane wave-front; the width of an output beam exceeds the size of planar mirror by a factor of $\sim|M|$. Such properties are characteristic of SFUR. Starting from $|M| \approx 3$, both resonators a similar not only qualitatively, but quantitatively as well. By this is meant that diffraction losses, the beam width and the divergence of radiation in SCR and SFUR are approximately the same. This general information holds for resonators with rectangular and circular mirrors. Improvement of the SCR with circular cross section may be achieved by apodization of the plane mirror aperture, Ref. [29]. The areas of application

of SCR are lasers with reasonable gains and moderate Fresnel numbers (solid-state lasers, some CO_2 lasers, metal-vapor and excimer lasers).
The following fact draws special interest to 3-D SCR when its mirror size is $2a_x \times 2a_y$ and $a_x \neq a_y$. Because the beam broadening mechanism here is not geometric as in unstable resonators, but diffractional, the dimension of the beam cross section is found to be larger along the direction of the shorter side of the rectangle. This creates almost the same potentials for varying the shape of the entrance aperture by resorting to rotating the field in the feedback loop by 90° in unstable resonators [1].
This reasoning is illustrated in Fig. 6, in which the cross section of a plane mirror (inner rectangle) and the central spot of light beam incident on the plane of this mirror (outside rectangle) are shown: the part of the beam cross section tapped from the resonator is shaded. Such a geometry of resonator can be especially useful when the requirement on resonator selectivity in one of the directions substantially lower than in the other. Such a situation occurs, in particular in flowing lasers, in the wave-guide lasers of slab configuration. Finally, by shifting the plane mirror slightly to one side, we can make the main portion of the radiation emerge in the form of a compact beam along one side of this mirror.

3. Resonators of Lasers with Annular Medium Cross Section

A need in such resonators arose in connection with the development gas-dynamic and chemical lasers based on outflow of an active medium ejected from many nozzles simultaneously. A quantity of considerations argue for a circular nozzle arrangement with radial ejection of the medium. Let us not consider here the well known works in this direction such as [33] - HSURIA and [34] - laser resonator for "star war" applications. Designed for special purposes this resonators are very sophisticated and can not be implemented in industry because of the
idea of axis splitting. Other types of resonators of lasers with annular medium cross section (one can find a detailed overwie in [1]) can not insure the desired beam quality even in theory.

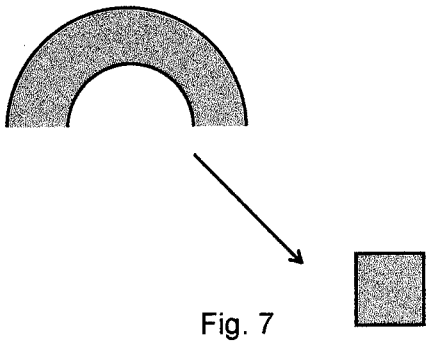


Fig. 7

3.1. NEW TYPE OF ASTIGMATIC TELESCOPE [35, 36]

Let us set ourselves the task of development of arrangement to convert the plane wave of ring sector cross section to the plane wave of rectangular cross section, Fig. 7. It is well known that usual types of polarization in coaxial lasers are radial or tangential, Fig. 8.

Therefore, desired arrangement must also transform the polarization type to linear one which is common for rectangular geometry. Such a task can be solved by comparatively simple two-mirror telescope. The reflecting surface of one of the mirrors of this telescope is shaped as a cone sector with a vertex angle about (but not equal to) $\pi/2$, while that of the other is a parabolic cylinder whose generating line is parallel to the cone axis, and the focal line coincides with this axis.

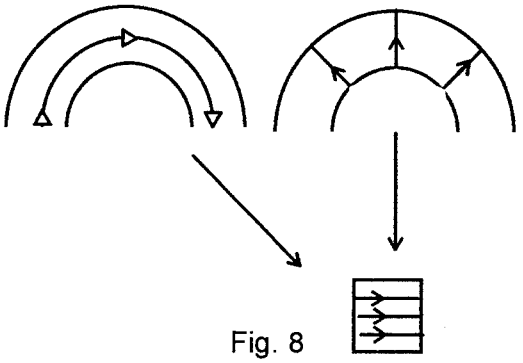


Fig. 8

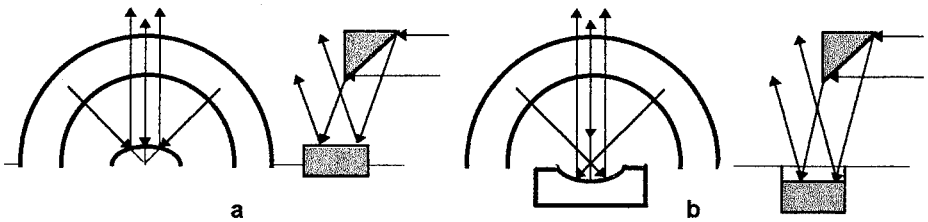


Fig. 9

The principle of operation of the astigmatic telescope is as follows, see also Fig. 9. The incident beam with a cross section shaped as a ring sector with a vertex angle less than π and with a plane wave front is transformed, upon striking the conical reflector, into a beam with cylindrical wave front which converges toward the cone axis. The converging cylindrical beam is next reflected from the parabolic cylinder whose focal line coincides with the focusing line and transforms to a beam with plane wave front
and rectangular (or square) form of cross section. Following the polarisation transformation it is easily to verify that radiation with tangential or radial type of polarisation becomes linear polarized. As shown in Fig. 10, the parabolic mirror of astigmatic telescope can be both concave and convex. Inside the telescope with convex parabolic mirror there is a region where the radiation is focused to a line.

The cone vertex angle has to be somewhat different from $\pi/2$ for convenience in coupling the radiation out of the telescope.

3.2. RESONATOR WITH HIGH EFFECTIVE LENGTH BASED ON THE STIGMATIC TELESCOPE [35,36]

To design a workable resonator arrangement for laser with annular cross section of active medium, one should take into account that such a resonator would have an output cross section of a reasonable shape (square, circle), would provide the polarisation

matching of the various parts of the arrangements and, at last, would have a common optical axis at the centroid of the beam.

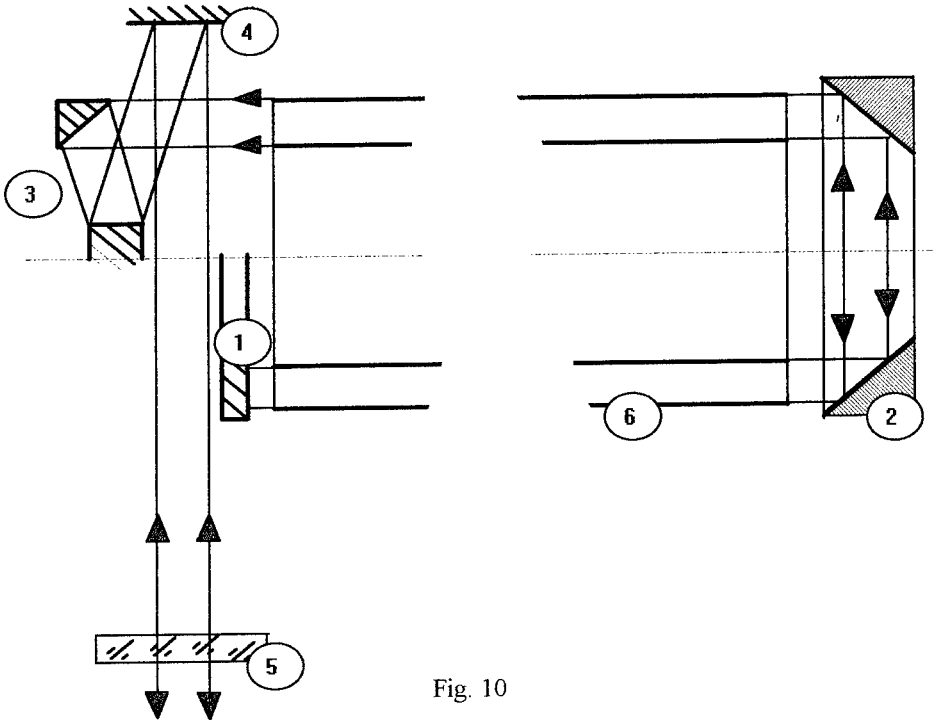


Fig. 10

Such a resonator can be developed using the astigmatic telescope. The arrangement shown in Fig. 10 was patented by Rofin Sinar with our participation [37] and was detailed in [38].

Here 1 is a plane mirror with a cross section of 180^0 ring sector, 2 is a usual conical reflector, 3 is the astigmatic telescope, 4 is a plane mirror, 5 is a coupler and 6 is the active medium of annular cross section. The proposed resonator is a resonator with high effective length for the azimuthal direction. Inside the active medium beam has a shape of a ring sector, inside the telescope it is subjected to compression, described in 3.1, and between plane mirror and coupler it is narrow.

The portion of the diagram from the output plane of the telescope to plane coupling mirror acts as spatial selector of azimuthal direction. The bandwidth of this selector is controlled by properly varying its length, thus permitting one to perform easily experimental optimization of resonator parameters.

4. Resonator Arrangements for Wave-guide CO_2 Industrial Lasers

4.1. INTRODUCTION

It is well known [37], that the best way to increase the efficiency of RF-pumped diffusion-cooled CO_2 lasers is to reduce the electrode gap to about $h = (1.5 - 2)$ *mm*. The representative length L of gain medium in powerful lasers is about 1 m. Such a relationship between h and L ($h^2/\lambda L >> 1$) causes the radiation to propagate through the gain medium in a purely wave-guide mode.

We shall start from the lasers of slab geometry and restrict our consideration to the case of radiation with vector $\boldsymbol{E}$ parallel to the wave-guide walls because of the high level of losses for the radiation with that perpendicular to the surface of electrodes. In absence of losses and with homogeneous medium inside the wave-guide (in this case its dielectric constant $\varepsilon = const$) these modes have the following field distribution

$$E_m(x, z, t) = u_m(x) \exp[-i(k_m z - \omega t), \qquad (21)$$

where the coordinate axis x and z are directed perpendicular to the walls and along the propagation, the wall coordinates are $x = 0$ and $x = h$, ω is the circular frequency, k_m is the real propagation constant and $u_m = \sin(\pi m x / h) \equiv \sin(\beta_m x / h)$, $m = 1, 2, \ldots$

Inside the electrode gap in the CO_2 laser the refractive index is essentially inhomogeneous because of heat deposition. In the general case this inhomogeneity produces a distributed negative lens and a distributed optical wedge (the latter appears if the cooling is nonsymmetrical).

Heat distribution calculations show that the difference between the refractive indices at the walls and between them may reach about $0.5 \cdot 10^{-5}$. Note that the presence of such a lens whose focal distance is, besides, pump-level dependent, casts doubt on the possibility of developing a laser with free (optical) light propagation in the electrode gap. Such a lens could also become a formidable obstacle on the way to producing a stable and efficient wave-guide laser.

An analysis has shown, however, that the presence of a distributed lens and wedge in a wave-guide do not qualitatively affects the pattern of light propagation. Indeed, general theory shows that modes of the type of (21) with the same electric field vector orientation continue to exist under these conditions. Any other wave with the same polarization satisfying given boundary conditions can also be represented as a sum of modes of this type (the completeness property of the eigen function set). Only the functions $u_m(x)$, while remaining real, will change; they can no more be written in analytical form and should be numerically calculated.

It can be shown that dimensionless parameter

$$\Delta\Phi \equiv k_0 \cdot \left(\frac{2\pi h^2}{\lambda}\right) \cdot \Delta\varepsilon \equiv k_0 \cdot L_{Fr} \cdot \Delta\varepsilon \qquad (22)$$

is a measure of optical inhomogeneity within a wave-guide. Here $\Delta\varepsilon$ is the maximum difference of dielectric constant across the gap and L_{Fr} is the Fresnel length for given h and λ. The value $\Delta\Phi$ in (22) presents the maximum phase difference over the Fresnel length which appears due to inhomogeneity of the medium.

It can be shown that inhomogeneity is "weak", if

$$\Delta\Phi << \pi^2 m^2 \qquad (23)$$

(m is transverse mode index, $\beta_m = \pi \cdot m$ is a transverse wave constant for unpertubed 2-D wave guide). As evident from Eq. (22), (23) the effect of perturbations on the properties of modes (the shape and propagation constant) becomes weaker when the

mode index increases or the gap width decreases. This may be considered as another argument for transition to gaps of minimum possible width. In addition, it has been found experimentally that wave-guide CO_2 lasers with a small $(h = 1.5 \div 2\ mm)$ electrode gap insure the single mode lasing in transverse direction. It is the third argument counts in favour of small h. It can be shown that propagation inside the coaxial wave-guides occurs in a similar way provided certain conditions hold. As we shall see later, for high power diffusion-cooled lasers these conditions are fully met in the gap between the operating electrodes.In summary of this general part it should be mentioned that there is one common problem for the wave-guide resonators. It is the problem of diffraction losses incurred in introducing into the wave-guide the radiation reflected from the mirrors. To reduce these losses the mirror should have cylindrical (or toroidal, in the case of coaxial wave-guides) surface with the generatrix curvature $R \approx h^2/2\lambda$ or be plane and placed as close to the wave-guide end as possible.

4.2. SOME RESONATOR ARRANGEMENTS FOR LASERS WITH PLANE WAVE-GUIDES

Representative dimensions of discharge region for powerful (1 - 2 kW) wave-guide laser are shown at Fig. 11. As is evident from the foregoing, the central problem with resonator arrangements for such a laser is to achieve a coherent lasing in lateral dimension. Let us take a brief look at some methods to solve this problem.

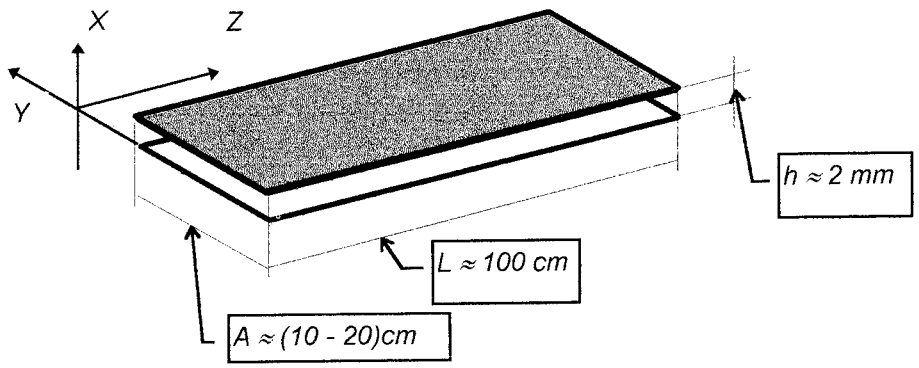


Fig. 11

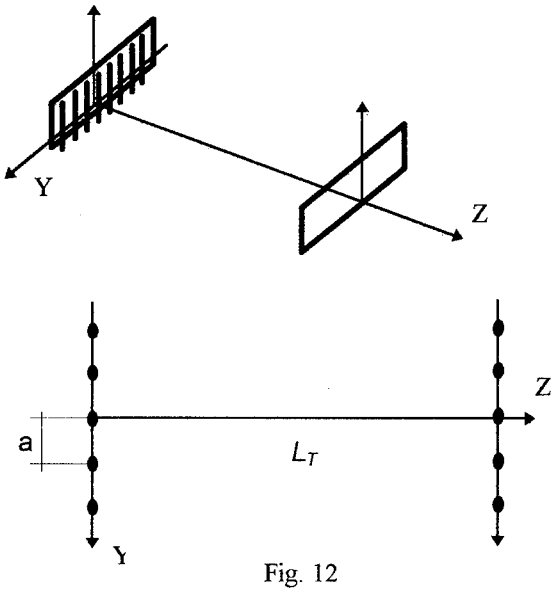


Fig. 12

4.2.1 *Resonator using Talbot effect.*
The idea of this method is a phase locking of a great many of independent single mode lasers of lateral dimension by Talbot effect. The effect implies that if one has a periodic amplitude distribution in reference plane perpendicular to z axis (see Fig. 11) so
- the lateral periodicity will hold along the whole length of propagation and
-the initial amplitude distribution is periodically repeated while the wave is spreading along z (the period is usually labeled L_T).

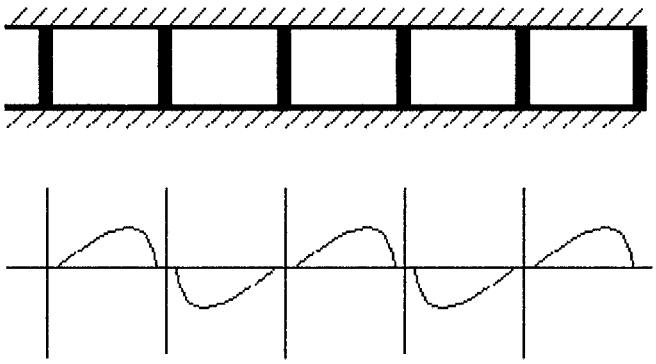


Fig. 13

To implement this effect for solving the problem, one can insert into the resonator a masc with periodical transmission function $F(y)$, Fig. 12. The period of $F(y)$ depends on the resonator dimensions in according with condition $L_T = L$, where L is a length of round trip through the resonator. If , for example, the mask is a sequence of transparent and opaque sections the zeros of the amplitude distribution will coincide with opaque sections to decrease the loss of power, Fig. 13. Therefore, the Talbot effect may be thought of as a mechanism of suppression of all modes which minimums do not coincide

with the opaque zones or as a desired mechanism of lateral spectrum contraction. It should be noted that $L_T = na^2/\lambda$, where n is a refractive index. So for $L = 200$ cm, $\lambda = 10^{-3}$ cm a ≈ 0.45 cm. The question of implementation of Talbot resonator in powerful lasers is still an open question.

4.2.2. *Two-dimensional unstable resonators*

The idea of implementation of the 2-D unsymmetric positive-branch unstable resonator (PBUR), Fig. 14, is the most evident for lasers shown in Fig. 11. However, two-mirror positive-branch unstable resonators are quite suitable for use in wide-aperture lasers with allowable losses of at least 20% [1]. In the case of diffusion cooled wave-guide lasers the allowable losses are only about 10%. This leads to the use of resonators with M close to unity. Such resonators are too sensitive to misalignments to be successfully employed here. The other problem is a disposition of the optical axis close to the perturbed bound of active medium. Both this problems can be successfully got over by the use of unsymmetric negative-branch unstable resonator (NBUR) shown in Fig. 16.

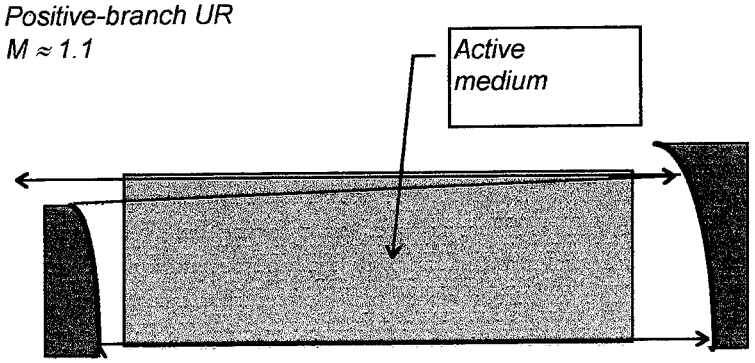


Fig. 14

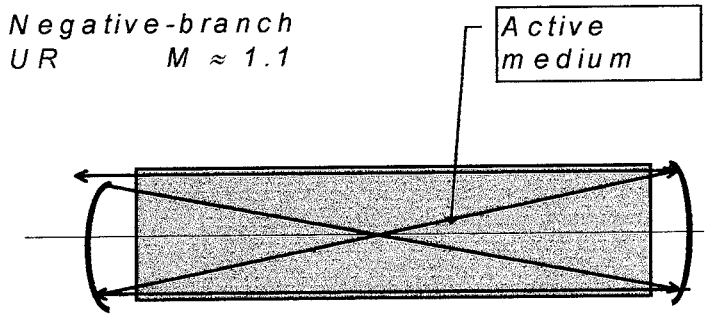


Fig. 15

The sensitivity to misalignments for NBUR is well below that for PBUR (the ratio is $(|M|-1)/(|M|+1)$); the optical axis is placed in the center of active zone. The arrangement shown in Fig. 16 appears to be the most reasonable solution of the problem for slab wave-guide CO_2 lasers.

4.3. LASERS WITH COAXIAL WAVE-GUIDES

The general view of the coaxial wave-guide laser is shown in Fig. 16. For powerful system with $P \approx 2.5$ kW $L \approx 100$ cm, $r_0 \approx 5$ cm, $h \approx 0.2$ cm (all information regarding the gap width from the previous section is valid for coaxial wave guides). Coaxial design of discharge structure offers few constructional advantages over the planar electrode system.

At given dimensions the electrode system shown is a coaxial wave-guide ($L > L_{Fr} = (h/2)^2/\lambda = 10$ cm). The problem on the rigorous description of the coaxial wave-guides modes, as applied to laser situation, is not simple. The point is that the field in coaxial wave-guide, generally speaking, is not transversal [38].It can be shown, however, that in certain situation ($\lambda/h << 1$, $h/r_0 << 1$ and $\nabla[\ln\varepsilon(r)] \parallel \boldsymbol{r}$; all these conditions are fulfilled for powerful lasers) the electric field may be considered as transversal TE mode with $\boldsymbol{E} = \boldsymbol{E}_\varphi$ only. In this case an azimuthal component of the electrical field can be expressed in terms of the only component of the magnetic field $\boldsymbol{H}_z$. Under these conditions the equations, describing the field propagation in coaxial systems, are scalar and no qualitatively different from that for planar 2-D wave-guides. The only difference in describing the modes lies in the fact that we have to consider helical waves in coaxial wave-guides instead of the plane waves in planar case. Once a discussed consistency

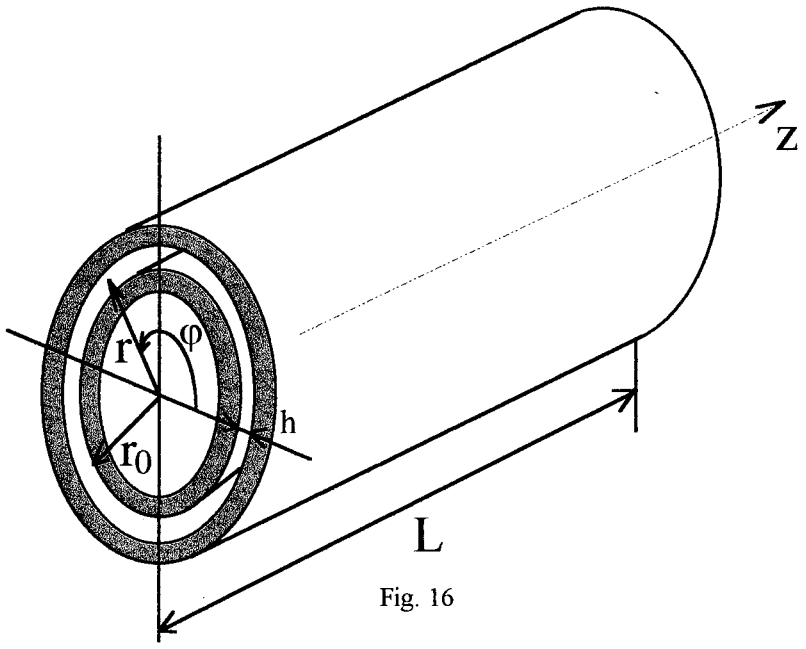


Fig. 16

between properties of planar and coaxial laser wave-guides has been established, the solutions for planar wave-guide lasers can be extended to the case of coaxial wave-guide resonators. The first attempt of such an extension was undertaken by the authors of [39]. In this paper the unstable in azimuthal direction resonator was described. The implementation of this resonator, however, can not solve the problem in all aspects: it has very high sensitivity to misalignments, unfavorable state of polarization and two output beams propagating at an angle to each other.

4.3.1. *Talbot resonator for coaxial wave-guide lasers*

The second extension is an idea to implement the Talbot effect in coaxial wave-guide resonators; this optical arrangement was patented by Rofin-Sinar with our participation[40]. Without going into mathematical detail we shall simply note that at the above specified conditions ($\lambda/h << 1$, $h/r_0 << 1$ and $\nabla[\ln\varepsilon(r)] \parallel r$) the Talbot effect exists for helical modes in coaxial wave-guides. What's more the formula for calculating of Talbot length is essentially coincident with that for planar case: $L_T = \left(\frac{2\pi\bar{r}}{m}\right)^2 \frac{1}{\lambda} = \frac{\bar{a}^2}{\lambda}$.

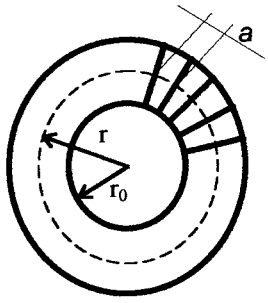


Fig. 17

Here $\bar{r} = \frac{r_0 + h}{2}$, $\bar{a}$ is a period of transmission function $F(\varphi)$ ($F[\varphi]=F[\varphi + 2\pi] = F[\varphi + p\cdot(2\pi/m)]$) at the $\bar{r}$ level, $2\pi/m$ is the least period, $p = 1, \ldots, m$, see also Fig. 17.

The optical arrangement using the Talbot effect is shown in Fig. 18. The W-Axicon serves to decrease the cross section of output beam and output coupler; $L_T = 2L$, where

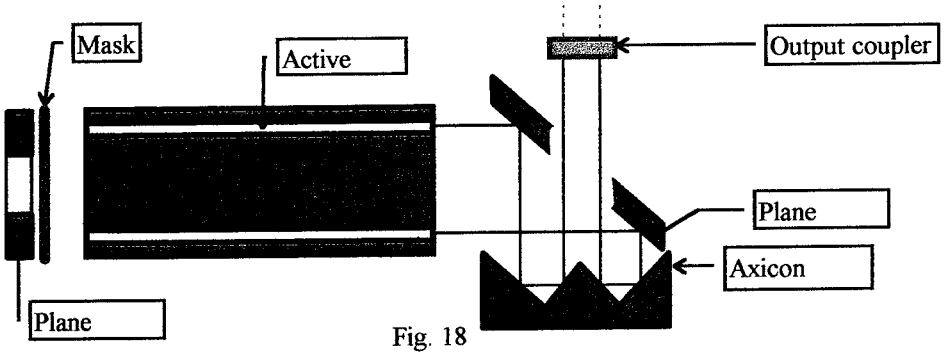


Fig. 18

L is a distance between mask and output mirror. It should be noted that if we chose the formula for L_T of the form $L_T = a^2/\lambda$, the output field will have an amplitude with alternating signs (the same is true for the planar case) This increases the divergence of

output beam. To correct this condition, one can use phase π-shift coating at the external surface of the output coupler.

4.3.2. *Optical arrangement to decrease the Fresnel number of coaxial wave-guide resonator* [41]

Now we shall enlarge on the resonator arrangement that can be used by itself or as a part of another type arrangement (for example, the Talbot resonator). The idea is to use two embedded wave-guides in RF pumped CO_2 laser. One of the possible arrangements using this idea is shown in Fig. 19. This resonator is the four-transit-type, with radiation propagation along two circular coaxial cylindrical wave-guides. The wave guide system shown in Figure permits making a multitransit resonator compact enough. In this arrangement, the required power is largely provided by the outer, and spatial coherence in the azimuthal direction, by the inner wave-guide. Laser operation in the lowest mode in azimuthal direction is achieved by properly choosing the radius of the inner wave-guide.

Radiation can be transported without losses from one wave-guide to another by properly using the translational properties of the telescopic system. The paraboloid of revolution transforms the beam of annular cross section into a similar beam while compensating at the same time for the optical wedge in the active medium. The reflecting axicon with paraboloid generating lines matches the inner and outer wave-guides (they may have different values of h). Output mirror should have an antireflecting coating on the outside.

4.3.3. *Possible implementation of astigmatic telescope for coaxial wave-guide lasers*

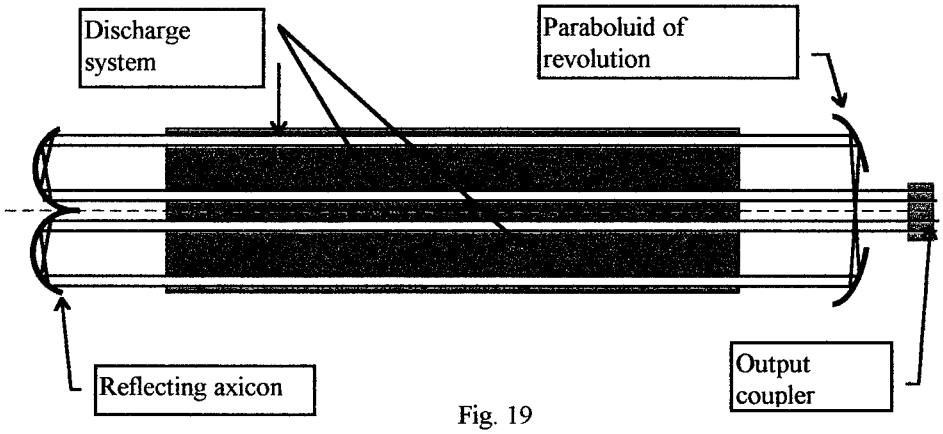


Fig. 19

Now we are ready to discuss the implementation of astigmatic telescope for coaxial wave-guide lasers. As is evident from the foregoing, in order for developing the wave-guide resonator arrangement one need take into account only the problem of the radiation injection into the wave-guide. To solve this problem the following procedure should be adopted: the axicon in Fig. 17 should be replaced by paraboloid of revolution

(see Fig. 20); the plane mirror 1 should be replaced by toroidal mirror and the plane mirror 4 - by cylindrical one, see part **4.1** of this paper.

Appendix 1.

Let us consider an optical structure of two parallel finite equal apertures. Let an arbitrary function $\psi_1 \in \mathfrak{H}$ ($\mathfrak{H}$ - a complete Gilbert functional space defined at the surface of the aperture) be a complex amplitude of an input wave; $\psi_2 \in \mathfrak{H}$ - an amplitude of an output wave. Obviously a power loss Δ due to the diffraction in that system can be defined as $\Delta = 1-(\psi_2,\psi_2)/(\psi_1,\psi_1) \equiv 1-\|\psi_2\|^2/\|\psi_1\|^2$. With the use only a basis property of $\{u_n^0\}$, it can easily be shown [7] that in the optical structure of two finite apertures the power loss of an arbitrary wave is subject to the inequality

$$\Delta \geq 1-|\gamma_0^0| \tag{1.1}$$

with $\Delta = 1-|\gamma_0^0|$ only if $\psi_1 = u_0^0$,where γ_0^0 is an eigen value and u_0^0 is a complex amplitude of a fundamental eigen mode of the operator $\mathfrak{P}_0$ for a confocal resonator limited by edges of the apertures. It is obvious that in the subspace $\{\mathfrak{H} \setminus \varphi(u_0^0,u_1^0,u_2^0,\ldots,u_{(n-1)}^0)\}$ (where $\varphi(s_1,s_2,\ldots,s_k) = \{\alpha_1 s_1 + \alpha_2 s_2 + \ldots + \alpha_k s_k\}$, $\alpha_i \in \mathbb{C}$), Eq. (1.1) is changing to a form

$$\Delta \geq 1-|\gamma_n^0| \tag{1.2}$$

$\Delta = 1-|\gamma_n^0|$ if $\psi_1 = u_n^0$, (eigen transverse modes are classified by their losses: $|\gamma_0| > |\gamma_1| > |\gamma_2| > \ldots \Leftrightarrow |\Delta_0 < |\Delta_1| < |\Delta_2| < \ldots)$. Now suppose that some operator $\mathfrak{P}' : \mathfrak{P}' \neq \mathfrak{P}_0$ of an open resonator has a basic sequence of eigen functions $\{u_n'\}$. It is obvious that we can repeat reasoning that led us to Eq.(1.1) , Eq.(1.2) for the new set of functions $\{u_n'\}$. When this result is compared with that of Eq.(1.1) - Eq.(1.2) for the set $\{u_n^0\}$, it is apparent that $u_n' = u_n^0$ and $\gamma_n' = \gamma_n^0$ $\forall\, n$. By this is meant that $\mathfrak{P}' = \mathfrak{P}_0$ [4], in other words the confocal resonator is the only resonator among hard-edged resonators with finite mirrors that has the basic set of eigen functions (or transversal modes). This property is valid in every reference plane z inside the resonator.

Appendix 2.

In the case of infinite interval the integral equation of the symmetrical 2-D stable resonator with a mirror width of $2a$ acquires the form

$$\gamma\, u(x_1) = \int_{-\infty}^{\infty} \mathfrak{K}(x_0,x_1)\cdot\left[1-h(x_0)\right]\cdot u(x_0)dx_0 \equiv \mathfrak{U}u(x_0), \tag{2.1}$$

where x_0 , x_1 are dimensionless transverse coordinates in the mirror planes measured in units of $w/2^{1/2}$,

$w^2 = \lambda L/(\pi(1-g^2)^{1/2})$, g is the configuration parameter,

$h(x) = 0$, if $|x| < \sqrt{c}$ and $= 1$, if $|x| > \sqrt{c}$, $\sqrt{c} = \sqrt{2}a / w$ is the normalized mirror size; $\mathfrak{U} \to \mathfrak{U}_0$ when $c \to \infty$, is an operator of a stable resonator with infinite mirrors. There is no point in using of the perturbation theory to solve Eq. (2.1) because of the eigen system $\{\varphi_n\}$ of $\mathfrak{U}_0$ is degenerated. Because of this we did not consider the equation $\mathfrak{U} = \mathfrak{U}_0 + \mathfrak{U}'$ [42]; we looked for the eigen modes of operator $\mathfrak{U}$ in a form

$u(x) = \sum_n b_n \varphi_n$, where $\varphi_n = \left(2^n \sqrt{\pi}\, n!\right)^{-1/2} \cdot H_n(x) \cdot exp\left(-x^2/2\right)$ are the solutions of Equation. (2.1) for $h \equiv 0$ and form an orthogonal basis of the space of square-integrable functions. Thereafter we calculated the matrix form of an operator $\mathfrak{U}$: $a_{lk} = (\mathfrak{U}\varphi_l,\ \varphi_k^*) = (\mathfrak{U}\varphi_l,\ \varphi_k)$.
The matrix elements a_{lk} may be analytically calculated. The next step is a numerical decision of usual eigen value problem for the q-dimensional approximation $\mathfrak{A}_q$ of matrix $\mathfrak{A}$: $\gamma\, \mathfrak{B} = \mathfrak{A}_q\, \mathfrak{B}$; $det(\mathfrak{A}_q - \gamma\, \mathfrak{E}_q) = 0$, where $\mathfrak{B}$, γ are respectively desired eigen vector and eigen value, $\mathfrak{A}_q = \left(a_{lk}\right)_{l,k=0}^{q}$, $\mathfrak{E}_q$ is an identity $(q \times q)$ matrix. The last equation has q complex roots, successive substitution of which in previous allows us to find q corresponding eigen vectors, whose components are expansion coefficients of the solutions sought.

References

[1] Anan'ev Yu. (1992) *Laser resonators and the beam divergence problem,* Adam Hilger, Bristol, Philadelphia and New York.
[2] Siegman A. E. (1986) *Lasers,* University Science Books, Mill Valley, CA.
[3] Fox A.G. and T. Li T. (1961) *Bell. Sys. Tech. J,* **40** 453-488.
[4] Hutson V. G. L. and Pym J. S. (1980) *Applications of Functional Analysis and Operator Theory*. Acad. Press.
[5] Gloge D. (1966), *Quasioptics*, Sov. Radio, Moscow, 266-279.
[6] Vainshtein L. A. (1966), *Open resonators and open wave-guides,* Sov. Radio, Mosc.
[7] Anan'ev Yu. A., Anikitchev S.G. (1986) *Optics and Spectroscopy* **61**, 856-860.
[8] Boyd J. D. and Gordon I.P.(1961) *Bell. Syst. Tech.* **40**, 489.
[9] Wilkinson J. H. (1965) *The Algebraic Eigenvalue Problem*, Oxford University Press.
[10] Fox A.G. and T. Li T (1966) *IEEE J. Quant Electron* **QE-2**, 774-783.
[11] Johnson M. M. (1974) *Appl. Opt.*, **13**, 2326.
[12] Siegman A. E. (1977) *Opt. Lett.* **1,** 13.
[13] Streifer W. (1965) *J. Opt. Soc. Am.* **55** 868.
[14] Anan'ev Yu. A., Anikitchev S.G. (1985) *Optics and Spectroscopy* **59,** 1331-1336.
[15] S. Solimeno, B. Crosignani, P. Di Porto (1986) *Guiding, Diffraction and Confinement of Optical Radiation,* (Academic Press, Inc, San Diego.
[16] Anan'ev Yu. A., Anikitchev S.G. (1988) *Optics and Spectroscopy* **64**, 390 -396.
[17] Lavigne P., N. McCarthy et al (1988) *Can. J. Phys.* **66**, 888.
[18] Anan'ev Yu. A., Anikitchev S.G. (1989) *Optics and Spectroscopy* **67,** 408-410.
[19] Anan'ev Yu. A., Anikitchev S.G. (1983) *Sov. Phys. Tech. Phys* **28,** 1205-1208.
[20] Anan'ev Yu. A., Anikitchev S.G., et al (1988), *Sov. Phys. Tech. Phys* **34,** 772-774.
[21] Anan'ev Yu. A., Anikitchev S.G.(1991) *Inventor's Certificate* No. 5014295 (USSR).
[22] Anan'ev Yu. A., Anikitchev S.G. (1993) *Optics and Spectroscopy* **74**, 116-118.
[23] Yausi K., Tanaka M. and Yagi S. (1988) *Appl. Phys. Lett.* **52**, 330.
[24] Yausi K., Tanaka M. and Yagi S. (1989) *J. Appl. Phys.* **65**, 17.
[25] Yagi S., Yausi K., Takenaka Y., Kuzumoto M. and Tagashira M. (1990) *Proc. SPIE,* **1225**, 357.

[26] Anan'ev Yu. A., Anikitchev S. G., and Solov'ev V. D. (1991) Laser resonator, *Patent SU 1790796 A3* (USSR)
[27] Anan'ev Yu. A., Anikitchev S. G., and Solov'ev V. D. (1990) *Optics and Spectroscopy* **68**, 710-711.
[28] Anan'ev Yu. A., Anikitchev S. G., and Solov'ev V. D. (1992) *Optics and Spectroscopy* **73**, 101-105.
[29] Gobbi P.G., Morosi S., Reali G.C., and Zarkasi A.S. (1986) *Appl. Opt.* **26**, 26.
[30] Gobbi P.G. and Reali G.C.(1986) *Opt. Commun.* **57**, 355.
[31] Anan'ev Yu. A., Anikitchev S. G., and Gorlanov A. V. (1988) *Optics and Spectroscopy* **64**, 572-573.
[32] Pax P. and Weston J. (1991) *IEEE J. Quantum Electron.* **QE-27**, 1242.
[33] Fink D (1979) *Appl. Opt.* **18**, 581.
[34] Bloembergen N. et al. (1987) *Rev. Mod. Phys.* 59 (3), pt 2 S41.
[35] Anikitchev S., Solov'ev V., Anan'ev Yu., Lopota V., Schanz K. (1994), *Pat. Appl. of Rofin-Sinar Laser GmbH* P 4421 600.9.
[36] Anan'ev Yu. A., Anikitchev S. G., and Solov'ev V. D. (1995) *Optics and Spectroscopy* **78**, to be published.
[37] Shackleton C.J., Abramsky K.M., Baker H.J., Hall D.R. (1992) *Optics Comm.* **89** 423-428.
[38] Pruzhanovskii V.A.(1970) *Sov. Phys.-Tech. Phys.* **15**, 897-900.
[39] Ehrlichmann D.R., Habich U., and Plum H.-D.(1993) *J. Phys. D: Appl. Phys.* **26**, 183-191.
[40] Anikitchev S., Solov'ev V., Anan'ev Yu., Lopota V., Schanz K. (1993) *Pat. Appl. of Rofin-Sinar Laser GmbH* P 4325 063.7-33.
[41] Anikitchev S., Solov'ev V., Anan'ev Yu., Lopota V., Schanz K. (1994) *Pat. Appl. of Rofin-Sinar Laser GmbH* P 4424 726.5.
[42] Vitkin A. I. (1967) *Optics and Spectroscopy* 7, 185-192.

VARIABLE REFLECTIVITY MIRROR UNSTABLE RESONATOR THERMAL LENS COMPENSATED BY A DEFORMABLE REAR MIRROR

N. PAVEL, T. DASCALU, V. LUPEI, and H. TOTIA
INSTITUTE OF ATOMIC PHYSICS, IFTAR-MALIRM Department,
Bucharest R-76900, Romania

ABSTRACT

In order to compensate for thermal lensing in Nd:YAG rod active media, placed in different positive-branch unstable resonators with a super-Gaussian reflectivity profile of the output mirror, a deformable thin glass plate was used as the rear mirror. Unstable resonators with magnifications of $M=1.5$ and $M=1.8$ were designed with a beam quality of 0.8-mm-mrad. For unloaded resonators the output energies of the laser working at a 10 Hz repetition rate and pump energies up to 50 J per pulse were close to those obtained for a 1 Hz repetition rate.

1. INTRODUCTION

Unstable resonators that use radial variable-reflectivity mirrors as output couplers have been demonstrated to be particularly successful for generating high-energy diffraction-limited beams with a smooth transverse profile [1-7]. By a suitable technology based on vacuum deposition of dielectric thin films on a transparent substrate, different reflectivity profiles such as parabolic, super-parabolic and super-Gaussian, were obtained [8-12]. The mirror reflectivity profile can be designed to provide an optimum balance between the energy and the beam quality of the laser output.

Due to the sensitivity of resonator properties to thermal lensing in the active media, unstable resonators were initially used in single shot operation or in Q-switched systems with low average output power. However, recently it has been demonstrated that the unstable resonators can be used in high-power solid-state lasers if the resonator is properly designed. These new unstable resonator configurations are: (i) the "*rod imaging unstable resonator*" [13] and (ii) the "*near-concentric unstable resonator*" [14]. From a pulsed Nd:YAG laser, output beams with divergence about twenty times lower than that obtained with a multimode stable resonator at an average power of 200 W have been obtained in the first configuration. The second configuration is characterised by much lower sensitivity to thermal lensing compared to other unstable resonator schemes. A

R. Kossowsky et al. (eds.), High Power Lasers – Science and Engineering, 283–292.
© 1996 *Kluwer Academic Publishers. Printed in the Netherlands.*

maximum output power of 420W and beam parameter products below 3-mm-mrad have been reported for a pulsed Nd:YAG laser [14].

This paper gives the results on the output beam characteristics obtained from Nd:YAG positive-branch unstable resonators with a super-Gaussian reflectivity profile of the output mirrors and with thermal lensing compensated by a deformable rear mirror. This method of thermal lens compensation has already been used in CO_2 stable resonators [15] and in Nd:$YAlO_3$ stable and unstable configurations [16]. Here we report the results on this thermal lens compensation method in unstable resonators with an output mirror of super-Gaussian reflectivity profile. This technique proves suitable for the resonator configurations used in our experiments: plane output mirror and convex total reflectivity rear mirror. The possibility of obtaining a concave radius of the deformable membrane is also discussed.

2. RESONATOR DESIGN

A schematic of the unstable configuration used in the investigation is presented in fig. 1.

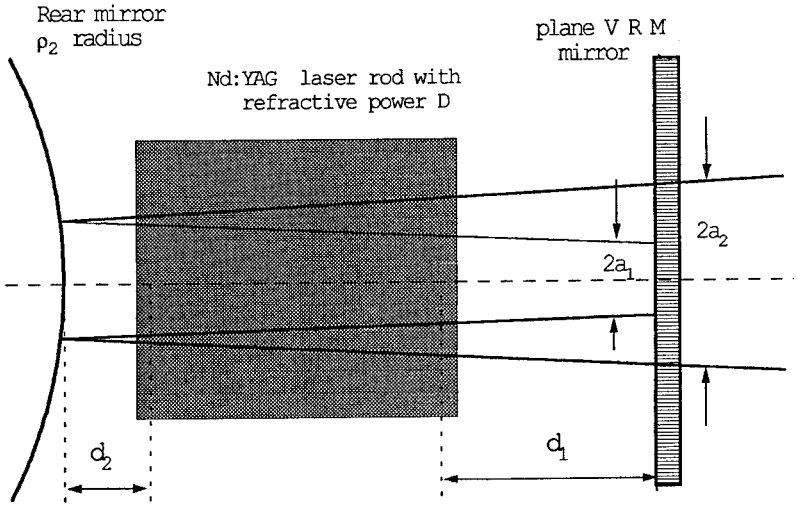


Figure 1. The super-Gaussian output mirror unstable resonator with the Nd:YAG lenslike active media. d_1 and d_2 are the distances between the mirrors and the adjacent principal planes of the Nd:YAG rod and $M=a_2/a_1$ is the resonator magnification.

The resonator with an internal variable lens of refractive power D has the same mode properties across the mirrors as the equivalent resonator with stability parameters g_i^* and length L^* given by:

$$g_i^* = g_i - Dd_j(1-\frac{d_i}{\rho_i}), \qquad i,j=1,2 \quad i \neq j \tag{1}$$

$$L^* = d_1 + d_2 - Dd_1d_2 \tag{2}$$

where $g_i = 1-(d_1+d_2)/\rho_i$ is the stability parameter for an empty resonator $(D=0)$, ρ_i is the curvature radius of mirror i, d_i is the distances between mirror i and the adjacent principal planes of the rod and D is the refractive power of the rod. The magnification M of the unstable resonator (fig. 1) can be calculated from the equivalent parameters g_i^* using the relation:

$$M = \left|2g_1^*g_2^* - 1\right| + \sqrt{4g_1^*g_2^*(g_1^*g_2^* - 1)} \tag{3}$$

For the laser performance, the sensitivity of the resonator magnification M to the variation of the rod refractive power is important. With increasing rod refractive power D, the magnification M decreases and the unstable resonator can become stable; under these conditions the laser beam quality decreases.

The output energy E_{out} is related to the input energy E_{in} by relation [4]:

$$\xi - 1 = \frac{\int_S [\varepsilon U - 1 + \exp(-\varepsilon U)]dS}{\int_S \frac{\varepsilon U - 1 + \exp(-\varepsilon U)}{\varepsilon U} dS} \tag{4}$$

where: $\xi = E_{in} / E_{th}$ is the pump energy normalised to the threshold pump energy E_{th}; $\varepsilon = \frac{2\sigma E_{out}}{\gamma_1 h\nu}$ is the normalised output energy with σ the stimulated emission cross section and $\gamma_1 = -\ln(R_0 / M^2)$ the logarithmic losses of the output mirror; $U(r)$ is the square of the mode amplitude of the resonator and dS is a surface element of the laser rod. Equation (4) is valid for any mode profile $U(r)$, not only the super-Gaussian. Due to the decrease of the resonator magnification M the mode volume in the active media and the output energy decreases too. Moreover the logarithmic losses of the output mirror are changed and this leads to inefficient energy extraction from the laser resonator.

A positive thermal lens inside the laser resonator modifies its optical configuration and the output beam characteristics. In order to keep the beam quality stable, without any decrease of output energy, the equivalent resonator configuration must be stabilised. One way to maintain the magnification M insensitive to the variation of D is to modify the rear mirror radius. The rear mirror radius and the resonator parameters for a given magnification M are related by the relation:

$$\frac{1}{\rho_2} = \frac{1}{(d_1 + d_2 - Dd_1d_2)}[1 - Dd_1 - \frac{1}{g_1^*}\frac{(M+1)^2}{4M}] \tag{5}$$

This equation was used in order to keep the magnification of the unstable resonators constant by modifying the radius of the rear mirror in accordance with the refractive power D of the rod.

3. EXPERIMENTAL RESULTS AND DISCUSSION

A Nd:YAG laser rod (Φ5x56 mm) placed in a cylindrical silver-coated cavity was optically pumped in a pulsed mode with an ILC 6F2 lamp. A plane super-Gaussian mirror of order n=5, with mirror spot-size of w_m=1.7 mm and peak reflectivity of R_0=35% (fig. 2), was used in two unstable resonators: (i) one with M=1.5 made by a total reflectivity convex mirror of -8 m radius, and (ii) the other with M=1.8 using a rear mirror of -5 m radius. The output beam characteristics obtained with these configurations were compared with those determined by using a classical plane-plane resonator of 30 cm length and 39% output mirror reflectivity.

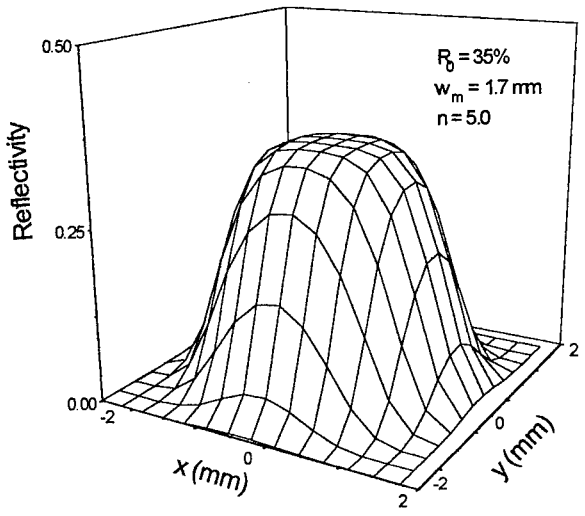


Figure 2. The reflectivity profile of the output mirror is described by the relation $R(r) = R_0 \exp[-2(r / w_m)^n]$ where r is the radial coordinate and R_o is the peak reflectivity, w_m is the mirror spot-size and n denote the order of the mirror.

The output energies and beam quality obtained at 1 Hz repetition rate and different pumping levels are presented in fig. 3. The output energies obtained from the unstable resonators were fitted with relation (4). The output energy was about 25% less than in the stable resonator, but the beam quality improved. The beam quality is defined as $\Theta w / 4$ where Θ is the full angle beam divergence (based on 86.5% energy in the focal plane of a 1000 mm focal lens) and w is the beam width, calculated from the near-

field intensity distribution (obtained by scanning the laser beam near the output with a pinhole and a photodiode).

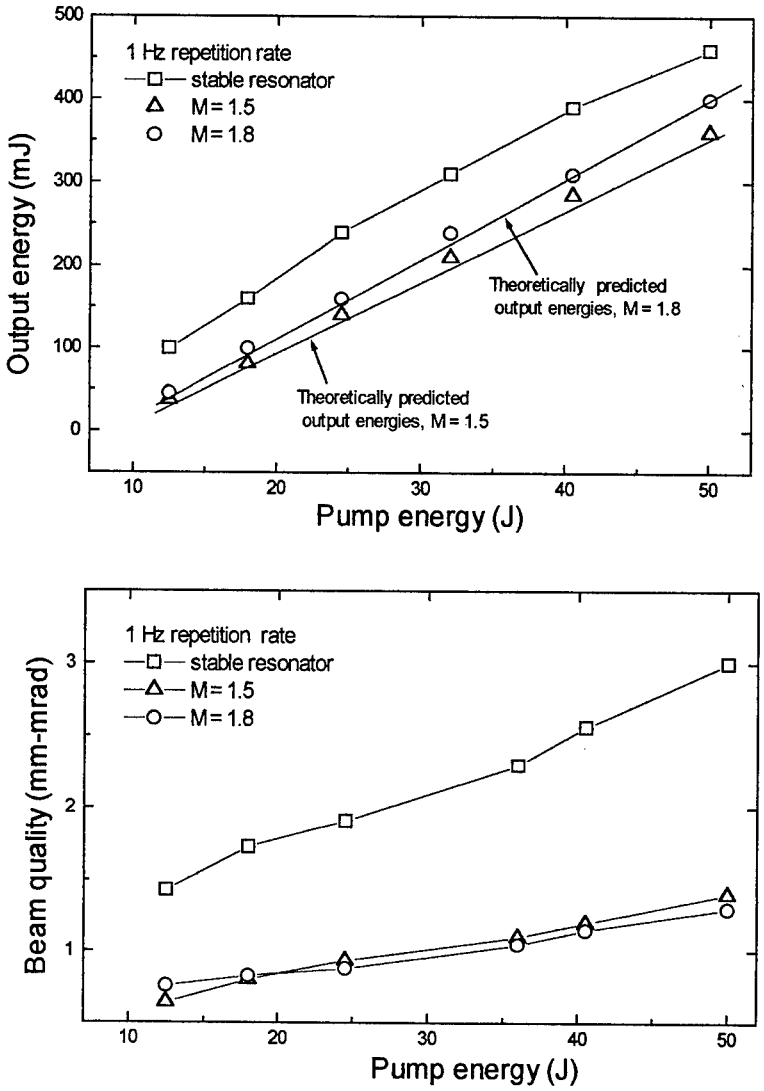


Figure 3. Output energy (upper fig. 3.a) and beam quality (lower fig. 3.b) at 1 Hz repetition rate. For unstable configurations the experimental energies are close to those predicted by relation (4).

The laser beam characteristics at 10 Hz are presented in fig. 4. With increasing pump power, the output energy decreases and the beam quality changes. To explain this behaviour, the position of the unstable resonators in the stability diagram was studied.

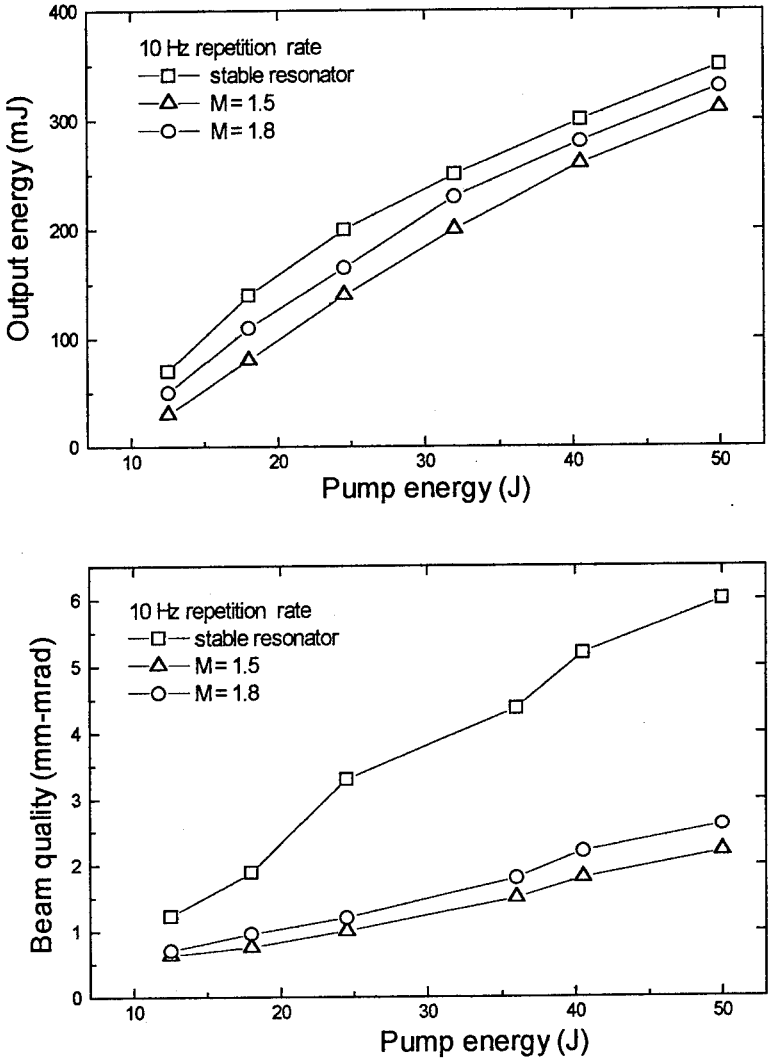


Figure 4. Output energy (upper fig. 4.a) and beam quality (lower fig. 4.b) obtained at 10 Hz repetition rate for the stable and unstable resonators.Compared to results at 1 Hz the output energy decreases and the beam quality changes.

At 10 Hz repetition rate the laser rod was considered as equivalent to a thick lens with a refractive power D, which depended on pumping level, and which was determined by the method described in [17]. The variation of the g_i^* stability parameters for the investigated resonators are presented in fig. 5 as a function of the pump level. Due

to the decrease of the magnification M the unstable configuration can became stable and decreases in the output energy and beam quality are expected.

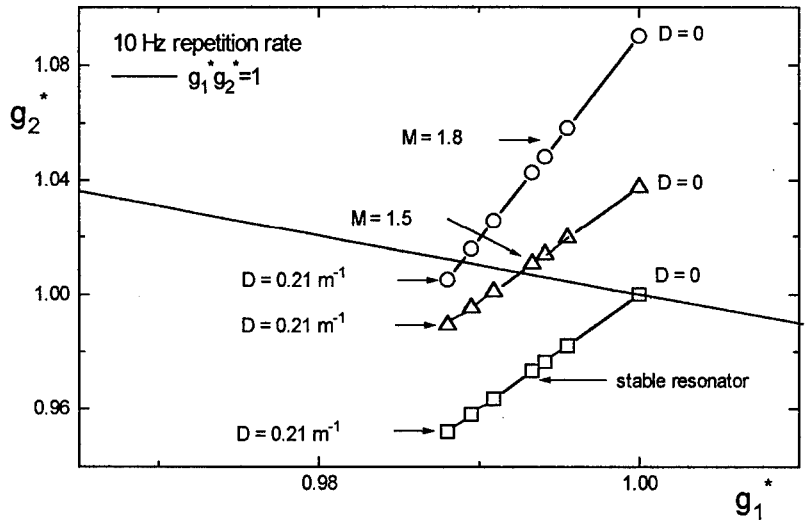


Figure 5. The equivalent stability diagram of the resonators for rod refractive powers, D, in the range 0 to 0.21 m^{-1}. Due to the refractive power of the rod the unstable resonators move into the stable region.

In order to keep the magnification of the unstable resonators constant, the radius of the rear mirror was modified as a function of the rod refractive power according to relation (5). The deformable optical mirror was made from a 0.65-mm-thick BK7 glass membrane with 22-mm diameter and fixed in a metallic mount. This base was constructed in such a way that the accuracy of the mirror contour is insensitive to the mounting; the pressure on the mirror was measured from the height of a water column. The experimental points on the mirror curvature as a function of the pressure on the mirror, are presented in fig. 6.a. where, for comparison, the theoretical curves are also plotted. This dependence is almost linear in the 1.04 to 1.16 bar pressure range. This deformable mirror was used in the unstable resonators in order to keep the magnification constant. The variation of the radius of curvature of the membrane as a function of the pumping level is presented in fig. 6.b.

The beam quality and the output energies obtained from these resonators are presented in fig. 7. By this procedure the beam quality was maintained constant at ≈ 0.8 mm mrad, characteristic for unloaded resonators. The output energies were close to those obtained for a 1 Hz repetition rate.

During the laser operation no degradation of the membrane total reflecting film was observed. The pump level used was not high but we estimate that this method can be successfully used for thermal compensation for high power unstable lasers. If a concave radius for the rear mirror is needed, new ways to exert the pressure on the membrane can be used (for example a pneumatic cell). The variation of the concave

membrane radius may be necessary in the construction of stable resonators for fundamental mode selection.

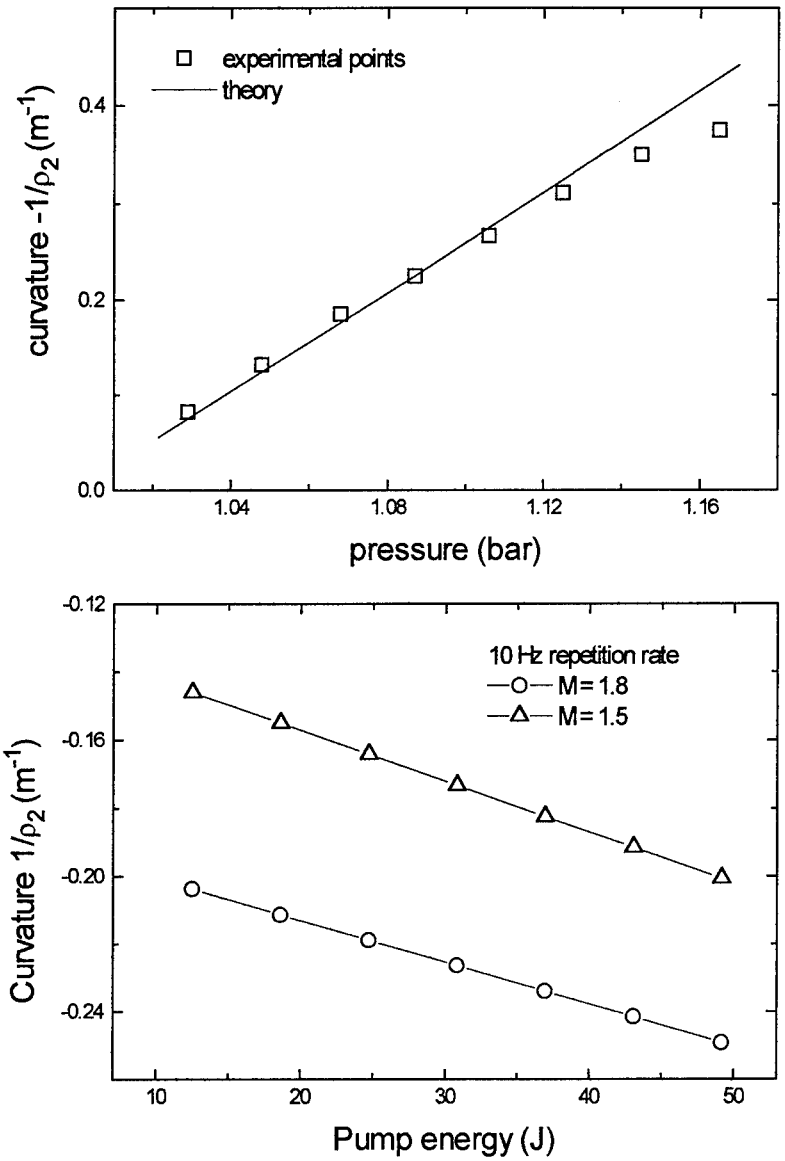


Figure 6. The dependence of the radius of curvature of the glass plate as a function of pressure is presented (upper fig. 6.a). The experimental points are close to the theoretical values. Fig. 6.b (lower figure) shows the variation of the rear mirror curvature at 10 Hz repetition rate.

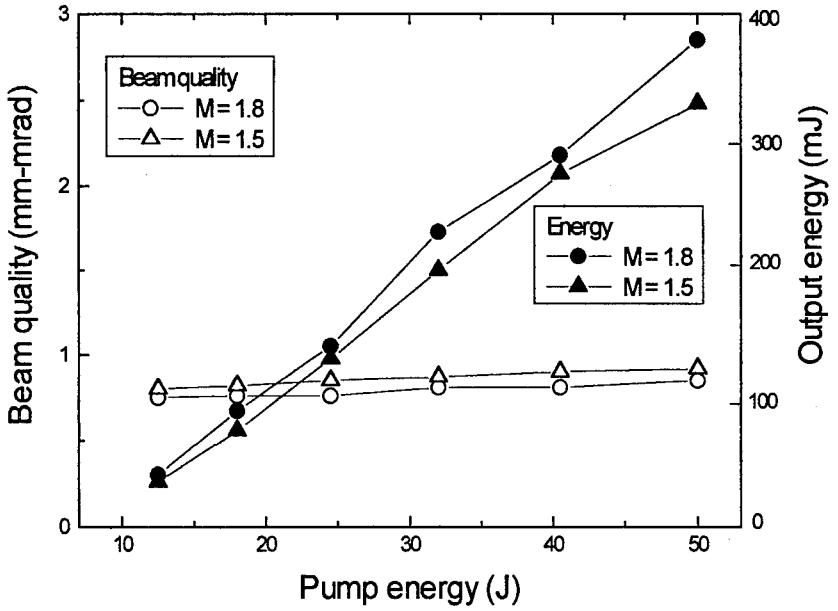


Figure 7. Beam quality and output energy for thermally compensated unstable resonators. A constant value of ~ 0.8 mm-mrad for the beam quality was maintained with output energies close to those obtained at a 1 Hz repetition rate.

The method of thermal lens compensation by a deformable rear mirror was recently used for a diode-side pumped Nd:YAG laser [18], and the pressure on the membrane was obtained by a simple screw placed in the centre of the plate. By fixing this screw on the thin plate glass, a concave profile of the mirror could also be obtained.

In our experiments the laser rod was considered as a thick lens with refractive power D, without taking into account any type of intracavity distortions. To compensate for these effects, a deformable mirror with control electrodes [19] can be used but with a substantial cost increase of the laser system.

In conclusion, a deformable thin glass plate was used as the rear mirror in different positive-branch unstable resonators with a super-Gaussian reflectivity profile of the output mirror. By this means, thermal lensing in Nd:YAG rod active media was compensated. For unstable resonators with magnification of 1.5 and 1.8 the beam quality was maintained at a value of 0.8-mm-mrad. For these resonators the output energies of the laser working at 10 Hz with pump energies up to 50 J per pulse were close to those obtained at a 1 Hz repetition rate.

Acknowledgements: This work was supported by the Romanian Ministry of Research and Technology under contract 151B/A434 (1995).

REFERENCES

1. Parent, A., McCarty, N., and Lavigne, P. (1987), Effects of Hard Apertures on Mode Properties of Resonators with Gaussian Reflectivity Mirrors, *IEEE J. Quantum Electron.* **QE-23,** 222-228.
2. De Silvestri, S., Laporta, P., Magni, V., Svelto, O., Arnone, C., Cali, C., Sciortino, S., and Zizzo. C (1988), Nd:YAG LASER WITH MULTIDIELECTRIC VARIABLE REFLECTIVITY OUTPUT COUPLER, *Optics Comm.* **67**, 229-232.
3. De Silvestri, S., Laporta, P., Magni, V., and Svelto, O. (1988), Solid-State Laser Unstable Resonators with Tapered Reflectivity Mirrors: The Super-Gaussian Approach, *IEEE J. Quantum Electron.* **QE-24**, 1172-1177.
4. De Silvestri, S., Magni, V., Svelto, O., and Valentini, G. (1990), Lasers with Super-Gaussian Mirrors, *IEEE J. Quantum Electron.* **QE-26**, 1500-1508.
5. De Silvestri, S., Magni, V., Taccheo, S., and Valentini G. (1991), Q-switched Nd:YAG laser with super-Gaussian resonators, *Opt. Lett.* **16**, 642-644.
6. Caprara, A. and Reali, G.C. (1992), Time-resolved M^2 of nanosecond pulses from a Q-switched variable-reflectivity-mirror Nd:YAG laser, *Opt. Lett.* **17**, 414-416.
7. Perrone, M.R., Mezzolla, F., Cali, C., and Pace, C. (1991), Super-Gaussian reflectivity unstable resonator for excimer lasers, *Appl. Phys. Lett.* **59**, 1153-1155.
8. Lavigne, P., McCarthy, N., and Demers, J.G. (1985), Design and characterization of complementary Gaussian reflectivity mirror, *Appl. Opt.* **24**, 2581-2586.
9. Lavigne, P., McCarthy, N., Parent, A., and Snell, K.J. (1988), Laser mode control with variable reflectivity mirror, *Canadian Journal of Physics* **66**, 888-895.
10. Emiliagni, G., Piegari, A., De Silvestri, S., Laporta, P., and Magni, V. (1989), Optical coatings with variable reflectance for laser mirrors, *Appl. Opt.* **28**, 2832.
11. Duplain, G., Verly, P.G., Dobrowolski, J.A., Waldorf A., and Bussiere, S. (1993), Graded-reflectance mirrors for beam quality control in laser resonator, *Appl. Opt.* **32**, 1145-1153.
12. Perrone, M.R., Piegari, A., and Scaglione, S. (1993), On the Super-Gaussian Unstable Resonators for High-Gain Short-Pulse Laser Media, *IEEE J. Quantum Electron.* **QE-29**, 1423-1427.
13. Magni, V., De Silvestri, S., Lie-Jia Qian, and Svelto, O. (1992), Rod-imaging supergaussian unstable resonator for high power solid-state lasers, *Optics Comm.* **94**, 87-91.
14. Hodgson, N., Bostanjoglo, G., and Weber, H. (1993), The near-concentric unstable resonator (NCUR) - an improved resonator design for high power solid state lasers, *Optics Comm.* **99**, 75-81.
15. Keming Ku, Loosen, P., and Koechner, H. (1994), Properties of a high-power CO_2-laser with an adaptive mirror, *Optics Comm.* **106**, 269-277.
16. Chetkin, S.A. and Vdovin, G.V., (1993), Deformable mirror correction of a thermal lens induced in the active rod of a solid state laser, *Optics Comm.* **100**, 159-165.
17. Subhash, N. and Sathianadnan, N. (1984), Thermal effects in a Nd:Glass Laser Rod Pumped in a Double Close-Coupled Cavity, *IEEE J. Quantum Electron.* **QE-20**, 111.
18. Greiner, U.J. and Klingenberg, H.H. (1994), Thermal lens correction of a diode-pumped Nd:YAG laser of high TEM_{00} power by an adjustable-curvature mirror, *Opt. Lett.* **19**, 1207-1209.
19. Kudryashov, A.V. and Panchenko, V. Ya (1994), Improvement the output beam parameters of excimer, copper-vapor, CO_2, and solid-state lasers by methods of adaptive optics, *Proc. IEEE* **94TH0614-8**, 209.

TWO-ROD VRM-UNSTABLE RESONATOR WITH DEFORMABLE MIRROR THERMAL COMPENSATION

N. PAVEL, T. DASCALU, V. LUPEI, and M. POTERASU
INSTITUTE OF ATOMIC PHYSICS, IFTAR-MALIRM Department
Bucharest R-76900, ROMANIA

ABSTRACT

The performance of a two-rod super-Gaussian positive-branch unstable resonator Nd:YAG solid - state lasers was investigated. A glass deformable pressure mirror was used for thermal lens compensation in the resonators.

1. INTRODUCTION

Unstable resonators that use super-Gaussian reflectivity mirrors as output couplers have been demonstrated to be the best way to generate high-energy diffraction-limited beams with a smooth transverse profile. Due to strong thermal lensing of Nd:YAG rods and its dependence on the pumping power, the application of unstable resonators to high average power Nd:YAG lasers is not trivial. For this reason new unstable resonator configurations were developed for high power solid-state lasers: (i) the *rod imaging unstable resonator* [1] and (ii) the *near-concentric unstable resonator* [2]. In a pulsed Nd:YAG laser [1], output beams with divergence about twenty times lower than that from a multimode stable resonator at an average power of 200 W have been obtained in the first configuration. The second configuration is characterized by a much lower sensitivity to thermal lensing as compared to other unstable resonator schemes; a maximum output power of 420W and a beam divergence products below 3-mm-mrad have been reported for a pulsed Nd:YAG laser [2].

This paper gives the results of a comparative investigation of the laser beam characteristics such as energy, divergence and beam-product quality for two Nd:YAG rods placed in variable reflectivity mirror (VRM) unstable resonators. With increased pumping energy a decrease of the unstable resonator magnification M, with a consequent alteration of the beam quality, was observed. This leads to a variation of the position of the focal point which is unacceptable for many materials processing applications and for fibre coupling. Compensation of the thermal lensing would keep the position of the focal

R. Kossowsky et al. (eds.), High Power Lasers – Science and Engineering, 293–301.
© 1996 *Kluwer Academic Publishers. Printed in the Netherlands.*

point constant and would also allow a fairly constant fill factor, independent of the pump energy.

By proper radii variation of a glass deformable pressure - controlled rear mirror [3, 4] the magnification of the positive branch unstable resonators was made insensitive to the thermal loading of the laser active media.

2. TWO-ROD VRM UNSTABLE RESONATOR

The schematic unstable configuration used in this study is shown in fig. 1. It consists of a Nd:YAG rod (Φ5x56 mm) and a Nd, Ce:YAG rod (Φ6x75 mm) placed in a cylindrical silver coated cavity and optically pumped in a pulsed mode with ILC 6F2 lamps. The resonator can be characterised by the following parameters: d_1, d_2 - the distances between the mirrors and the principal planes of the rods; d_m - the distance between the principal planes of rod 1 and 2; ρ_1, ρ_2 - the curvature radii of the mirrors, and D_1, D_2 - the refractive power of the laser rods. One must take into account that the total resonator length L is always shortened because the principal planes are located inside the rods.

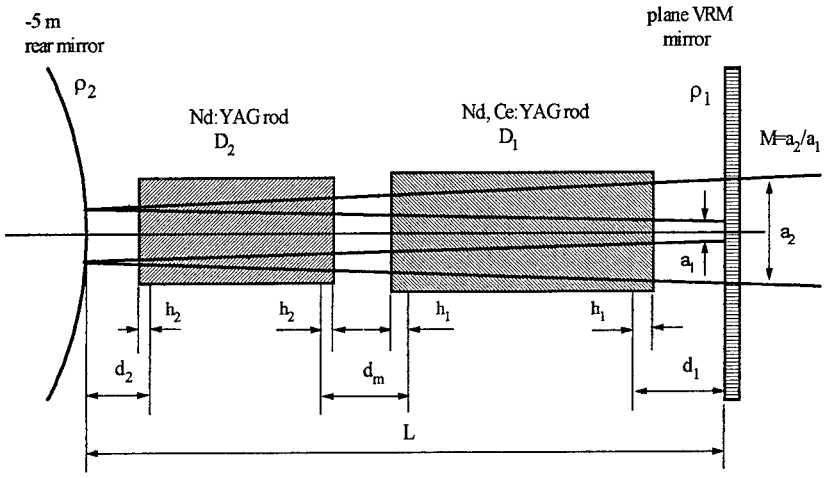


Figure 1. Unstable resonator with the lenslike active media. h_1 and h_2 are the distances between the principal planes of the rods and their faces.

A plane super-Gaussian mirror of order n=5, mirror spot-size of w_m=1.7 mm and peak reflectivity of R_o=35% (figure 2) was used in the unstable resonator with magnification M=1.8. The distance d_2 is 7 cm and the rods were placed close to each other. The results on output beam characteristics obtained with this configuration are

compared with those determined by using a classical plane-plane resonator of 45 cm length and 39% output mirror reflectivity.

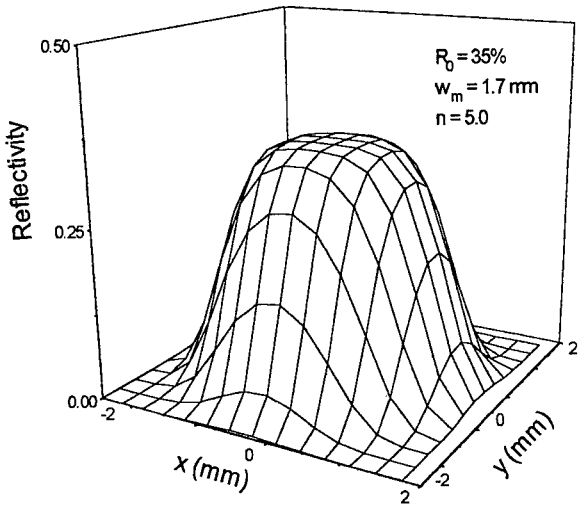


Figure 2. The reflectivity profile of the output mirror is described by the relation $R(r) = R_0 \exp[-2(r / w_m)^n]$ where r is the radial coordinate and R_o is the peak reflectivity, w_m is the mirror spot-size and n denote the order of the mirror.

2.1. REFRACTIVE POWER OF THE RODS

It is well known that a considerable amount of heat is generated in the laser rod, due mainly to low pump quantum efficiency and to the nonradiative loss of energy between the pumping bands and the laser levels. The heat removed from the surface of the rod generates a radial thermal gradient, which produces the following effects: (1) temperature-induced variation of the refractive index; (2) strain-dependent variation of the refractive index; (3) end-face curvature. The term due to end-face curvature is, in general, less than 10 percent of the total refractive power for typical dimensions of the rod and can thus be neglected.

If the heat generation is uniform, the rod acts as a lens-like medium, because of the quadratic variation of the refractive index as a function of the radius. The rod can thus be treated as a lens whose refractive power is independent of its length and is related solely to the optomechanical properties of the material, its cross section and the efficiency factors of the pumping cavity. Because the thermal relaxation time of the Nd:YAG rod is relatively long (τ~1.5-2 sec) the active medium can be considered like a thick lens even at a low repetition rate of pumping (> 5 Hz). The refractive power of the rods was determined by the method presented in [5]. The results obtained for D_1 and D_2

at 5 Hz and 10 Hz repetition rates and the pump energies used in our experiments are presented in figure 3.

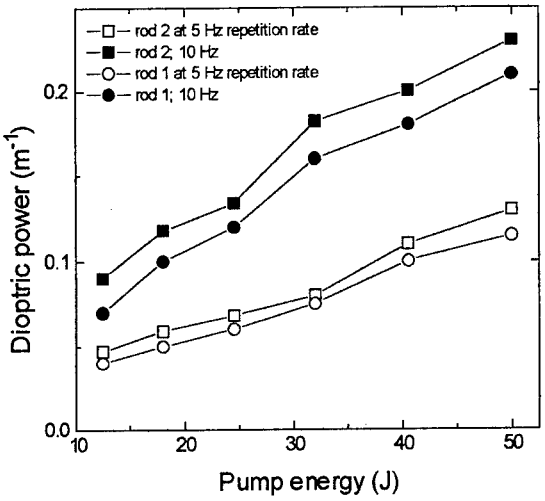


Figure 3. Refractive power of the rods as a function of the pump energy at 5 Hz and 10 Hz repetition rates.

3. EXPERIMENTAL RESULTS AND DISCUSSION

The output energies and beam quality obtained at 1 Hz repetition rate for different pumping energies are presented in fig. 4. The output energy from the unstable resonator was about 20% less than that from the stable one, but the beam quality was better. The beam quality is defined by $\Theta w / 4$ where Θ is the beam divergence (determined as 86.5% of the energy encircled in the focal plane of a 1000 mm focal lens) and w is the beam parameter, calculated from the near-field intensity distribution. For the unloaded resonator the near-field profile, predicted by geometrical optics, is shown also in fig. 5.

At a 10 Hz repetition rate a decrease of the output energy and an alteration of the beam quality was observed. To explain this behaviour, the position of the unstable resonators in the stability diagram has been studied. The resonator presented in fig. 1 has the same mode properties across the mirrors as the equivalent resonator with stability parameters g_i^* and length L^* given by [6]:

$$g_i^* = g_i + d_m D_j \{\frac{d_j}{d_m}(1-\frac{d_i}{\rho_i})[d_m D_i - (1+\frac{D_i}{D_j})] - \frac{D_i}{D_j}(1-\frac{d_i + d_j D_j / D_i}{\rho_i})\} \qquad (1.a, b)$$

$$L^* = L' - d_m D_2 \{d_1 \frac{D_1}{D_2} + d_2 - \frac{d_1 d_2}{d_m}[d_m D_1 - (1+\frac{D_1}{D_2})]\} \qquad (2)$$

where $L'=d_1+d_2+d_m$, $g_i=1-L'/\rho_i$, i, j=1, 2, i≠j.

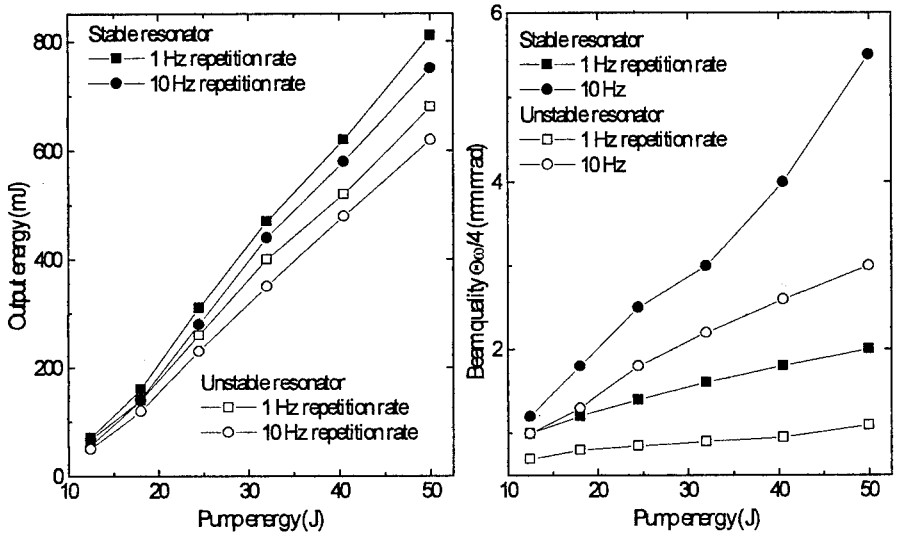


Figure 4. Output energy (left) and beam quality (right) at 1 Hz and 10 Hz repetition rate for the stable and unstable resonators. At 10 Hz repetition rate a decrease of the output energy and an alteration of the beam quality are observed.

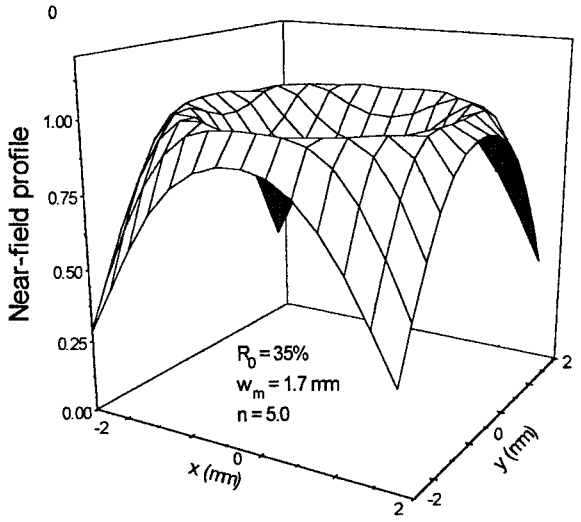


Figure 5. Near-field intensity profile for the super-Gaussian resonator with M=1.8 is presented.

If the refractive powers of the rods are equal, $D_1=D_2=D$, the stability parameters become:

$$g_i^* = g_i + d_m D[\frac{d_j}{d_m}(1-\frac{d_i}{\rho_i})(d_m D-2)-(1-\frac{d_1+d_2}{\rho_i})] \quad (3.a, b)$$

$$L^* = L'-d_m D[d_1+d_2-\frac{d_1 d_2}{d_m}(d_m D-2)] \quad (4)$$

and the stability curve of the resonator is a parabola [7].

The magnification M of the unstable resonator (fig. 1) can be calculated from the equivalent parameters g_i^* using the relation:

$$M = |2g_1^* g_2^* - 1| + \sqrt{4g_1^* g_2^*(g_1^* g_2^* - 1)} \quad (5)$$

In laser operation the sensitivity of the resonator magnification M to the variation of the rod refractive power is important. With increasing D_1 and D_2 the magnification M decreases and the unstable resonator may become stable; in these conditions a decrease of the laser beam quality takes place. Moreover, the logarithmic losses of the output mirror are changed and leading to inefficient energy extraction from the laser resonator.

The variation of the g_i^* stability parameters (eq. 1.a, b) for the resonators investigated are presented in fig. 6. Due to decrease in magnification M the unstable configuration can become stable and a decrease in output energy and beam quality is expected.

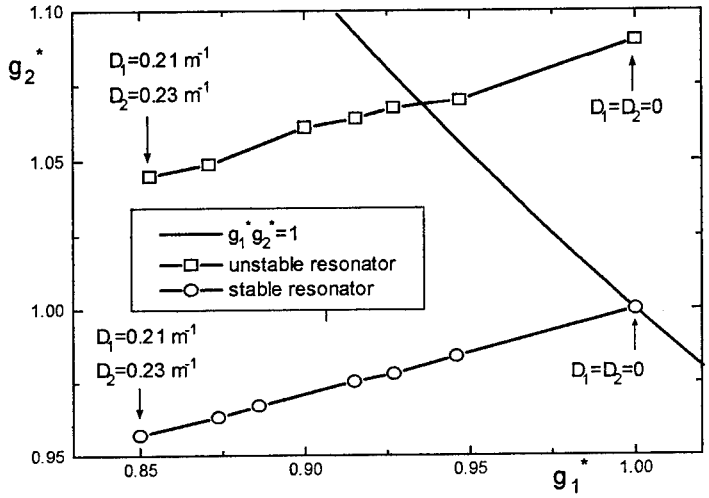


Figure 6. The equivalent stability diagram of the resonators at 10 Hz repetition rate. As the refractive power of the rods changes, the unstable resonator may become stable.

In order to keep the beam quality stable, without any decrease in output energy, the equivalent resonator configuration must be stabilised. One way to maintain the magnification M insensitive to the variation of refractive powers of the rods is to modify, the rear mirror radius. We consider a deformable mirror, which consists of a

BK7 glass membrane whose curvature is adjustable with the pressure of the cell medium. The design of the membrane mirror used is shown in figure 7.

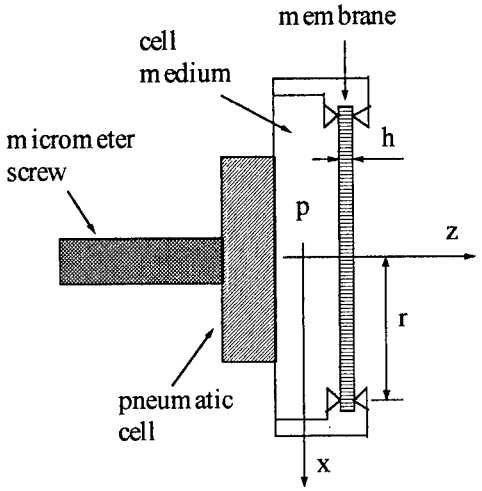


Figure 7. Schematic of the used mirror. p is the pressure of the medium, h is the thickness of the plate and r is the radius of the plate.

At a given pressure p of the mirror medium, the elastic deformation of the membrane clamped on the circumference is described by the following equation [8]:

$$z = \Psi \frac{pr^4}{Eh^3}\left(1 - 2\frac{x^2}{r^2} + \frac{x^4}{r^4}\right) \qquad (6)$$

where h and r are the thickness and the radius of the membrane, E denotes the elasticity modulus, and Ψ is a constant depending on the mounting. The three terms in eq. 6 should be interpreted in the following way:

(i) the first term $\Psi pr^4/Eh^3$ represent a pressure dependent change of the resonator length, causing a shift of axial modes;

(ii) the second term $-2\Psi(pr^4/Eh^3)x^2/r^2$ is the parabolic term and is used for the adjustment of the resonator parameters by varying the pressure p. The radius is:

$$\frac{1}{\rho} = -\frac{4\Psi pr^2}{Eh^3} \qquad (7)$$

(iii) the third term $\Psi(pr^4/Eh^3)x^4/r^4$ represents the spherical aberration which should be held below $\lambda/10$ for most laser applications.

The rear mirror radius and the resonator parameters for a given magnification M are related by the relation:

$$\frac{1}{\rho_2} = \frac{1}{b}\left[a - \frac{1}{g_1^*}\frac{(M+1)^2}{4M}\right] \qquad (8)$$

where for an unstable resonator with two rods the parameters a and b are given by:

$$a = 1 + d_1 D_1 [d_m D_2 - (1 + \frac{D_2}{D_1})] - d_m D_2 \qquad (9.a)$$

$$b = (d_1 + d_2 + d_m) + d_1 d_2 D_1 [d_m D_2 - (1 + \frac{D_2}{D_1})] - d_m D_2 (d_2 + d_1 \frac{D_1}{D_2}) \qquad (9.b)$$

In order to keep the magnification of the unstable resonators constant, the radius of the rear mirror was adjusted for the rods' refractive powers according to relation (8). The deformable optical mirror was made from a 0.65-mm-thick BK7 glass membrane with 22-mm diameter and fixed in a metallic mount. This base was constructed in such a way that the accuracy of the mirror contour is insensitive to the mounting; the pressure on the mirror was obtained with a water pneumatic cell whose dimensions are controlled by a micrometer screw.

The variation of the curvature radius of the membrane as a function of pumping energy is presented in figure 8. The beam quality obtained from the unstable resonator at 5 Hz and 10 Hz repetition rates is shown in figure 9. By this thermal lens procedure the beam quality was maintained at a low value, characteristic of an unloaded resonator. For comparison the beam quality of the stable resonator with two active media at 1 Hz repetition rate is presented in fig. 9. The output energies were close to those obtained at 1 Hz.

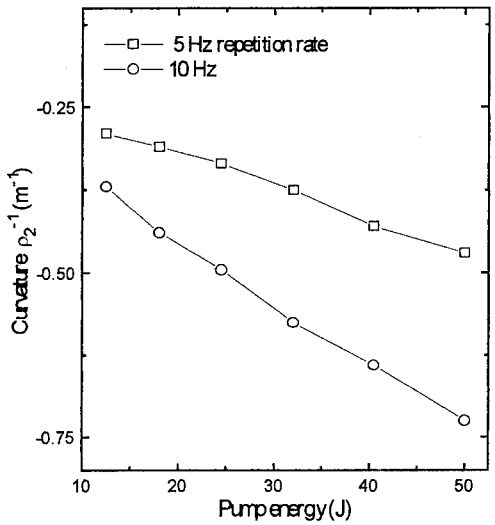


Figure 8. The variation of rear mirror radius for the unstable resonator with M=1.8 at 5 Hz and 10 Hz repetition rates with pumping energy.

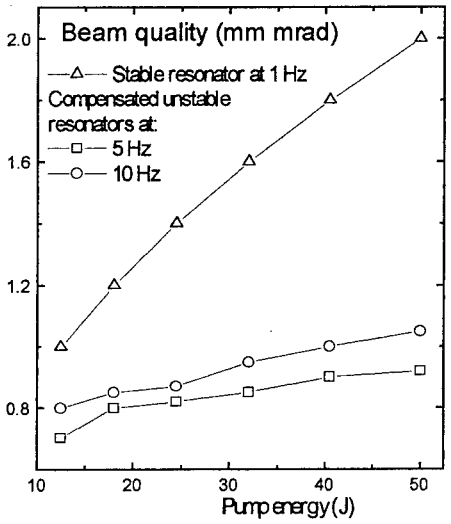


Figure 9. Beam quality for a thermal compensated unstable resonator. For comparison the beam quality of the stable resonator at 1 Hz repetition rate is also shown.

4. CONCLUSIONS

The performances of a two-rod super-Gaussian positive branch unstable resonator for Nd:YAG solid-state lasers were investigated in the free-generation regime. With increasing pump energy a decrease of the unstable resonator magnification M with an alteration of the beam quality was observed. By the proper radii variation of a glass deformable pressure-controlled rear mirror, the magnification of the positive branch unstable resonators was made insensitive to the thermal loading of the laser active media.

Acknowledgements: This work was supported by the Romanian Ministry of Research and Technology under contract 151B/A434 (1995).

REFERENCES

1. Magni, V., De Silvestri, S., Lie-Jia Qian, and Svelto, O. (1992), Rod-imaging supergaussian unstable resonator for high power solid-state lasers, *Optics Comm.*, **94**, 87-91.
2. Hodgson, H., Bostanjoglo, G., and Weber, H. (1993), The near-concentric unstable resonator (NCUR)-an improved resonator design for high power solid state lasers, *Optics Comm.*, **99**, 75-81.
3. Chetckin, S.A. and Vdovin, G.V. (1993), Deformable mirror correction of a thermal lens induced in the active rod of a solid state laser, *Optics Comm.*, **100**, 159-165.
4. Pavel, N., Dascalu, T., Totia, H., Florescu, R., and Lupei, V. (1994), Adaptive optical mirror for unstable resonators with thermal effects, CLEO/Europe '94, *Technical Digest*, **IEEE TH0614**, 115.
5. Subhash, N. and Sathianadan, K. (1984), Thermal Effects in a Nd:Glass Laser Rod Pumped in a double Circular Close-Coupled Cavity, *IEEE J. Quantum Electron.*, **QE-20**, 111-116.
6. Dascalu, T., Pavel, N., and Lupei, V. (1994), Laser Resonators with High Beam Quality, *Balkan Physics Letters*, (in press).
7. Driedger, K.P., Ifflander R.M., and Weber, H. (1988), Multirod Resonators for High-Power Solid-State Lasers with Improved Beam Quality, *IEEE J. Quantum Electron.*, **QE-24**, 665-674.
8. Keming Du, Loosen, P., and Kochmann, H. (1994), Properties of a high-power CO_2-laser with an adaptive mirror, *Optics Comm.*, **106**, 269-277.

BEAM TRANSPORT OPTICS FOR HIGH-POWER LASER SYSTEMS

JOHN R. TAYLOR
Lawrence Livermore National Laboratory
Livermore, California 94550

1. Abstract

Beam transport optics receive output energy from the laser cavity and deliver it to the work site. Depending on the application, this may require a few simple elements or large complex systems. Collection of the laser energy depends on the spatial and temporal energy distribution as well as the wavelength and polarization of the laser cavity and output coupler. Transport optics can perform a variety of functions, including beam formatting, frequency doubling, and distribution to one or more work sites while maintaining or even improving the beam quality. The beam may be delivered to work sites as focused spots or images, projected to distant targets, or propagated through various media for sensing or photochemical processing.

Design may involve optical modeling of the system, including diffraction effects and thermal management. A Gaussian beam profile is often used for convenience in modeling. When deviations from this ideal profile need to be considered, it is necessary to characterize the laser beam in detail. Design of the transport system requires understanding of the interaction of the laser energy with optical materials and components. Practical considerations include mounting the optics without stress and with the stability suitable for the intended application. Requirements for beam direction, stability, size, shape, and quality dictate the design approach for each specific situation.

Attention also must be given to reliability, environmental, and commercial requirements. Damage to optics in high-power laser systems is a common concern. Environmental problems such as atmospheric turbulence, contamination by dust or vapor from the work site or other sources, or absorption of water vapor can directly degrade beam quality. Other potentially significant optical performance effects may result from instability and aging of the optics, temperature, humidity, pressure, transmitted vibration, and contamination from the work site or other sources. Optimizing beam transport systems may include cooling active components or subsystems that provide automated pointing, centering, and wavefront control.

Design of optical components includes material selection, fabrication tolerances, and coating requirements. Component specifications are sometimes best handled by describing the performance requirements for the optics. Testing optics performance and qualifying vendors to meet system requirements and specifications are important to ensure total laser system performance.

Visible beams can be added to provide a safe and simple method of aligning the high-power laser beam on the work site or to maintain alignment and quality over long distances.

Work performed under the auspices of the U. S. Department of Energy by the Lawrence Livermore National Laboratory under Contract W-7405-Eng-48.

R. Kossowsky et al. (eds.), High Power Lasers – Science and Engineering, 303–329.
© 1996 *Kluwer Academic Publishers. Printed in the Netherlands.*

Several beam transport optics systems and examples of component specifications and methods of testing important performance requirements illustrate these fundamental and practical issues.

2. Introduction

The development of lasers provided a vastly improved light source which allowed advances in many areas, opened up new applications, and spawned new industries. Prior to the laser, high-power applications were generally limited to simple illumination and projection systems using broadband, noncoherent sources. The optical systems were often relatively sophisticated in order to deal with large area-, diverging-, and broad-band sources. Material selection, design, and coatings were optimized to provide efficiency, control and reliability. Over the past forty years, the development of lasers and thermal their applications have increased the demands on beam transport systems and components particularly at high-power and pulse energies over a broad range of wavelengths. New developing applications require more complexity in the transport system and more reliability in the optical components in order to provide a flexible delivery path, to transport over long distances, and to utilize multiple lasers for increased power, frequency, and reliability.

3. The Optical Transport System

The requirements and physical constraints for the optical transport system are defined by the laser and the application. The interface with both the laser and work site must be understood in order to define the beam characteristics. This interface also determines how the optical system will be designed to format the beam, to maintain required beam quality and stability, and to provide beam scanning or positioning. Optical component specifications are then derived from the system requirements in the design process.

This approach is utilized to describe the optical transport system and optical components for high power laser systems. Common issues involve diffraction, efficiency, and thermal management. Optical components for high-power applications have some unique manufacturing and performance issues. A diagram of a typical laser system, illustrated in Figure 1, shows the laser, transport system, and work site divided into major elements.

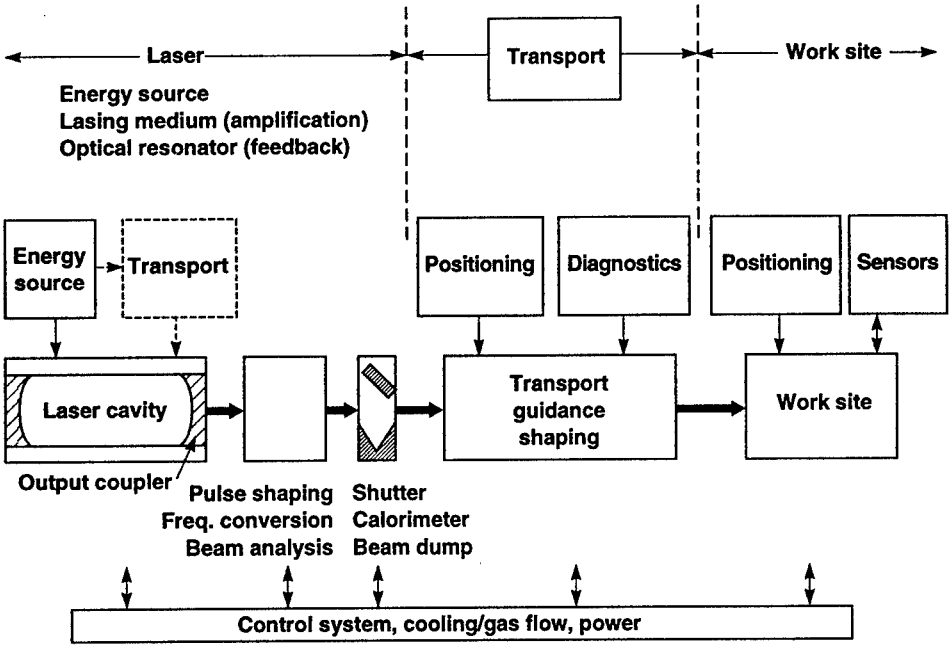


Figure 1. Typical laser system.

Although some functions such as pulse shaping and frequency conversion can occur within the transport system, they will be considered part of the laser function and not discussed in detail. The transport functions apply to the common applications for high-power lasers as a heat source (cutting, welding, and surface treatment), for power transmission, and for a variety of applications that increasingly extend into the high-power regime such as inspection, distance measurement, printing, pollution monitoring, and holography. High-power laser sources for this range of applications usually include CO_2, Nd-YAG, Nd-glass, ruby, and, increasingly, excimer for industrial applications.

There is a growing need for intermediate wavelength sources in the visible and near IR region such as copper vapor, dye, Argon and Ti:Al_2O_3. Lasers that do not produce usable high power in a single cavity can sometimes be operated with multiple stages of amplification or multiplexed to deliver high power to the work site. The transport functions will be described and illustrated in several laser systems currently under development: (a) the use of a laser to create an artificial guide star, (b) Atomic Vapor Laser Isotope Separation (AVLIS), and, (c) the National Ignition Facility (NIF).

4. System Considerations

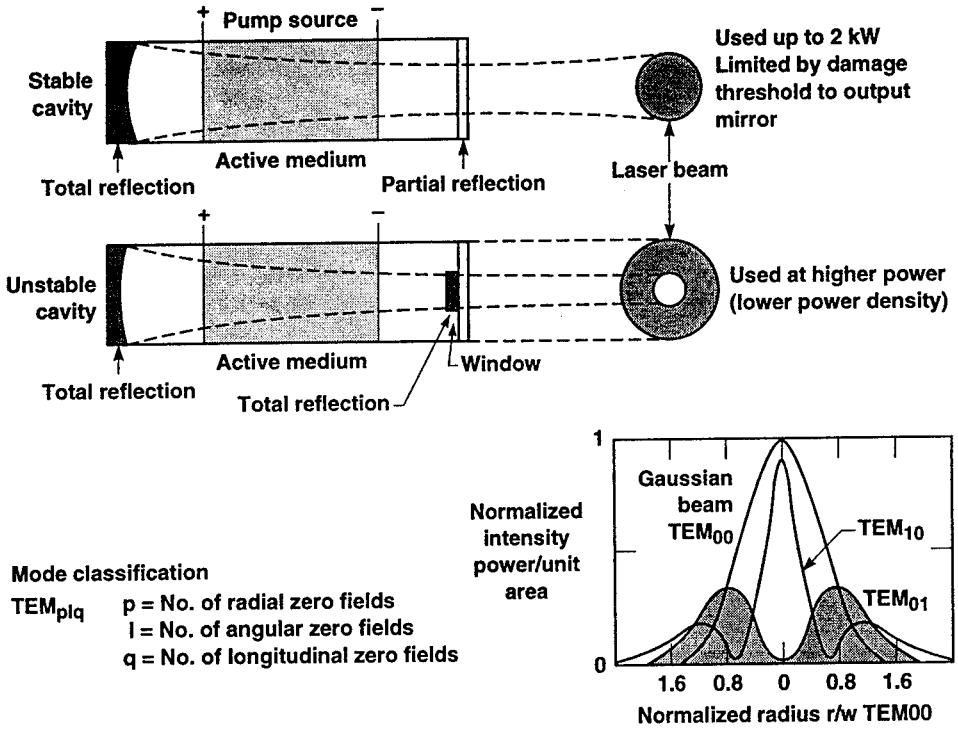
4.1 INTERFACE WITH THE LASER

The laser diagram in Figure 1 illustrates the fundamental elements of the laser: an energy source, a laser medium for amplification, and an optical resonator or cavity to

provide feedback. Lasers are also used as the energy source to pump other lasers in some applications, which means that the transport of the pump laser light must also be engineered. The laser may also include a number of other elements such as beam analysis, apertures to improve mode quality, gratings to narrow the spectral bandwidth, temporal pulse shaping, frequency conversion, power measurement, and shutters. The important interface requirements for beam transport are largely determined by the cavity design. The resonator cavity usually consists of at least one curved reflective surface and an output coupler used to extract useful light from the cavity as illustrated in Figure 2.[1] A partial reflector is one of the most convenient methods to maintain a stable cavity. At high power, other methods are sometimes required that may make the cavity unstable and degrade mode quality. The cavity length (L) and the width at the output aperture (a) determine the number of off-axis modes that can oscillate in the cavity. The Fresnel number (N) represents the number of fringes in the output aperture, where λ is the cavity wavelength.

$$N = \frac{a^2}{\lambda L} \tag{1}$$

The Transverse Electromagnetic Mode (TEM) structure of the power distribution across the beam describes the off-axis modes illustrated in Figure 2.



1.1.3.0695.1577pb01

Figure 2. Cavity design and mode quality.

4.2 INTERFACE WITH THE WORKSITE

Applications utilizing high-power laser energy typically require a beam format optimized for either delivery to a spot (cutting, welding, surface melting, surface texturing, non-contact bending, magnetic domain control, stereo lithography, and atomic fusion), uniformity over a surface (heat treatment, surface alloying, electroplating, chemical or vapor deposition, paint stripping, holography, or inspection), or propagated to a distant location or through a medium (distance measurement, pollution monitoring, laser guide star, or isotope separation).[1,2]

Beam power, wavelength, and quality for cutting depend on the material and method used. Vaporization is usually used with pulsed lasers and materials that don't melt. Fusion cutting uses a gas jet to blow melted material away from the cut and requires less power. Reactive fusion cutting adds a gas like oxygen to react with melted material as well as blow it away to increase the cutting speed. Controlled fracture is used with brittle materials. Scribing weakens a part to permit a well-defined break. Cold cutting is a growing application for excimer lasers to reduce heat transfer to the part. Beam requirements affecting performance are usually power, traverse speed, spot size, and material thickness. A small beam size reduces cut width and increases absorption of energy. Since cutting is generally found to be much faster in the direction of polarization, circular polarization can be used to produce uniform cut width and speed. Shorter wavelengths allow smaller spot size assuming the same mode structure. Advances are being made in precision micro drilling using a 30-watt copper-vapor laser for percussion drilling, trepanning, and advanced laser beam quality control, and wavefront tilting technologies.[3]

For thicker materials, the best cuts may occur when the beam is focused below the surface. Material properties such as the surface finish and reflectance, oxide layers, and plasmas produced during cutting effect the choice of cutting method, wavelength, and power required. Air breakdown can be a limiting factor in these applications at high power and small-beam size. When beam quality is high, near diffraction limited spot sizes can produce a power density that exceeds the ionization potential for gas molecules. When beam quality is very non-uniform, individual areas in the beam can produce high power with a similar result. Mode quality and intensity variations can sometimes be controlled through design of the laser, transport system (such as imaging the output aperture), or phase plates to improve energy distribution.

Welding imposes a similar set of requirements. The energy can be delivered continuously or in pulsed format but the pulses are usually longer and shaped to have a smaller initial peak than for drilling. When welding in a "keyhole" or joint, there is relatively little dependence on wavelength because of high absorption due to the geometry. Offsetting this high absorption in a keyhole is the formation of plasma that blocks the beam which reduces the quality of the weld. When using a conduction limited weld, the preference is for high absorption, usually obtained at shorter wavelengths.

For surface treatment or long propagation applications, beam power and uniformity are of major importance. This application usually requires a uniform distribution of energy at the surface or through a volume of space. The power level must be controlled so that it is above a minimum level required to perform the process (annealing or paint stripping) but below a level that could cause melting, damage, or other unwanted effects. This application is typically sensitive to mode quality and near-field beam

quality. It is often useful to image the laser or output aperture either at the surface being treated, into the medium, or to a distant point. Atmospheric turbulence can significantly affect the beam quality in practical applications and may require active wavefront sensing and correction or operation in low-pressure enclosures. A promising high rate, pulsed laser deposition technique using a copper vapor laser to produce diamond-like-carbon coatings has been demonstrated.[4]

4.3 BEAM CHARACTERIZATION

Laser beams are characterized by a variety of parameters which define the wavelength, phase, and electric field relationships as well as the distribution in space and time:[1,5]

- Spatial energy profile (mode/diameter).
- Temporal energy profile (pulse width, wave shape, repetition rate).
- Spectral profile (wavelength).
- Phase relationship (coherence).
- Electric field relationship (polarization).

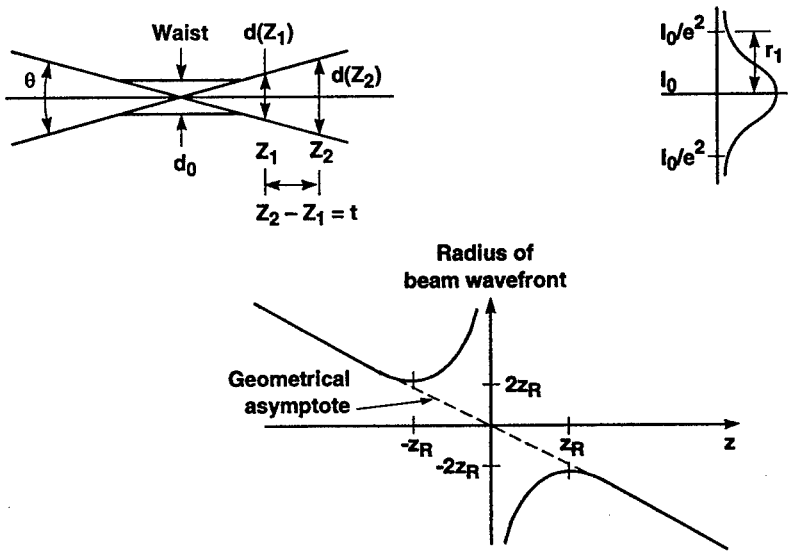
Practical beams are typically made up of components that produce a range of these values. Spectral bandwidth ($\Delta\lambda$) is the width of the spectral line at half the maximum power (half width). Narrow spectral bandwidth is a feature of lasers that is rarely utilized in high-power applications with the notable exception of isotope separation. Stability of phase in both space and time can be an important parameter. The coherence length is defined as $\Delta s = \lambda^2/\Delta\lambda$. Coherent beams also have their electric field vectors all lined up. Beams are also characterized by the extinction ratio of desired to unwanted polarization.

Mode quality plays a major role in how well the beam can be transported, focused, or distributed in space. The higher the order of the mode, the more difficult it is to focus the beam to a small spot. Lasers may run at a continuous (cw) power level or in pulses defined by intensity (or fluence), pulse energy (or power), pulse width (Δt), pulse period (t') or repetition rate ($R = 1/t'$).

The simplest type of beam is the lowest mode (TEM_{00}). Gaussian describes the profile of the beam through its center as shown in Figure 3.[6] Irradiance is symmetric about the beams axis and varies radially, I(r).

$$I(r) = I_o e^{-2(r/r_1)^2} \qquad (2)$$

The beam radius is defined where the irradiance is $1/e^2$ of the maximum value. A beam either diverges from or converges to the narrowest region called the beam waist. The divergence (or convergence) far from the waist ("far field") is defined as the full angle (θ) subtended by the $1/e^2$ points.



1.1.3.0695.1580pb01

Figure 3. Gaussian beam characteristics.

Here $d \equiv \theta z$. Diffraction defines a minimum spot size that can be produced at the waist, $d_0 = 4\lambda/\pi\Theta$, rather than the theoretical point predicted by geometrical optics. To decrease the waist spot size, λ can be reduced or θ can be increased. As beams become more collimated, the waist size increases. Near the beam waist ("near field"),

$$d = \sqrt{d_0^2+\Theta^2 z^2} \tag{3}$$

The beam waste region is called the Rayleigh range and is defined as the distance from the beam waist to

$$d = \sqrt{2}\, d_0 \tag{4}$$

$$\text{where } Z_R \equiv d_0/\Theta. \tag{5}$$

The wavefront in the beam is planar at the waist and becomes flatter again in the far field as shown in Figure 3.[6] The radius of the beam wavefront is a minimum at the Rayleigh points $\pm Z_R$. An ideal Gaussian beam is completely defined by this information. The initial Rayleigh range is defined by the radii (R_1 and R_2) and spacing (L) of the cavity mirrors. For a stable cavity, $Z_R^2>1$. For an unstable cavity, $Z_R^2<1$.

$$Z_R^2 = \frac{L(R_2+L)(R_1-L)(R_2-R_1+L)}{(R_2-R_1+2L)^2} \tag{6}$$

In order to use the beam, it usually has to be expanded, focused, or recollimated using lenses, mirrors, prisms, or plates of glass. When reimaging the waist with a lens, the size, convergence angle, and Rayleigh range can easily be derived from the initial waist and lens characteristics.[6] The beam waist for a laser is not always well known but is often assumed to be near the output mirror of the laser.

A Gaussian beam is "collimated" by making the divergence as small as possible and distance to the next beam waist as far as possible. A telescope that initially strongly converges or diverges a basically collimated beam with a short focal length lens and uses a long focal length lens for recollimation can improve collimation and expand the beam size. The first case is a Kaplarian telescope and the second case is a Galilean telescope.

Beams with high modes have the same Rayleigh range but a larger spot size and divergence than the TEM_{00} mode. Higher order modes are hard to transport and shape which eventually results in a loss of energy. Higher order can be suppressed using a limiting aperture in the laser cavity or in the near-field beam with a corresponding loss of energy.

Where uniform energy distribution is required at the worksite, flat-top beams can be made from a Gaussian beam by using an aperture to block the outer edges of the beam. This is very inefficient but can be effective when followed by further stages of amplification, as in a master oscillator/power amplifier (MOPA) configuration. Flat-top beams can also be made using a phase grating to produce an electric field distribution that becomes flat top in the far field. Diffraction limited beam quality can be maintained in transport systems by following several principles:

- Relay an image of the laser or system aperture to each amplifier, worksite, or to the center of the illuminated medium.
- Use optics with low wavefront distortion.
- Use optics in the far field large enough to avoid diffraction losses.

4.4 INTERACTION WITH OPTICAL MEDIA

When light interacts with optical media, it is generally divided into components that are reflected, transmitted, and absorbed. The law of reflection predicts that the angle of specular reflection equals the angle of incidence. The law of refraction predicts the angle of the specular transmitted component on the basis of the relative index of refraction (n_1 for the initial medium of transmission and n_2 for the material on which it is incident): $n_1 \sin \theta_1 = n_2 \sin \theta_2$. In addition to the specular (defined by a single direction) components, small scale deviations from a flat surface or bulk properties produce diffuse nonspecular components which scatter the light over wide angles. Nonspecular loss is normally small for good quality optical components but can play a role when the number of components in a system is large or the surface of the optics become contaminated.

The refractive index for any material varies with wavelength (dispersion = $\Delta n/\Delta\lambda$ and temperature ($\Delta n/\Delta t$). The dispersive power describes the spectral variation for the material.

$$\text{Dispersive power} = \frac{n(F) - n(c)}{n(d) - 1} \tag{7}$$

where n(F) is the index at the Hydrogen F line (4861Å)
n(c) is the index at the Hydrogen C line (6563Å)
n(d) is the index at the Helium d line (5893Å)

The Abbe number = 1/dispersive power

For a material of absorption coefficient α, the intensity of a beam of initial intensity (I_0) that has traveled a distance x in the material will have an intensity of $I = I_0 e^{-\alpha x}$. Optical material normally has a band-pass region of low absorption limited in the best cases by impurities, phase changes, voids, boundaries, and inhomogeneities.

The reflection and transmission characteristics of an optical surface can be enhanced by optical coatings. Highly polished metal surfaces and coatings tend to be reflective over broad spectral regions but can lead to large, accumulated energy loss when many reflections are required and absorb a significant amount of energy, a problem for high-power lasers. Thin dielectric films are used to control reflection through constructive or destructive interference. These coatings are optimized for specific applications. Scattering and absorption can be controlled to a high degree through proper design, selection of materials, and deposition techniques.

5. System Design

5.1 SYSTEM REQUIREMENTS

High-power, optical-transport systems usually share several common goals. For applications requiring control of the energy distribution, typical performance goals include:

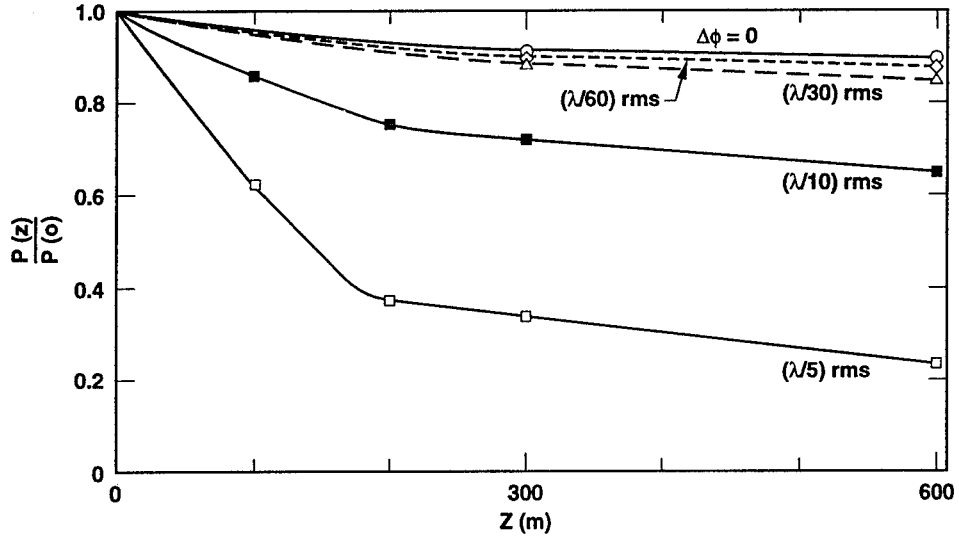
- High efficiency.
- Good beam uniformity and wavefront quality.
- Accurate beam pointing and position control.
- Images at specific locations.
- Ability to handle high fluence or average power density.
- High reliability for maximum system availability and lowest maintenance cost.

The design of the transport system proceeds using these goals, specific performance requirements, and the interface constraints with the laser and worksite. Simple systems for monochromatic Gaussian beams can be performed using the guidelines already provided. Complex input beam characteristics or system requirements quickly require more sophisticated design tools for geometric ray tracing and diffraction analysis. At this point, experienced designers are required because the project can become a significant effort to document, procure, test, install, align, and operate the system.

It is useful to be able to model the thermal response of the system in order to help optimize the selection of optical materials and predict their effect on the system. Since computer codes for this application are not available commercially, we developed a code called TSO (for Thermal, Structural, Optical analysis) to aid in the analysis of laser optical systems whose operating characteristics are altered by absorption of the applied beam energy[7]. TSO is a VAX-based code that integrates three exisiting programs, CODE V®, NIKE 3D, and TOPAZ 3D. CODE V® is a three-dimensional implicit finite element code for analyzing the static and dynamic response of solids.

TOPAZ 3D is a three-dimensional implicit finite element heat-transfer-analysis code. TSO analyzes the optical system sequentially. The laser beam footprint on the first optic is determined from the optical design code, a finite element mesh is generated for the optical component, the thermal and structural effects are analyzed, and the lens data base is modified to show these effects. This is repeated for each optic with the beam footprint determined by a geometric ray trace through the distorted system. The end result is a lens file distorted by the heating effects due to the incident laser beam. Incident beam power, material bulk absorption and surface absorption, environment temperature, convection properties, and element mesh parameters are provided by the designer. This modeling has allowed us to understand and minimize wavefront distortion as well as guide us in designing our optical systems for high-power laser beam transport. The model predicts that a fused silica window can transmit almost ten times as much laser power at a wavelength of 600 nm as a BK7 window of the same thickness producing the same wavefront distortion due to lower bulk absorption. The model predicts that a 645 watt beam that is 1.3 mm diameter is distorted about 0.04 waves peak-to-valley through a 13 mm thick uncoated fused silica window (mostly due to the temperature dependence of the index) which agrees with operating experience.

The ability to model diffraction effects is also useful in the design process. The loss of power versus transport distance is shown in Figure 5 for a variety of wavefront quality beams. A transport system that can maintain the wavefront quality of the beam can approach the diffraction limit for transport efficiency.



1.1.3.0995.2200pb01

Figure 4. Power loss from a 2 x 5 cm aperture: initial phase vs distance.

5.2 COMPONENT SPECIFICATION

In order to specify the transport optics for high-power laser systems, it is important to understand how the optical system is affected by component performance. This is illustrated in Table 1.[8]

TABLE 1. Effect of optical components on system performance

Optical component characteristics	Optical system efficiency	System wavefront quality
Bulk index variation	√	√
Surface roughness / defects	√	—
Surface shape errors	√	√
Reflectance / transmittance	√	—
Absorptance	√	√

The optical design process provides the nominal size, material, surface curvatures, and often the thickness of the optic and maximum wavefront distortion. Tolerances for these parameters are usually provided as guidelines from a sensitivity analysis. Completing the specification process requires a detailed understanding of the application, operating environment, mechanical constraints, stability requirements, budget, and schedules. In addition to understanding the application and system performance, other considerations in the specification process include:

- Who will be reading the specification?
- How should the requirements be stated (as manufacturing steps or performance)?
- How can the requirements be verified?
- How are production cost, schedule, and yield effected by the specifications?
- What form and standards should be used to document the requirements?

There are a variety of administrative issues to resolve such as referenced standards, test requirements, marking, packaging, shipping instructions and interface issues such as size, wedge, chamfer, environment, and cleaning requirements. In addition, decisions must be made between performance-based requirements and secondary [nonfunctional] specifications. Performance requirements might include beam deviation rather than wedge or centering specifications; focal length and wavefront quality rather than radius of curvature, surface figure, striae, and homogeneity; reflection, transmission, scatter, or absorption rather than coating design and surface roughness; or survivability (damage threshold) rather than coating design, surface defects, or material impurities. Performance based requirements are preferred if they can be tested and if their importance is well understood.

6. System Optimization

6.1 THERMAL MANAGEMENT

Several steps can be taken to minimize the amount of heat introduced into the transport optics and deal with the residual effects. These steps include the following:

- Minimize transmission in optical media; use reflective optics.
- Use the lowest absorption optical media when transmission is unavoidable (vacuum windows, beam combiners/splitters, waveplates, etc.).
- Design coatings for minimum absorption (<10 ppm, visible).
- Control stray light from secondary reflections and scatter; use masks and beam dumps.
- Control the conductive cooling path from the optic. Conduction to the mount through the edge of the optic lowers the optic temperature but increases radial temperature gradients and wavefront distortion.
- If passive control is not sufficient, consider active cooling: forced air convection, water flowing through interior channels, or immersion in a transmissive cooling fluid.
- If passive control and active cooling are not sufficient, a deformable mirror may be required to correct wavefront errors.

The use of fused silica and low absorption coatings has been effective in our applications. Significant improvements in coating absorption shown in Figure 6 was demonstrated as a result of an effort to optimize the designs[9]. Several attempts to actively cool the optics have been tried but results were not satisfactory due to turbulence induced wavefront errors with forced air cooling and shortened coating life for immersed optics. Relatively inexpensive deformable mirrors and wavefront sensors have been developed that are very useful in dealing with residual thermal effects.

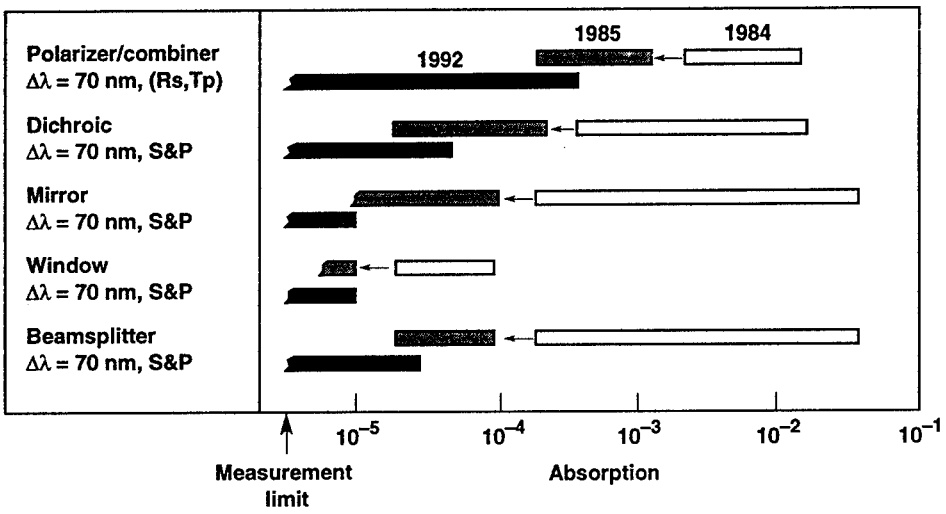


Figure 5. Improvement in coating absorption for thermal management.

6.2 FIBER TRANSPORT

Low-loss optical fibers have proven to be very useful in providing multiplexing and system flexibility. Fused silica fibers with 1 mm core diameter routinely transport up to

several hundred watts of visible laser light in the AVLIS transport system. This network of fiber discussed in the examples can be easily reconfigured to redistribute the laser light and no longer requires that the lasers and transport system be in a fixed relationship to each other.

Several important efficiency and reliability issues are in development. These include cleaning and preparing the fiber faces for maximum coupling and damage threshold, antireflection coating of fiber ends, and improvements in the reliability of the fibers from various sources of deterioration and damage. The fibers are part of a large power distribution network.

6.3 MOUNTING AND STABILITY

All the efforts to manufacture high-quality optics to minimize wavefront distortion can easily be defeated by improper mounting. The design of the mount should hold the optic at three opposed points or by edge grooves in the optics and isolate the optic from stresses and temperature variations in the mount. The best approach is to test the optic for wavefront distortion before and after it is assembled in its mount. Only minimal changes should be observed after mounting. This provides confidence that the mounted optic will not contribute to system errors.

Stability should be provided for the laser, transport system, and worksite, as well as isolation from all sources of transmitted or acoustic vibration. Various isolation techniques are possible. Direct measurement of beam stability at the worksite and vibration measurements along the beam path are useful ways to verify performance (or track down problems). Remaining instability may require correction by using a fast response, closed-loop pointing system.

6.4 POINTING AND CENTERING

Active correction of beam pointing and centering may be required to compensate for system instabilities, thermal response, or anticipated movement between the laser and worksite.[10] Although simple in concept, the use of numerous closed loops in large laser systems represents a challenging control problem. Examples of large laser systems are described later.

Sampling of the beam position is required using a beamsplitter or diffractive optic to separate a small percentage of the beam power. This can adversely affect total system efficiency in large systems where numerous diagnostic systems are required.

Additional low-power laser beams can be added to the high-power transport path as pointer or pilot beams. There are several advantages to this approach. The transport system can be maintained in alignment with or without the high-power beams. The lower power beams can be smaller and of better quality which improves the diagnostic function. They can be used continuously with low repetition rate, short pulse systems to precorrect future pulses based on the quality of past measurements.

6.5 WAVEFRONT CONTROL

Closed-loop wavefront control of the beam may be useful to correct for many of the same sources that can affect pointing and centering. This type of system can provide flexibility for addressing other system parameters such as beam size, shape, and image location. Wavefront control can also be the whole purpose of the system, as in the

guide-star programs. Several applications will be discussed later. This system involves beam sampling and the addition of pilot beams for pointing and centering diagnostics. Beam wavefront is typically controlled by deforming the surface of a mirror to introduce the desired amount of correction. The design of these mirrors can often involve independent actuators that bend a thin plate consisting of the mirror surface or separate mirror segments. To provide feedback to the control mirror, the beam wavefront can be measured using an interferometer or hartman sensor optimized in the design with the mirror actuator system.

6.6 RELIABILITY AND ENVIRONMENTAL EFFECTS

The performance of the transport optics and how that performance changes with time, environment, and system power level has a major impact on system performance and reliability.

The extreme case is optical damage to the coating or bulk material at high-power levels that degrades or interrupts system operation. Failure may occur slowly in some cases of antireflection coatings or more often catastrophically for mirrors.[11] Material selection and coating design should be optimized for high-power operation. System reliability can be obtained by the following steps:

- Test optimized coatings and selected materials to determine the highest level of fluence or power for which the optics survive without degraded performance.
- Design optical transport systems within this region of reliable survivability.
- Establish a testing program to ensure that each optic meets this minimum level of performance with damage.

A development program to lower coating absorption for thermal management provided more reliable operation (less change in the beam wavefront) over a wide range of operating power and also improved the survivability of the coating at high power in a high-repetition rate laser system.[12] Damage in low-absorption coatings is now usually associated with coating defects or contamination, a relationship familiar to single-pulse, high-fluence laser systems.

Enclosing the transport system in vacuum introduced two environmental effects for the optical coatings. As is well known, the spectral curve shifts to shorter wavelengths as water molecules are withdrawn from the relatively porous evaporated coating at low pressures. For coatings used for their spectral shape to combine different wavelengths, this can require adjusting the angle of incidence between operation in air and operation in vacuum. In measuring this effect, we found the magnitude and time to stabilize greater than expected.[13]

In addition to the spectral shift, we observed a change in coating stress during this process, which could be very significant, as shown in Figure 7. Since almost all of the coatings we use have a compressive stress forcing the optical surface into a slightly convex shape, operation in a low pressure environment tends to reduce the stress which causes all of the optical surfaces to become more concave. The effect is additive and can become significant for large systems. Coating processes that densify the coating, reduce the amount of water which can be absorbed and can minimize the spectral shift and stress changes as shown for the ion beam sputtered (IBS) coating in Figure 7.[13]

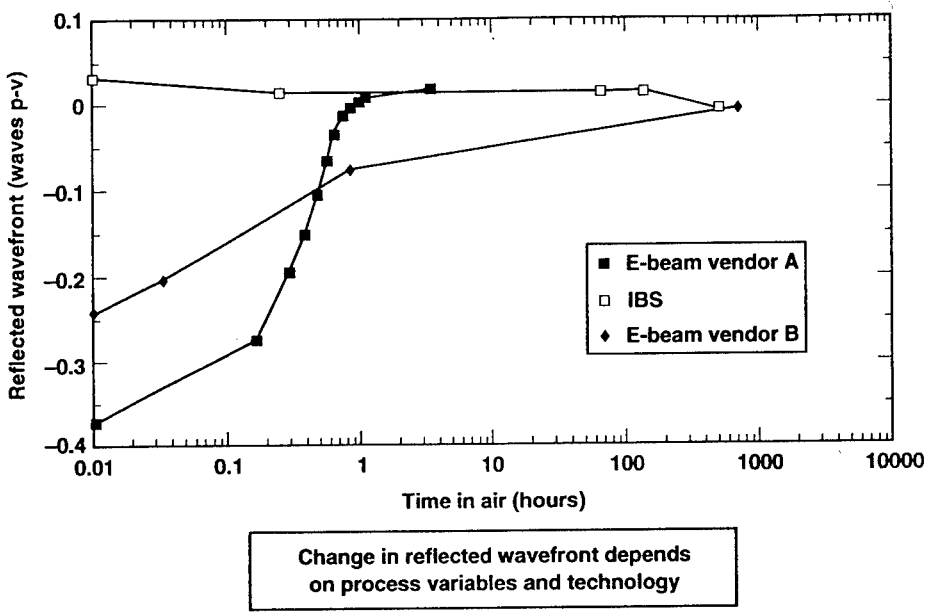


Figure 6. Change in stress from vacuum to air.

We have observed an increase in absorption over time for a few coatings. This observation prompted us to monitor absorption for a number of coatings over a 5-year period. This problem has been associated with a specific coating material (Ta_2O_5) although the problem was not observed for all vendors using the material. The cause is not known but this knowledge will help us avoid the problem in our transport system.

A similar problem was observed when measuring absorption over a range of power levels. One coating material (Ta_2O_5) in particular was found to increase in absorption at higher-power densities. Absorption measurements at low power may not reveal this power dependent problem. High-power tests are required to identify this problem.

Dust and vapor that deposits materials on optical surfaces can dramatically increase absorption and lower reliable survivability. Optics with contamination on the optical surface have been measured with absorption 10,000 times higher than clean surfaces. Laser damage was observed at 1/20 of the expected value due to contamination.

7. Components

7.1 COMPONENT PERFORMANCE

Typical optical component specifications for the AVLIS laser system described later are shown in Table 2.[9]

TABLE 2. Typical optical component specifications

Parameter	Mirror	Window or lens	Beamsplitter, dichroic,or polarizer
Bulk absorption (cm^{-1})	—	$\leq 5 \times 10^{-5}$	$\leq 5 \times 10^{-5}$
Subsurface damage	*	*	*
Coating microdefects	*	*	*
Surface roughness (Å rms)	<10	<10	<10
Visual defects, scratch/dig	10/5	10/5	10/5
Wavefront distortion (waves p-v at 633 nm)	0.05–0.10	0.05–0.10	0.05–0.10
Reflectance	>0.998	<0.003	>0.99 or ±0.02
Coating absorption	$\leq 10^{-5}$	$\leq 10^{-5}$	5×10^{-5}
Survivability (kW/cm2)	>10	>10	2 - 10

*Minimized through vendor qualification.

Transmitted wavefront quality can be predicted from the variation (or inhomogeneity) in the refractive index. An 18-mm thick fused silica window with 2 ppm inhomogeneity, can cause a wave-front error of about 1/20 wave (peak-to-valley). Similarly, the amount of energy lost in scatter can either be measured directly or it can be predicted from surface roughness:

$$\text{Total integrated scatter} \propto (4\pi r/\lambda)^2 \tag{7}$$

where r is the surface roughness. Optical surfaces with a roughness of 5Å rms should produce less than 0. 01% loss due to scatter. Commercially available optics can have scatter loss four times higher than this. In systems where scatter loss is important, it should be measured directly.

The importance of coating efficiency in large laser systems can be understood by an example transport system of N mirrors each with a reflectance (R). Efficiency of this system is R^N. For 27 commercial quality optics (R=0.995), system efficiency is 87.3%. For an optimized coating design (R=0.999), system efficiency is 97.3%. This can save significantly in the cost of the laser system needed to make up this difference and helps keep heat out of the transport optics.

7.2 OPTICAL COMPONENT MANUFACTURING

Manufacture of high-quality optical components along with preparing drawings, placing orders, shipping, and testing can require 6 - 9 months. Manufacture typically consists of the raw material, fabricating the optic shape and optical surfaces, and coating the optical surfaces. It is important to understand the relationship between the size and specifications and the impact on cost, schedule, and yield. Yield refers to the probability of an optic successfully being manufactured as specified and scheduled. The lower the yield, the higher the cost to produce the required quantities and the greater the chance of encountering program delays. Good planning and managing for this area of optics manufacturing can save money and keep the laser system on schedule.

The relative cost of the material, fabrication, and coating depends dramatically on size, quantity, substrate material, and quality of the surface, complexity of the coating, and testing requirements. An indication of these relationships can be obtained by reviewing prices in catalogs of commercial optics. Fully utilizing fabrication tooling capacity and filling coating chambers can keep prices down.

7.3 TESTING AND QUALITY ASSURANCE

Optics for high-power transport systems often involve requirements that are hard for a manufacturer to verify. Very high levels of reflectance, subsurface polishing damage, material and coating absorption, and levels of reliable survivability are examples. One approach is described in Table 3 for coating fabrication.[8,9]

Table 3. Coating Vendor Qualification Plan

Step 1 - Market Survey:	Survey, visit, and select potential vendor. Define vendor requirements.
Step 2 - Prequalification:	Vendor demonstrates ability to meet reflectance, durability, and surface quality requirements.
Step 3 - Development:	Assist prequalified vendor to develop special capabilities such as low absorption/low stress technology.
Step 4 - Qualification:	Vendor demonstrates 2 test runs on near-production size test samples that meet all requirements. The vendor is then added to the list of qualified vendors for that specific coating to be included on the bid list for production optics.
Step 5 - Qualification Review:	a) Periodic review of the performance of qualified vendors through production evaluation or requalification, b) Review of potential new vendors.

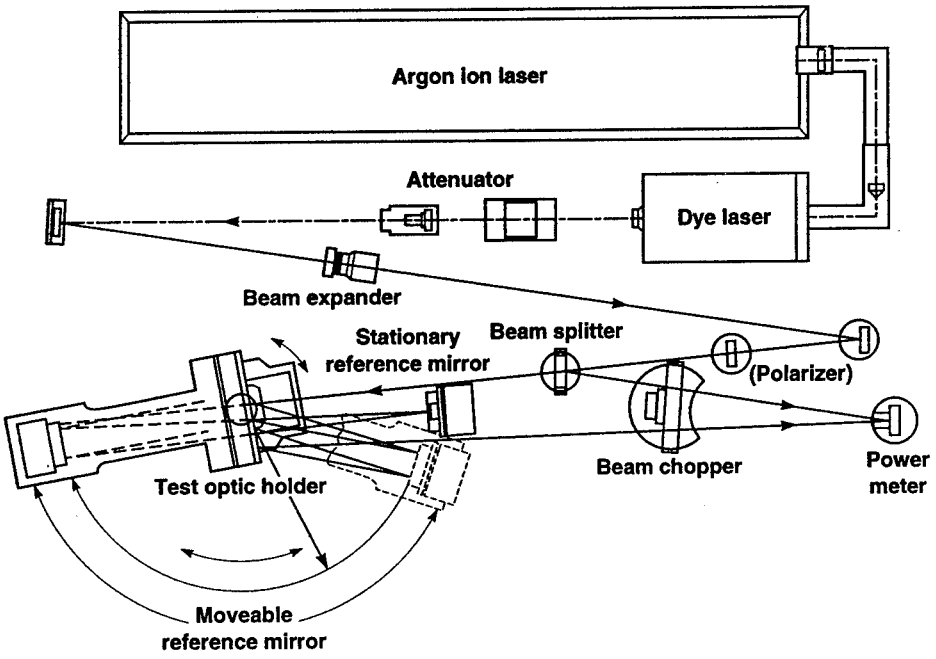
This type of qualification process is applied separately to procurement of the material, fabrication, and coating since manufacturers are often not equipped to provide all phases of the work. This involves an extensive program to qualify vendors and regularly assess their performance. It also requires up to three separate procurements for each type of optic. The advantages are seen in the confidence that optics will be delivered as scheduled which meet performance requirements at the lowest price. Qualification ensures fair and effective competition in the procurement process and better assurance that performance, budgets, and schedules will be met.

An important element of this process is having the capability of verifying performance of the optical component. To ensure that test results are a good indication of performance of the optical components in the laser transport system, a practical approach has been developed. Test samples are selected from production lots for nondestructive tests. When witness samples are required, they should be of the same basic substrate material and approximately the same size and shape as the production parts they represent. Coating samples are polished to the same specifications as the production parts. Test equipment is designed to be large enough to test production size parts and versatile enough to test the parts exactly as they will be used in the optical

transport system. Test data and witness samples are maintained on file for future reevaluation in the event that optical performance problems are later observed during operation. Where possible, the optical manufacturer should have the test capability to verify performance. This gives the manufacturer the direct feedback to optimize manufacturing processes and routinely monitor process control. As a last resort, the user should develop a test or screening method for optical performance that meets their needs. When problems are identified, this information can be provided to the manufacturer as feedback. This is a slow way to try to control the manufacturing process but, without some method of feedback, the process is not in control and performance problems in the optical transport will be the result. These problems can be very hard to track down in operation.

Several areas of testing have been particularly useful. Subsurface damage in the polished surface of optical components has been associated with damage in high-power operation. This is evaluated by etching samples polished with the production parts or sample parts from the production run. This destructive evaluation is being replaced by a microscope method of observing scattered light from defects just below the surface under test.[14]

For evaluating reflectance of high performance coatings, a multi-bounce, self-referencing laser photometer has been developed which can test reflectance of coatings on production optics with a high level of accuracy while simulating all operating parameters (wavelength, polarization, and angle of incidence). This is shown schematically in Figure 8.[9]



1.1.3.0695.1696pb01

Figure 7. Schematic of a ratioreflectometer.

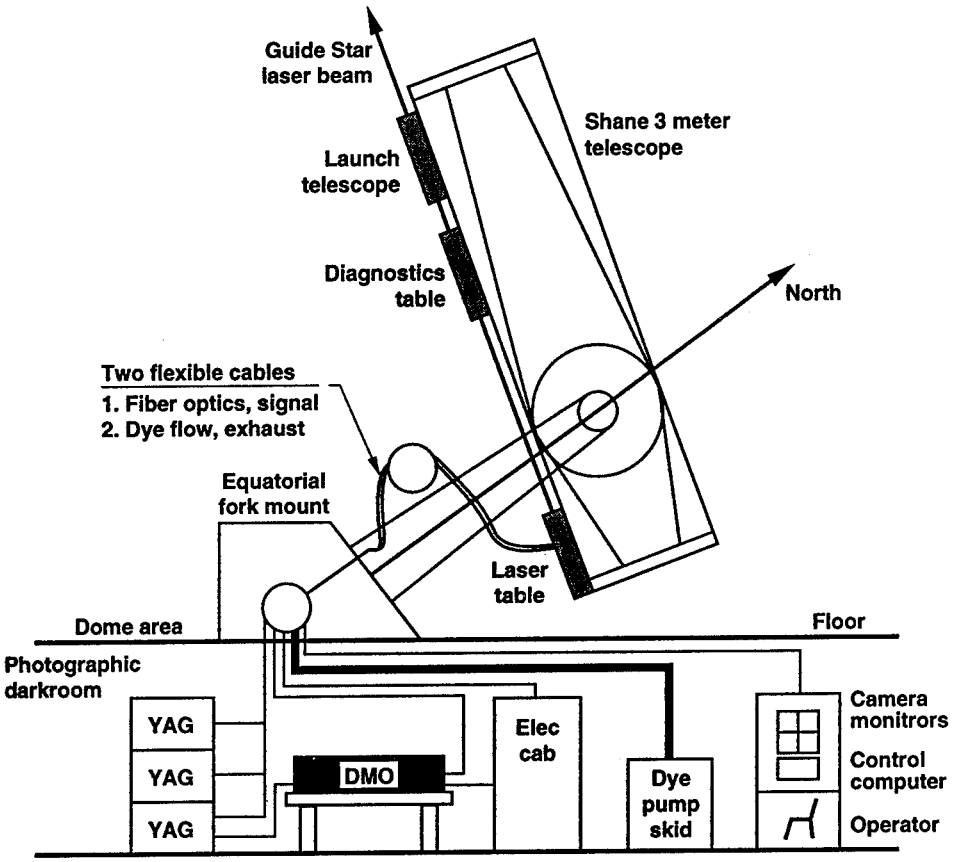
Absorption and damage tests of optical coatings have supported development of optimized coatings by coating vendors which help to verify performance for production. These tests use the same high-power lasers used in the high-power laser system to ensure that test conditions are the same as operating conditions.

An example of the importance of understanding the quality at each step in the manufacturing process was a transmitted wavefront problem traced to the selection of the fused silica blanks. The fused silica was typically graded for homogeneity in a thick sample and then sectioned into thinner plates with the assumption that the index homogeneity of each plate would be representative of the thick piece. A study of the index homogeneity for five plates cut from a single 79 mm thick core indicated that the homogeneity varied from 1.5 to 10 ppm, the best occurring at the center.[15] This indicated the need to measure the homogeneity of each plate in approximate final thickness. The fused silica manufacturer made major improvements in interferometry to support this requirement and drastically reduced wavefront problems from this source.

8. Examples

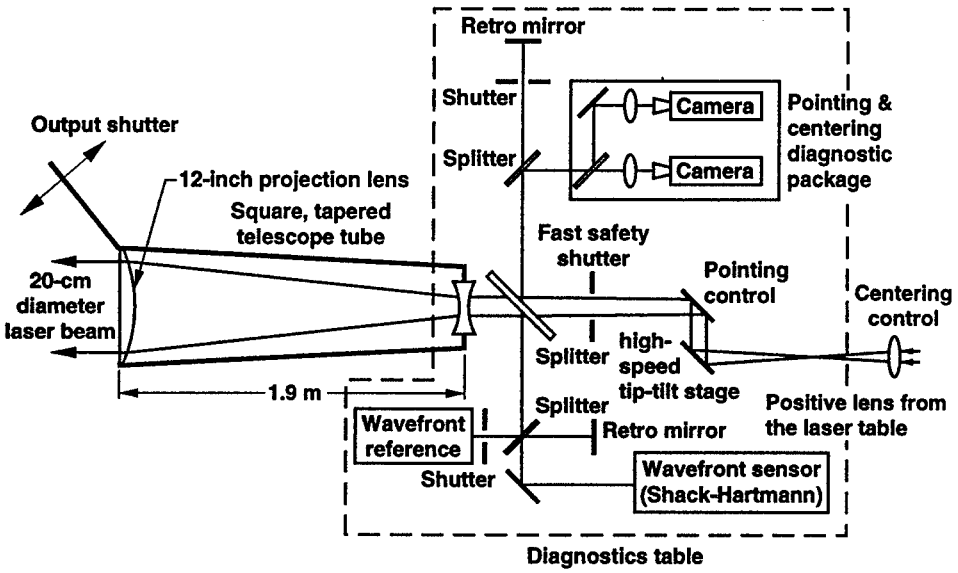
8.1 LICK LASER

The objective of this program is to demonstrate the ability to correct for atmospheric turbulence in astronomy using an adaptive optical system and an artificial source of light for a reference in areas of the sky where natural stars of sufficient magnitude are not available. The artificial "star" is created using a 25-watt dye laser tuned to a wavelength of 589 nm to stimulate a layer of sodium high in the atmosphere. Figure 9 shows schematically how the laser, diagnostic table, and launch telescope are attached to the Shane 3-meter telescope at Mt. Hamilton, California. The laser consists of a YAG pumped dye master oscillator transported by fiber to two stages of amplification. Figure 10 shows the optical transport system that provides automatic pointing and centering including a high-speed tip-tilt mirror and a wavefront control system using a built-in wavefront reference source. The beam is then enlarged to 20-cm diameter and collimated to produce a 1-meter size spot of reradiated light from the sodium layer approximately 100 km above the earth. The primary lens is hyperbolic in shape and reversed from normal orientation to provide a diagnostic sample of the beam that is reflected back to the diagnostic package. The adaptive optics system has demonstrated the capability for dramatic improvements in image quality for the 3-meter telescope at the Lick Observatory. The artificial guide star created by the 25-watt laser is predicted to yield Strehl ratios >0.5 at a wavelength of 2.2 μm. This system was developed at Lawrence Livermore National Laboratory (LLNL) in conjunction with the University of California Lick Observatory.



1.1.3.0995.2202pb02

Figure 8. Guide Star Laser installed on the Shane Telescope at Lick Observatory.



1.1.3.0995.2201pb01

Figure 9. Optical schematic of the Lick laser dianostic system and output telescope.

8.2 NATIONAL IGNITION FACILITY (NIF)

This system now in design at LLNL is planned to demonstrate laser fusion on a large scale and provide a scientific test facility for this technology (Figure 11). NIF is a large system consisting of 192 separate lasers and optical-transport systems that converge on a single, small target for each shot. The system is based on many years of laser fusion research at LLNL and elsewhere. The Laboratory currently operates the NOVA laser system which started testing in the mid-1980s and the Beamlet laser system which represents a prototype of one of the NIF laser systems and started operating about a year ago.

The laser system architecture utilizes a four-pass amplifier and contains 39 large-aperture optical components per beamline (as illustrated in Figure 12). This architecture involves beam transport through the amplification system and blurs the distinction between the laser and beam transport functions. A low energy pulse is injected into a spatial filter aperture, through a booster amplifier into a cavity consisting of a polarizer, Pockels cell, switch amplifier, spatial filter, and cavity amplifier as well as mirrors at the end of the cavity. After four passes through the amplifiers and spatial filter, the Pockels cell switches beam polarization and the polarizer optic reflects the beam out of the cavity, and through the remaining transport optics including frequency conversion crystals to the target.

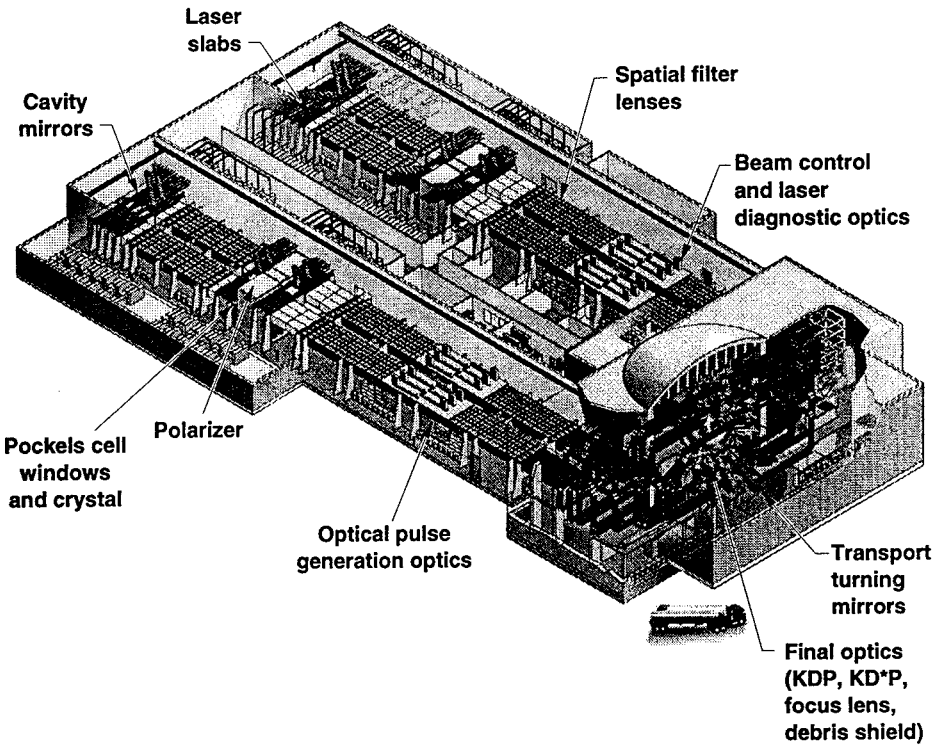
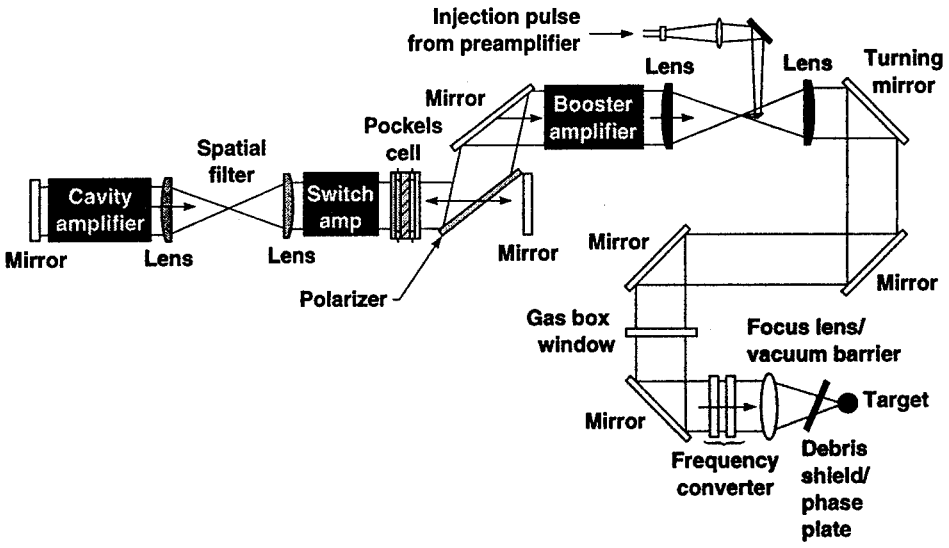


Figure 10. Optical components in the National Ignition Facility.



70-39-0195-0158pb01

Figure 11. The NIF four-pass laser architecture contains 7500 large-aperture optical components in 192 beamlines like the one shown.

NIF will utilize 7500 large-aperture (40 cm) optical components. Most of the components are slabs of laser-glass amplifiers and mirrors. The remainder of the large optics are lenses, polarizers, crystals, windows, and debris shields. Amplifiers are uncoated. Lenses, crystals, windows, and shields are expected to be antireflection coated with Sol-gel material that can be easily applied, stripped, and reapplied as needed at the NIF facility. Mirrors and polarizers utilize dielectric coatings optimized to survive high-fluence pulses (>25 J/cm^2). Transmissive optics also must be tightly controlled for strain birefringence (<4-6 nm/cm), inclusions (<100-500 μm), and wavefront distortion (<0.2 waves peak-to-valley transmitted, <0.4 waves peak-to-valley reflected). Several different materials must be optimized for this high-fluence, low-distortion application and coatings must be optimized for high-efficiency and high-damage thresholds including a major emphasis on defect reduction.

Alignment, wavefront, and power diagnostics are performed at numerous points in the system. Because the NIF laser system is fired intermittently, precorrection of wavefront and alignment for the high-fluence operation must be performed using low-power laser sources (pilot beams).

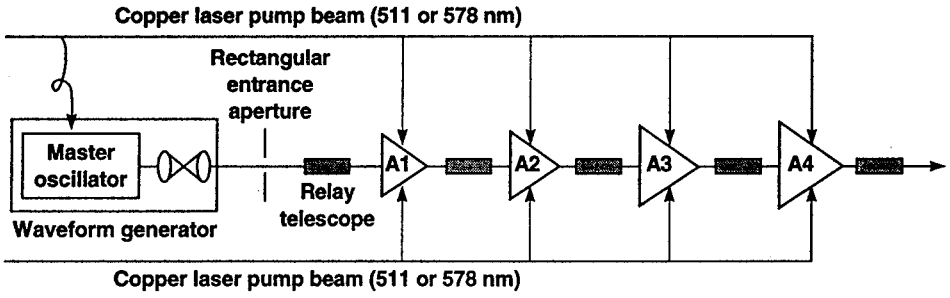
8.3 ATOMIC VAPOR LASER ISOTOPE SEPARATION (AVLIS)

This system has been in development for the past twenty years and may be deployed in an advanced Uranium enrichment facility within the next ten years. The isotope separation process has been demonstrated for a number of materials. The design of a large photochemical processing plant based on this technology offers advantages over current methods in reduced capital and operating costs resulting in significantly lower nuclear fuel costs. Copper laser (or possibly solid state lasers in the future) are used to pump energy into the dye lasers that are precisely tuned to produce the wavelengths and

beam quality for efficient ionization of the material to be processed. Both the copper lasers and dye lasers operate in master oscillator, power amplifier or MOPA configuration to produce over 1000 watts of power in each laser chain. Three stages of amplification are used for the copper vapor laser chains and three to four amplifiers are used in the dye chains as shown in Figure 12. Copper lasers produce pulsed power at 4.4 kHz that is transported to the dye chains using large core optical fibers. This transport system provides flexibility in the plant architecture. It also multiplexes the light into each dye-laser amplifier to minimize the impact of copper-laser maintenance and allows higher pulse rates for dye-laser operation.

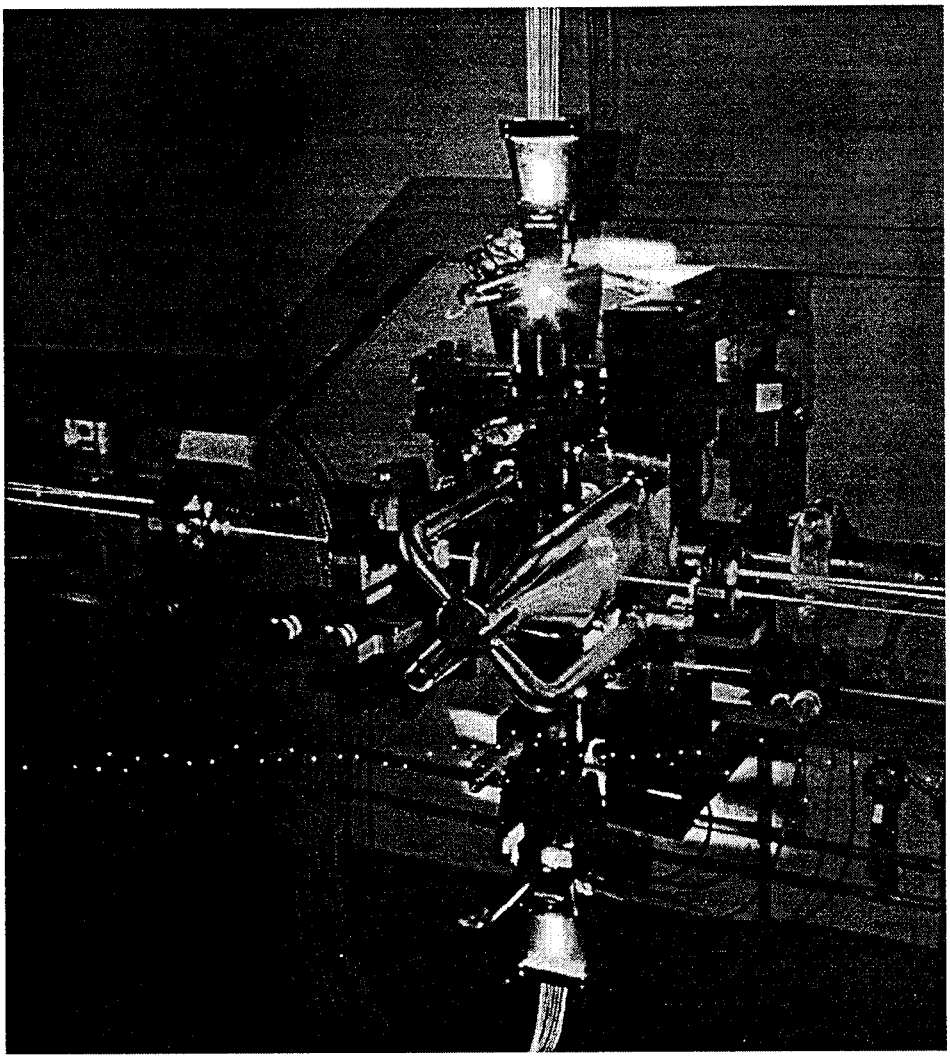
Figure 13 shows the basic elements of the dye laser and transport system. Multiple wavelength beamlines produced by the dye laser chains are combined and transported to the separator where they are used to illuminate and ionize vaporized atoms of material in the separator. Ionization of selected isotopes is the method used to separate or enrich the material by increasing the percentage of the desired isotope. This process is optimized for lowest production cost and depends on precise wavelength control, efficient production and transport of the light, and uniform illumination of the vapor. Transport efficiency and wavefront quality of the optical components has been discussed in several previous examples. The fiber transport systems include optics for insertion of the light into the fiber and receiving the light from the fiber, formatting it, and relaying it into the dye amplifier to uniformly excite the dye molecules. The light from each copper laser is divided into numerous fibers which are routed to different dye chains and different amplifiers. A complex utility network of fibers is involved in this transport system.

Total power on many of the thousands of optics in this system reach several thousand watts but reliability is ensured by low-absorption, high-survivability optics, a cleanroom or vacuum environment, and beams sized to reduce power densities to safe operating levels.



1.1.3.0695.1693pb01

Figure 12. Schematic diagram of the AVLIS dye-laser amplifier chain.



1.1.3.0594.2482pb02

Figure 13. AVLIS dye laser and optical transport system.

An extensive control system is used to control laser beam alignment, wavefront, and power levels. Beam control must be maintained while the system is normally operating on a continuous high-power basis and also when the high-power lasers are turned off for maintenance. This requires several pilot beams operating at different wavelengths than the high-power lasers so that the control system can operate independently of the main system. Tight tolerances for alignment accuracy and beam pointing are maintained. The beam wavefront can be corrected over a range of ±5 waves with an accuracy of 0.1 waves rms at a bandwidth of 1 Hz. Direct calorimetric power measurements are made up to 4000 watts ±5% with secondary monitoring using photodiodes on a continuous basis at lower power. Numerous closed-loop control points

photodiodes on a continuous basis at lower power. Numerous closed-loop control points are provided over long beam paths for numerous lasers operating simultaneously on a continuous basis making the control system a significant part of the laser and transport system in order to ensure reliable operation and high system availability.

9. Summary

Optical transport systems for high-power lasers perform a variety of functions and utilize many different types of optical components. Some common design and interface issues have been discussed, along with system optimization, and several systems used as examples. These examples, current projects at the Lawrence Livermore National Laboratory, illustrate the transport functions and precision transport optics.

10. Acknowledgments

These projects represent the efforts of hundreds of individuals over many years. These projects are moving from laboratory research to routine and useful applications. This work was performed under the auspices of the U. S. Department of Energy by Lawrence Livermore National Laboratory under contract No. W-7405-Eng-48. Since 1993, the AVLIS technology development has been sponsored by the United States Enrichment Corporation.

References

1. Steen, W. M. (1991) *Laser Materials Processing*, Springer-Verlag, London.
2. Warner, B. E. and Sheng, P. S. (July 1993) Better lasers create new applications and improve existing uses, *Industrial Laser Review*, PennWell Publishing Co.
3. Chang, J. J., Martinez, M. W., Warner, B. E., Dragon, E. P.,Huete, G. , and Solarski, M. E., (Oct. 1994) Micro Drilling with Copper Vapor Lasers, IALEO'94, Orlando, Florida.
4. McLean, W. II, Fehring, E. J., Dragon, E. P.and Warner, B. E. (Oct. 1994) High Rate PLD of Diamond-Like-Carbon Utilizing Copper Vapor Lasers, IALEO'94, Orlando, Florida.
5. Meyer-Arendt, J. R. (1972) *Introduction to Classical and Modern Optics*, Prentice-Hall, Englewood Cliffs, NJ.
6. O'Shea, D. C. (1985) *Elements of Modern Optical Design*, Wiley & Sons, New York 230 266.
7. Cohen, S. J.,English, Jr., R. E. , Stolz C. J., Taylor J. R. (July 1992) Thermal Analysis of Transmissive Elements, *SPIE Conference, Vol. 1739-50*, San Diego, CA 400 – 407.
8. Taylor, J. R. and Stolz, C. J. (1993) High-efficiency high-reliability optical components for a large, high-average-power visible laser system, *SPIE Proc., Vol. 1869-12*, 104-114.
9. Taylor, J. R. (1989) Specification and testing facilities for optical components used in a high average power visible laser system, *SPIE Proc. , Vol 1047*, 250-265.
10. Bliss, E. S., Peterson, R. L., Salmon, J. T. and Thomas R. A. (1993) Laser beam control and diagnostic systems for the copper-pumped dye laser system at Lawrence Livermore National Laboratory, *SPIE Proc. Vol 1859*, 130-144.
11. Aikens, D. M. and Taylor, J. R. (1987) Causes of damage in multilayer dielectric coatings exposed to high average power visible laser radiation, *NIST Special Publication (756)*, 419-429.
12. Taylor, J. R., Stolz, C. J. and Sarginson, T. G. (1991) Limits of survivability and damage for optical components used in a high repetition rate visibility laser, *SPIE Proc. Vol. 1624*, 411-422.
13. Stolz, C. J., Taylor, J. R., Eickelberg, W. K., Lindh, J. D. (1993) Effects of vacuum exposure on stress and spectral shift of high reflective coatings, *Applied Optics 32(28)* 5666-5672.
14. Liao, Z. M., Cohen, S. J. and Taylor, J. R. (Oct. 1994) Total internal reflection microscopy (TIRM) as a nondestructive subsurface damage assessment tool, *SPIE Proc. Vol. 2428* 43 – 53.
15. Tesar, A. A., Eickelberg, W. K. and Taylor, J. R. (April 1991) Interferometric Measurements of Refractive Index Inhomogeneity in fused silica, *Symposium on Solid-State Optical Materials*, Cincinnati, Ohio.
16. Bliss, E. S., Peterson, R. L., Salmon, J. T. and Thomas, R. A. (1993) Laser beam control and diagnostic systems for the copper-pumped dye laser system at Lawrence Livermore National Laboratory, *SPIE Vol. 1859*, 130 – 144.

HIGH-POWER UV EXCILAMPS

V.F. TARASENKO, M.I. LOMAEV, A.N. PANCHENKO, V.S. SKAKUN, AND E.A. SOSNIN
High Current Electronics Institute,
4 Academichesky ave., Tomsk 634055, Russia

Abstract

The results of an experimental study of coaxial exciplex lamps pumped by various types of discharge (the longitudinal discharge, barrier discharge, or continuous glow discharge) are presented. The mixture compositions and pressures as well as the pumping pulse parameters have been optimized for the production of radiation with λ = 193, 222, 249, 308 and 350 nm. Exciplex lamps with a radiating surface area of 570, 840, and 1300 cm^2 have been created. The average radiation power achieved for λ = 222 and 308 nm is up to 100 W and for λ = 350 nm is ~20 W. The application of an inductive energy store with a semiconductor opening switch being used for pumping a longitudinal-discharge-based exciplex lamp has been demonstrated.

1. Introduction

There has been concidarable research interest in creating of powerful spontaneous radiation sources operating in the UV and VUV regions [1–12]. The drawback of these sources compared the lasers is that they produce light beams of lower quality, showing comparatively wide radiation bands and large divergence. However, the spontaneous radiation sources are distinguished for their simplicity, high efficiency, broad spectra of operating conditions and radiator designs, as well as for the possibility to use the atomic and molecular transitions and the pumping conditions that are not appropriate for the production of laser radiation. These sources can be pumped by the barrier discharge [1, 5, 13–16], transverse discharge with UV preionization [6, 10, 12, 17–19], pulsed longitudinal discharge [16, 20], continuous longitudinal discharge [4, 6, 8], microwave discharge [2, 3, 21, 22], or spark discharge [11].

To produce light beams from spontaneous radiation sources within the UV and VUV regions, having minimum band widths at maximum efficiencies, it is most profitable to use the radiation on the bound-free transitions of noble-gas-halide exciplex molecules of the type RX* [23] or inert-gas-dimer excimer molecules of the type R_2^* [24]. That is why in [18] it was proposed to call such spontaneous radiation sources that use RX* and R_2^* type molecules radiation as "exciplex" and "excimer" lamps (excilamps).

R. Kossowsky et al. (eds.), High Power Lasers – Science and Engineering, 331–345.
© 1996 *Kluwer Academic Publishers. Printed in the Netherlands.*

In this work were discribed the creation and study of coaxial excilamps with various designs of radiators and pumping generators.

2. Experimental equipment and techniques

2.1. PUMPING GENERATORS

For the excitation of the excilamps under investigation three types of pumping generator and a dc voltage source were used. A simplified circuit diagram of the generator No 1 (Fig.1) where the type Ekstra-2 or Ekstra-3 (TGI1–10,000/25) thyratron has used as a switch. These thyratrons were capable of switching currents up to 10 kA and showed stable operation at voltages of 10–30 kV and pulse repetition rate up to ~2 kHz. The capacitance of the storage capacitor C_0 was varied from 0.1 nF to 12 nF. The discharge circuit inductance L_0 was made as low as possible and generally equal to ~30 nH. The peaking capacitor capacitance was varied from 20 pF to 6.6 nF; in some tests, no peaking capacitor was used. The total inductance L of the peacking capacitor circuit connected with load L_0 did not exceed 10 nH. The charging of the capacitor C_0 carried out from the special source, which was capable to charge capacitive energy stores by not more the 10 kHz repetition rate pulses. In the process, once the thyratron had operated, a ~500 μs pause in the charging of C_0 established automatically.

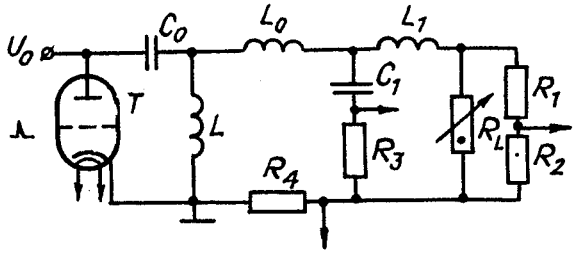


Figure 1. Circuit diagram of a pumping generator: T – thyratron, C_0 – storage capacitor, C_1 – peaking capacitor, L – charge inductance, L_0 – inductance of the discharge circuit with the storage capacitor, L_1 – inductance of the circuit with the peaking capacitor, R_L – excilamp, $R_1 - R_4$ – voltage divider and shunt resistors, V_0 – high voltage input.

The generator No 2 produced alternatively positive and negative voltage pulses of peak value ~15 kV with the pulse repetition rate varied from 2 to 10 kHz. The duration of the current pulse through the excilamp was ~500 ns.

The generator No 3 (Fig. 2) used the energy stored in the inductance. The capacitor C_0 discharged on the operation of the switch SG through the inductance L_0 and the

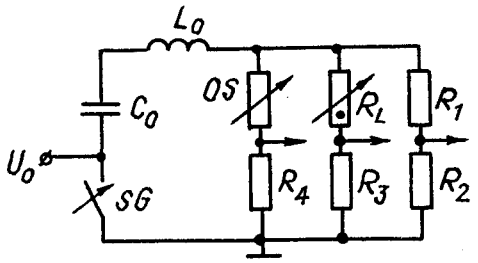


Figure 2. Circuit diagram of a pumping generator with a semiconductor opening switch: C_0 – storage capacitor, L_0 – inductance, OS – opening switch, R_L – excilamp, SG – spark gap switch, R_1 – R_4 – voltage divider and shunt resistors, V_0 – high voltage input.

opening switch OS whose function was performed by commercial semiconductor diodes of the type SDL–0.4/800 [25]. These diodes, once they have passed current in the forward direction, continued, for a certain time (generally ~ 700 ns), to pass current in the inverse direction and them they interruped it (in the best modes in a time of ~ 200 ns ($dI/dt \sim 10^9$ A/s)). The current through a single diode peaked at 600 A; the pulsed overvoltage across the load was ~3 times greater than the charge voltage of the capacitor C_0. The parameters of the excilamp pumped from the inductive energy store were investigated at pulse repetition rates of a few hertz.

The power supply of the excilamps pumped by continuous glow discharges was accomplished from a controllable (0–40 kV) dc voltage source with a current of up to 100 mA.

2.2. RADIATORS

The experiment was carried out using radiators of three types (Fig. 3) fabricated from quartz tubes. In the case of barrier discharge pumping, excilamps consisting of two coaxial quartz tubes were used (see Fig. 3a). The internal diameter of the outer tube was generally 66 mm and the external diameter of the inner tube was 50 mm. The length of the external grid electrode was 40 cm, so the radiating surface had an area of ~ 840 cm^2. The second excilamp had a radiating surface of diameter 54 mm and a grid electrode of length 75 cm, so the radiating area was ~ 1300 cm^2. The inner solid electrode, electrode I, served simultaneously as an additional reflector. The excilamp was cooled with water circulated through the inner quartz tube.

Figure 3b presents a schematic diagram of a longitudinal-discharge-pumped radiator having a single discharge gap. The radiator, like in the above case, consisted of two coaxial quartz tubes. The internal diameter of the outer tube was 60 mm and the external diameter of the inner tube was ~ 55 mm. The discharge was initiated between

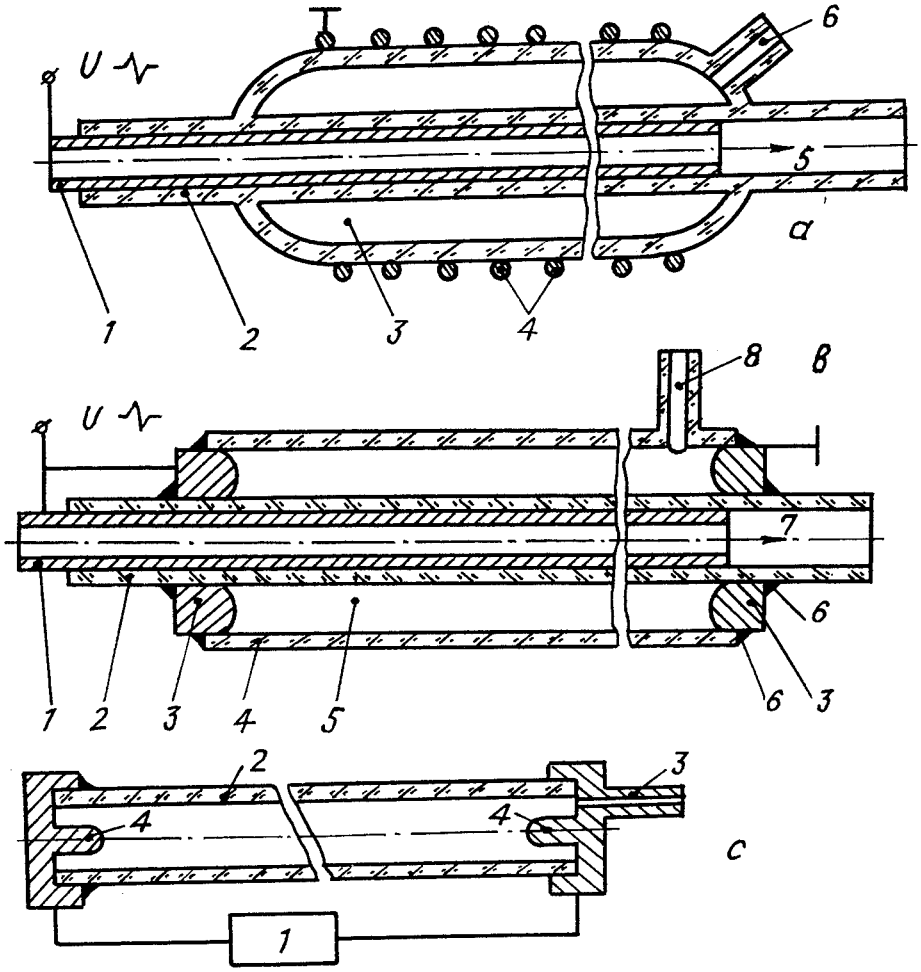


Figure 3. Schematic diagram of excilamps with the barrier discharge (*a*), pulsed longitudinal discharge (*b*), and cntinuous glow discharge (*c*). (*a*): *1* – metallic tube (reflector), *2* – case consisting of two quartz tubes, *3* – gas chamber, *4* – external grid electrode, *5* – water flow direction, *6* – gas-feeding sleeve. (*b*): *1* – metallic tube (reflector), *2* – inner quartz tube, *3* – electrodes, *4* – outer quartz tube, *5* – gas chamber, *6* – splice, *7* – water flow direction, *8* – gas-feeding sleeve. (*c*): *1* – power supply, *2* – quartz tube, *3* – gas-feeding sleeve, *4* – electrodes.

electrodes *3* placed 30 cm apart. In some tests we used an excilamp with three electrodes one of which was centrally located , at a distance of ~ 15 cm from each of the outer electrodes placed at the edges of the excilamp. In this case, metallic reflector *1* placed into the inner quartz tube was connected only with the central electrode, and a pulsed voltage was applied to the external electrodes. Cooling, like in the barrier-discharge-

pumped excilamp, was performed by water circulated through the inner tube. The radiating surface area for the longitudinal-discharge-pumped excilamps was 570 cm^2.

By the pumping for stationary-glow-discharge, we was used the excilamp shown in Fig. 3c. The internal diameter of the quartz tube was 9 mm and the tube length was varied from 17 to 40 cm. A high dc voltage was applied between electrodes *4*. The experiment was performed without additional cooling of the radiator.

It should be noted that quartz tubes with a comparatively low transmittance (10–60%) for the wavelength shorter than 260 nm were used for the manufactoring of the radiators; therefore, the powers reported below can be increased substantially when using quartz tubes of better quality.

2.3. WORKING MIXTURES

To produce radiation in the range ~ 350 nm, gas mixtures consisting of the halide carrier, NF or F_2, xenon, and a buffer gas, neon or helium were used; the mixture components for the range 308 nm were HCl, Cl_2, xenon, helium or neon; for the range 250 nm – NF_3 or F_2, krypton, helium or neon; for the range 222 nm – HCl, Cl_2, krypton, helium or neon; and for the range 193 nm – F_2, argon, helium or neon. The working mixtures were generally prepared directly in the excilamps. Since the radiator length was much in excess of its cross dimensions, it was necessary to try to get mixing of the components. Before the working mixture was fed into a lamp, the latter was evacuated, treated with a blow of helium or neon, and conditioned by a discharge at a pressure below 1 Torr.

2.4. MEASURING TECHNIQUES AND INSTRUMENTS

The time and amplitude characteristics of the spontaneous emission at λ ~350, 308, 250, 222, and 193 nm were measured with the use of a calibrated photodiode of the FEK22SPU type whose signal was applied to an oscilloscope of the C8-14 type. Current and voltage measurements were performed using shunts and resistive voltage divider fabricated from TVO-type low-inductance resistors whose signals also applied to the oscilloscope. The average radiation power was measured by calorimeters of the IMO-2N and TPI-2M.1 type; the electric signal from the latter was applied to a digital millivoltmeter of the Shch 300 type. To select specified spectral regions, light filters were used. The spontaneous radiation spectra in the range 210–600 nm were recorded on the type RF-3 film by a spectrograph of the ISP-30 type. The type IFO-451 microphotometer was used for sketching of the films to produce density records.

3. Amplitude-time and spectral characteristics of excilamps

3.1. THE BARRIER-DISCHARGE-PUMPED EXCILAMPS

The amplitude-time characteristics of barrier-discharge-pumped excilamps were investigated in detail with the use of the generator No 1; the length of the excited region

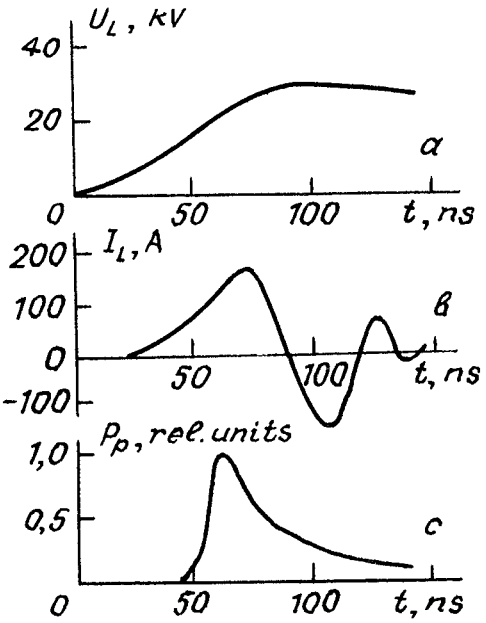


Figure 4. Waveforms of pulsed voltage (*a*), current (*b*), and radiation intensity at λ = 222 nm (*c*) for a barrier-discharge excilamp with a He-Kr-HCl mixture.

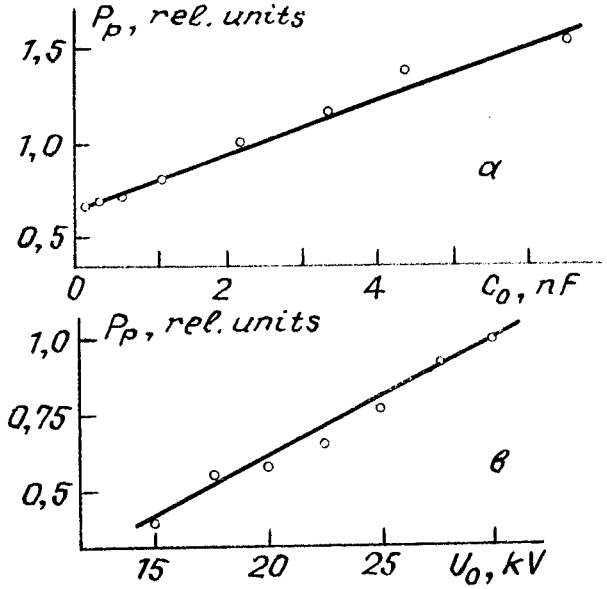


Figure 5. Pulsed radiation power versus the capacitance C of the storage capacitor for λ = 222 nm; V_0 = 20 kV and He-Kr-HCl mixture (*a*), and versus charge voltage for λ = 250 nm; C_0 = 1.1 nF and He-Kr-F_2 mixture (*b*).

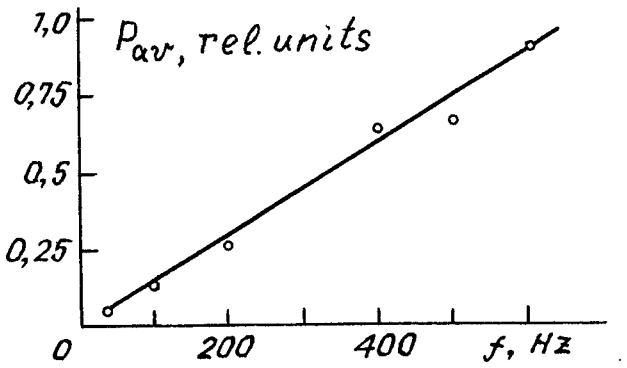


Figure 6. Average radiation power versus pulse repetition rate for λ =222 nm, mixture He-Kr-HCl, V_0 = 20 kV, C_0 = 1.1 nF; a barrier-discharge excilamp and the generator No 1.

was 40 cm; the working mixtures used were He(Ne)-Ar-F_2 (λ = 193 nm), Ne(He)-Kr-HCl (222 nm), and He(Ne)-Kr-F_2(NF_3) (250 nm). Figure 4 presents typical waveforms of the pulsed voltage across the excilamp, discharge current, and radiation intensity at λ = 222 nm. These waveforms were recorded in the absence of the peaking capacitor C_1. When C_1 was connected in the circuit it involved sometimes in an increase of spontaneous radiation power, but the pulse energy in this case did not increase. Since the capacitance C_L of the excilamp, when it is filled with plasma, cannot be in excess of 400 pF (which is calculated by the formula for the capacitance of a coaxial capacitor), and the storage capacitor capacitance in the most of tests was ~ 1 nF or more, the voltage across the excilamp was 1.5–2 times greater than the charge voltage (Fig. 4a). The current pulse

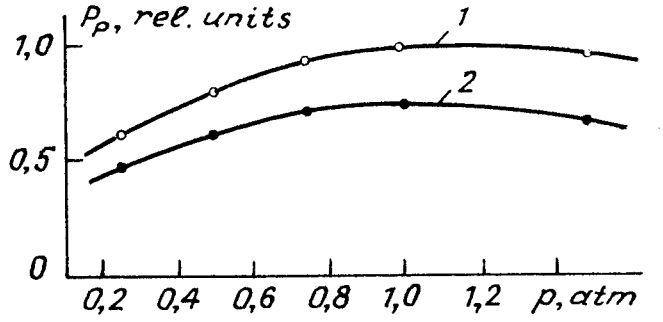


Figure 7. Pulsed radiation power at λ = 193 nm versus helium pressure for a mixture F_2:Ar:He = 4.5 Torr:150 Torr:He (*1*) and versus neon pressure for a mixture F_2:Ar:Ne = 3 Torr:100 Torr: N_2 (*2*). V_0 = 20 kV, C_0 = 1.1 nF.

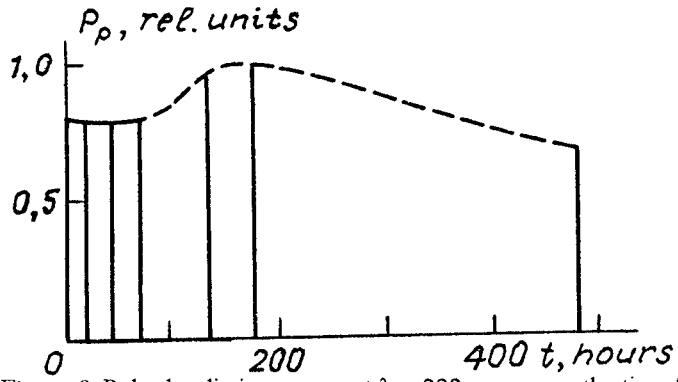


Figure 8. Pulsed radiation power at λ = 222 nm versus the time for which one portion of the working mixture retains in repetitive short-time operations for a mixture of HCl:Kr:He = 8 Torr:60 Torr:1 atm. V_0 = 20 kV, C_0 = 1.1 nF, number of shots ~ 10^6.

duration was as a rule no longer than ~ 200 ns, and the FWHM duration of the radiation pulse varied from 20 to 300 ns. It should be noted that only a certain part of the energy stored in the capacitor C_0 was transferred to the barrier discharge plasma. The appearance of the gas discharge plasma was typical of the barrier discharge; the plasma consisted of numerous filament channels chaotically migrating on the background of a space discharge. Figure 5 presents the pulsed radiation power as a function of the storage capacitor capacitance and charge voltage. Increasing C_0 and V_0 increases the radiation energy; however, the efficiency reaches its maximum at a low C_0 and low charge voltage. Figure 6 illustrates the effect of the pulse repetition rate on the pulse radiation power. It can be seen that increasing repetition rate increases linearly the average power. The dependence of the radiation power at λ = 193 nm on the buffer gas pressure is plotted in Fig. 7. The pressures of argon and fluorine as well as the buffer gas pressure were chosen such that the radiation power be a maximum at atmospheric pressure. Figure 8 gives the radiation pulse power as a function of the time for which one portion of the working medium retains at repetition short-time operations of the excilamp. It can be seen that the pulse power remains almost unchanged for a long time.

With the generator No 2, the radiation power in a single pulse was about one-third of that produced with the generator No 1. However, the average power achieved in the operation at a pulse repetition rate of 10 kHz was higher than the average power produced with the generator No 1. It should be noted that when excilamps were pumped by a barrier discharge from the generator No 1, the pulse repetition rate was limited to 600 Hz, because of the circuit effects. The maximum average radiation powers produced by barrier-discharge excilamps were ~ 0.5 W with the generator No 1 at λ=222 nm and ~ 0.6 and 1.0 W with the generator No 2 at λ= 222 and 250 nm, respectively. These average radiation powers may increased with the growth of the pulse repetition rate, and by increasing of the lamp dimentions, and by choosing of the qualitative quartz.

3.2. THE LONGITUDINAL-DISCHARGE-PUMPED EXCILAMPS

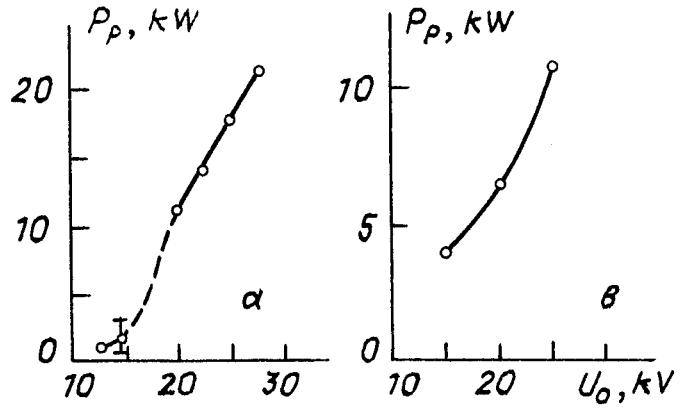


Figure 9. Pulsed radiation power versus charge voltage. (*a*) P1-type excilamp, $f = 50$ Hz, $C_0 = 4.4$ nF, $C_1 = 0.47$ nF, mixture Ne-Kr-HCl, FWHM radiation ulse duration 250 ns. (*b*) P2-type excilamp, $f = 50$ Hz, $C_0 = C_1 = 1.1$ nF, mixture Ne-Kr-HCl.

The amplitude-time characteristics of these excilamps were investigated in detail at $\lambda = 222$ nm with mixtures of Ne(He)-Kr-HCl pumped from the generator No 1. In this experiment we used the excilamps with one discharge gap of length 30 cm (P1-type excilamp) and with two discharge gaps, each ~ 15 cm long (P2-type excilamps). The characteristics obtained were in general identical for both types of excilamp,; however, the working mixtures and pressures were noticeably different.

Figure 9a presents the dependence of the radiation pulse power on the charge voltage obtained for a P1-type excilamp. When the voltage is increased to 20 kV, the low-current space discharge in the excilamp changes into a discharge consisting of several bunches, without the sertain locations. The radiation power therewith is small and, with an inhomogeneous discharge, unstable. Starting from the voltage 20 kV, the discharge takes the whole volume of the excilamp and the radiation power has a fast risetime; however, the discharge is not entirely homogeneous but it consists of numerous diffuse channels evently distributed over the cross section of the discharge region. Figure 10a shows the average radiation power as a function of the neon buffer gas pressure for various concentrations of krypton. The greatest pulse power was achieved at a krypton pressure of 36 Torr.

When the P2-type excilamp was used, the best results were obtained with a peaking capacitor, C_1, connected in the circuit, whose capacitance was the same as that of the capacitor C_1. Also characteristic of the P2 excilamp were a highly homogeneous discharge and a nonlinear dependence of the radiation power on charge voltage (Fig. 9b). The dependence of average power on Ne-pressure for this case are shown in the Fig. 10b. However, the radiation pulse powers achieved on excilamps with one and two discharge gaps were practically the same for the same C_0 values. The radiation pulse duration depended on C_0 and it was longer for the P1 excilamp. Figure 11 presents the average radiation power as a function of pulse repetition rate. It can be seen that the average radiation power increases linearly with repetition rate. The P2 excilamp was also

investigated at pulse repetition rates up to 2 kHz; however, when the pulse repetition rate was increased to above ~ 800 Hz, the water cooling of the inner tube failed to the operating of the excilamp. Duaring the certain time the excilamp operated stably and after that due to the overhearting the discharge ceased to be homogeneouse. At a repetition rate of ~ 2 kHz, the excilamp with $C_0 = 2.2$ nF and $C_1 = 0.47$ nF could operate without overheating for ~ 10 s. In this mode, the average radiation power was ~ 4 W; then it almost halved in 20 s and a channel appeared in the discharge region, which led to a nonuniform heating of the tube and a further decrease in average radiation power. If the lamp was switched off after 10–20 s of operation, cooled, an then switched on again, the radiation parameters recovered.

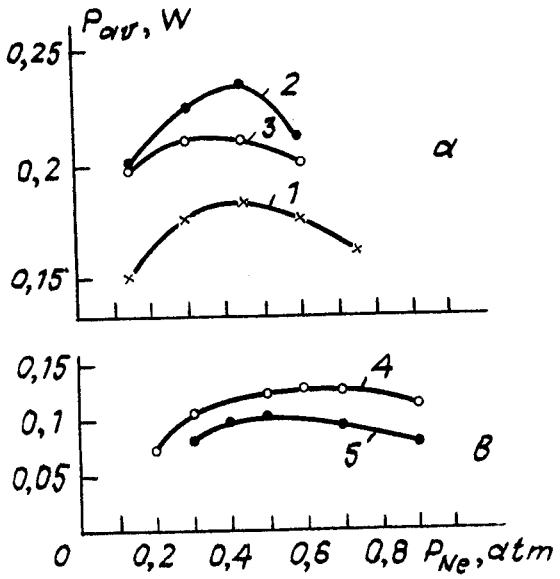


Figure 10. Average radiation power versus neon buffer gas pressure. (*a*) P1-type excilamp, $f = 50$ Hz, $C_0 = 4.4$ nF, $C_1 = 0.47$ nF, HCl pressure = 1 Torr, Kr pressure = 30 (*1*), 36 (*2*), and 45 Torr (*3*). (*b*) P2-type excilamp, $f = 50$ Hz, $C_0 = C_1 = 1.1$ nF, HCl pressure = 0.5 Torr, Kr pressure = 21 (*4*) and 45 Torr (*5*).

Figure 12 presents a density record of the radiation of a Ne-Xe-HCl mixture pumped by a longitudinal discharge. (The density record was taken on the ISP-30 spectrograph.) It can be seen that the most intense radiation is the radiation with $\lambda = 308$ nm generated

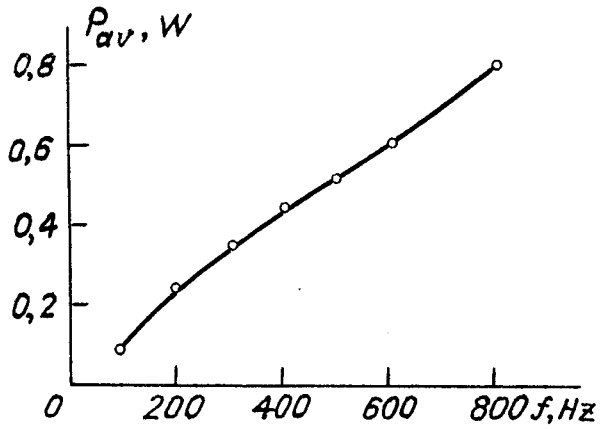


Figure 11. Average radiation power versus pulse repetition rate. P2-type excilamp, $C_0 = C_1 = 1.1$ nF, Ne:Kr:HCl = 0.5 atm:18 Torr:18 Torr. $V_0 = 20$ kV, FWHM radiation pulse duration ~ 160 ns.

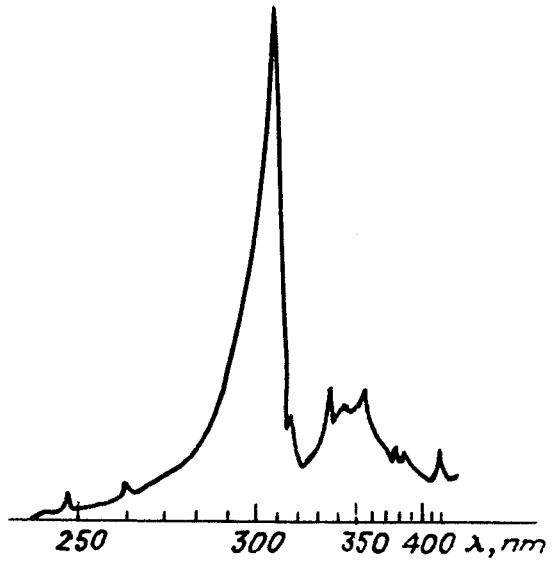


Figure 12. Density record for the radiation in the region 240–450 nm of a He-Xe-HCl mixture pumped by a longitudinal discharge.

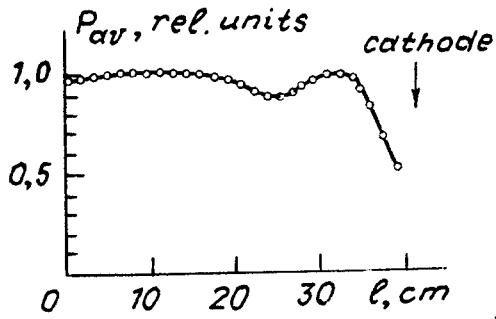


Figure 13. Average radiation power distribution along the length tube. λ ~ 308 nm, discharge current = 30 mA, tube voltage = 4,5 kV, mixture Xe:HCl = 3:1, p = 18 Torr.

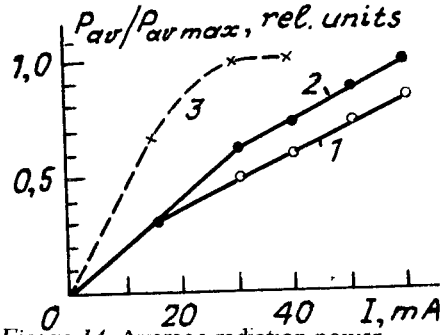


Figure 14. Average radiation power versus discharge current for λ ~ 308 (*1*, *2*) and 350 nm (*3*). Mixture Xe:HCl = 3:1, p = 24 Torr (*1*); Xe:HCl = 3:1, p = 18 Torr (*2*); Xe:NF_3 = 2:1, p = 9 Torr (*3*).

by the *B-X* transition of XeCl* molecules. Other gas mixtures show similar radiation spectra.

3.3. THE CONTINUOUS-LONGITUDINAL-DISCHARGE-PUMPED EXCILAMPS

Many technical applications call for radiation on UV-range, with high average power and with more higher bandwidth of radiation than produced by laser devices. In special cituations the pulse power is not essential. In these cases, it is most profitable to use glow discharges for pumping the lamps [7, 8]. We investigated the radiation of this type of discharge in mixtures of Xe-HCl(Cl_2), Kr-HCl(Cl_2) and Xe-NF_3 with helium and neon buffer gases as well as in double mixtures. Figure 13 gives the average radiation power as a function of the current through the gas discharge tube for λ = 308 and ~ 350 nm. The voltage across the plasma for the current 40 mA and the excilamp length 20 cm was 3–5 kV. The curves show a characteristic bend whose position depends on the mixture composition and pressure. In optimized modes, the discharge features homogeneity and the radiation power for mixtures with HCl as a halide carrier remains unchanged for a long time. The power distribution along the length of the excilamp is shown in Fig. 14. The radiation power in the UV region is the same throughout the most part of the lamp and only near the cathode it decreases. When the tube length is decreased, the character of the cathode glow does not change, but the anode region contracts. The efficiency of emission therewith drops. The highest average radiation power was achieved on a tube with the discharge region length 40 cm; for the spectral region with λ = 350 nm it was ~ 20 W and for the spectral region with λ = 308 nm it was ~ 25 W. The radiant efficiency with respect to the pumping power reached 3 %. In closing it may be said that we have achived an average output power of 100 W (spectrum range ~ 250 and ~ 308 nm) with the radiation efficiency between 10 to 15% for going from discharge tube to the coaxial cylindrical geometry of excilamp.

3.4. USE OF INDUCTIVE ENERGY STORES FOR PUMPING EXCILAMPS

In the above sections we dealt with capacitive energy stores used for pumping excilamps. It is well known that inductive energy stores allow an increase in pumping power and form unipolar current pulses through the load. However, the application of inductive energy stores is hindered by the absence of reliable opening switches capable of operating in repetition pulse modes. Recently, it has been reported [25] on the use of commercial semiconductor diodes as opening switches. The present section outlines the results of first model tests on the pumping of a longitudinal-discharge excilamp from the generator shown in Fig. 2. These tests were performed with an excilamp similar to that shown in Fig. 3b but smaller in size. The electrode separation was 20 cm and the diameter of the radiating region was 3.5 cm. Figure 15 gives waveforms of the pulsed current through the excilamp, the voltage across the excilamp, and the pulsed radiation

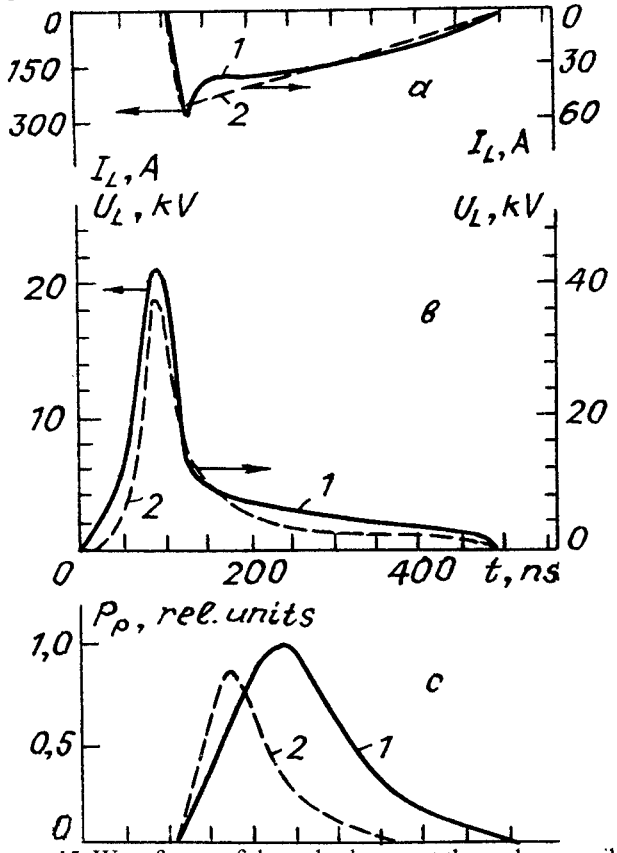


Figure 15. Waveforms of the pulsed current through an excilamp (*a*), voltage across the lamp (*b*), and radiation intensity at $\lambda \sim 308$ nm (*c*) for mixtures Ne:Xe:HCl = 30 Torr : 6 Torr 0.5 Torr (*1*) and Ne:Xe:HCl = 150 Torr : 6 Torr 0.5 Torr (*2*). $V_0 = 16$ kV.

intensity at λ = 308 nm for two mixture pressures. For the excilamp pumped from an inductive-energy-storage generator, the excitation is accomplished by unipolar pulses; an increase in board resistance shortens the excitation pulse, and the voltage across the excilamp prior to the breakdown of the gas mixture is several times greater than the charge voltage. The latter is highly important for the formation of a space discharge. It should also be noted that using the generator shown in Fig. 2 makes it possible to realize the pumping mode where the space discharge is initiated at the expense of the energy stored in the inductance during the rise of the current through the gas-discharge load, while the main energy input in a matched mode is from the capacitor C_0 [26].

4. Conclusion

A study of excilamps pumped by various types of discharge (the barrier discharge, longitudinal discharge, and continuous glow discharge) has been carried out. Working gas mixture components and pressures optimal for the production of radiation at λ = 350, 308, 250, 222, and 193 nm as well as the best pumping pulse parameters have been found. Excilamps with a radiating surface area of 570, 840, and 1300 cm^2 have been created. The most average radiation power achieved with longitudinal-discharge pumping is 4 W for λ = 222 nm and with barrier-discharge pumping 0.6 W for λ = 222 nm and 1 W for λ = 250 nm. The most average radiation power achieved with a glow discharge is λ = 350 nm is ~ 20 W and ~ 100 W for λ = 222 and 308 nm.The possibility has been demonstrated that an inductive energy store with a semiconductor opening switch can be used successively for pumping longitudinal-discharge excilamps.

5. References

1. Boyunov, V.I., Volkova, G.A., and Podmoshensky, I.V. (1991) VUV Radiation pulse coaxial lamp, *Zh. Priklad. Spektroskopii*, **54**, No 1, 164-166.
2. Hatakeyama, T., Kannari, F., and Obara, M. (1991) Theoretical study of vacuum ultraviolet F_2 excimer lamp (157 nm) excited by microwave discharge, *Appl. Phys. Lett.*, **59**, 387-389.
3. Kumagai, H. and Toyoda, K. (1991) Properties of a new high-efficiency vacuum ultraviolet fluorine lamp excited by a microwave discharge, *Ibid.*, **59**, 2811-2813.
4. Teylor, R.S., Leopold, K.E., and Tan, K.O. (1991) Continuous *B-X* excimer fluorescence using direct current discharge excitation, *Ibid.*, **59**, 525-527.
5. Gellert, B. and Kogelschatz, V. (1991) Generation of excimer emission in dielectric barrier discharges, *Appl. Phys. B*, **52**, 14-21.
6. Koval', B.A., Skakun, V.S., Tarasenko, V.F., Fomin, E.A., and Yankelevich, E.B. (1992) High-power wide-aperture exciplex lamp, *Prib. Tekh. Eksper.*, No 4, 244-245.
7. Golovitsky, A.P. (1992) Possibilities of production of effective UV sources based on continuous glow discharge in mixtures of inert gases and halogens, *Pisma Zh. Tekhn. Fiz.*, **18**, 72-76.
8. Golovitsky, A.P. and Kan, S.N. (1993) Characteristics of UV excimer radiation of continuous glow low-pressure discharge, *Optika i Spektroskopiya*, **75**, 604-609.

9. Boichenko, A.M., Tarasenko, V.F., Fomin, E.A., and Yakovlenko, S.I. (1993) Broadband emission continua in rare gases and in mixtures of rare gases with halides, *Quant. Electr.*, **23**, 3-25.
10. Kuznetsov, A.A., Skakun, V.S., Tarasenko, V.F., and Fomin, E.A. (1993) Excimer electro-discharge lamp with λ = 126, 146, or 172 nm, *Pisma Zh. Tekh. Fiz.*, **19**, 1-5,.
11. Rulev, G.V. and Saenko, V.B. (1993) UV radiation generation initiated by spark discharge in mixtures of inert gases with halogens, *Ibid.*, **19**, 53-56,.
12. Boichenko, A.M., Skakun, V.S., Tarasenko, V.F., Fomin, E.A., and Yakovlenko, S.I. (1993) Powerful exciplex flashlamps, *Laser Physics*, **3**, 838-843.
13. Volkova, G.A., Kirillova, N.N., Pavlovskaya, E.N., and Yakovleva, A.V. (1984) VUV-lamps pumped by a barrier discharge in rare gases, *Zh. Priklad. Spektroskopii*, **41**, 681-695.
14. Eliasson, B. and Kogelschatz, U. (1988) UV excimer radiation from dielectric-barrier discharges, *Appl. Phys. B*, **46**, 299-303.
15. Kogelschatz, U. and Esrom, H. (1990) New incoherent ultraviolet excimer sources for photolotytic material deposition, *Laser and Optielektronik*, **22**, 55-59.
16. Vizir', V.A., Skakun, B.S., Smorudov, G.V., Fomin, E.A., Tarasenko, V.F., and Chervyakov, V.V. (1995) Coaxial excilamps pumped by barrier and longitudinal discharges, *Kvant. Elektr.*, **22**, 512-522.
17. Skakun, V.S., Tarasenko, V.F., and Fomin, E.A. (1992) Pulsed wide-band emission sources, *Zh. Prikl. Spektroskopii*, **56**, 331-333.
18. Boichenko, A.M., Skakun, V.S., Tarasenko, V.F., Fomin, E.A., and Yakovlenko, S.I. (1993) Spatial characteristics of the emission from exciplex lapms, *Quant. Electr.*, **23**, 532-534.
19. Kuznetsov, A.A., Skakun, V.S., Tarasenko, V.F., and Fomin, E.A. (1993) A pulsed source of high-power VUV spontaneous emission, *Optika atmosfery i okeana*, **6**, 694-698.
20. Gerber, T., Lüthy, W., and Burkhard, P. (1980) High efficiency KrF excimer flashlamp, *Opt. Commun.*, **35**, 242-244.
21. Kumagai, H. and Obara, M. (1989) New high-efficiency quasi-continuous operation of KrF(*B-X*) excimer lamp excited by microwave discharge, *Appl. Phys. Lett.*, **54**, 2619-2621.
22. Kumagai, H. and Obara, M. (1989) New high-efficiency quasi-continuous operation of ArF(*B-X*) excimer lamp excited by microwave discharge, *Ibid.*, **55**, 1583-1584.
23. *Excimer Lasers* (1979) Ch.K. Rhodes (ed.), Springer-Verlag, Berlin, Heidelberg, New York.
24. Gerasimov, G.N., Krylov, B.E., Loginov, A.V., and Shchukin, S.A. (1992) Ultra-violet emission of excited rare gas molecules, *Usp. Fiz. Nauk*, **162**, 123-159.
25. Kotov, Yu.A., Mesyats, G.A., Rukin, S.N., and Filatov, A.L. (1993) Solid state current interrupter for powerful nanosecond pulses generation, *Dokl. RAN*, **330**, 315-317.
26. Panchenko, A.N. and Tarasenko, V.F. (1990) Pumping of gas lasers by generator using inductive energy storage, *Kvant. Elektron.*, **17**, 32-34.

REPRODUCIBLE ULTRASHORT PULSES AND MULTISTABLE MONOCHROMATIC EMISSION FROM SOLID-STATE LASERS WITH SATURABLE ABSORBER AND NEGATIVE FEEDBACK LOOP

K.P. KOMAROV, A.S. KUCH'YANOV, V.D. UGOZHAYEV
Institute of Automation and Electrometry
of the Russian Academy of Sciences
Universitetckii Pr. 1, Novosibirsk 630090, Russia

Abstract

We present the overview of our investigations on various operation regimes of solid-state lasers with saturable absorber and an inertial negative feedback loop suppressing Q-switching instability. The stabilized passive mode-locking and the multistable monochromatic generation hold a central position among these regimes. The stabilized passive mode-locking of such solid-state lasers is similar in their characteristics to passive mode-locking of dye lasers: after transient evolution the reproducible regime of single stationary pulse is realized, and extremely short duration of pulses are reached. Another typical instabilities (the self-phase modulation instability and the instability of transverse spatial structure of radiation) are studied and the methods of theirs suppression are investigated. The passive mode-locking in colliding pulse regime is analysed. Experimental peculiarities of stabilized passive mode-locking for various lasers (ruby, Nd:phosphate and Nd:silicate glasses, potassium gadolinium tungstate, Nd:YAG) are presented.

It is shown that in the case of the sufficiently slow saturable absorber the multistable monochromatic generation is realized (in a linear resonator the saturable absorber acts as a nonlinear intracavite selective component with the transmission maximum at the emitted mode frequency, and the single mode regime is reached). Required parameters of the laser and the negative feedback loop for origin of this regime have been determined.

The regimes under study are of interest in the development of solid-state laser sources of reproducible power ultrashort pulses and high-power monochromatic radiation with a stable frequency. Furthermore, laser system under investigation provides a way of studying the nonlinear light dynamics under longtime self-influence of radiation in nonlinear media.

R. Kossowsky et al. (eds.), High Power Lasers – Science and Engineering, 347–364.
© 1996 *Kluwer Academic Publishers. Printed in the Netherlands.*

1. Introduction

Solid-state lasers have good energy characteristics and considerable intracavity amplification of radiation. Thanks to these qualities, without breaking down the laser condition one can insert various additional nonlinear elements into a laser resonator and by this means can exert control over the formation of intracavity radiation. However, if nonlinear element produces a saturable absorption, then Q-switching instability results, that prevents the efficient realization of such control. Because of this instability, the radiation decreases periodically in intensity to level of spontaneous emission. And transient evolution begins again and again remaining in the initial stage of its way (when the saturable absorber is sufficiently dense, Q-switching instability is manifested by the emission of a giant pulse).

Suppressing Q-switching instability by inertial negative feedback loop we realized the stable regime of stationary single pulse. All parameters of ultrashort pulse independent of initial noise radiation. They are stationary and controlled by laser parameters: gain bandwidth, time of saturable absorber recovery, pump rate, etc. This stationary regime exists without interruption till the end of pumping, hence extremely small pulse durations are obtained.

In our experiments we had also observed the other type of instability, namely, the instability of transverse spatial distribution of radiation. This instability results from long-continued self-influence of intracavity radiation through inertial nonlinearity of refractive index of dye solution used as saturable absorber. For our lasers the increment time of this instability is equal to $10 \div 100$ μs. The transverse instability is suppressed by pumping of the dye solution through the saturable absorber cell.

In Nd:glass lasers we had also observed self-phase modulation instability. The peculiarities of laser operation due to this instability are presented in Section 5.

In our theoretical papers it is shown, that solid-state laser with saturable absorber and stabilizing negative feedback loop can demonstrate multistable regimes in the case of linear resonator. In the case of fast saturable absorber the steady state of laser can be the stable intracavity train of equal-spaced stationary pulses. Number of pulses in train depends on initial conditions of generation. In the case of sufficiently inertial saturable absorber the transient evolution of laser generation is finished with the single mode stationary monochromatic operation. The realization of operation of one or other mode depends on the initial lasing conditions.

2. Experimental Arrangement, Inertial Feedback Loop, and Supression of Q-Swithing Instability

Fig.1 represents the optical scheme of experimental arrangement. The Kepler telescope increases the nonlinear self-influence of intracavity radiation into saturable absorber. The inertial feedback loop consists of the photodiode 8, an electronic amplifier 9, and an intracavity electrooptic modulator 2. A part of output radiation is directed onto the photodiode.

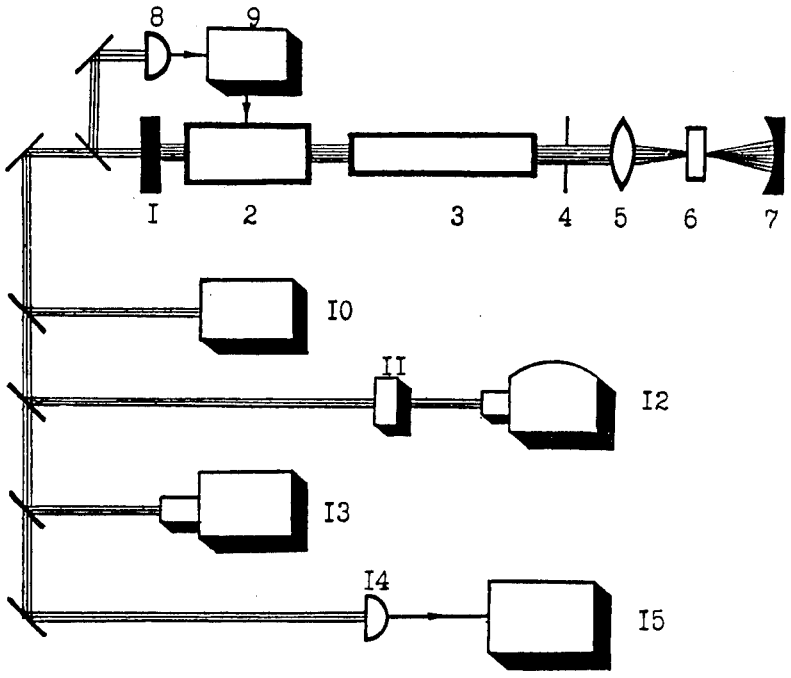


Figure 1.

1 is the plane mirror. Together with the intracavity lens 5 the mirror 7 forms a Kepler telescope. Cell 6 with saturable absorber has 0,2 mm gap thickness. 3 is active medium, which is pumped with two direct impulsive lamps (the pump time is ≈0,5 ms). 8 is a photodiode. 9 is an electronic amplifier. 2 is an intracavity electrooptic modulator containing Pockels cell. 10–15 are control equipment. 10 is an energy measuring instrument (calorimeter IMO-2). 11 is a Fabry-Perot interferometer. 12 is high-speed camera SFR. 13 is high-speed streak camera. 14 is a photodiode. 15 is an oscillograph S1–75.

An electrical signal from the photodiode is amplified and directed to

the intracavity electrooptic modulator. The feedback loop becomes closed. The response time of the electronic circuit is equal to several radiation round-trip times in resonator. As result, the loss due to the electrooptic modulator follows closely the cavity-averaged intensity. There are optimal values for depth, response time (time of averaging for signal), and time of delay of inertial feedback loop. Fig.2–4 demonstrate typical oscillograms of the output under different parameters of the feedback loop.

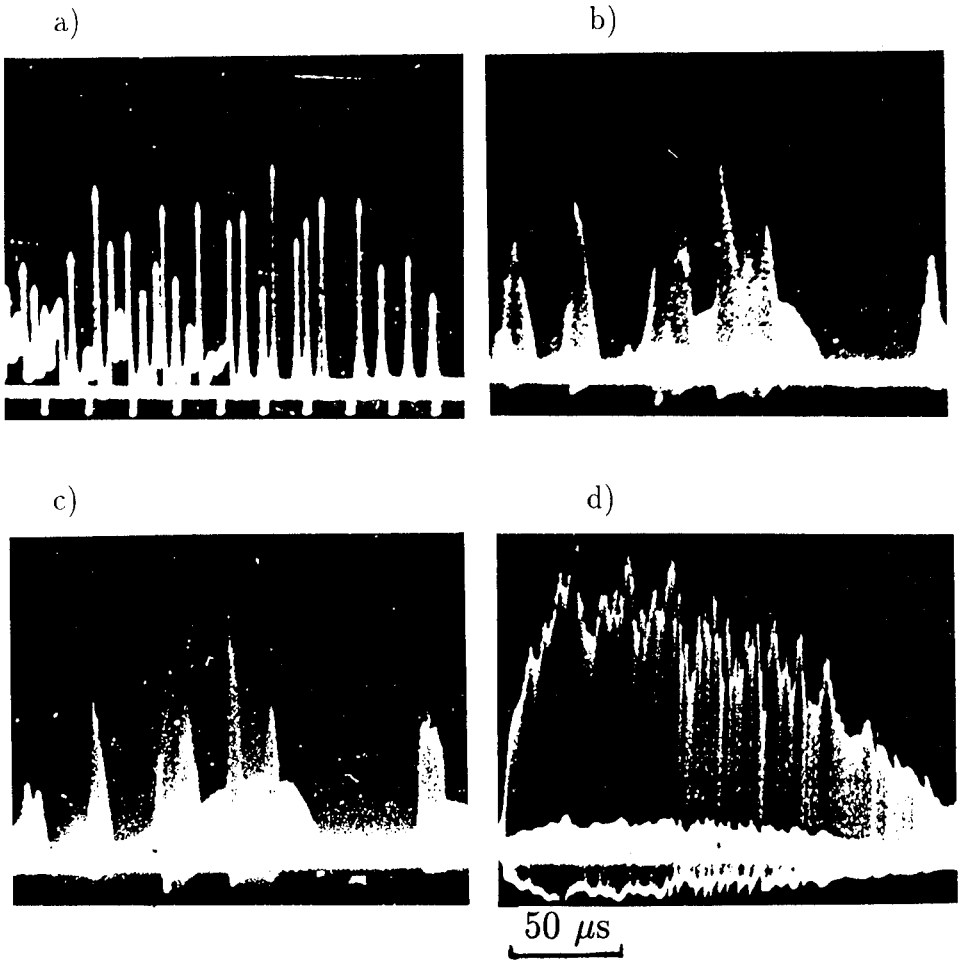


Figure 2. Typical oscillograms of the output under different depth of the feedback loop. The linear loss of a saturable absorber equals $\approx$ 8% in a single pass. a) – the feedback loop is switched off; b) – the loss due to the feedback loop equals 6% in a single pass; c) – the loss due to the feedback loop equals 8% in a single pass; d) – the loss due to the feedback loop equals 10% in a single pass.

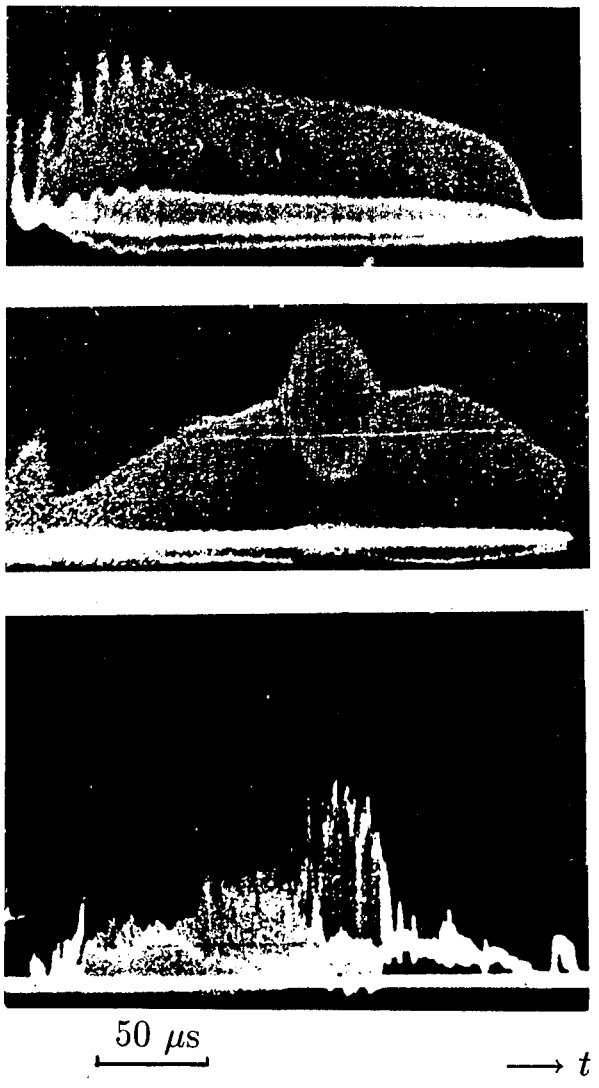


Figure 3. Typical oscillograms of the output under different parameters of laser system.

a – optimal depth of feedback loop;
b – regime of saturation of electronic amplifier;
c – high excess of pumping above the threshold.

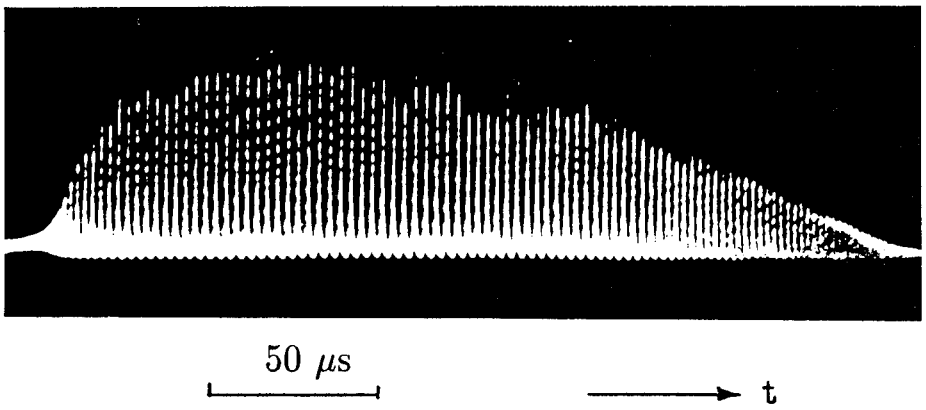


Figure 4. Oscillogram of the output from solid-state laser under high depth of feedback loop and high saturation of electronic amplifier.

3. Transient Evolution and Regime of Stationary Pulse

Fig.5 and Fig.6 represent the temporal dependencies of the output power. As can be seen from Fig.5b there exists the single ultrashort pulse into resonator (time resolution of oscillograph ~100 ps). As illustrated in Fig.6, at the initial stage of transient evolution there are many ultrashort pulses into resonator. Then number of pulses decreases. At the final stage of transient evolution there are only two pulses colliding in saturable absorber. And lastly, the regime of stable single pulse is realized. This picture is typical for solid-state lasers under study.

A slit scanning of radiation spectrum (see Fig.7,9,10) reveals peculiarities of generation for various lasers.

The potassium gadolinium tungstate laser has the shortest time of transient evolution. There is the drift of central frequency of radiation in the case of Nd:phosphate glass laser. Estimations of the mode-locked pulse durations were made from the spectral width of stationary pulse. For the ruby laser the experimental spectral width 1,4 cm^{-1} corresponds to the pulse duration of 7,5 ps, for Nd:phosphate laser with dye № 3955 the spectral width 4 cm^{-1} corresponds the duration of 2,5 ps (in the case of dye № 3274 the spectral width 20 cm^{-1} corresponds to 500 fs), for Nd:potassium gadolinium tungstate laser the experimental spectral width 1,9 cm^{-1} corresponds to the pulse duration of 5 ps.

For all cases the average intracavity power is 50÷100 W. For the purpose of increase of pike intensity of shaped ultrashort pulses we switch off the feedback loop after the completion of transient evolution (see Fig.8).

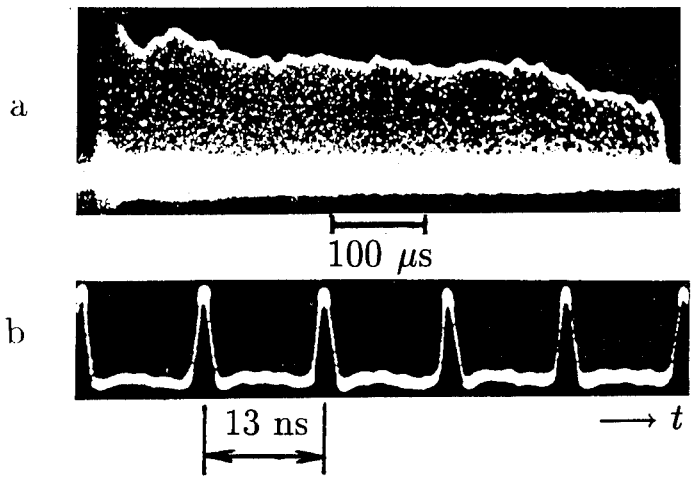


Figure 5. Oscillograms of the output recoded at (*a*) low and (*b*) high rate scanning.

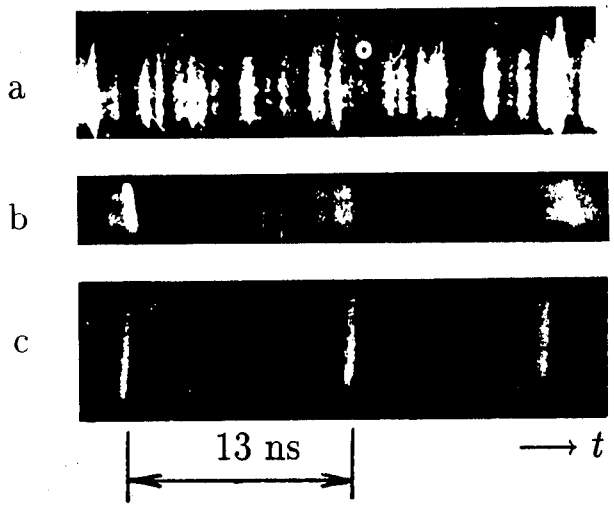


Figure 6.

Streak camera recodings of the output power at (*a*) the initial and (*b*) the final stages of transient process, (*c*) at the stage of stationary single ultrashort pulse.

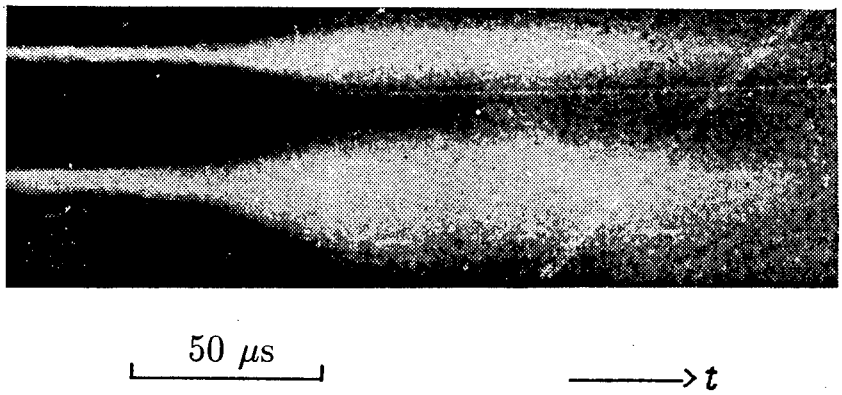


Figure 7. Slit scanning of radiation spectrum for ruby laser.

The width of quasistationary spectrum is 1,4 cm^{-1}. Free dispersion range of the etalon is 2,5 cm^{-1}. The solution of cryptocyanin in ethanol is used as saturable absorber.

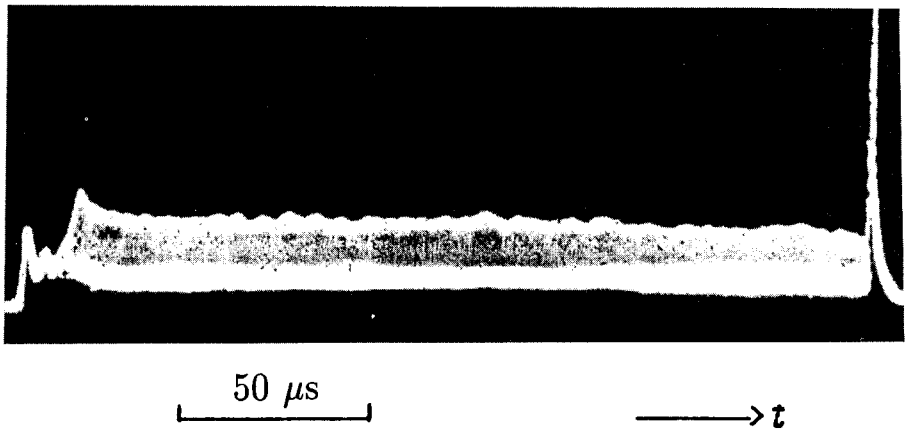


Figure 8.

Oscillogram of the output from potassium gadolinium tungstate laser.

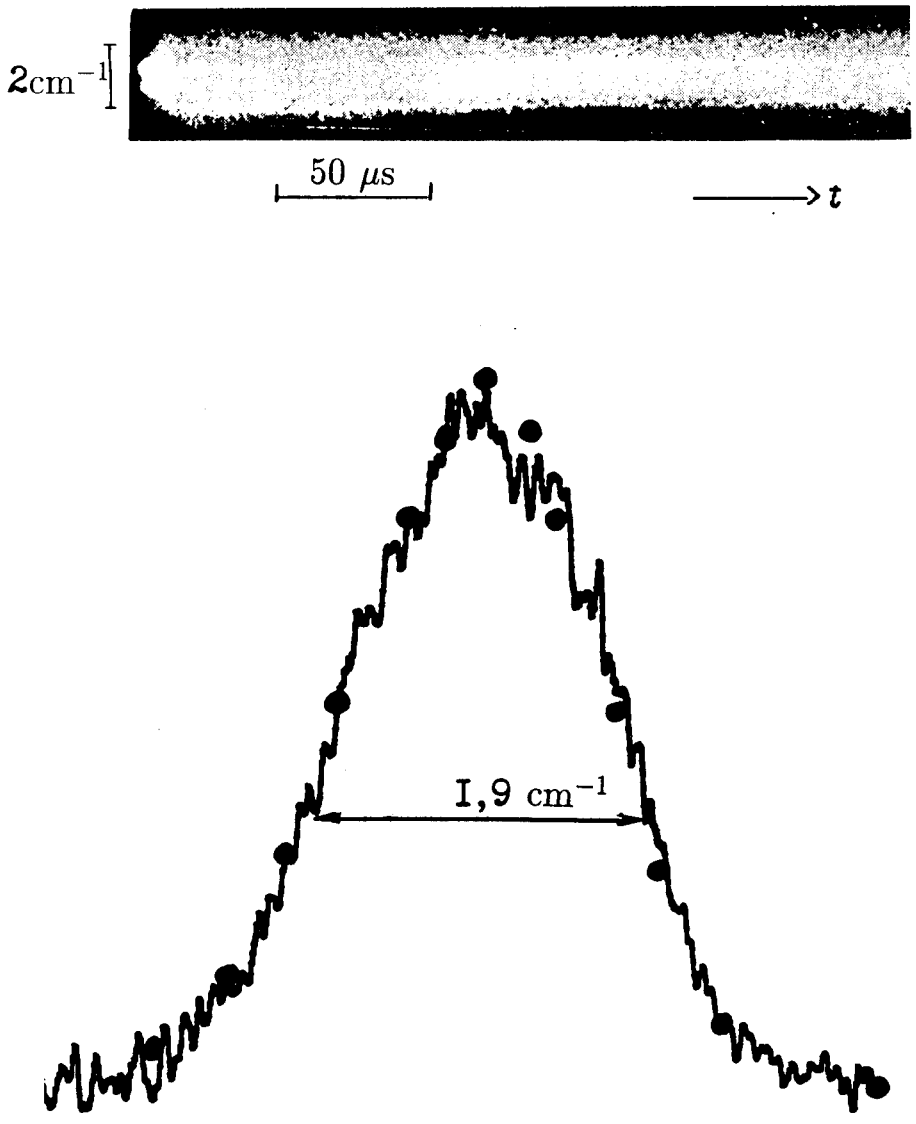


Figure 9.

Slit scanning of generation spectrum from stabilized passive mode-locked potassium gadolinium tungstate laser and densitogram of spectrum for stationary ultrashort pulse. Dependence in the form of square of hyperbolic secant is marked by dots.

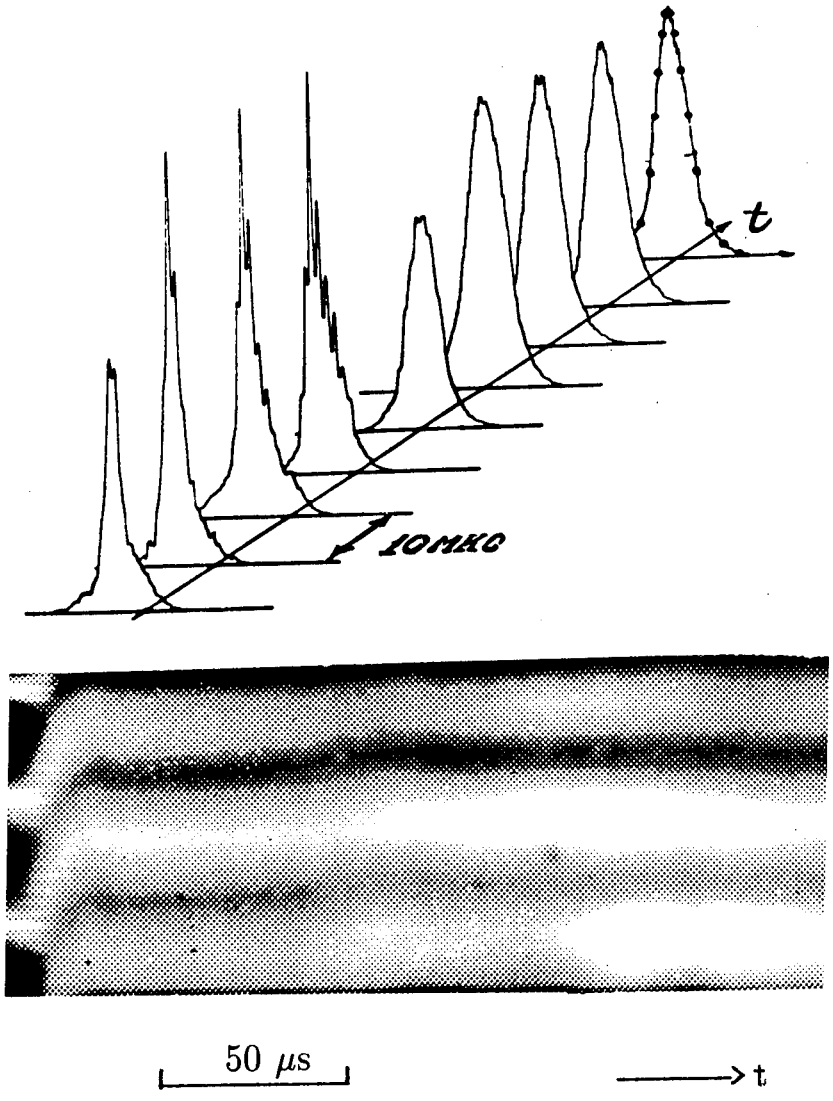


Figure 10.

Slit scanning of generation spectrum from Nd:phosphate glass laser with dye № 3955 in spirit as saturable absorber and transient evolution of spectral shape of output radiation. Steady state spectral shape has the form of square of hyperbolic secant (the function is marked by dots). The width of stationary spectrum is 4 cm^{-1}.

4. Instability of Transverse Spatial Distribution of Intracavity Radiation

Fig.11 illustrates the transverse instability of radiation. Transition of generation from transverse zero-order mode to chaotic transverse distribution is realized. We connect this instability with nonlinear self-influence of intracavity radiation through heat nonlinearity of refractive index of the dye solution used as saturable absorber. Accumulated transverse spatial inhomogeneity of the refractive index results in the considerable scattering intracavity radiation. As a result, the loss increases, that leads to the decrease of intensity and then to the generation frustration (see Fig.12).

The transverse spatial instability is suppressed by pumping of the dye solution through the saturable absorber cell (see Fig.13). The required velocity of the solution is $\approx$3 m/s.

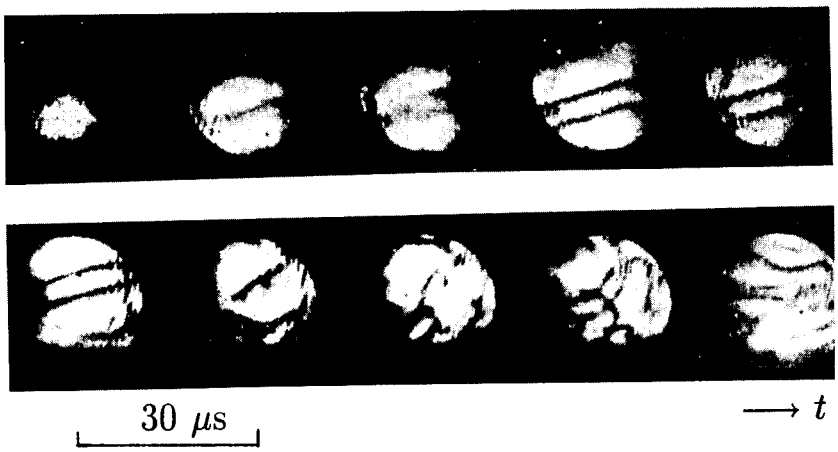


Figure 11.

Evolution of transverse spatial distribution of intracavity radiation connected with transverse instability.

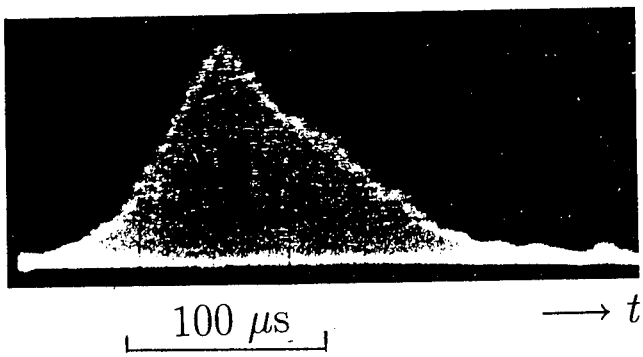


Figure 12.

The decrease of intensity and the generation frustration due to the transverse instability of intracavity radiation of ruby laser.



Figure 13.

Suppression of transverse spatial instability of intracavity radiation by pumping of the dye solution through the saturable absorber cell.

5. Self-Phase Modulation Instability

In the case of the Nd:phosphate glass laser we observed also more considerable drift of central radiation frequency than for the case presented in Fig.9. This effect induces the instability illustrated in Fig.14. This instability arises under considerable focusing of intracavity radiation into a saturable absorber. More considerable drift occurs in the case of Nd:silicate laser (see Fig.15).

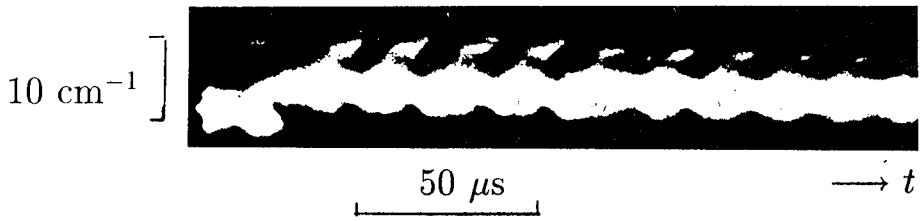


Figure 14.

Repeated drifts of radiation frequency in Nd:phosphate glass laser under considerable focusing of intracavity radiation into saturable absorber (the self-phase modulation instability).

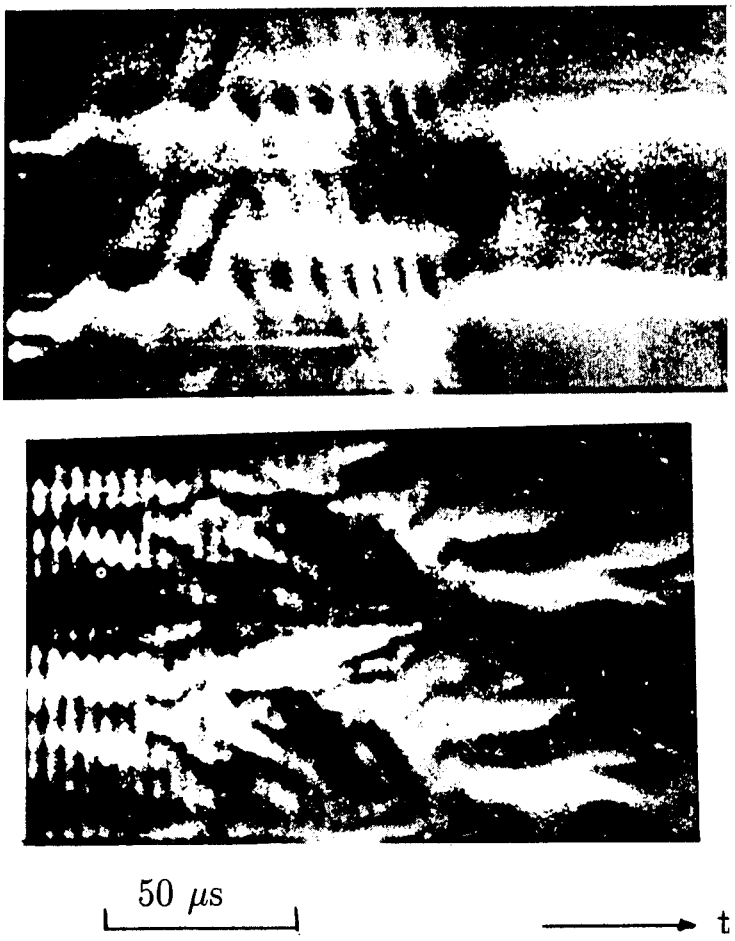


Figure 15.

Spectral drift of radiation frequency due to the self-phase modulation instability in Nd:silicate glass laser. Free dispersion range of the etalon is 25 cm^{-1}.

6. Multistability Monochromatic Generation

In the case of passive mode-locking the fast saturable absorber result in selection of the strongest peak from initial noise radiation, so that finally a single ultrashort pulse with stationary parameters is realized. In the case of a slow-responce saturable absorber there exists selection of the strongest laser mode from initial spontaneous radiation. This effect is due tu the "burning-out", in saturable absorber, of a spatial loss grating by the standing-wave field of the strongest laser mode of linear resonator. The losses experienced by the weak modes, which have a different spatial distribution of the field, are higher than for the strong mode. In such way there arises the effect of suppression of the weak modes, that can result in single-mode lasing at the end of the transient evolution.

In the case of single-mode lasing the spatial distribution of the losses in a saturable absorber can be described by the following expression

$$S(x) = \frac{S^0}{1 + \eta I_i \sin^2(i\pi x L^{-1})}, \qquad (1)$$

where S^0 и η are, respectively, the unsaturated losses and the reciprocal of the intensity of the absorption saturation; I_i is the intensity of emitted mode; the function $\sin(i\pi x L^{-1})$ governs the spatial distribution; i is the number of antinodes in the standing wave of the ith mode in question; x is the longitudinal coordinate; L is the optical length of the resonator cavity.

In the case of weak saturation of the absorber ($\eta I_i \ll 1$) the difference between the absorption coefficients for the kth and the lasing ith modes is

$$\delta S_k = 3^{-1}\eta I_i S^0 \left\{1 - \frac{\sin \pi(k-i) l_s L^{-1}}{\pi(k-i) l_s L^{-1}} \cos\left[\pi(k-i)(l_s + l_m) L^{-1}\right]\right\}, \qquad (2)$$

where l_m is the distance between a cavity resonator mirror and the saturable absorber.

Fig.16 shows the dependence of eq.(2) obtained for the saturable absorber position next to one of the cavity mirrors $l_m = 0$. We can see that an absorber with a spatial loss grating, "burnt-out" by the lasing mode, is an intracavity nonlinear selective component with the transmission maximum at the lasing mode frequency and a passband width amounting to L/l_s intermode spacing. The contrast of the frequency profile of the transmission is governed by the product of the factor representing the unsaturated losses in the absorber S^0 and the saturation parameter ηI_i. If saturable absorber entirely fills the resonator cavity ($l_s/L = 1$), the losses experienced by the lasing mode are minimal and are a factor of $3^{-1}\eta I_i$ larger for the other modes.

The "burning-out" of the spatial grating in the distribution of the population in the active medium has the opposite effect: the gain is higher for the uncontrolled modes, compared with the gain for the lasing mode, so that multimode lasing is observed. The spatial distribution of the gain $G(x)$ and of the gains experienced by the various modes G_k and difference between the gains for the nonlasing and lasing modes δG_k can be all obtained from eqs (1), (2) when $S(x)$, S^0, l_s, η, S_k, δS_k, l_m are replaced with $G(x)$, G^0, l_a, χ, G_k, δG_k, l_n, where G^0, l_a, χ represent the unsaturated gain, the length of the active medium, and the saturation intensity in the medium, and l_n is the distance between a resonator cavity mirror and the active medium.

The positioning of active medium next to a cavity mirror $l_n = 0$ is optimal for preventing the participation of new modes in the lasing process.

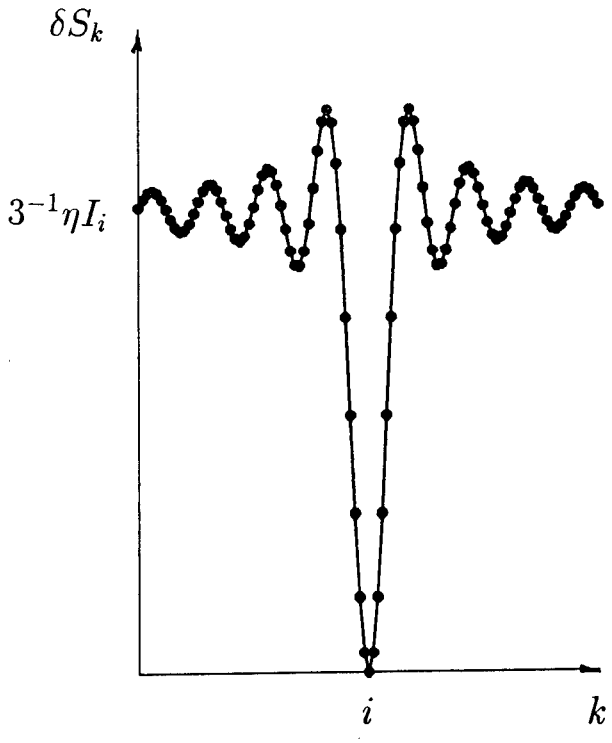


Figure 16. Dependence of the loss difference δS_k on the mode number k.

In a linear resonator the slow saturable absorber acts as the nonlinear selective component with the transmission maximum at the emitted ith mode frequency.

It is obvious that in the single-mode lasing case the condition for prevention of generation of additional modes is the inequality $\delta S_k \geq \delta G_k$. This inequality is definitely satisfied if the width and contrast of the spectral profile of the losses described by (2) are greater than the corresponding parameters of the spatial profile of the gain:

$$l_s > l_a, \qquad \eta S^0 > \chi G^0. \tag{3}$$

7. Conclusions

Solid-state lasers operating in regime of stabilized stationary ultrashort pulses are good basis for the construction of reliable practical sources of picosecond and femtosecond reproducible power light pulses.

The regimes with the self-phase modulation and transverse spatial instabilities are of considerable research interest as systems described by one- and two-dimensional nonlinear Schrödinger equation with complex parameters, consequently. Nonlinear dynamics of these systems is much investigated. Similar instabilities can be manifested, for example, in fiber lines of communications.

The multistable lasing mentioned above may be of interest in the development of solid-state laser sources of high-power monochromatic radiation with a stable frequecy and with the feasibility of switching lasing from one frequency to another.

If our theoretical and experimental investigation of stabilized passive mode-locking is in a sufficiently advanced stage development, then experimental research of multistable monochromatic generation is in the initial stage. The main problem consists in the search for saturable absorber with suitable parameters (recovery time, intensity of an absorption saturation, section of an absorption).

8. References

1. Komarov, K.P., Kuch'yanov, A.S. (1995) Formation of ultrashort pulses in lasers with nonlinear diffraction loss, *SPIE's Proceedings* **2513,** 512–519.

2. Komarov, K.P. (1994) Multistable single-mode emission from solid-state lasers, *Sov.J.Quantum Electron.* **24,** 975-976.

3. Komarov, K.P. (1992) Soliton mechanism for compression of ultrashort light pulses in passive mode-locked solid-state lasers with wide gain bandwidth, *Izvestiya Rossiiskoi akademii nauk, seriya fizicheskaya* **56,** 2–6.

4. Komarov, K.P., Kuch'yanov, A.S., Ugozhayev, V.D., Pavlyuk, A.A., Nesterenko, V.F. (1992) Stationary picosecond pulses from Nd:potassium gadolinium tungstate laser, *Izvestiya Rossiiskoi akademii nauk, seriya fizicheskaya* **56,** 135–139.

5. Komarov, K.P., Kuch'yanov, A.S., Ugozhayev, V.D. (1991) High-performance picosecond and femtosecond solid-state lasers with feedback-controlled passive mode-locking, *SPIE's Proceedings* **1501,** 135-143.

6. Komarov, K.P., Kuch'yanov, A.S. (1991) Limiting duration of ultra-short optical pulses generated by passively mode-locked solid-state lasers, *Sov.J.Quantum Electron.* **21,** 182–185.

7. Komarov, K.P. (1991) Transient evolution, stability for disturbances, multistability, chaos of transverse spatial structure of a light wave propagating in a ring system with inertial nonlinear medium, *The OSA Proceedings on Nonlinear Optical* **7,** 271–276.

8. Komarov, K.P. (1990) On transient evolution and shaping of transverse spatial distribution of a light wave propagating in a ring resonator with inertial nonlinear medium, *Journal of Modern Optics* **37,** 1159–1162.

9. Komarov, K.P., Kuch'yanov, A.S., Ugozhayev, V.D. (1990) Solid-state lasers for reproduced picosecond and femtosecond light pulses, *SPIE's Proceedings* **1223,** 274–278.

10. Komarov, K.P. (1989) On the theory of passive mode-locking in regime of colliding pulses, *Optika i spektroskopiya* **66,** 648–654.

11. Komarov, K.P., Kuch'yanov, A.S., Ugozhayev, V.D. (1986) Generation of stationary ultra-short pulses by a passive mode-locking solid-state lasers, *Optics Communications* **57,** 279–284.

12. Komarov, K.P., Kuch'yanov, A.S., Ugozhayev, V.D. (1986) Generation of stationary ultra-short pulses by a passive mode-locking solid-state lasers, *Optics Communications* **57,** 279–284.

13. Komarov, K.P. (1986) On the theory of steady-state ultrashort pulses in passively mode-locked lasers, *Optika i spektroskopiya* **60,** 379–383.

14. Komarov, K.P. (1986) On transient evolution and steady-state generation of passive mode-locked lasers, *Kvantovaya elektronika* **13,** 166–169.

15. Komarov, K.P. (1985) On the theory of transient evolution of passive mode-locking, *Optics Communications* **54,** 233–235.

AN EXTENDED CHARACTERIZATION OF FLATTENED GAUSSIAN BEAMS

S.-A. AMARANDE
Laser Department
Institute of Atomic Physics
P.O. Box MG-6, RO-76900 Bucharest-Mãgurele, Romania.

Abstract

The characterization of flattened gaussian beams is extended. The representation of these beams in cartesian coordinates contains only even Hermite-Gauss modes. Two parameters, beam propagation factor M^2 and kurtosis, both specific to the method of moments are evaluated. The calculation is using mode coefficients of the representation by a superposition of Hermite-Gauss modes. Parameters evolution, as functions of beam order, start, as expected, for the zero order with the well known values of the pure gaussian beam, one, respectively three. Then they increase, respectively decrease. Arriving to a beam order approximately 5, the kurtosis variation slow down and, after an order around 10, remains nearly constant at approximately 1.85.

1. Introduction

High power lasers are characterized by high gains and large apertures. Therefore, efficient mode filling of the active media deserves special attention when designing the optical cavities, the oscillator-amplifier configurations, the nonlinear conversion experiments, etc. An uniform or flat-topped beam intensity profile represents a solution for such cases.

Flat-top beams can be produced for example: i) by stable optical resonators oscillating highly multimode [1,2] and ii) by unstable optical resonators with supergaussian graded reflectivity mirror [3,4]. The beam propagation has been treated in the first case analytically [2] and, in the second case, numerically [5]. More recently, the supergaussian beam was approximated by the generalized flattened gaussian beams for which the propagation can be treated analytically in a simpler manner [6].

Because the design of laser systems requires appropriate evaluation of beam characteristics, much work was devoted especially recently [7], to beam

R. Kossowsky et al. (eds.), High Power Lasers – Science and Engineering, 365–372.
© 1996 *Kluwer Academic Publishers. Printed in the Netherlands.*

characterization methods. Among these, the method of moments, which rely mainly on the concepts of the beam propagation factor, M^2, [8] and of the effective radius of curvature [9], has important advantages [10]. We think that, the existence of such kind of characterization parameters provides in principle an appropriate opportunity to compare further supergaussian beams with flattened gaussian beams. To do this one must first to identify or to deduce the suitable relations and then to apply them. Following this objective, the characterization of flattened gaussian beams (FGB's) is extended in this paper. In the next section we will introduce the representation of FGB's in cartesian coordinates. In Sec. 3 and 4, the M^2-factor and, respectively, the flatness of FGB's are evaluated as a function of beam order. Finally, in Sec. 5, we present the conclusions.

2. Representation of flattened gaussian beams in transverse cartesian coordinates

To introduce FGB's [11], a superposition of N suitably weighted Laguerre-Gauss beams was carried out, N representing the beam order. The field distribution across the waist plane is similar to that produced by an ordinary gaussian beam except that the central region is flattened. The flat zone occupies a larger fraction of the cross section as the order of beam increases.

Many of already existent results concerning beam characterization parameters are obtained by using cartesian coordinates rather than cylindrical coordinates. Therefore, we will trace back FGB's to Hermite-Gauss beams by using the standard procedure. For the sake of simplicity, we restrict ourselves to the bidimensional case (x, z). Then, by the multiplication of the two distributions, flattened independently along x and y, we could obtain a tridimensional FGB whose cross section is in the form of a rectangle.

We begin by representing optical field amplitude, $u_N(x,z)$, at z=0 as a truncated local expansion (around the origin)

$$u_N(x,0) = A\cdot\exp\left(-x^2\right)\cdot\sum_{k=0}^{N}\frac{x^{2\cdot k}}{k!}, \qquad N=0,1,\ldots, \tag{1}$$

where the beam width at the waist was considered w_0=1. We then express x^{2k}, starting from a decomposition relation in Hermite-Gauss functions [12], by

$$x^{2\cdot k} = \frac{(2\cdot k)!}{2^{3\cdot k}}\cdot\sum_{n=0}^{k}\frac{1}{(k-n)!\cdot(2\cdot n)!}\cdot H_{2\cdot n}\left(\sqrt{2}\cdot x\right). \tag{2}$$

One can see that only even Hermite polynomials, H_{2n}, are involved.

The Hermite-Gauss beam of order n [13], say $\Psi_n(x,z)$, has the following spatial distribution (at z=0)

$$\Psi_n(x,0) = \left(\frac{2}{\pi}\right)^{1/4}\cdot\left(2^n\cdot n!\right)^{-1/2}\cdot H_n\left(\sqrt{2}\cdot x\right)\cdot\exp\left(-x^2\right). \tag{3}$$

One obtain finally, after a straightforward calculation, the amplitude of FGB represented in cartesian coordinates

$$u_N(x,0) = \sum_{n=0}^{N} c_n \cdot \Psi_{2\cdot n}(x,0), \qquad N=0,1,\ldots . \tag{4}$$

where

$$c_n = A \cdot \left(\frac{\pi}{2}\right)^{1/4} \cdot \frac{2^n}{[(2\cdot n)!]^{1/2}} \cdot \sum_{k=n}^{N} \frac{1}{2^{3\cdot k}\cdot k!} \cdot \frac{(2\cdot k)!}{(k-n)!}. \tag{5}$$

Drawing the field distribution for a few values of N we obtain the curves presented in Fig. 1.

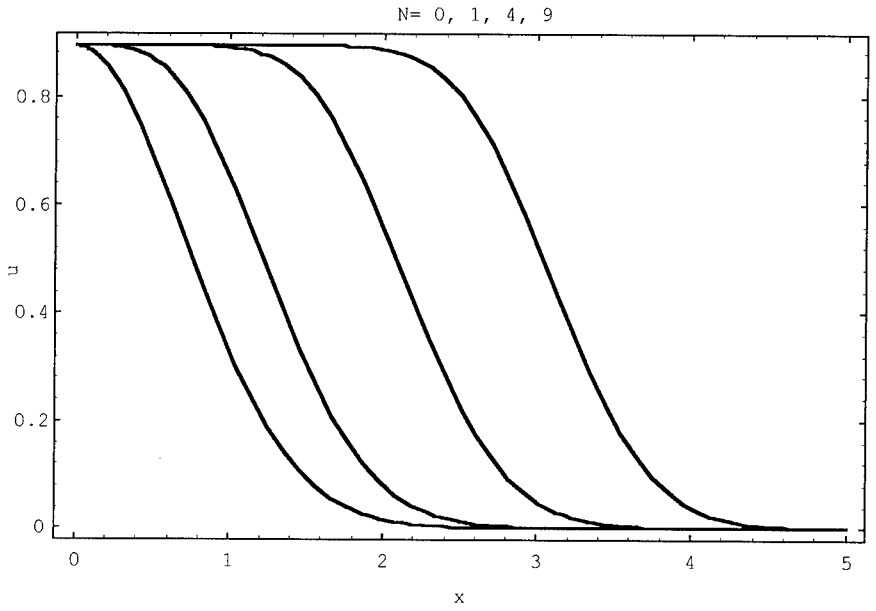


Figure 1: FGB transverse intensity profiles with different beam orders versus x.

3. Evaluation of beam propagation factor M^2

As FGB's are a superposition of Hermite-Gauss beams, suitably weighted, we can consider them formally as a kind of multimode beams. Then we can normalize mode coefficients, c_n, so that the total power $\Sigma|c_n|^2=1$, obtaining for the constant A the expression

$$A=\left(\frac{\pi}{2}\right)^{-1/4}\cdot\left\{\sum_{n=0}^{N}\frac{2^{2n}}{(2\cdot n)!}\cdot\left[\sum_{k=n}^{N}\frac{1}{2^{3\cdot k}\cdot k!}\cdot\frac{(2\cdot k)!}{(k-n)!}\right]^2\right\}^{-\frac{1}{2}}, \qquad N=0,1,\ldots \quad (6)$$

The graphs of field distribution corresponding to these normalized FGB's are presented in Fig. 2.

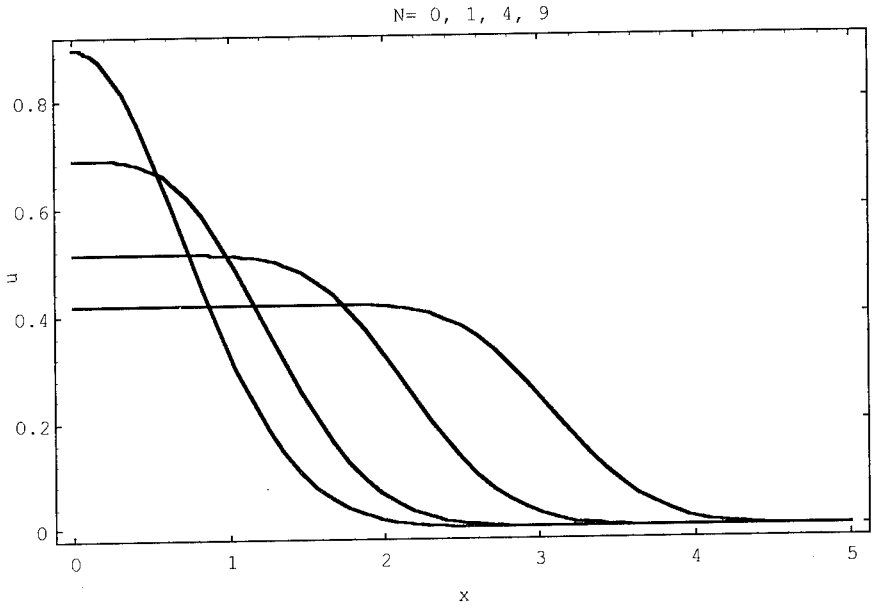


Figure 2: Normalized FGB's profile versus *x*.

Flat-top beams could be in principle represented by a superposition of Hermite-Gauss (or Laguerre-Gauss) modes. The superposition could be either i) coherent, and the transverse field profile is changing in propagation [6], or ii) incoherent, and the intensity profile will retain the same transverse shape at all planes z (propagation axis) [2]. Now we will evaluate M^2 factor for every beam order N by using the relation which is valid for a general beam represented either by coherent or by incoherent superposition [14,15]

$$M^2=\left(\left[\sum_{n=0}^{N}(2n+1)|c_n|^2\right]^2-4\cdot\left\{\sum_{n=0}^{N}\left[(n+1)(n+2)\right]^{1/2}\mathrm{Re}\left(c_n\cdot c_{n+2}^{*}\right)\right\}^2\right)^{1/2} \quad (7)$$

The results appear in Fig. 2.

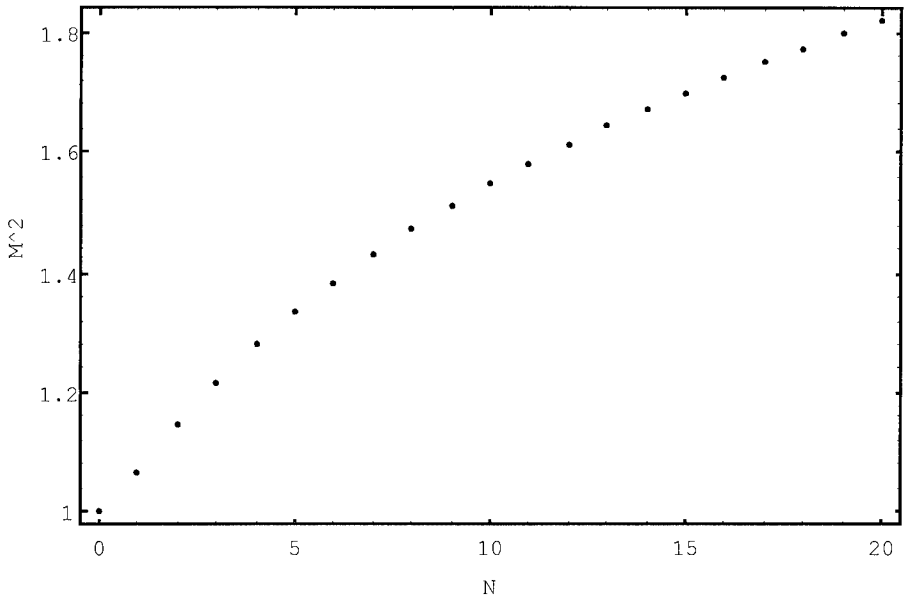


Figure 3: Beam propagation factor M^2 versus beam order N.

As expected, for N=0 we encounter a pure gaussian beam for which M^2 equals 1, the minimum value for this parameter.

4. Evaluation of FGB flatness

The parameter which describes the degree of flatness (or sharpness) of any beam intensity distribution is the so-called kurtosis parameter, K, [16]. This parameter is defined as

$$K = \overline{x^4} \Big/ \left(\overline{x^2}\right)^2, \tag{8}$$

where

$$\overline{x^n} = \int_{-\infty}^{\infty} x^n |u(x)|^2 \, dx, \tag{9}$$

denotes the n-th order moment of the intensity distribution $I(x)=|u(x)|^2$.

Let us now recall the relations expressing the two necessary moments in terms of Hermite-Gauss modes coefficients [14]

$$\overline{x^2} = \left(\frac{w_0}{2}\right)^2 \cdot \left\{ \sum_{n=0}^{N} (2n+1)|c_n|^2 + 2 \cdot \sum_{n=0}^{N} \left[(n+1)(n+2)\right]^{1/2} \mathrm{Re}\left(c_n \cdot c_{n+2}^*\right) \right\}, \qquad (10)$$

and

$$\overline{x^4} = \left(\frac{w_0}{2}\right)^4 \cdot \left\{ 3 \cdot \left[1 + \sum_{n=0}^{N} \left(2n^2 + 2n\right) \cdot |c_n|^2 \right] \right.$$

$$+4 \cdot \sum_{n=0}^{N} (2n+3)\left[(n+1)(n+2)\right]^{1/2} \cdot \mathrm{Re}\left(c_n \cdot c_{n+2}^*\right)$$

$$\left. +2 \cdot \sum_{n=0}^{N} \left[(n+1)(n+2)(n+3)(n+4)\right]^{1/2} \cdot \mathrm{Re}\left(c_n \cdot c_{n+4}^*\right) \right\}. \qquad (11)$$

By introducing Eqs. 10 and 11 in Eq. 8, and by representing the kurtosis parameter, K, as a function depending of FGB order, N, one obtain the graph presented in Fig. 4.

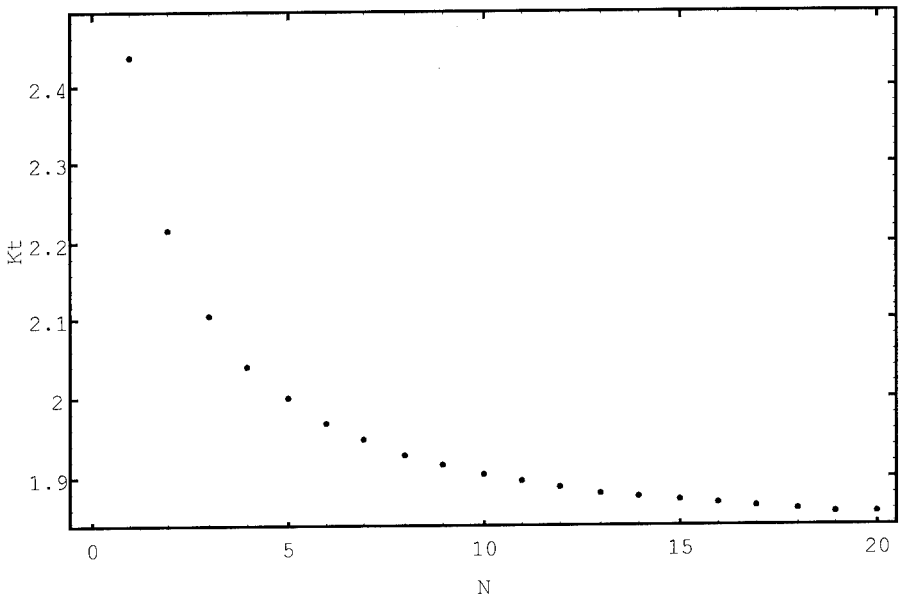


Figure 4: Kurtosis parameter K versus beam order N.

For N=0 the FGB is a pure gaussian beam and K has the maximum value equal with 3, which was not included in the graph. This profile is denoted as mesokurtic. The

beam profiles for which K is lower are denoted as platykurtic. After a mode order around 5 the kurtosis decreases slowly, and after a mode order approximately 10 this parameter is rather constant and equal with 1.85.

5. Conclusions

An extension of FGB's characterization is presented. The representation of FGB's in cartesian coordinates contains only even Hermite-Gauss modes. Two parameters, beam propagation factor and kurtosis, both specific to the method of moments are evaluated. The evolution of M^2 and K as functions of beam order start, as expected for N=0 with the well known values of the pure gaussian beam. Then they increase, respectively decrease. Arriving to a beam order approximately 5 the kurtosis variation slow down and, after a beam order around 10, remains nearly constant at approximately 1.85. These results could be usefull to evaluate further the approximation of the supergaussian beam by the generalized FGB by using a parameter which describe globally the beam propagation such as the M^2 -factor.

The evaluations here presented provide some figures which could add information useful for the design of laser systems. Especially for the design of optical resonators and systems of the high power lasers for materials processing where beam characteristics are important in application performances.

Aknowledgements

The research work leading to this paper was supported by the Ministry for Research and Technology of Romania, under contract No. 152B-B407.

References

1. Lamberton, H.M and Roper, V.G. (1978) Beam divergence of a highly multimode CO_2 laser, *J. Phys. E: Sci. Instrum.* **11**, 1102-1103.
2. Siegman, A. E., and Townsend, S. W. (1993) Output beam propagation and beam quality from a multimode stable-cavity laser, *IEEE J. Quantum Electron.* **29**, 1212-1217.
3. De Silvestri, S., Magni, V., Svelto, O., and Valentini, G. (1990) Lasers with super-gaussian mirrors, *IEEE J. Quantum Electron.* **26**, 1500-1509.
4. Parent, A. and Lavigne, P. (1989) Variable reflectivity unstable resonators for coherent laser radar emiters, *Appl. Optics* **28**, 901-903.
5. Parent, A., Morin, M. and Lavigne, P. (1992) Propagation of super-Gaussian beams field distributions, *Opt. and Quantum Electron.* **24**, S1071-S1079.
6 Palma, C. and Bagini, V. (1994) Propagation of super-Gaussian beams, *Optics Comm.* **111**, 6-10.
7. Weber, H. (ed.) (1992) Special issue on Laser Beam Quality; *Opt. and Quantum Electron.* **24,** No. 9;
   Mejías, P.M., Weber, H., Martínez-Herrero, R. and González-Ureña, A. (eds.) (1993) *Laser beam characterization*, SEDO, Madrid;
   Weber, H., Reng, N., Lüdtke, J. and Mejías, P.M. (eds.) (1994) *Laser beam characterization* FLI, Berlin.
8. Siegman, A.E. (1990) New developments in laser resonators, in D. A. Holmes (ed.), *Optical Resonators*, Proc. SPIE **1224**, pp. 2-14.

9. Bélanger, P.A. (1991) Beam propagation and ABCD ray matrices, *Optics Lett.* **16**, 196-198;
Siegman, A.E. (1991) Defining the effective radius of curvature for a nonideal optical beam, *IEEE J. Quantum Electron.* **27**, 1146-1148;
Porras, M.A., Alda, J. and Bernabeu, E. (1992) Complex beam parameter and ABCD law for non-Gaussian and nonspherical light beams, *Appl. Optics* **31**, 6389-6402.
10. Siegman, A.E. (1993) Defining and measuring laser beam parameters, in Mejías, P.M., Weber, H., Martínez-Herrero, R. and González-Ureña, A. (eds.) *Laser beam characterization*, SEDO, Madrid, pp. 1-21.
11. Gori, F. (1994) Flattened gaussian beams, *Optics Comm.* **107**, 335-341.
12. Morse, P. M. and Feshbach, H. (1953) *Methods of Theoretical Physics*, McGraw- Hill, New York, vol. 1, chap. 5.
13. Siegman, A. E. (1986) *Lasers*, Univ. Sci., Mill Valley, CA, p. 646.
14. Du, K. -M., Herziger, G., Loosen, P., and Rühl, F. (1992) Coherence and intensity moments of laser light, *Opt. and Quantum Electron.* **24**, S1081-S1093.
15. Martínez-Herrero, R. and Mejías, P. M. (1992) Expansion of the cross- spectral density function of general fields and its application to beam characterization, *Optics Commun.* **94** 197-202.
16. Martínez-Herrero, R., Mejías, P.M., Sánchez, M. and Neira, J.L.H. (1992) Third and fourth order characterization of partially coherent beams propagating through ABCD optical systems, *Opt. and Quantum Electron.* **24**, S1021-S1026.

OPTICS FOR X-RAY LASER AND LASER PLASMA SOFT X-RAY RADIATION

L. PINA
Faculty of Nuclear Sciences and Physical Engineering, Czech Technical University in Prague
Brehova 7, CZ-115 19 Praha 1
Czech Republic

A. INNEMAN
Koma, Prague
K lesu 965, CZ-142 00 Praha 4
Czech Republic

R. HUDEC
Astronomical Institute
Czech Academy of Sciences, Ondrejov
CZ-251 65 Observatory Ondrejov
Czech Republic

Abstract: Focusing X-ray grazing incidence optics for X-ray laser and laser plasma soft X-ray radiation has been studied. Theoretical model including reflectivity dependence on the x-ray photon energy, grazing incidence angle and surface microroughness was used for intensity and trajectory calculations in a ray-tracing computer code. Parabolic axisymmetric mirror for focusing Princeton X-ray laser beam and ellipsoidal axisymmetric mirror for focusing soft x-rays from nanosecond laser plasma were modelled in details. Test samples of flat and ellipsoidal mirrors were developed and made using electroformed replication process. Following experimental results showing possible efficiency of conversion of the laser light to broad-band X-rays the grazing incidence focusing optical element was designed in order to obtain gain in the X-ray beam intensity.

1. Introduction

For more than two decades laser plasma belongs to the sources generating extremely intense broad-band soft X-ray (SXR) radiation. Its spectrum features lines as well as bremsstralung part. X-ray photons from a laser plasma have energy typically between

R. Kossowsky et al. (eds.), High Power Lasers – Science and Engineering, 373–380.
© 1996 *Kluwer Academic Publishers. Printed in the Netherlands.*

50 eV and 10 keV. Reported conversion efficiency from laser light to the X-ray radiation reached more than fifty percent as e.g. already in [1]. Recently also X-ray lasers matured to become available sources of a monochromatic radiation opening new challenging opportunities for the development and applications in the soft X-ray band of electromagnetic radiation spectrum. However, some applications demand even more intense X-ray beams, or sources cheaper and smaller than that presently available, namely big lasers and synchrotrones.

Therefore, not only mirrors for laser resonators, but also focusing optics for X-ray beams became the important issue. In principle it is possible to consider multilayer mirrors, zone plates, crystals and grazing incidence mirrors as X-ray optical elements. All of them are nowadays more or less developed to a certain state of acceptability. If one wants to scale their use to the very high intensities and thus to possible damage threshold, one comes to focusing with a use of the X-ray grazing incidence optics.

2. Computer model and ray-tracing

Theoretical model including reflectivity dependence on the X-ray photon energy, grazing incidence angle and surface microroughness was used for intensity and trajectory calculations in a ray-tracing computer code written in our lab. Two cases were studied. Parabolic axisymmetric mirror for focusing monochromatic beam of the old version of X-ray laser developed by S. Suckewer in the Princeton Plasma Physics Laboratory in 1988 (Figure 1.), and elliptical axisymmetric mirror for focusing broad-band soft X-rays from laser plasma spot. The old type of Princeton laser was chosen for the study due to the shape of its beam (hollow cylinder) which is especially compatible with the grazing incidence conical optics considered here. Calculated maximum intensity is of the order of 10^9 Wcm^{-2} for considered 50 μm focal spot.

In case of elliptical mirror the ray-tracing program was used for preliminary calculations of the distribution of the irradiance in the chosen focal plane. The simulations showed that the image of the X-ray source (laser plasma, disk 100 μm dia, uniform distribution, 100 MW of 1.5 nm wavelength X-rays into 2π solid angle) has a reasonable intensity distribution (Figure 2.) and intensity gain of the order of thousands.

3. Electroformed replication

Continuing our previous research [2], test samples of flat and ellipsoidal mirrors were developed and made using electroformed replication process (Figure 3.). It is rather

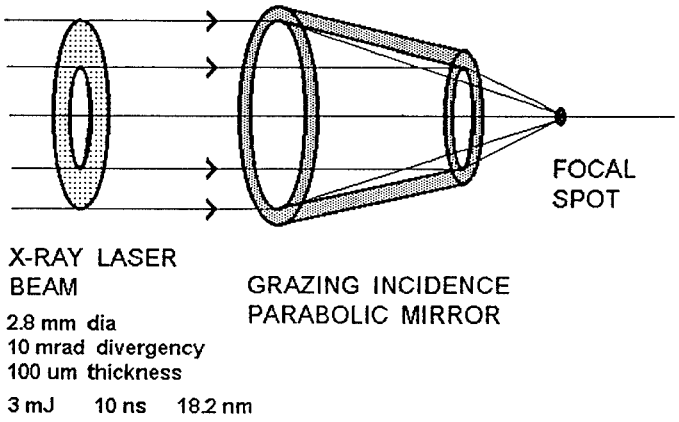


Figure 1. Focusing Princeton X-ray laser by a parabolic axisymmetric mirror.

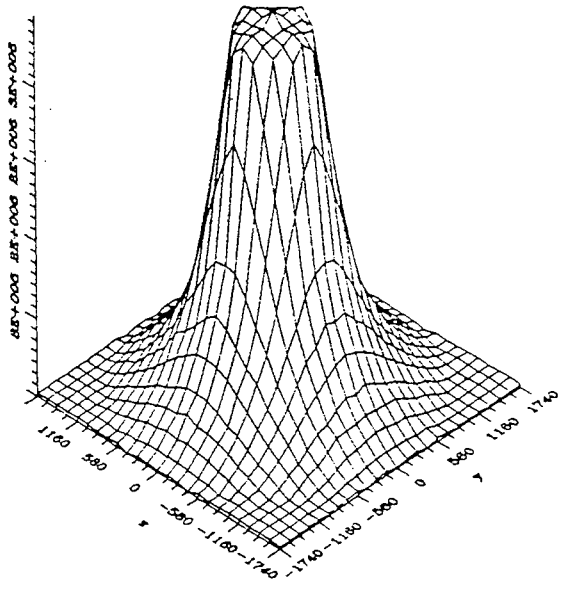


Figure 2. Intensity distribution I(x,y) of soft X-rays from laser plasma spot focused by an elliptical axisymmetric mirror (x and y in micrometers, I in $MWcm^{-2}$).

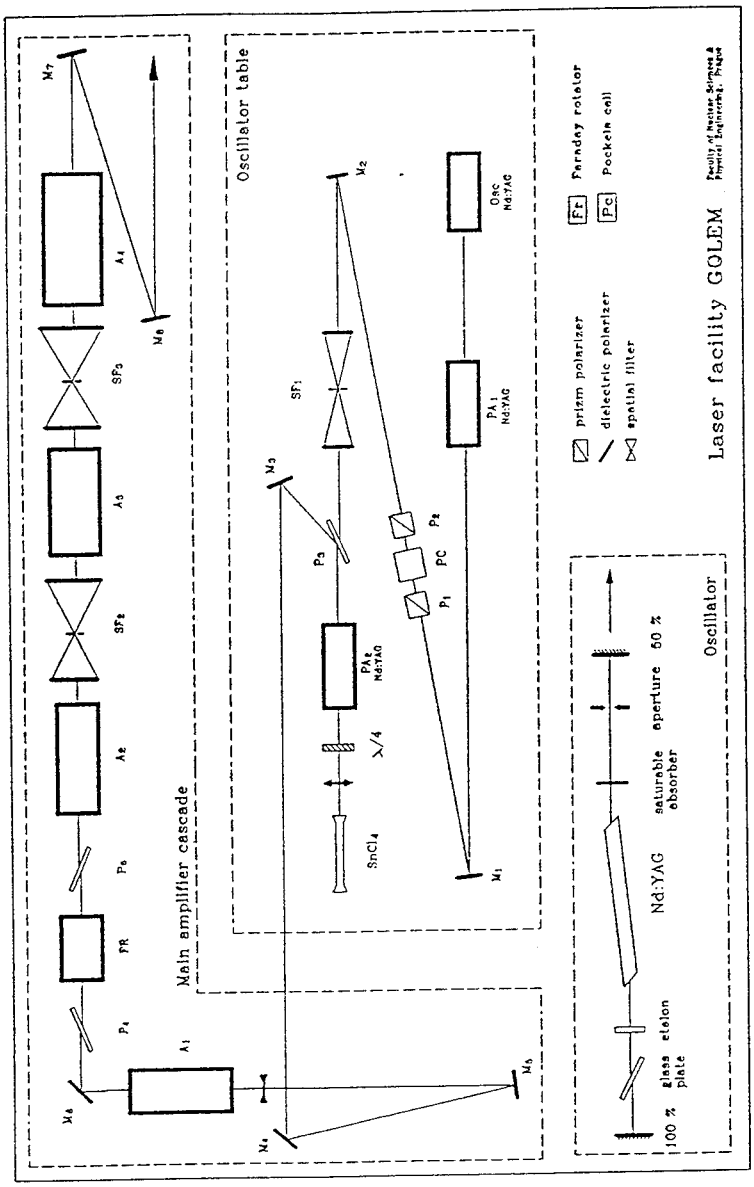


Figure 4. High power Nd:glass laser system GOLEM at CTU Prague.

difficult and expensive to produce high-quality polished internal cavity with diameters below 10 mm. This problem is efficiently solved thanks to the above mentioned method. Electroformed replicas are made of a master mandrel which has an external shape which is that of the cavity of the final mirror. The advantages of this method are following: it is not necessary to polish the cavity and many copies from only one master can be produced. Nickel or gold metal layers with good reflectivity serve as reflecting surfaces. Unlike most of the thin evaporated layers, the electroformed nickel layer is highly resistant to environmental and laboratory influences.

The facility for measurements of masters and shells is based on a microfocus X-ray tube with the X-ray source diameter of the order of 10 micrometers. A 2D CCD serves as a X-ray detection system and the measured signal is processed by a computer.

4. Experimental

Laser intensity dependence of the X-ray conversion efficiency for nanosecond pulses was studied by many authors giving the best integral conversion efficiency at intensities of the order of 10^{13} Wcm^{-2}. The most suitable pulse durations were found to be around 3 ns. It was also confirmed that using target materials with different atomic numbers leads not only to different integral conversion efficiencies, but this approach may be used to tune the peak intensity of the emitted X-rays to the desired wavelength. This last feature is of considerable importance for X-ray lithography, X-ray microscopy, X-ray radiobilogy etc. These results are being modified by the continuing research.

Laser plasma in our experiments was created by the high power laser system GOLEM at the CTU Prague (Figure 4.). Laser pulse duration was 5 ns and the energy of pulses was in the range of 0.5 to 5.0 Joules. This parameters together with the focal spot diameter of approx. 80 micrometers provided intensities in the range of 0.2 to $2x10^{13}$ Wcm^{-2}. Planar targets made from C, Al, Cu and W were mounted on a rotary holder inside a vacuum target chamber equipped with suitable diagnostics of laser beam and emitted X-rays.

Following our experimental results confirming attainable efficiency of conversion of laser light to broad-band X-rays (Figure 5.) the grazing incidence focusing ellipsoidal mirror was designed and optimized (central lambda = 1.5 nm, critical angle = 33 mrad, output dia = 4.7 mm, plasma-mirror distance = 10 mm, excentricity = 375 mm) in order to obtain collimation and the high gain in X-ray beam intensity. According to performed computer simulations laser plasma source created by GOLEM laser combined with properly designed grazing incidence long focus X-ray mirror can give at the focus collimated broad-band (0.1 - 2 keV) pulsed X-ray beam with maximum

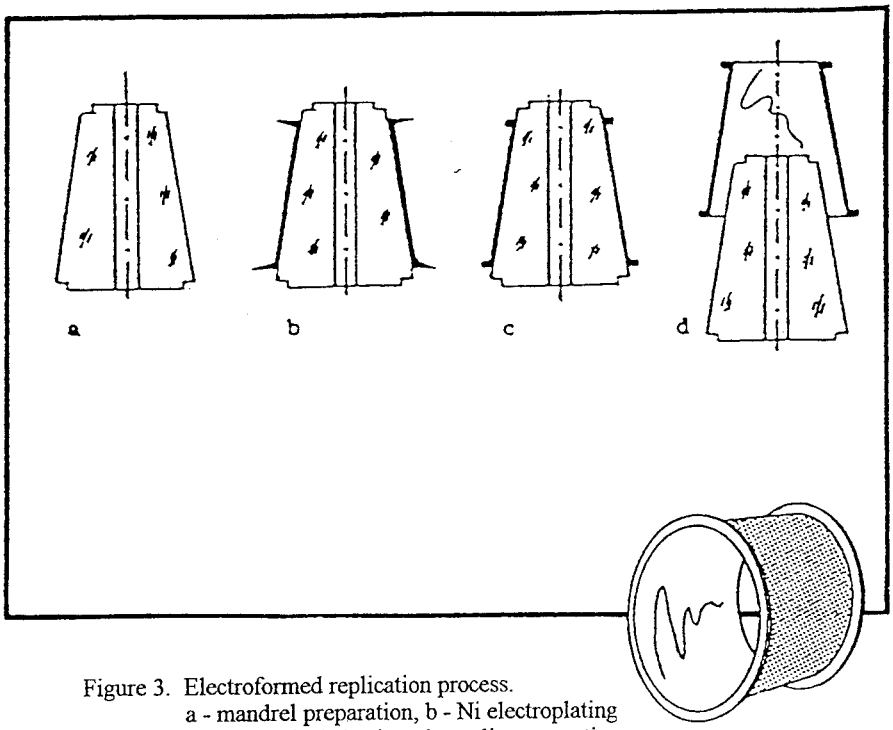


Figure 3. Electroformed replication process.
a - mandrel preparation, b - Ni electroplating
c - mechanical shaping, d - replica separation.

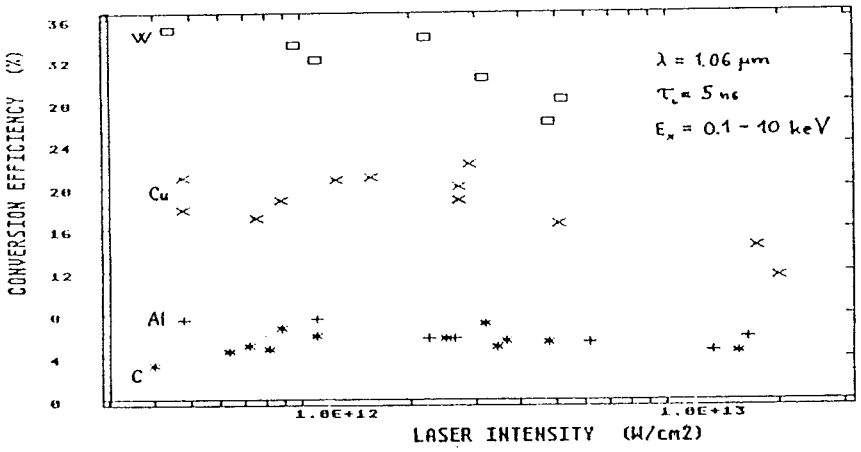


Figure 5. Laser light to X-rays integral conversion efficiency (0.1 - 10 keV photon energy band).

intensity of the order of 10 $MWcm^{-2}$ (Figure 6.). Experiments based on applications of the developed mirrors are under preparation.

5. Conclusion

Two selected applications of the grazing incidence X-ray axisymmetric mirrors to laser and laser plasma were studied in order to develop some of possible ways for obtaining very high intense X-ray beams using focusing or collimation. Laser systems like GOLEM which was used in our experiments can be nowadays made as a tabletop and repetition ones still featuring 10 $MWcm^{-2}$ maximum spectrally integral X-ray intensities at the focus. Scaling towards bigger laser systems and higher intensities is possible.

The suitable replication technology for making special axisymmetric grazing incidence X-ray mirrors was developed and tested. Results should find applications e.g. in laser plasma research, solid state physics, X-ray lithography and molecular biology.

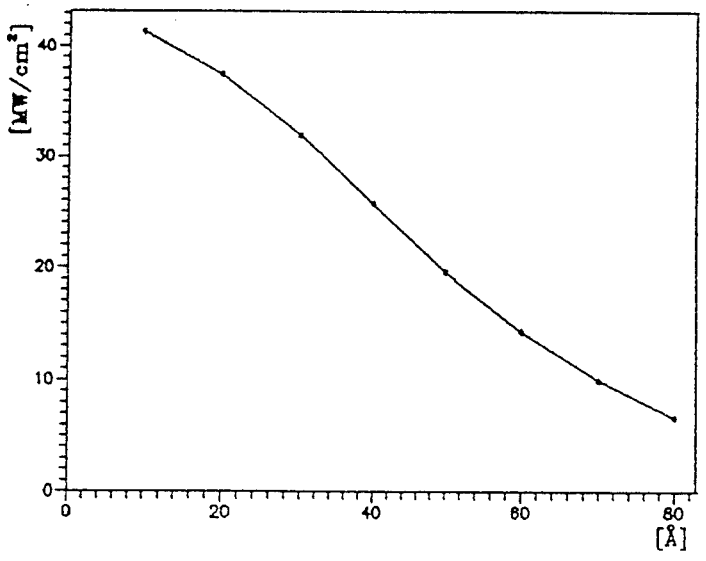


Figure 6. Maximum intensity I ($MWcm^{-2}$) of soft X-rays from laser plasma spot focused by an elliptical axisymmetric mirror as a function of the mirror surface microroughness σ (Angstrom).

6. Acknowledgments

Research leading to the development of improved electroformed replication method used in the work reported herein was supported in part by the U.S. - Czech Science and Technology Program under grant number 930 37. In addition, the authors wish to acknowledge support in the present work from the Medical Research Council, Cambridge.

7. References

1. Kishimoto, T. (1985) Absolute Measurement of Spectra Emitted by Laser-Produced Plasmas, *MPQ Garching Report No. 108.*

2. Hudec R., Inneman A., Arndt U. and Pina L. (1992) Compact Laboratory X-ray beam line with focusing microoptics, *Inst. Phys. Conf. Ser. No 130*: Chapter 7, Int. Congr. X-ray Optics and Microanalysis, Manchester.

COMPUTER SIMULATION OF THE LASER BEAM INTENSITY DISTRIBUTION IN RESONANT CAVITIES

M. ENESCU, S. AMARANDE, I. FARCAS, C. VASILESCU*
Institute of Atomic Physics, Laser Department
P.O. Box MG-6, RO-76900, Bucharest 5, ROMANIA

**University of Bucharest, Faculty of Physics*
P.O. Box MG-11, RO-76900, Bucharest 5 , ROMANIA

Abstract

In order to determinate the stationary modes of active resonator, we have developed a computer model based on the iterative solution of a generalized Kirchhoff-Fresnel integral equation.

The model is tested for a linear resonator whose parameters (resonator length, diameter and radius of curvature of concave mirror, diameter and output mirror transmission) are known.

The computer program was drawn up in the FORTRAN and Mathematica languages with a modular structure in order to facilitate testing and generalization to the more complex case of U-folded resonant cavities.

1. Introduction

The CO_2 laser in recent years has continually gained importance as a tool for material processing. The output power of the laser beam as well as the modal distribution are the crucial points for the success of any processing operation with laser. Thus, for the improvement of the output parameters of the laser beam there have been proposed different models in the laser design, with certain geometry of the resonant cavities. One of these geometry is the folded resonators, which should have the advantage of a smaller size for a given output power. This type of lasers are very sensitive to the misalignment of the mirrors, therefor requiring a careful design and rigorous execution.

There have been proposed some techniques to analyze different aspects of resonators: Fast Fourier Transform method [1], Finite Differences method [2], Computer Simulation for Z-folded resonators [3], Thin-sheet gain approximation [4].

The purpose of our paper is to present a computer simulation providing criteria for the choice of parameters in designing an U-folded resonator CO_2 laser.

R. Kossowsky et al. (eds.), High Power Lasers – Science and Engineering, 381–388.
© 1996 *Kluwer Academic Publishers. Printed in the Netherlands.*

2 The model for linear resonators

The electromagnetic field at a point (x,y) on one mirror can be expressed in terms of an integral of the linear polarized field on the other, using the scalar formulation of Huygens' principle [5].

Laser resonators are of the Fabry-Perot interferometer type (Figure 1) with two mirrors: O_1-concave (radius of curvature r_1, reflection coefficient R_1, aperture d_1) and O_2-plane ($r_2 = \infty$, R_2, d_2). L is the length of resonator.

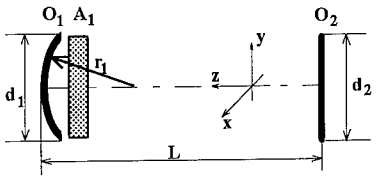


Figure 1. Linear active resonant cavity.

The electric field vector in the resonator is represented by:

$$\vec{E} = \vec{p} \cdot E(x,y,z) \cdot e^{i\cdot(\omega\cdot t - k\cdot z)} + c.c. \qquad (1)$$

where $\vec{p}$ is the unit polarization vector, $k = 2\cdot\pi/\lambda$, the magnitude of the wave vector, ω and E(x,y,z) are the frequency and, respectively, the complex amplitude of the field.

In order to calculate the intensity distribution and the mode pattern of a linear active resonator, we use the following procedure:

Beginning with an arbitrary amplitude and phase distribution at one of the mirrors (O_2) of the laser cavities, field propagation through the resonator is calculated taking into account the propagation properties of the laser medium and mirrors' parameters.

The resulting field distribution at mirror O_2 is calculated after each round-trip and compared with that of the previous round-trip. This procedure is repeated until the relative difference between the intensity field distributions for two successive iterations is less than 1% in every point of the grid, indicating that a stationary mode has been obtained:

$$\frac{\left|\vec{E}_i - \vec{E}_{i+1}\right|^2}{\left|\vec{E}_i\right|^2} \le 1\% \qquad (2)$$

The most important problem of this procedure is to calculate the electric field distribution after one resonator round-trip. This problem can be further subdivided in the following three steps:

2.1. WAVE PROPAGATION IN FREE SPACE

We calculate the resulting field distribution $E_1(x_1,y_1)$ at the plane P_1 of the mirror O_1 from a given field distribution $E_2(x_2,y_2)$ at the plane P_2 of the mirror O_2 by evaluating the Kirchhoff-Fresnel integrals (3):

$$E_1(x_1,y_1) = \frac{i\cdot k}{2\cdot\pi\cdot L}\cdot e^{-i\cdot k\cdot L}\cdot \int_{(x_2)}\int_{(y_2)} E_2(x_2,y_2)\cdot e^{-\frac{i\cdot k}{2\cdot L}[(x_1-x_2)^2+(y_1-y_2)^2]}\cdot dx_2 dy_2 \tag{3}$$

where k is the magnitude of the wave vector and L is the distance between the mirrors.

The electric field at point $P_1(x_1,y_1)$ can be calculated as the sum of elementary waves from all points $P_2(x_2,y_2)$ of plane P_2. Equation (3) is valid under the assumption that the transversal dimensions of the resonator are small compared to the distance L.

2.2. AMPLIFICATION IN THE LASER MEDIUM

If we assume an active medium between the two planes, the amplitude of the resulting electric field $E_1(x_1,y_1)$ has to be modified by taking into account the amplification. Using the *"thin sheet approximation"* [4], the active medium of length *l* between the two planes is assumed to be concentrated in a small space adjacent to plane P_1. This approximation is a good one for not too large values of *g*, the gain factor per passage through the active medium.

For large values of the gain factor (high power laser), the approximation is no longer valid and the procedure has to be modified: the resonator is subdivided into small elements so that the gain per element is small enough [4] for the above mentioned approximation to hold. It is obvious that for this procedure the calculation time drastically increases.

Using the thin sheet approximation, the amplitude of the resulting electric field at plane P_1, E_1', is given by:

$$E_1'(x_1,y_1) = A(x_1,y_1)\cdot E_1(x_1,y_1) \tag{4}$$

The amplification factor, A, depends exponentially on the length of the active medium between planes P_1 and P_2, and on the gain factor g(x,y,I), where *I* is the intensity of the radiation field in the resonator. The gain factor, g(x,y,I), depends on the small signal gain, g_0, and on the saturation intensity, I_S:

$$A(x,y,I) = e^{g(x,y,I)\cdot\frac{l}{2}} \tag{5}$$

$$g(x,y,I) = \frac{g_0(x,y)}{1+\frac{I(x,y)}{I_S}} \tag{6}$$

2.3. REFLECTION AT THE CONCAVE MIRROR

Taking steps 2.1 and 2.2, one can calculate the amplitude of the resulting field distribution $E_1'(x_1,y_1)$ at plane P_1. The reflection of the field at the mirror O_1 can be described by a complex reflection coefficient [3], M(x,y).

$$E_1''(x_1,y_1) = M(x_1,y_1)\cdot E_1'(x_1,y_1) \tag{7}$$

The absolute value of the mirror's complex reflection coefficient is determined by the properties of the mirror surface (geometry and reflection coefficient):

$$M(x_1,y_1) = \sqrt{R_1}\cdot e^{-2\cdot i\cdot k\cdot d(x,y)} \tag{8}$$

In case of a plane mirror, the phase factor reduces to unity and the mirror coefficient reflection becomes $\sqrt{R_1}$. Following the three steps described above, one can calculate the field distribution after a round-trip.

3. Computation method

The method for determination of an active resonator' stationary mode requires a large amount of computation time. We have optimized the procedure for obtaining reasonable computation times and accurate results. Now we will discuss the most important features of the computer program.

The most time consuming part of the procedure is evaluation of the Kirchhoff-Fresnel integral. We have evaluated the integral numerically on a two-dimensional grid of size N×N. The number of grid points has to be large enough to get a good approximation of the true value. The minimum number N_{min} of grid points is proportional to the Fresnel number,

$$F = \frac{d_1\cdot d_2}{4\cdot\lambda\cdot L}, \tag{9}$$

$$N_{\min} = \frac{8\cdot\pi\cdot F}{\delta\phi}, \tag{10}$$

where $d_{1,2}$ are the diameters of the mirrors, λ is the wavelength and $\delta\phi$ is the required accuracy for the phase of the kernel in equation (3) ($\delta\phi << \pi/\lambda$).

The direct evaluation of (3) would require N^2 complex operations to calculate the resulting amplitude for one grid point at plane P_1. To get the field distribution for the whole grid, the total amount of computation time increases as N^4. For large Fresnel number resonators, this method would require unacceptable large computation time. To avoid this, some more sophisticated methods have been proposed, such as the algorithms using the Finite Differences Method [2] for high Fresnel numbers, or the Fast Fourier Transform Method [1] for low Fresnel numbers, which allow the calculation of wave propagation in this case.

The computer program was drawn up in the FORTRAN language with a modular structure in order to facilitate testing and generalization to the more complex case of folded resonant cavities.

The test program starts with an arbitrary field distribution ('top hat') at one of the mirrors (O_2). After one round-trip (the first iteration) the results are stored into a data file, this file representing the new input for the second iteration. The program can be tested for different configurations of the resonant cavity (passive or active) and runs until the stationary mode is obtained.

A separate program drawn up in the Mathematica language [6] makes the contour plot representation of the modal distribution and also the three-dimensional representation of the intensity distribution of the electric field.

The right choice of the grid size was tested by doubling or halving the number of grid points in one dimension and following the effect on the results. The time required for one iteration using a grid size of 22×22 was about 2.2 seconds on an AT 486 DX4/100 MHz computer.

4. Numerical results for the linear resonator

In order to test the computer program we use the following data: length of the resonator, L = 250 cm, length of the active medium, l = 180 cm, saturation intensity, I_S = 160 W/cm^2, small signal gain, g = 0.45 %·cm^{-1}, O_1 (aperture, d_1 = 2.6 cm, radius of curvature, r_1= 15 m, reflectivity, R_1 = 100 %), O_2 (d_2= 1.95 cm, r_2= ∞, R_2= 80 %).

For a constant initial electric field distribution at the mirror' surface (Figure 2.a), we expected the intensity distribution in a passive resonator to be a gaussian one (the transversal distribution of the electric field is described by the Hermite-Gauss polynomials). This shows that the distribution corresponds to the fundamental mode TEM_{00} (Figure 2.c). Figure 2.b shows an intermediary electric field distribution. This distribution stabilizes after about five iterations.

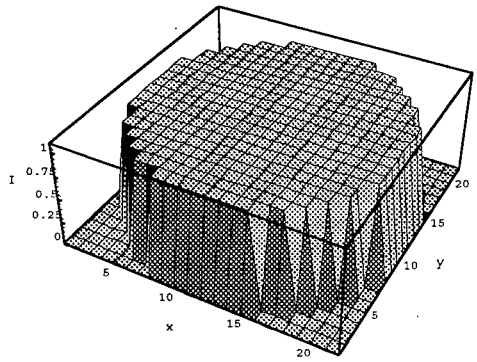


Figure 2.a. Initial intensity distribution

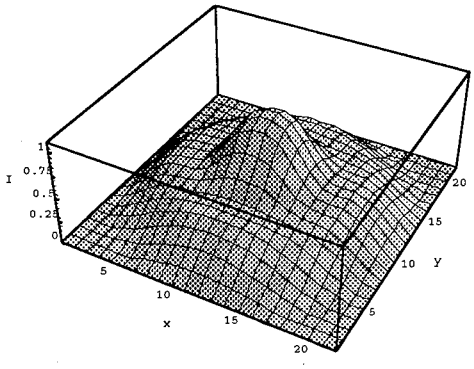


Figure 2.b. Intermediate intensity distribution

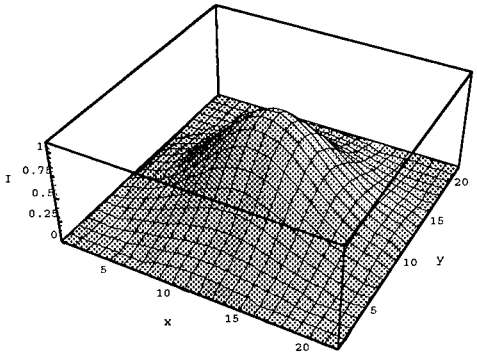


Figure 2.c. Stable intensity distribution of a linear passive resonator.

For an active resonator with the same parameters, using the thin sheet approximation described above, we have obtained an intensity distribution which corresponds to the TEM_{01} mode (Figure 3).

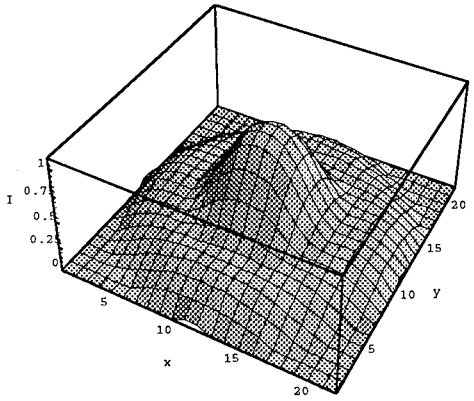


Figure 3. Intensity distribution of a linear active resonator.

5. The model for the folded lasers

In this work we consider the type of folded resonator shown in Figure 4 ('U-folded') [7] using two 45° mirrors O_3 and O_4). The length of the resonator is L' = 2·L and the apertures for both mirrors (O_3 and O_4) are $d_3 = d_4 = \sqrt{2} \cdot d_2$.

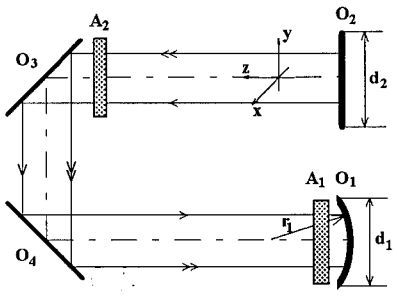


Figure 4. U-folded active resonant cavity.

To emphasize the advantages of a folded resonator as compared to a linear one, we made simulations of a folded resonator under the same conditions as the active resonator discussed above. Figure 5 shows the resulting mode pattern (modes superposition) for a folded resonator.

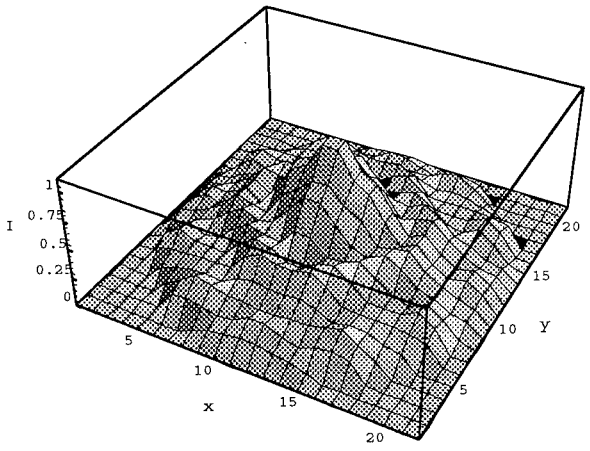


Figure 5. Intensity distribution of an U-folded active resonator.

7. Conclusions

We propose a calculation procedure for finding the three-dimensional mode pattern and output beam characteristics of a linear and folded high power CO_2 laser resonators.

Our procedure allows for the determination of the influence of the laser resonator parameters on the stationary mode and output intensity.

One can observe that our results are similar with the existing results, are obtained with a good precision and the computational times are substantialy improved.

8. References

1. Siegman, A.E. and Sziklas, A. (1975) Mode calculations in unstable resonators with flowing saturable gain. Fast Fourier transform method, *Applied Optics*, **18**, 1874-1889.

2. Rensch, D.B. (1974) Three-dimensional Unstable Resonator Calculation with Laser Medium, *Applied Optics*, **13**, 2546-2561.

3. Meisterhofer, E. and Lippitch, M.E. (1973) Computer simulation of a CO_2 high power laser with folded resonator, *Industrial application of High Power Laser, SPIE Proceedings*, **455**, 29-36.

4. Milonni, P.W. (1987) Criteria for the thin-sheet gain approximation, *Applied Optics*, **16**, 2794-2795.

5. Siegman, A.E. (1971) *An introduction to Lasers and Maser*, Chapter 8, McGraw-Hill Book Company.

6. Wolfram, S. (1991) *Mathematica-A System for Doing Mathematics by Computer*, Addison-Wesley Publishing Company, Inc., New York.

7. Hall, D.R. and Jackson, P.E. (1989) *The Physics and Technology of Laser Resonators*, Adam Hilger, New York.

PART III: Measurements

LASER MEDIUM QUALITY CONTROL

In Excimer Lasers

B. FORESTIER
IRPHE
CNRS / Aix-Marseille Universities I and II
Campus de Luminy
Marseilles 13009 France

1. Introduction

The main topic is related to the influence of laser medium quality on the average power and the laser beam features in the case of high average power excimer lasers. The wavelength (UV domain) and the energy density levels of pulsed excitations justifies this restriction.

Taking into account the other contributions to the excimer lasers in the same NATO ASI the following elements will be approached :
- short presentation of flow loop component,
- visualisation of pressures waves induced by the active medium excitation,
- pressure waves analysis in a one shot experiment,
- few words on numerical studies,
- pressure waves history in repetitive regime and correlation between residual pressure fluctuations and extracted laser energy,
- influence of acoustic waves damping on extracted laser energy.

2. Flow loop components

The use of closed-cycle laser flow system allows high output power, conserves expensive rare gas mixtures, and permit to handle poison gas : (HCl, F2, NF3, ...). A closed-cycle laser flow system has to :
- provide flowing gas to the laser cavity with sufficient medium homogeneity
- remove the thermal energy put into the gas
- minimise gas consumption
- provide minimum weight laser system for long run time applications
- be compact and efficient.

At least two sets of requirements have to be elaborate to achieve the required flow conditions to obtain the discharges stability and laser beam quality:
- the lasing medium in the cavity must be completely exchanged between successive pulses by flowing the gas in the closed cycle loop with an optimisation of pressure drops,

R. Kossowsky et al. (eds.), High Power Lasers – Science and Engineering, 391–412.
© 1996 *Kluwer Academic Publishers. Printed in the Netherlands.*

- acoustic suppression and flow conditioning devices in the flow system must permit to achieve residual density fluctuations as low as 10^{-2} (discharge stability) or 10^{-4} (laser beam quality). These requirements are basically in conflict and the overall objective of the flow system studies can be viewed as an attempt to find the optimal trade-off between the two requirements in the minimum volume.

Optimisation of flow loop components has been undertaken in the EUREKA and AMMTRA programs. Different descriptions are given in other contributions to the same NATO ASI. In the figure 1 the mains components are all visible ; the device corresponds to a prototype defined, a long time ago, to study aerodynamic and acoustic problems, at IMF in Marseilles.

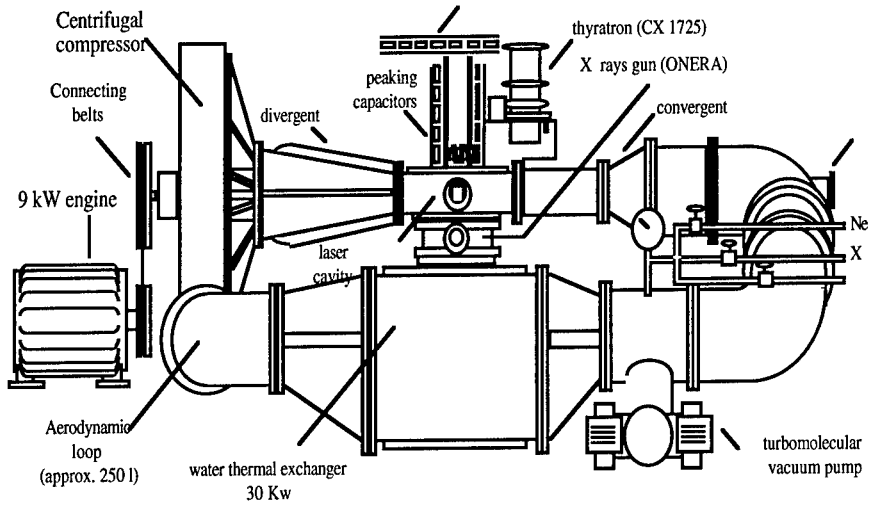


Figure 1. "LUX" closed cycle loop with X rays preionization

3. Aero-acoustic waves, definition, visualisation

As soon as an energy amount is deposited in a finite gas volume; heating will produce waves which may be summarised for an excimer laser by the figure 2. The different families of waves are identified in this figure. The waves of family 2 are induced by the excess of energy deposited in the cathode and anode electrical sheets of the discharge, commonly used for excitation.

The propagation of the waves is mainly controlled by the flow and the geometry of loop. The design of devices in the immediate vicinity of discharge volume plays as we will see later, a leading role.

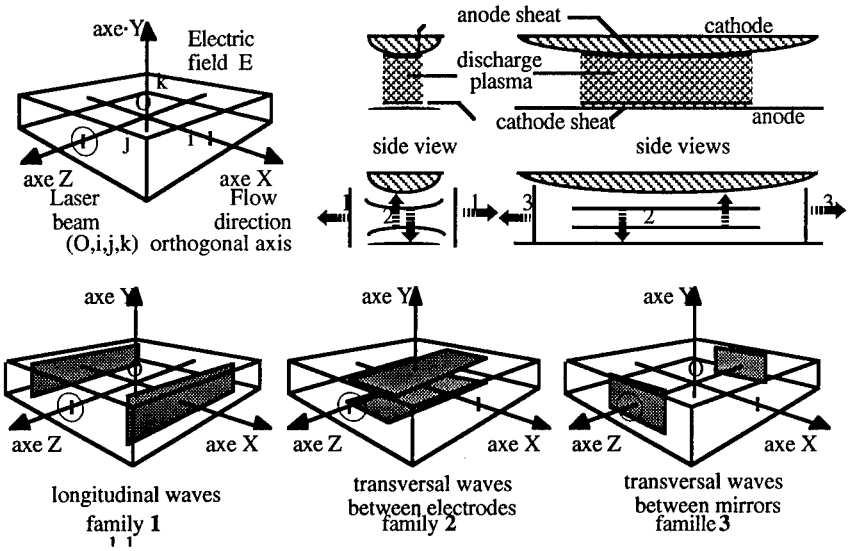


Figure 2 Schematic representation of waves induced by discharge excitation

The waves of families 1 and 2 are clearly visible on an interferometric snapshot recorded many years ago on "LUX" testbed. This interferogram associates with a schematic representation is shown on figure 3.

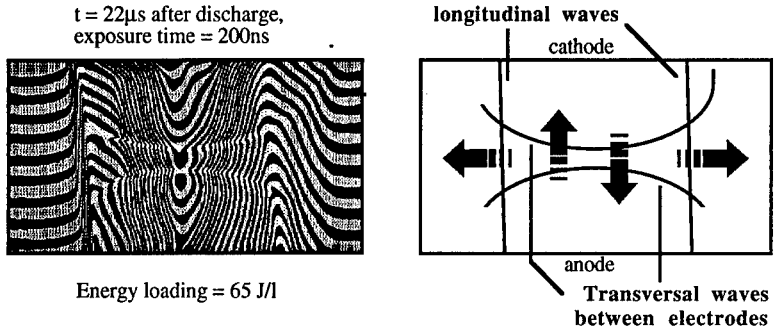


Figure. 3 Interferometric visualisation of families 1 an 2 waves

:

These waves are too shown on an x,t interferogram (figure 4) and a sequence of schlieren snapshot on the figure 5 corresponds to a recent study achieved in the frame of AMMTRA program in Japan.

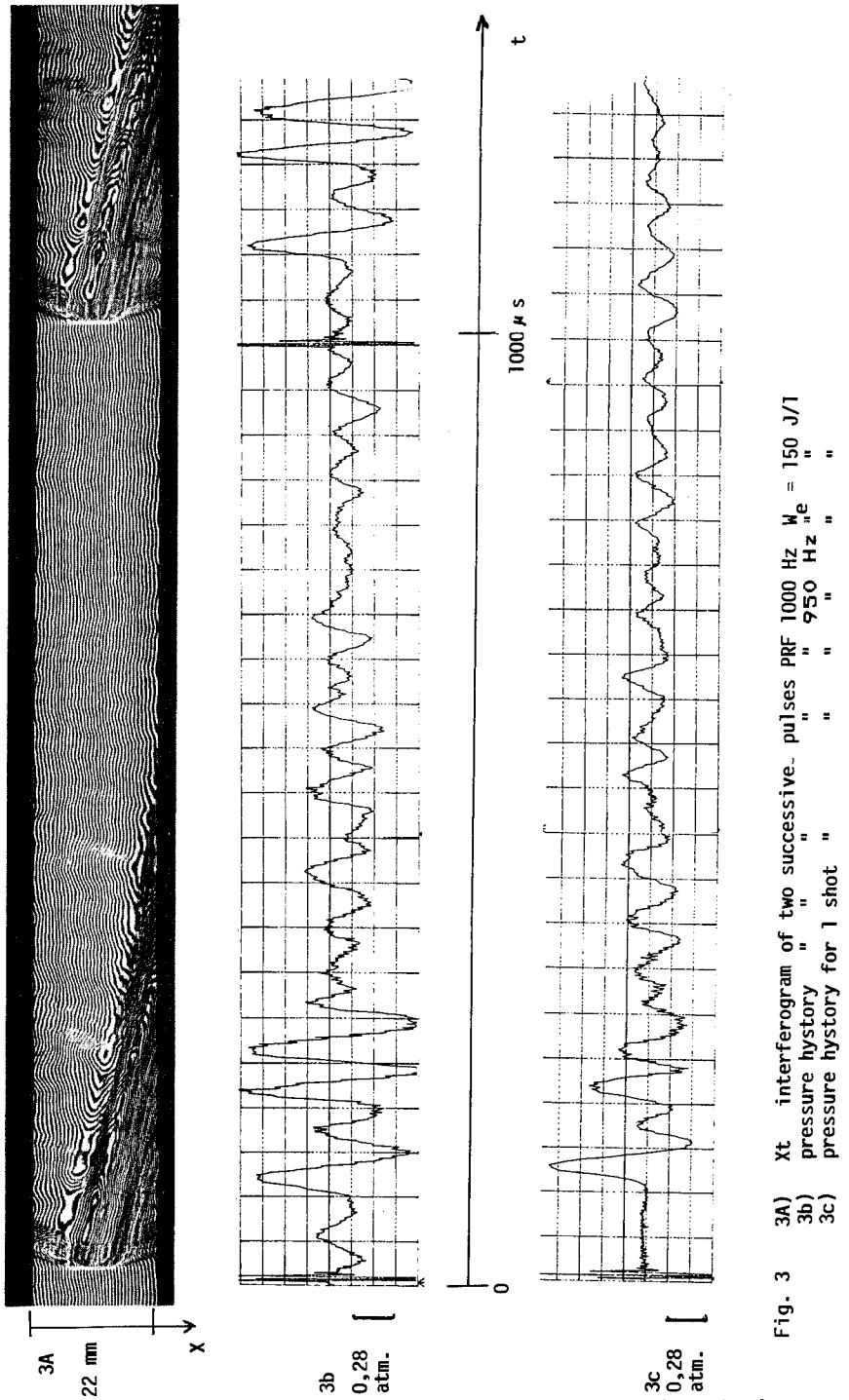


Fig. 3 3A) Xt interferogram of two successive pulses PRF 1000 Hz W_e = 150 J/l
3b) pressure hystory " " " 950 Hz " "
3c) pressure hystory for 1 shot " " " " "

Figure 4. x,t interferogram of two pulses of a burst and pressure histories for two shots and one shot. Data recorded in « LUX I » laser cavity

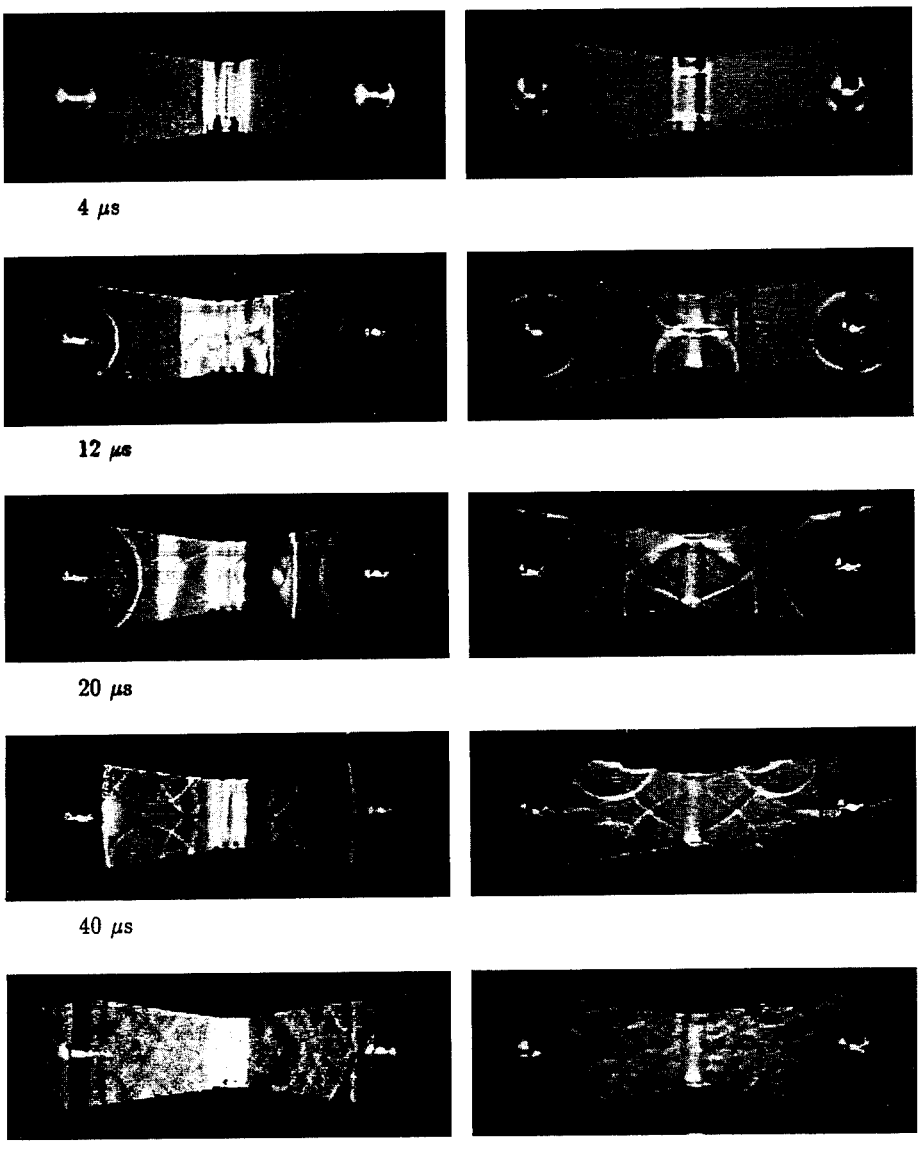


figure 5 Schlieren photographies recently recorded, in the frame of AMMTRA program, a few microseconds after the energy deposition in a laser cavity with a uv preionisation by lateral pin discharges associated to the main discharge.

It is not very easy to directly visualise the family 3 waves which beat between optics. It is possible to deduce their influence from pressure histories in the laser cavity at it will be shown hereafter.

Initial strength of longitudinal waves varies directly with the input energy loading. Typical values of initial overpressure are relatively high ; in the neon at 4 bars an energy input of few tens of Joule by litre leads to a few bars overpressure. Pressure disturbances are so, well above acoustic levels, and non linear analysis must be undertaken. Associated entropy waves and contacts surfaces have to be take into account as well as density disturbances that result from the interaction of pressure waves with regions of non isentropic flow or discontinuities, current returns, preceding pulses, heated plasma slug.....

3. Pressure waves recording in a one shot experiment

The possibility to dispose high frequency small piezoelectric transducers (PCB 20 to 300 mv/PSI) relatively near of the discharge volume permit to record pressure histories at different locations inside the laser cavity, the loop and even inside the acoustic dampers.

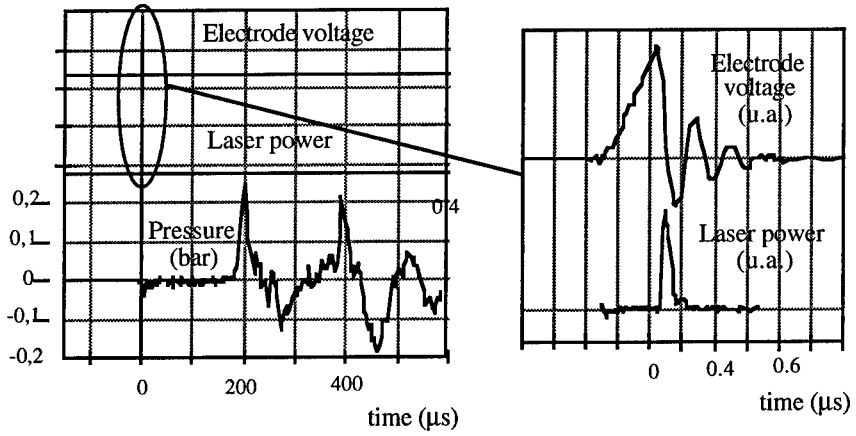


Figure 6 Correlation between pressure and electric parameters

The figure 6 shows up, in the lower part, a comparison between on one hand a pressure trace and on the other hand voltage and laser energy histories. The analysis of time scales underlines the non influence of aerodynamic phenomena for a one shot experiment.

Before to give a precise analysis of pressure fluctuations it is usefully to analyse the homogeneity of energy deposition in the active medium. The figure 7 represents, in parallel, the visible light emitted transversally by the discharge plasma and voltage and laser power histories.

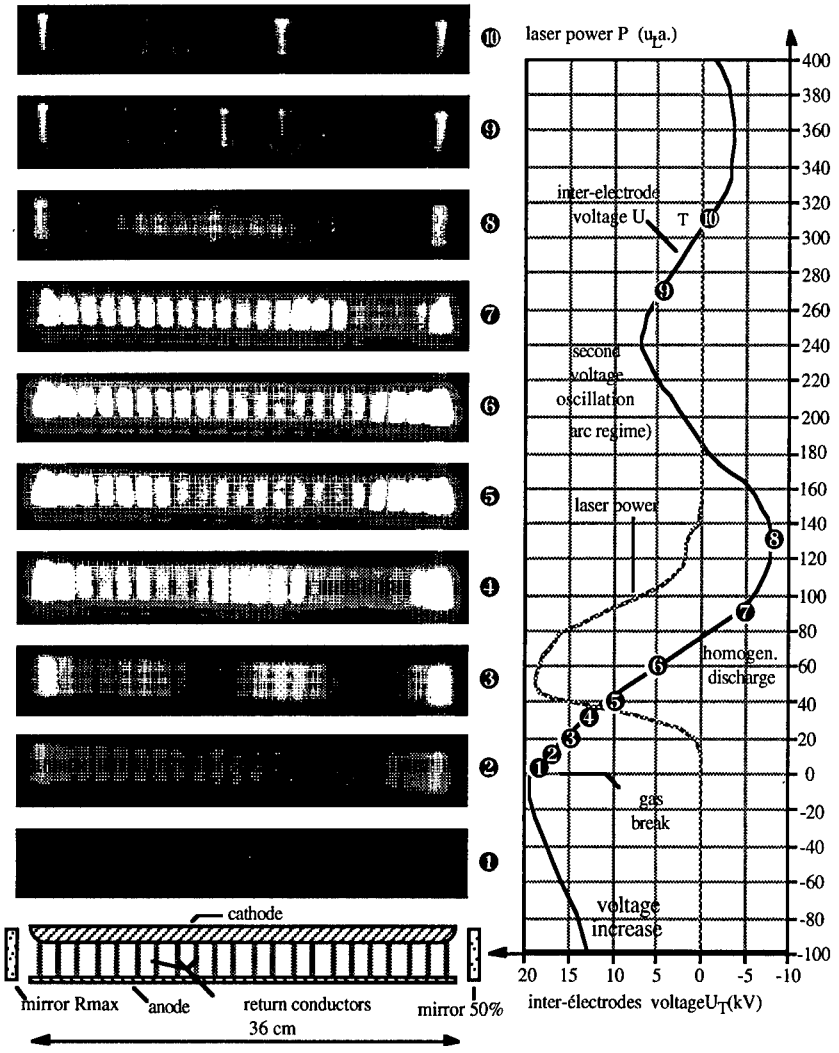


Figure 7. Photographs of discharge plasma and electric parameters

Ten successive photographs of the discharge plasma recorded with a CCD camera, through a window fitted in the upstream elbow of "LUX" testbed, are marked by a N° traced back on the voltage curve, on the right part of the figure, in order to show the chronology. The plasma is relatively homogeneous during the snapshots 5 and 6 corresponding to the laser emission. The regularly spaced vertical bars are related to the electric conductors, crossing the flow channel in order to minimise the discharge impedance to an acceptable value.

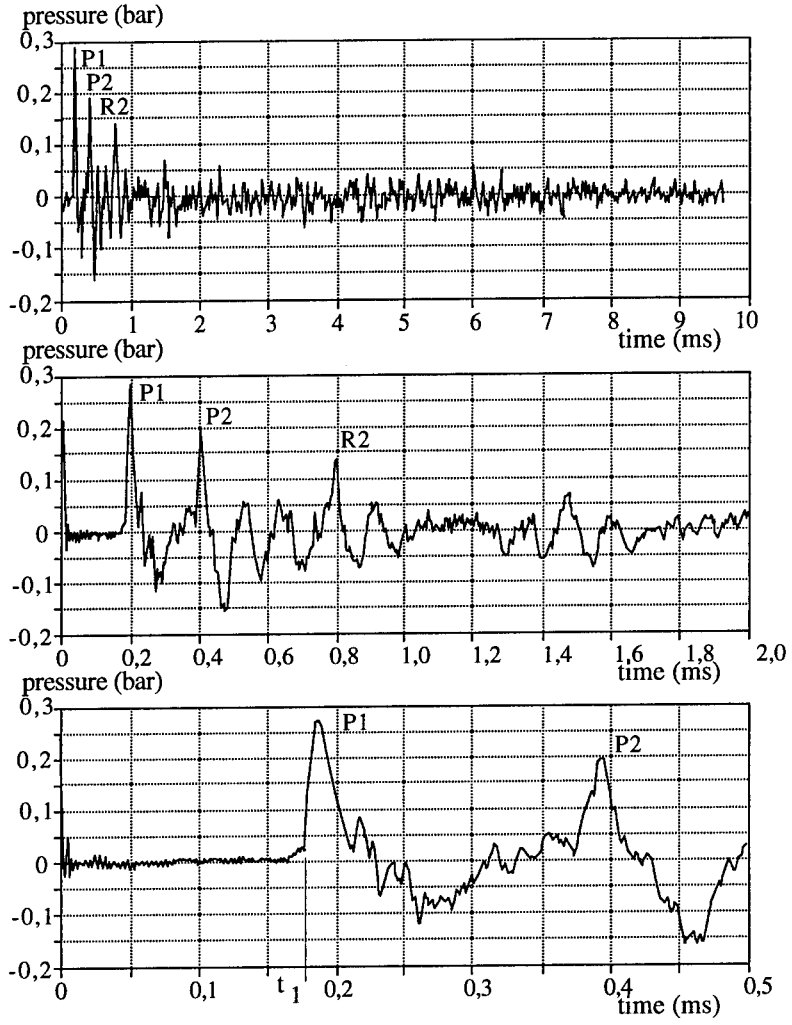


Figure 8. Pressure history at three different base time

A pressure history, for a one shot experiment at an energy loading of 110J/l is given on the figure 8.

The first pressure maximum P1 corresponds to the time when arrive both the waves induced by the homogeneously heated plasma and by the post and pre discharge arcs generated in the central part of discharge zone.

The second maximum P2 is induced by the superposition of cylindrical waves induced by pre and post discharge arcs at the extremities of electrodes (cf figure 7).

The maximum R2 is related to the reflection of previous cylindrical waves on optics

and corresponding channel side walls.

The additive or subtractive interactions of waves after reflections on the different parts of closed cycle loop generate the other recorded fluctuations. The main frequency, after a few ms, is determined by the lowest characteristic length i. e. the height of discharge volume (family 2 waves).

The comparison of figures 9 and 10 underlines the strong correlation between pressure fluctuations and discharge quality. A simple piezo transducer permit to control in real time the discharge degradation.

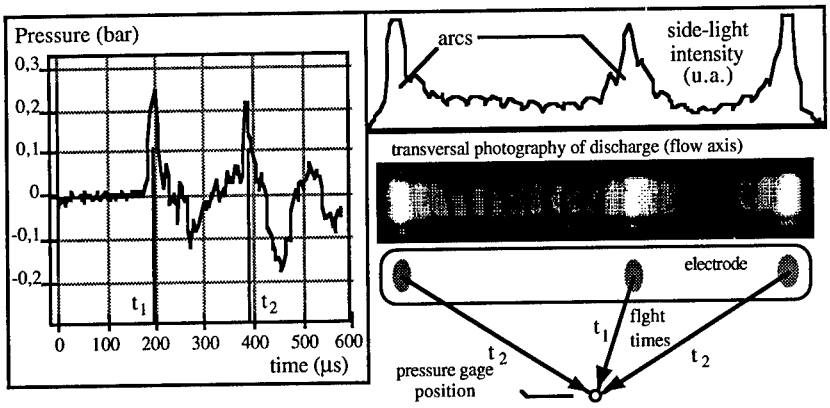


Figure 9. Pressure history and integrated transversal discharge light when pre and post discharge arcs are relatively well localised

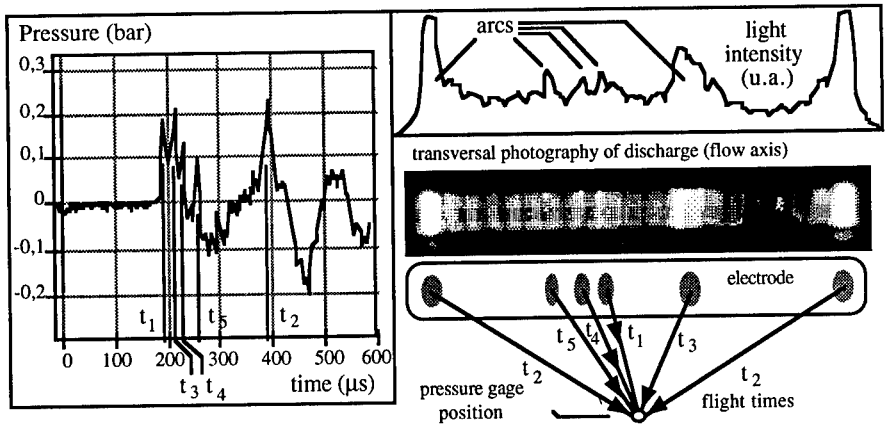


Figure 10. Pressure history and integrated transversal discharge light when pre and post discharge arcs are badly controlled

The diagram of the figure 17 (see paragraph 6) clarifies the origin of cylindrical waves.

The lecture of pressure signatures is a powerfully means to evaluate the discharge quality. The figure 11 shows up a trace when discharge device has been optimised to decrease arc generation by better fitting of discharge circuit and electrodes profile.

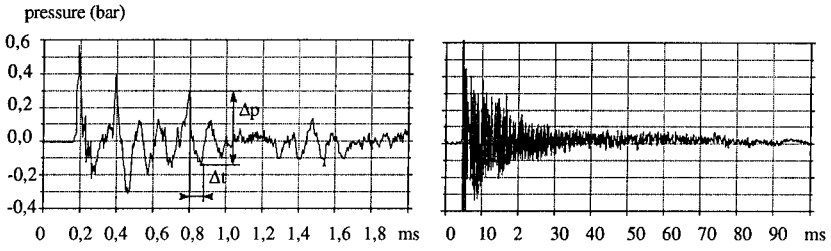


Figure 11 Pressure evolution in Laserdot cavity , energy injected = 140 J/l

The analysis of aerodynamic phenomena through these pressure signatures, is simplified by the deduction of pressure waveforms from the evolution of most important pressure fluctuations in a given time window (approximatively the period of waves of family 2). The maximum amplitude of fluctuations in this window is then drawn on log-log representation (figure 12) or on log-log representations if needed.The decreasing rate follows on large scale of time an exponential law. The parameters of the law depend from energy loading and from the geometry of laser device.

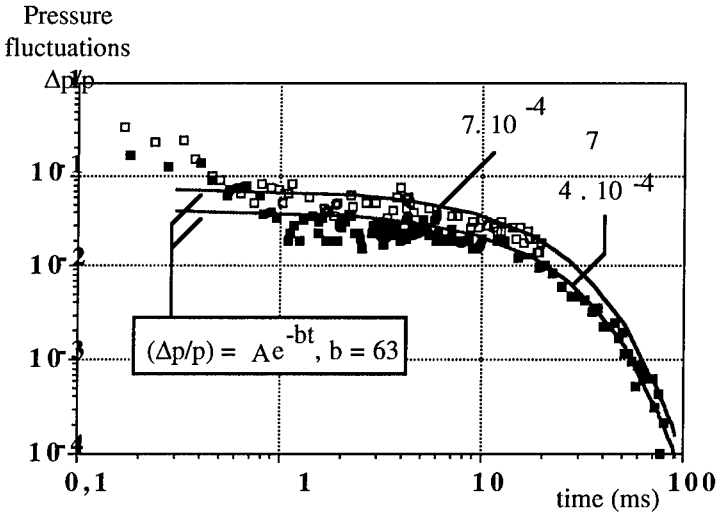


Figure 12. Comparison between the pressure decreasing rates for two energy loading 150 and 110 J//l respectively up and down

5. Some words on numerical studies of aerodynamic phenomena

Before to study the aerodynamic phenomena in high repetition rate regime it is interesting to briefly comment the numerous numerical studies undertaken since many years.

A first attempt has been made, in a one dimension and unstationnary model, to manage the shock waves and associated contact surfaces induced by the rapid heating of active medium by the classical characteristics method. These methods were only able to follow the waves of family one which have been overestimated by the "excimer community". Any way it was completely impossible to apply these methods on multishots experiments.

An other classical algorithm has been applied to simulate an unsteady two-dimensional flow in an excimer laser. The flow is, here too, described by the Euler equations. These equations are solved by numerical method based on a finite difference scheme with a flux corrected transport algorithm (SHASTA method).

This method permit to simulate waves of families 1 and 2 . The waves of family 2 being produced in the simulation, by a non uniform energy deposition, deduced of comparison between experimental and numerical results, and related to the electrode sheets. The figure 13 shows up a comparison of results for one shot.

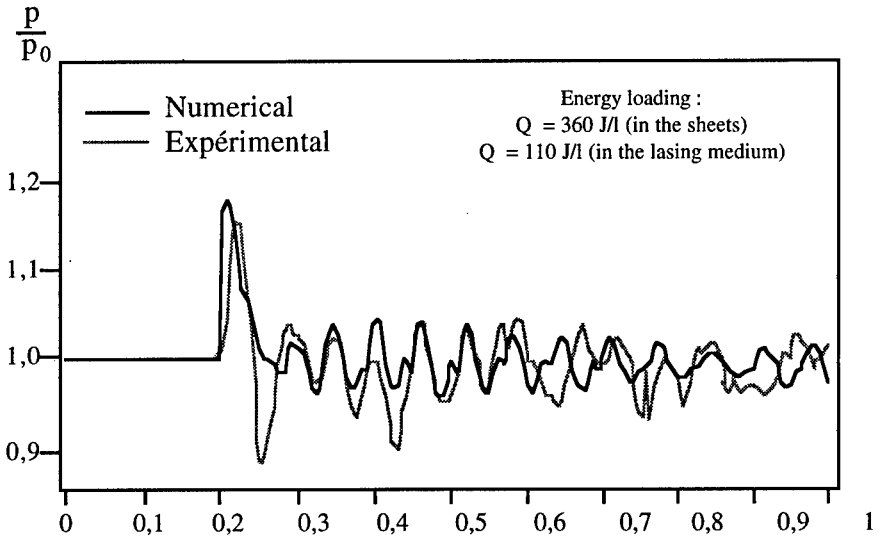


Figure 13. Comparison of numerical and experimental values of pressure

A typical pressure field in the cavity of an excimer laser is given on the figure 14. The transversal waves are long lived in the discharge zone as shown by the pressure history of figure 8.

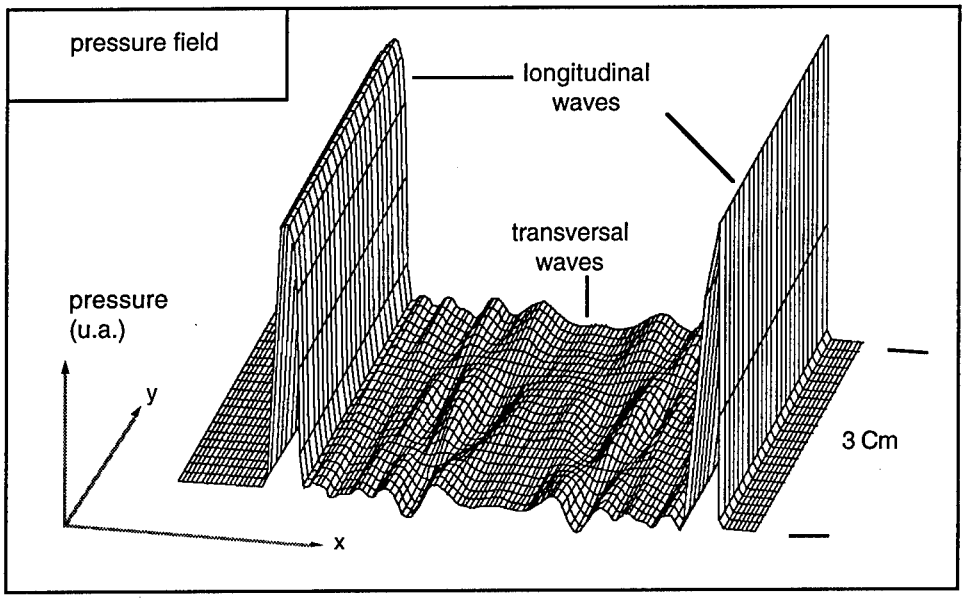


Figure 14. Pressure field in laser cavity deduced from SHASTA method

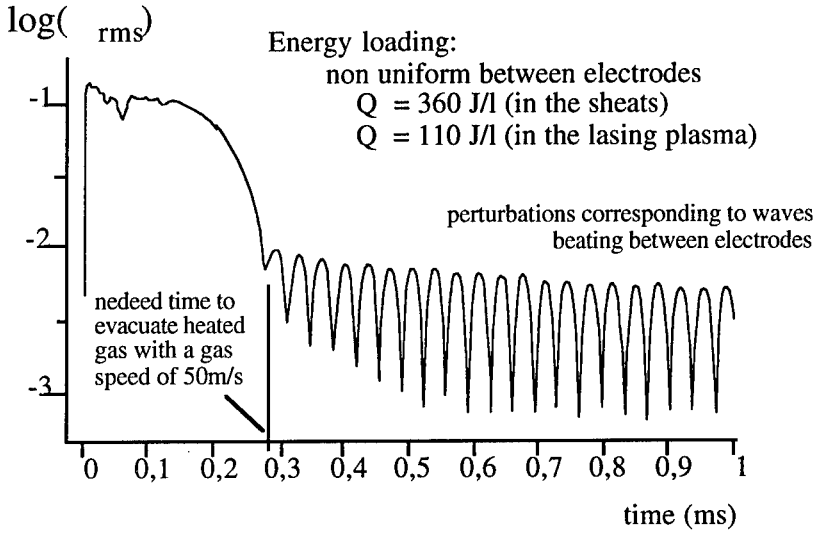


Figure 15 Numerical evolution of density after the excitation

The SHASTA FCT method is powerfulness. This method has been used by many authors to calculate the flow characteristics as well in the laser cavity than in the laser loop but, as soon as it is envisioned to study multi pulses experiments the time consumption is very high and it is too difficult to take into account both the three dimensional effects and the large time depth needed to evaluate the cumulative

aerodynamic perturbations induced by previous shots .

The mach number of shock waves induced by the excitation of an excimer laser is very low and as soon as we are away of the initial longitudinal waves we have to handle very little fluctuations of gas parameters and it is not absolutely useful at least when we are looking for qualitative results to struggle with Rankine Hugoniot equations and gas real effects.

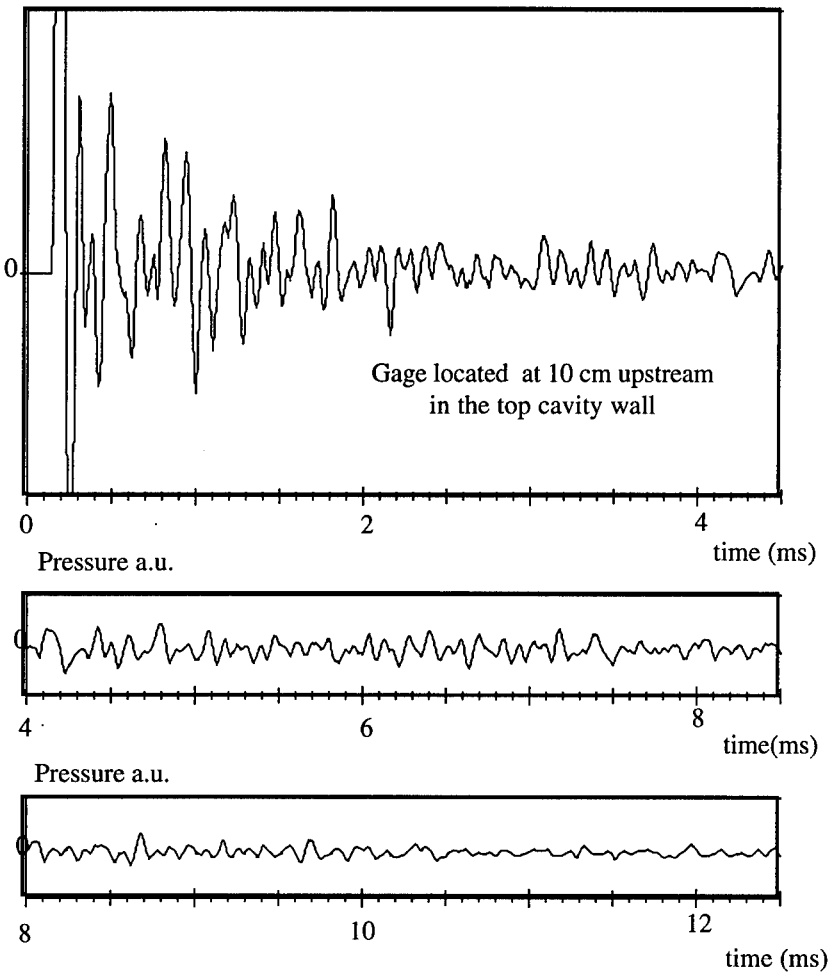


Figure 16. Amplitude fluctuations with a very simple linear modelisation

The idea to use very simple and linear laws has been proposed by a student of IMFM (J.P.Truong). A punctual wave source has been located in the middle of a parallelipedic volume, whose dimensions are approaching those of laser head (36*10*48cm3). The wave, propagating at sound speed, is supposed sinusoidal and the amplitude decreases as k/r^2, the reflections of the wave on walls are supposed to

follow the optic laws ; very simple calculations on a P.C. gives for the fluctuations the curves of figure 16 which are to be compared to the one of figure 8. Whatever the excitation, the main time evolution are geometrically imposed ; and a very simple approach permit to qualify aerodynamic phenomena time dependence.

The model is simple enough to choose a more complicated "source" of waves. The photography of time integrated side light from plasma discharge shown on figure 17 leads to propose to dispose three different sources located as explicated on the accompanying schemes. The sources are considered as punctual and not cylindrical, in fact this hypothesis permit to generate the waves of family 2 due in the reality to the electrode sheets.

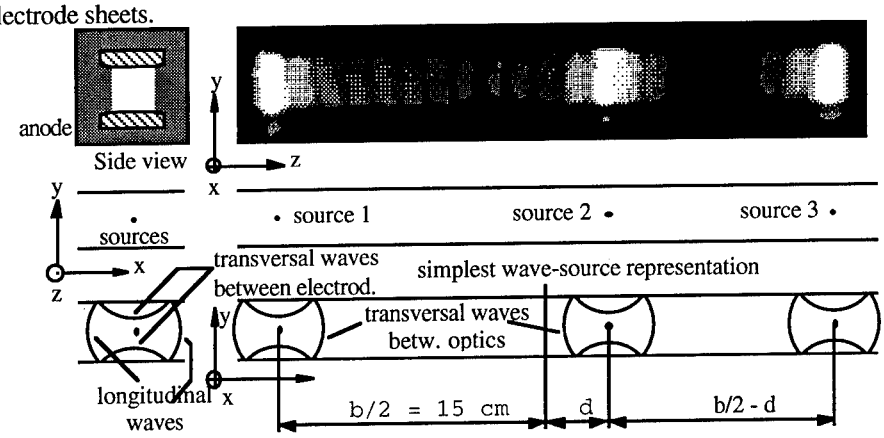


Figure 17. Sources of wave production for the 3D simplified model

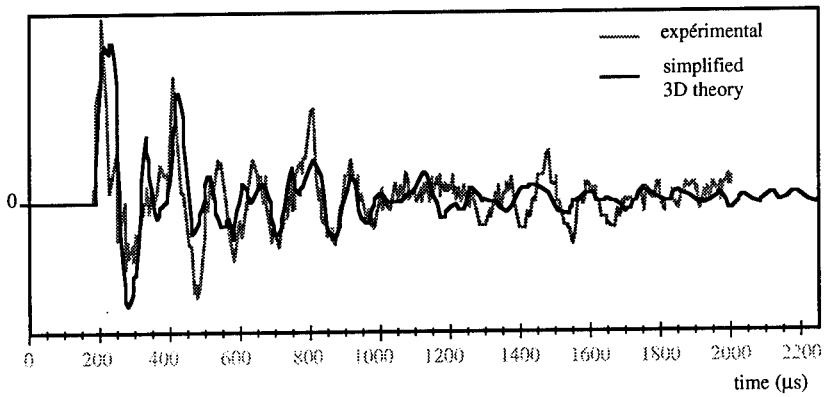


Figure 18. Comparison of experimental and numerical values of time evolution

A comparison of experimental and numerical results is given on figure 18. For this comparison the amplitudes are normed at the same value, the model is just able to predict the time behaviour of waves reflections. These predictions seems to be good enough to try to follow what happens when many shots are added. A semi-log

representation is given on figure 19 which is to be compared with the experimental values of figure 12 .

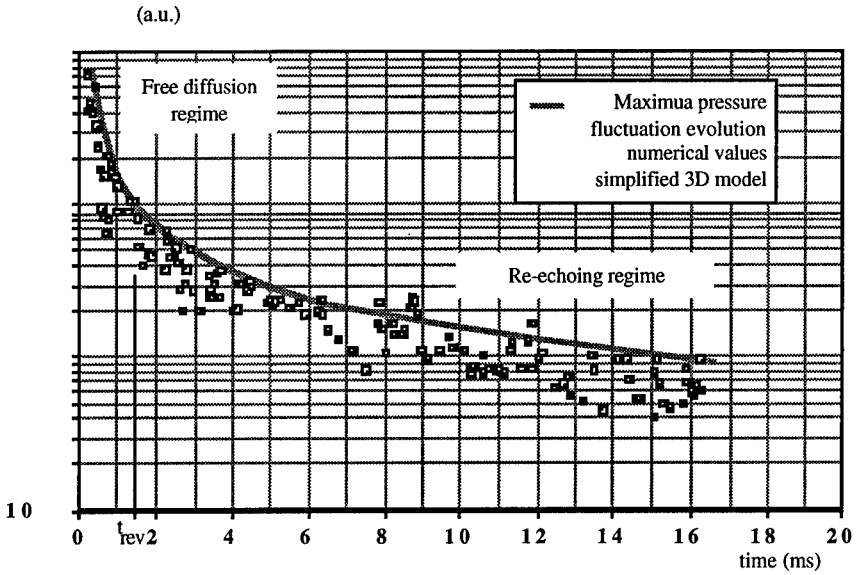


Figure 19 Waves evolution 3D simplified model

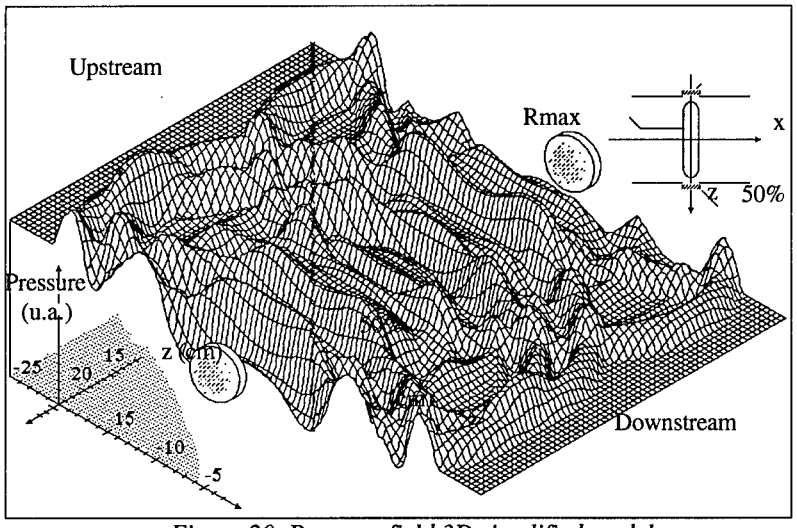


Figure 20. Pressure field 3D simplified model.

This simplified three dimensions modelisation looks to be useful to predict easily and without large time consumption the decreasing rate of perturbations induced in a laser device. The pressure field of figure 20 would be very difficult to achieve with classical methods.

6. Pressure waves history in repetitive regime

Many studies have been undertaken in the frame of different programs described in companion papers. We will focus only on the amplification of residual pressure fluctuations in high PRF experiments. This amplification is clearly visible on the figures 21 and 22. The figure 21 shows up pressure traces for 6 shots of a burst at a pulse repetition rate of 500 Hz. The pressure fluctuations level at the time of different shots, marked by the vertical bar (short electromagnetic noise), increases shot to shot.

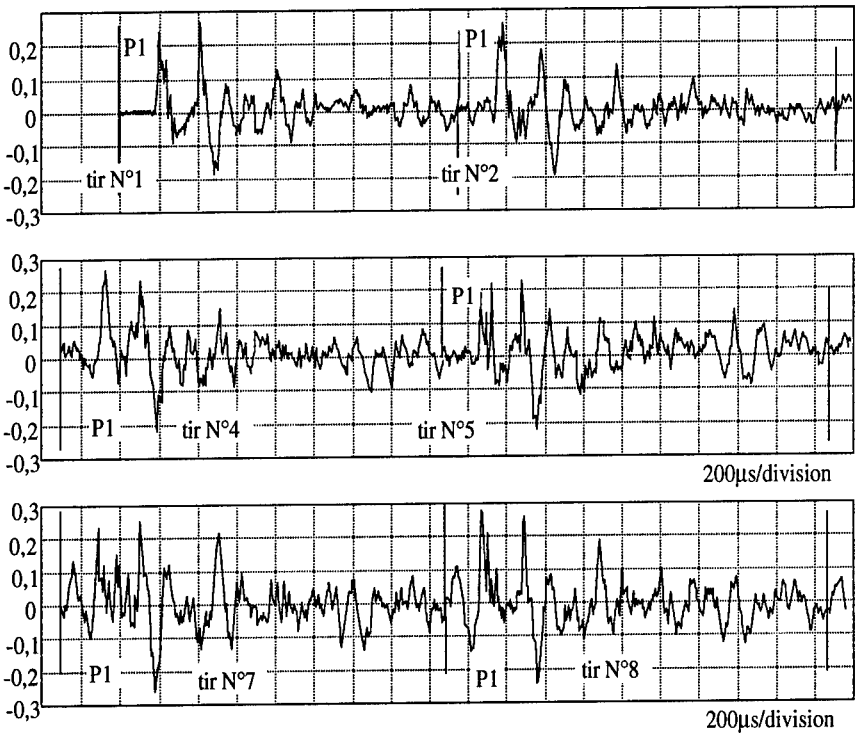


Figure 21. Pressure histories for some shots of a burst at PRF= 500 Hz

On the figure 22 the evolution of this residual pressure fluctuations level is shown for 100 successive shots ; the pressure fluctuations are recorded only during a time window of 0.5ms, just before the occurrence of the next shot. The amplification process occurs, on « LUX » device, during a tenth of shots before to saturate. This level is dependent of repetition rate as shown on the experimental results of figure 23.

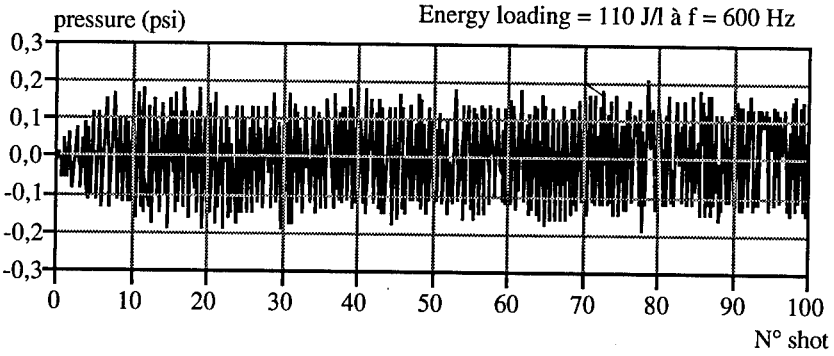


Figure 22. Residual pressure fluctuations versus shot number in a burst at 600 Hz

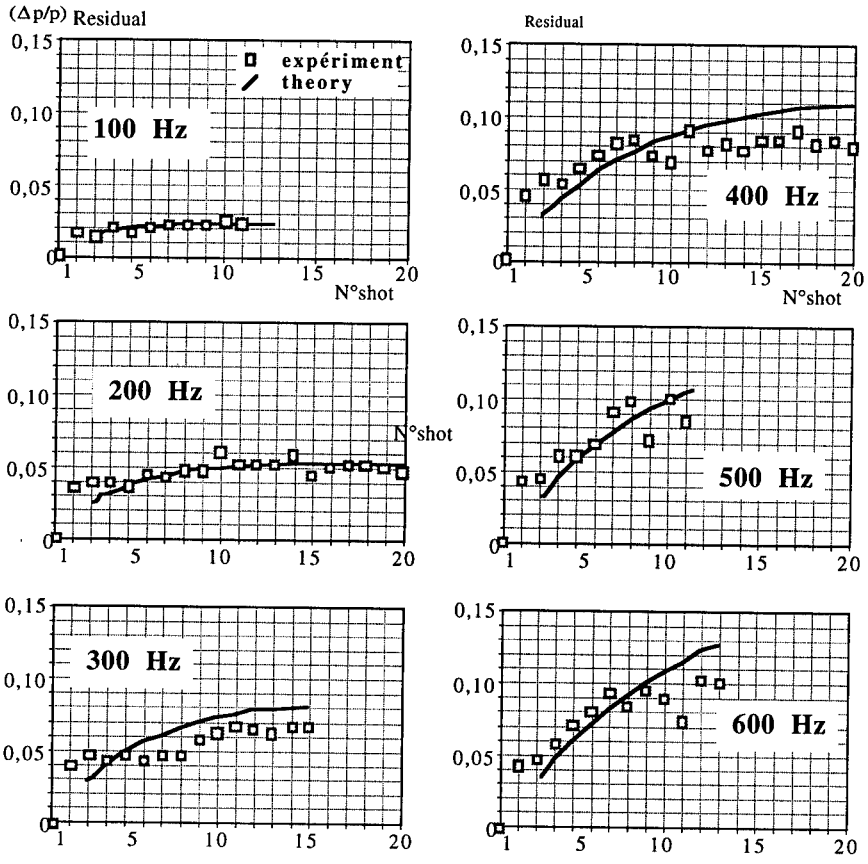


Figure 23. Residual pressure fluctuations versus shot number for different PRF

The curves in full line, on the figure 23, correspond to the simple numerical addition

of pressure perturbations induced by each one of the previous shots. The decreasing rate has been experimentally found (cf fig : 12) :

$$(\Delta p/p)(t) = A e^{-\beta t}, t > 0 \quad (1)$$

and as an approximation , f being equal to pulse repetition frequency :

$$) = \frac{1}{2} \sum_{i=0}^{n-1} (\frac{\Delta p}{p})(t - \frac{i}{f}) , \qquad n-1 < tf \leq n \text{ et pour } tf > 1$$

A et β are parameters controlled by the laser geometry and the energy loading. Their values may be determined for a given device by very simple one shot experiment. The value of b, leading parameter of re-echoing regime, may be enhanced by fitting damping material on sidewalls or in mufflers. This opportunity will be envisioned in the next part.

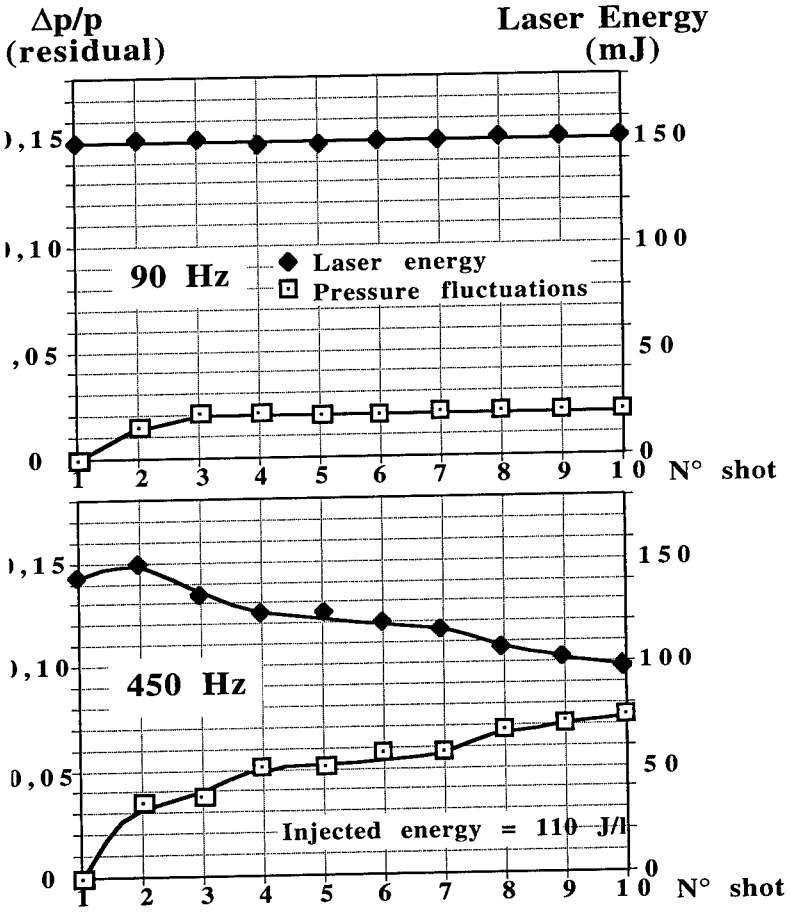


Figure 24. Correlation between pressure fluctuations and laser energy at two PRF

The correlation between residual pressure fluctuations and extracted laser energy is clearly shown on the figure 24

This comparison underlines the leading role of aeroacoustics phenomena in a high repetition rate excimer laser with relatively high loading. In the next paragraph the use of damping material in laser head to decrease waves effects is made clear.

7. Damping of acoustic waves and benefit for extracted laser energy

A laser cavity has been designed (LUX III) to have the possibility to dispose porous material in the immediate vicinity of discharge volume in order to increase the energy losses of acoustic waves. The figure 25 shows up the locations of the damping materials. Different materials have been used, the best results have been recorded with felt ceramic (Al2O3 96%, SiO2 4% Goodfellow AL633790).

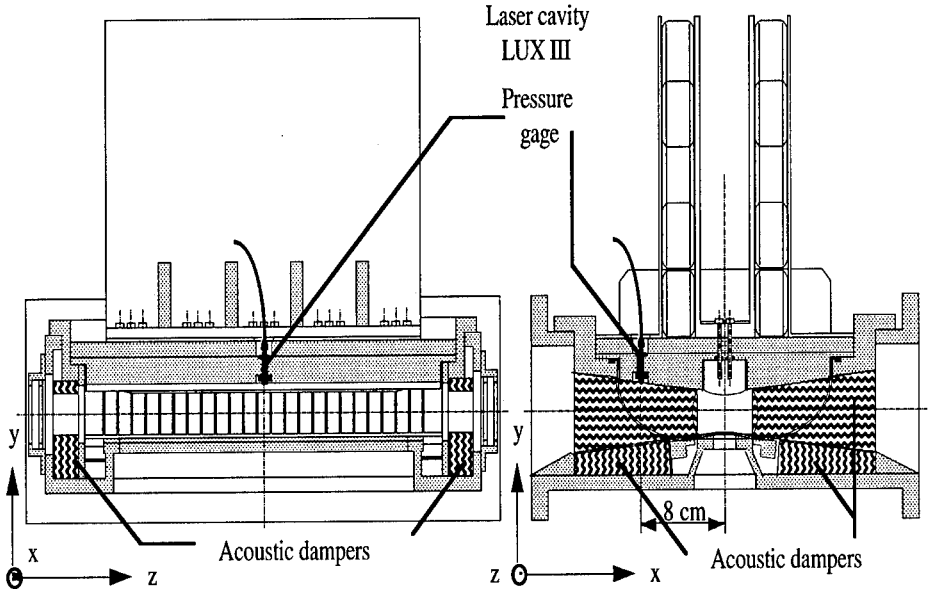


Figure 25. Laser cavity with acoustic dampers

The pressure fluctuations recorded in "LUX III" laser cavity, without and with damping materials, are compared on the figure 26, when all the disponible cavities are full of damping material. The benefit is clearly visible ; at 10 ms the level of residual pressure fluctuations is decreased by a factor 5.

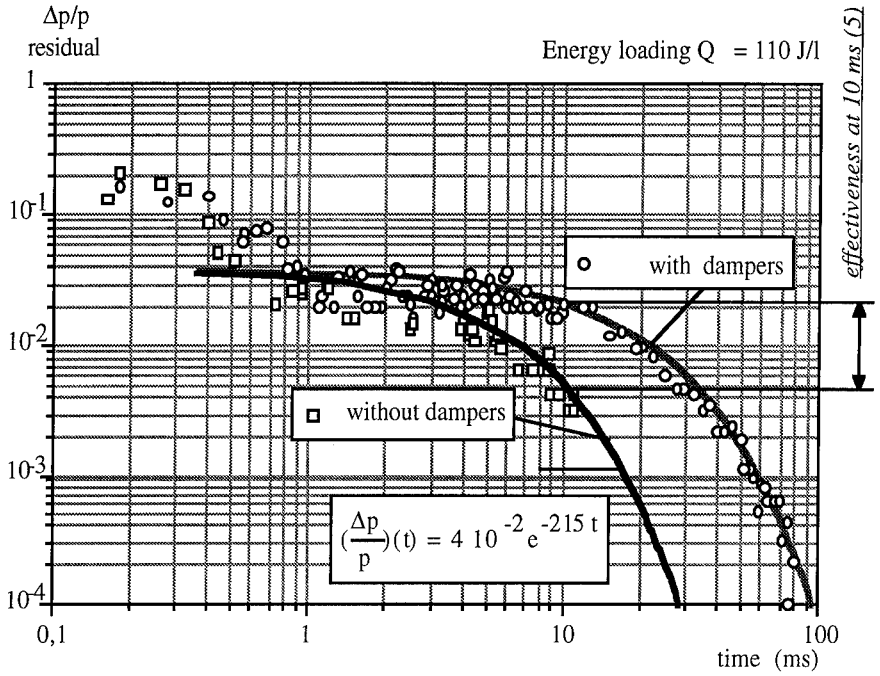


Figure 26. Residual pressure fluctuations with and without dampers

	$\mathcal{A}$	β
without damper	$4\ 10^{-2}$	63
with dampers	$4\ 10^{-2}$	215

Figure 27. Comparison of waves decreasing parameters in laser cavity LUX III with and without damping materials

The parameters of the exponential decreasing rates are compared in the figure 27 . These decreasing rates have been recorded in a one shot experiment ; the value corresponding to the re-echoing regime is strongly increased when damping material is used.

Due to the cumulative processes underlined in the previous section the effectiveness of the damping must be of high interest in repetitive regime. The figure 28 shows up the comparison of residual pressure fluctuations at different PRF ; higher is the PRF higher is the benefit.

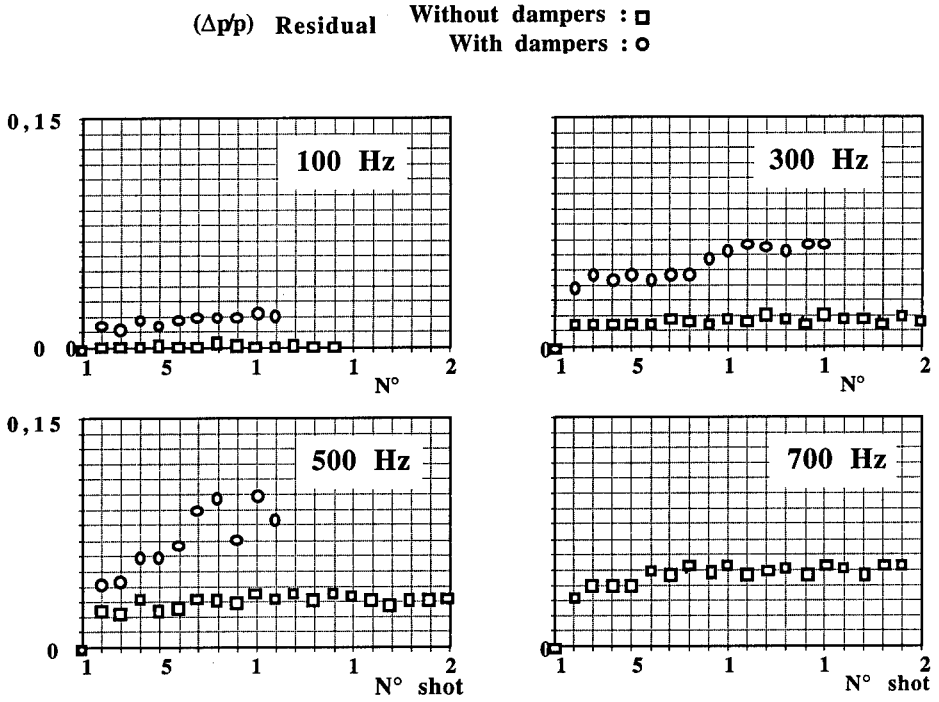


Figure 28 Residual pressure fluctuation versus the shot number of a burst at different PRF (energy loading 110J/l)

The experimental values of pressure fluctuations are compared on the figure 29 with the curves deduced from the cumulative processes. As soon as the parameters of figure 27 are known, a simple one shot experiment is needed, the pressure history in repetitive regime may be easily evaluated.

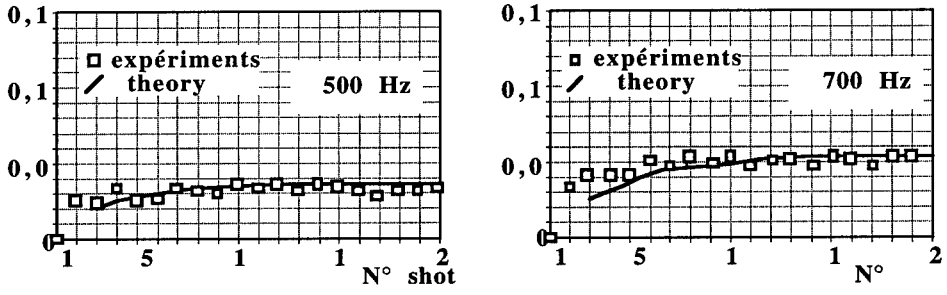


Figure 29. Comparison of experimental and expected values of residual pressure fluctuations at two PRF (energy loading 110J/l).

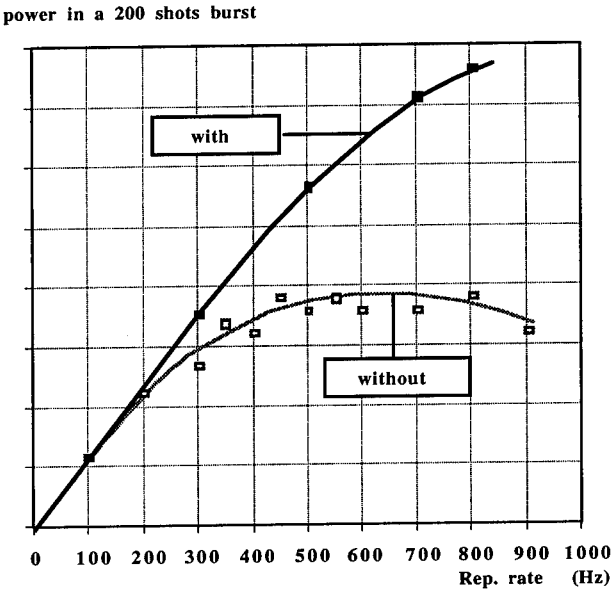


Figure 30 average power of 200 shots burst with and without dampers

The average power of 200 shots burst has been recorded in the same experimental conditions without and with dampers ; the results are presented on the figure 3O.

8. Conclusions

A careful study of pressure fluctuations in "LUX" testbed had permit to underlines the detrimental effects of acoustic waves on extracted laser energy in a high average power excimer laser. Simple analysis, with piezotransducers and very simplified and crude 3D modelisation, have focused the idea on the leading role of waves reflections in the immediate vicinity of discharge volume and damping materials permit to strongly increase the laser energy. In order to control the active medium homogeneity a careful design of excitation scheme is needed to minimise the long term heating of active medium in the discharge volume. The concepts studied in a non optimised laboratory prototype has been successfully applied in the device described in a companion paper by B. Lacour.

Nota Bene

1. An exhaustive bibliography of the subject may be found in :
   - The numerous papers presented at the specialised sessions of International GCL symposia
   - In the reports of EUREKA and AMMTRA programs described in companions papers
2. The results presented here are extracted from the Thesis of Jean Pierre Truong

LASER THERMAL-WAVE DIAGNOSTICS OF STRESSED STATES IN METALS

A.P.KUBYSHKIN
Russian Academy of Sciences
Scientific Research Centre for Technological Lasers
NICTL RAN
Shatura, Moscow Region
140700 Russia

A possibility is being investigated to reveal the local inner stresses in subsurface regions of metallic parts by nondestructive noncontact laser thermal-wave technique. Anisotropy of thermal diffusion of metal caused by mechanical load has been studied. Local fatigue stress region in aircraft turbine blade has been obtained.

1. Introduction

The investigation of stressed states in metals is a very important problem in modern machine-building. Inner stresses can arise as a result of thermal and mechanical actions in parts processing, as well as a result of fatigue transformations of metal structure at its exploitation. In the most cases the presence of inner stresses is undesirable, because of it decreases strength and reliability of constructions. In this connection, the development of methods, that enable to reveal the inner stresses, their localization and value, seems is now topical.

There are some different methods for evaluation of stressed states: optical polarimetry [1], tensometry; the use of fragile tensosensitive coatings; opto-elastic coatings, optical holography [2], X-ray scattering [3]. Nevertheless, the methods based on tensometric measurements and on the analyses of fragile coatings modification require the contact with the object surface, that is often impossible. The optical polarimetry and holographic methods demand the surface treatment by special compounds, changing their optical properties under stresses and deformations in the inspected materials, so these are not fully contactless. The X-ray diffraction method enable to investigate strains at the microlevel with high locality, but it demands for special preparation of samples (in form of thin films, for example) and does not apply to real objects testing.

At the latest time, the new laser thermal-wave methods have been widely used for non-contact testing and material structure evaluation [4]. These methods are based on

R. Kossowsky et al. (eds.), High Power Lasers – Science and Engineering, 413–421.
© 1996 *Kluwer Academic Publishers. Printed in the Netherlands.*

the excitation of local nonstationary thermal fields by modulated laser beam and on the analysis of thermal diffusion in the vicinity of laser heating region. Owing to the possibility of wide-range variations of the laser beam focusing and modulation conditions, as well as to high locality of thermal waves in laser heat zone, the thermal-wave method is very promising for application in local control of construction materials and machine parts. In particular, these methods are widely used in defectoscopy for investigation near-surface layers, see for example [5] The present paper considers the possibility of using laser thermal-wave diagnostics to study the stressed states in metallic samples (model and real objects).

2. Method description

To study the stressed states we use the method of laser thermal-wave IR radiometry based on the foundations worked out earlier [6]. The presented paper shows that this method can be used both for the study of anisotropy of thermal waves propagation and for recording and investigation of inner stresses in metals.

Show now qualitatively how the relation between laser-induced thermal waves and stresses manifests itself. Consider the laser beam action on the thermally thick extended sample subjected to contraction. In this case, it convenient to use the cylindrical symmetry task and to direct the coordinate axis Z deep into the sample, then to bring the X-Y plane in coincidence with the sample surface. The sample can be considered to have some infinite thickness. The action of external load causes the stresses emergence along Z axis.

Periodically modulated laser radiation being absorbed at the surface of metallic sample produces its periodical heating. The thermal field in the laser action area described by the equation of heat conduction having the form:

$$\rho c_p \frac{\partial T}{\partial t} - \nabla\left(\hat{\kappa}\,\nabla T\right) = (1-R) I_0 H\left(r_\perp\right) e^{i\omega t} e^{-\alpha z} \qquad (1)$$

where: ρ is density; c_p is heat capacity; α is the absorption coefficient; R is the reflection coefficient; I_0 is laser beam intensity; $H\left(r_\perp\right)$ is the normalized function of laser beam profile; ω is beam modulation frequency. In (1), $\hat{\kappa}$ is the tensor of heat conduction depending in the general case on mechanical strain in the medium [7,8]. The main axes of tensor $\hat{\kappa}$ are considered to be coincident with coordinate axes.

Mechanical stresses can produce strain, that produce variation in thermal conductivity and, respectively, the peculiarity of heat diffusion in the laser heating area. As, on the assumption, the load is directed along Z axis, the task geometry, nevertheless, remaining cylindrically symmetric - the change is only the in the values of components of heat conduction tensor. In paper [9] has been shown that in this case, the component of heat conduction tensor is related to the corresponding load

component by relationship $\kappa_{zz} = \kappa_0 + \eta S_{zz}$, where κ_0 is the value of thermal conductivity without load, η is the coefficient defined by medium properties, S_{zz} is the active load.

In the spectral presentation for the semi-infinite medium solution (1) can be written in the form

$$\tilde{T}(\omega, k_\perp, z=0) = \frac{(1-R)I_0 H(k_\perp)}{\kappa_{zz}\sqrt{-i\,\omega/\chi_{zz} + k_\perp}} \tag{2}$$

here $\chi_{ii} = \kappa_{ii}/\rho c_p$ are the components of thermal diffusivity tensor, $k_\perp$ is the wave vector in plane direction. With the gaussian profile of the laser beam exciting the thermal wave $H(k_\perp) = \pi a^2 \exp\left(-k_\perp{}^2 a^2/4\right)$ the surface temperature dependence on coordinate takes the form:

$$\tilde{T}(\omega, r_\perp, z=0) = \frac{\pi a^2 (1-R) I_0}{\kappa_{zz} \cdot 2\pi r_\perp} \int_0^\infty \frac{I_0(\xi)\xi d\xi}{\sqrt{\xi^2 - i\omega r_\perp{}^2/\chi_\perp}} \exp\left(-\frac{a^2\xi^2}{4 r_\perp{}^2}\right) d\xi, \tag{3}$$

where a is diameter of the beam. With temperature recording at the distance $r_\perp \rangle\rangle a$ this expression goes into a simple enough relationship

$$\tilde{T}(\omega, r_\perp, z=0) = \frac{\pi a^2 (1-R) I_0}{\kappa_{zz} \cdot 2\pi r_\perp} \exp\left[-i\left(\sqrt{-i\omega/\chi_\perp}\right) r_\perp\right] \tag{4}$$

from which it follows that both the amplitude and phase of heat vibrations depend on variation in heat conduction and thermal diffusivity. Thus, when recording the dependence of temperature amplitude and phase on the load it is possible to evaluate both variations in thermal wavelength and corresponding thermal diffusion coefficient.

With the IR radiometry method the temperature field in the laser excitation area is recorded by detection of variations in the surface heat flux, related to temperature changes. In accordance with Stefan-Boltzmann law, the evaluation of IR radiation flow is related to the temperature change by the expression

$$dW = 4\varepsilon\sigma T^3 dT \tag{5}$$

where ε is the coefficient of emissivity of the surface, σ is the Stephan-Boltzmann constant.

Thus, when recording variations in the thermal flow on the modulation frequency of laser radiation and analyzing its spatial distribution, it is possible to estimate the

distribution of nonstationary temperature field over the object surface. The temperature distribution over the surface, when related to heat diffusion under the object surface, enables to study the distribution of stress field in it.

3. Experiment description

The experiments were conducted on the setup shown in Figure 1.

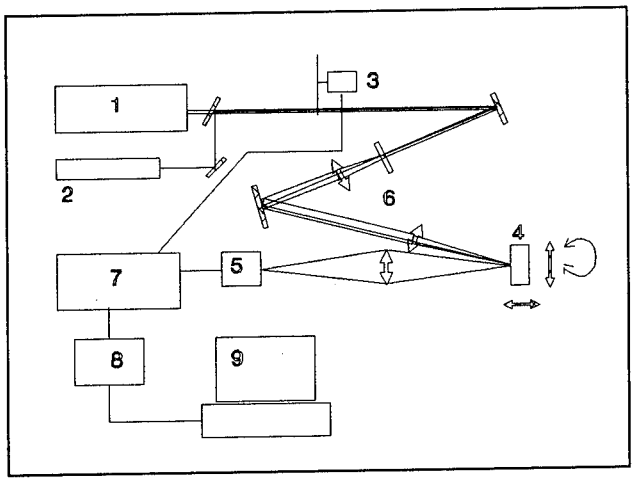


Figure 1. Scheme of laser thermal-wave IR radiometry diagnostics setup
1- heating Nd:YAG laser; 2 - He-Ne laser; 3 - chopper; 4 - movable/rotatable table; 5 - IR photodetector; 6 - optical focusing system; 7 - two connected lock-in amplifiers; 8 - A/D converter; 9 - computer

As the source of thermal waves excitation, a cw Nd:YAG laser was used with the parameters λ=1.06 μm, W=10 watt, TEM_{00}. The radiation was attenuated to the level W ~ 100 mW, modulated by chopper with frequency varying in the range of 10-300 Hz and focused to the sample surface with the lens F=10 cm. The focused spot diameter was 50 μm. The IR radiation induced by laser heating was recorded with the cooled HgCdTe photodetector having the sensitive area of 50 μm size. The relative position of laser heating point and point of IR recording on the object could be regulated with 10 μm accuracy. So, the total spatial resolution of the system was of the order of 100 μm. The electron system of data acquisition consisted of two one-channel lock-in amplifiers synchronized from modulator and mutual phase tuning. Their output was fed to computer through A/D converter. This permitted to evaluate the amplitude and phase of the measured signal by a software. The object was placed on the table, movable in X-Y direction and rotatable around Z axis. In the experiment on the model, sample was stressed in special contraction device placed on the table. The load was evaluated with the calibrated piezosensor.

3.1. MODEL EXPERIMENT

To find out the possibility of inner stresses revealing, a model experiment was carried out. The scheme of the geometry of measurements is given in Figure 2. The experiment is aimed at recording variation in the thermal wave propagating from the centre of laser heating area to periphery under the defined external load causing inner stresses in the sample. The mechanical load in the direction transverse to the plane of laser action in breaking the symmetry in heat diffusion transverse the heating area. This can be found out when rotating the point of IR registration around the heating point at some fixed distance. Anisotropy of heat diffusion induced by stress will manifest itself in signal dependence upon the rotation angle.

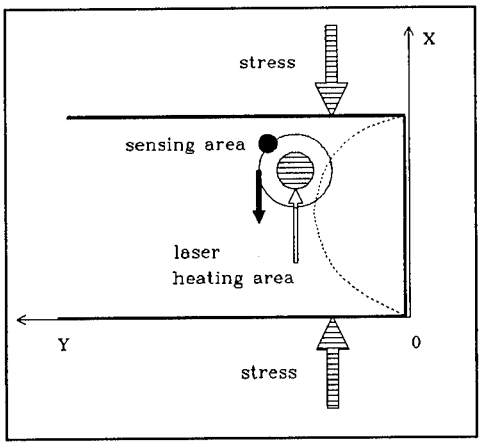


Figure 2. Scheme shows the geometry of laser induced thermal waves propagation measurements in model experiment

As the model, a steel bar (St-20) was used (10x10x40 mm^3) that was placed into the contraction device. The contraction load was apply to the 0-5 mm region from the bar edge and accounted for 150 MPa. The laser beam was directed to the arbitrary chosen point in the area in the vicinity of load application. The point of thermal wave recording was offset by 100 μm from the centre of laser beam focal point and rotated around it. The signal was measured as depended from the angle.

Figures 3a-c present the results of measurements. As evident from the figures, the angular curves of thermal wave response show the pronounced peaks due to external load. By the way, these peaks appear at some typical angles multiple to 60°, that agrees with the directions of load isolines under the considered geometry (the dashed curve in Figure 2 shows schematically the its direction). There exist some proportional dependence between these peaks amplitudes and the load value. Besides, their size is a function of location of heating and recording points. After the load removal any peculiarities in the dependencies disappeared The observed dependencies can be

interpreted as a manifestation of heat diffusion anisotropy caused by inner stresses owing to external forces application. As the stress value and direction are changed from point to point, this is the reason for variation in the signal value. When recording the distribution of these dependencies within the sample boundaries, it is evidently possible to map the relative distribution of stress field in the near-surface layer.

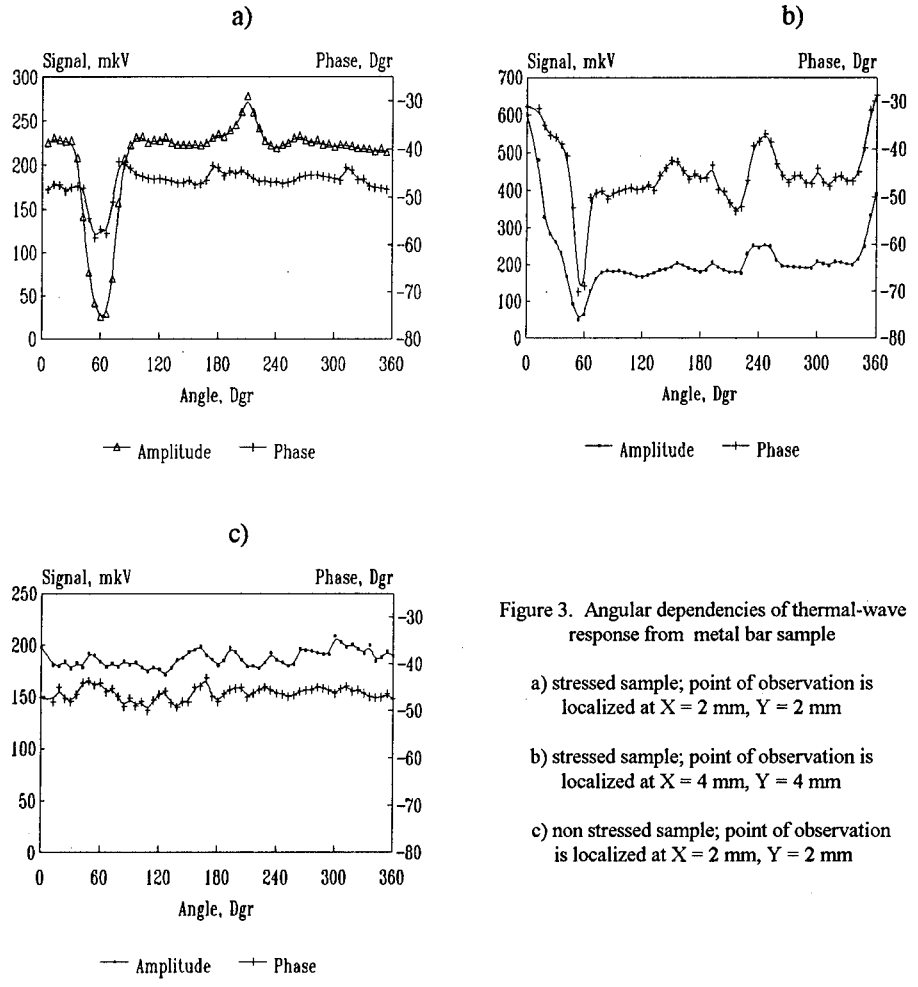


Figure 3. Angular dependencies of thermal-wave response from metal bar sample

a) stressed sample; point of observation is localized at X = 2 mm, Y = 2 mm

b) stressed sample; point of observation is localized at X = 4 mm, Y = 4 mm

c) non stressed sample; point of observation is localized at X = 2 mm, Y = 2 mm

Attention should be paid to asymmetry of thermal diffusion angular dependence, as by the angle 60° the amplitude and phase of the signal decreased 2 or 3 times, thus implying the reduction of thermal wave length in this direction and, respectively, the same decrease in heat diffusion coefficient. At the same time, in the opposite direction (angle is 240°) the signal changes slightly. As yet, there is no clear explanation of this phenomenon. It is possibly related to the presence of essential gradients of stress field.

It is unlikely that the mechanism of relation between the stresses and variation in heat diffusion can be determined on the basis of this experimental results. In polycrystalline materials like that used the stress induced anisotropy of heat diffusion can be a consequence of variation in thermal resistance at the grain boundaries. Some other mechanisms can be possible, e.g. SIPA [10] related to generation of defects in crystalline structure, caused by inner stresses with their subsequent effect upon heat transfer conduction. So, clarification of mechanisms of observed phenomena requires the future studies at the microlevel both on mono- and polycrystalline samples.

3.2 INVESTIGATION OF TURBINE BLADE

The laser thermal-wave method was applied to reveal the regions of stresses states concentration in a real object, i.e. turbine blade of aircraft IL-76 engine (D30-KL-2). A study was conducted on turbo-engine blade that had served its term of 1000 hours. It is known that in the blade of this kind variations in the material structure are observed that are due to high mechanical and thermal shocks on engine operation. The results of metallographic studies also show that the main region of highest stresses is located at the front edge of the blade. So, the measurements were performed by scanning the control point along this edge from its base to boundary. Figure 4 shows schematically the control geometry. The spatial resolution defined by thermal wave length was 0.8 mm.

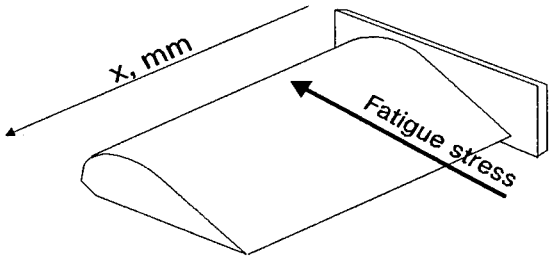


Figure 4. Scheme of turbine blade thermal wave inspection point of registration is scanning along frontal edge along X axis; arrow shows the position of fatigue stress region of weary blade

The results of measurement on the weary blade are shown in Figure 5a. We notice that the maximum related to localization of stress region manifests itself in both amplitude and phase dependencies on the control point coordinates. It is located at approximately 1/3 of the distance from the blade base, i.e. in the place where the node of swelling of the blade flexural vibration is sate. The region suffers the highest loads in operation resulting in accumulation of fatigue stresses, and, finally, can become a place of blade destruction.

The revealed peculiarity showed itself at the laser beam modulation frequencies up to 100 Hz. At higher frequencies (above 120 Hz) the signal disappear. This is,

evidently, due to reduction of thermal wave length (in accordance with (4)) to the value lower than the depth of stresses concentration region. This permits to estimate the depth of stress region location as about 0.1-0.2 mm.

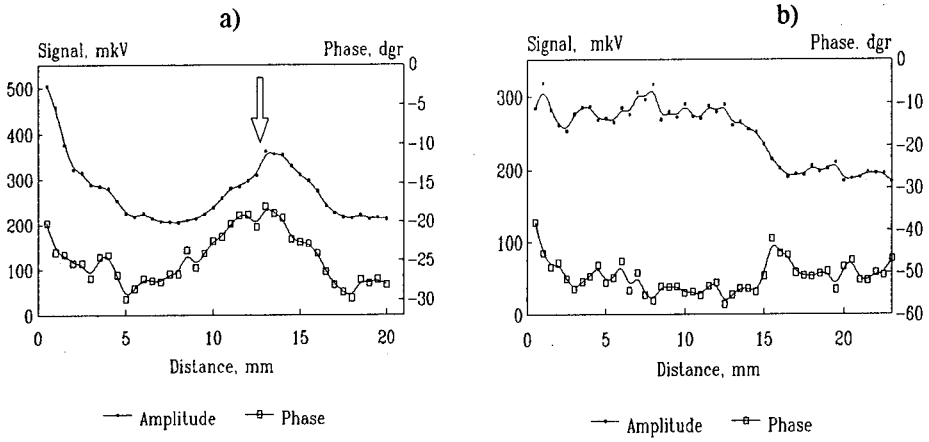


Figure 5. Spatial dependencies of thermal-wave response from turbine blade
a) weary blade; arrow shows the position of fatigue stress zone location;
b) reconstructed blade; no peculiarities connected with fatigue stress are observed

Then, the blade under study was reconstructed by thermal annealing that removed stresses. The repeat measurements showed that the region of stresses state has actually disappeared (see Figure 5b), and blade is restored.

The results of nondestructive thermal-wave inspection were supported by the results of metallographic (destructive) analysis of the similar samples having the served term and restored.

4. Conclusion

The results of experiments on the model sample and real object showed that the laser thermal-wave IR radiometry method cam be used to study of stressed states in metallic construction elements. A distinguishing feature of this method is its full non-contactness and no necessity of the object destruction on inspection. The method is effective in investigation of the state in the material undersurface area - for metals depth of the order of 1-2 mm, - where the application of other alternative methods (i.g. ultrasonic) is problematic. In particular it can find application in surface layers inspection in surface laser heat treatment and facing to study the stresses distribution over the depth of laser treatment area, as well as to investigate the areas of stresses induced by thermal loads near the weld joint on laser welding of metallic parts. Thus, the method under consideration is of considerable promise for inspection in laser technology.

5. References

1. Netrebko, V.P. (1988) *Photoelastivity of anisotropic bodies*, Moscow State University Publishing, Moscow.
2. Makhutov, N.A., Ed. (1992) *Experimental investigations of stresses in constructions,* Nauka, Moscow.
3. Ferrari, M. and Lutterotti, L. (1994) Method for the simultaneous determination of anisotropic residual stresses and texture by x-ray diffraction, *J.Appl.Phys.* **76**, 7246-7255.
4. Mandelis, A., Ed. (1992, 1993) *Progress in photothermal and photoacoustic science and technology* **1**, **2**, Elsevier, New York.
5. Fournier, D., Ed. (1994) *Proceedings of 8 International Topical Meeting of Photothermal and Photoacoustic Phenomena*, Guadelupa, France.
6. Busse, G. (1980) Photothermal transmission probing of a metal, *Infrared Phys.*, **20**, 419-422.
7. Landau, L.D. and Lifshits, U.M. (1987) *Elasticity theory*, Nauka, Moscow.
8. Grimvall, G. (1986) *Thermophysical properties of materials,* North-Holland Physics Publishing, Amsterdam.
9. Qian, M. (1994) Use of photoacoustic technique for detection of residual stress distribution, In. *Proc. of 8 ITMPPP*, Guadelupa, France, 221-222.
10. Ibragimov, Sh.Sh., Kirsanov, V.V. and Piatiletov, Yu.S. (1985) *Radiation induced damage of metals and alloys*, Energoatom Publishing, Moscow.

EXPERIMENTAL STUDIES OF REFLECTION ABILITY OF LIQUID METAL TARGETS IN VACUUM UNDER CONDITIONS OF NEODYMIUM LASER PULSE RADIATION.

KOZLOVA A.S.
Ph. doctor
Moscow Aviation Institute, Volokolamskoe shosse 4, Moscow 125871
Russia.

Abstract

Melting and evaporation stages of metals are in the basis of numerous technological processes developed in the field of metal treatment. Lasers enable to heat the surface of metals by powerful short-term radiation that considerably changes the properties of their surface. The necessity to study the optical characteristics of metals and alloys subjected to such treatment becomes of vital importance.

This paper considers the method and represents the measurement results of solid and liquid metal target reflection ability in vacuum under neodymium laser impulse effect acting in the mode of free generation. The techniques presented are based on the comparative method of reflection factor RF measurement and a widely-spread method of measuring a reflection factor of diffusionally scattering surface described by Taylor . The measurements were taken during a hundred ms after the laser impulse effect on the target using a system of laser synchronization with spectral RF measurement. The RF temperature dependence for fermenting metals (tin, indium) within the interval of 20'C to 350'C has been obtained for optical ranges of scanning emission in vacuum no more 10^{-4} Torr under the neodymium laser effect (facility GOS-1001), the beam energy up to 1 kJ and maximum emission power density at the target being 10^5 W/cm^2.

R. Kossowsky et al. (eds.), High Power Lasers – Science and Engineering, 423–432.
© 1996 *Kluwer Academic Publishers. Printed in the Netherlands.*

Introduction

Powerful radiation of optical quantum generators results in different non linear phenomena appearance and contributes to a number of non-optical effects (evaporation, subsurface layer structure change, etc.).

Unfortunately, even current experimental measurements of particle energy dependence on laser radiation power and its spatial distribution for different targets often has a wide spread in the data causing a surprise [1]. That is why the problem of studying target reflection ability in different aggregate state before, during and after a powerful pulse laser effects remains vital. However, it is still difficult to obtain and keep metals in a liquid state. This is achieved by carrying out experiments in vacuum or neutral gas media.

Experiment

To perform sufficiently accurate measurements a system of reflection registering synchronous with the laser pulse has to be developed.

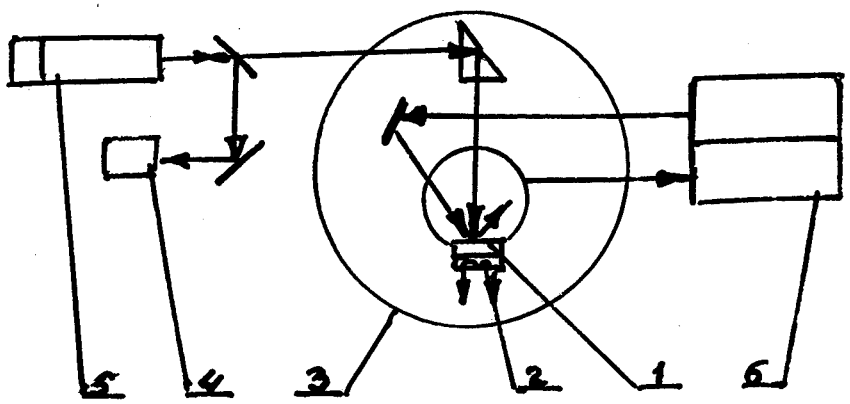


Fig. 1. Test Pattern.

1 – target; 2 – furnace for target heating; 3 – vacuum chamber; 4 – system for measuring energy, heating laser radiation and its time distribution; 5 – GOS-1001 source of heating laser radiation; 6 – system for measuring light reflection factor of the target

This paper considers a method and the results of reflection ability measurements of solid and liquid targets in vacuum not worse than 10^{-4} Torr in conditions of neodymium laser pulse effects operating in the mode of free generation (Fig. 1).

Determination of reflection factor (RF) is based on comparative techniques allowing to find reflected probing radiation beam, falling radiation beam ratio. A source of probing radiation is He-Ne type laser, a gas-filled lamp or a light-emitting diode. Every source has been designed so that they generate pulse low-power radiation in optical and IR range.

The reflected and falling radiation are registered either by PEM-85- type photomultiplier first passing through UM-2 monochromator, or photodiode. The whole information of these two values goes to analog-digital converter (ADÑ) and to DVK-2M computer, where RF is computed. Simultaneously, with the help of a thermocouple the sample-target temperature is measured. The reflected radiation is collected and averaged by a diffusion ally-dispersing surface of a spherical shape described by Taylor [2]. The wall of the sphere is replaced by the sample surface. Besides the orifice for probing radiation input and the output of the averaged reflected radiation the sphere has an additional orifice opposite the

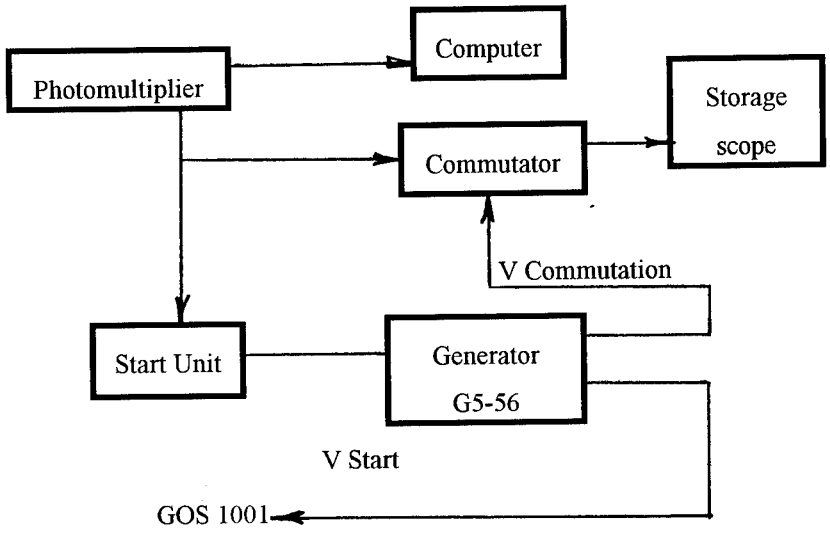


Fig. 2(a).

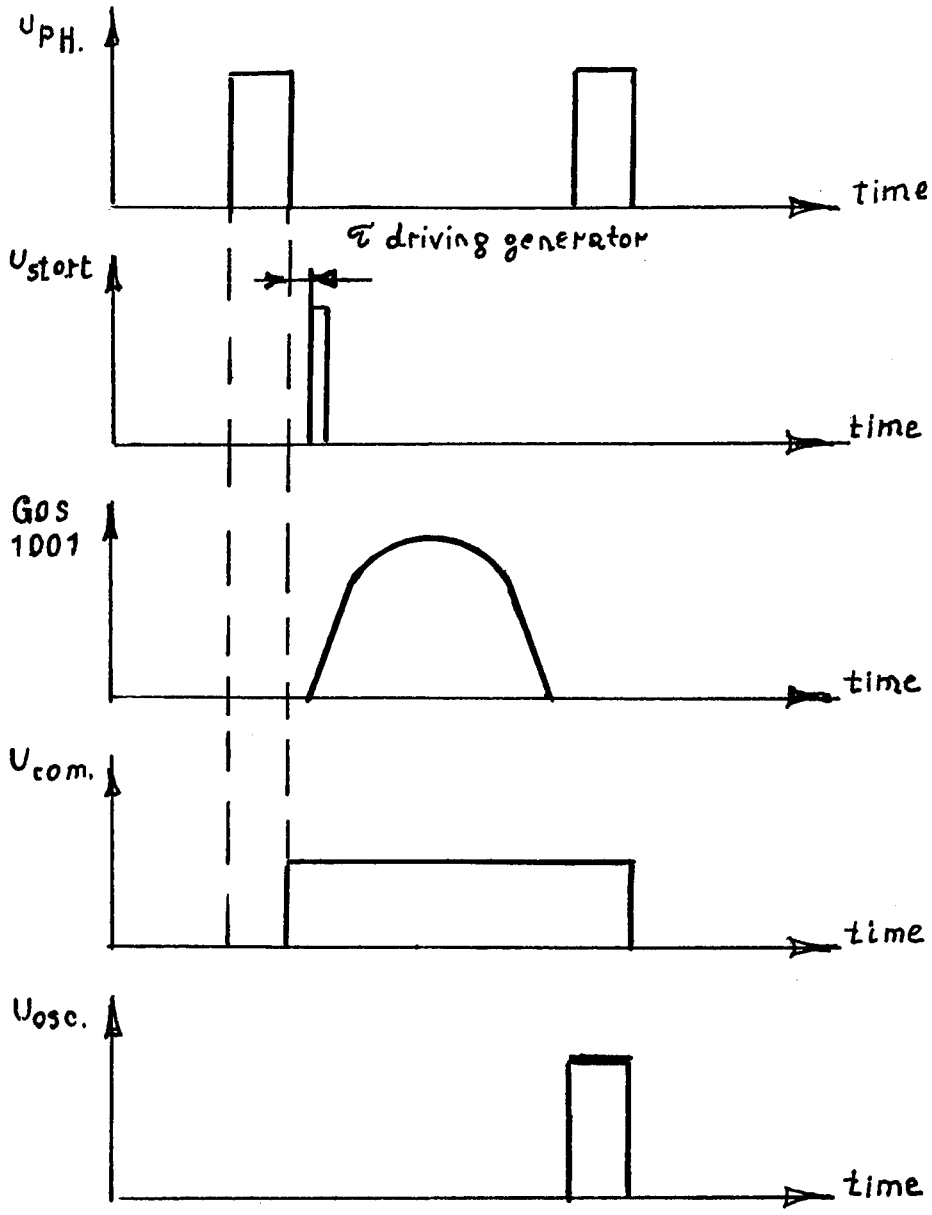


Fig. 2(b)

Synchronization unit of heating laser radiation

and reflection factor measurement system

sample surface. Heating pulse laser radiation is supplied through this additional orifice from GOS-1001 device. This unit on the neodymium glass produces power up to 1 kJ with the wavelength 1,06 μm up to 1,5 ms. Maximum power density of laser radiation on the target is 0,1 kJ/cm^2 (~10^5 W/cm$^{2)}$. The target is a cylinder 30 mm in diameter and 10 mm height which is placed in a tab made of a refractory ,e.g. niobium.

Due to the fact that the processes taking place on the surface of materials heated by pulse laser radiation are fast the reflected light signal intensity has to be registered, in an ideal case, just after the laser pulse completed . To obtain this effect a system was developed to synchronize GOS-1001 laser with a spectral reflection factor measurement unit. Signals of photomultiplier reflected from the sample enter the start circuit and commutator (Fig.2).

The start circuit generates a synchronization pulse connected with the reflected signal measured. A synchronization pulse enters the generator that produces a commutator control pulse 0,33 s detained and 1÷3 s long and for Laser starting pulse. Generator delays in respect to a start pulse have been chosen in such a way that a commutator control pulse appears in synchronism with GOS-1001 pulse and due signals coming from photomultiplier.

Registration of 10÷20 due signals reflected from the sample surface after the effect of GOS-1001 laser beam lasted 100÷200 μs. That is an averaged signal out of 10 ÷20 registered reflected from the sample signals is recorded.

Experimental data

Measurements of spectral reflection factor were carried out under different laser beam power effects upon tin possessing different surface temperature before laser heating (Table 1). RF value was registered by two independent channels: 1 - computer, 2 - storage scope. Under such density of laser radiation energy flow [3] for easy-melting metals the melting and evaporation processes were observed [4].

TABLE 1. The spectral reflection factor under different laser beam power effects upon tin possessing different surface temperature before laser heating

	Computer	Storage scope	
Pulse energy GOS-1001 kJ	Reflection factors %	Reflection factors %	Sample temperature °C
-	47.5	47.5	20
20	47.5	47.5	20
30	47.5	49.7	20
-	47.5	49.5	20
40	45.5	46.4	20
-	47.5	49.7	20
50	43.5	45.3	20
50	41.5	-	20
-	45.5	49.7	13.0
-	45.5	51.8	169.0
-	45.5	51.8	177.0
20	45.5	51.8	176.0
30	47.5	51.8	170.0
40	47.5	51.8	157.0
50	47.5	51.8	149.0
-	47.5	51.8	153.0
30	47.5	51.8	155.0
-	47.5	51.8	157.0
before the shot	47.5	51.8	161.0
50	45.5	49.7	162.0
120 s after the shot	47.5	54.0	176.0

Fig.3 demonstrates Indium and tin RF dependence obtained by the method described. The RF values were measured at room temperature and they are in satisfactory agreement with the data known [5].

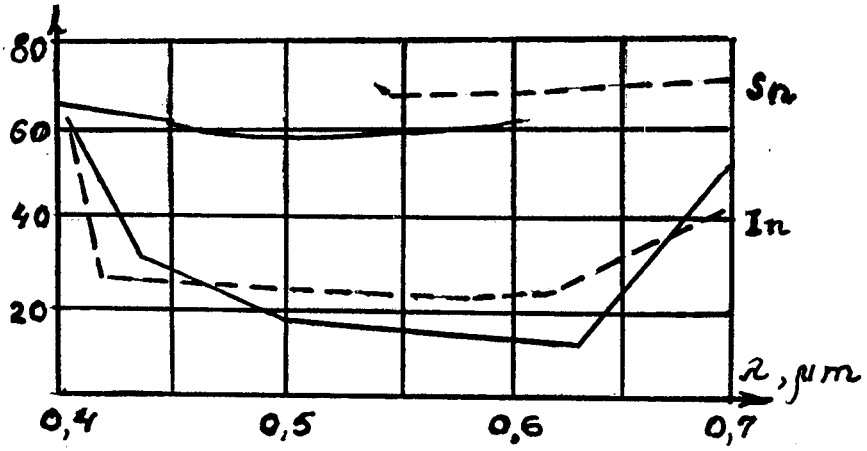


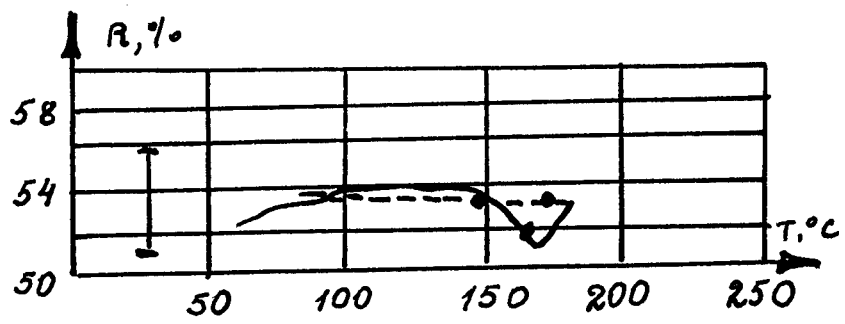
Fig. 3. Indium and tin reflection factor spectral dependence
(dispersion) at room temperature
...the data of [6,**5**]; -- experimental data

With continuos heating the Indium and tin reflection ability temperature dependence of graphs were built including temperatures of melting (Fig. 4,5). The specified RF values were measured after laser pulse effects.

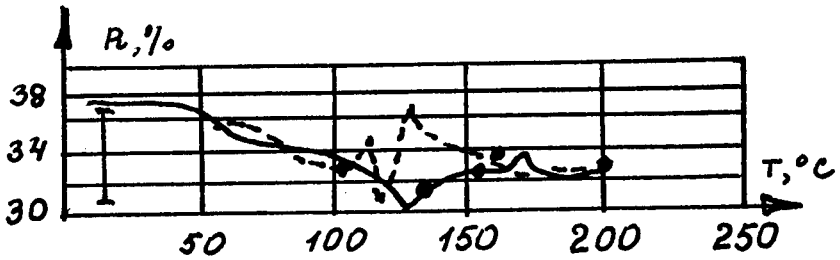
Conclusion

In and Sn diffuse reflection factors are constant with temperature increase. Reflection ability of easy-melting metals does not change both under long-term heating including melting and powerful pulse laser effects.

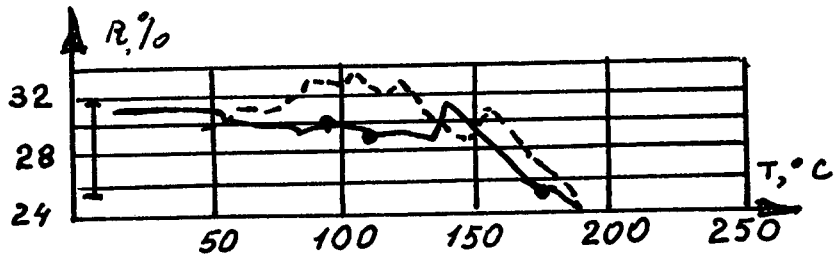
If to consider a phenomenon of metal RF conservation under the effect of pulse laser without taking into account the results of stationary heating, the explanation can be the following. Firstly, RF increases after the metal surface has melted, and on account of probing light absorption by metal vapors the difference is compensated. Secondly, RF remains constant during transition solid-liquid state phase and it does not depend on the rate of this transformation. Besides when was over the surface under both



a) λ = 0.4300 μm



b) λ = 0.6400 μm

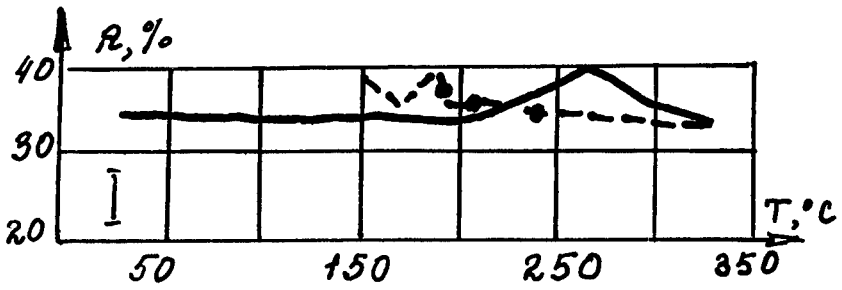


c) λ = 0.6328 μm (He-Ne laser)

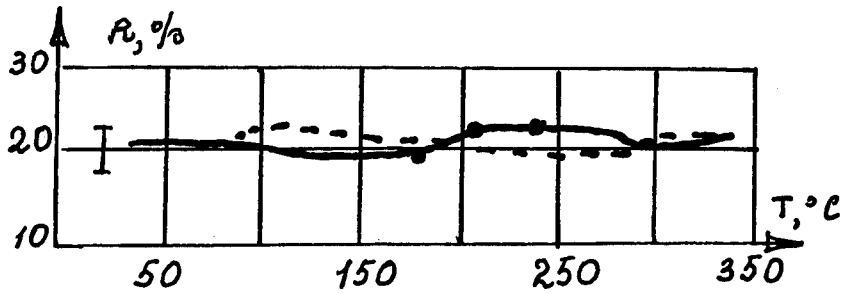
Fig. 4. Graphs of indium temperature dependence

for different wavelengths of optical range. ($T_{melting}$=156° C)

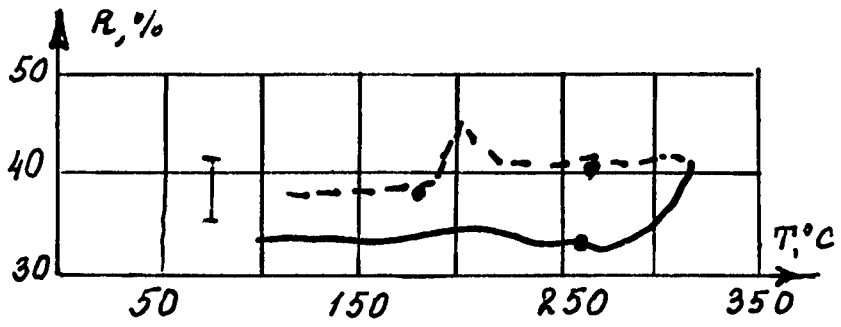
— heating; -- cooling.



a) $\lambda = 0.4200$ μm



b) $\lambda = 0.6328$ μm (He-Ne laser)



c) $\lambda = 0.58$ μm

Fig. 5. Graphs of tin temperature dependence for different wavelengths of optical range.($T_{melting}$=232° C)

— heating; -- cooling.

longterm heating a low density of metal's vapour can't provide the scattering of falling radiation beam. Obtaining RF temperature dependencies under long stationary thermal heating of metals undergoing transition transformations support the second conclusion with the accuracy of experimental measurement.

The diffuse reflection factor of easy-melting metals (tin, Indium) keeps constant values at transition phase irrespective of the heat character and rate.

References

1. Khora H. (1986) Physics of Laser Plasma: Trans. from Eng., Energoatomizdat, Moscow, pp. 272
2. Taylor A.H. (1920) The Measurement of Diffuse Reflection Factors and a New Absolute Reflectometer , J. Opt. Soc. of Amer., v. 4; (1920), Sci. Bur. Stand, v.16.
3. Grigoryants A.G. (1989), Fundamentals of Material Laser Processing, Mashinostroyeniye. Moscow, pp. 302.
4. Delone N.B. (1989) Laser Radiation Interaction with the substance: Course of lectures: Teach. Inst., Nauka. Publ. House Phys.-Math. Lit., Moscow, pp. 238.
5. Motulevich G.P. (1971), Optical Properties of Intransitional Metals. Intemolecular Interaction, Nauka, Moscow, pp. 242.
6. The properties of substances, Handbook, (1985), in prof. M.E. Dritz (ed.), Metallurgia, Moscow.

RECONSTRUCTION OF A LIGHT BEAM WAVE FRONT BY SYNTHESIS OF A SHEAR INTERFEROGRAM

V.N.SHEKHTMAN, A.YU.RODIONOV, A.G.PEL'MENEV

Laboratory of Engineering Physics, St.Petersburg,189620 Russia

1.Introduction

The interferograms produced by the reference light beam, actually, contain the information not on the shape of the wavefront but on phase aberrations introduced by the test object. The latter is generally the goal of interferometric measurements. However, in most cases the required information is that on the shape of the wavefront of the investigated beam. Such necessity arise, for example, when measuring the shape and quality of optical elements without reference pieces, or, in the case of linear adaptive systems operating on the phase conjugation basis.

For problems of wavefront reconstruction the advantages of using shear interferometers, rather than those with reference beam, are quite obvious, since the formation of the reference beam, coherent to the investigated one, with the known wavefront shape, appears to be a very complicated technical task. Shear interferometers are simple to produce, however, in this case, reconstruction of the wavefront is more complicated and shear interferograms are less informative compared to those produced with reference beam interferometers.

The loss of information when using shear interferometers is caused by several factors [1].

One of the reasons for the information loss is the selective sensitivity of shear interferometers to various spatial frequencies of the wavefront including a complete loss of sensitivity at certain frequencies [2-4].

R. Kossowsky et al. (eds.), High Power Lasers – Science and Engineering, 433–447.
© 1996 *Kluwer Academic Publishers. Printed in the Netherlands.*

Another source of information loss is an incomplete filling of the aperture of the investigated light beam with the interference pattern. This actually results in a discrete representation of the reconstructed wavefront with a step equal to the shear magnitude. This feature of shear interferometers makes it impossible to evaluated wavefront aberrations with a spatial period smaller than the minimal shear.

The third factor lowering the information content of shear interferograms is that, in general case, the reconstruction of the wavefront can be performed with a first-order-aberration accuracy due to an unknown order of interference within the interference pattern region. Data of the first order aberrations can be obtained using either non-monochromatic light sources [5], or some additional optical elements in the lateral shear interferometer with a monochromatic light source [6].

This paper presents a method of producing and processing lateral shear interferograms which allows to avoid any information losses and thus to perform a complete reconstruction of a light beam wavefront.

2. Informative character of shear interferograms depending on the type of shear.

For the analyze of the wavefront information losses in shear interferograms, consider the four types of interferometers of lateral, radial, rotary and reverse shear.

Out of three above-mentioned types of information losses, the first one occurs in lateral, rotary and reverse shear interferometers, the second one in radial and lateral shear interferometers and the third one in lateral shear interferometers.

Let's carry out the formal analysis of information losses in various interferograms by representing the function of spatial distribution of the light wave $\varphi(x)$ the corresponding interference order function $h(x)=\varphi(x)-\varphi(x-s)$ as Fourier spectrum and let's assume that the direction of the coordinate x coincides with the direction of the shear vector s. Note that the analysis of information losses can be also carried out by other types of expansion of $\varphi(x)$ and $h(x)$ into basic functions.

In all the investigated cases the lack of information on $\varphi(x)$ function is due to two physical reasons: mutual subtraction of certain spectral components of $\varphi(x)$ function during the shear operation and the presence of regions on the test aperture with interference patterns being not defined. The first reason is characteristic of lateral, rotary and reverse shear interferometers and the second one for lateral and radial ones.

In the case of lateral shear, Fourier spectra of the interference order $H(\nu)$ and wave phase $\Phi(\nu)$ functions are connected by the relationship following from the Fourier transform properties:

$$H(\nu)=\Phi(\nu)(1-\exp(-i2\pi s\nu)) \qquad (1)$$

where: $H(\nu)=F[h(x)]$, $\Phi(\nu)=F[\varphi(x)]$

s is the shear vector magnitude.

It can be seen from equation (1) that the sensitivity of the lateral shear interferometer to spatial frequencies of distortions of the wavefront analyzed is a periodic function having maximal at the frequencies $\nu_K=(k+0.5)/s$, $k = 0,1,...$ At the frequencies $n_k = k/s$ information on the amplitude of wavefront aberration is entirely absent in the lateral shear interferograms. To avoid this loss of information, a pair of interferograms with non-multiple shears should be jointly processed [4], or an interferometer with spatially variable shear (e.g., a radial shear interferometer [3]) should be used. The other two mentioned reasons of information loss are retained because $\varphi(x)$ and $h(x)$ are spatially constrained functions in actual practice: the function $\varphi(x)$ is defined over the entire entrance pupil area (see Fig.1) and $h(x)$ is known only on the segment $[s,D]$. In this case, formula (1) takes the form

$$H(\nu)=\Phi(\nu)(1-\exp(-i2\pi s\nu)) + L(\nu) \qquad (2)$$

where:

$$L(\nu)=\int_0^s \varphi(x)\, e^{-i2\pi\nu x}\, dx + e^{-i2\pi\nu s}\int_{D-s}^{D} \varphi(x)\, e^{-i2\pi\nu x}\, dx$$

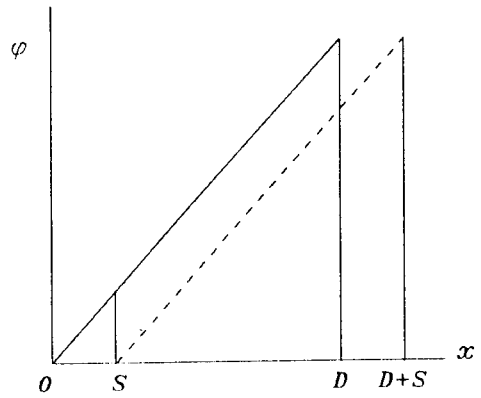


Fig. 1. Wave-front section along the shear vector

One can show that when the function $h(x)$ is known, the additional term on the right side of equation (2) can be completely determined, provided $\varphi(x)$ is specified at each segment of length s within the domain of definition $[0,D]$.

Thus, the problem of wavefront reconstruction using a shear interferogram can be solved for a spatially restricted function only if the wavefront profile is known at any segment of the length s over the light beam aperture.

In practice, an interferogram is interpreted at the limited number of points N. In this case, equation (2) can be written in the form

$$H_j = (1 + e^{-i 2\pi j \frac{k}{N}}) \Phi_j + L_j ; \qquad (3)$$

where:

$$H_j = \frac{1}{N} \sum_{k=0}^{N_h - 1} h_k e^{-2\pi j \frac{k}{N}}; \quad h_k = h(x_k); \quad x_k = k \frac{D-s}{N_h}; \quad k = 0, 1, ..., N_h - 1;$$

$$\Phi_j = \frac{1}{N} \sum_{k=0}^{N-1} \varphi_k e^{-2\pi j \frac{k}{N}}; \quad \varphi_k = \varphi(x_k); \quad x_k = k \frac{D}{N}; \quad k = 0, 1, ..., N-1;$$

$$L_j = -\frac{1}{N} \sum_{k=0}^{k_0 - 1} \varphi_k e^{-2\pi j \frac{k}{N}} + \frac{1}{N} e^{-2\pi j \frac{k_0}{N}} \sum_{k=N-k_0}^{N-1} \varphi_k e^{-2\pi j \frac{k}{N}};$$

$$N = N_h + k_0; \quad k_0 = \frac{sN}{D};$$

In expression (3) the parameter N_h and N determine the numbers of points on the net, i.e., representations of the functions $h(x)$ and $\varphi(x)$ at the section, respectively. The parameter $k_0 = N - N_h$ indicates the number of the representation steps in the section within the shear s.

At $k_0 = 1$ (i.e., when the step of the net equals the shear) L_j vanishes; hence using equation (3) and the known H_j coefficients one can calculate the coefficients Φ_j and reconstruct the wavefront represented in N points section:

$$\Phi(x_n) = \sum_{j=0}^{N-1} \Phi_j e^{i 2\pi j \frac{k}{N}};$$

In spite of the fact that L_j vanishes, the information on the wavefront aberration on a scale less than the shear value is lost. Moreover, identification of the fringe pattern belonging to the unperturbed interferogram and to one of the objects under study is sometimes impossible owing to the absence of the pattern on part of the aperture (within the intervals $[0,s]$ and $[D,(D+s)]$ shown in Fig.1). This results in an uncertainty of the optical wedge type at the wavefront reconstruction [6].

If $k_0 \neq 1$, L_j is non zero in the general case and, as was noted above, the interferogram interpretation requires information on $\varphi(x)$ and φ_K behavior at any one of segments $[c,c+s]$. In number of cases, e.g., when the unperturbed field is presented at the fringe pattern, such information is available; however if the entire interference field is occupied by an optical inhomogeneity, the interferogram whose step is smaller than the shear cannot be interpreted without additional data on the wavefront.

In spite of the high sensitivity of a lateral shear interferometer to wavefront aberration with spatial frequencies $\nu_C = (n+0.5)/s_C$, $n = 0,1,2,...$, information on these frequencies can be erroneous or lost in the process of wavefront reconstruction because of the masking effect arising in attempting to satisfy the condition $k_0 = 1$, $L_j = 0$. In this case, zero or near-zero amplitudes at these frequencies can be obtained at the net nodes, which results in corresponding errors in the reconstructed wavefront. To avoid such information loss, one should choose the shear $s << 1/\nu_C$. However, in this case the accuracy of interpretation is lowered because of a decrease in the interferometer sensitivity to the distortions with the spatial frequency ν_C and an increase in the relative error of the shear vector determination with decreasing shear.

For radial shear interferograms the expression similar to (1) takes the form:

$$H(\nu) + L(\nu) = \Phi(\nu) - g\,\Phi(g\nu) \qquad (3)$$

where: $$L(\nu) = -\int_{D/g}^{D} \varphi(x)\, e^{-i2\pi\nu x}\, dx \quad ,$$

g is the ratio of the linear size of the larger image to the smaller one.

As it is also obvious, in the expression connecting the spectra of the interference order function and wave phases there is an unknown component L(ν) describing the lost piece of information. Thus, both radial and lateral shear interferograms are characterized by information loss due to the second factor. Therefore, the assumption [3] that the radial shear interferometer has no information losses on spatial frequencies is not true. Radial shear interferograms, indeed, feature information losses not only of the first type.

In rotary and reverse shear interferometers where the localization region of the interference pattern coincides with the aperture of the test beams the information loss due to the second and third reason is not possible.

In rotary shear interferograms, just as in case of the lateral shear, a periodic sensitivity loss is observed for spatial frequencies satisfying the equation $(1 - e^{-i2\pi s\nu}) = 0$ (see expr.(1)): $\nu_k = \kappa / \alpha r$, $k = 0,1,2,....$

where: αr -angular shear.

In case of the reverse shear , we obtain the relation between the spectra of the wavefront and the interference order functions: $H(\nu)=\Phi(\nu)-\Phi^{*}(\nu)$, from which it follows that the reverse shear interferometer is not sensitive to even harmonics and twice as sensitive to odd harmonic components of the wavefront compared to the reference beam interferometer.

Consider below a method for the interferogram producing which allows to eliminate the wavefront information loss using a lateral shear as an example.

3. Elimination of the wavefront information losses by synthesis of the interference pattern

First, consider the condition with the elimination of the interferometer sensitivity due to an incomplete filling of the beam aperture with the interference pattern.

As it follows from (2), such information can be eliminated under the condition that

$$L(\nu) \quad 0, \text{ or } \varphi(x) \quad \varphi(x+2D) \qquad (4)$$

Let us transform the function φ(x) into the function satisfying the condition (4). For this purpose we perform the mirror reflection $\varphi(x)$ with respect to the points $x = 0$ and $x = D$ specifying the boundaries of the domain of definition. Then we obtain a new function $\psi(x)$ (Fig.2). Performing this procedure an infinite number of times, we finally obtain a continuous periodic function $\psi(x)$ with period $2D$, $\psi(x) = \psi(x+2D)$, which corresponds to a periodic function of the interference orders $h_D(x) = h_D(x+2D)$. The function $\psi(x)$ synthesized in such a way satisfies the condition (4), i.e., its spectrum is related to the spectrum of the function of interference orders by a simple equation:

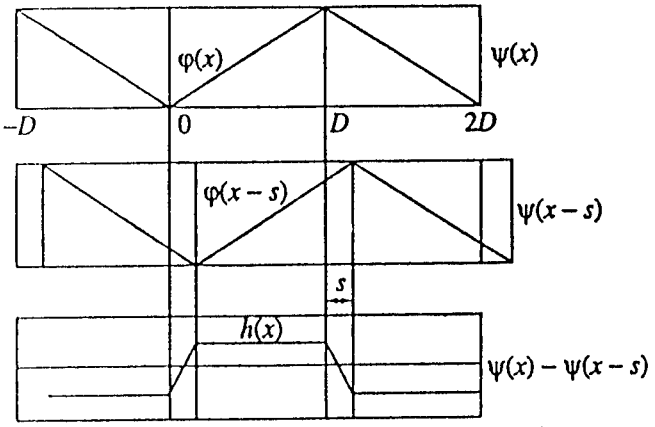


Fig.2. Wave-front section of the synthesized beam along the shear vector.

$$H_D(\nu_x) = (1 - e^{-i2\pi \frac{k}{f}}) \Phi_D(\nu_x)$$

which allows one to obtain information on the phase aberration amplitudes for the enter spectrum of spatial frequencies, including $\nu < 1/s$, from a shear interferogram with any specified accuracy. The function

$h_D(x)$ is an odd one (with respect to the points $x_n = s/2 + nD$, $n = 0,1,2,...$) for any form of the wave front measured

$$h_D(x + x_n) = -h_D(-x + x_n).$$

Two conclusions follow from this property:

(i) Determination at the segment $[s/2, s/2 + D]$ is sufficient for reconstruction of the whole function of interference orders $h_D(x)$ using its periodicity and party properties.

(ii) Because the function $h_D(x)$ is odd at any $\varphi(x)$, it takes on zero values at the points $x_0 = s/2 + nD$, $n = ..., -1,0,1,...$ Owing to the symmetry of φ (x) with respect to $x = nD$, the lateral shear results in local reverse shear (see Fig.2) at the segments of $\varphi(x)$ domain $[nD, nD + s]$, its value varying linearly from $-s/2$ to $s/2$. The shear is zero at $x = s/2 + nD$ and the function of interference orders vanishes.

A well - known disadvantage of lateral shear interferometers [6] is the complexity of determination of a wave front tilt. In contrast to interferograms with a reference beam, a shear fringe pattern is by aberrations of the wedge type as a whole without changing its structure. To determine the value of this shift (and consequently the optical wedge angle) one should identify the fringe order using specially designed optical systems. For example, a technique using pattern areas with zero shift fringes are fixed relative to the probe aperture is reported in [6]. It is this situation that is realized for the function of interference orders $h_D(x)$ at the points $x = s/2 + nD$, which enables the wavefront tilt to be determined.

Therefore, the algorithm of measuring the light beam wave front can be reduced to the following sequence of operations:

(i) Synthesis of a new beam satisfying the condition (4) from the initial light beam with the wave front $\varphi(\mathbf{x})$ and the aperture $[0,D]$ using successive mirror reflections.

(ii) Production of a lateral interferogram and reconstruction of the function of interference orders $h_D(x)$ from it. In practice, a double mirror reflection from the $\varphi(x)$ domain boundaries is sufficient. This provides

information on the function $h_D(x)$ behavior over half of a period $[s/2, s/2 + D]$, which is sufficient for complete determination of $h_D(x)$ because $h_D(x) = h_D(D - x)$. Apparently, a restriction $s < D$ should be imposed on the shear magnitude in this case.

(iii) Reconstruction of the functions $\psi(x)$ and $\varphi(x)$ from the known function $h_D(x)$ using a spectral method based on equation (3).

To conclude this section note that condition (4) is automatically satisfied for a rotational shear interferogram when it is interpreted along the circles centered at the rotation axis. However, such an interferogram used for reconstruction of a two - dimensional wave - front should be supplemented by a lateral or radial shear interferogram with its characteristic information loss.

Thus the method of synthesis of an interferogram in the general case allows to avoid the information loss of the second and third type. However, a correct adjustment of the interferometer makes it possible to eliminate also the first type of losses.

In a synthesized interferogram the function $\psi(x)$ and the corresponding interference order function $h_D(x)$ are periodic, therefore, their spectra are discrete. For a discrete spectrum expression (1) takes form:

$$H_D(\nu_k) = (1 - e^{-2\pi k s/T})\,\Phi_D(\nu_k) \qquad (5)$$

where: $\nu_k = k/T$, $T = 2D$ is the interference pattern period and $k = 0, +1, +2, \ldots$

It is easy to notice that an interferometer with a synthesized aperture loses the sensitivity to all spatial frequencies ν_k for which the equality $p = ks/T$ is satisfied, where p is an integer. In particular, at $s = T/2$ this equality is satisfied for all even harmonics ν_{2k}, i.e. when carrying out the synthesis operation a reverse shear interferogram is produced, allowing to obtain information only on odd harmonic components of the wavefront.

Formally, such relationship of s and T can be selected that the equality $p = ks/T$ will not be satisfied at any p and k integers (s/T is an irrational number). In this case, the spectrum $\Phi_D(\nu_k)$ will not contain the harmonics for which the factor $(1 - e^{-i2\pi\kappa s/T})$ in expression (5) turns into zero, thus

the loss of information will be completely eliminated. In practical use, it is sufficient to choose such relationship of s and T, so that the condition $p = ks/T$ would be satisfied only at sufficiently high k for the frequencies $\nu_k = k/T$ being beyond the domain of spatial resolution of optical system and wavefront reconstruction.

Thus, using a synthesized interferogram at a certain relationship of T and s values we can obtain information necessary for complete reconstruction of a light beam wavefront.

4. Practical implementation of the method

The proposed method of synthesis of a shear fringe pattern was used for wave - front analysis of a light beam transmitted by a test object with phase inhomogeneities. The optical setup consisted of three mirror interferometers of the Mach - Zehnder type used in tandem (see Fig. 3b, d and f). The mirrors in two interferometers were replaced by prisms. The first pair of reverselateral shear interferometers formed a light beam with the wave front satisfying the condition (5). The third interferometer produced the lateral shear fringe pattern in the detection plane. the sequence of wave front synthesis for the beam passing through the optical system is shown schematically in Fig. 3a, c, e and g. The synthesized

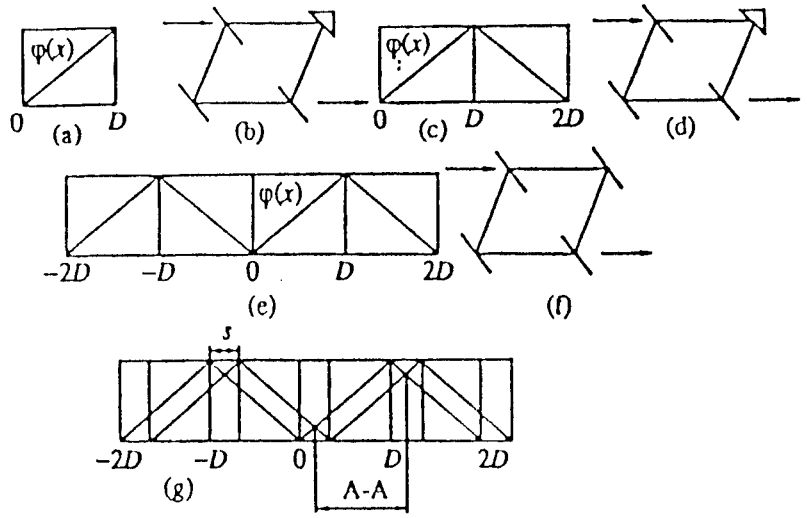


Fig.3. Diagram of optical synthesis of a shear interferogram.

lateral shear interferogram and the respective interferogram recorded using a reference beam (Michelson) interferometer are shown in Fig. 4a, b.

The shear interferogram was interpreted along the section parallel to the shear vector. One such section is shown in Fig. 4 by the line A-A. The

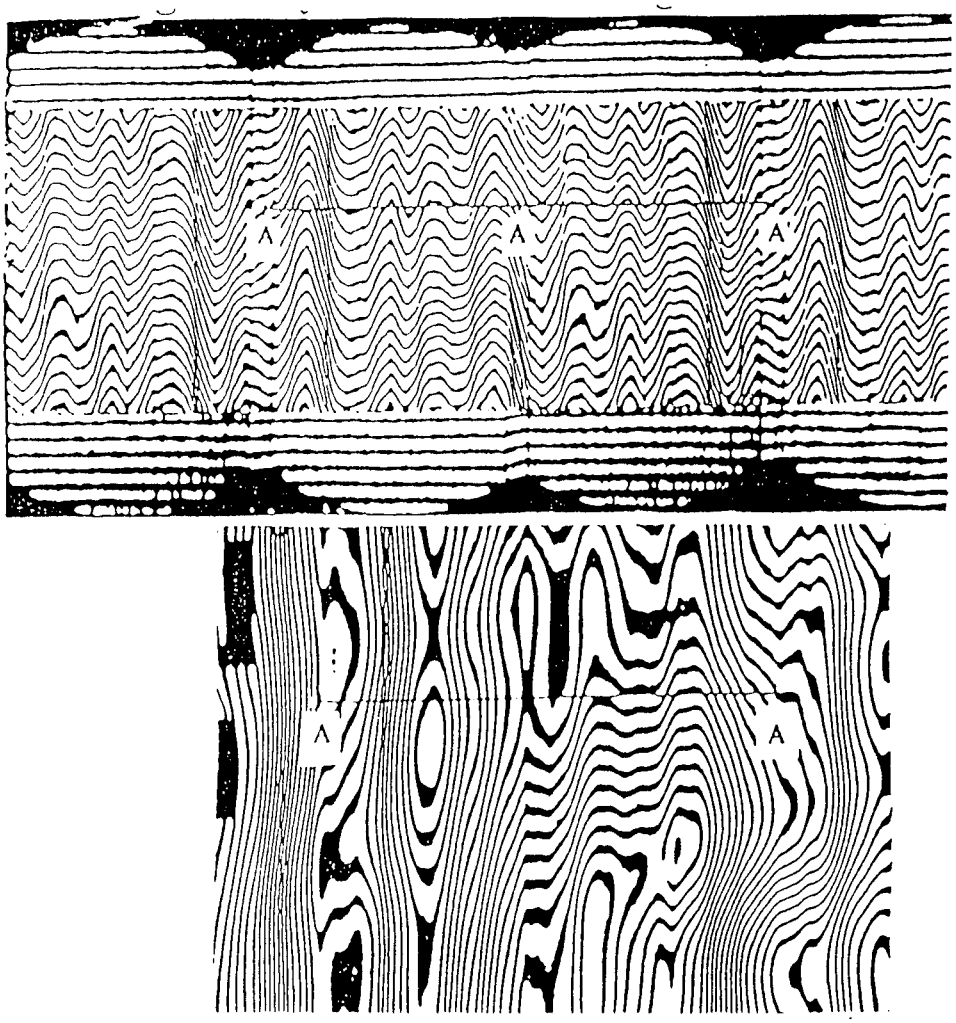


Fig.4. Interferograms of a phase object obtained by interferogram synthesis shown in Fig.3. (a) and using a reference beam for the same object (b).

points Λ confining the segment in the shear interferogram (Fig. 4a) belong to the region of reverse shear and correspond to its zero value. The interference fringe in these points does not change its position relative to regardless of the phase aberrations caused by the interference fringe in the absence of distortions introduced by a phase object.

Figure 5 shows the results of the shear interferogram interpretation along the path Λ - Λ using the spectral method based on equation (5) with the step $D/N << s$. The reconstructed wave front $\psi(x)$ that is identical to $\varphi(x)$ at the segment $[0,D]$ is shown by curve 1; curve 2 is the function

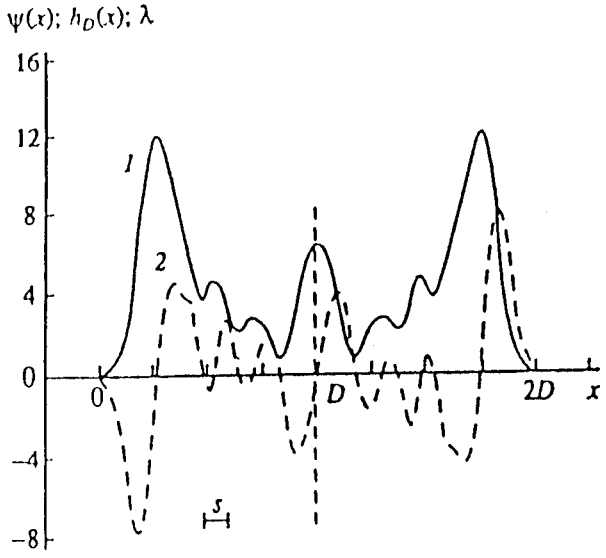


Fig.5. Result of interpretation of the synthesized lateral shear interferogram $\psi(x)$ (1) and the function of interference orders $h_D(x)$.

of the interference order $h_D(x)$. These data coincide with the interpretation of the interferogram depicted in Fig.4b with an accuracy determined by the technique used for interpretation of deference wavefront interferograms.

For experimental illustration of the informative character of interferograms produced by shear interferometer with shear aperture synthesis, phase (bleached) holograms were manufactured and placed

within the object plane of an interferometric synthesizing system similar to that described in [1]. The holograms represented a one-dimensional phase grating similar to a sinusoidal one. Fig.6 shows interferograms of one of these holograms produced with different adjustments of the interferometer. All the interferograms are presented for the domain of definition of the interference order function $[0,D+s]$. Since the function $h_{D}(x)$ is odd in respect to the points $x=n$, $D+s/2$, $n=0,1,2,...$, this information is sufficient for a full reconstruction of $h_{D}(x)$.

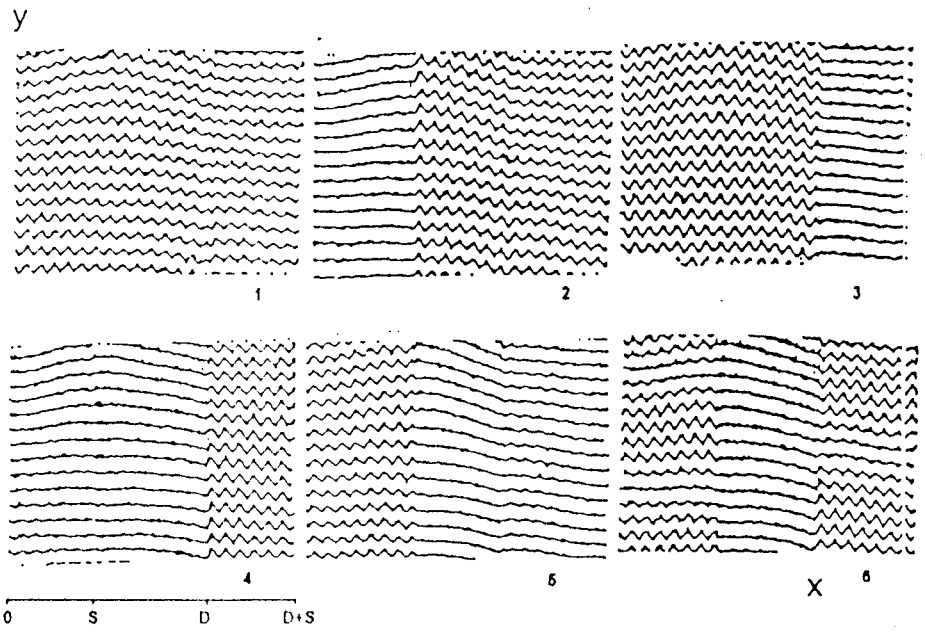


Fig.6. Shear interferograms of a sinusoidal phase object.

On each interferogram three characteristic segments can be distinguished. The segment of the length $[s,D]$ belongs to an ordinary lateral shear interferogram, and in the intervals $[0,s]$ and $[D,D+s]$ the reverse shear interferograms are produced. The interferograms 1-3 are produced at the magnitude of the shear s being not multiple of the period of the object phase spatial modulation. For the interferogram 1, the hologram location was chosen in such a way that the phase modulation was observed at the three segments of the interferogram necessary for wavefront reconstruction. In this case the curve of interference fringes is

of sinusoidal character with a period equal to that of the object phase modulation. Phase aberrations on the size of the hologram are due to inhomogeneity of the glass substrate. Note that a high sensitivity of the interferometer to the phase aberrations is due to the large magnitude of the shear s.

On interferogram 2, the hologram position makes the sinusoidal phase modulation even in respect to the zero shear point $x=s/2$ at the left segment of the interferogram, therefore, the information on the modulation of this segment is absent. At the middle segment the information remains intact, since the shear magnitude and the modulation period are not multiple. In respect to the zero shear point at the right segment of the interferogram $x=D+s/2$ phase modulation is odd and therefore a corresponding fringe modulation is observed. The interferogram 3 is different from the second one only by variation of phase modulation parity in respect to zero shear points at the extreme segments of the interferogram.

On the interferograms 4, 5 and 6 the lateral shear magnitude is multiple of the modulation period, therefore, at the middle segment of the interferogram the information on the latter is absent. However, with the interferometer adjustment the relationship of s and $T=2D$ is chosen so that in Fourier spectrum of the wavefront function of the test beam there were no harmonics with frequency $\nu=1/s$. Therefore, the information on the wavefront modulation on the interferogram remains intact. It is shown as a fringe bend at the right segment of the interferogram 4 or at the left segment of the interferogram 5 depending or the parity of wave phase modulation in respect of the zero shear points at these segments. The interferogram 6 was produced with the deviation of the direction of the constant phase of holographic grating from the direction perpendicular to the shear.

Like in case of the interferograms 4 and 5, the middle segment contains no information on phase modulation of the wavefront due to the shear being multiple to the modulation period. The extreme segments, in turn, contain such information depending or parity variation in respect of their zero shear points.

Thus the mentioned synthesized lateral shear interferograms illustrate their property to reflect the aberrations of the light beam wavefront with a characteristic period multiple of the shear magnitude with the interferometers adjustment according to the above recommended ratio of the aperture size to shear magnitude.

5. Conclusion

The proposed [1] method of synthesized interferogram of lateral shear, in particular, with an additional condition of selecting the relation ship of the shear magnitude and linear size of the aperture, described in this work, allows to perform a full reconstruction of the light wave shape in the observation plane of the interference pattern.

Since the synthesized by the proposed method interferogram reflects the entire spectrum of the spatial frequencies of the wavefront, it is sufficient to have in a shear interferometers a limited (down to a single) number of definitions of the shear magnitude. These peculiarities of the synthesized interference pattern make it possible to produce compact, vibration-resistant and easily-operated light beam wavefront analyzers without light beam information losses.

6. References:

1. Shekhtman, V.N., Rodionov, A.Yu., and Pel'menev, A.G.(1994) Optics and Spectroscopy, 76, No 6, 884-888.

2. Kromin, S.I., Pel'menev, A.G., Shekhtman, V.N. (1988) Abstracts of Papers, Vsesoyuznaya Konferentsiya po Optike Laserov (All-Union Conf. on Laser Optics), , Abstracts, p.149.

3. Hariharan, P. (1988)Appl.Opt., 27, No17, 3594-3596.

4. Shugang Lin, Zenquang Li, and Yu Liu(1990) Acta Opt. Sin., 10, No3, 267-275.

5. Shekhtman, V.N. (1982)Opt.-Mekh.Prom-st., No10, 1-4.

6. Kolyshkina, L.I., Kromin, S.I. and Shekhtman, V.N. (1986) Opt.-Mekh.Prom-st., No10, 51-54.

EXPERIMENTAL INVESTIGATIONS OF THE OUTPUT BEAM PROPERTIES FROM A HIGH POWER CW CO_2 LASER

G. RABCZUK, P. KUKIEŁŁO, G. ŚLIWIŃSKI
Polish Academy of Sciences, Institute of Fluid-Flow Machines, Fiszera 14, Pl 80-952 Gdańsk, Poland

1. Introduction

Results of a laser material processing are strongly affected by spatial properties of a laser beam, including the beam waist dimensions, far-field divergence, the amplitude and phase of a mode distribution. They determine the quality of a beam, its propagation and focusing properties. A correct specification of the basic beam parameters is required for the proper designing of a beam handling optics as well as for the optimization and efficient controll of the particular technological process.

The the real laser beam characteristics are difficult to predict theoretically due to their complex mode structure as well as rather unpredictable influence of the laser optical components on the beam parameters, especially in the case of the high power beams. Therefore the beam measurements are necessary.

The purpose of our measurements was to determine the propagation and focusing characteristics of the output beam from an industrial, transverse-flow, cw CO_2 laser working in the range up to 1.5kW [1]. The laser excited by dc glow discharge operates with a multipass stable resonator. The focusing conditions of the output beam were investigated for two resonator configurations described by the different optical and active medium length. Standard knife-edge method was adopted for determination of the laser output beam characteristics. From the recorded far-field laser beam caustics the propagation factor, far-field divergence as well as focused beam parameters were concluded and compared for both investigated resonator configurations.

2. Resonator configurations and theoretical beam properties.

The beam of radiation is extracted from the laser by a stable plano-concave resonator folded in the flow direction by means of flat reflectors into three- or four-pass configuration. The resonator optics comprises mirrors of circular

R. Kossowsky et al. (eds.), High Power Lasers – Science and Engineering, 449–454.
© 1996 *Kluwer Academic Publishers. Printed in the Netherlands.*

symmetry with the effective diameter of 2 cm. In the three-pass configuration the rear high reflectivity, flat mirror is placed at 3.9 m from the concave-convex ZnSe outcoupler of 50% reflectivity. In the four-pass configuration the resonator mirrors are separated by the distance of 5.2 m. In both cases the radii of curvature of the concave-convex outcoupler surfaces are 10 and 7.5 m. The outcoupler acts as a positive lens of a long focal length, collimating the resonator beam. The active medium length is 3 m and 4 m, respectively.

In the study of a real laser beam characteristics it is useful to specify the properties of the corresponding, theoretical Gaussian beam, describing an ideal limit that can be approached by a laser. Real beams have diameter-divergence products larger than the ideal Gaussian beam by a factor of M^2 [2]. The gaussian mode parameters are uniquely determined by the resonator mirrors curvatures and their distance. For the considered resonators the TEM_{00} mode diameter at the plane of the outcoupler, predicted by the Gaussian beam optics is equal to 10.4 mm for n = 3 configuration and 11.9 mm for n = 4. The waist beam diameters, located at the plane of the rear mirror are only slightly different and they are 8.1 and 8.2 mm. Respectively; the far field divergence values (full angle) are 1.7 and 1.6 mrad. These resonator beams are transformed by the meniscus outcoupler to the beams of lower divergence (1.4 and 1.3 mrad) and the beams diameters at the end of the optical train are abt. 13.9 and 15.4 mm . If the lens of 127 mm focal length is used (at the distance of 4.3 m from the laser enclosure) the theoretical focus has a diameter of 0.14 mm for n = 3 and 0.12 mm for n = 4 (with spherical aberrations taken into account).

Although the TEM_{00} beam parameters calculated for the cavities under consideration are only slightly distinct the real experimental beams, both of multi-mode structure, differ considerably. This is mainly due to the differences in the diffraction losses of the systems, which are described by the Fresnel number (or the ratio of the resonator mirror diameter and the gaussian mode size over the concave outcoupler).

The theoretical mode field distributions found as the superposition of the Laguerre-Gaussian modes with different ratio coefficients of the modes content are shown on Fig. 1. They simulate, approximately, the experimentally recorded intensity patterns. The analysis of the theoretical patterns indicates that the TEM_{00} and TEM_{02}^* modes are mainly responsible for the beam profile from the three-pass cavity while TEM_{00} and TEM_{01}^*dominate when the laser operates with the four-pass resonator. Then; as it is predicted by the theory [3] the propagation factor is $M^2 \leq 2$ for the beam from the four-pass cavity and $M^2 \leq 3$ when the three-pass cavity is employed. As the uderlying gaussian beam parameters are given, the respective characteristics of these theoretical multimode beams can be calculated. These theoretical laser beam parameters can differ considerably from the experimental ones because the exact prediction of the mode

content is difficult. Also optical distortions due to heat absorbed by the laser optics can influence the beam parameters, especially for high power lasers.

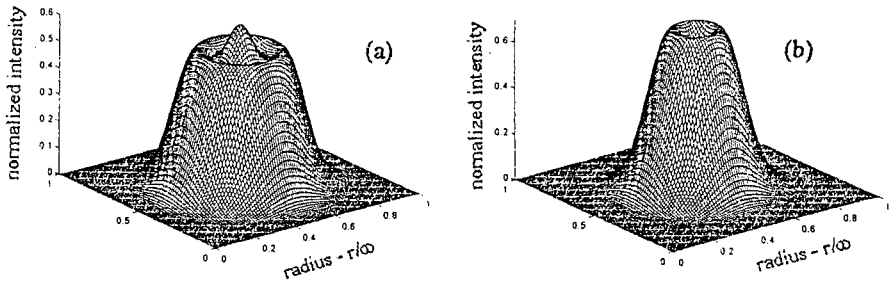


Figure 1. Theoretical mode distributions simulating the experimental patterns recorded for investigated resonators;
(a) three-pass cavity, $M^2 \approx 2.4$, $\alpha TEM_{00} + \beta TEM_{02}^*$, $\alpha / \beta = 1.5$
(b) four-pass cavity $M^2 \approx 1.6$, $\alpha TEM_{00} + \beta TEM_{01}^*$, $\alpha / \beta = 1.5$

3. Laser measurements

The beam parameters were measured in the laser processing region. The schematic diagram for the experimental condition is shown on Fig.2.

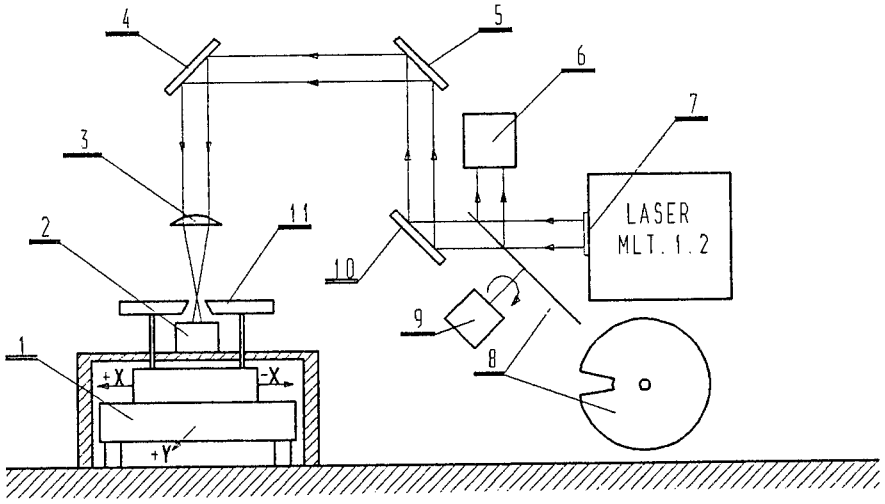


Figure 2. Schematic diagram of the experimantal setup; (1) X-Y table, (2) power detector, (3) focusing lens, (4), (5), (10) flat mirrors, (6) absorber, (7) output window , (8) chopper disc, (9) chopper engine, (11) knife

The beam emitted from the resonator after passing through the ZnSe window (7), closing the vacuum discharge chamber, is directed by three reflectors (4,5,10) of the beam guiding system to the ZnSe focusing lens (3) of 127 mm focal length. The length of the optical train, measured from the laser enclosure is 4.3 m.

The scanning knife-edge technique [4] was implemented for measuring the width of the laser beam at various distances from the focusing lens. A moving edge (11) cuts the beam in front of a fixed, large area power detector (2) so that the detector measures the transmitted power as a function of the edge position. The knife edge was translated by a mechanical, numerically controlled X-Y table (1) at a step of 0.05 mm along the principal directions perpendicular to the beam propagation axis. In order to reduce the power density at the surface of the power meter as well as to avoid the effect associated with the heating of the knife edges which are located in the focus region, the beam was modulated at the laser output by a specially designed rotating chopper disc (8-9). The aperture in the disc was chosen experimentally; properly larger than the beam size at the laser output, in order to minimalize diffraction influence on the beam parameters. The ratio of the aperture dimension and disc diameter was selected to reduce the power up to 5% of the cw laser output power.

From the curves fitting to the experimental data for the detected power versus the knife position, a distance defined by the points at which 16% and 84% of the total beam power is intercepted by the knife edge was found. This distance multiplied by the clip coefficient of 2 is a measure of a beam diameter. The associated scale factor for converting the obtained beam diameter value into the second moments width of the laser beam was choosen in agreement with ISO standards [5]. The above procedure was used for determination of the beam size at different knife locations in realation to the lens focus position.

The laser beam parameters were concluded from the law of the multimode beam propagation from a stable-cavity through any arbitrary paraxial optical train, saying that the square of the beam diameter increases linearly with the square of the distance away from the waist. The three beam constants (the beam waist, its location and M^2 value) can be obtained, in principle, by measuring the beam diameter at three different locations along the propagation axis. Under experimental conditions more measurement points on both sides of the focus are required in order to minimalize the influence of diffraction effects. In our case the beam diameters were measured at seven locations, then a data smoothing routine was used to generate a hyperbolic fit curve from which the parameters were concluded.

The results of the measurements are comprised on Fig. 3, where the focused beam caustics measured for the three- and four-pass resonator are presented. In the case of the four-pass resonator the M^2 parameter was estimated to be in the range from 2.2 to 2.4., while for the three-pass resonator the value of M^2 concluded from our measurements was abt 3.2-3.4.

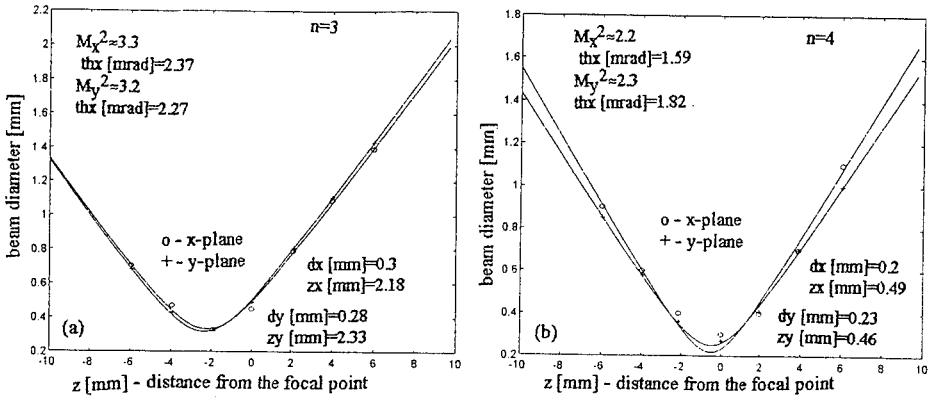


Figure 3 Beam diameter vs distance from the focal plane of the focusing lens (f=127mm), measured for the 1.2 kW CO_2 laser operating with (a) -three-pass and (b) four-pass stable plano - concave resonator

The far field divergence angles of the laser source beams (indicated on Fig.3 as *thx* and *thy*) were abt 1.6-1.8 and 2.2-2.4 mrad, respectively. The data concerning the waist size (*dx* and *dy*) and its location (*zx*, *zy*) for the focused beams are also gathered on the respective figures. In the case of the three-pass cavity with Fresnel number of 2.42 the output beam contains higher order modes than the beam emitted from the four-pass cavity (of Fresnel number equal to 1.81) characterized by the higher diffraction losses. It results in the higher value of M^2 parameter for the beam emitted from three-pass resonator. For both investigated resonators the values of M^2 are higher than those predicted theoretically. It can be explained by the contribution of higher order modes than those only assumed in the model. It is also known that the knife-edge method become gradually less accurate for the increasing higher order mode content or poorer-quality beams. The error of our measurements of the laser beams parameters is estimated to be abt +/- 10%. The values measured in the x- and y-direction are only slightly different. The ratio of the measured beams diameters in x and y is smaller than 1.15/1 and the beams may be cosidered as circular. The measured waist size of the focused beams seems to be correct, and correspond within an experimental error to those estimated on the base of the laser cutting results.

4. Concluding remarks

As the results of the performed analysis the propagation characteristics of the output beam were estimated for an industrial transverse-flow cw CO_2 laser employing a stable multipass resonator. The beam properties were compared for

two different resonator configurations of different diffraction properties described by Fresnel number and stability parameter.

Measurements confirmed that the resonator of lower Fresnel number and better conditions for mode selection alows for the better quality beam. The lower far-field divergence and smaller focus spot were measured, and better technological effects were recorded when the four-pass cavity was used. But in this case the conditions of the long-term, stable laser operation are more difficult to obtain due to the higher sensitivity of a longer resonator to any of the optical cavity and medium distortions. The experimental results agree well with theoretical predictions.

In order to improve the beam quality from the resonators considered, the Fresnel number of the systems should be reduced (e.g. by inserting a properly designed mode selecting diaphragm) which will allow to aproach the conditions for TEM_{00} oscillation. High quality beam operation of the laser at the nominal output power level (1.5kW) requires simultaneously some optimization of the laser excitation system.

5. References

1. Kukiełło, P., Rabczuk, G. (1992) An industrial transverse flow 1.2kW CO_2 laser, *Electronica (in polish),* **33**, 14-17
2. Siegman , A.E. , (1990) New Developments in laser resonators, in SPIE Proc. **1224,** D.A. Holmes (ed.) *Optical Resonators,* pp. 2-14
3. Sasnett, M.W., (1989) Propagation of multimode laser beams - the M^2 factor, in Hall and P.E.Jacson (eds.) *The Physics and Technology of Laser Resonators,* Adam Hilger, Bristol and NY, pp. 132-142
4. Siegman, A.E., Sasnett, M.W., and Johnston, T.F., (1991) Choice of clip levels for beam width measurements using knife-edge techniques: *IEEE J. Quantum* Electronics, **27,** 1098-1104
5. ISO-Norm, Document ISO/TC 172/SC 9 WG 1, (1991), Test method for width, divergence and radiation characteristic factor of laser beam

THE APPLICATIONS OF A NEAR-IR LASER TO RAMAN SPECTROSCOPY: FT-RAMAN SPECTROSCOPIC STUDIES OF ADSORBED SPECIES BY CLAYS.

T. BULAT*, S. AKYÜZ*, T. AKYÜZ** and J. E. DAVIES+

* Physics Department, Istanbul University, Vezneciler 34459, Istanbul, Türkiye

** Çekmece Nuclear Research and Training Center, P.K. 1 Havaalanı, Istanbul, TÜrkiye

\+ Environmental Science Division, Lancaster University, LA1 4YQ, U.K.

ABSTRACT

This paper reviews the investigation of adsorption of bipyridyls (4,4'- bipyridyl and 2,2'- bipyridyl) by some natural clay minerals from Anatolia (Turkey), using vibrational spectroscopy. The advantages of using FT-Raman spectrometers operating by near-IR laser excitation has been discussed.

1. Introduction

The use of IR spectrocopy for the analysis of clays is well known, and has been established over a long period of time. However, Raman spectroscopy has found little use to date for the study of clays, due to the weakness of the Raman scattering signal, the occurrence of thermal or photodegradation of the sample, and the occurence of fluorescence which swamps the Raman signal, although it has several advantages. The advantages of Raman lie in the fact that it detects primarily the symmetric vibrations and results in simpler spectra without overtone and combination bands.

Recently, FT-Raman spectrometers, operating by near-IR laser excitation, has been introduced to overcome the problems: Fluorescence is dramatically reduced, signal-to-noise can be improved by the co-adding scans and the use of the longer wavelength of exciting light reduces the problems of sample degredation under the laser. In this study both FT-Raman and FT-IR spectra of adsorption of bipyridyls (4-4' - and 2-2' bipyridyl) by sepiolite and smectite group clay minerals from Anatolia has been investigated. Raman spectroscopic investigation has been found to be very useful in shedding light on the host-guest interaction, since it enables one to analyze clearly the 1100-950 and 600-400 cm^{-1} regions of the spectra of adsorbed molecules, regions which are obscured in the IR spectrum by the host vibrational modes of aluminosilicate[1].

R. Kossowsky et al. (eds.), High Power Lasers – Science and Engineering, 455–460.
© 1996 *Kluwer Academic Publishers. Printed in the Netherlands.*

2. Experimental

Bipyridyl treated samples were prepared by immersing air-dried clays in a benzene solution of bipyridyl (B.D.H) in sealed bottles, at room temperature, for two days. They were then filtered and washed several times with benzene and dried[1, 2]. During the course of this study it was found that bipyridyl molecules can also be intercalated in the clays by solid-solid exchange reactions.

The FT-IR spectra of KBr discs of samples were recorded on a Nicolet 510 spectrometer. The FT-Raman spectra were recorded on a Bruker IFS 66 FT-Raman instrument using 1.06 μm excitation from a Nd:YAG laser. Five hundred scans were accumulated at 4 cm^{-1} resolution using a laser power of 100 mW. No spectra could be obtained using visible 488.0 and 514.5 nm excitation due to strong fluorescence.

3. Results and Discussion

Free 4-4' bipyridyl and 2-2'-bipyridyl (which is in trans conformation) molecules are in D_{2h} and C_{2h} point groups, respectively, thus both are centro-symmetric (see Figure 1 a and b). For molecules with a center of symmetry, transitions that are allowed in the Raman spectrum are forbidden in the IR and conversely, transitions that are allowed in the IR spectrum are forbidden in the Raman. If free 4,4' - bipyridyl molecule coordinates to a metal as unidentate ligand its symmetry drops to C_{2v} (which is not centro-symmetric), but if it coordinates to two identical metal atoms as bidentate ligand its symmetry point group is not altered and be D_{2h} as free molecule. Its well known[3] that 2,2' bipyridyl molecule is in trans position while it is free (C_{2h}) thus centro-symmetric but it turns to cis position when it coordinates to a metal as bidentate ligand so dpors to C_{2v} point group which is not centro-symmetric. Therefore it is possible to obtain information about the coordination state of the adsorbed 4,4'-bipyridyl and 2,2'-bipyridyl molecules by investigation of both IR and Raman spectra of the clays. On the other hand the vibrational spectroscopic studies on the adsorption of pyridine[4], 4,4'-bipyridyl[5] and 2,2'-bipy-

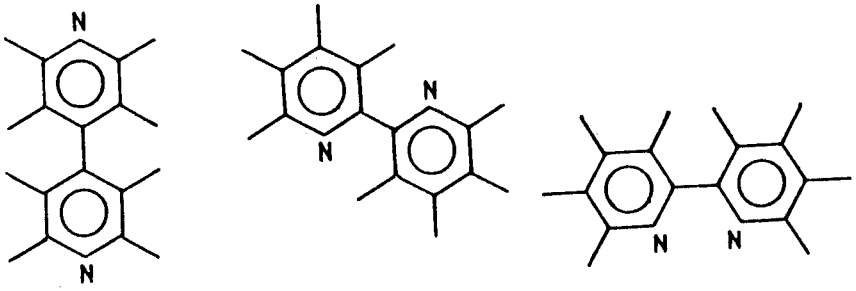


Figure 1: 4,4'-bipyridyl (a) and 2,2'-bipyridyl (b) molecules

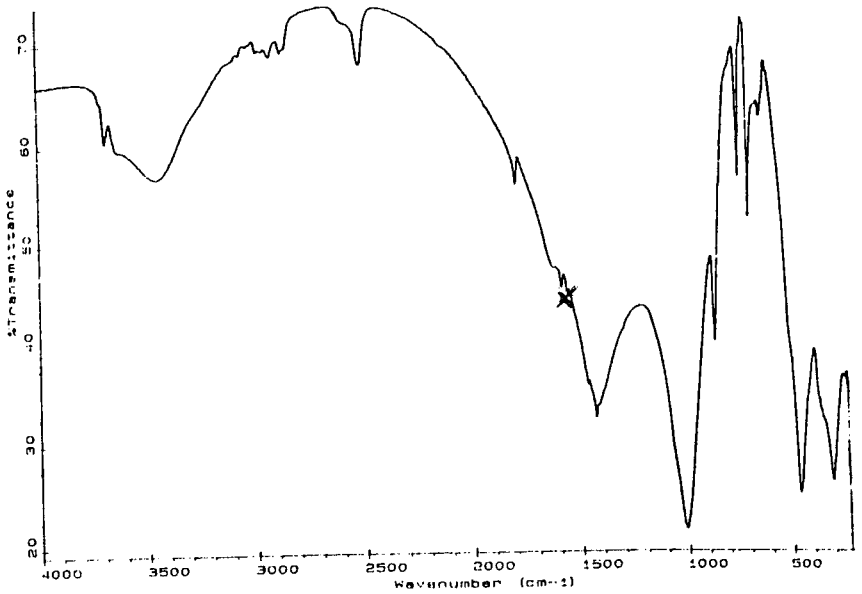


Figure 2: The IR spectrum of 2,2'-bipyridyl treated hectorite.
The 2,2'-bipy bands are indicated (x)

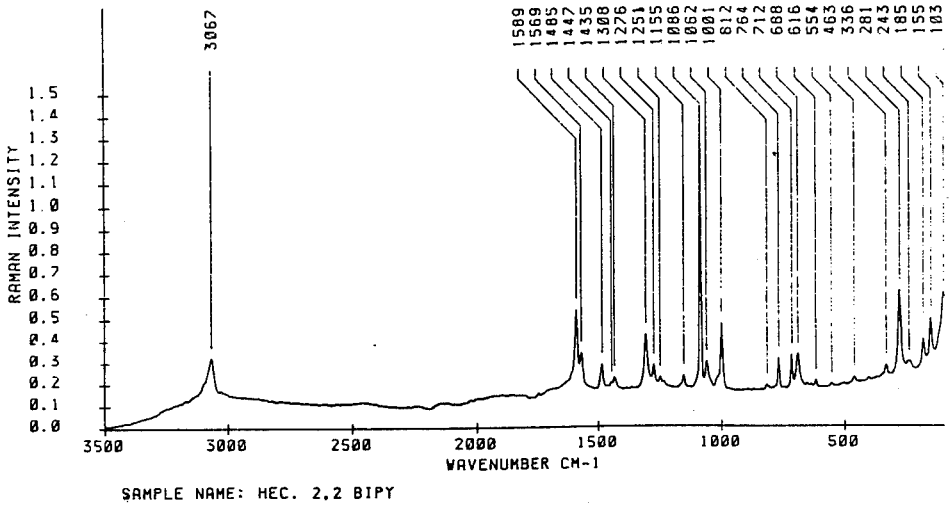


Figure 3: The Raman spectrum of 2,2'-bipyridyl treated hectorite.

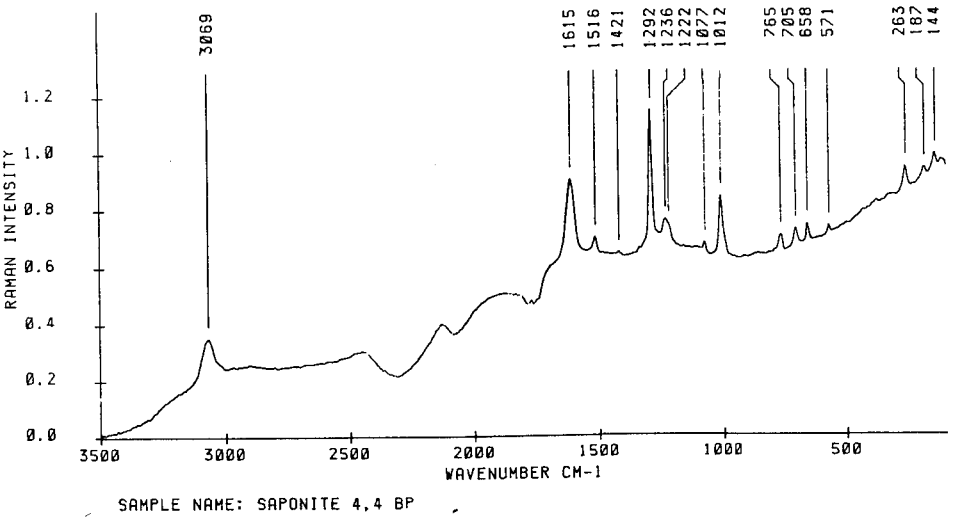


Figure 4: The Raman spectrum of 4,4'-bipyridyl treated saponite

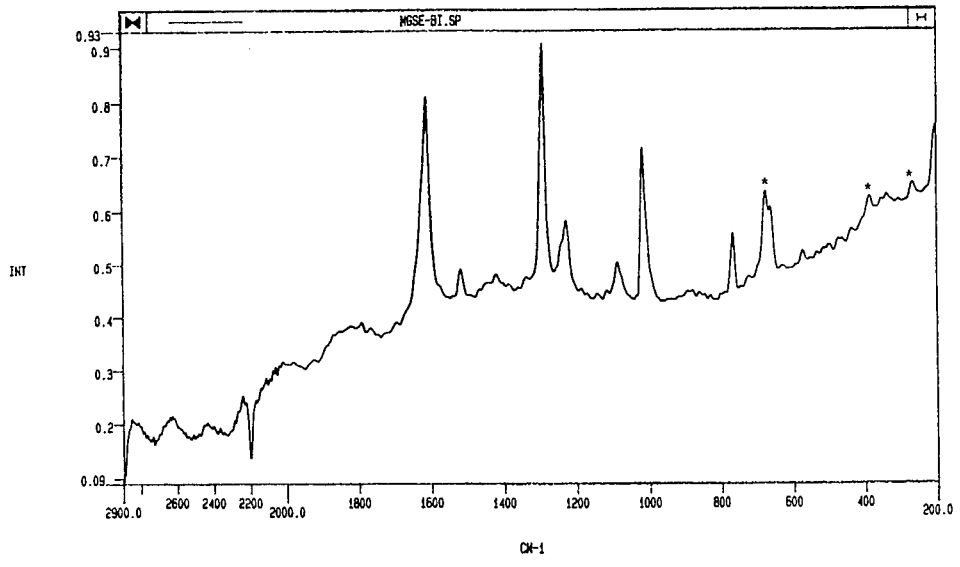


Figure 5: The Raman spectrum of 4,4'-bipyridyl treated sepiolite.
Marked bands belong to host structure

ridyl[6, 7] on oxide surfaces showed that the ring breathing mode of the aromatic molecule around 990 cm^{-1} and the two ring stretching modes observed in 1500-1600 cm^{-1} region are very sensitive to the interaction with the absorbing sites. They exhibit upward frequency shifts upon coordination of the lone pair on nitrogen atom to Lewis acidic sides or upon formation of H-bonds through the nitrogen lone pair to surface OH groups. However, the ring breathing mode of bipyridyls (around 990 cm^{-1}) is obscured by the broad absorption band of the silicate framework (ν (Si-O)) in the IR spectra of bipyridyl treated clays, but it can be clearly observed in the Raman spectra. Figure 2 shows the IR spectrum of 2,2'-bipyridyl treated hectorite and Figure 3, the FT-Raman spectrum of the same sample. Although we could hardly pick up the few bands of the adsorbed molecule at the IR spectrum (Figure 2), most of the vibrational modes are clearly observed in the Raman spectrum (Figure 3).

The FT-Raman spectrum of 4,4'-bipyridyl treated saponite and sepiolite are given in Fifure 4 and 5 respectively.

The rign breathing mode in-phase component of 4,4'-bipyridyl (Ag) was observed at 1000 cm^{-1} in the Raman spectrum of crystalline 4,4'-bipyridyl[8] and was observed as a strong band around 1009-1012 cm^{-1} in the 4,4'-bipyridyl treated sepiolite, bentonite, hectorite and saponite. On the other hand the coordination sensitive ring stretching modes out-of-phase components of 4,4'-bipyridyl were observed around 1602-1603 (ν_3 ; ν_{ring} , B_{3u}), 1536-1539 (ν_{12} ; ν_{ring} , B_{2u}) and 1490-1492 cm^{-1} (ν_4 ; ν_{ring} , B_{3u}) in the IR spectrum of 4,4'-bipyridyl treated clays, wheras the corresponding modes were observed at 1598, 1532 and 1481 cm^{-1}, respectively, in the IR spectrum of microcrystalline 4,4'-bipyridyl. Thus, spectroscopic results indicated that the vibrational wevenumbers of adsorbed bipyridyl exhibited all the characteristics of coordinated molecule. In the case of sepiolite, no coincidences were observed between the IR and Raman wevenumbers of adsorbed 4,4'-bipyridyl, showing that it possessed a centre of symmetry. However in the cases of hectorite, saponite and bentonite few coincidences were observed indicated that absorbed molecule did not possess a centre of symmetry. Based on these spectroscopic investigations we proposed that the molecules adsorbed on sepiolite are centro-symmetric and act as a bidentate ligand, whereas the molecules adsorbed on hectorite, saponite and bentonite coordinate to exchangeable cations as monodentate ligand.

In the case of adsorption of 2,2'-bipyridyl by clays we have observed upward shifts up to 18 cm^{-1} in the coordination sensitive ring stretching modes of 2,2'-bipyridyl in the vibrational spectra of treated clays in comparison to those of free molecule. Thus the vibrational wavenumbers of adsorbed molecule were found to be closer to those of coordinated molecule, than the free molecule. We have also observed 2,2'-bipyridyl anion bands, but comparatively very low.

Conclusion

It is found that both IR and Raman spectroscopic analysis sheds much light on the nature of the surface species formed on clays. The use of an FT-Raman spectrometer enables the Raman spectra of these samples to be obtained and in particuler the vibrational modes of the bipyridyl molecules in the 950-1100 cm^{-1} region, which is obscurd by broad absorption band of the silicate framework in the IR spectre of the clays.

Acknowledgement

We would like to thank Dr. Paul Turner of Bruker Spectropsin Limited for recording the Raman spectra.

4. References

1. Akyüz S., Akyüz T. and Davies J.E.D. (1993) A Vibrational Spectroscopic Study of the adsorption of 4,4'-bipyridyl by sepiolite and smectite group clay minerals from Anatolia, *J. Incl. Phenom.* **15,** 105-119.
2. Akyüz S., Akyüz T. and Davies J.E.D. (1994) Adsorption of 2,2'-bipyridyl. onto sepiolite, attapulgite and smectite group clay minerals from Anatolia, *J. Incl. Phenom.* **18,** 123-135.
3. Neto N., Moniz-Miranda, M. Angeloni L and Castellucci E., (1983) Normal mode analysis of 2,2'-bipyridyl, *Spectrochimica Acta* **39A** 97-106.
4. Morterra C., Ghiotti G., Boccuzzi F. and Coluccie S. An İnfrared Spectroscopic investigation of the surface properties of magnesium aluminate spinel *J. Catalysis,* **51,** 299-313.
5. Coluccia S., Garrone E. and Morterra C., (1981), Adsarption of 4,4'-bipyridyl *Z. Phys. Chem. Neue Folge,* **124,** 201-206.
6. Coluccia S., Chiorino A., Guglielminotti E. and Morterre C., (1979) Adsorption of 2,2'-bipyridyl on magnesium oxide and calcium oxide, Infrased spectre of neutral and anionic surface species, *J. Chem. Soc. Faraday Trans I,* **75,** 2188-2198.
7. Bagshaw S. A. and Cooney R. P., (1994), FTJR and Roman Spectroscopic investigation of 2,2'-bipyridine adsorption on silica, alumina, zirconia and titania, *J. Mater. Chem.* **4(4),** 557-563.
8. Topaçlı A. and Akyüz S., (1995), 4,4'-bipyridyl vibrational assigaments and force field, *Spectrochimica Acte* **51A,** 633-641.

PART IV: Applications

HIGH-POWER LASERS IN MATERIALS PROCESSING - AN AUTOMOTIVE PERSPECTIVE

D. M. ROESSLER
General Motors Research & Development Center
30500 Mound Rd., Warren, MI 48090-9055, USA

Abstract

We broadly review the growth and current status of laser processing in the automotive industry. The first section introduces the primary aspects of the interactions of laser beams with materials and the concept of different processing regimes. The main part of the review draws heavily on relatively high-powered laser applications within the automotive industry, especially surface treatment, welding, and cutting. The concluding section speculates on future developments, in terms of both laser technology and vehicle manufacture.

1. Introduction

In 1969, less than ten years after the first operation of a manmade laser, the automobile industry began using lasers as manufacturing tools on factory production lines. A steady expansion of activity since then has led to a situation where, although precise numbers are not available, well over 4,000 lasers are currently engaged in machining activities related to the automotive industry. These account for about 15-20% of all lasers involved in material processing but exclude lasers used for measurement, inspection, and other non-machining purposes. We will regard as automotive lasers any which are used for materials processing in the fabrication or assembly of vehicles, whether by the automobile manufacturers themselves or by their suppliers.

Figure 1 shows the steady increase in the total number of automotive lasers installed since the first three in 1969. Note the semilogarithmic plot: although the ***rate*** of increase may have slowed in recent years, there are no signs that the field has matured or that demand is slackening. Although North America currently has about a third of the world's automotive lasers, Japan has over half (Figure 2). This is all the more remarkable because there was little use of lasers in the Japanese automotive industry until the early 1980s. While Europe has most of the remaining lasers, the numbers are also increasing in the rest of the world. For example, over forty are being used just in Brazil for automotive cutting and welding.

R. Kossowsky et al. (eds.), High Power Lasers – Science and Engineering, 463–504.
© 1996 *Kluwer Academic Publishers. Printed in the Netherlands.*

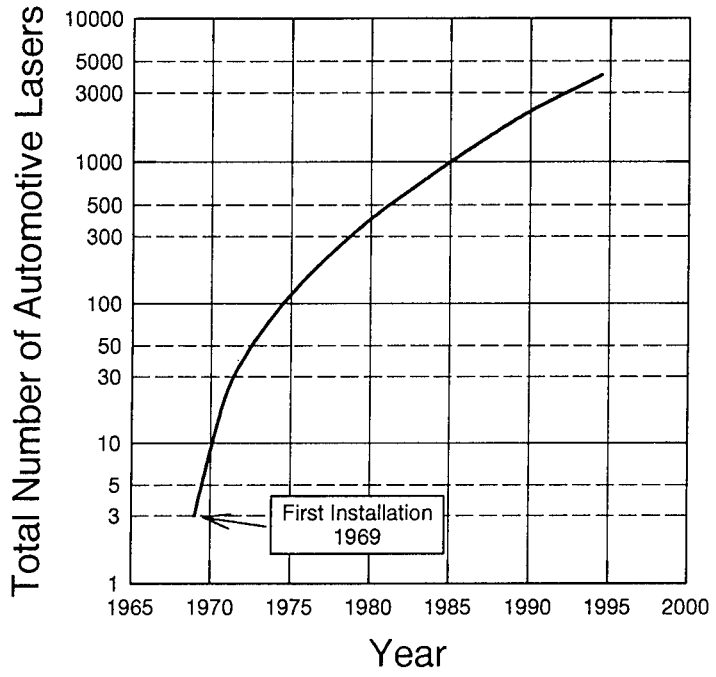


Figure 1. The growth in the number of lasers supporting automotive materials processing (global total).

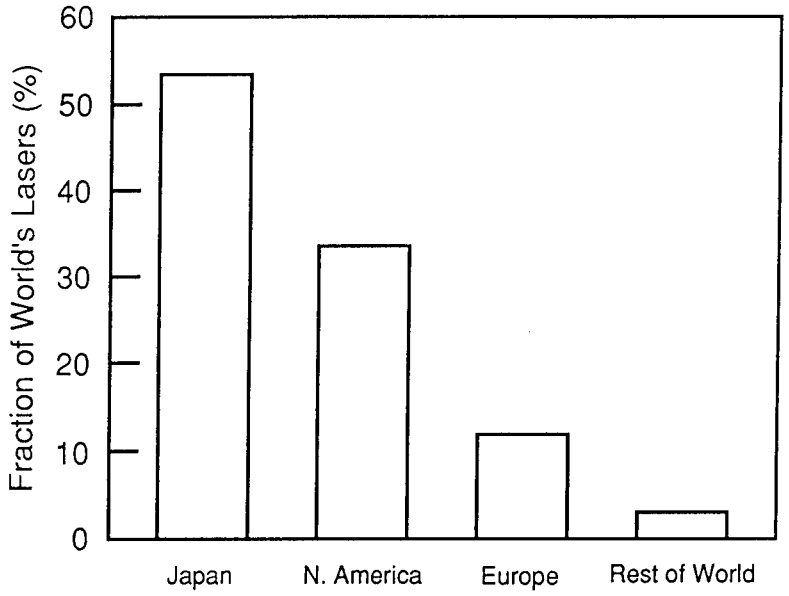


Figure 2. Distribution of automotive lasers by geographic region.

The most common machining use of lasers on a global average basis, by both industry in general and the automotive industry in particular, is cutting. However, there are important regional differences in their use, as shown in Figure 3. For example, the North American automotive industry uses more lasers for welding (from small parts in electronic circuits to large transmission components) than for any other single purpose. Cutting and marking are the next most common applications, with drilling employing slightly fewer lasers. The "other" category in Figure 3 covers a very broad miscellany of applications, from the scribing of ceramic substrates and resistor trimming to surface treatment and rapid prototyping.

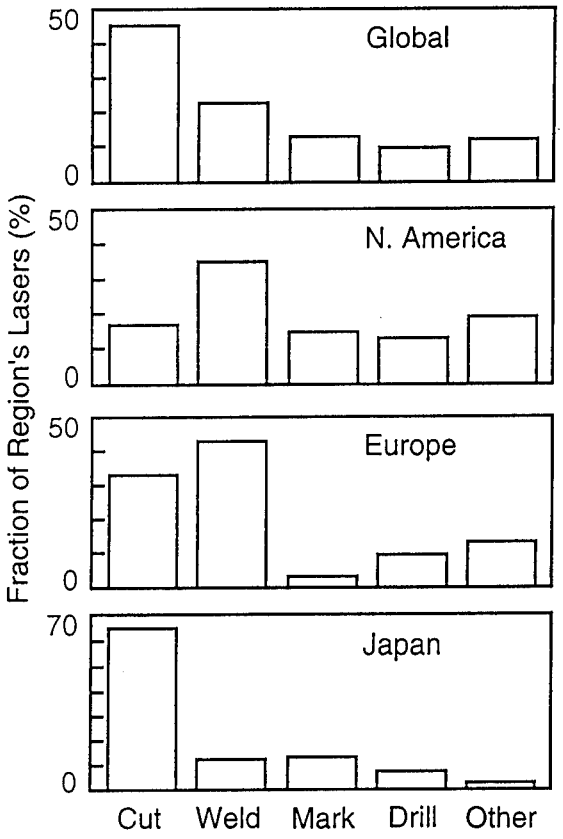


Figure 3. Primary uses of automotive lasers as a function of geographic location.

By contrast, in Europe, the number of lasers used for welding is only marginally greater than that for cutting. The role of the latter is very clear in Japan, where Figure 3 shows that, for every laser involved in welding applications, there are five or six being used for cutting. Thus, because of Japan's present lead in the total number of automotive lasers, cutting is currently also the dominant process on a global basis.

In this paper we shall focus on high-power laser applications in the automotive industry and will somewhat arbitrarily define high power as 500 W and above. First, however, we shall review some of the very elementary principles of laser-material interaction relevant to materials processing.

2. Basic Principles

2.1. LASERS

The role of the laser in materials processing is to produce permanent changes in a material. The laser may provide nearly all, or only a small part, of the total energy required, the remainder being supplied by mechanical or chemical forces. Over 95% of the lasers used for materials processing in the automotive industry nowadays are either Nd:YAG or CO_2, there being very approximately equal numbers of each.

The CO_2 gas laser was discovered in 1964 and was the first to be used on automotive production lines. It has been commercially available since 1966 and output powers presently range from only a few watts up to tens of kilowatts. The CO_2 laser has a high overall power efficiency, is less expensive than other lasers in the same power class, and has proved industrially rugged and reliable. In some applications, these factors may offset the disadvantage of the long wavelength of its light emission.

The Nd:YAG laser, discovered in 1964 also and commercialized in 1967, has several potential attractions: its output wavelength is only a tenth that of the CO_2 laser and it offers the benefits inherent in solid-state systems. The overall power efficiency is only a few percent, however, and, until recently, the maximum available output power for commercial applications was limited to a few hundred watts. Further, the capital cost of Nd:YAG lasers per output watt is about double that of CO_2 lasers. In practice, the economic viability depends on additional factors such as operating costs over the lifetime of the laser together with the costs of the associated equipment (beam delivery systems, etc.). The reliability of YAG lasers has steadily increased and one customarily expects them to be operational at least 97% of the time scheduled. This is also true for the CO_2 laser and partly accounts for the widespread industrial acceptance of these two lasers.

Numerous other lasers find uses in material processing, including automotive applications. They include the ruby, Nd:glass, argon ion and excimer lasers. However, most of them operate with average output powers of well under 100 W and will not be considered further. The allure of the ultraviolet wavelengths characteristic of excimer lasers has stimulated efforts to improve their industrial ruggedness and to increase their maximum output powers. The excimer laser was not discovered till 1975 and may not yet be mature in terms of industrial use. Nonetheless, powers of over 1 kW have already been achieved at 308 nm from XeCl. Costs remain significantly higher, and the reliability less, than for either the CO_2 or the Nd:YAG laser. Consequently, the use of

the excimer laser is restricted to special applications, particularly those where material processing involves mechanisms which are not necessarily purely thermal.

2.2. BEAM PROPERTIES

The high spatial and temporal coherence of laser light distinguishes it from other light sources. For many processing applications, the most important characteristics are its high radiance and low beam divergence. Not only can a laser beam be efficiently propagated and steered over long distances if necessary, but it can also be focused to a very small spot, producing a high irradiance (intensity or power density). Even moderate focusing can give power densities well above those available from other light sources. A 1-kW CO_2 laser beam, focused to a spot of 0.1-mm radius, has an intensity of over 10^6 W/cm^2, enough to melt and vaporize most solids.

The properties of laser beams which are associated with the various longitudinal and transverse resonances that occur in the laser cavity are well known and will be mentioned only cursorily here. It is worth noting, however, that the automotive industry has been relatively slow to appreciate the subtleties associated with mode structure and process control. In the early days, low order modes were generally assumed to be desirable for most processes (other than surface treatment) but were not usually available at high power levels.

The term "spot size" has often been used only in a vague sense. For the TEM_{00} mode, it can be defined simply in terms of a parameter a where the beam has a radial intensity $I(r)$ given by:

$$I(r) = I(0) \exp\left(\frac{-r^2}{a^2}\right). \qquad (1)$$

At $r = a$, the intensity is $1/e$ (i.e., 36.8%) of its peak value $I(0)$. The total beam power P is simply $\pi a^2 I(0)$, with 63.2% (that is, $1\text{-}1/e$) of this power being contained in a circle of radius a. Some workers, particularly when dealing with material processing applications, prefer to use a spot radius equal to $a\sqrt{2}$. A spot of this size would contain 86.5% (that is, $1\text{-}1/e^2$) of the beam power. Higher order and mixed modes have more complex spatial intensity distributions and attempts to derive analytic expressions for an effective spot size have limited value. For practical purposes, it is probably better to determine spot size in terms of the radius of that circle whose area encompasses some appropriate fraction of the total beam power.

The divergence of laser beams profoundly affects their propagation to the workpiece and their focusability. For industrial lasers, the full angle divergence, i.e. the vertex angle of the conical envelope of the spreading beam, varies from well under 1 mrad to well over 10 mrad. Although the minimum focused spot size can, in principle, be made comparable to the wavelength of the light, it will in practice be drastically

affected by the beam divergence. Regardless of beam mode, and with good optics underfilled by the beam, the spot diameter *w* is linearly proportional to the divergence:

$$w = f\theta, \tag{2}$$

where *f* is the focal length of the relevant optic.

Figure 4 shows simple focusing of a laser beam. Because the width increases on either side of the focal plane, the laser beam intensity decreases correspondingly. An increase in beam width by 5% leads to an intensity decrease of 10% and, at some distance, the intensity will be too low to support the laser-material interaction of interest. This distance can regarded as the working depth of focus δ and, for a Gaussian beam, can be expressed as:

$$\delta = \pm \frac{\pi w^2}{\lambda} \sqrt{(\rho^2 - 1)}, \tag{3}$$

where ρ is the ratio of the beam width at the distance δ to its value at the focal plane.

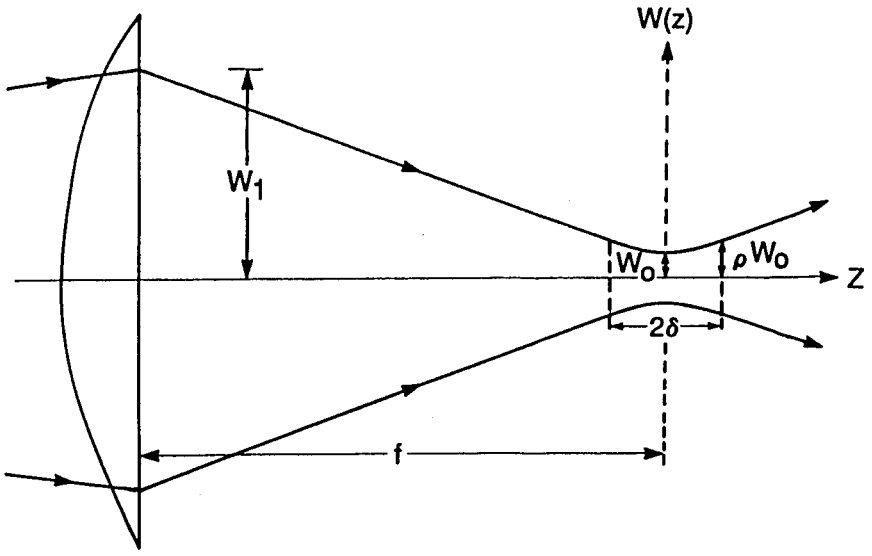


Figure 4. Schematic depiction of simple focusing of a Gaussian beam, defining the depth of focus.

The parameter δ is somewhat arbitrary but clearly has a major influence on the tolerance of a process to variations in the "stand-off" distance between the last laser optic and the workpiece. Usually one would like this to be large and there may be some benefit in buying this through a higher-powered laser and long focal length optics. Achieving high power densities by "tight" focusing leads to a limited working range.

2.3. BEAM DELIVERY

Delivering a laser beam to the workpiece is not necessarily trivial in terms of technical feasibility and is often expensive in terms of raw cost. It is not uncommon for the beam delivery system to cost as much or more than the laser and its power supply in many industrial plants. Safety enclosures and related features may also be added.

Processing applications commonly entail relative motion between the beam and the workpiece. There are three possibilities: the beam is fixed and the part is moved; the beam is moved and the part is fixed; or both the beam and the part are moved. In low-power systems, the laser head itself, not just the beam, may be moved. Other refinements include the possibility of a single laser servicing several workstations, via beam-splitting or time-sharing. A further general classification occurs depending upon the laser wavelength and the availability of suitably transmissive or reflective optics for beam manipulation.

Beam manipulation via mirrors is possible for all laser wavelengths, and considerable flexibility is afforded by the use of articulated arms. The disadvantages increase with the number of mirrors. They include: the cumulative loss of power when many successive reflections are involved; the need for added cooling (increasing mass and complexity) in high-powered laser systems to avoid distortion and damage to the optics; difficulties in alignment of the beam within the system; and difficulties in maintaining pointing accuracy and reproducibility over long path lengths.

Beam manipulation via flexible fibers requires the availability of low-loss optical light guides which have mechanical properties compatible with the bending and durability requirements. Currently, no economically viable fiber systems for high-power CO_2 industrial lasers are available. However, many substances, including quartz and some glasses, are quite transmissive at wavelengths of 1 μm. Fiber optics made from these materials have greatly increased the usefulness of high-power Nd:YAG lasers. These fibers have diameters of only a few hundred microns but are typically packaged with thick cladding and protective armor. They can transmit average powers exceeding 1 kW and enable the output from a single laser to be shared in power or time between several workstations or the outputs from several lasers to be combined. Further, the optical losses are primarily at the end faces rather than via absorption in the bulk. The latter may be only 6 dB/km whereas end face losses may approach 10%.

Metallized wave guides, hollow channels with highly reflecting internal walls, have been used primarily with low-power lasers. These guides can be flexible and may transmit over 90% of the initial power per meter of length. Numerous other systems have been investigated or deployed but, in the automotive industry, articulated mirrors and fiber optics predominate. Perhaps the most significant recent development, other than fiber optics, has been the better integration of the laser with the beam delivery system. This can reduce costs and enhance performance. Several laser-robot devices are now available which give at least 5 axes of motion for the laser beam but where only four or five internal mirrors are required. Telescopic and articulated arms give flexibility but, where reach is extensive, positioning accuracy may suffer.

Within the laser and the beam delivery system, the optical components are key factors in determining ultimate processing capabilities and control. They include mirrors, lenses, beam splitters, polarizers and fiber optic guides. Ideally, the diameter of such components should be at least twice that of the effective laser beam width to minimize edge effects. In all cases, absorption should be low to avoid thermal distortion or damage by the beam. Air or water cooling may be used to limit temperature increases and a slight over-pressure of gas is often used to prevent contamination of the optics.

Lenses are sometimes anti-reflection coated to increase their transmittance; mirrors may have dielectric coatings to enhance their reflectance and damage threshold. These coatings improve the initial optical characteristics but, once degradation starts, failure may be more pronounced and catastrophic than in their uncoated counterparts. Quartz is commonly used as the lens material for visible and near-IR lasers: GaAs or ZnSe is used for medium- or high-power CO_2 lasers. ZnSe is partially transparent to visible light and its use can permit the inclusion of a He-Ne laser beam collinear with that from a CO_2 laser to permit easier alignment of the latter.

Mirror substrates should have high thermal conductivity: copper is frequently used, with or without coatings. Bare copper can withstand irradiances of 10^5 W/cm^2 but is soft and oxidizes readily. Surface coatings such as molybdenum may improve the durability but at the expense of lowered reflectance.

3. Laser - Material Interaction

Of the laser light which is initially incident on a surface, only the fraction which is absorbed can contribute to changes in the material. This determines which laser wavelengths are appropriate for a given material. In some cases, the absorbed photons may dissociate bonds directly and be accompanied by only minor heating effects. In most automotive applications, however, the absorbed laser radiation produces significant heat. It is the subsequent thermal changes, either in the solid state or through melting and vaporization, which determine the process that can occur [1].

3.1. COUPLING COEFFICIENT

The fraction, γ, of the total incident laser energy which is transferred to the workpiece is variously termed the coupling coefficient or energy transfer efficiency. It depends on numerous parameters, including the angle of incidence and the polarization of the radiation, the optical properties of the material (which vary with wavelength, temperature and surface condition) and the presence of any intervening matter. Its instantaneous value may change considerably during the course of the irradiation. In deep-penetration welding, for example, the value of γ prior to surface melting may be much less than 0.1, but be close to unity once substantial vaporization has occurred.

Determining the value of the coupling coefficient is nontrivial in high power processing applications once the surface of the workpiece melts and vaporization

increases. The energy transfer is no longer determined solely by the direct absorption of the incident laser beam at the surface of the material in its solid state. There will be interactions of the beam with material in liquid, vapor or plasma phases, in both direct and indirect processes, as will be apparent below. In some cases, there may be little if any optical absorption directly by solid material.

3.2. THERMAL EFFECTS

At low power densities, the incident laser light produces negligible heating and the interaction with the workpiece surface is purely optical. As the power density is increased, atomic diffusion increases and, in some materials, there may be solid-state phase transformations. Further increases produce melting and vaporization. The power densities and times needed for these phase changes vary widely with the material. For example, vaporization can occur at intensities of only 10^3 W/cm^2 in some materials, but 10^6 W/cm^2 is more typical for automotive metals.

At high irradiances, particulate matter, ions and electrons emitted from the surface create a dense vapor. Light is absorbed and scattered by the condensing droplets and orange-white, glowing plumes of hot gas appear above the workpiece. At 10^7 W/cm^2 there is partial ionization of the vapor: it becomes more opaque, rapidly increases in temperature, and readily undergoes thermal ionization. A plasma is formed, characterized by temperatures near 20,000 K and an intense blue-white light. It may absorb nearly all of the incident laser beam and become a significant source of radiative heat transfer to the workpiece. If the plasma moves away from the surface, the laser beam may become completely decoupled from the workpiece [2].

As long as the surface remains solid, the temperature increase can be calculated as a function of depth and described by quite simple analytic expressions for a variety of incident light profiles. Shkarofsky and others [3-5], for example, discuss a number of situations, varying from continuous to pulsed radiation and from spatially uniform to circular and Gaussian distributions. These models usually ignore the temperature-dependence of the thermal and optical properties of the irradiated material and have limited value once melting or vaporization occur. However, they can offer a little insight as to the role of the basic parameters.

For a semi-infinite, isotropic slab which has been uniformly irradiated for a time τ there are two limiting cases. They depend on the relative values of the optical and thermal penetration depths. If β is the optical absorption coefficient of the material and the light intensity decreases exponentially with penetration z into a material, then $1/\beta$ is the optical depth, at which the beam intensity has decreased to $1/e$ of its initial value. The thermal depth will be defined as $\mu = \sqrt{(4\alpha\tau)}$ where α is the thermal diffusivity.

For short irradiation times and deep optical penetration, $\mu\beta \ll 1$, and the temperature increase is given by:

$$\Delta T(z, t) = \left(\frac{H\alpha t}{k}\right)\beta e^{-\beta z} , \qquad (4)$$

where H is the heat flux density at the surface and k is the thermal conductivity. This expression could also have been derived from a simple energy balance analysis of a heated slab. The temperature-depth profile matches that of the light intensity within the material because there is very little thermal diffusion that can occur during a short irradiation pulse. It is also worth noting that the rate of heating is independent of the pulse duration, τ, for short pulses.

The second limit, $\mu\beta >> 1$, applies to many laser machining applications, particularly for metals. The incident light is absorbed within a very shallow surface region and the heat may be regarded as a surface rather than a volume source. The temperature-depth profile is then given by:

$$\Delta T\,(z, t) = \left(\frac{H\mu}{k}\right) \text{ierfc}\left(\frac{z}{\mu}\right), \qquad (5)$$

where "ierfc" denotes the first integral of the complementary error function. At a depth $z = \mu$, the temperature increase is about 8.9% of its value at the surface, hence the use of μ as an effective thermal penetration depth. It should be noted that some workers prefer to define the thermal penetration depth as $\sqrt{(\alpha\tau}$, i.e., half of the value used here. This corresponds to the depth at which the temperature increase is about 35.4% of that at the surface.

For the surface temperature increase, equation 5 reduces (for $z = 0$) to:

$$\Delta T\,(0, t) = \frac{H\mu}{k\sqrt{\pi}} \; . \qquad (6)$$

Thus the temperature increase varies as the square root of irradiation time. Figure 5 illustrates the basic features of this heating process for the spatially uniform, constant irradiance of a highly absorbing semi-infinite solid for a time τ. The data in Figure 5 are based on equation (5), modified to take account of the condition $H = 0$ for $t > \tau$, and have been normalized for convenience. Immediately following the irradiation, the surface begins to cool even while deeper regions of the solid have not yet reached their maximum temperatures. Note that, even after the irradiation has stopped, the temperature below the surface at the effective thermal penetration depth, $\mu = \sqrt{(4\alpha\tau)}$, continues to rise for a time at least as long as that of the original irradiation.

The data also show the rapid initial rate of heating and, after irradiation stops, the very rapid initial rate of cooling. Note that these data assume that the material remains solid throughout the heating process. Direct differentiation of equation (5) provides the corresponding heating and cooling rates, and the temperature gradients. Inserting typical values for practical irradiation and material parameters shows that heating and cooling rates can be well in excess of 10^5 °C/s and approach values many orders of magnitude greater than obtainable by traditional heating techniques.

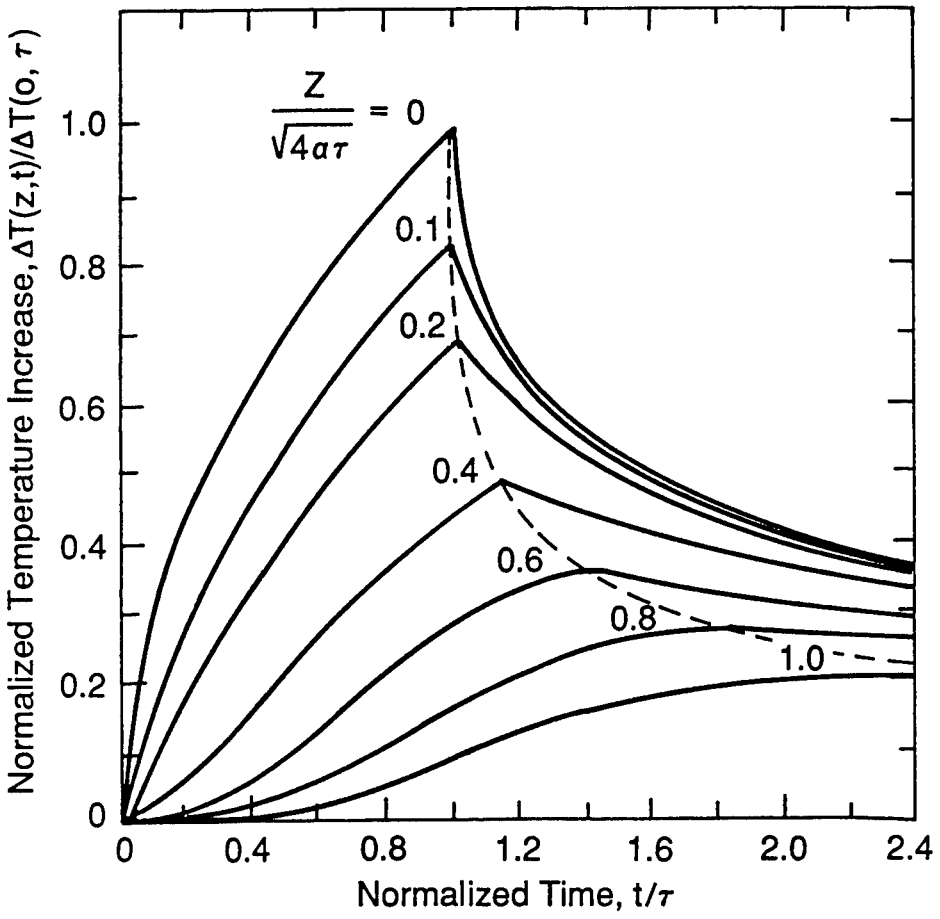


Figure 5. The heating and cooling of material irradiated by a uniform power density for a period τ. The temperature profiles are shown as a function of time t at various depths z beneath the surface.

In practice, laser beams do not irradiate surfaces uniformly and there is significant lateral diffusion of heat. The temperature will increase less rapidly than implied by equation (5) and, further, will not increase indefinitely. For example, if the laser beam is contained within a spot of radius a, the temperature-depth profile at the center of the beam ($r = 0$) has an asymptotic limit given by:

$$\Delta T\,(0, z, \infty) = \frac{H}{k}\left(\sqrt{\left(z^2 + a^2\right)} - z\right) . \qquad (7)$$

The maximum surface temperature that can be obtained, even for prolonged irradiation, is therefore:

$$\Delta T\,(0, 0, \infty) = \frac{Ha}{k} = \frac{P}{\pi a k} \quad . \tag{8}$$

It should be noted that the above expressions underestimate the temperature rise if the thermal penetration during the irradiation is comparable with the thickness of the workpiece (i.e., if it may no longer be considered to be semi-infinite).

It is an interesting exercise to refine the models to include relative motion between the beam and the workpiece, and so on. Indeed, it is remarkable to see how the spatial and temporal characteristics of the incoming radiation, together with those of the thickness of the workpiece, can be varied whilst still permitting analytic expressions for the temperature profile. It is quite trivial, of course, to invert expressions such as equation (6) and obtain a lower bound for the time for the surface to reach its melting or vaporization temperatures. The time will generally be an underestimate because such models neglect latent heats.

Nowadays, most predictive models of laser-material interactions must rely heavily on numerical techniques for the determination of temperature profiles and so on. Numerous summaries of laser processing models are available [1, 6-9], ranging from those that consider only conduction processes to those which include convective flow and radiative losses. In many processes, such as cutting, the last two represent only a few percent of the losses. It remains true, however, that lack of knowledge of some of the crucial parameters (and their temperature dependence), such as the coupling coefficient, limits the predictive value of even the most sophisticated models.

3.3. PROCESSING REGIMES

In general, energy densities of at least 0.1 J/cm^2 are needed to produce permanent changes in materials. Significantly higher energy densities (10^2 - 10^5 J/cm^2) are needed for many common applications such as cutting or welding. The energy density alone does not define what process occurs. The power density, i.e. the ***rate*** at which the energy is supplied to the workpiece per unit area, is also a key factor.

Figure 6 shows how different processes are controlled by the incident intensity and the interaction time. Note that it is only a very general guide: in practice, it ignores such critical factors as the differences between materials. Further the processes themselves may involve varying mechanisms and phenomena. Cutting, for example, may proceed by several distinct mechanisms: the laser may provide only a small part of the total energy involved. Thus the actual processing domains for cutting, welding, and so on, will depend strongly on the particular application.

Low power densities and long interaction times allow significant thermal penetration prior to any surface melting. Thus this regime is useful for various solid-state changes. High intensities and short interaction times will steepen the temperature

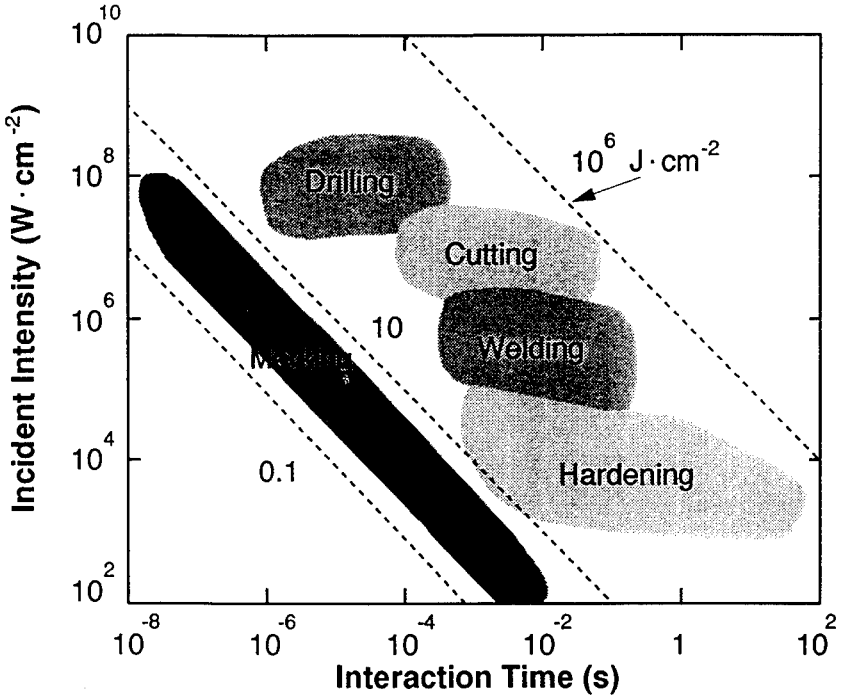


Figure 6. The roles of incident power density (intensity) and interaction time in determining laser processes.

gradient within the material. This can be deduced from equation (6), which can be rewritten as:

$$\Delta T\,(0, t) = \left(\frac{1}{k}\sqrt{\frac{4\alpha}{\pi}}\right)\frac{E}{\sqrt{\tau}}\ . \qquad (9)$$

Here, we have replaced the power density H of equation (6) by the energy density E (= $H\tau$, where τ is the duration of the radiation), and the thermal penetration depth μ by $\sqrt{(4\alpha\tau)}$. Thus for a given energy density, higher surface temperatures are achieved with shorter pulses. This simply reflects the fact that short irradiation times do not permit deep thermal penetration during the pulse.

Once the surface melts, processes such as welding can occur. For intensities near 10^7 W/cm^2 or so, surface vaporization may occur before there is significant thermal penetration and will initiate ablation. The high intensity, short duration regime is therefore best suited for applications such as drilling or other types of material removal. If peak intensities are too high, or if pulse lengths are too long, plasma formation may

disrupt the process. High intensities (10^8 W/cm^2 in metals) can cause violent expulsion of both vapor and other material, molten and particulate [2, 10].

4. Major High Power Applications

4.1. SURFACE TREATMENT

In many applications the surface properties of a component (optical, electrical, mechanical and so on, including cleanliness) are critical. Much industrial interest has focused on improving resistance to impact, wear, corrosion, and oxidation. Materials which intrinsically possess satisfactory properties are often expensive and may be difficult to machine by virtue of the very attributes desired (hardness, for example).

The surface properties of some common materials can be improved by laser irradiation and made comparable to those of more expensive ones. This modification may require only a thermally-induced change in the material or it may involve addition of other materials to the surface. Only a thin surface region is affected and the process can be precisely controlled [11]. The major types of hardening include transformation hardening (also known simply as heat treating), surface melting, alloying and cladding (also termed "hardfacing"). Despite early and successful applications of lasers for surface treatment in the US most of the recent advances have been in Europe and Japan.

4.1.1. *Transformation Hardening*

The hardness of certain ferrous alloys can be significantly altered by heat treatment. The laser can be used to induce thermally the solid-state metallurgical changes responsible and has been used for heat treatment since the early 1960s. It offers several benefits over traditional furnace, flame or induction hardening. Distortion is low because only the area of interest need be heated; the case depth (hardened thickness) can be tightly controlled; and there is often no need for forced cooling.

The microstructure of many steels is dominated by a mixture of bcc ferrite (α-Fe) and carbides such as cementite (Fe_3C). When heated above a critical temperature, this material transforms into an fcc structure, austenite, which more readily dissolves carbon interstitially. The required temperature depends upon the original carbon content and is about 912 °C for pure ferrite but only 727 °C for eutectoid steel (0.77 % C). The time required for the carbon to dissolve completely and become uniformly dispersed throughout the austenite also depends on the composition of the initial alloy.

If the austenite is now cooled ("quenched") to its original temperature sufficiently rapidly, usually within a second or so, the carbon is retained in solution and a hard, metastable phase, martensite, results. In laser hardening, the optical absorption is confined to a very thin surface layer. The heat generated then rapidly diffuses into the underlying metal, in a self-quenching process. The carbon content must usually exceed about 0.2% by weight for a mild steel to be transformation-hardened. The maximum Rockwell C hardness in fully martensitic steels is less than 40 if there is only 0.1% C but over 60 when the carbon content exceeds 0.5%. The martensite may be ***too*** hard for

some applications but can be tempered to reduce brittleness: the reheating allows controlled decomposition and relieves stress.

Laser powers must usually exceed several hundred watts to give adequate surface coverage rates. Typically the beam is only weakly focused, to give a spot up to 1 cm in diameter and an incident intensity of 10^4 W/cm^2 or less. The relative linear speed between the laser beam and the workpiece is typically 5 - 150 mm/s. Dwell times are 0.01 - 1 s and hardened regions are up to several millimeters thick. If the laser heating is too rapid, the surface may melt before there has been adequate thermal penetration at deeper levels and the case depth (hardened region) will be too shallow.

Figure 7 shows the depth profile of a steel alloy which has been transformation-hardened by a 2-kW CO_2 laser which scanned at 12.7 mm/s across the surface. The alloy contained about 0.4% C and, initially, was mainly pearlitic in structure, i.e., a lamellar mixture of ferrite (α-Fe) and carbide (Fe_3C, cementite) phases. After the laser treatment, the surface zone was fully martensitic with a Vickers hardness approaching 700 (or a Rockwell C hardness of about 60). The hardness remains above 600 HV (55 R_C) to depth of about 0.5 mm, i.e., the case depth. The underlying layer shows decreasing hardness with depth, corresponding to incomplete dissolution of cementite (Fe_3C) and diffusion of carbon. At depths greater than about 0.9 mm, temperatures did not increase enough during the heating period for austenite to form: the material therefore retains its original structure and softness.

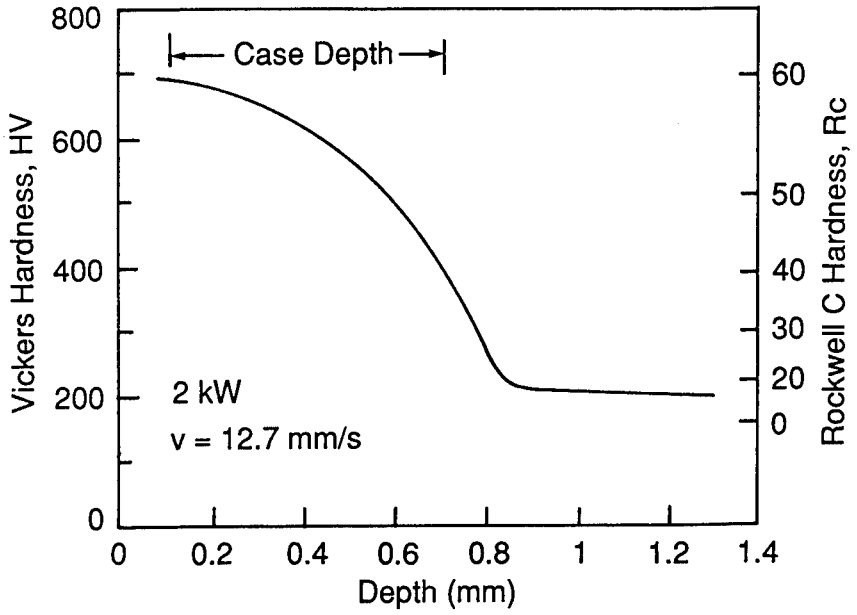


Figure 7. Hardness versus depth below surface for a laser-hardened iron-carbon alloy. (Adapted from work of J. R. Bradley, General Motors R&D Center.)

The first intensive automotive application of transformation hardening by a laser was probably that of the malleable cast iron housing of automobile power-steering gears, begun in 1973 to contend with higher front-end loads on vehicles. In a typical system, a 1-kW cw CO_2 laser puts a stripe pattern in the housing, selectively hardening only those regions known to experience high stress [12]. Heat input is thus minimized, less than 0.1% of the total housing mass being significantly affected. Distortion is very low and there is little scrap. The rate of wear was decreased by 90% at a cost which was only 20% of that of alternative techniques, such as furnace hardening or nitriding. Furthermore, castings can be ordered on the soft side of their hardness specifications to improve machinability. Although redesign of this component for some models has reduced the amount of heat-treating needed, over 20 lasers were so employed at one time and some remain active today.

This experience was useful for a later application when, in 1976, several 5-kW CO_2 lasers installed at GM's Electromotive Division (LaGrange, Illinois) began hardening the bores of cylinder liners for turbocharged diesel-electric locomotive engines [13].

4.1.2. *Surface Melting*

When surface temperatures are allowed to rise above the melting point, a much wider range of materials (not just ferrous alloys) can be made to undergo significant changes. During the molten state, homogenization of material occurs. Then, for high laser intensities and short interaction times, the subsequent very rapid cooling rates (typically 10^6 - 10^{10} °C/s) "freeze" in this uniformity and metastable glassy or amorphous phases can be formed which have wear and corrosion resistance markedly different from that of the bulk material [14].

The technique is relatively new and still only little exploited, although interest is growing for applications such as automotive camshafts and tool steels, and in the modification of coatings applied by conventional plasma and flame-spray. While pre- and post-process heating can reduce surface stress cracking and warping (from the rapid heating and cooling), there is generally more distortion than in transformation hardening. A recent automotive application in Germany used a 12-kW CO_2 laser for the surface remelting of camshafts.

4.1.3. *Alloying*

Major surface modifications are possible when chemical additions are made. The desired material may be added in diverse ways: as a powder, wire, sheet or coating prior to the laser scan; or it may be injected or blown in during the irradiation. All of the additive flows into the surface region of the substrate when the laser traverses the workpiece. Strong convection currents in the melt pool ensure thorough mixing. The alloyed material forms a dense, fine-grained, homogeneous layer extending up to 1 mm or so below the surface [15].

Although not yet widespread in the automotive industry, the technique has been applied to various engine components such as valves and piston rings. Typical industrial applications commonly employ kilowatt-class CO_2 lasers and interaction times of 10-50 ms. The primary advantage is the ability to use components made from

inexpensive steels but provide them with the surface characteristics normally obtained only in much more costly materials.

4.1.4. *Cladding (Hardfacing)*

Like alloying, laser cladding requires addition of a new material to the workpiece surface: unlike alloying, not all of the additive is mixed into the substrate. Some remains undiluted and constitutes the new surface, which therefore has the same properties as those of the added material. The laser provides enough heat to produce a metallurgical bond between the cladding material and the base metal. The heat input must be carefully controlled: extensive melting of the base metal will result in undesirable dilution of the cladding material and possible loss of desired properties. A good bond demands some dilution but this is typically less than 10%.

Laser cladding has been investigated since 1974 and has advantages over alternatives such as plasma spraying and arc welding [16]. Many of the applications are similar to those for alloying, such as the automotive valve seats used in high-performance engines [17].

4.2. WELDING

4.2.1. *Process Parameters*

If a laser beam of adequate power is scanned across the surface of a metal, material melts and the melt front propagates some distance below the surface. In most welding applications, the surface will begin to melt within about a microsecond. Figure 8 shows

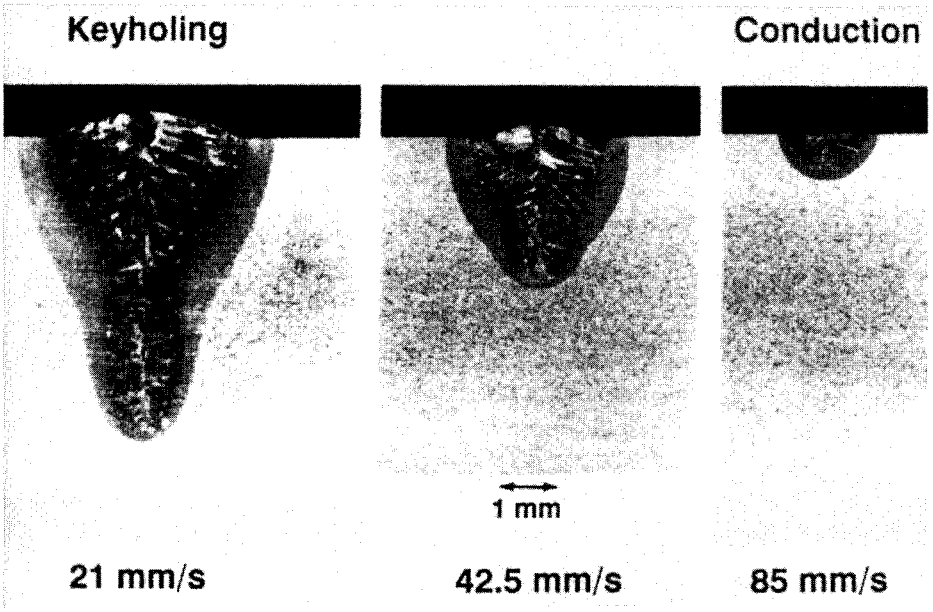


Figure 8. Cross sections of an AISI 4140 steel plate traversed by a cw 5-kW CO_2 laser at various speeds.

cross sections of a 6.5-mm-thick AISI 4140 steel plate whose surface was traversed by a 5-kW CO_2 cw laser beam at speeds of 21 - 85 mm/s. The new microstructures correspond to material which melted and then resolidified (the fusion zone), and to metal which was modified by the heat but did not melt (the heat-affected zone, HAZ).

At the highest speed, where the laser energy absorbed per unit volume of material is least, the melt front propagates uniformly into a hemisphere. This is the conduction welding regime where the fusion zone has a somewhat semi-circular cross section with an aspect ratio of less than about 1.5. As the scanning speed decreases, and the energy delivered per unit volume increases, there is an elongation of the melt zone directly beneath the beam. This is the "keyhole" welding regime and gives weld profiles resembling those from electron beams. For a focused cw CO_2 laser, the transition from conduction to keyhole welding occurs at powers near 1 kW and power densities of about 10^6 W/cm^2.

Numerous models of laser welding have appeared since the early 1970s [18-20] and have become increasingly sophisticated as they have tried to include more of the complex phenomena in the melt pool and plasma [21-24]. There are now excellent reviews of such research [6, 25]. In the keyhole regime, the irradiated surface begins to evaporate during the propagation of the melt front. The vapor produced creates a cavity

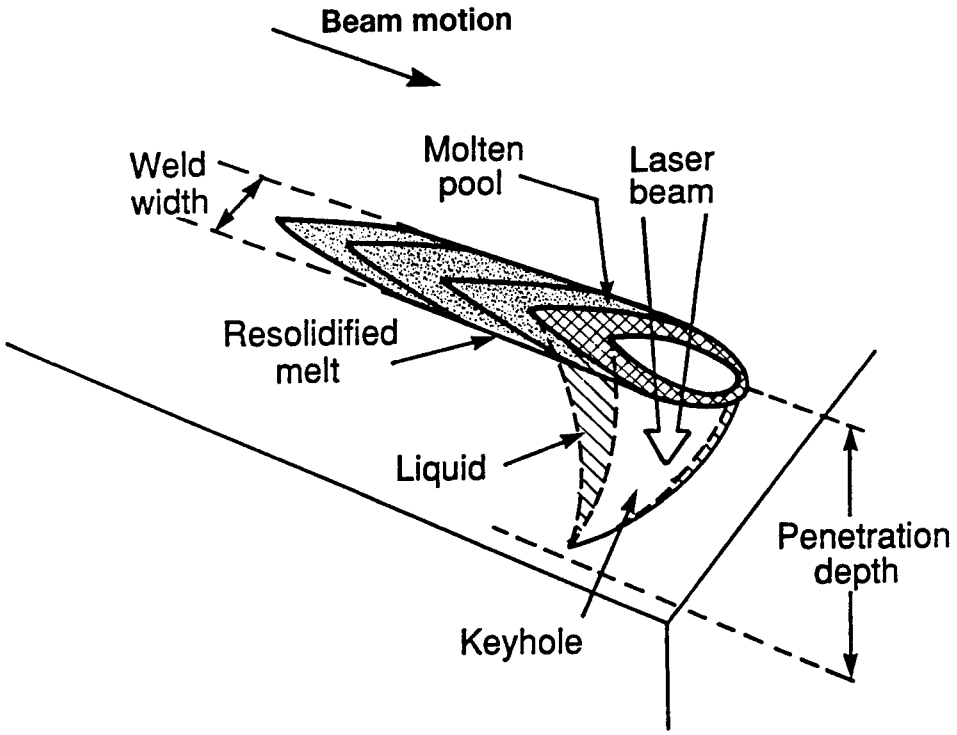


Figure 9. Depiction of keyhole welding.

below the beam by forcing molten material aside and allows the incident beam to penetrate deeper. The liquid flows around the keyhole, collapses back into the hole and resolidifies while the latter moves forward (Figure 9). The cavity is dynamically stable for a restricted range of scanning speeds. If the speed is too low, the amount of molten material is too great to be supported by the vapor pressure and no cavity can be sustained. If too fast, inadequate vaporization occurs and again no cavity is formed.

The keyhole regime has considerable practical value. The penetration is much deeper than in the conduction mode, giving aspect ratios as high as 10:1. The heat-affected zone is narrowed to less than a quarter of the weld width and the welding efficiency increases. Simple energy balance considerations predict that penetration depth should increase linearly with power and inversely with speed. Empirical data for CO_2 laser powers up to 45 kW and for a wide range of speeds are in general agreement but give a slightly sublinear dependence on power.

Figure 10 shows the approximately inverse relationship between penetration depths

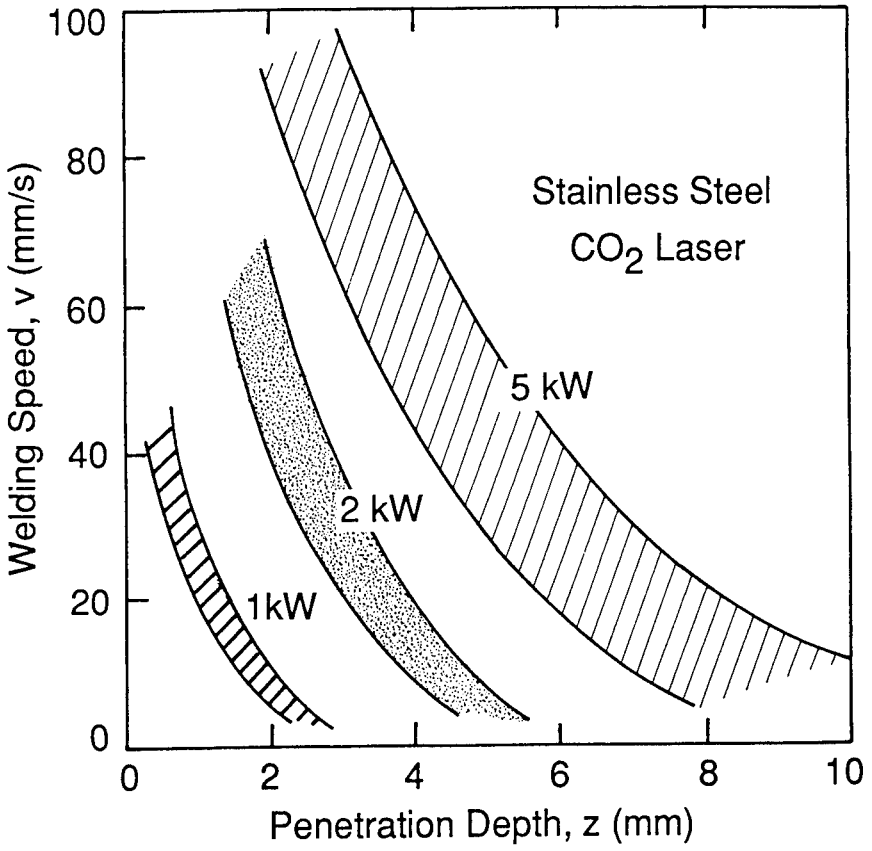


Figure 10. Welding speed versus penetration depth of the melt zone for CO_2 laser scans across a 304 stainless steel plate.

and welding speeds, at a given beam power, for a cw CO_2 laser beam scanned across a thick 304 stainless steel plate. The large bandwidth for each curve reflects the dependence upon other processing variables (focal spot size, assist gas parameters - such as type of gas, flow rate and direction - and so on).

Laser welding parameters depend, *inter alia*, on the thermal diffusivity of the materials to be joined. Alloys tend to have lower diffusivities than pure metals and longer irradiation times may be needed to ensure adequate penetration. On the other hand, high diffusivities may result in too much heat being wasted by being rapidly conducted away. In copper, for example, it is usually necessary to use high powers and short interaction times. However, the metallurgical properties of the material also play a crucial role and one must be aware of sensitivity to embrittlement, cracking, porosity, and so on. In some serendipitous cases (low carbon steel, for example), the welded region exhibits properties such as tensile strength, toughness and hardness, which may exceed those of the parent metal. In many other cases, or where one is welding parts made from dissimilar metals, or where the mechanical fit-up of the parts is poor, it may be necessary to add filler metals to strengthen the joint or improve the metallurgy.

Various gases and flow geometries, from coaxial to cross flow, are utilized in laser welding. Purposes include protection of the focusing optics from contamination (especially by debris and spatter from the workpiece), protection of the weld bead from contamination, reduction in porosity, and control of the plasma or weld plume.

Inert gases are often used to blow the plasma out of the path of the incident laser beam. The direction must be controlled to avoid disruption of the weld pool. Helium reduces oxidation and plasma effects, but is expensive. Argon has a much higher molecular weight and gives excellent coverage against oxidation. However, it ionizes more readily and produces a strong plasma. Results with CO_2 lasers show that the type of assist or shield gas used greatly affects the weld penetration depth. Penetration is least with argon, moderate with nitrogen or carbon dioxide and greatest with helium. Plasma effects are generally weaker with Nd:YAG, than with CO_2, laser welding.

4.2.2. *Advantages and Limitations*

The laser provides considerable flexibility in joint configurations, allowing considerable materials and costs savings if the component can be designed to take advantage of the beam's unique properties. Figure 11 shows a view of the many variants of joint design that can be considered, the lap and butt joints still being most common. Lasers also offer one-sided access to the workpiece, precise positioning and localized heat input. No mechanical contact is needed and the material can be isolated if desired, the laser beam being introduced via a window or other optical means.

The low heat input results in narrow heat-affected zones, little distortion and negligible thermal damage to surrounding areas, an especial advantage in the welding of fragile components. Heat inputs can be reduced further by the use of a pulsed rather than a continuous beam. The laser avoids some of the limitations imposed by electron beams (e-beams): there are few X ray hazards or potential problems from strong electric and magnetic fields, and the welding does not require a low pressure ambient.

Not all metals are easily laser welded, as has been noted above. The rapid changes

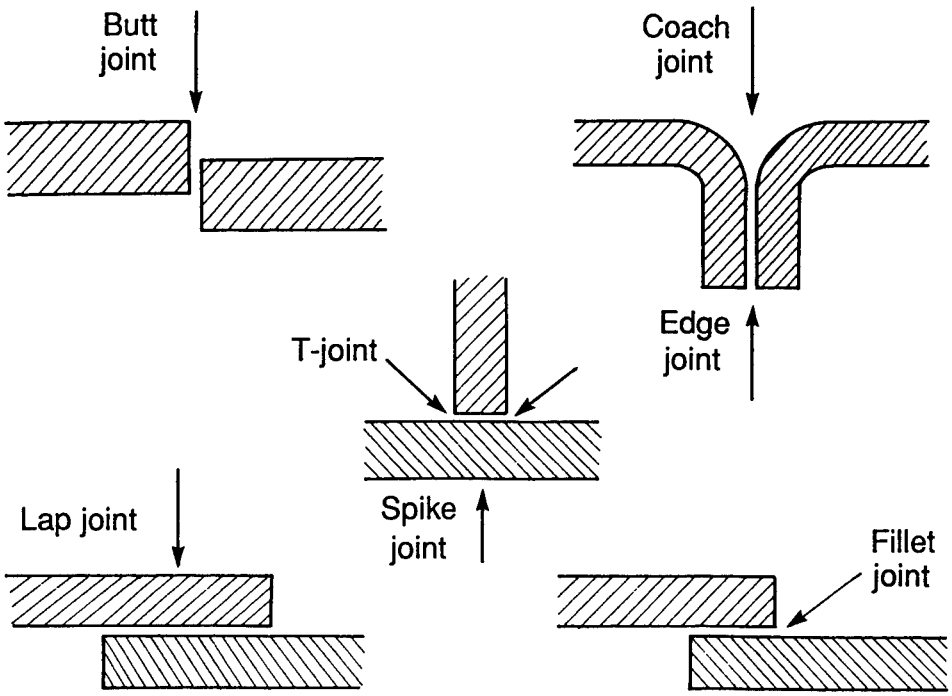


Figure 11. Miscellaneous joint configurations amenable to laser welding.

in temperature induced by laser irradiation can lead to very hard, brittle, weld beads in some metals and can also produce hot and cold cracking - especially in high carbon steels. There may be unacceptably high porosity (especially in the lap welding of zinc-coated steels), embrittlement and cracking, or the metallurgical properties of the weld may be inadequate in general. Filler metals may not always solve such problems.

The advent of Nd:YAG lasers with average powers at the kilowatt level means that high-powered CO_2 lasers are no longer the only option for some deep welding applications, although they continue to dominate for continuous welding at high speed. However, lasers are generally inefficient at making very deep welds. Many industrial processing lasers can make shallow penetration welds (less than a few mm) but depths above 1 cm usually require lasers with very high powers. Even though 100-kW-level CO_2 lasers have achieved weld depths in steel of several centimeters at speeds exceeding 1 m/min, their high capital costs usually make them less attractive than electron beams. Finally, unlike arc welding processes, the energy transfer in laser welding is far more dependent on factors such as the type of laser, its power density, material surface conditions, and so on. In fact, there has been considerable interest in augmenting the laser with an arc for welding to minimize the individual disadvantages of each and to maximize energy transfer and welding speed.

4.2.3. *Press-Fit Component Applications*

Many automotive components to be welded are designed to fit tightly together, often have circular or other simple symmetry, and can be easily positioned and manipulated beneath a fixed laser beam. These factors greatly simplify the beam delivery system and parts handling. Initially, laser welding was used on relatively small components and required only modest average laser powers. However, by the late 1970s, a wide variety of components were being laser welded, ranging from electrical terminals, electronic circuits and alternators to fuel injector adjustment screws, air-conditioner parts and pulsair valves. While the welding was done primarily with CO_2 and Nd:YAG

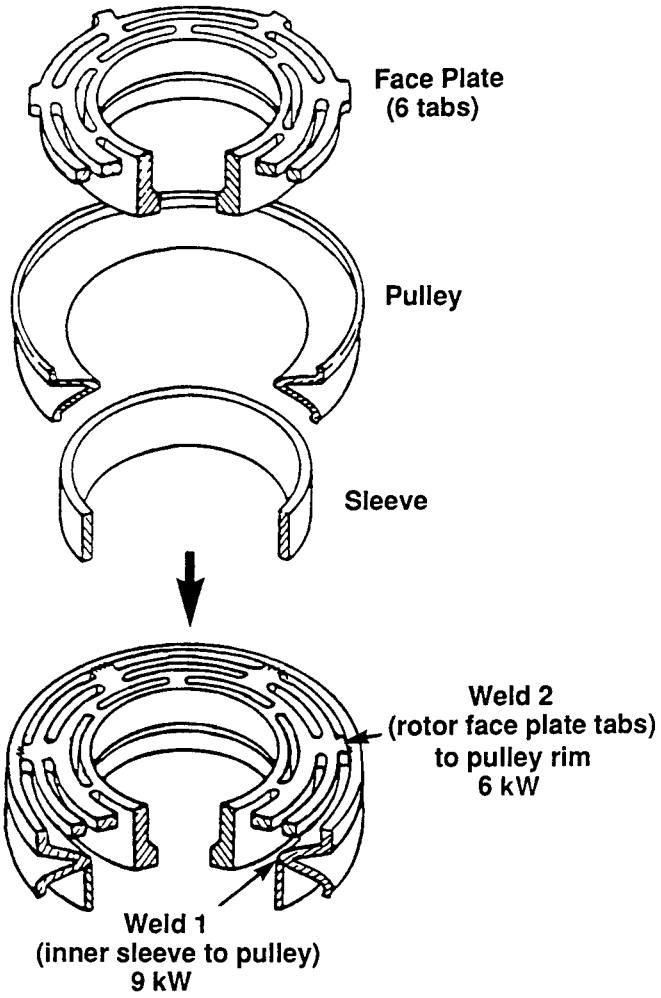


Figure 12. Air-conditioner compressor clutch pulley assembly.

lasers, the Nd:glass laser was also used. For example, by 1979, the Packard Electric Division of GM was using as many as 30 Nd:glass laser heads to weld lugs on emission control components.

The laser welding of automobile air-conditioner pulleys in the late 1970s was an important development [26], not because of the very high laser powers employed (four CO_2 lasers at 5 kW each, five at 9 kW and three more at 6 kW) but because of the impact of proper design. In 1978, a General Motors team responsible for developing a new lightweight air-conditioner clutch package for three basic air compressors was given the freedom to design the compressor clutch specifically to be laser-welded in its assembly. (Figure 12). The laser produces very localized heat input and minimal part distortion, allowing the use of thin-walled subassemblies. Further, joints could be made via small tabs which would have had too little contact area for conventional welding techniques. As a result, the group was able to design an assembly which had only 50% of the mass needed previously. Also, the high welding speeds achievable meant that use of lasers required fewer workstations and less factory floor space. Quick changeover tooling allows the production of various models, ranging from 12 to 15 different pulley configurations at any one time.

Nowadays, multikilowatt CO_2 lasers are in wide use, especially in the welding of transmission components. All of the major domestic US automobile manufacturers now have large capital investments in such systems. The first GM production-line laser welding of gears was in 1978. Ford began using a laser in 1984, instead of an electron-beam, to weld the sun-gear-and-shell assembly in an overdrive transmission [27], and steadily expanded its use of lasers for transmission component welding. It added fifteen more in 1991 to supplement its existing half-dozen and simultaneously announced plans to order at least as many more [28]. Chrysler Corporation had just ten lasers installed for welding transmission components at the end of 1989 but, by 1996, will have about twenty-five in total with a combined total power of 182 kW. They will include several CO_2 lasers having output powers of 14-kW.

In principle, either a laser or an electron beam can give the narrow deep welds needed for transmission components without producing significant distortion. However, the much greater flexibility in parts processing afforded by laser welding (typically, one laser beam can service more than one workstation and more than one type of transmission part) gives it an advantage. Further, the high uptimes (over 97% is common) and productivities achieved by laser systems offset their higher initial cost.

Lasers are also being used where other welding techniques might disturb needed electrical or magnetic properties. Stator cores, for example, are built up from thin laminated sheets which are about 0.5 to 1 mm thick. A multikilowatt CO_2 laser is used to weld the edges of the finished stacks, thus keeping them aligned while being transferred. The laser welds at about 30 mm/s, giving a smooth bead about 1 mm deep. Whereas plasma-arc welding alters the electrical properties of the assembly, the narrowly confined heat input of the laser minimizes such effects.

There has been a steady increase in demand for higher and higher power lasers for the welding of components. However, the recent advances in Nd:YAG lasers with multikilowatt outputs and fiber-optic delivery (4-kW power levels were already

becoming available commercially by 1995) mean that the high-power welding regime is no longer solely the domain of the CO_2 laser, unlike the situation in the past.

4.2.4. 3-D *Body Sheet Metal Applications*

Typical automobile bodies contain from 1000 to 4000 resistance spot welds along 40 m of pinch weld flanges. The laser offers potential advantages and unique opportunities to improve structural properties and weld consistency, while at the same time reducing weight and costs. Reducing the width of pinch weld flanges, for example, could eliminate up to 50 kg of metal [29]. Other benefits include smaller heat-affected zones and less thermal distortion, single-sided access and good design flexibility. Further, the high speeds obtainable with lasers, typically 5 m/min or more in full penetration lap welds of body sheet metal with a few kilowatts of laser power, indicate that one laser welding station can replace several resistance spot welders.

The above advantages are often offset by the particular problems posed by body sheet metal, such as poor fitup or the presence of coatings. For example, the theoretical advantage of one-sided access offered by laser beams may not be realized in practice if expensive fixturing and clamping is required. Initial work by Ford Motor Company in the mid-1970s clearly demonstrated difficulties which have persisted ever since.

General Motors began production line laser welding 3-D body sheet metal in 1987. The application was the welding of bare steel roofs to two-sided galvanized steel quarter panels and used two 2.5-kW CO_2 lasers and gantry-mounted robots to lap-weld a 0.3-m section on the left- and right-side ditch joints simultaneously [30]. The system allowed either laser to weld both sides of the vehicle if one laser were not operational. The ditch joint design eliminated metal finishing operations and could therefore save costs in principle. However, the primary purpose of this system was to permit a direct comparison between laser welding and resistance spot welding.

Subsequently, a number of integrated, multikilowatt, CO_2 laser-robot systems were installed to gain additional field experience in laser welding body sheet metal subassemblies. These were "learning" systems run in parallel with existing resistance spot welding lines and no design changes were made to take advantage of the laser's unique characteristics. Sheet metal subassemblies were selected which could be done off-line and which presented least problems in terms of fitup or coatings. Several became mainline production activities.

One example was a radiator support assembly where laser beam welding was substituted directly for resistance spot welding, about 45 "laser stitches" replacing the original 55 spot welds [31]. Because no design changes were made (such as flange width reduction, joint configuration, etc.), any benefits realized by use of the laser beam rather than by resistance spot welders can be regarded as conservative. However, only one laser station was required in place of three resistance spot welders, freeing up both manpower and floor space.

Also at GM, a 3-kW CO_2 laser was used with a robot to weld a rear shelf panel subassembly. The laser welded the rear seat to back window panel, two hinge boxes and the back window drain panel, all of them being lap welds in bare steel. Each of the original resistance spot welds was replaced by a 25-mm-long laser stitch weld. Filler

metal was not used so good part fitup was needed. Floor space use was minimized by having several system components, including the laser generator and chiller, mounted on a platform above the workstation. The consistency and integrity of the laser weld permitted extensive nondestructive weld evaluations (via electrical resistivity) and reduced the amount of destructive testing needed. Although laser welding was successfully implemented as an alternative to resistance spot welding, it still represented only a small fraction of the over one million spot welds that were being made every day in this plant, averaging about 2700 per vehicle.

The use of lasers for welding in production operations is normally justified only if there are demonstrable economic benefits. However, there have been situations where they have been used because no other technique can provide as satisfactory a weld or as unique a design. For example, a recent installation employed a 3-kW cw Nd:YAG laser to weld a 2-m-long roof channel on GM's Oldsmobile Auroras. The laser is used because of its unique accessing capabilities.

A slightly older application was introduced with the 1992 Cadillac Seville decklid and continued in later models. This vehicle has a very distinctive appearance and stringent design criteria must be met in order to preserve the styling. The center high-mounted stop lamp (CHMSL), a federal requirement, is comprised of a narrow array of light-emitting diodes which span the full width of the lid (Figure 13). This array fits into the recess formed from the reinforcement which must be welded to the outer upper

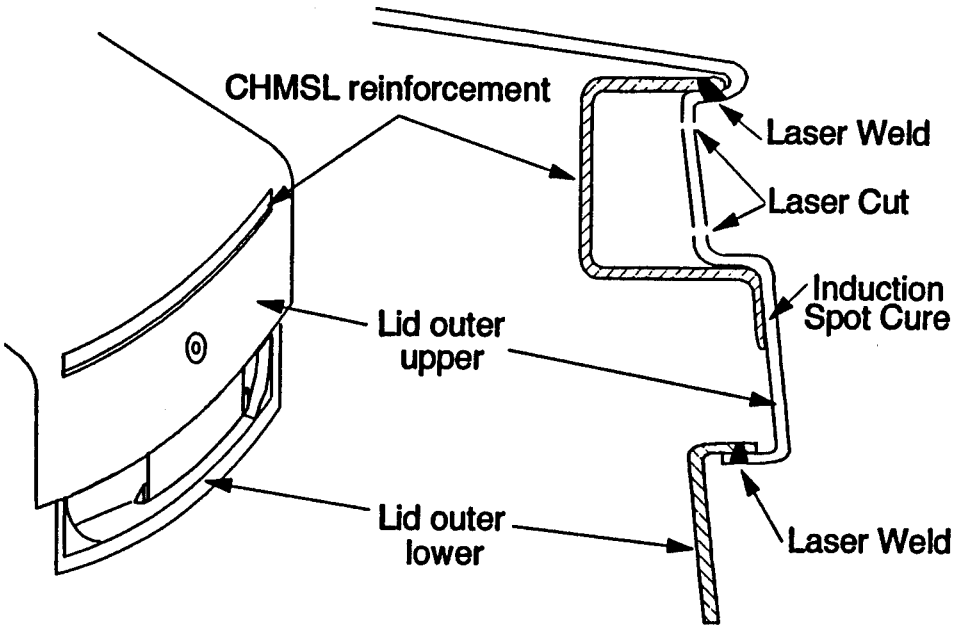


Figure 13. Schematic of center high-mounted stop lamp (CHMSL). Both laser cutting and laser welding are employed.

lid panel. The two pieces are of 1-mm-thick, two-side-galvanized steel, and there is limited access to the joint (thus precluding conventional resistance welding). Also, there is a need to avoid marring the smooth exterior surface. A 3-kW CO_2 laser is able to meet these exacting conditions with seven stitch welds. The same laser is also used for the easier weld between the outer upper and the outer lower (0.8-mm thick, two-side-galvanized steel), thereby eliminating the originally anticipated need for a resistance spot welder. In a later operation, a second laser-robot cuts out a 19-mm-high x 1236-mm-long opening in the reinforcement, to allow insertion of the lamp array itself. While the laser processes are expensive, they have been justified by the unique fit, finish and appearance [32].

4.2.5. *Tailored Blank Welding Applications*

Much current interest in automotive laser processing centers on the use of tailored blanks - metal sheets which, by being formed of component blanks, exhibit localized physical and chemical properties as needed in various parts of the total area. Fabricating a part by butt-welding together constituent steel sheets, each of which is selected to have just those properties required, offers substantial savings in materials costs and weight. The lasers used initially to butt-weld the component blanks had output powers of about a kilowatt. More recent applications, driven by speed and other considerations, have led to the use of lasers with 5 - 10 times that power.

The first laser welding of tailored blanks is believed to have been in Germany in 1985 when Thyssen Stahl AG began butt-welding two pieces of hot-dipped-galvanized steel to make a blank wide enough for an Audi floor pan [33]. By the late 1980s, the laser welding of tailored blanks gained wide attention with its use by Toyota, who may have been the first to use the laser for butt-welding together steels of ***different*** thicknesses and coatings on the production line [34].

In some automotive operations, much of the material originally purchased ends up as "engineered scrap." In practice, only half of the original sheet metal may be left in some stamping operations. The laser can be used to weld together some of the scrap into blanks big enough for other components. For example, the blank cut-outs from some truck door inner panels (made from two-side-galvanized steel) are individually too small to be used and would normally be scrapped [35]. However, when trimmed and then laser-butt-welded together, two of these cut-outs make a 0.13 m x 1.14 m blank which is big enough for use as a door reinforcement anti-flutter bar (Figure 14).

In this application, the 0.75-mm thick parts are welded at 5 m/min by a 3-kW CO_2 laser, the cycle time being about 20 s. About four welded pieces out of every thousand are subjected to a tensile test: thus far, none of the welds have failed [36]. Despite the cost of the laser welding operation, the use of a tailored blank fabricated from the two cutouts is less expensive than the purchase of a new blank.

In a separate application, laser-welded tailored blanks were used to eliminate the reinforcement pieces for center pillar inner, and motor compartment rail inner upper, panels in the 1992 and later Cadillac Seville and Seville STS models [37]. The center pillar inner requires considerable strength in the upper part where the shoulder belt is anchored. This can be achieved by spot-welding a reinforcement in this region, but this

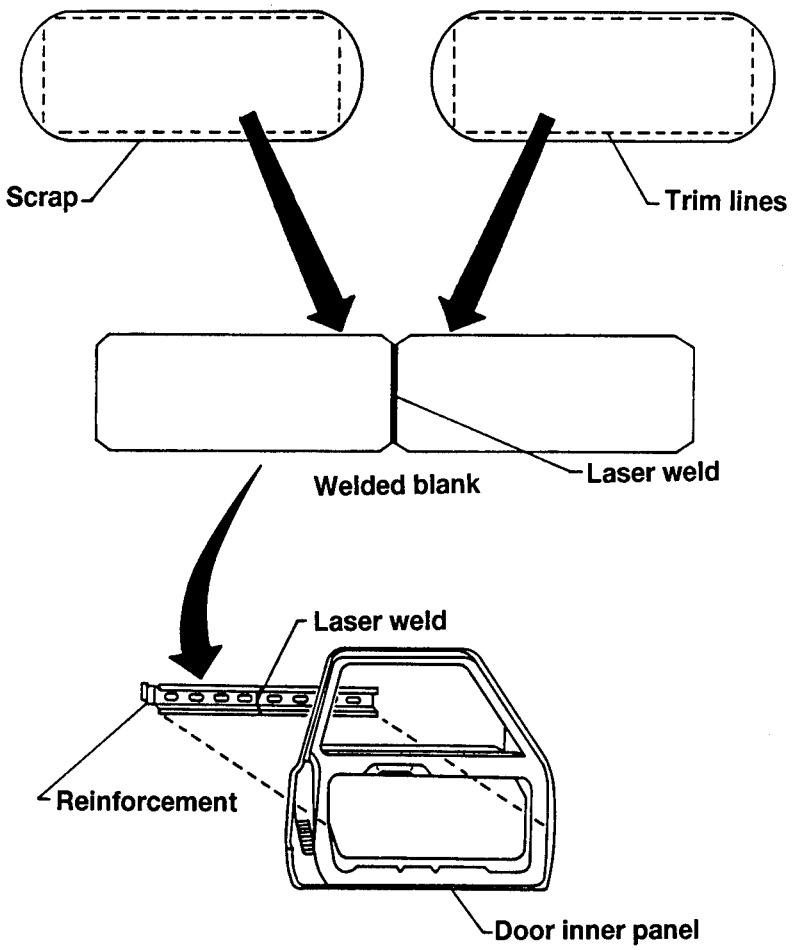


Figure 14. Engineered scrap from truck door cut-outs is laser welded and reused as a door reinforcement bar.

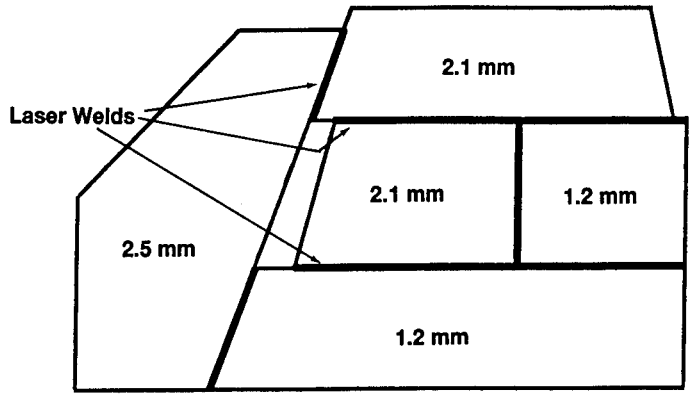
would require additional fabrication costs. The present design eliminates this reinforcement by use of a cold-rolled tailored steel blank composed of a 1.8-mm-thick upper piece which is laser-butt-welded to a 1.0-mm-thick lower section. Two center pillars are produced every minute, at a welding speed of about 3.5 m/min. Use of the laser-welded blank allows thickness to be distributed as required and results in a net savings of about 0.7 kg in mass. Further, no reinforcement piece is needed, eliminating the attendant fabrication costs of dies, assembly tooling, and plant facilities.

In a similar application, the motor compartment rail inner upper consists of a 0.8-mm-thick blank which has been laser-butt-welded to one which is 2.0 mm thick. The heavier metal is placed in the higher stress area and eliminates the need for a reinforcement patch in this region. In practice, both the right-hand and left-hand panels are contained in the laser-welded blank, which is then split apart in a subsequent die

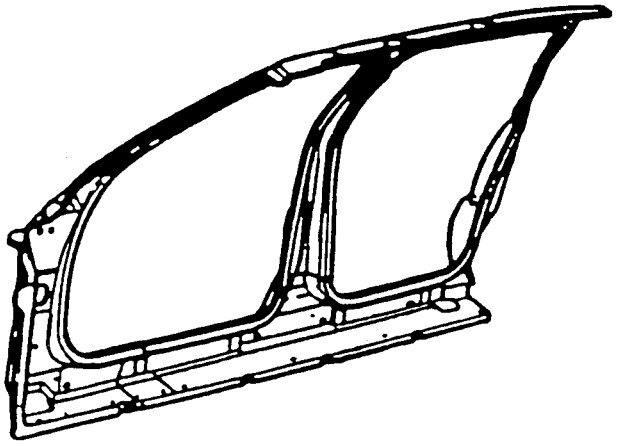
operation. Such applications typically save a kilogram or so of mass, in addition to the cost reductions obtained by part elimination.

Since 1994, Cadillac DeVille and DeVille Concours models have included not only these applications but an additional eight tailored blanks [38]. The Cadillac frame-body-side application is broadly similar to that employed in the Toyota Lexus in that it also involves five laser-welded blanks of varying thicknesses and alloy content. It does differ in some details (no filler metal is used, all surfaces are galvanized, and so on).

Figure 15 shows how the body side ring (or frame body side) is made up from these



a) Tailored Blank



b) Stamped Part

Figure 15. 5-piece tailored blank approach for the Cadillac DeVille frame body side.

five blanks butt-welded together by a CO_2 laser. Three different thicknesses of galvanized steel are used for this part. The thickest piece (2.5 mm) is used in the hinge attachment area and eliminates the previously required reinforcements. It not only provides strength here but, by extending to the front of the rocker area, makes the latter a very strong structure also. Two of the remaining sections are from light-gauge sheet (1.2 mm) while the other two are of intermediate thickness (2.1 mm), providing the appropriate structural properties where needed.

The use of the tailored blanks eliminates three components and reduces the dimensions of two reinforcements Apart from direct mass and cost savings, there are also advantages such as improved structural integrity, dimensional consistency and appearance. The welding operation should not be regarded as trivial, however. Each blank has four welds and, because of the geometry and varied gauges, each has to be made separately. Further, stamping a one-piece side frame of this complexity is more demanding than stamping smaller parts.

Both the front and rear door inner panels of the Cadillac DeVilles are made from laser-welded tailored blanks. The primary purpose is to remove the need for any reinforcement parts in the hinge pillar area. The conventional design, by calling for such strengthening, necessitated the fabrication of these separate additional parts, with all of their associated costs. The tailored blank design utilizes two component blanks of different thicknesses, 0.8 mm and 1.8 mm, the heavier gauge providing the additional strength required in the hinge pillar areas.

In the case of the front door, the thicker section of the tailored blank also provides appropriate strength in the mirror attachment area by being wider at the top than at the bottom. Thus both the mirror and hinge reinforcement parts can be eliminated. Conventional fabrication of these door panels requires between twenty and thirty dies (the front door needing a few more than the rear) to cover both left- and right-hand sides. This represents a major investment cost and the tailored blank design, by requiring far fewer dies, is very attractive, particularly for low-volume niche markets. Not only are the additional costs associated with these parts removed, but there is also much better material utilization. Each separate blank in the traditional design must include sufficient area for the binder material (for clamping in the die). Use of a single composite blank provides steel savings of up to 30%.

The final example of laser-welded tailored blanks to be discussed here eliminates no reinforcements, dies or tooling: it saves no mass; and it cannot be justified in terms of quality improvements. However, it does yield a very obvious benefit - direct savings in materials costs by a dramatic reduction in steel scrap. Conventional stamping of the frame-windshield-side results in about 50% steel scrap, primarily because the shape does not permit efficient nesting in the steel coils. This curved, 2-mm-thick part is almost eight feet (2.4 m) long and, nested conventionally, requires a wide coil - six feet (1.83 m) - to furnish the blanks (Figure 16a).

If the desired blank is considered to be composed of two shorter blanks, one of which has a purely rectangular shape, then a much more efficient nesting pattern is possible. Indeed, the straight section can be nested with an almost 100% efficiency in a 46.25-inch-wide (1.17 m) coil (Figure 16b). The total amount of steel scrapped is much

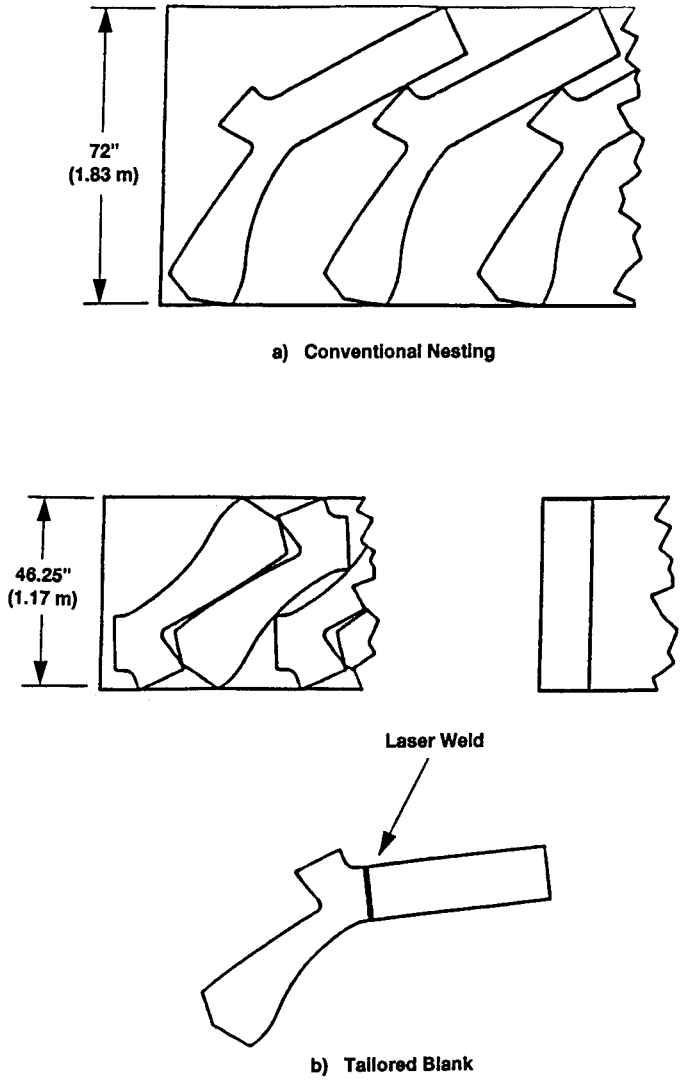


Figure 16. Reduction of scrap by tailored blank design of the Cadillac DeVille frame windshield side panel.

reduced and less steel need be purchased. Partly offsetting this, of course, is the cost of butt-welding the two same-gauge cutouts together in order to form the final blank.

4.3. CUTTING

In laser cutting, the beam fully penetrates the material, there is relative motion between the beam and the workpiece, and the goal is complete removal of material from beneath

the beam. The label "trimming" is used for some cutting applications specifically involving the removal of flash and burrs from curved parts.

4.3.1. *Process Parameters*

The laser may provide part, or all, of the energy required for material removal, the remainder being contributed by assist gases or by exothermic reactions at the cutting surface [7, 39]. Of the total energy delivered to the material, up to half is subsequently "lost" through conduction and a few percent is lost through convection or radiation. Two broad classes of cutting can be defined: sublimation cutting, in which material is removed primarily by vaporization; and fusion cutting, in which molten and other material is flushed out by assist gases.

Sublimation cutting is suitable for materials such as plastics, which have low vaporization temperatures and small latent heats of vaporization. Fusion cutting includes the use of either inert gases, to provide the mechanical force to flush out material, or reactive gases, which additionally promote exothermic or other chemical reactions at the surface.

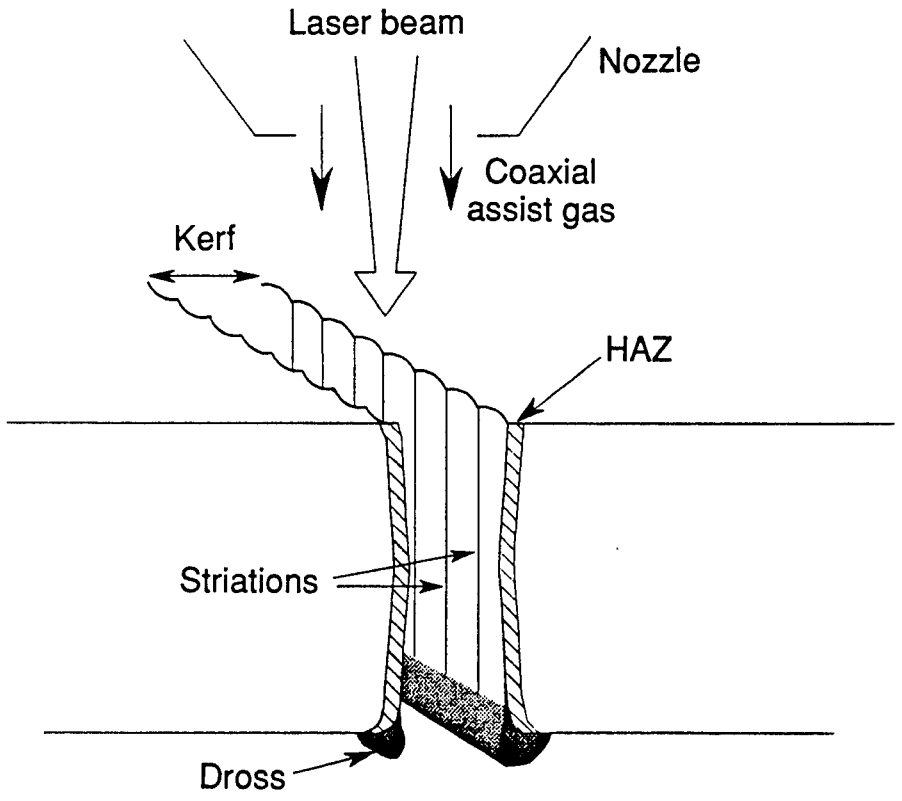


Figure 17. Schematic of laser cutting, defining the kerf (width of cut), and showing dross on the underside and striations on the walls.

Assist gases are often used to accelerate removal of loose or molten material and to flush out the hole, by contributing substantial amounts of mechanical energy to the cutting process. They are commonly directed into the kerf by a jet which is coaxial with the laser beam (Figure 17), though off-axis flows have been used with high pressure jets.

Inert gases (such as argon) are used to reduce unwanted oxidation and are imperative if burning is to be avoided in flammable materials. Further, they cool the cut edges, serve to reduce backspatter, and protect the focusing optics. If chemically reactive gases are used, energy released in exothermic reactions supplements that from the laser and from mechanical processes and can dramatically increase cutting rates. With oxygen, for example, the laser may be required only to raise the temperature high enough to initiate "self-burning." While the cutting speed may increase, this process can become difficult to control. Surface quality may suffer (through the formation of dross or undesirable oxides) and there may also be periodic striations on the cut edges in some materials (Figure 17), resulting from differences in propagation speeds between the melt front and the laser beam.

Even quite low concentrations of some impurities have been found to affect cutting performance and careful control of both the physical and chemical parameters of the assist gases may be critical in some applications.

In many applications, the characteristically narrow cut width (kerf) provided by lasers is an important benefit. The beam quality and mode structure, which affect focusing, are therefore significant. High power densities are required and are best provided by low-order-mode beams. Focal control is critical to good cutting. If the workpiece is not flat, some type of automatic height adjustment may be needed to ensure continuous control of the focal plane position with respect to the workpiece surface. This may be provided by mechanical means, such as rollers supporting the focusing head, or via optical and electrical sensors monitoring the distance to the workpiece (not shown in the figure).

Often, the laser beam is not perpendicular to the material being cut. This can result in uneven cutting around curves because the rate at which energy is absorbed depends on the polarization of the beam and the angle of incidence. If edges are distorted, material being cut out may remain wedged in the hole rather than freely falling through. The problem is often remedied by use of a circular polarizer in the beam, ensuring uniform cutting independent of direction.

In general, the speed of cutting, like welding, increases with incident laser power but decreases with material thickness. Figure 18 indicates typical ranges of cutting speeds as a function of the laser power normalized by the material thickness. The width of the bands indicates dependence on individual materials and on laser and on gas assist parameters. As noted above, a compromise may often be necessary between maximum speed and optimum cut quality, depending on the particular application.

The cutting of metals is usually slower than that of nonmetals because the laser coupling efficiency is often poorer and because the heat generated diffuses rapidly away from the interaction zone. High beam quality and high peak power densities are needed for the cutting of metals such as copper and aluminum which have both high optical reflectance and high thermal conductivity.

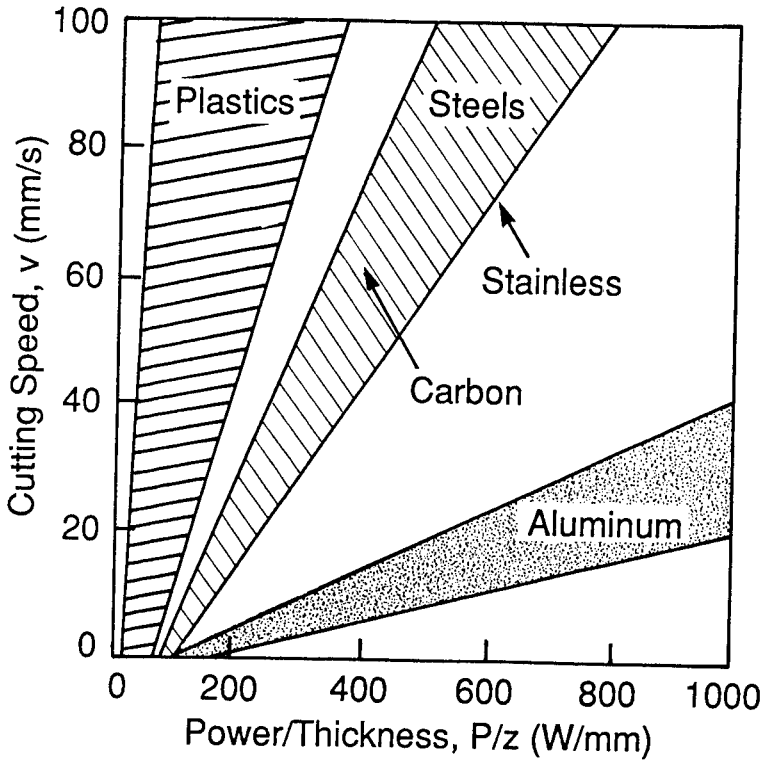


Figure 18. Cutting speed for diverse materials as a function of power per unit sheet thickness.

4.3.2. *Advantages and Limitations*

There are numerous advantages that can be exploited in laser cutting. The laser offers precise control and restricted heat input, and exerts negligible pressure on the workpiece, enabling intricate patterns to be cut in thin materials. Positioning accuracy and dimensional control can be held to within 50 μm even with kilowatt-class lasers. The ability to cut materials does not depend on their mechanical hardness and there is no tool wear. Edge quality is often good enough to obviate further finishing or cleaning operations. The process offers flexibility, easy automation, and rapid reprogramming for different contours. Shapes need not be circular. The narrow kerf (typically 0.5 mm) minimizes debris and maximizes material usage, and environmental concerns can be readily addressed. Multiaxis laser cutters can handle three-dimensional parts, whereas most conventional cutting systems are restricted to cutting flat workpieces.

Cutting speeds are fast, particularly for thin materials, but vary strongly with material and processing parameters. Speeds decrease rapidly as thickness increases but metals up to 10 mm thick have been cut both by CO_2 and by Nd:YAG lasers. However, it is difficult to expel molten debris in deep kerfs and, when left, it absorbs the incident beam and lowers the cutting efficiency. The formation of recast layers and dross can

seriously degrade edge quality. Laser cutting also generates internal stresses which may need to be removed prior to later bending and fabrication operations. Finally, the high capital cost of laser cutting systems and, if large amounts of oxygen assist gas are needed, significant operating costs, are always a major concern.

4.3.3. *Applications*

As already noted, cutting is the most common automotive application of laser processing. Most of the uses stem either from its flexibility and minimal requirement for fixturing, or on its ability to access difficult geometries and to limit heat input.

One of the earliest production-line cutting operations was in 1972, when several cw CO_2 lasers of a few hundred watts were used to cut paper secondary ignition coils. Current applications can be broadly classified as prototype work (relying on the laser's flexibility and speed), low volume (where hard tooling would be uneconomic), option holes and special situations.

The process of developing new vehicles requires extensive use of prototypes during the early design and testing stages. It is often an iterative procedure and the resulting continual modification of dies and hard tooling represents a major cost. The laser is valuable in enabling parts to be cut and subsequently modified with only simple reprogramming of the cutting path. Once the correct geometry has been established, only one die need be fabricated and used for the subsequent production line stamping or cutting. Trimming tools are routinely used in automotive manufacture to remove excess material from deep-drawn parts. Establishing the necessary contour to the required precision can be time-consuming and expensive. The final contour can be established very quickly with a laser cutter, because of the ease with which it can be programmed to accommodate modifications in the contour. The corresponding coordinates are then used to build the trim tool.

Similarly, for low volume markets, the capital cost of stamping dies is often a disproportionately large expense. Thus the Cadillac Allante, introduced in 1987, was aimed at a low-volume market (less than 10,000 per year) but has a shorter underbody than standard Cadillacs. To avoid the need for separate dies, the procedure adopted was to take the two basic components (floor pan and rear compartment pan) of a standard Cadillac underbody and cut off a strip from each of them with a 1.5-kW CO_2 laser [40]. These two shortened sections were then resistance-welded together with a reinforcement to produce the underbody required for the Allante. The laser was also used for some additional cutting and trimming, such as on the 1.1-mm-thick, two-side galvanized rear end panel.

Late option hole cutting lowers manufacturing costs by deferring customized features to a late stage in the vehicle production. It enables a much wider use of common parts. A well-known early example was its use by Volkswagen to provide either left-hand or right-hand drive options for its Golf vehicles [33]. Less than 15% of these vehicles required a ventilation-system cutout on the left, rather than the right, side of the dash-support structure. Since 1986, the cutting operation has been done by a 400-W CO_2 laser mounted such that the beam delivery arm can access the car body interior via the windshield opening.

A later (1990) German application employed a laser-cutting gantry system in a body shop production line [41]. This incorporated a 600-W CO_2 laser to cut a variety of holes in the Opel Omega: one for the antenna, four for rear tow hooks, two for turn indicators, four for air conditioner outlets, and one for a sunroof water drain outlet [42]. The system replaced manual drilling and cuts holes to a ±0.1-mm tolerance.

Figure 19 shows an example from the US, where Ford uses a 400-W CO_2 laser in its St. Louis (Missouri) plant to make roof rack attachment holes in some of its Aerostar

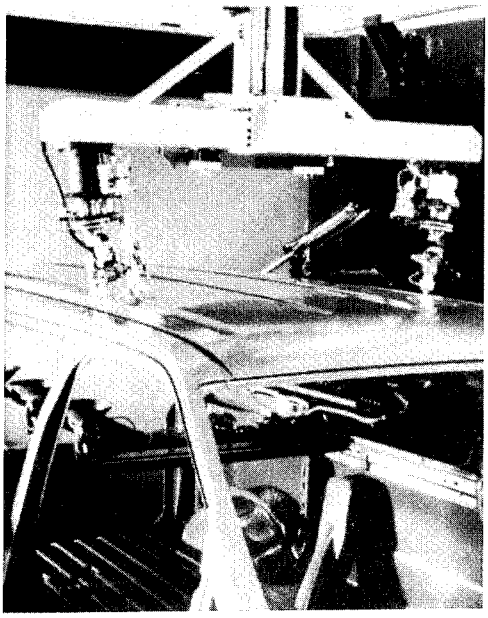


Figure 19. Late option hole cutting of roof rack mounting holes with a 400-W CO_2 laser.

vans. About 40% of these vans are ordered with the roof luggage-rack option and the holes are made, as needed, while the vehicle is on the production line. In practice, the beam is shuttled from side to side to make the two rows of five holes (Figure 19). The holes have 10-mm diameters and are laser-trepanned rather than pierced, the complete operation taking 30 seconds per vehicle.

Several of GM's pickup truck and utility vehicles are offered with a wide variety of customer options, including choices such as 2- or 4-door, extended or standard cab, bench or bucket seats, 2- or 4-wheel drive, and manual or automatic transmission [43]. As a result, there are many different hole patterns that must be available in the 1-mm-thick, two-side-galvanized, steel floor pans to accommodate these variations. A total of 89 different configurations is required to satisfy all choices for these vehicles and a typical floor pan contains about 24 holes, not all circular (Figure 20), with dimensions ranging from 2.8 mm to 39 mm.

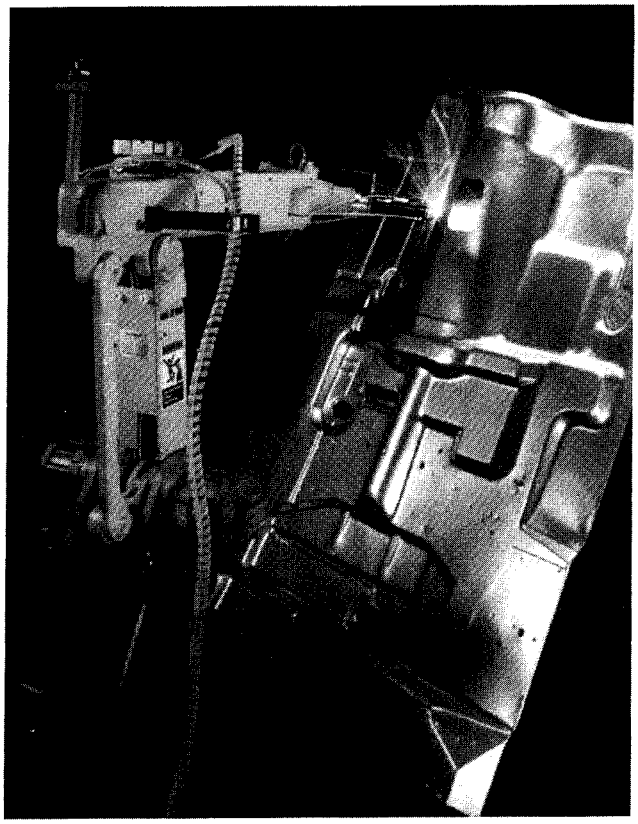


Figure 20. Nd:YAG laser cutting of holes in truck floor pans. Nearly 90 different hole configurations are needed to satisfy all customer options.

The flexibility of the laser and the ease with which cutting paths can be programmed enables all of these holes to be made from only five basic floor pan stampings and greatly reduces die design and tryout costs. A typical laser cell contains two 500-W Nd:YAG lasers, each with a 10-m-long fiber-optic (600-μm-diameter) beam delivery and a robot. The use of two lasers enables each floor pan to be processed in just under one minute. The previous technique, which used electrical and hydraulic drill-and-pierce tooling, mandated substantially more maintenance because of its high mechanical impact nature and consequent wear.

Special situations occur when, for example, distortion must be minimized. The laser cutting of exhaust pipes provides high speed, reduced scrap, and negligible distortion. One German auto manufacturer bevel-cuts chrome-nickel steel alloy head tubes which are to be butt-welded to the inlet of catalytic converters. A robot feeds the pipe sections to a fixed 500-W CO_2 laser beam which both cuts the pieces and drills a

hole needed for a sensor. Cycle times are only a third of those with the earlier technique, the cut taking about 10 s. Further, there is negligible distortion and excellent cut quality.

Similarly, use of an 800-W CO_2 laser avoided deformation in the cutting of mounting holes in the rear spoilers of some GM vehicles introduced in 1987. The spoiler has a complex curvature, to meet aerodynamic needs, but must also have the center high-mounted stop lamp (CHMSL) attached to it. The 3-axis laser system cuts the mounting holes in just one side of the spoiler with minimal distortion [44].

In some cases, laser cutting permits holes to be located correctly in components which may have already undergone distortion. Up to about 30 holes and notches are cut in the 1.5-mm-thick cold-rolled steel brackets which are welded to the 1.6-m-long stamped tube forming the main beam of instrument-panel hangers for two luxury model cars [45]. This beam is attached to the firewall by four bolts, two at each end, and helps support the instrument panel and other accessories (such as an airbag).

Initial attempts to punch the holes in the stamped brackets prior to MIG welding proved unsatisfactory because the deformation produced by the welding process caused positioning problems and variances in the holes. The laser cell contains two 500-W cw Nd:YAG lasers teamed with two 5-axis robots. Each robot is equipped with a 2-axis trepanning head having a combined cutting tip and height sensor. The cell is fully automated and the system provides a cutting rate of up to 4 m/min per laser, with a processing time of 3 seconds per hole (some of which are rectangular) and a scrap rate of less than 1%. The holes have dimensional tolerances in the range ±0.1 mm to ±0.25 mm and positioning tolerances (relative to the mounting holes) in the range ±0.5 mm to ±1.0 mm. The cutting task is shared simultaneously between the two lasers, each of which can operate in an enhanced square-wave mode in addition to cw. This is particularly useful in the case of two holes where the pulsed mode provides enhanced power but also the reduced heat input needed to obtain good edge quality.

5. Current Trends and Prognostications

The future use of laser material processing in the automotive industry depends on several factors: developments in laser technology, improvements in our understanding of how best to utilize the laser-material interaction, and new approaches to automotive manufacturing.

5.1. LASER TECHNOLOGY

The Nd:YAG and CO_2 lasers are expected to continue to dominate laser material processing in the automotive industry for the foreseeable future. Their compactness and reliability will remain key considerations even while output powers may increase. There is growing interest in the processing capabilities of lasers with tens of kilowatts of output power [46]. However, even greater attention will be given to refinements such as pulse shaping and beam spatial control.

The short wavelength of the excimer laser, enabling it to process a wide variety of materials, often with minimal thermal damage, has led to some automotive applications, despite early limitations of power and durability. The latter have both been increased dramatically recently and we expect this trend to continue. The major impediments to their use outside of specialized areas will continue to be their high capital cost and maintenance requirements. Similar comments apply to the copper vapor laser, which has not as yet entered the automotive field. Like the excimer laser, its attraction is its short-wavelength emission (510.6 nm and 578.2 nm). The future of other gas lasers, such as iodine (λ = 1.315 μm) and carbon monoxide (λ = 5-7 μm), is uncertain because the original needs (high power and efficiency, fiber optic transmission) are being increasingly met by developments in CO_2 and Nd:YAG lasers.

The compactness of the newer kilowatt-class lasers is greatly simplifying beam delivery problems. Quite apart from the economic benefits from requiring less plant floor space, they offer the possibility of much closer proximity to the workpiece. Sealed, RF-excited CO_2 lasers, for example, with adequate power for many operations, can be mounted directly on the end of robot arms and access even interior parts of vehicles and components at a late stage in manufacture.

Other developments in CO_2 lasers include the scaling up of output power from diffusion-cooled slab lasers. Their design allows simplicity, by the elimination of fast gas circulation and cooling systems. Operational costs are greatly reduced and, further, very low beam divergences can be obtained.

The versatility of Nd:YAG lasers has greatly increased in recent years with the availability of output powers no longer limited to a few hundred watts and with improvements in fiber-optic beam delivery. A continuing concern is the general difficulty of obtaining high beam quality at high output powers, although advances in slab laser technology have certainly helped in applications such as drilling.

There is currently great interest and activity in the use of diode laser arrays, rather than flash lamps, to pump Nd:YAG lasers [47], whether in slab or rod form. Flash lamps must usually be replaced after a few hundred hours of operation or a few million pulses, and this is a significant item in the operating costs of these lasers. They also have a broad spectral output. Diode-lasers both last much longer than flash lamps and have a spectral emission which is much more efficiently matched to the absorption lines of the neodymium. There are challenges: the technical ones include dissipation of heat from these very high-powered compact devices, and improvement of beam quality. The economic problems include the present high cost of the diode arrays. Nonetheless, average powers of about 1 kW have already been achieved from diode-pumped Nd:YAG lasers and near-cw levels of 6 kW are expected in 1996.

The diode arrays themselves can be used directly for some laser processing applications, such as hardening or soldering, and offer the advantages of compactness, solid-state longevity and relatively short wavelengths (thus improving coupling of the beam to the workpiece). Yearly sales have been doubling since the late 1980s but their high cost, together with limitations imposed by beam divergence, may delay their widespread implementation in the automotive industry, though not necessarily in certain other applications.

5.2. PROCESS TECHNOLOGY

The laser is often still being used in a primitive fashion, because many applications in welding, cutting, and so on, ***are*** possible even in such a manner. We still need to learn more about optimizing parameters such as the rate of energy delivery, assist gas flow and so on. Pulse shapes and frequencies can be tailored to deliver energy at the right rate for a particular process. Similarly, beam shapes, mode structures and polarization can be optimized, and nozzle design can be perfected for given cutting and welding applications. It is intriguing to note that even now, so long after lasers were first implemented for welding automotive steel on the production line, such fundamental aspects as which shielding gas to use are still very fertile areas of basic research [48].

The automatic positioning and sensing of parts to be laser-machined is of increasing importance. For example, some welding and cutting applications require very precise positioning of the beam with respect to the workpiece. This is stimulating development of seam tracking [49] and stand-off height control devices. Future developments may allow much more "forgiving" processing. With adequate power and high beam quality, for example, a laser beam's depth-of-field might be increased to the point where there is no longer need for tight control of the focal plane and the stand-off distance from the last focal head optics to the workpiece.

As noted earlier, in connection with some of the challenges of laser welding 3-D sheet metal, some of the potential advantages of the laser are not always being obtained in practice. Poor metal fitup leads to the need for elaborate and expensive fixturing and clamping, and can largely offset benefits anticipated from one-sided access.

Many current laser applications are very inefficient in the use of what is certainly a rather expensive energy source. For example, the actual time for which a laser beam may be welding is often only a small part of total process cycle time. For much of the time the beam may simply be idle and little thought may be have been given to time-sharing the beam between several applications. This has proved very effective in the welding of components such as transmission parts, but could be used more widely.

There is a need for real-time, *in situ*, process monitoring. The first step is to ensure that the operating parameters (laser power, mode, gas pressures, etc.) are maintained within specific ranges. It is usually more difficult to conduct real-time *in situ* monitoring of the workpiece itself but several diagnostic techniques, notably optical, thermal and acoustic, are being assessed. They include visual appearance of the irradiated spot, the brightness and spectral distribution of the plasma, temperatures at the workpiece, noise in various frequency ranges and so on. While this information helps and can be used in closed loop control systems, it seldom distinguishes adequately between acceptable and unacceptable conditions and post-process evaluations may still be needed.

5.3. NEW MANUFACTURING TECHNOLOGY

The prospects for rethinking the manufacturing process for automobiles are currently very strong because of the increasing need to reduce the time it takes to bring new

models to market, the need to have much more flexibility in providing customized options and to satisfy small or niche markets, and the shorter 'in vogue' lifetime expected for many future models.

Additionally, there have been increased expectations regarding fuel economy, safety and environmental responsibility: these are motivating work on alternative materials and new designs. Although steel has been a prime structural material for the automobile in the past, the mass reductions needed to obtain the fuel economies desired for future vehicles mandate increased use of lighter-weight materials. Traditional cutting and joining methods may need to be re-evaluated and other technologies, such as the laser, considered.

Not only materials but new vehicle designs and assembly processes are stimulating different ways to manufacture automobiles. Only one will be considered here, hydroforming, though there are many others. This process enables closed metal tubes of circular cross section to be shaped into components of complex or varying cross sections along curved paths. It differs from conventional stamping in that it employs only a single full-sized, shape-defining die. Historically, stamping has been a major feature of automotive manufacturing, with the attendant high cost of hard tooling such as dies. Tubular components having varying cross section are usually constructed from individual pieces which must then subsequently be joined to make the final part. Each separate stamping requires its own die - a major expense. Further, these costs are increased by those of the various joining operations, parts handling, inventory, and so on.

The hydroform process offers reduced tooling costs (one hydroform die replaces several stamping dies and eliminates joining operations), less mass (the elimination of several joining operations means that the flanges needed for MIG or resistance spot welding can be reduced), and higher structural integrity and product quality (there are fewer parts and higher strength and stiffness). The laser offers a convenient and flexible way to perform many of the post-trimming and piercing operations. Some holes can be put in by the hydroform die itself but many previously made during conventional stamping will now be produced in a later operation. Contoured end trimming and irregular cuts can be made in a simple and completely agile fashion with tools such as the laser.

In concluding this overview, we note that the laser currently plays only a fraction of its potential role in the automotive industry. Increasing awareness of its successes in the past, its flexibility and its industrial reliability, together with ongoing developments and anticipated vehicle needs, bode well for the future of high-power lasers in automotive materials processing.

Acknowledgments

I am indebted to numerous colleagues both within and outside of General Motors for their generous sharing of information with me.

References

1. von Allmen, M. (1987) *Laser-Beam Interactions with Materials*, Springer-Verlag, Berlin.
2. Ready, J. F. (1978) *Industrial Applications of Lasers*, Academic Press, New York.
3. Shkarofsky, I. P. (1975) Review on industrial applications of high-power laser-beams, *RCA Review (USA)* **36**, 336-368.
4. Duley, W. W. (1976) *CO_2 Lasers: Effects and Applications*, Academic Press, New York.
5. Modest, M. F. and Abakians, H. (1986) Heat conduction in a moving semi-infinite solid subjected to pulsed laser irradiation, *Trans. ASME. J. Heat Transfer (USA)* **108**, 597-601.
6. Mazumder, J. (1983) Laser welding, in M. Bass (ed.), *Laser Materials Processing*, North-Holland, Amsterdam, pp. 113-200.
7. Steen, W. M. and Kamalu, J. N. (1983) Laser cutting, in M. Bass (ed.), *Laser Materials Processing*, North-Holland, Amsterdam, pp. 15-111.
8. Chryssolouris, G. (1991) *Laser Machining: Theory and Practice*, Springer-Verlag, New York.
9. Ion, J. C. (1992) Modeling of laser material processing, in D. Belforte and M. Levitt (eds.), *The Industrial Laser Handbook (1992-1993)*, Springer-Verlag, New York, pp. 39-47.
10. Rykalin, N., Uglov A., and Kokora, A. (1979) *Laser Machining and Welding*, Pergamon, Oxford.
11. Steen, W. M. (1985) Surface engineering with a laser, *Metals and Materials* **1**, 730-736.
12. Miller, J. E. and Wineman, J. A. (1977) Laser Hardening at Saginaw Steering Gear, *Metal Progress* **111**, 38-43.
13. Strong, E. J. (1983) How General Motors Decided to Heat Treat with Lasers on the Assembly Line, *Laser Focus/Electro-Optics* **19**, 172-180.
14. Breinan, E. M. and Kear, B. H.(1983) Rapid solidification laser processing at high power density, in M. Bass (ed.), *Laser Materials Processing*, North-Holland, Amsterdam, pp. 235-295.
15. Draper, C. W. and Poate, J. M (1985) Laser surface alloying, *International Metals Reviews* **30**, 85-108.
16. Li. L. J. and Mazumder, J. (1985) A study of the mechanism of laser cladding processes, in K. Mukherjee and J. Mazumder (eds.), *Laser Processing of Materials*, The Metallurgical Society of AIME, Warrendale, PA, pp. 35-50.
17. Shibata, K. (1990) Laser Applications in the Japanese Automobile Industry, *Proc. 2nd Intl. Application Forum on Laser-Material-Processing in the Automotive Industry, 15-16 Nov. 1990, Bremen, Germany*, pp. 22-29.
18. Swift-Hook, D. T. and Gick, A. E. F. (1973) Penetration welding with lasers, *Welding J.* **52**, 492s-499s.
19. Klemens, P. G. (1976) Heat balance and flow conditions for electron beam and laser welding, *J. Applied Phys.* **47**, 2165-2174.
20. Cline, H. E. and Anthony, T. R. (1977) Heat treating and melting material with a scanning laser or electron beam, *J. Applied Physics* **48**, 3895-3900.
21. Mazumder, J. and Steen, W. M. (1980) Heat transfer model for cw laser material processing, *J. Applied Physics* **51**, 941-947.
22. Dowden, J., Postacioglu, N., Davis, M., and Kapadia, P. (1987) A keyhole model in penetration welding with a laser, *J. Phys. D: Applied Physics* **20**, 36-44.
23. Mazumder, J. (1991) Overview of melt dynamics in laser processing, *Optical Engineering* **30**, 1208-1219.
24. Kapadia, P., Ducharme, R., and Dowden, J. (1992) The theory of radiative transfer in the plasma of the keyhole in penetration laser welding, in *Proc. ICALEO '91, Vol. 74*, Laser Institute of America, Orlando, FL:, pp. 53-63.
25. Schuocker, D. (1992) Physical mechanism and modeling of deep-penetration laser welding, in D. Belforte and M. Levitt (eds.), *The Industrial Laser Handbook (1992-1993)*, Springer-Verlag, New York, pp. 67-73
26. Friermood, E. (1993) Production Laser Welding of Automobile Air-Conditioner Pulleys, *United Technologies Industrial Lasers' Fourth International Focal Spot Users' Seminar, Orlando, Florida, 21-24 October 1993.*
27. Anon. (1991) The Auto Industry: A World Market, *Welding Design & Fabrication* **64**, 38-46.

28. Anon. (1991) Ford Buys Laser Systems for Transmission Welding, *Industrial Laser Review* **6**, 24.
29. DiPietro, F. A. (1989) Robotic Laser Welding Systems, *Paper #89504, Proc. Conf. on Laser Applications in the Automotive Industries, 21st ISATA, Wiesbaden, Germany, 6-10 November 1989*, **1**, 39-60.
30. Uddin, N. M., Berardi, E., Ducharme, R. C., Salada, D. A., and Speranza, J. J. (1986) A Five-Axis Robotic Laser and Vision Integrated "On-Line" Welding System, *Proc. SPIE Conference on Laser Processing, Quebec City, Canada, 3-6 June 1986*, **668**, 260-264.
31. Anon. (1991) Why General Motors is Investing in Laser Beam Welding, *Welding Journal* **70**, 65.
32. Anon. (1991) Integrated CHMSL, *Automotive Industries* **71**, 39.
33. Vaccari, J. A. (1992) CO_2 and YAG Lasers Tackle Tougher Tasks, *American Machinist* **136**, 37-48.
34. Schreffler, R. (1990) Toyota Tahara, *Automotive Industries* **170**, 42-44.
35. Neiheisel, G. and Cary, R. (1991) From Scrap Reclamation to Tailored Blanks, *Industrial Laser Review* **6**, 5-9.
36. Irving, B. (1991) Blank Welding Forces Automakers to Sit Up and Take Notice, *Welding Journal* **70**, 39-45.
37. Roessler, D. M., Jenuwine, W. C., Koons, J. N., and Speranza, J. J. (1992) Laser Material Processing in General Motors Corporation, *Paper #921053, Proc. Conf. on Laser Applications in the Automotive Industries, 25th ISATA, Florence, Italy, 1-5 June 1992*, pp. 37-51.
38. Koons, J. N. and Roessler, D. M. (1994) Body Sheet Metal Applications of Laser Welding," *Proc. International Body Engineering Conference (IBEC '94), Detroit, Michigan, 26-29 September 1994*, **10**, 97-100.
39. Schuocker, D. (1987) The physical mechanism and theory of laser cutting, in D. Belforte and M. Levitt (eds.), *The Industrial Laser Handbook (1987)*, PennWell Books, Tulsa, OK, pp. 65-79.
40. Anon. (1990) Prima Industrie Seeks Growth in Lasers, *Auto Industry Newsletter* **12**, 12.
41. Manthey, S. (1991) Dimensional Gauging of Reference Features for Laser Cutting, *Paper #911265, Proc. Conf. on Laser Applications in the Automotive Industries, 24th ISATA, Florence, Italy, 20-24 May. 1991*, pp. 665-672.
42. Aberman, Z. (1990) Laser Cutting and Welding Systems for JIT Production, *The Fabricator* **20**, 33-34.
43. Vasilash, G. S. (1992) GM Truck & Bus: On the Cutting Edge of Laser Cutting Technology, *Production* **104**, 38-40.
44. Owen, J. V. (1992) Cutting It with Lasers, *Manufacturing Engineering* **108**, 35-41.
45. Miller, P. C. (1994) Beam versus Stream, *Tooling & Production* **60**, 38-46.
46. Banas, C. (1993) Laser Welding to 45 kW, *United Technologies Industrial Lasers' Fourth International Focal Spot Users' Seminar, Orlando, Florida, 21-24 October 1993.*
47. Marabella, L. (1995) Status Report on Technology Reinvestment Project for High Power Diode Pumped Solid State Lasers, *Automotive Laser Applications Workshop (ALAW '95), Dearborn, Michigan, 6-7 March 1995.*
48. Abbott, D. H. and Albright, C. E. (1994) CO_2 Shielding Gas Effects in Laser Welding Mild Steel, *J. Laser Applications* **6**, 69-80.
49. Juptner, W. and Falldorf, H. (1991) A Seam Tracking System for Laser Beam Welding, *Paper #911280, Proc. Conf. on Laser Applications in the Automotive Industries, 24th ISATA, Florence, Italy, 20-24 May. 1991*, pp. 691-698.

LCVD WITH COPPER VAPOUR AND COPPER BROMIDE VAPOUR LASERS - REVIEW

B. IVANOV, C. POPOV, V. SHANOV, D. FILIPOV

Higher Institute of Chemical Technology, Dept. of Semiconductors, 8 Kliment Ohridski St., 1756 Sofia, Bulgaria

1. Introduction

Recently, metal organic chemical vapor deposition (MOCVD) has become a successful competitor to the classical sputtering method for aluminium [1]. Information concerning the photolytic decomposition of Al alkyls with excimer laser radiating in the UV range of wavelengths predominates in the literature, while experiments on the basis of pyrolysis of these compounds by laser emission are treated in far fewer papers. Besides, there is no definite answer as to what is the mechanism of thermal decomposition of trimethylaluminium. In the literature there is a lack of information concerning the use of pulsed visible lasers and in particular a Copper Vapour Laser (CVL) or Copper Bromide Vapour Laser (CBVL) in the wavelength range 510 - 578 nm for LCVD of any materials. This has motivated our research into the activation of chemical processes by such a laser for deposition of aluminium and silicon.

2. LCVD of Al from trimethylaluminium (TMA)

The deposition of aluminum stripes in closed reaction cell was carried out by the pyrolytic LCVD process using a focused beam of copper vapor laser up to 130 μm on the surface of an Si (111) monocrystalline wafer. The experimental set-up for LCVD of aluminum is given on Fig. 1. The scanning speed was varied from 10 to 400 μm/s, the laser power was between 0,8 and 2 W. The partial pressure of the precursor was in the range of 0.5 to 10 mbar and the background temperature of the substate was changed from 300 to 573 K. More details are presented in Refs. [2] and [3].

R. Kossowsky et al. (eds.), High Power Lasers – Science and Engineering, 505–526.
© 1996 *Kluwer Academic Publishers. Printed in the Netherlands.*

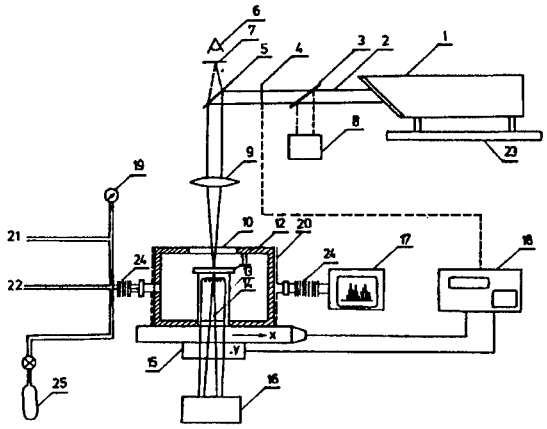


Fig. 1. Schematic of the experimental set-up for LCVD

1 pulsed visible laser; 2 laser beam; 3 beam splitter; 4 optical shutter; 5 mirror; 6 observer; 7 optical filter; 8 power meter; 9 quartz lens; 10 quartz window; 11 wafer holder; 12 chamber; 13 heater ; 14 thermocouple; 15 stepping stage; 16 temperature control unit; 17 quadrupole mass spectrometer; 18 computer; 19 pressure gauge; 20 heating tape; 21 turbomolecular pump; 22 gas supply system; 23 granite table; 24 flexible vacuum connection; 25 metalorganic precursor.

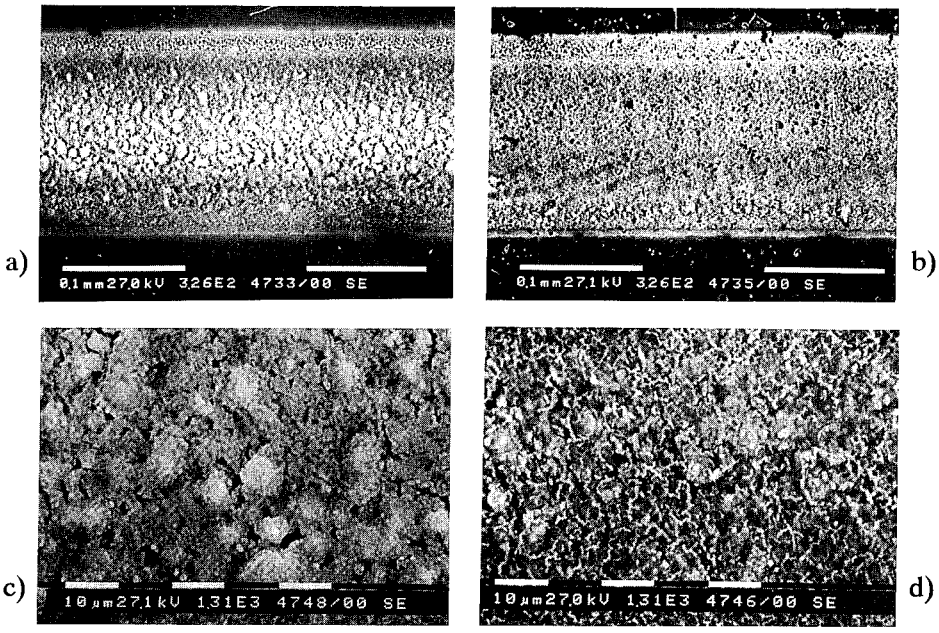


Fig. 2 Scanning electron micrographs of aluminium lines (background temperature, 300 K; laser power 1.0 W): a) TMA pressure of 0.1 kPa and writing speed of 20 µm / s; b) TMA pressure of 0.1 kPa and writing speed of 60 µm / s; c) TMA pressure of 0.1 kPa and writing speed of 20 µm / s; d) TMA pressure of 1 kPa and writing speed of 20 µm / s.

2.1. Morphology of LCVD aluminum

The morphology of the deposited aluminum shows well-definite grains which are more typical for photolytic deposition of metals [2-4]. The grain size depends strongly on the process parameters. This was the first time, we believe, that the layer structure was observed using pyrolysis of metal alkyls with visible laser light. This type of morphology most probably originates from the pulsed time structure of the light source, in which the power flux to the substate for the time of single pulse is about several hundreds GW/m^2. This may cause an increase in supersaturation and a high nucleation rate, which favors the granular structure. The size of the grains decreases with the increase in the writing speed as result of a decrease in the surface temperature (Figs. 2 a) and 2 b)). The increase in the partial pressure of TMA from 1 to 10 mbar results in almost halving of the grain size which could be caused by the increase in supersaturation (Figs. 2 c) and 2 d)). The profile of the deposited material approximately follows the laser beam intensity distribution. As shown on Figs. 3 and 4 , the height and the width of the lines decrease with increases in the writing speed. This is an expected effect due to the decreases in laser exposure time.

2.2.Geometric parameters and growth rate behaviour of the deposited stripes

Careful evaluation of the geometric parameters of the profile was necessary for further calculation of the vertical growth rate, Vg [5]. The expression used for this calculation was:

$$V_{vg} = h / \tau \qquad \{ 1 \}$$

where h is the heights of the stripes in micrometers, obtained for the time of deposition, τ in seconds.The time of deposition in the center of the laser spot, t , can be determined:

$$t = wo / Vsc \qquad \{ 2 \}$$

where wo is the laser spot diameter in micrometers and Vsc - the scanning speed in micrometers per second. Using Equation 1 and 2 we obtained:

$$V_{vg} = h \; Vsc / wo \qquad \{ 3 \}$$

The laser spot diameter can be calculated from the formula:

$$wo = f \; \theta \qquad \{ 4 \}$$

where f is the focal length in micrometers and θ is the laser divergence in radians. For the laser used in this work $f = 3.7 \times 10^4$ μm/s and $\theta = 3.5 \times 10^{-3}$ rad. The obtained value was experimentally verified. As shown on Figs. 5 growth rate shows tendency of increasing with a rise of the scanning speed

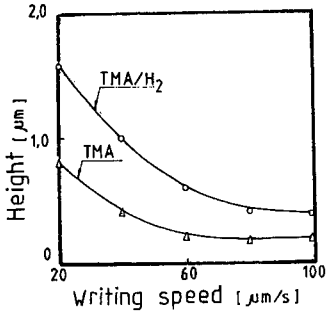


Fig. 3 Average line height as a function of writing speed (background temperature, 373 K; laser power 1.6 W); Δ - 0.1 kPa - TMA; O - 0.1 kPa - TMA + 0.1 MPa - H_2.

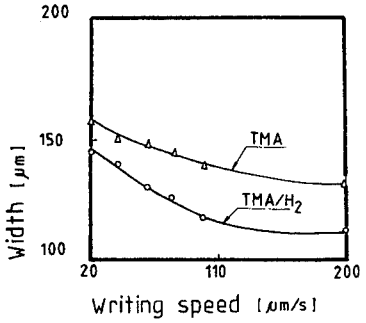


Fig. 4 Line width as a function of writing speed (background temperature, 373 K; laser power 1.6 W): Δ - 0.1 kPa - TMA; O - 0.1 kPa - TMA + 0.1 MPa - H_2.

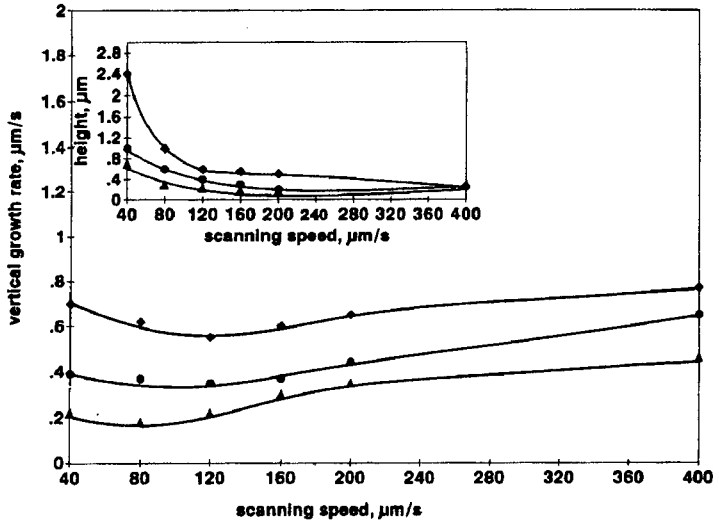


Fig. 5. The vertical growth rate and the height of the stripes as a function of the scanning speed at 1.6 W laser power and 473 K background temperature ● - 0.1 kPa TMA + 0.1 MPa H_2; ◆ - 0.1 kPa TMA + 0.1 MPa Ar; ▲ - 0.1 kPa TMA.

from 120 μm/s up to 400 μm/s. We believe this behavior is due to the change of the deposition conditions (mainly the optical and thermal properties of the substrate surface) when varying the scanning speed. The growth of the deposited layers could be provisionally divided into two basic stages: deposition on pure silicon surface that predominate at high scanning speeds, and deposition on the aluminum layer already grown during the first stage. The second stage prevails at low scanning speeds. Boundary cases could be considered to be those at which *V*sc tends to extremely high values and when *V*sc = 0. It is assumed that the deposition for which vertical growth rate was calculated includes the processes that occurs during both stages. When heating the substrate the maximum temperature rise in the center of the spot can be given by:

$$To = P(1\text{-}R) / \{(2p)^{1/2} k wo\} \qquad \{ 5 \}$$

where P is the laser power, R is the refractively of the substrate, wo is the laser spot diameter and k is the thermal conductivity. The use of the average power, P, for a pulsed laser such as a copper laser is not correct, and does not give the real temperature rise. Due to the pulsed time structure of laser irradiation, the temperature on the substrate oscillates between high and low values with each pulse. This behavior complicates the real temperature determination. Nevertheless Equation 5 shows the influence of the substrate properties (R and k) on the surface temperature. For deposition on silicon substrate (R_{Si}=0.38; k_{Si}=1.4W.cm^{-1}.K) the maximum temperature would be higher compared with that for deposition on already grown aluminum layer (R_{Al} = 0.92; k_{Al} = 2.35 W.cm^{-1}.K). A competing trend, which influences the growth rate, is the surface temperature increase when the scanning speed of laser beam is decreased, which is the case without deposition. This effect could be substantially disturbed by the deposition of materials with thermal and optical properties different from those of the substrate. It is supposed that this is the reason for growth rate behavior of the deposited Al stripes on Si surface at scanning speed between 120 μm/s and 400 μm/s. In the range between 40 μm/s and 120 μm/s probably increasing of carbon contamination with decreasing of scanning speed is responsible for increasing of surface temperature and deposition rate. The growth rate of aluminum stripes obtained in hydrogen atmosphere is lower than that in an argon atmosphere at the same process parameters (Fig. 5). Hydrogen is probably not an inert component during the pyrolytic LCVD. Suzuki at al. supposed formation of active intermediates containing Al as result of TMA decomposition. It is assumed that these radicals can interact with hydrogen and the final result is their deactivation so they do not contribute to the layer growth. Argon as an inert gas does not affect the decomposition chemistry and, in this case the growth rate is higher. The results in Fig. 5 indicate the lowest vertical growth rate when absence an additional gas. Following the hypothesis for intermediates, it is assumed that there is an increase of their molecular diffusivity at lower total pressure. This effect

enhances the diffusion of the intermediates away from the laser spot and decreases their dwell time on the surface reaction area. In this way, the probability for further decomposition to Al decreases. The growth rate is seen to increase with an increase of the total pressure in the chamber as it is shown in Fig. 6. It is supposed that in this case the total pressure effect dominates over the competing trend of intermediates chemical deactivation with hydrogen. The growth rate of the stripes is lower at higher temperatures for the same process parameters (Fig. 7). This is probably a result of the enhanced desorption of TMA molecules at higher temperatures which causes decrease in the surface concentration of the precursor.

2.3. New experimental approach for growth rate determination of LCVD written Al stripes

For kinetic studies of CVD processes is of great importance the precise evaluation of the layer thickness or the mass of the deposit. These approaches are inconvenient for applications that use direct writing based on LCVD. The problems are caused mainly by the non-uniform thickness of the deposit following the Gaussian distribution across the laser spot [6]. Weight measurement of the deposit is not reliable for laser direct writing because of micrometric dimensions of the features obtained. Our experience in LCVD of Al showed that for deposition of reasonable quantity of Al (e.g. 1 mg), which could be precisely weighted by a microscale, line 80 μm wide , 2 μm thick and 231.5 cm. long should be written. This would take 6.4 h at a scanning speed of 100 μm/s, which will slow down the data collection for different process parameters. We consider that in the case of kinetic investigations of laser induced direct writing , reliable method is inductively coupled plasma atomic emission spectroscopy (ICP-AES). The dedection limits of this analytic technique for most of the metals is about $5x10^{-2}$ μg / ml. and lower [7]. A special technique was developed for mass determination of the aluminium deposit [8]. A 3 in. monocrystaline silicon wafer was cut into 16 uniform square pieces (13 mm X 13 mm) and set up in a holder placed in the reaction cell. Aluminium meander stripes with length 80 mm was written on each of the silicon pieces. The conventional sample introduction into an ICP as a liquid required a preliminary dissolution of the deposited material. The usual solvent for Al, like hydrochloric acid did not work efficiently because of the presence of insoluble residues of Al compounds. We found that mixture of concentrated nitric and hydroflouric acids was suitable for a total dissolution of the deposit. The emission intensity of the most sensitive line (Al 396.152 nm) was measured. The relative standard deviation of Al determination was in the range 0.71-3.20 %. The Al concentration in the samples was determined after calibration procedure. Fig. 8 illustrated the quantity of the deposited Al per meander obtained at different partial pressures of TMA. This behaviour

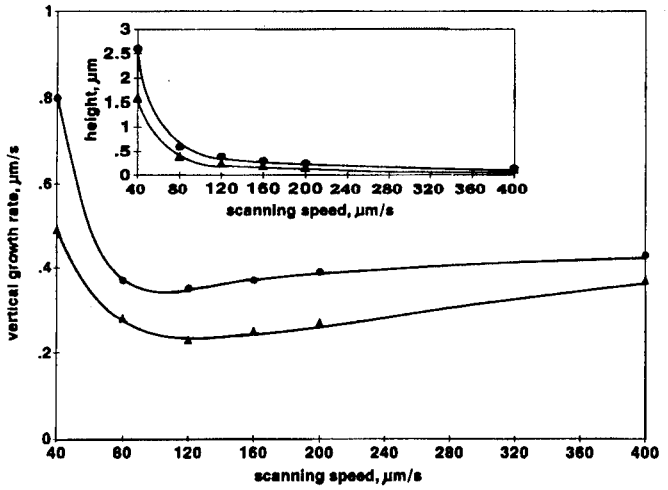


Fig. 6. The vertical growth rate and the height of the stripes as a function of the scanning speed at 1.2 W laser power and 373 K background temperature: ▲ - 0.1 kPa TMA + 10 kPa H_2; ● - 0.1 kPa TMA + 0.1 MPa H_2.

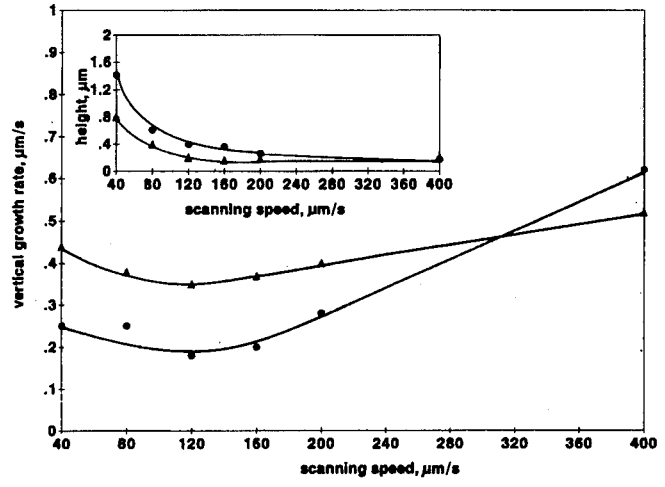


Fig. 7. The vertical growth rate and the height of the stripes as a function of the scanning speed 1.6 W laser power and 0.1 kPa partial pressure of TMA ▲ - 300 K; ● - 373 K.

suggests surface kinetics as a rate limiting step. In this case the chemical reaction rate is proportional to the surface concentration of the reagent, which is determined by its partial pressure via a certain adsorbtion isotherm. Fig. 9. presents the dependence of deposited Al quantity per meander on the laser beam power. As shown in this figure the increase of the laser power causes a rapid rise of the deposit quantity and hence the growth rate. The ICP-AES method could be used for growth rate evaluation of laser induced direct written Al. The calculation of the growth rate was based on the expression:

$$V_g = G / (b \; l \; t) \qquad \{ 6 \}$$

Where G is the quantity of the deposited Al per meander, b is the width of the stripe, l - the length of the meander and t is the deposition time. In the case of pulsed laser one should consider the total duration of the pulses per second, which could be obtained by multiplying the repetition rate f_r by the pulse time t. Than the real laser exposure time t for writing of the meander will be:

$$t = l \; f_r \; t \; / Vsc \qquad \{ 7 \}$$

This expression could be refined by taking into account the time for temperature decrease between the pulses down to the decomposition temperature of TMA. If we assume the surface kinetics as a limiting step for LCVD of Al, the growth rate can be expressed by applying of Freundlich`s isotherm:

$$V_g = k \; p^{\alpha} \qquad \{ 8 \}$$

Taking the logarithm of Equation 8 we obtain:

$$\ln V_g = \ln k + \alpha \ln p \qquad \{ 9 \}$$

Fig. 10 shows the logarithm of growth rate as a function of the logarithm of the partial pressure of TMA. In this case the growth rate could be expressed by

$$V_g = 0.93 \; X \; 10^{-3} \; p^{0.68} \qquad \{ 10 \}$$

which fits the experimental data with an accuracy of ± 2.5% and confirms the accepted isotherm. When changing the laser power to the 1.9 W, the expression for the growth rate is converted to:

$$V_g = 1.28 \; X \; 10^{-3} \; p^{0.755} \qquad \{ 11 \}$$

The reason for increasing of k is the raise of the power. We believe that the reason for the change of α is alteration of the mechanism of the chemical reaction.

2.4. Element analysis of LCVD aluminum

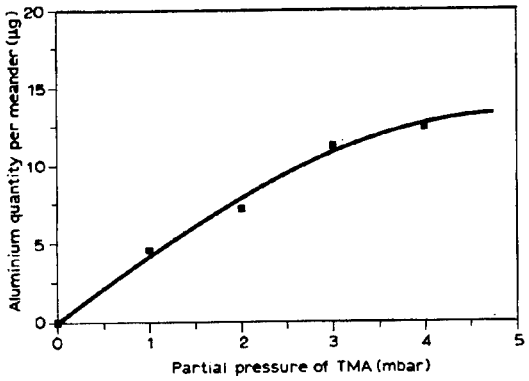


Fig. 8 Deposited aluminium quantity per meander as a function of partial pressure of TMA at 160 µm/s scanning speed, 1.7 W laser power and 373 K background substrate temperature.

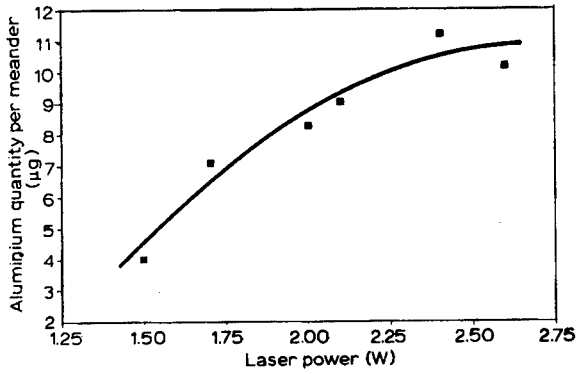


Fig. 9 Deposited aluminium quantity per meander as a function of laser power at 120 µm/s scanning speed, 2 mbar partial pressure of TMA and 373 K background substrate temperature.

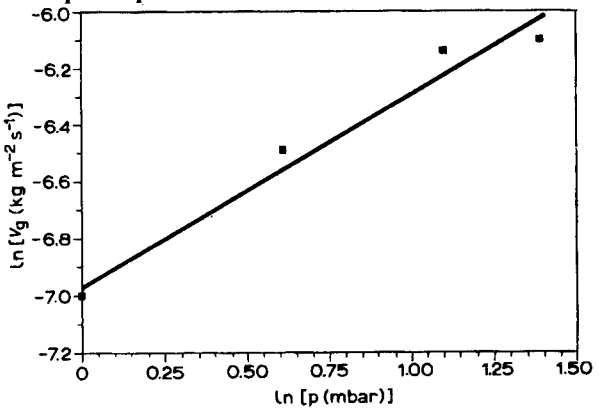


Fig. 10 Growth rate of aluminium as a function of partial pressure of TMA at 160 µm/s scanning speed, 1.7 W laser power and 373 K background substrate temperature.

The element analysis of the Al deposits from TMA were obtained by AES and the depth profile of the basic elements are shown on Fig. 11 (a). The top layer of the film exhibits the usual oxide coating, which results from exposure to air prior to the analysis. Relatively high carbon contamination in LCVD written aluminum stripes using TMA was probably due to the unconventional way of the precursor decomposition caused by pulsed laser irradiation and secondary reaction of the products. It was confirmed by *in situ* mass spectrometric studies of the gaseous phase composition during the deposition process.

2.5. Mass spectrometric study of LCVD process from TMA

The photofragmentation mass spectrometric data for TMA show mostly gaseous products like: ethane, ethylene and methane. In the case of pyrolysis of this compound the mechanism of the decomposition differs substantially from that of photodecomposition and the reported gaseous products were mainly methane and hydrogen [9], methane [10] or methane, hydrogen and small amounts of ethane and ethylene [11]. A different mechanism and different products of the chemical reaction are expected when pulsed laser irradiation with extremely high power density per pulse is used. In the case of deposition this will cause high peak surface temperature [12]. For LCVD of Al from metal organic precursors we used Quadrupol Mass Spectrometer (QMS 200 - Inficon) to determine *in situ* the gas composition. The experimental arrangement for the sampling gaseous products during laser pyrolysis of TMA is shown on Fig. 12. A sampling capillary is introduced in to a stainless steel cell adjacent to the surface of silicon wafer, on which pyrolysis takes place. A high vacuum gas-dosing needle valve was set up at the end of this capillary for precise and reproducible pressure maintenance in the QMS sensing head. The room temperature mass spectrum of TMA showed patterns similar to those presented in Ref. [13]. The detected characteristic peaks at m/e = 57, 43, 42, 41, 29, 28, 27 and 15 are assigned to the fragments: Al $(CH_3)_2^+$; $AlHCH_3^+$, $AlCH_3^+$, $AlCH_2^+$, AlH_2^+, AlH^+, Al^+ and CH_3^+. We observed total pressure rise in the closed reaction cell during LCVD. This effect is due to the gaseous products released during laser pyrolysis of TMA [14]. Fig. 13 shows mass spectrum obtained after 8.58 min. of laser processing. The "bar subtract" mass spectrum illustrated the differences between the current data and the previously saved data which are obtained immediately prior to the beginning of the pyrolysis. As presented in Fig. 13, the basic mass peaks of various intensities are found in three groups: first group, m/e = 30, 29, 28, 27 and 26; second group, m/e = 16, 15, 14 and 13; and third group, m/e = 2 and 1. The second and third groups are typical mass spectra of methane and hydrogen. The mass peaks at m/e = 30, 29, 28, 27 and 26 can be assigned to ethane. In accordance with the tabulated data for ethane, the intensity of the mass peak at

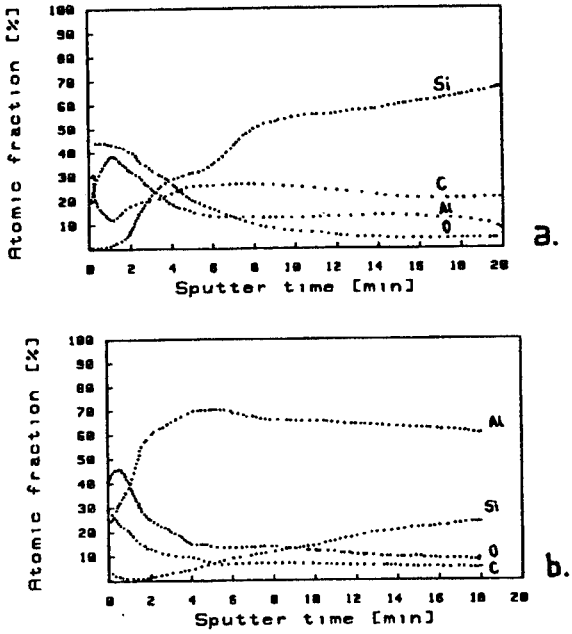


Fig. 11 Auger electron intensity as a function of sputtering time: (a) Al stripe deposited from TMA 1 mbar, scanning speed 100 μm/s, laser power 0.8 W, (b) Al stripe deposited from TMAA 0.1 mbar, scanning speed 20 μm/s, laser power 1.3 W.

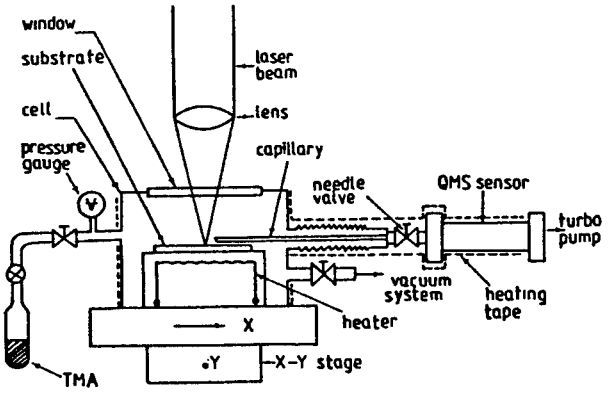


Fig. 12 Experimental set-up for LCVD coupled with quadrupole mass spectrometer for *in situ* analysis.

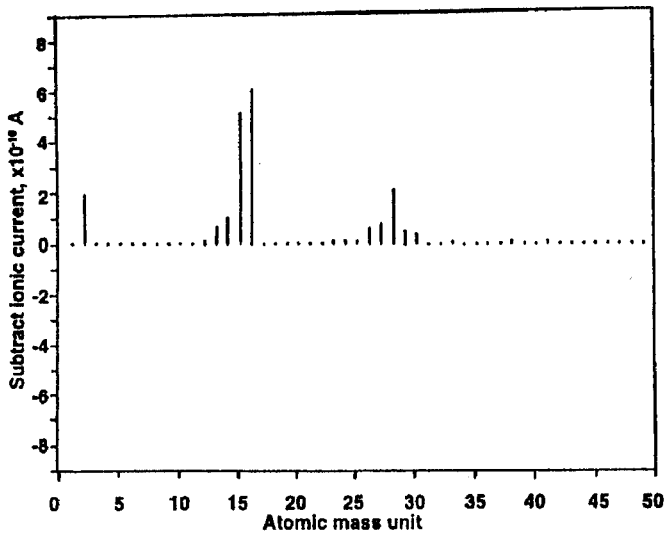


Fig. 13 Bar-subtract mass spectrum of products from TMA pyrolysis after 8.58 minutes laser processing time at 0.22 GW/m^2 average power density, 120 μm/s scanning speed and 100 Pa - - (1 mbar) TMA.

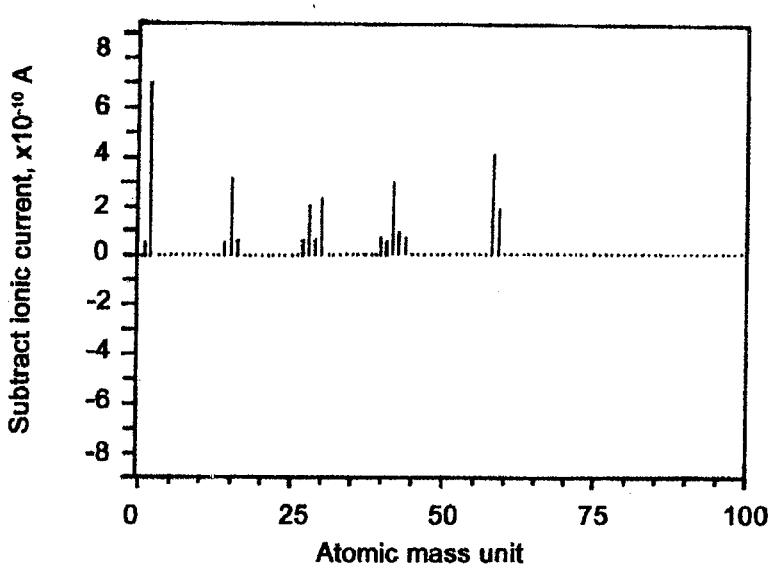


Fig. 14 Bar-subtract mass spectrum of products from TMAA pyrolysis after 1000 s laser processing time at 98 MW/m^2 average power density, 10 μm/s scanning speed and 10 Pa (0.1 mbar) TMAA.

m/e = 28 should be 3.3 time higher that at m/e = 30 [15]. Estimation of this ratio from Fig. 13 gives a value of 4.5. This discrepancy is probably due to the simultaneous presence of fragments with m/e = 28 originating from molecules of ethane and ethylene[15]. As shown on Fig. 13 (for m/e = 2), the presence of hydrogen as a product of LCVD process is considerable, while in the literature are reported only traces of this gas for a short decomposition time (5 - 40 min.). When pyrolysis with a pulsed laser takes place, the high peak surface temperature could cause decomposition of the resulting hydrocarbon products to hydrogen and carbon. Such a secondary pyrolysis of hydrocarbons depends strongly on the laser power density and is responsible for additional carbon contamination of the growing aluminum layers. Auger elemental analysis of the deposit confirmed that the carbon content varied in the range 10-25 at. %.

2.6. Resistivity of the Al stripes.

The resistivity of each line was calculated after the evaluation of geometric parameters and resistance. The lowest value obtained was 90 μΩ.cm. This resistivity occupies an intermediate place regarding the classical materials used for interconnection in IC technology: doped polycrystalline silicon (2000 μΩ.cm) and silicides of titanium, cobalt, molybdenum and tungsten (13-35 mΩ cm) [16] In general the resistivity decreases with increase the writing speed in the range 20 -80 μm/s (Fig. 15). This behaviour is probably due to the decrease in the grain size, causing the densification of the Al layers.

3. LCVD of Al from trimethylamine alane (TMAA)

This precursor offers some advantages over the common alkyl Al sources of being less air sensitive, having simple decomposition pathway, and decomposing at temperature below 120^{O}K. Layers of III-V compounds and Al, grown from TMAA, showed greatly reduced levels of carbon and oxygen contamination. This is due to the absence of a direct Al-C bond in its molecule and relatively weak donor-acceptor bond between Al and N. From the other side, oxygen contamination is suppressed by the formation of involatile Al-OH species and by high surface atomic hydrogen concentration. We selected TMAA for LCVD of Al in order to improve the quality of the Al deposit [17].

3.1. Geometric parameters and morphology of LCVD aluminium

The dependence of geometric geometric characteristic on the process parameters are almost the same like in the case of TMA with the exception of width stripe behavior - Fig.16 a) and b). The morphology of the layers have similar granular structure. but additional "volcano" effect could be recognised on SEM micrographs Fig. 17 (a) and (b) [2, 17]. As it can be seen from Fig. 11

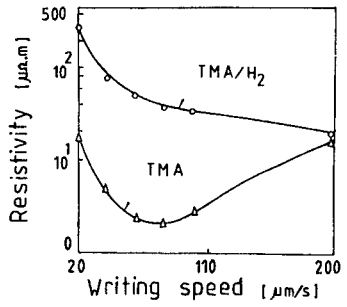


Fig. 15 The resistivity as a function of writing speed (background temperature, 373 K; laser power 1.6 W): Δ - 0.1 kPa - TMA; O - 0.1 kPa - TMA + 0.1 MPa - H_2.

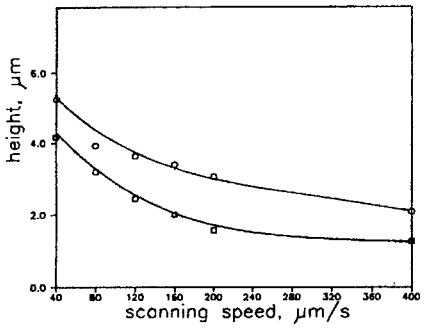


Fig. 16 a) Average stripe heights as a function of scanning speed at 1 mbar TMAA; laser power: □ - 1.3 W; O - 1.8 W .

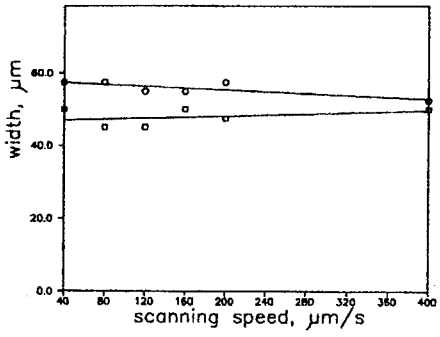
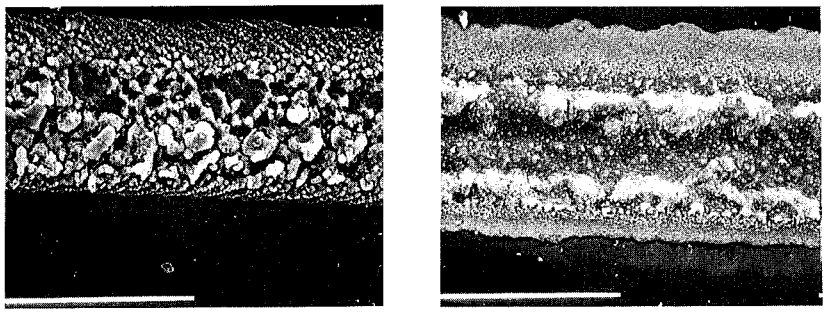


Fig. 16 b) Stripes widths as a function of scanning speed at 1 mbar TMAA; laser power: □ - 1.3 W; O - 1.8 W .



a) b)

Fig. 17 Scanning electron micrographs of aluminium stripes a) TMAA pressure of 0.1 mbar, scanning speed - 10 μm / s, x 44, b) TMAA pressure of 0.1 mbar, scanning speed - 60 μm / s, x 44.

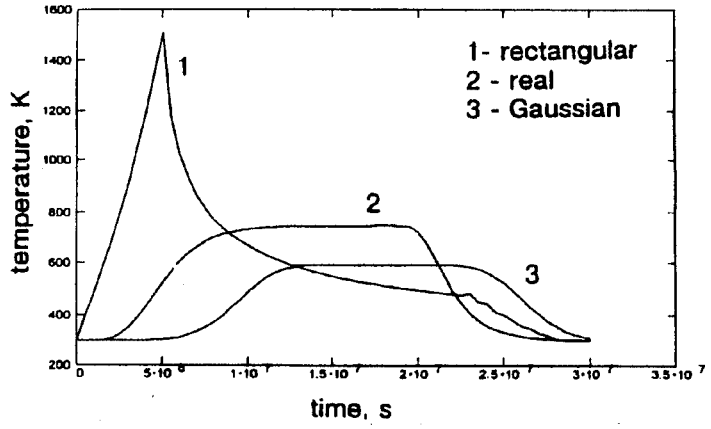


Fig. 18 Temperature in the laser spot center as a function of time. Laser power - 0.490 W, spot diameter 100 μm.

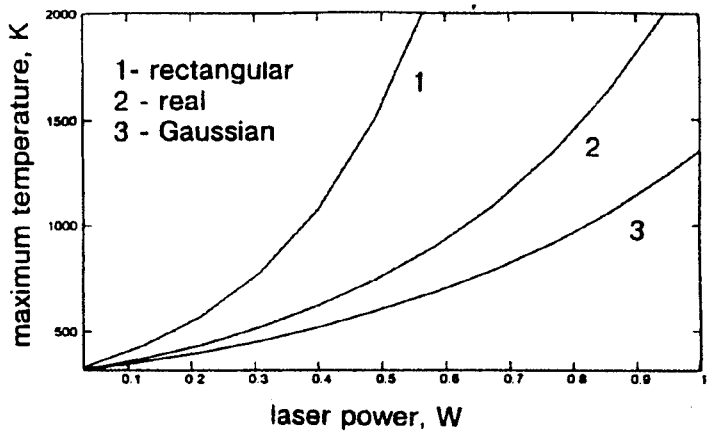


Fig. 19 Maximum temperature in the laser spot center as a function of laser power.

(b), the carbon contamination in the layer is considerably reduced due to the absence of direct Al-C bond and easy cleavage, weakly coordinated Al-N bond.

3.2. Mass spectrometric study of LCVD process from TMAA.

The detected characteristic peaks for room temperature mass spectrum of TMAA at m/e = 59, 58, 56, 42, 30, 28, 27 and 15 could be assigned to the fragments $N(CH_3)_3^+$ $N(CH_3)_2CH_2^+$ $N(CH_2)_3^+$ $N(CH_2)_2^+$; NCH_3H^+/AlH_3^+; NCH_2^+/AlH^+; NCH^+/Al^+; CH_3^+, respectively. Fig. 14 shows "bar subtract" mass spectrum of the gaseous products released during the laser pyrolysis of TMAA [18]. The basic mass peaks which change their intensities are m/e = 58, 42, 59, 15, 30, 28, 43, 41, 2. These peaks indicate formation of usual products of TMAA decomposition - trimethylamine and hydrogen. In accordance with the tabulated data for trimethylamine, the intensity of the mass peak at m/e = 58 should be 2.9 time higher that at m/e = 15 [15]. Estimation of this ratio from Fig. 14 gives a value of 1.3. This discrepancy is probably due to the simultaneous presence of fragments with m/e = 15 originating from molecules of trimethylamine and methane [15]. The mass peak at m/e = 16 indicates presence of methane in the gaseous phase during LCVD of Al from TMAA. The tremendous energy flux adsorbed by the substrate during the deposition probably changes the decomposition mechanism compared with that at moderate temperatures. At high surface temperature the liberation of CH_3 groups is possible due to the break of nitrogen-carbon bond. A secondary gas phase reaction of CH_3 groups is quite likely to form CH_4, which is presented on the spectra. The calculated values of the resistivity were 1.5-3.5 times higher that of bulk Al (2.8 $\mu\Omega$ cm) and the lowest value reached was 4.0 $\mu\Omega$ cm. The resistivity was almost independent on the scanning speeds in the range of 10-60 μm/s , where the best results were obtained.

In conclusion, it should be stressed that the average power density for deposition of Al from TMAA with copper vapor laser is about 100 times lower compared to that obtained with an Ar^+ laser. We consider this as a significant advantage of the pulsed visible laser [17].

4. LCVD of Si from silane.

In order to model LCVD with CVL and CBVL, we choose relatively simple and well studied chemical system - CVD of Si from silane. We developed new model for temperature distribution at Si surface induced by CBVL laser, taking in to account the shape of laser pulse. The latest leads to quite different results in comparison with data from the literature based on rectangular shape pulse structure. Analytical model, describing different kinetic systems, are proposed also. The analytical approach is based on the Kirhoff transform and Green function analysis of nonlinear heat diffusion problem [19].

4.1. Modelling of the temperature distribution

The temperature T in the irradiated zone can be described by the following equation:

$$T(\theta) = b + (T_0 - b)\exp\left[\frac{\theta}{T_0 - b}\right] \qquad \{12\}$$

$$K(T) = \frac{a}{T - b} \quad ; a = 299\ \frac{W}{cm} \quad ; b = 99\ K$$

Where θ is the linearized temperature, which is expressed by next equation {13}:

$$\theta = \frac{P_a(1-R)}{2\pi K_0 \lambda f I_f} \int_0^t \int_{-\infty}^{+\infty} \int_{-\infty}^{+\infty} \int_0^{\infty} GF(X,Y,Z,\tau;X',Y',Z',\tau')SF(X',Y',Z',\tau')dX'dY'dZ'd\tau'$$

where the Green's function GF is defined in the next equation {14} as:

$$GF(X,Y,Z,\tau,X',Y',Z',\tau') =$$
$$= [4\pi(\tau-\tau')]^{-3/2} \exp\left[-\frac{(X-X')^2+(Y-Y')^2}{4(\tau-\tau')}\right]\left\{\exp\left[-\frac{(Z-Z')^2}{4(\tau-\tau')}\right] + \exp\left[-\frac{(Z+Z')^2}{4(\tau-\tau')}\right]\right\}$$

The consideration of the pulsed character of the irradiation is accomplished by defining of the source function SF. In case of round spot and Gaussian beam it's form will be:

$$SF(x,y,z,t) = \frac{P(t)(1-R)}{\pi w_o^2 \lambda f} \exp\left[-\frac{(x - V_{sc}t)^2 + y^2}{w_o^2}\right] \exp(-z/\lambda) \qquad \{15\}$$

where P(t) is the laser power in pulse, R the reflectance, wo the laser spot radius, Vsc - the scanning speed and λ the absorption depth. The experimentally obtained shape of the laser pulse is fitted and expressed mathematically. The introduction of the obtained expression in {15} allows to estimate the real temperature distribution. Temperature distribution in the time course for different approximations of the pulse shape (rectangular and

Gaussian) compared with the temperature distribution for the real pulse is shown on Fig. 18 . As it can be seen from Fig. 19, the pulse shape substantially influences the maximum temperature in the laser spot center of the irradiated zone.

The obtained time evolution of temperature distribution on Si surface for real pulse shape is presented on Fig. 20. On the basis of the obtained temperature distribution at the end of the pulse, the distance from the spot center to the point where T = 548 ^{O}K (the temperature above which the decomposition of SiH_4 on the surface takes place [20]) is determined. It corresponds to the half-width of the deposited stripe. The theoretically calculated and the experimentally measured widths of the stripes are compared on Fig. 21. As seen from this figure the model predicts well the experimental widths.

4.2. Modelling of the kinetics

The determination of kinetic parameters during the LCVD process is very difficult task. That is why we used cited data from the literature. The results of several investigations concerning the thermal decomposition of SiH_4 on heated silicon substrate show that the process has a complex mechanism [21] and different pathways. According to the most of models the process could be considered from the point of view of Langmuir - Hinshelwood kinetics, including: adsorption, surface chemical reaction and desorption. Our model for laser pyrolysis of SiH_4 using a pulsed laser is based on the following assumptions: (a) process of homogeneous pyrolysis of SiH_4 does not occur; (b) the obtained hydrogen is not adsorbed; (c) LCVD of Si is entirely pyrolytic process; (d) the gas phase diffusion is not taken into account.

According to Buss et al. [22] the heterogeneous decomposition of SiH_4 includes dissociative adsorption, desorption and surface reaction. In this work, analytical expression for the reactive sticking coefficient (RSC) as a function of the substrate temperature are presented. In our case the process is non-isothermal and non-stationary and it is necessary the RSC distribution along x and y directions and in the time course to be known.

The temperature field and it's time evolution already described in paragraph 4.1. are involved in the model of Buss et al. and RSC distributions as a function of coordinates and time are determined. Since RSC is time dependent function, an effective time t_{eff} for the reaction run by one pulse with an average value of RSC (for x = 0 and y = 0 where RSC is maximum) could be defined.

$$t_{eff} = \int_0^{t_p} RSC(t)\, dt \qquad \{16\}$$

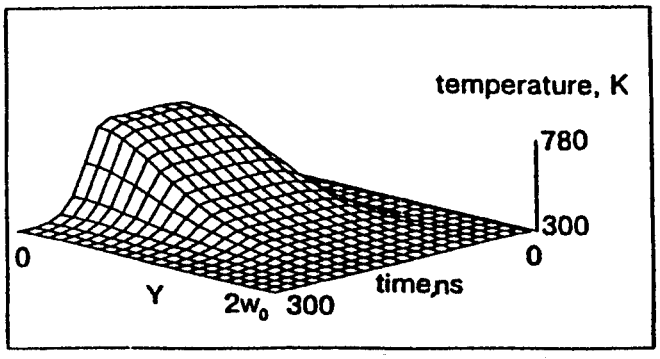


Fig. 20 Temperature as a function of coordinate Y and time.

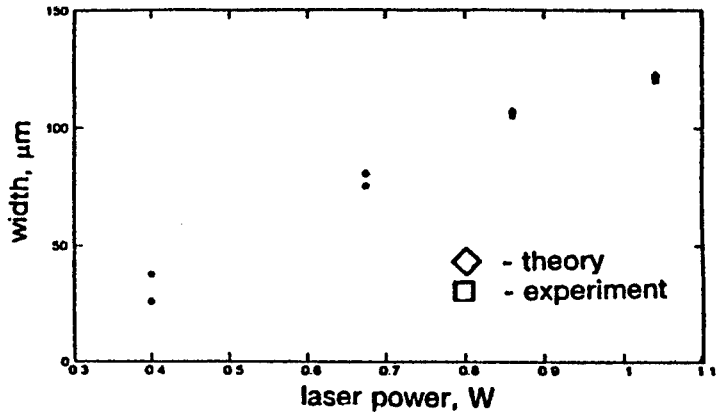


Fig. 21 Theoretical and experimental widths of silicon stripes as a function of laser power. Pressure of 5 % SiH_4 in Ar - 1000 mbar.

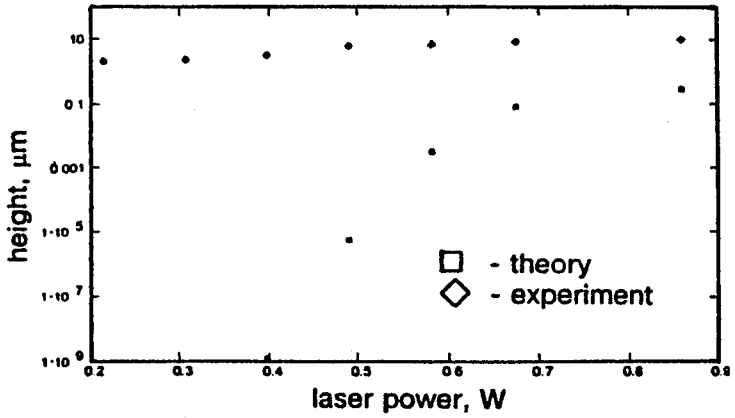


Fig. 22 Theoretical and experimental heights of silicon stripes as a function of laser power. Pressure of 5 % SiH_4 in Ar - 1000 mbar.

It is convenient the introduction of another parameter Vm, which is constant for a definite gas partial pressure:

$$V_m = F M / (\rho N_A) \qquad \{17\}$$

where F is SiH_4 molecules flux to the surface, M the atomic mass of silicon, ρ the density of monocrystalline silicon and N_A Avogadro's constant. The physical meaning of Vm is the maximum deposition rate assuming that RSC = 1 and its value is 2.71x10-3 m/s for 50 mbar partial pressure of SiH_4.

The height of the deposited stripe for one pulse Hp in the center of the laser spot (x = 0, y = 0) will be product of t_{eff} and Vm

$$Hp = t_{eff} V_m \qquad \{18\}$$

The X-Y stepping stage used in the experiment performs step of 2 μm so the number of translations for which the laser beam spot (with diameter 2wo) will pass through a geometric point is wo. It means that for 100 μm laser spot the number of translations will be 50.

The number of pulses at a point Np can be determined by the following expression

$$N_p = s f / V_s \qquad \{19\}$$

where s is the step of X-Y stepping stage, Vs the scanning speed and f the laser frequency. Having in mind the character of translation of the X-Y stepping stage and RSC as a function of the coordinate x, along which this translation is carried out, the height of the deposited stripe H can be determined by the expression

$$H = Hp N_p \frac{\sum_{i}^{50} \int_{0}^{t_p} RSC(t, X_i)\, dt}{\int_{0}^{t_p} RSC(t, X = 0)\, dt} \qquad \{20\}$$

The obtained results from {20} presented on Fig. 22 show substantial discrepancy with the experimental data in contrast to the width modelling. Our opinion is that the kinetics of LCVD of Si from SiH_4 using copper bromide

vapour laser is complicated probably by non-linear photolytic effects and can not be defined with the known kinetic parameters. In literature there is information about photolytic effect during the deposition of silicon from silane induced by a cw Ar^+ laser, but this effect takes place only at low laser powers [23]. To the best of our knowledge pyrolytic LCVD of silicon from silane, using CBVL is reported from our group for the firs time. The influence of process parameters on the geometry of the obtained stripes are presented and some conclusion for the process mechanism are made.

In conclusion, we consider the copper vapor lasers as a power tool for enhancement of CVD and for materials processing. There is still a lot to be done in this area and new research is in progress.

5. References

1. Levy, R.A. Green M.L. and Gallagher, P.K., (1984) Characterisation of LPCVD aluminium for VLSI processing, *Journal of Electrochemical Society* **No 9**, 2175 - 2182.

2. Shanov, V., Popov, C and Ivanov B. (1993) LCVD of aluminium stripes obtained by pyrolysis of TMAA and TMA, *Journal de Physique IV,* **3** 255 - 260.

3. Shanov, V., Ivanov B. and Popov, C (1992) Laser chemical vapour deposition of thin aluminium coatings , *Thin Solid Films* **207**, 71 - 74.

4. Shanov, V., Ivanov B. and Popov, C. (1991) Laser induced direct writing of aluminium, *Journal de Physique II* **1**/7, 373 - 380.

5. Shanov, V., Ivanov B. and Popov, C (1993) Growth rate behavior of LCVD aluminium, *Processing of Advanced Materials* **3**, 41 - 44.

6. Allen, S. , (1981) Laser chemical vapor deposition: A technique for selective area deposition, *Journal of Applied Physics* **52**, 6501 - 6505.

7. Thomson, M. and Walsh, J., (1983) *A Handbook of Inductively Coupled Plasma Spectroscopy*, Blackie, Glasgow.

8. Shanov, V., Popov, C, Ivanov, Souleva, A. and Peev, G. (1993) An experimental approach for growth rate determination of LCVD written aluminium stripes, *Journal of Materials Science: Materials in Electronics* **4,** 55 -58.

9. Suzuki, N., Anayama, C., Masu, K., Tsubouchi, K. and Mikoshiba, N., (1986) *Japanese Journal of Applied Physics,* Pyrolysis and photolysis of trimethylaluminium **25**, 1236 - 1242.

10.Squire, D.W., Dilcey, C.S. and Lin, M.C., (1985) Mechanistic studies of the decomposition of trimethylaluminium on heated surfaces, *Journal of Vacuum Science and Technology* **B3**, 1513 - 1518.

11. Yeddanapalli, L.M. and Schubert C.C., (1946) Thermal and photochemical decomposition of gaseous aluminium trimethyl, *Journal of Chemical Physics*, **14**, 1 -8.

12. Haba, B., Hussey, B.W. and Gupta, A., (1991) Temperature distribution during heating using a high repetition rate pulsed laser, *Journal of Applied Physics* **69**, 2871 - 2876.

13. Tanaka, J. and Smith, S.R., (1969) Mass spectra of Bridge-bonded aluminium compounds, *Inorganic Chemistry* **8**, 265 - 270.

14. Ivanov, B., Popov, C. and Shanov, V., (1992) Mass spectrometric study of laser induced pyrolytic decomposition of TMA, *Journal of Advanced Materials for Optics and Electronics* **1**, 287 - 292.

15. Grasselli, J.G. and Ritchey, W.M., (1975) *Atlas of Spectral Data and Physical Constants for Organic Compounds,* 2end ed., CRC Press, Cleveland OH.

16. Pauleau, Y., (1987) Interconnect materials for VLSI circuits, *Solid State Technology*, **No 2**, 61 -67; **No 4**, 155 -162; **No 6**, 101 - 105.

17. Popov, C., Ivanov, B. and Shanov, V., (1994) Laser-induced chemical vapor deposition of aluminium from TMAA, *Journal of Applied Physics* **75**, 3687 - 3689.

18. Popov, C., Ivanov, B. and Shanov, V., (1993) Mass spectrometric study of laser induced pyrolytic decomposition of TIBA and TMAA, *Journal de Physique IV* **3**, 107 - 112.

19. Ivanov, B., Popov, C., Shanov, V. and Filipov, D., (1993) Pyrolytic LCVD of silicon using a pulsed visible laser - experiment and modelling, Mat.Res.Soc.Symp. W Vol. **334** - *Gas Phase and Surface Chemistry in Electronic Materials Processing* - November 29 - December 4, 1993, Boston, USA.

20. Gates S.M., Greenlief, C.M., Beach, D.B. and Holbert P.A., (1990) Decomposition of silane on Si(111)-(7X7) and Si(100)-(2X1) surfaces below 500^{O}C, *Journal of Chemical Physics* **92**, 3144 - 3153.

21. Jasinski, J.M. and Gates S.M., (1991) Silicon chemical vapor deposition one step at a time: Fundamental studies of silicon hydride chemistry, *Accounts of Chemical Research* **24**, 9 -15.

22. Buss, R.S., Ho, P., Breiland, W.G. and Coltrin, M.E., (1988) Reactive sticking coefficients for silane and disilane on polycrystalline silicon, *Journal of Applied Physics* **63**, 2808 - 2819.

23. Auger, G., Tonneau, D. and Patella, Y., (1988) Evidence of a photon effect during the visible laser-assisted deposition of polycrystalline silicon from silane, *Applied Physics Letters* **52**, 1062 - 1064.

LASER DEPOSITION AND CHARACTERIZATION OF A-C AND A-C:N FILMS

J. BULÍŘ, M. JELÍNEK, V. PEŘINA*,
Institute of Physics, Academy of Sciences of the Czech Republic, Na Slovance 2, 180 40 Prague 8, Czech Republic.
**Institute of Nuclear Research, Řež by Prague, Czech Republic*

1 Introduction

The interest of amorphous carbon (a-C) films is stimulated by the search of new protective coatings of the mechanical tools by the reason of their high hardness and low friction coefficient. The a-C films are also applicable as the protective anti-reflection coatings for IR optics because of their low optical absorption in IR.

The high energetic particles injected to the film produce high compressive stress in the film [1], [2] that induce a buckling of the films [3]. The value of the stress depends on the substrate temperature and on the pressure of the environmental gas during deposition [4], and on the thickness of the film [5]. The a-C films prepared by various deposition methods possess usually intrinsic stress between 1 and 10 GPa [1] [5] [6]. The intrinsic stress produces a shear stress at an interface between the substrate and the film. The shear stress is proportional to the film thickness. There exists a critical value of the film thickness above which the shear stress exceeds the adhesion of the film and delamination occurs. Adhesion of a-C films to substrate that depend on the material of the substrate, on the pretreatment of the surface, and on the substrate temperature during deposition, is usually poor. Consequently it is very difficult to produce thick a-C films without buckling.

Investigation of the effect of nitrogenation on the properties of hard carbon films became since Jones and Stewart published the first paper on nitrogenated hydrocarbons in 1982 [7]. Nitrogenated carbon films without hydrogen (a-C:N) were studied for the first time by Cuomo et al. in 1979 [8], but great increase of the interest can be noticed after Liu and Cohen (1989) predicted theoretically the superior hardness of the hypothetical β-C_3N_4 material [9].

Laser ablation and deposition is a suitable method for preparation of thin film with high quality for material research. Ablation dynamics depend besides of target material and laser parameters also on the presence of the environmental gas [10]. The enhanced pressure causes collisions between the ablated atoms and background atoms, and the coating atoms arrive at the substrate in randomized directions that promote a shadowing effect and void formation [4]. As it is simulated in [11] the amorphous films contain a number of voids.

R. Kossowsky et al. (eds.), High Power Lasers – Science and Engineering, 527–532.
© 1996 *Kluwer Academic Publishers. Printed in the Netherlands.*

The amorphous germanium behaves as a weak p-type semiconductor [12]. The amorphous carbon has similar behavior. Nitrogen doping change it to n-type semiconductor. At certain doping level the a-C semiconductor is compensated. An increase of an electrical resistivity is observed at this level [13] [14].

Aim of this work is concerned on the investigation of an influence of nitrogen pressure on the properties of the a-C:N films. Electrical resistivity, intrinsic stress, and UV-Vis transmission of the films were measured. Nitrogen concentration were determined from RBS measurement.

2 Experimental details

2.1 PREPARATION OF SAMPLES:

The experimental setup consists of a KrF excimer laser (EAK, type ELI-94) and vacuum chamber, in which a heating substrate holder is placed in the distance of 3 cm from a graphite target. The laser beam (pulse duration 20 ns, repetition rate 5 Hz) was focused by the quartz lens on the target at an angle of 45°. The target was rotated during deposition. The power density of the beam on the target was $3x10^8$ Wcm^{-2}.

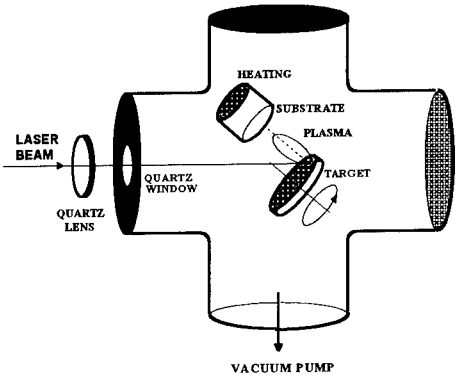


Figure 1. Scheme of the deposition set up.

The substrates were optically polished and cleaned in acetone, toluene and ethanol before deposition. At first, the vacuum chamber was pumped out to a pressure of $2x10^{-3}$ Pa by an oil diffusion pump. Before deposition the substrate was heated at temperature 300°C for an hour in order that faster degassing of the substrate surface was reached. After preheating the substrate was cooled near to room temperature. Films were deposited on fused silica substrates in vacuum pressure of

TABLE 1. Summary of deposition conditions.

Laser Source	KrF (248 nm)
Pulse Duration	20 ns (FWHM)
Repetition Rate	5 Hz
Pulse Energy	200 mJ/pulse
Spot Size on Target	1.2 x 2.5 mm^2
Power Density	~3 x 10^8 W/cm^2
Target	Graphite (99.99% C)
Substrate	fused silica 10x10mm^2
Substrate Temperature T_s	40°C
Target-Substrate Spacing	3 cm
Base Pressure	2 x 10^{-3} Pa
Nitrogen Pressure	0.5-100 Pa
Deposition Rate	0.02-0.05 nm/pulse

$2x10^{-3}$ Pa (a-C) or in nitrogen atmosphere of pressure p_N from 0.5 to 100 Pa (a-C:N). The thickness of the films ranged from 90 nm to 350 nm.

2.2 CHARACTERIZATION OF THE FILMS:

The samples were analyzed using the standard Rutherford backscattering (RBS), UV-Vis transmission, electrical resistivity, Raman spectra, and.intrinsic stress measurement.

The RBS was accomplished with 2 - 2.35 MeV proton beam to get the best precision of the analysis. The measured area was 1-2 mm^2 and supposed accuracy 5-10%.

The UV-Vis transmission measurements were carried out on the films using Specord spectrometer.

The electrical resistivity measurement was performed on the films deposited on the quartz substrate. Silver contacts were created on the film surfaces. A multimeter was used for determining resistivity lower than $10^3\,\Omega$cm. Resistivities higher than $10^3\,\Omega$cm were determined from the voltage drop at a known ohmic resistance electrically connected in series with the films. A voltage of 35 V was applied, and the voltage drop at the ohmic resistance was measured.

Raman spectra were measured in near-backscattering geometry using 488 nm line of Kr-ion laser of the power below 100mW. The scattered light was analyzed by the double-grating spectrometer (Spex 14018) and detected by a Quantacon photomultiplier (RCA C31034) operating in the photocounting regime. The spectral slitwidth never exceeded 6 cm^{-1}.

The intrinsic stress was determined from the curvature of the substrate. The curvature was measured using optical leverage method. The two parallel laser beams were aimed on the substrate and the deflection of the reflected beams was measured. The radius of the substrate curvature was calculated from the deflection of the beams. The intrinsic stress of the film is given by Stoney's equation [5]. .

3 Results

RBS with 2-2.35 MeV protons was chosen to characterize a-C:N layers. The main reason were the enhancement sensitivity for light elements (e.g. non-Rutherford cross-section), which enables more precise estimation of stoichiometry for layers thicker than several hundreds of nm. Only some uncertainty of cross-section of carbon near resonance for our geometry (i.e. scattering angle 160°)

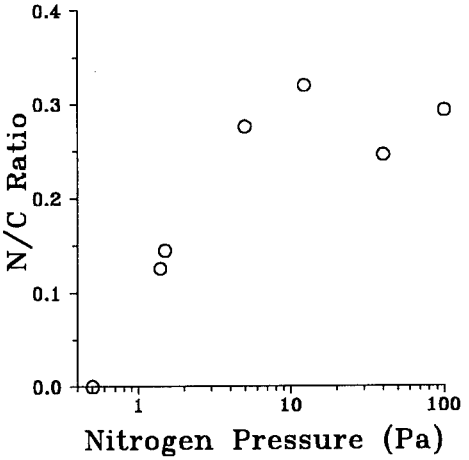


Figure 2. Influence of the nitrogen pressure p_N on the ratio N/C in the film.

is a little disadvantage. The FWHM of detector is 12 keV.

An influence of the nitrogen pressure p_N on the ratio N/C in the film is on Fig.2. At first the increase of nitrogen pressure p_N has strong influence on increasing amount of nitrogen incorporated in the films till p_N reaches 5-10 Pa. Above this pressure is ratio N/C saturated on value of around 0.3 and the next increase of the nitrogen pressure has no contribution to amount of nitrogen in the film.

The presence of the nitrogen in the a-C:N films is confirmed by the Raman spectra. Example of the spectra is on Fig.3. The weak peak at 2220 cm^{-1} is characteristic of triple bonded C-N stretching mode and indicates that nitrogen is chemically bonded to carbon [15] [16].

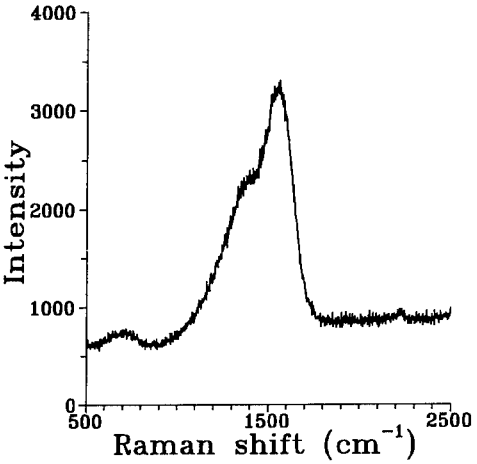


Figure 3. Example of fitted Raman spectra of a-C:N films deposited by laser ablation. (T_s=40°C, p_N=12.2 Pa).

The films exhibit good transparency in visible region. The absorption edge of the nitrogen free a-C film is located around 0.4 μm. In agreement with [17], the nitrogenation of the a-C leads to decrease of the optical band gap and refractive index.

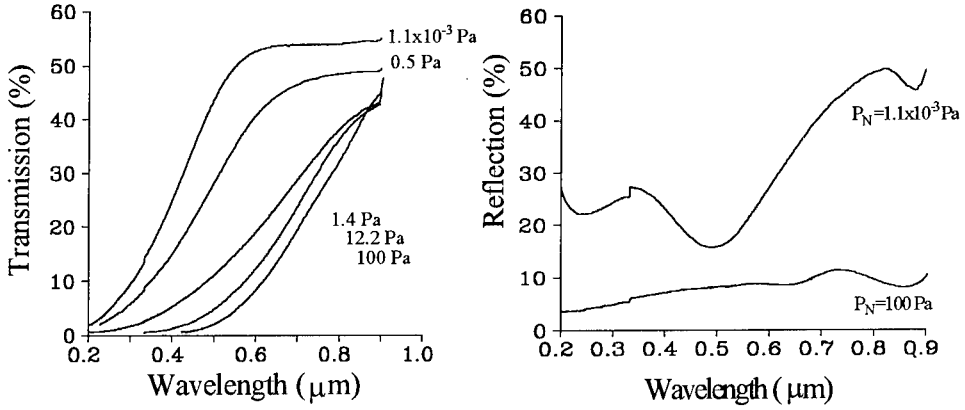


Figure 4. UV-Vis transmission and reflection of the a-C and a-C:N films deposited on the quartz substrate. The a-C:N films were deposited at various nitrogen pressure p_N (T_s=40°C).

It is seen on Fig.4 that absorption edge shifts from UV region to IR region with increasing p_N. The shift is accompanied with a shrinkage of the optical gap. The nitrogenation also influences the reflectivity of the film-substrate system. The reflectivity of the a-C:N films on fused silica substrate is lower than that of the a-C film (Fig.4).

The a-C films possess high electrical resistivity. The resistivity even increases with increasing nitrogen pressure p_N during deposition process (Fig.5).

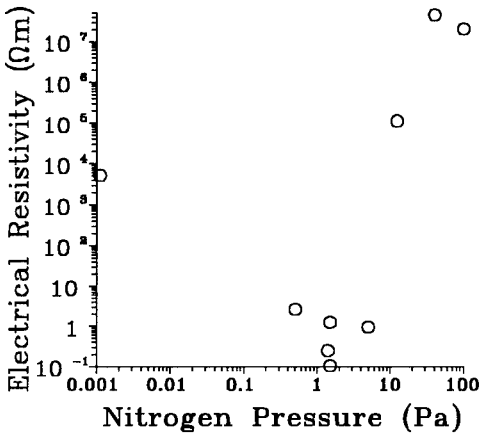


Figure 5. Electrical resistivity of the a-C and a-C:N films deposited on the quartz substrate versus nitrogen pressure p_N (T_s=40°C).

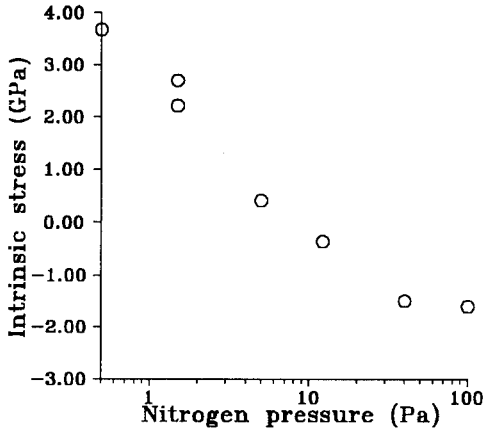


Figure 6. Change of the intrinsic stress in the a-C:N films deposited on the quartz substrate (T_s=40°C) with nitrogen pressure p_N.

The nitrogen free films possess high intrinsic compressive stress. The stress strongly depends on the p_N. With increasing nitrogen pressure the compressive stress around 4 GPa changes to tensile stress around 2 GPa. It was found by interpolation of the points that it can be reached a zero stress in a film deposited at a pressure of 10 Pa. In this manner the thick a-C films without buckling and cracking can be prepared.

4 Discussion

Some properties, for example electrical resistivity and intrinsic stress, change their value with p_N above 5-10 Pa while the concentration of the nitrogen in the structure is saturated. This result implies that the change of the properties is due to a change of the deposition mechanism. When the nitrogen pressure p_N is elevated the traveling particles are disturbed due to collisions with the nitrogen gas [10]. The fact, that the particles arrive at the substrate in randomized directions, promote shadowing effect and formation of voids in the structure [4]. The created porous structure yields tensile stress [4]. In agreement with the results our samples created at enhanced pressure possess tensile stress. The compressive stress produced by injection of the particles into the films [18] is reduced and even changed to tensile stress by formation of the voids in the film.

The rapid increase of the electrical resistivity can be explained by the presence of the voids reducing the effective cross-section of the film. The increase of the resistivity is not evocated by compensation effect of the nitrogen doping because the resistivity rapidly increases in the region where the concentration of nitrogen is saturated. In addition the compensation effect is established at much lower concentration of nitrogen.

5 Conclusion

The nitrogen content of the films is in the range from 0% to 25%. Presence of nitrogen in the films is confirmed by appearance of weak peak around 2220 cm^{-1} in the Raman spectra. The films exhibit increasing N/C ratio with increasing nitrogen pressure p_N.

The absorption edge shifts from UV to IR region with increasing p_N. The increase of the p_N influence increase of the electrical resistivity of the films.

The films internal compressive stress reduces and change to the tensile stress with increasing pressure p_N. A thick films with a zero stress can be obtained.

6 References

1. Scheibe, H.-J. and Schultrich, B. (1994) Thin Solid Films **246**, 92
2. McKenzie, D.R., Muller, D., and Pailthorpe, B.A. (1991) Phys.Rev.Lett. **67**(6), 773
3. Iyer, S.B., Harshavardhan, K.S., and Kumar, V. (1995) Thin Solid Films **256**, 94
4. Thornton, J.A. and Hoffman, D.W. (1989) Thin Solid Films **171**, 5
5. Puchert, M.K., Timbrell, P.Y., Lamb, R.N., and McKenzie, D.R. (1994) J.Vac.Sci.Technol. A **12**(3), 727
6. Veerasamy, V.S., Amaratunga, G.A.J., Milne, W.I., Robertson, J., and Fallon, P.J. (1993) J.Non-Cryst.Solids **164**, 1111
7. Jones, D.I. and Stewart, A.D. (1982) Philos.Maq B **46**, 423-434,
8. Cuomo, J.J., Leavy, P.A., Yu, D., Renter, W., and Frisch, M. (1979) J.Vac.Sci.Technol.**16**, .299-302,
9. Liu, A.M. and Cohen, M.L. (1989) Science **245**, 841-842,
10. Ohkoshi, M., Yoshitake, T., and Tsushima, K. (1994) Appl.Phys.Lett. **64**(24), 3340
11. Henderson, D., Brodsky, M.H., and Chaudhari, P. (1974) Appl.Phys.Lett. **25**(11), 641
12. Tauc, J., Grigorovici, R., and Vancu, A. (1966) Phys.Stat.Sol. **15**, 627
13. Amaratunga, G.A.J., Veerasamy, V.S., Davis, C.A., Milne, W.I., McKenzie, D.R., Yuan, J., and Weiler, M.. (1993) J.Non-Cryst. Solids **164-166**, 1101
14. McKenzie, D.R., Yin, Y., Marks, N.A., Davis, C.A., Kravtchinskaia, E., Pailthorpe, and B.A., Amaratunga, G.A.J. (1993) J.Non-Cryst. Solids **164-166**, 1119
15. Chen, M.Y., Li, D., Lin, X., Dravid, V.P., Chung, Y.-W., Wong, M.-S., and Sproul, W.D. (1993) J.Vac.Sci.Technol. A **11**(3), 521
16. Kaufman, J.H., Metin, S., and Saperstein, D.D. (1989) Phys.Rev. B **39**, 13053
17. Stenzel, O., Wallendorf, T., and Petrich, R. (1993) Optical Materials **2**, 21
18. Davis, C.A.. (1993) Thin Solid Films **226**, 30

ANISOTROPIC MELTING OF SEMICONDUCTORS AT IRRADIATION BY POWERFUL LIGHT PULSES

YA. V. FATTAKHOV, R. M. BAYAZITOV,
I. B. KHAIBULLIN, T. N. L`VOVA
Kazan Physical-Technical Institute of the Russian Academy of Sciences
Sibirsky Trakt 10/7, Kazan, 420029, Tatarstan, Russia
Tel: 7-8432-761241, Fax: 7-8432-765075

1. Introduction

One of the interesting physical effects observed at the interaction of powerful optical irradiation with substance is the the effect of anisotropic local melting of the surface of semicondurtors [1-6] .

The essence of the effect is that as a result of homogeneous irradiation by coherent or incoherent light with pulse durations ~ 0.2 ms - 10 s melting has inhomogeneous character: on the surface of semiconductor local regions of melting (LRM) are formed. They are separated by regions of non-melted substance.

Many papers are devoted to studing an other but a very similar effect - generation of the surface periodical structures. In this case the change in the surface morphology of semiconductor at laser irradiation takes place due to the interference of incident irradiation and the difracted surface electromagnetic wave, surface acoustic wave, capillar

R. Kossowsky et al. (eds.), High Power Lasers – Science and Engineering, 533–548.
© 1996 *Kluwer Academic Publishers. Printed in the Netherlands.*

wave, and evaporation waves. The parameters of such surface structures depend on characteristics of laser irradiation (irradiation wave length, polarization, incidence angle). As a rule, these structures are observed at the shorter pulse durations of about nanoseconds (see, for instance, [7]). However, the main regularities of anisotropic local melting do not depend on the type of light irradiation (lasers or incoherent light sources).

At first the effect was observed at irradiation of semiconductors by powerful lasers: cw CO_2 laser [4], free-running Nd:YAG and Nd:glass lasers with pulse duration 0.2 ms [5] and 1.5 - 6 ms [6], respectively. With using powerful incoherent light sources for annealing of ion-doped layers, the papers appeared where the mechanism of the effect was studied at using various lamps: tungsten - halogen lamps with pulse duration ~10 s [2], flash lamps used for pumping lasers those working in regime of singular flashed with the pulse duration 10 ms [1] and those working in the stroboscopic regime (pulse duration~20 ms - 20 s) [3].

Up to now, however, the mechanism of this important effect is not understood enough. Several models of this effect are proposed at present.

In [8] the following model is proposed. Laser radiation generates the point defects in the subsurface layer of a semiconductor. When concentration of point defects reaches the threshold value, the process of defect clustering begins. Due to high compressive strain inside the vacancy cluster the melting temperature inside the cluster on the Si surface is lowered. Accordingly, the cluster regions are melted prior to the melting of other regions.

Other authors [6] consider that at pulse laser irradiation, due to the modulation of the absorption coefficient by self-diffusion of carriers and their self-location in the subsurface layers caused by local curvature of zones, the inhomogeneous fields are formed. This should result in local melting of a semiconductor in the points, corresponding to the maxima of the thermal field.

In [1], it is supposed that local regions of melting are formed at superheating of silicon samples by several tens of degrees. The necessity for superheating in due to the presence of the barrier of nucleation of the liquid phase on the boundary silicon - native silicon oxide. The authors distinguish two possible mechanisms of the appearance of the local nuclei of the liquid phase - homogeneous and heterogeneous nucleation.

Only three of various models of local melting are given above. Thus additional investigations should be carried out in order to establish the mechanism of the effect, the nature of the nucleation centres of the liquid phase and the main regularities of local melting.

Taking into account that the main regularities of the effect do not depend on the type of irradiation to study the mechanism we have used a battery of flash lamps which enabled us to provide homogeneous irradiation of the whole silicon wafer with 76 and 100 mm diameter during one pulse.We have specially modernised the equipment in order to precisely change the density of the irradiation power and consequently the duration of the light pulse causing melting of silicon surface.To exclude the boundary effects the experiments were mainly carried out on whole silicon wafers and not on small samples as usual for laser experiments.

2. Experimental

Light pulse irradiation of semiconductor wafers in the regime of LRM formation was carried out by three xenon-filled flash lamps, operating in the stroboscopic regime. Lamp feeding is carried out directly from the three-phase alternating current circuit through double-wave detector and thyristor commutator. The total pulse duration of light irradiation - the duration of the exposure (τ)- ranged from 20 ms to 20 s by setting the corresponding number of flashes (see inset in Fig. 3). The

radiation power density I_o was regulated in the range of 20 to 2000 W cm^{-2} by changing the duration of the connected state of lamps through the thyristor commutator to the circuit (Δt) within a half-period of the circuit voltage.

Polished monocrystalline silicon wafers 400 and 500 μm thick with a diameter of 76 and 100 mm, of n- and p- type conductivity, 1 to 10 Ω cm specific resistivity, with surface orientations (100), (130), (111), etc., as well as germanium monocrystalline (111) wafers with 45 Ω cm specific resistivity were irradiated and analyzed by optical microscopy.

The control samples by method of rapid thermal diffusion from spin-on source were prepared.

Determining the dependence of the LRM density on the regimes of local melting, the measurements were carried out at 20 points of each of the 90 investigated wafers. A number of samples were treated in Sirtl etchant before and after light irradiation (including the melting regime) to reveal defects of dislocation type.

3. Results and Discussion

3.1. LOCAL MELTING OF MONOCRYSTALLINE SILICON

It is known that LRM formed on monocrystalline silicon have definite facets and their forms are unambiguously connected with the crystallographic surface orientation [1-3], Figure 1.

Studies of the dependence of LRM density and size on the light pulse duration leading to local melting, were carried out both with a fixed value of the power density (Figure 2a) and with its variation from 20 to 2000 W cm^{-2} (Figure 3). It can be seen that (at a fixed power density) with increasing exposure (and sample temperature) the LRM density increases sharply and then remains approximately constant. Their maximum sizes increase linearly with the increase of exposure. The side of the equilateral triangle has been chosen to be the characteristic LRM size L. The results of

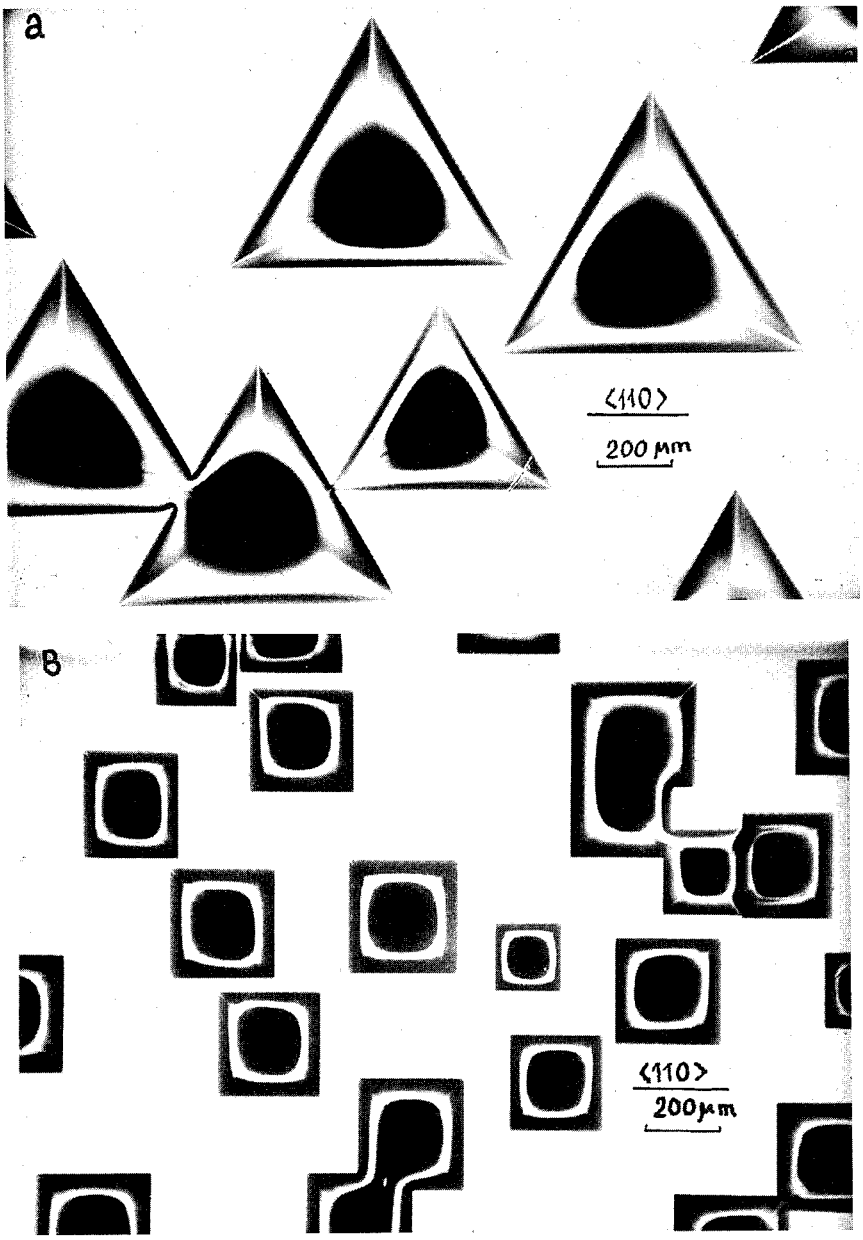


Figure 1.Micrographs of the surface of monocrystalline silicon, subjected to local melting. Surface orientation a - (111), b - (100).

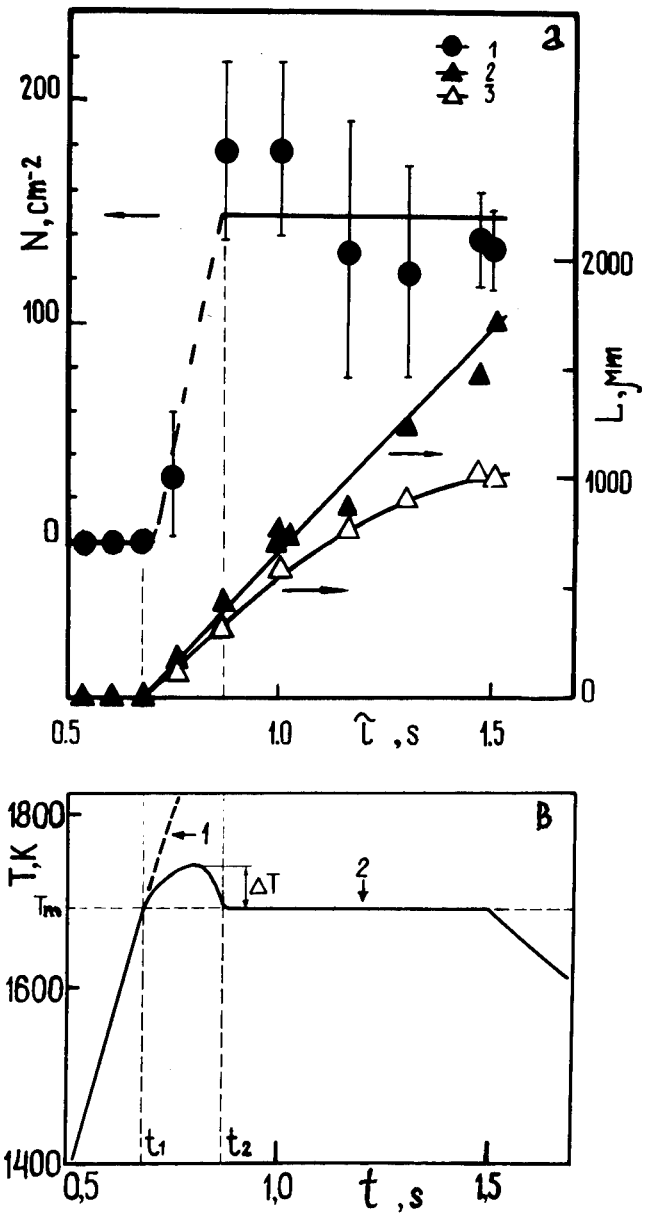


Figure 2.a) The dependences of density N (1) maximal (2) and middle (3) sizes of local regions of melting on the duration of light pulses τ at fixed power density I_0=250 W cm^{-2}. Monocrystalline phosphorus doped (111) silicon with the specific resistivity of 1Ω ϵm and (111)+4° surface orientation.
b) The calculated temperature dependence of the sample not accounting for LRM formation (1) and hypothetical temperature dependence accounting for nucleation in the time interval from t_1 to t_2 (2).

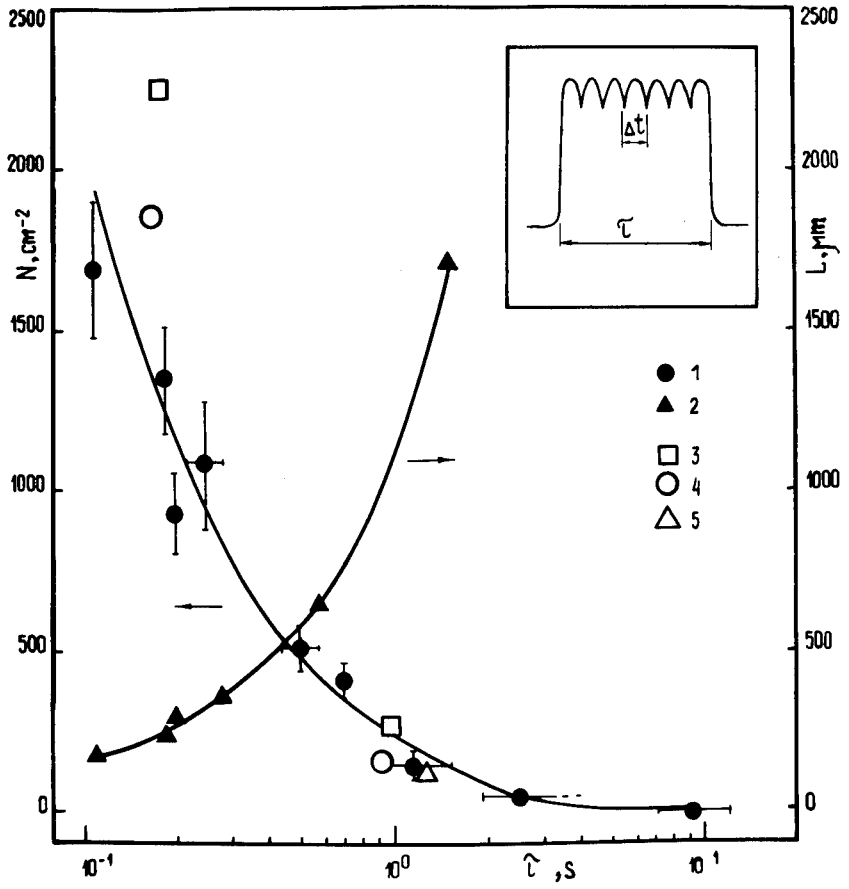


Figure 3. The dependences of the density N (1, 3-5) and maximal sizes L (2) of local regions of melting on the duration of light pulses at different power densities.
Monocrystalline silicon: 1, 2 - phosphorus doped, 1Ω cm, (111)+4° orientation;
3-5 - boron doped, 10 Ω cm, with surface orientation (100), (111) and (130), respectively.
The inset shows the shape of light pulse.

a number of analogous experiments for nine different power densities are presented in Figure 3. The decrease of the output power and, as a result, an increase of the light pulse duration necessary for the sample to reach the temperature of local melting (i. e. the state corresponding to the "plateau" in Figure 2a), leads to a decrease of LRM density, while their sizes increase sharply.

Similar dependences for other surface orientations, specific resistivities, and conductivity types of monocrystalline silicon have been established.

We can explain these dependence $N = f(\tau)$ (Fig. 2a,3) by different degrees of semiconductor superheating, with respect to the equilibrium melting temperature. Due to superheating conditions are established for overcoming the barrier for the formation of the liquid phase nuclei.

By convention the formation of the local regions of melting may be divided into two stages. At the first stage (t_1-t_2 , Fig. 2b), the velocity of the growth of liquid phase is determined by the work of formation of the critical nucleus, which in turn depends on the temperature of superheating with respect to the equilibrium melting temperature. The centers formed (nuclei with dimentions exceeding the critical one) mainly grow due to absorption of the heat of surrounding superheated zones. At the second stage ($t>t_2$) the density of centers reaches the value $N=1/Dt$, where D is coefficient of thermal conductivity of a crystal. The thermal fields of separate centers overlap, the temperature of the overheated regions lowers down to the melting point, formation of new centers stop and the further increase in the sizes of centers may be only due to absorption of the energy of the pulse light irradiation. Fixing the density and average size of LRM to the end of the first stage (the start of a "plateau"), one may find the value of superheating ΔT from the balance of the quantity of energy:

$$\Delta T c d \rho = N V \rho H, \qquad (1)$$

and consequently

$$\Delta T=0.12NL^3H/(cd), \qquad (2)$$

where H, c, ρ are the latent heat of melting, specific heat, and the crystal density, respectively, d is the wafer thickness, and V average volume of LRM (for a tetrahedron $V = 0.12L^3$).

Let us estimate ΔT for two values of pulse duration corresponding to the moment t_2: τ= 0.85 (Figure 2) and 0.46 s (power densities are 250 and 380 W cm^{-2} respectively). Assume that H = 1780 J/g, c = 0.98 J/gK, d = 0.04 cm, N = 150 and 515 cm^{-2}, L = 0.03 and 0.023 cm respectively. The value of superheating is ΔT = 22 and 34 K for τ = 0.85 and 0.46 s respectively.

Thus our calculations and the results of a number of scientists (see, for example, [9]) demonstrated that the value of superheating in the solid phase decreases as the light pulse duration increases and in practice a stationary equlibrium regime characterized by the absence of superheating is established at τ > 10 s. The larger the value of superheating, the greater is the number of surface defects which become centres of liquid phase nucleus formation. Vice versa, the decrease in the degree of superheating which takes place at longer pulse durations provides melting only on defects with low nucleation barriers and, correspondingly, leads to the decrease in the number N of LRM.

3.2. ABOUT THE NATURE OF LMRs NUCLEUS

The question about the nature of centres of the growth of local liquid phase is also under discussion: homogeneous nucleation, heterogeneous nucleation on the defects, existing before the pulse light irradiation, or on defects, created by irradiation itself.

Our analysis shoved a correlation between the location of local regions of melting on the crystal surface and periodic distribution of

dopants occuring at crystal growth from melt; and methods and quality of treatment of surface of the wafers of monocrystalline of semiconductor. These results and those of [1] enable us to conclude that the dominant centres of nucleation of the liquid phase are defects of the semiconductor surface present before pulse thermal treatment.

It should be noted that the light pulse itself creates additional centres of formation of liquid phase. These are dislocations resulting from mechanical stresses in a sample due to enhanced temperature gradients under pulse heating. Treatment of wafers with 76 mm diameter in Sirtl etchant showed that dislocations were observed on the perimeter of wafers in a ring with about 5 mm width. At separate gliding lines formation of a dense claim of local regions of melting is observed. The density of local regions of melting at the sample periphery is about 6 times higher than that in the centre. The density of etching pits is 2-3 orders of magnitude higher than the density of local regions of melting.

Using small samples or lasers with irradiation beam diameter comparable with the diffusional thermal length at a given pulse duration one can observe dislocation net or local regions of melting occurring only on dislocations generated by light.

3.3. LOCAL MELTING OF IMPLANTED SILICON

An important feature of implanted silicon, as an object of local melting investigation is the following. During a light pulse when the sample is heated up to the local melting temperature T_{lm} the annealing of radiation defects and the creation of secondary defects in implanted layer take place simultaneously.

It is shown that the distortion of initial geometrical shape of LRM appear (Figure 4) and increases gradually with increase of implantation fluence in (111) Si. Also we observed an increase of LRM density with ion dose for species with different mass solibility and ion energy (Figure 5).

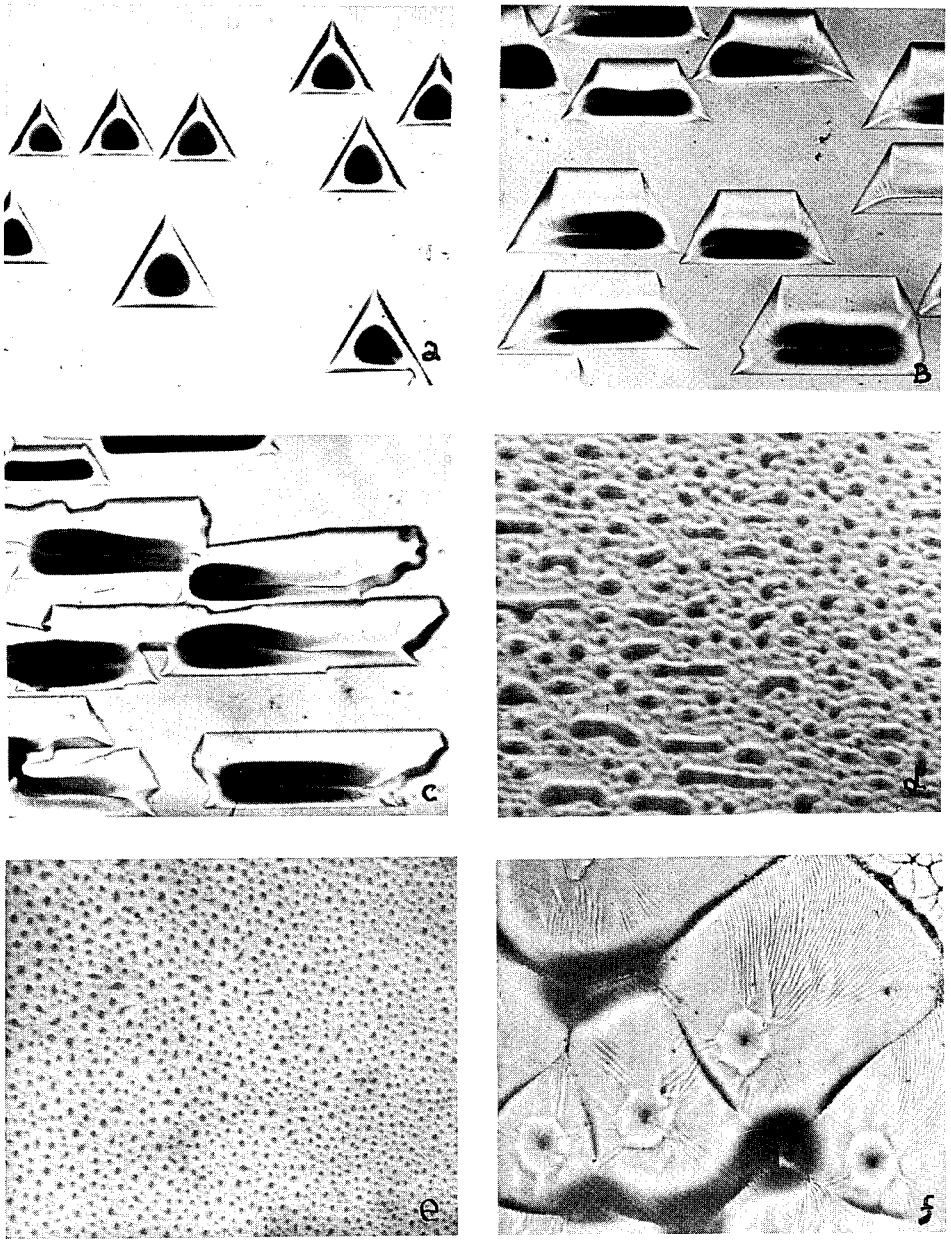


Figure 4. Micrographs of the surface of monocrystalline silicon (a) and phosphorus doped (b - f) 10 Ω cm; (111)+4° orientation. Regimes of implantation: E=40 keV, Φ, cm^{-2}: a)0; b)3.1 10^{14}, c)5.0 10^{14} , d)3.0 10^{15}, e)6.2 10^{15} , f)3.1 10^{15}.
Light pulse irradiation in the regime of local melting: a-e) τ =0.75 s, f) τ =0.22 s.

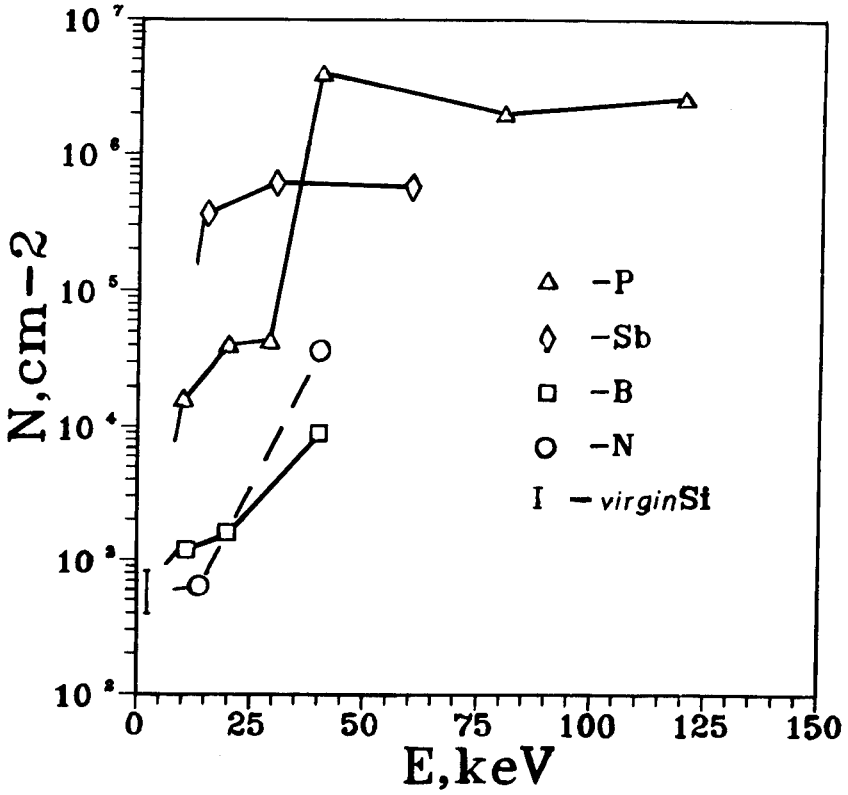


Figure 5.The dependence of LMR density N on the surface of implanted Si versus energy of implanted elements of III -V groups.
Substrate: (100) Si, boron doped, 10Ω cm.
Local melting regime: I_o=200 W cm^{-2}, τ =0.8 s.

There are the correlation between this process and degree of Si surface layers disorder.

Investigation of the dependence of the density and shape of LRMs on τ demonstrated (Figure 6a) that an increase in τ (with a corresponding decrease in I_o) led to a decrease in density two orders of magnitude. When τ rises in value, the LRMs shape changes from dendritic to nearly regular geometric, which corresponds to a virgin silicon crystal (Figure 6b,c).

To evaluate the degree of implanted layer recrystallization at the onset of local melting, the time dependences of sample temperature during and after light pulse irradiation with different sets of I_o and τ were calculated. Then we compared these results with those obtained when implanted layers subjected to rapid thermal annealing (RTA) were investigated by the TEM method. For all values of τ, the RTA temperature was chosen to be as close possible to the temperature of local melting. It was established by TEM that the increase of τ in the interval from 100 ms to 10s (and the corresponding decrease of I_o) results in a threefold decrease of the dislocation density. For $\tau < 1$ s, the duration of the back side of the thermal pulse, determined by heat radiation being the mechanism of cooling, is essentially longer than τ. For these values of τ, the main contribution to the recrystallization process will be due to the back side of the thermal pulse. As a result, the structural differences detected by TEM are more pronounced at the end of light pulse, i.e. at the end of the front side of the thermal pulse. Thus, LMR density reduction for τ ranging from 0.1 to 10 s is caused by a decrease of implanted layer defects when the temperature T_{lm} is achieved at longer light pulse durations [3].

In our opinion, depending on the duration and power density of light pulse, as well as the type of ion, fluence and energy of implantation, at local melting of amorphized implanted layers the following phase transitions are possible: (a) amorphous phase - partially recrystallized

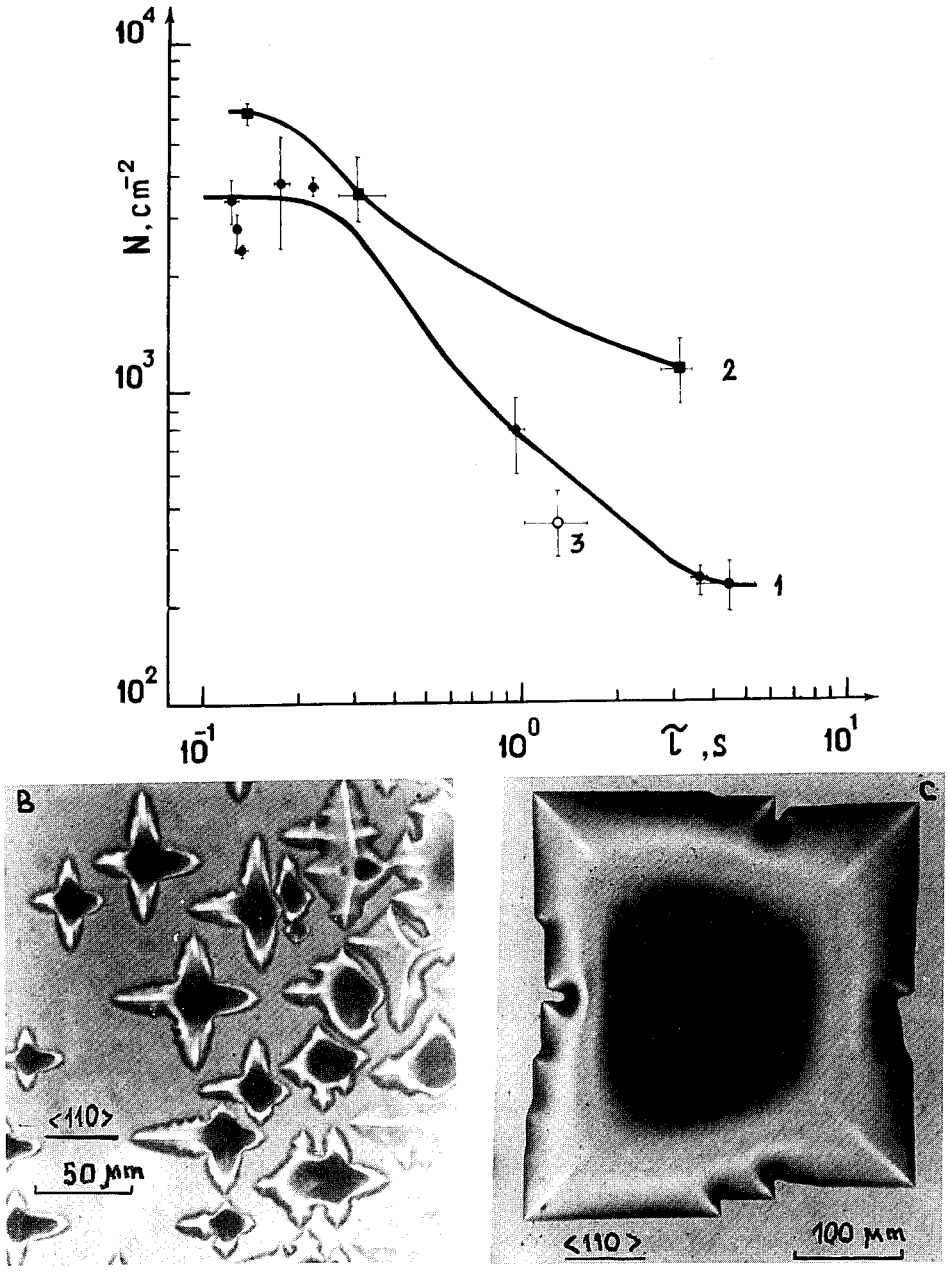


Figure 6. a) The dependence of LMR density N in the implanted Si on light pulse duration τ at different I_o. Implanted layer (IL) 1: (100)Si, n- type, 4.5 Ω cm doped by B^+ with E= 40 keV, Φ= 4.4 10^{15} cm^{-2}; IL, 2: (100)Si, p- type, 10 Ω cm doped by P^+ with E= 50 keV, Φ= 3.7 10^{15} cm^{-2}. For comparison, the value N is shown for monocrystalline (100) silicon, P doped, 4.5 Ω cm, - 3.

b, c) The shape of LRM (IL, 1 from fig.a) for τ [s]: (b)0.10; (c)5.01; I_o, W cm^{-2}: (b)1800; (c)60.

semiconductor - local supercooled liquid phase, or (b) amorphous phase - monocrystal with different concentration of secondary defects - local liquid phase.

Correlation of this processes will determine mainly the density, size and shape of the LMRs.

4. Conclusion

The mechanism and the main features of the effect of anisotropic local melting of semiconductor surfaces which can be observed at definite regimes of homogeneous irradiation by powerful pulses of coherent and incoherent light - are investigated. The results can be explained by the different degree of semiconductor superheating with respect to the equilibrium temperature of melting. It is demonstrated that under certain conditions light pulse itself generates centers for the formation of liquid nuclei.

5. Acknowledgments

This work was supported partially by Ministry of Science of Russian Federation, Russian Foundation of Basic investigations, Commercial Banks "Spurt" and "Avers". The autors would like to thank Dr. Ram Kossowsky, Prof. Miroslaw Jelinek and Dr. Robert Walter for possibility to participate in the work of "High Power Lasers".

6. References

1. Heinig, K.-H. (1985) Effect of local melting on semiconductor surfaces, in K. Hennig (ed.), *Energy Pulse Modification of Semiconductors and Related Materials,* Zentralinstitut für Kernforshung, Dresden, pp 265-279.

2. Celler, G. K., Robinson, Mc. D., Trimble, L. E., Lishner, D. J. (1983) Spatial melt instabilities in radiativiey melted crystalline silicon, *Applied Physics Letters* **43**, 868-870.

3. Fattakhov, Ya. V., Khaibullin, I. B., Vasil`yeva, T. N. (1991) The influence of the ion type on the anisotropic local melting of implanted silicon, *Nuclear Instruments and Methods in Physics Research B* **59/60**, 1072-1076.

4. Preston, J. S., Van Driel, H. M., and Sipe, J. E. (1987) Order- disoder transitions in the melt morphology of laser- irradiated silicon, *Physical Review Letters* **58**, 69-72.

5. Von Almen, M., Lüthy, W., and Affolter, K. (1978) Anisotropic melting and epitaxial regrow of laser-irradiated silicon, *Applied Physics Letters* **33**, 824-825.

6. Bonchik, A. Yu., Gafijchuk, V. V., Kiyak, S. G., Savitski, G. V. (1986) Surface morphology of semiconductors at laser pulse irradiation of millisecond duration, *Poverkhnost. Fizika. Khimiya. Mekhanika* (in Russian) **5**, 142-144.

7. Gorodetsky, G., Kanicki, J., Kazyaka, T., Melcher, R. (1985) *Applied Physics Letters* **46**, 547-549.

8. Emel`yanov, V. I., (1992) Generation-diffusion-deformational instabilities and formation of ordered defect structures on surfaces of solids under the action of strong laser beams, *Laser Physics* **2,** 389-466.

9. Karpov, S. Yu., Kovalchuk, Yu. V., Pogorelsky, Yu. V. (1986) Melting of semiconductors by laser pulses irradiation, *Fizika technika poluprovodnikov* (in Russian) **20**, 1945-1969.

EXCIMER LASER ASSISTED DEPOSITION AND CHARACTERIZATION OF MOLYBDENUM FILMS - FABRICATION OF MOLYBDENUM COATINGS ON OPTICAL FIBRES

CHRISTOS GRIVAS, PANTELIS PAPADOPOULOS, AND ARGIRO KLINI
Foundation for Research and Technology - Hellas (FO.R.T.H)
Institute of Electronic Structure and Laser (I.E.S.L)
P.O. BOX 1527, GR-71110 Heraklion, Crete, GREECE

ABSTRACT: The fabrication of molybdenum thin films on quartz substrates using a KrF excimer laser (248 nm) is reported. The influence of the substrate temperature (25-500°C) the energy density (3-10 Jcm^{-2}) and the target-substrate distance (3.5-9 cm) on the film properties has been investigated. The surface properties of the ablated layers have been studied by scanning electron microscopy (SEM), atomic force microscopy (AFM), X-ray diffraction (XRD) and scratch test. The excimer laser deposition technique has also been successfully employed for the formation of molybdenum coatings on bare optical fibres. Scanning electron microscope photographs reveal layers with smooth structure, and low droplets density.

1. Introduction

Formation of hermetic coatings on optical fibres is of great importance in the context of conservation of their initial optical and mechanical properties after exposure to the environment. Efficient hermetic coatings can considerably reduce or even stop the formation and the growth of microcracks on optical fibres which in conjunction with bending stresses can cause catastrophic failure of the fibres, and also prevent possible intrusion of water through them. The latter is mainly responsible for premature aging. Molybdenum is an attractive material for surface metallization particularly in very large scale integration (VLSI) technology. However, to our knowledge there is no publication on laser techniques employed for the deposition of molybdenum (or other metallic) protective coatings on optical fibres. Various molybdenum deposition techniques such as conventional chemical vapor deposition (CVD) [1-3] and laser chemical vapor deposition (LCVD) [4-6] has been proposed and investigated.

An alternative technique that has not yet been investigated in detail for the fabrication of molybdenum films is pulsed laser deposition (PLD) [7]. The

R. Kossowsky et al. (eds.), High Power Lasers – Science and Engineering, 549–559.
© 1996 *Kluwer Academic Publishers. Printed in the Netherlands.*

latter has attracted increasing attention in recent years since it is distinguished by a number of unique advantages such as: excellent control on the stoichiometry of even very complex materials, simplicity, low cost and great experimental versatility, high growth rates for the deposited materials and insignificant film contamination due to the fast, localized heating of the target's substrate by the focused laser beam [8]. A typical arrangement employed in such experiments comprises a laser source and a reaction chamber inside which the target and substrate are mounted. Upon laser irradiation material is ejected from the target and is deposited on the substrate, thus forming a thin film. The whole process may take place under vacuum conditions or at inert or reactive environment (reactive ablation).

In the present article we study the fabrication of molybdenum coatings on flat glass substrates (i.e, quartz, and microscope slides) as well as on optical fibres by means of the pulsed laser deposition technique (PLD). The paper is organized as follows: After a description of the experimental set up in Section 2, the experimental results are outlined and discussed in Section 3. Section 4 summarizes the results of the present investigations.

2. Experimental details

Thin films were deposited inside a stainless steel vacuum chamber (Figure 1) that could be evacuated to 1-2 $\times 10^{-6}$ mbar by means of a turbomolecular pump. Samples of very pure molybdenum (99.9%) were ablated with a KrF excimer laser (Lambda Physik LPX 200) operating at 248 nm and emitting pulses of ~20 ns duration. Irradiations were performed at a repetition rate of 10 Hz and the laser beam was focused on the target surface at an angle of 40°. Quartz and microscope slide glass as well as bare optical fibres were used as substrates. Immediately before mounting, the flat substrates were cleaned with aceton, ethanol, rinsed in distilled water and then dried in a jet of pure inert gas. The molybdenum targets were mounted on a vacuum stepper motor and during the irradiation were rotated to prevent drilling by the focused laser beam.

The distance between target and substrate varied between 3.5 cm and 9 cm. The laser energies employed to carry out the experiments were in the range of 200 mJ to 600 mJ per shot, at energy densities between 3 Jcm^{-2} to 10 Jcm^{-2}. The substrate temperature was varied between 25°C (room temperature) and 500°C. The surface deposited molybdenum layers were investigated by a scanning electron microscope (SEM) and an atomic force microscope (AFM). Investigations on the microstructure of the deposited films were performed by low angle x-ray diffraction. The molybdenum target was also characterized by x-ray diffraction. For the determination of the thickness of the deposited films an α-step profilometer was employed. The adhesion of

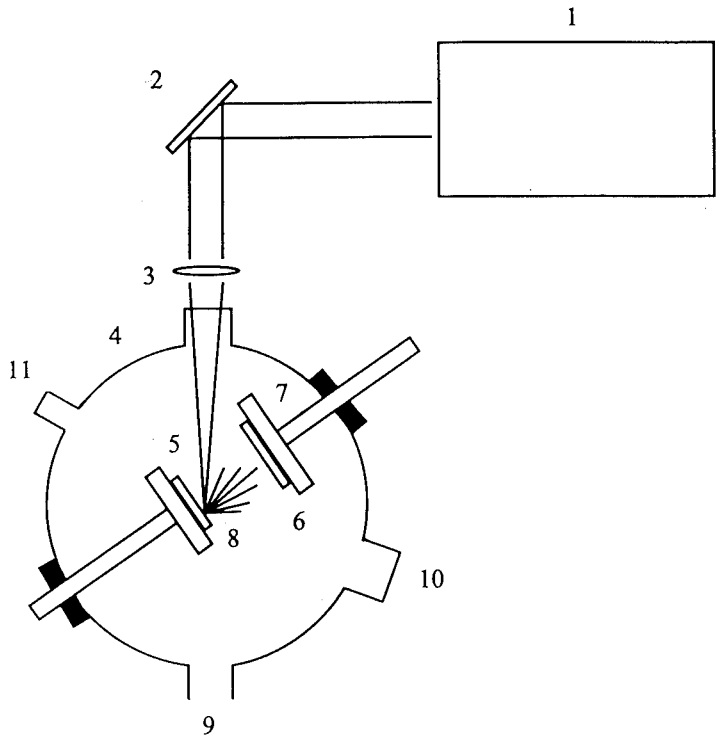


Fig. 1. Schematic of the experimental arrangement for pulsed laser deposition of molybdenum coatings on glass substrates; 1: KrF excimer laser 2: mirror 3: focusing lens 4: chamber, 5: molybdenum target, 6: glass substrate, 7: heated substrate holder, 8: ejected plume 9: pump out, 10: visual inspection / pyrometer 11: venting port

the deposited films on glass substrates was studied by scratch test.

3. Results and discussion

As far as the deposition on flat glass substrates is concerned interesting buckling phenomena were observed when the thickness of the fabricated molybdenum films exceeds a certain limit. The formation of such patterns is attributed to the existence of compressive stresses in the deposited layers. High compressive stresses causing similar buckling phenomena have been reported in carbon films [9-12]. Analysis of the stress relief in these films was made either by using the linear theory of buckling of shells and plates [10] or by describing the buckling as an instability phenomenon [9]. Four different stress relief patterns were observed in our experiments: (i) buckled-up wrinkles with sinusoidal form (ii) parallel continuous or dotted lines presenting slight buckling (iii) dense buckled-up deformed coatings (iv) peeling. For film grown under the same conditions the appearance of each of these patterns depends

strongly on the hickness of the deposited material. Thickness dependance of the buckling patterns has been reported and studied in carbon films [10,12].

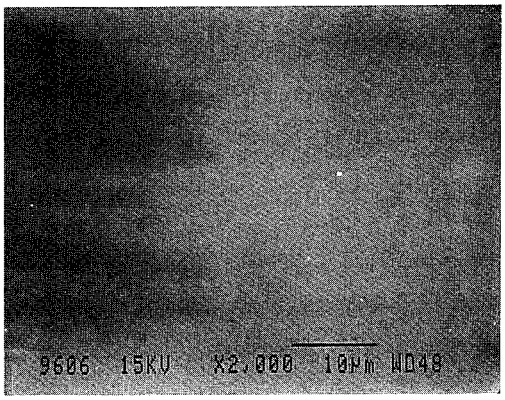


Fig. 2. Scanning electron micrograph a 700 Å thick molybdenum film on glass substrate obtained after 5000 pulses of 248 nm KF-excimer-laser radiation. The energy density and the substrate-target distance were fixed at 5 Jcm^{-2} and 7 cm respectively.

Figure 2 demonstrates scanning electron microscope (SEM) pictures of a 700 Å thick molybdenum film obtained at room temperature after 5000 pulses of KrF laser radiation of 5 Jcm^{-2}. The surface of the deposited layer shows enhanced smoothness and uniformity and presents very few of the particles and droplets often reported for other materials grown via laser ablation. However with increasing the number of pulses (that means for thicker deposited layers) the coating fails by buckling and peeling demonstrating the existence of stresses in the film. The first stage of the evolution of this failure behavior is clearly shown in Figure 3. Figure 3(a) shows a typical stress relief profile observed on a film obtained after irradiation with 10000 pulses of KrF laser pulses of 5 Jcm^{-2}. The thickness of this coating was approximately 900 Å. As it is shown the buckled structures have a sinusoidal form with well-defined shapes and widths. They do not present any preferential orientation in their propagation and after traveling over some distance they undergo branching. Where they cross each other they turn onto either of them or branch into both of them. The absence of any preferential propagation argues for the existence of isotropic compressive stress in the molybdenum layers. Figure 3(b) demonstrates another stress relief pattern also observed in a 900 Å molybdenum film. The latter presents wide regions covered with buckled-out parallel lines continuous or dotted which consist the starting points for the formation of sinusoidal stress relief patterns. These wavy wrinkles propagate perpendicular to the direction of the buckled lines, they cross other lines and wrinkles and later they begin to branch.

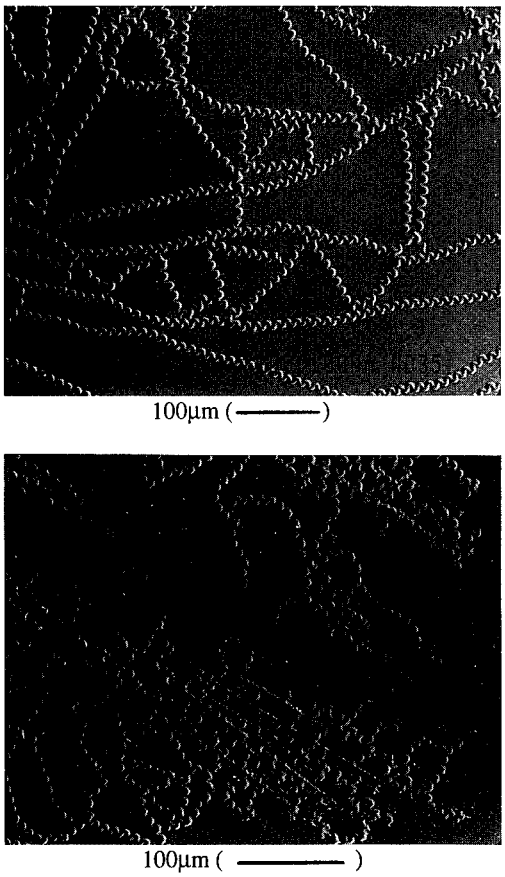


Fig. 3. Scanning electron micrographs of 900 Å thick molybdenum films on glass substrates obtained after 10000 pulses of 248 nm KF-excimer-laser radiation. The energy density and the substrate-target distance were fixed at 5 Jcm^{-2} and 7 cm respectively

At longer irradiation times for films with thickness exceeding 1000 Å more pronounced and dense formation of the aforementioned branched wavy wrinkles is observed [Fig. 4a]. With increasing thickness of the deposited coating and the width of the sinusoidal patterns becomes larger and sometimes they superimpose to form extended buckled areas [Fig. 4b]. Finally, when the curvature of the buckled layer becomes too large cracking and peeling occurs.

The appearance of these buckling phenomena is more pronounced for small substrate-target distances and laser energy densities higher than 5 Jcm^{-2}. As far as the evolution of the buckling is concerned, it was observed that it usually starts at the film edge or at defects on its surface and its extent depends on the thickness of the deposit. It should be also mentioned, that failure behavior of the deposits usually initiates after exposure to the atmospheric pressure and their deterioration is particularly accelerated by humidity.

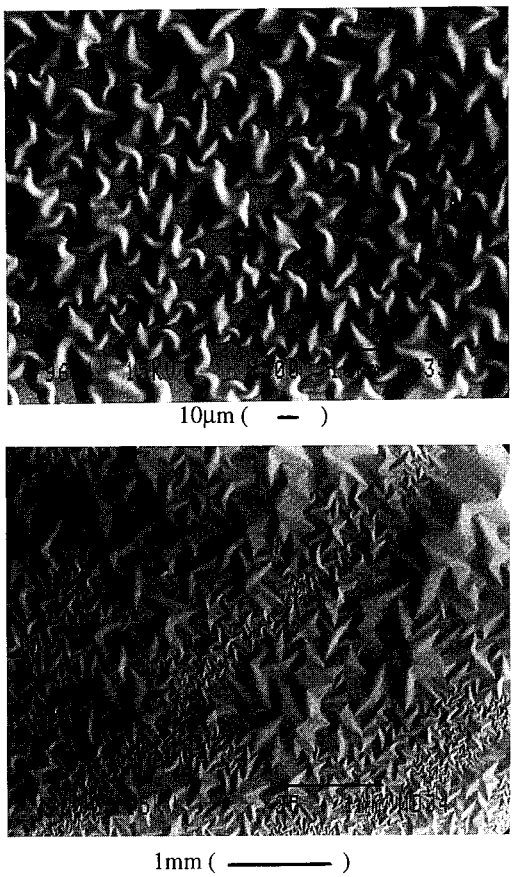


Fig. 4. Scanning electron micrographs of molybdenum films on glass substrates obtained after 248 nm KF-excimer-laser radiation of (a) 12000 pulses, (b) 15000 pulses. The energy density and the substrate-target distance were fixed at 5 Jcm^{-2} and 7 cm respectively

The temperature of the glass substrate is another parameter with influence on the formation of branched structures on the deposit. Figure 5 shows SEM-pictures of molybdenum films deposited on glass substrates with different temperatures. By keeping the energy density, and the distance from target to substrate fixed at 5 Jcm^{-2} and 9 cm respectively, molybdenum films deposited at substrate temperatures higher than 400°C reveal very smooth surface features [Fig. 5a] and very low density of droplets, whereas layers obtained at lower substrate temperatures reveal region with the aforementioned dendritic structure [Fig. 5b].

Figure 6 shows AFM profiles of molybdenum coatings deposited at room temperature with a laser energy density of 4 Jcm^{-2} after 5000 pulses [Fig. 6a] and 10000 pulses [Fig. 6b]. As it is shown both films are very smooth and they have grains with a height of about 2 nm and 3 nm respectively. The film

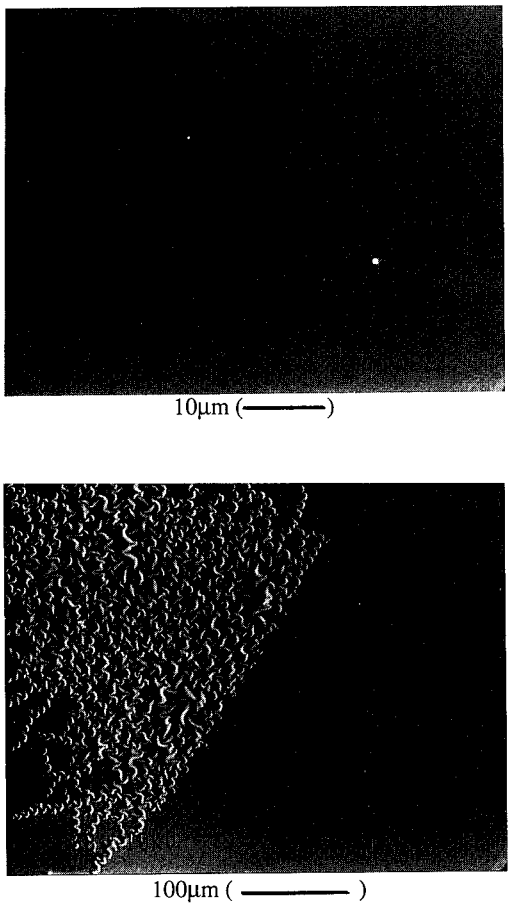


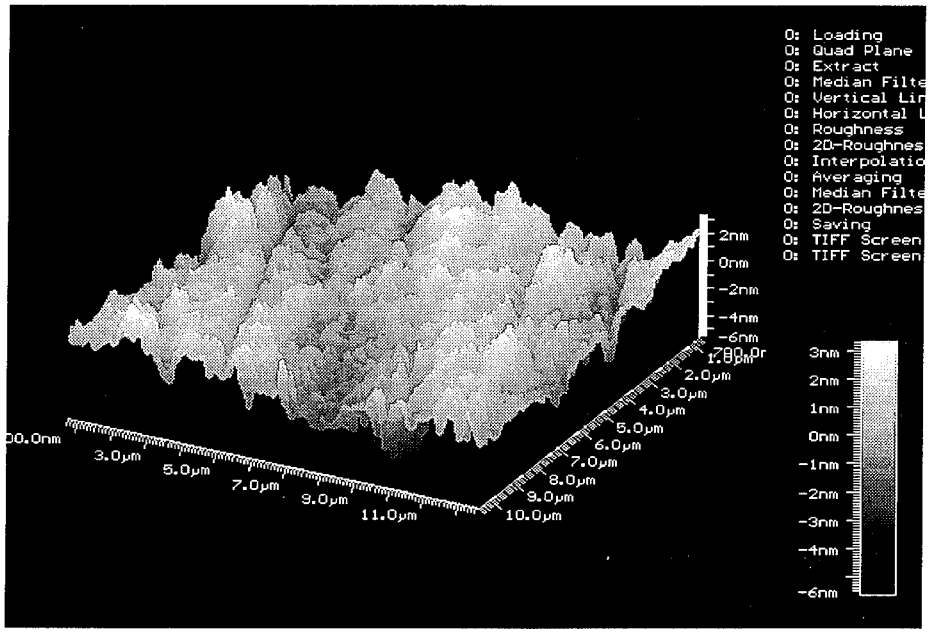
Fig. 5. Scanning electron micrographs of molybdenum films on glass substrates by means of 248nm KF-excimer-laser radiation for different substrate temperatures (a) 400°C and (b) 150°C.

obtained with shorter irradiation time reveals smoother surface structure in comparison with that deposited with 10000 pulses.

Contrary to deposits presenting failure behavior films with enhanced surface quality (or the parts of the films having smooth surface structure) present good adhesion since they withstood successfully the tape test. Scratch test performed with a 200 μm diamond tip revealed that the molybdenum layers were ductile and particularly adhesive since no flaking effects on their surface or removal from the glass substrate were observed. However quantitative determination of the adhesion was not feasible due to the influence of the small film thickness on the accuracy of the measurements.

The diffractometer trace for a molybdenum film deposited at a substrate temperature of 400°C is recorded in the angular range of 9° to 143° (2θ) as

(a)



(b)

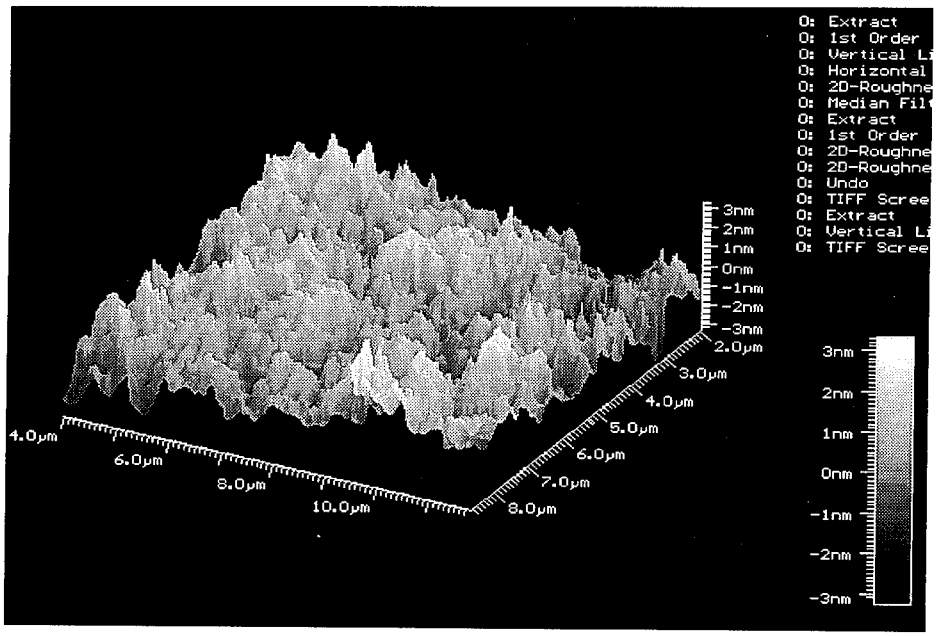


Fig. 6. AFM-pictures of molybdenum films grown on glass substrates after (a) 5000 pulses and (b) 10000 pulses of 248 nm KF-excimer-laser radiation. The energy density and the substrate-target distance were fixed at 4 Jcm^{-2} and 9 cm respectively.

shown in Figure 7(a). The x-ray peaks in this pattern correspond to the (011), (002), (112), (022), (013), and (123) planes of molybdenum. Figure 7(b) shows

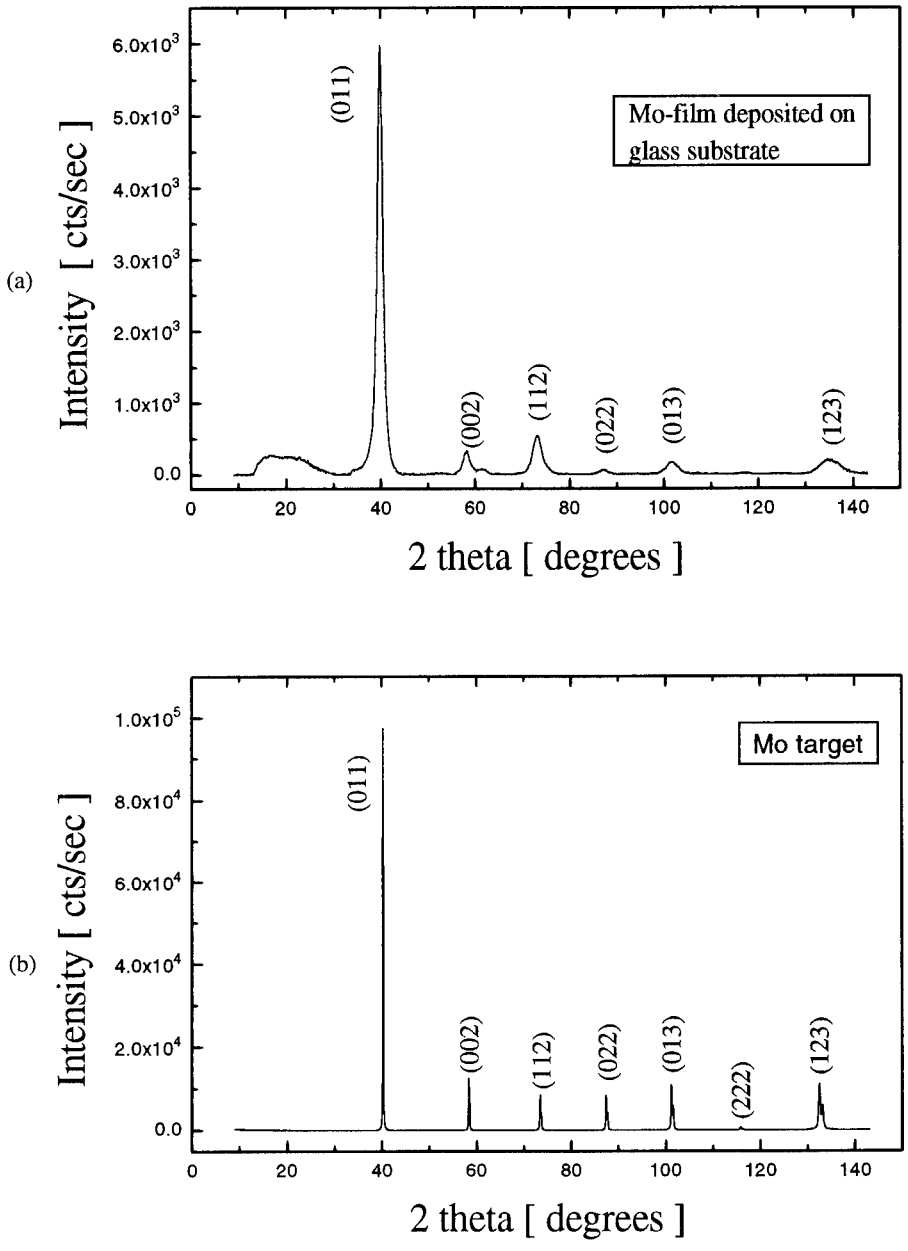


Fig. 7. X-ray diffraction patterns of (a) a molydbenum film deposited on glass substrate and (b) of the molybdenum target. The film was fabricated by 248 nm KF-excimer-laser radiation at a substrate temperature of 400°C

the result of x-ray diffraction measurements on a molybdenum target employed to perform depositions. In this pattern the peak of the (222) plane is also noticed.

The molybdenum deposits on bare optical fibers, shown in Figure 8, correspond to different number of laser pulses and energy density regimes. Coatings obtained after 6000 pulses of laser density 6 Jcm^{-2} have smooth substrate structure with low particle density, as shown in Figure 8(a). We have succeeded in depositing molybdenum coatings with thickness up to 500 Å possessing such enhanced quality. The layer shown in Figure 8(b) was produced after 50000 laser pulses of energy density 8 Jcm^{-2}. As it is shown ribbons of the deposited coating are peeled off revealing poor adherence on the surface of the bare optical fiber.

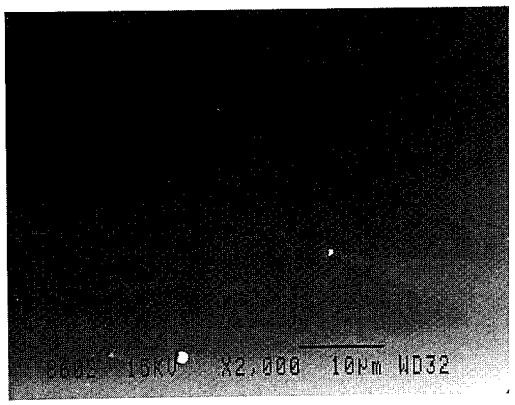


Fig 8. Scanning electron micrographs of bare optical fibres coated with molydbenum layers produced by (a) 6000 and (b) 50000 pulses of 248 nm KF-excimer-laser radiation. The energy density was 6 Jcm^{-2} and 8 Jcm^{-2} respectively. The substrate-target-distance was fixed at 5.5 cm.

4. Summary

In conclusion, pulsed laser deposition technique can be successfully used to fabricate molybdenum thin films on both flat glass substrates and bare optical fibers. The optimum parameters for deposition of good quality films, that is, films with smooth surface features, low particle density and enhanced adhesion, were determined. Under these conditions, the thickness of the deposited films
for the case of the flat samples was about 700 Å whereas for the optical fibers 500 Å. Deposits with thickness exceeding these values present regions where the film is debonded or even peeled off. Flat substrates reveal various stress relief patterns with profiles strongly dependent on the film thickness.

5. Acknowledgements

We wish to thank Dr. G. Kotrotsios (CSEM S.A) and Mrs. A. Patentalaki (FORTH-IESL) for the AFM and the SEM pictures respectively.

6. References

1. Sahin, T., Flanigan, E.J., and Sears J.T. (1987) in E.K.Broadbent (ed) *Tungsten and other refractory materials for VLSI Applications II,* Materials Research Society (Pittsburgh), pp 199-205.
2. Lifshitz, N., Brown, J.M., Williams, D.S. (1987) in E.K.Broadbent (ed) *Tungsten and other refractory materials for VLSI Applications II,* Materials Research Society (Pittsburgh), pp 215-223.
3. Kaplan, L.H., d' Heurle, F.M. (1970) The deposition of molybdenum and tungsten films from vapor decomposition of carbonyls, *J. Electrochem.Soc.* **117**(5), 693-700.
4. Baeuerle, D. (1986) *Chemical processing with laser,* Springer Verlag (Berlin, Heidelberg). 5. Radloff, W. Below, E. Duerr, H. and Stert, V., (1990) Laser Photolytic Deposition of Molybdenum and tungsten thin film microstructures, *Applied Physics A* **50**, 233-235 .
6. Gluck, N.S., Wolga, G.J., Bartosch, C.E., Ho, W., and Ying, Z. (1987) Mechanisms of carbon and oxygen incorporation into thin metal films grown by laser photolysis of carbonyls, *J.Appl.Phys.* **61**(3), 998-1005.
8. Chrisey, D.B., Hubler, G.K. (eds) (1994) *Pulsed laser deposition of thin films,* John Wiley & Sons, Inc. (New York).
7. Gaponov, S.V., Luskin, B.M., Nestorov, B.A., and Salashchenko, N.N. (1977) Morphological features and structures of films condensed from a laser plasma, *Sov.Phys.Solid State* **19**(10), 1736-1738.
9. Gille, G., and Rau, B. (1984) Buckling instability and adhesion of carbon layers, *Thin Solid Films* **120**, 109-121.
10. Nir, D. (1984) Stress relief forms of diamond-like carbon thin films under internal compressive stress, *Thin Solid Films* **112**, 41-49.
11. Matuda, N., Baba, S., and Kinbara, A. (1981) Internal stress, Young's modulus and adhesion energy of carbon films on glass substrates, *Thin Solid Films* **81**, 301-305.
12. Iyer, S.B., Harshavardhan, K.S., and Kumar, V. (1995) Bucling patterns in diamond-like carbon films, *Thin Solid Films* **256,** 94-100.

PULSED LASER-INDUCED SYNTHESIS OF METAL SULPHIDES IN SULPHUROUS LIQUIDS UNDER ACTION OF SHOCK WAVES

M. I. Markevich, F. A. Piskunov
Institute of Electronics, Minsk, Belarus

.Laser processing of materials in chemically reactive surrounding mediums has been marked with growing interest. using a pulsed laser in conjunction with a proper liquid makes it possible to induce rapid and often non - equilibrium reactions at the solid-liquid interface. It is believed that temperature, pressure and phase transformations in the liquid are the key parameters necessary to understand the interface reactions.

Recent research into laser processing of materials in a chemically reactive surrounding medium has been marked with growing interest /1/. In most of the studies on laser-induced reactions the main emphasis has been laid on the interaction at the vapour-solid interfaces and hardly any attempts have been made to explore the possibilities of synthesising new materials by pulsed-laser-induced reactions at liquid-solid interfaces /2/. Using a pulsed laser in conjunction with a proper liquid makes it possible to induce rapid and often non-equilibrium reactions at the solid-liquid interface and consequently to form compound layers with metastable phases and desirable properties /3/.

The basic processes in the liquid at the interface affected by pulsed laser irradiation are still largely unknown, but it is believed that temperature, pressure and phase transformations in the liquid are the key parameters necessary to understand the interface reactions /4/. The purpose of the present investigation is to determine the effects of pulsed laser processing in different power density regimes and, particular, to study the formation of several phases in circumstances where violent shock waves are generated causing great transient pressures.

We have chosen the Ni- sulphur containing liquid interface as a model system for the pulsed processing experiments both because the Ni-S phase diagram has been described in sufficient detail and because a considerable number of nickel sulphide phases have already been discovered /5/. Moreover nickel sulphides have been extensively studied in their applications as catalysts and in coatings for photo galvanic cells /6,7/. 1 mm thick nickel discs which were 20 mm in diameter and had a more than 99.5% purity were used in experiments. Their working surfaces were successively grounded and polished to a mirror finish. Sulphur and sodium sulphide were simultaneously dissolved in a water-glycerine mixture (1:2) to form a sodium

R. Kossowsky et al. (eds.), High Power Lasers – Science and Engineering, 561–565.
© 1996 *Kluwer Academic Publishers. Printed in the Netherlands.*

polysulphide solution used as a chemically reactive liquid. The ration and concentrations of the components were calculated to insure a high transparency of the solution for a laser wavelength of λ = 1.06 μm. The solution contained 80 g per litre of sulphur element in the form of sodium polysulphide. Its transmittance value was equal to 56% for a wavelength of λ = 1.06 μm in a layer of 1 cm in depth.

An Nd-glass laser used in experiments (λ =1.06 μm) was capable of giving a maximum energy per pulse of 700 J in free running regime for a 1 ms pulse width and 5 J in Q- switched regime for a 50 ns pulse width. The beam was collimated to ensure a homogeneous energy density and focused to a spot size which corresponded to the incident power density required by the experiments. While processing the samples in a liquid ambient, the depth of the liquid covering the sample surface was maintained at 1,0 - 1,5 mm. The experimental arrangement is shown in figure 1.

The growth of the chemical compound layer in the sample causes the initial conditions of the pulsed event to change within nanoseconds of high intensity irradiation /8/. Samples were therefore irradiated by a single pulse to obtain comparable results. The incident inten-sities of single pulsed va-ried from 2.5 10^8 to $4 \cdot 10^8$ W/cm^2 for a pulse width of 50 ns in the Q-switched mode and from 1.3 10^5 to 3.1 10^5 W/cm^2 for a pulse width of 1 ms the free- running mode to determine the effect of such variatiation on the composition of the surface compounds.

The temperature in the laser-induced area was calculated from the non-stationary equation of heat conduction with a source of heat and the corresponding initial and marginal values. The computation techniques have been described in greater detail in /9/. Calculated temperature values varied from 620 K to 1050 K depending on the experiment parameters.

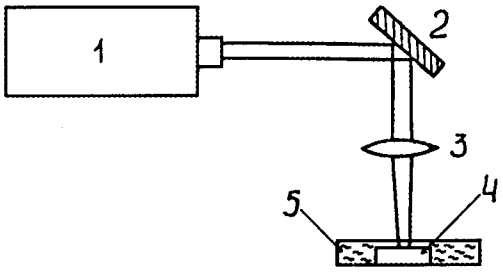


Fig.1 Schematic illustration of the experimental set-up for liquid mediated pulsed laser processing: 1, Nd-glass laser; 2, mirror; 3, lens; 4 substrate; 5, reactant liquid.

To detect the formation of the compounds, the laser irradiated nickel samples were analysed using X-ray diffraction in glancing angle geometries. The glancing angle X-ray patterns were obtained on a DRON-3 (USSR) machine by keeping the glancing angle of incidence fixed at 1o. For the results of the X-ray analysis of the laser processed nickel samples see figures 2, 3.

The outlines of the roentgenograms apparently depend on the processing mode. A 1 ms irradiation with power densities of $(1.3\text{-}3.1) \cdot 10^5$ W/cm^2 resulted in the detection of NiS reflections in the sample. At the same time, a 50 ns irradiation of the sample by a single pulse in the Q-switched mode produced additional Ni_3S_4 reflections.

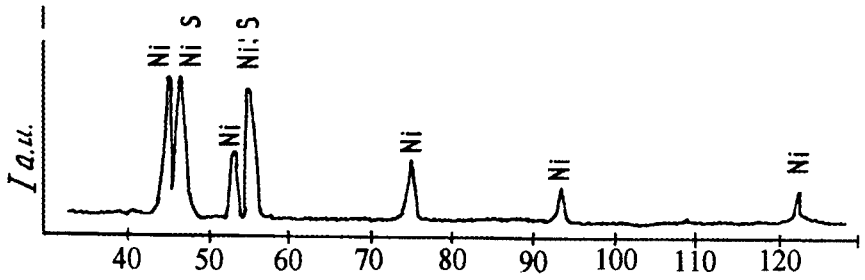


Fig.2 Glancing angle XRD pattern of nickel disc laser-treated in a sulphur containing liquid at a power density value of $3 \cdot 10^5$ W/cm^2 and a pulse duration of 1 ms.

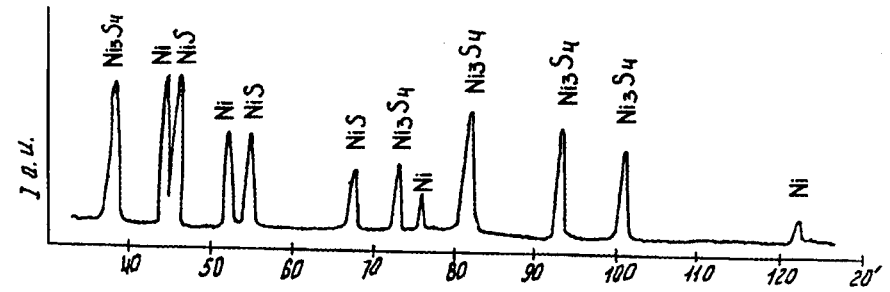


Fig.3 Glancing angle XRD pattern of a nickel disc laser-treated in a sulphur containing liquid at a power density value of 4 10^8 W/cm^2 and a pulse duration of 50 ns.

The interaction of nickel with sulphur at high temperatures (450-750 K) in steady-state conditions produces the NiS, Ni_3S_2, Ni_6S_5 and NiS_2 phases. The proportion of the Ni_3S_2, Ni_6S_5 and NiS_2 phases increases with the duration of treatment /10/. The Ni_3S_4 and Ni_5S_6 sulphides will not form. The formation of the single NiS phase (i.e. phase selection) appeared to be natural and in agreement with the theory of retarding "chemical relaxation" of a system in the disequilibrium conditions during pulsed laser processing. Phase selection also occurred during laser synthesis at solid-solid interface /10/

A variation of time and energy scales of laser processing in the Q-switched mode led to the formation of the additional Ni_3S_4 phase which is stable below 673 K.
In this mode of treatment the decrease in pulse duration is sharp (about 5 orders of magnitude, to 50 ns) and incident power density high (>10^8W/cm^2). These conditions are known to be conducive to shock ware generation /11/ The shock ware pressure amplitude at the absorbing surface in a nearly transparent condensed medium (TCM) can be calculated as follows /11/

$$p = \frac{2}{n+1}\left[\frac{(n-1)H}{n\Lambda F}+1\right]^{-1}\left[nAg_0\frac{\gamma-1}{\gamma}\frac{ZZ_0}{Z+Z_0}\right]^{1/2},$$

where n - is the index of refraction, H- is the depth of the TCM, ΔF is the direct lens distance, g_0 is the irradiation intensity value on the surface of the sample in the absence of the TCM, γ is the vapor adiabatic index, A is the efficient absorption power on the sample, Z, Z_0 are the acoustic resistance values of the TCM and the absorbing medium, respectively. The pressure amplitude in the experiments was calculated at 1 GPa. The morphological analysis and our calculations proved that the temperatures in both sets of experiments were approximately equal and rose to the melting point. In these conditions, the presence of roentgenographically detectable amounts of NiS and Ni_3S_4 in the samples after their processing with a 50 ns laser pulse suggests that the acceleration of the synthesis reaction and a change in its direction have been caused by the transient pressure created by the shock wae. We believe that the accelerating effect of the shock wae generated by very short high-power laser pulses is similar to that of explosion compression /13, 14/. Besides affecting the kinetics of the reaction, the chock wave may also intensify the migration of reacting particles into the base /15/. Such a conclusion is suggested by the date on low temperature synthesis of some metal sulfides affected by high pressure with applied shear action /17/.

CONCLUSIONS

1. Phase selection occurred when nickel samples were processed in a sulphur containing liquid medium with laser pulses of a 1 ms duration and (1.3 - 3.1)*10^5W/cm^2 power density form a single NiS phase.

2. Laser processing of nickel samples with pulse duration equal to 50 ns and power density to 4*10^8 W/cm^2 leads to the formation of the additional Ni_3S_4 phase due to the emergence of shock wave with an estimated pressure amplitude of 1 GPa.

REFERENCES

1. Bauerle, D. (1986) *Chemical processing with lasers* (Springer series in material sciences; v.1), Springer-Verl.,Berlin-Hheidelberg.
2. Ogale, S.B. (1988) Pulsed laser-induced and ion-beam-induced surface synthesis and modification of oxides, nitrides and carbides, *Thin Solid Film* **163**, 215-227.
3. Chan, S.W.,Dijkkamp, D,.Wu, X.D, Venkatesan, T.and Chang, C.C. (1987) Synthesis induced by laser irradiation at liquid/solid interfaces, *Mat .Res. Symp. Proc. Materials Research Society,* **74,** Pittsburgh, PA, 287-292
4. Polman, A, Sinke, W, Uttormark,M.J. and Thompson, M.O. (1988) Transient processes at the Si-water interface during pulsed laser irradiation, *Mat.Res.SoC.*

Symp. Proc. , Material Research Society ***100***, Pittsburgh, PA 555-560.
5. Hansen, M., Anderko, K. (1958) *Constitution of binary alloys*, McGraw-Hill Book Co., Inc., New-York.
6. Samsonov, G.V.,Drozdova, S.V. (1972) *The Sulphides Metallurgiya-Publ.*, Moscow .(in russian).
7. US Patent 4 814 259
8. Biunno, N., Narayan, J.,Singh, R.K., Hofmeister, S.K. ,.Schreiner,A.F., Sito, M.L. and .Auciello, O.H (1988) Liquid mediated pulsed laser processing of silicon, *Mat. Res.Sos. Symp. Proc, Materials Research Society, Pittsburg, PA* ***100,*** .567-572.
9. Podoltsev, A.S., Zheltov, G.I. (1989) Effects of infrared rariation on the cornea *Sov. J. Qquantum Electron* (USA), **19,** 1376-1378.
10. Preiffer, I. (1958) Attack of sulphur on nickel and nickel alloys, *Z. Metallkunde* **49,** 267-275.
11 Laude, .L.D.,Wautelet, M.,Andrew, R. (1986) Laser-induced synthesis of compound semiconducting films, *Appl.Phys.A*, **40,** 133-143.
12. Zhiryakov, B.M., Obesnyuk, V.F.(1984) Effect of transparent coatings on the generation of laser-induced shock waves in metals, *Phys. Chem. Mater . Treat.(GB)*, **18,** 487- 489.
13. Ivanov, E.E.,Simakov, Yu.M.,Yanushkevich, V.A. (1985) Laser-induced formation of pores in aluminium samples, *Fiz. Khim. Obrab. Mater.* **5,** 35-27
14. Batsanov, S.S. (1967) Physical chemistry of pulse pressures, *Inzh.-Fiz. Zhurnal*, **12**, 104-119
15. .Batsanov, S.S. (1967) Physical chemistry of shock compression, *Izv. Sib.Otd . Akad. Nauk SSSR, Ser. Khim. Nauk*, **6**, 22-35.
16. Dijkkamp, D.,Wu, X.D.,.Chan, S., Venkatesan, T. Rapid (1987) Laser-induced growth of nitride and oxyde layers at a berillyum/liquid interface, *J.Appl. Phys.*,.**62**, 293-295.
17. Zubova, E.V.,Korotaeva, L.A.(1958) Chemical transformations in the solid phase at pressures of 50.000 kg/sq. cm with applied shear action, Zhur. Fiz. Khim.,**32**, 1576-1579.

LASER PATTERNING OF THIN FILMS

J.Lančok, M.Jelínek, V. Trtík, L. Jastrabík
Institute of Physics, Academy of Sciences of the Czech Republic
Na Slovance 2,180 40 Prague 8

1. Introduction

Advances in the development of high T_C superconducting, diamond like carbon (DLC) and ferroelectric thin films and components and devices for electronics have led to the optimalization of patterning techniques. The laser patterning has a number of advantages over the other techniques. This technique is high perspective because a laser beam can cause various processes in this materials such as melting, ablation, evaporation and modification. The superconducting structures are suitable specially for subsequent studies of superconducting phenomena [1] and electronics device production (superconducting resonators, filters, AD and DA converters and SQUIDs [2],[3],[4]). The DLC film structures are suitable for infrared optics, resists and micromechanical devices [5],[6].

In this study we have used the thin films prepared by using of pulsed laser deposition (PLD). The superconductive films were created on $SrTiO_3$ (100) and sapphire (1-102) substrates; thin DLC film was deposited on steel, and thin $SrTiO_3$:Cr^{3+} (doped Cr^{3+} ions) were deposited on Si substrates [7,8,9]. We have studied the influence of laser (laser regime cw or pulsed, wavelength λ, energy and power density, repetition rate) and optical and thermodynamic parameters of films and substrate materials on the physical properties and morphology of created structures in order to optimalize patterning process (narrow cutted structures). The dependence of depth profile of laser traces on laser fluence was also studied and ablation threshold and absorption length of YBaCuO/$SrTiO_3$, YBaCuO/sapphire and DLC/steel were determinated. Simple structures as bridges in superconductive films was created.

2. Experimental setup

The schema of laser patterning system is shown in Figure 1. The pulsed, single-mode, Q-switched Nd:YAG and continual Ar^+ ion lasers were used. Nd:YAG laser of pulse duration of 10 ns and output energy of 1-7 mJ was used. The Ar^+ ion laser was operable in multimode regime with maximum output power of 3 W. The laser beam were focused to a spot of diameter of 10-20 μm by an optical objective. A video monitor was used to display the patterns simultaneously. Two computer-controlled stepper motors were employed to translate the film through the sample holder. The laser fluence was

R. Kossowsky et al. (eds.), High Power Lasers – Science and Engineering, 567–574.
© 1996 *Kluwer Academic Publishers. Printed in the Netherlands.*

attenuated to vary the laser energy or power density. The scanning rate of the x-y holder system was possible to change in the range 0.1-50 μm/s.

Measurement of etched profiles were performed using mechanical stylus (Talystep) and the morphology structures was observed by scanning electron microscopy (SEM). The electrical properties of superconductive thin films were measured by the standard four- probe method.

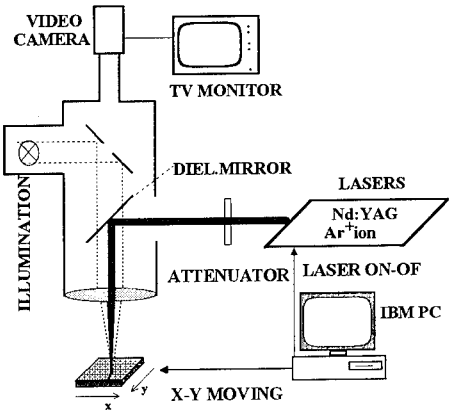


Figure 1. Experimental set-up for laser lithography system

3. Experimental results with Nd:YAG laser

3.1 DETERMINATION OF ABLATION THRESHOLD AND ABSORPTION COEFFICIENT

In order to create high quality patterning structures the laser energy density, x-y translation rate and laser repetition rate were varied. At first step we have investigated the dependence of depth profile of laser traces on laser fluence. This dependence is necessary to known the number of laser pulses and energy density needed to reach the required depth profile in thin layer. Examples of cutted traces in YBaCuO/sapphire and DLC/steel are shown in Figure 2. and 3. respectively.

By following the Beer-Lambert relation of absorption, the attenuated energy density at depth z, given by:

$$E(z) = E_{inc} e^{-\alpha z} \qquad (1)$$

where E(z) is attenuated energy density at depth z, E_{inc} is the incident energy density and α is the absorption coefficient or alternatively the inverse absorption length. Patterning is characterised by the ablation of the film material which is achieved by light absorption according to Beer-Lambert law [10]. Equation (1) at E_{th}, the absorption threshold energy we can write per one puls:

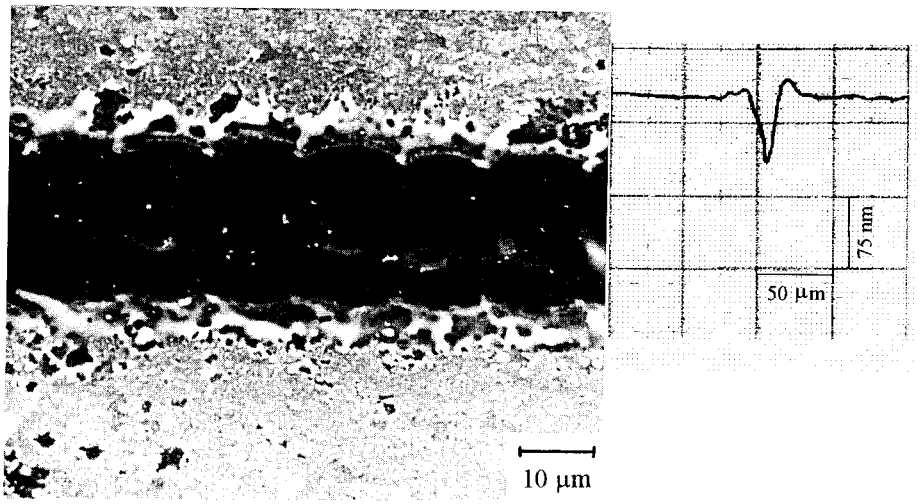


Figure 2. SEM photo and depth profile of Nd:YAG laser trace on YBaCuO/sapphire (thickness 300 nm), E=191.7 J.cm^{-2}, f=2 Hz, v=25 μm/s, 1000 x magnification).

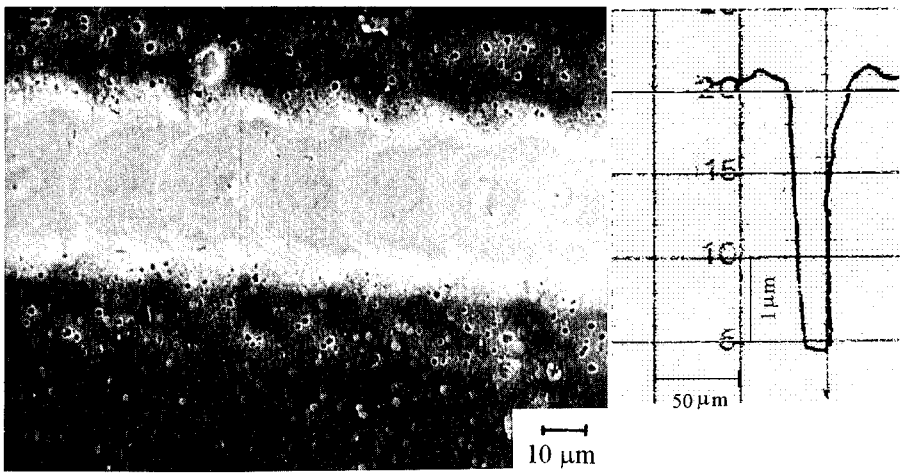


Figure 3. SEM photo and depth profile of Nd:YAG laser trace on DLC/steel (thickness 3 μm, E=19 J.cm^{-2}, f=2 Hz, v=25 μm/s, 720 x magnification).

$$abl.depth = \frac{1}{\alpha} \ln \frac{E_{inc}}{E_{th}} \qquad (2)$$

From graphs in Figure 4. and according to equation (2) we have determinate the absorption coefficients (from the slope) and ablation thresholds (by extrapolation).
The following ablation thresholds and absorption coefficients were determined:
1.YBaCuO/sapphire:
ablation threshold 85.3 J.cm^{-2}, absorption coefficient 0.6×10^5 cm^{-1}

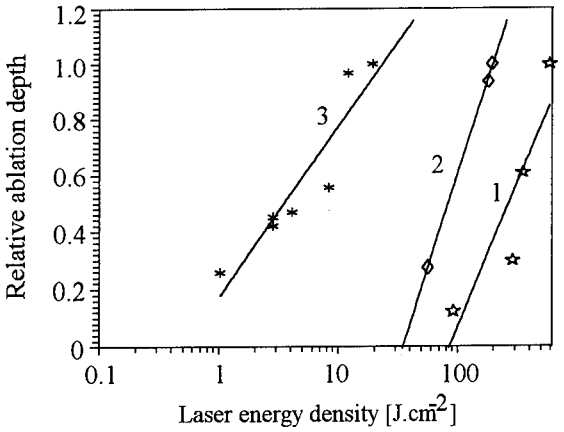


Figure 4. Relative ablation depth as a function of laser density for Nd:YAG laser for following films: 1 YBaCuO on sapphire (stars), 2 YBaCuO on $SrTiO_3$ (rhombs) (thickness of films 300 nm.), 3 DLC on steel (asterisks)(thickness of films 3 μm).

2.YBaCuO/$SrTiO_3$:
ablation threshold 35.1 J.cm^{-2}, absorption coefficient 0.55x105 cm^{-1}
3. DLC/steel:
ablation threshold 0.52 J.cm^{-2}, absorption coefficient 0.12x10^5 cm^{-1}.

As it is seen from graph on Figure 4. (graphs for YBaCuO films on and on sapphire) the ablation threshold depends on substrate material and its value depends on substrate temperature conductivity [11]. Because the temperature conductivity of $SrTiO_3$ is lower in comparison with that of sapphire, the ablation threshold for YBaCuO/$SrTiO_3$ is also lower than ablation threshold of YBaCuO/sapphire.

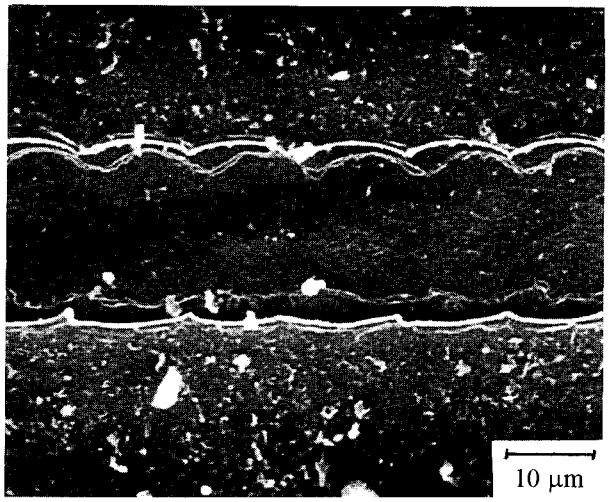


Figure 5. SEM photo and of Nd:YAG laser trace on $SrTiO_3$:Cr^{3+} /Si (thickness 100 nm, E=5.73 J.cm^{-2}, f=2 Hz, v=25 μm/s, 1200 x magnification).

For cutting of structures the laser intensity was adjusted slightly above the ablation threshold and the required ablation depth was achieved by manifold laser pulses at the same place.

The $SrTiO_3$:Cr^{3+} /Si film was very thin (thickness of about 100 nm), so the determination of the ablation threshold using this method was impossible. The best created structures is in Figure 5.

3.2 CREATION OF MICROBRIDGES IN SUPERCONDUCTIVE FILM

For some applications of thin supeconductive films the microbridges in the films is necessary to create. We have studied the influence of laser patterning on physical properties of superconducting film (degradation of superconducting properties). The microbridges were created gradually with width d of 240, 150, 80, 50, 40, 30 and 10 μm - see Figure 6.

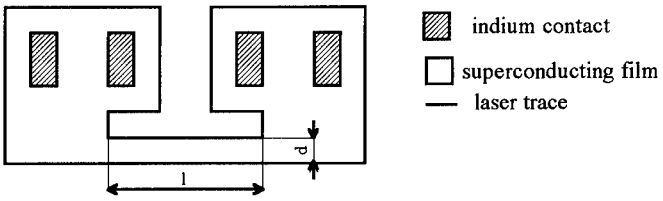


Figure 6. Geometry performed on film to measure electrical parameters of superconducting bridges, where d is flexible width and l is length of bridge. Length of bridge l was 1 mm.

The microbridges were created on $YBaCuO/SrTiO_3$. The original film showed a zero resistance temperature T_C= 89.2 K and Γ=2.64 (Γ is a slope of R(T) function in normal state).

The patterning technique based on local damaging has tendence to degrade the properties of the remaining structure, resulting in "dead layers" at the edges [12]. These degradation can be minimised e. g. by using liquid-nitrogen cooling during the patterning process [13]. Schema of our system for patterning of thin films cooled liquid nitrogen temperature is in Figure 7.

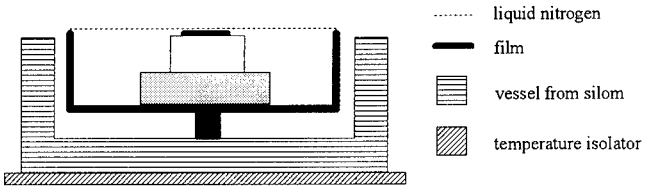


Figure 7. Design of vessel on liquid nitrogen, in which film has been inserted in process of bridge creating..

Relative degradation T_C and Γ was studied as a function of width of bridges at room temperature and at 77 K. The results are shown at Figure 8. The degradation of T_C for various width of bridges was found to be smaller than 1% and was independent on film temperature. The degradation of Γ at room temperature for bridge d=150 μm was approximate 20%, opposite to 4% degradation at 77 K seen graph on Figure 8.

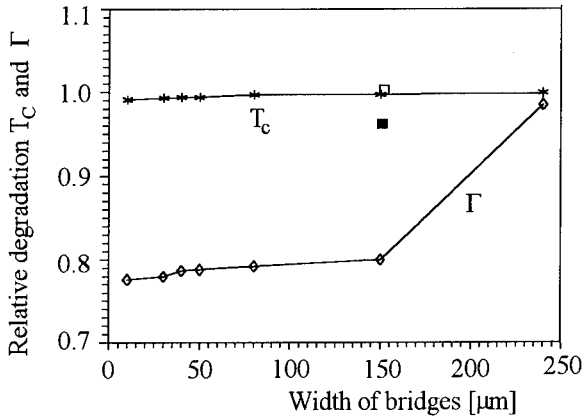


Figure 8. Relative degradation of critical temperature T_c (asterisks) and parameter Γ (rhombs) as a function of microbridges width. Closed field is Γ and open field is T_c for 150 μm wide bridge, which were performed at liquid nitrogen temperature.

3.3 MODIFICATION OF SUPERCONDUCTING FILM

The laser induced modification of properties of superconductive layers in open air atmosphere was studied. The four-point resistant method was used for the measurement of R(T) dependence. The film geometry and schema of equivalent electrical circuit of film are shown in figure 9.a respectively 9.b. The resistance of the illuminated part R_{illum} of film are was determined from the total resistance R_T:

$$R_{illum}(n) = R_T(n) - 2R_1 \tag{3}$$

where R(n) indicates the resistance after n pulses.

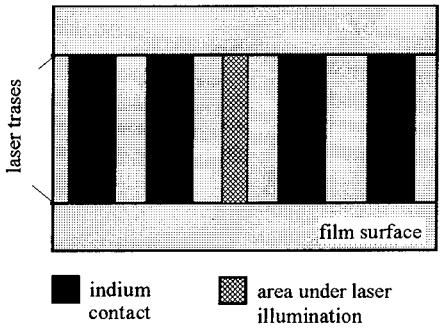
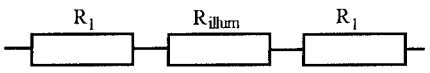


Figure 9.a Film geometry created on YBaCuO film on $SrTiO_3$ substrate



R_1 - resistancce of non-irradiated part of film
R_{illum} - resistence of irradiated part of film

Figure 9.b Equivalent circuit created on film

The relation between relative degradation depth D(n) [14] and R_{illum} is following:

$$D(n) = \frac{h(0)-h(n)}{h(0)} = 1 - \frac{R_{illum}(0)}{R_{illum}(n)} \quad (4)$$

where h(n) is the thickness of non-degenerated film after n pulses. In accordance with [14] we have found that h(n) is proportional to $R_{illum}^{-1}(n)$.

Dependence of relative degradation depth as a function of the number of laser pulses for three different intensities is shown in Figure 10.

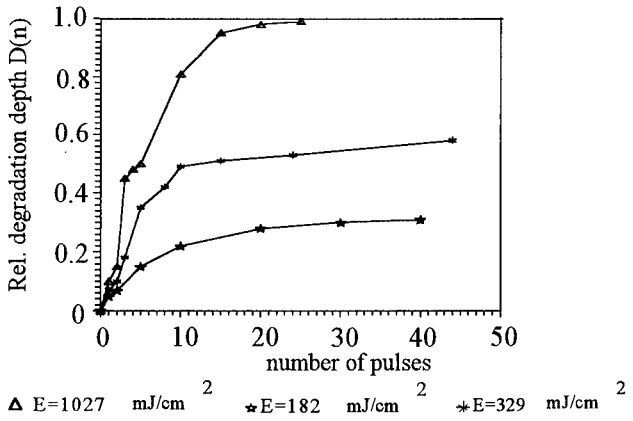


Figure 10. Relative degradation depth as a function of 10 ns pulses for three different laser intensities.

4. Experimental results with Ar^+ ion laser



Figure 11. SEM photo of trace for Ar^+ ion laser on YBaCuO/sapphire P=3.0 x 10^6 W/cm^2 (thickness 300 nm, v=25 μm/s, 1000 x magnification).

Because the absorption of light in ferroelectric or DLC films was very low only YBaCuO layers was possible to pattern using cw Ar^+ laser. The laser power density was in the range 3.0 - 4.0 x10^6 W/cm^2 . The line of 12 μm wide on sapphire substrate was possible to cut- see Figure 11.

5. Conclusion

Using Nd:YAG laser we have created the following laser traces in films: YBaCuO/sapphire, YBaCuO/$SrTiO_3$, DLC/steel, $SrTiO_3$:Cr^{3+}/Si with width of 17 μm, 30 μm, 20 μm and 18 μm. Ablation threshold and absorption coefficient of different film/substrate combination were determined. For higher substrate thermal conductivity the higher value ablation threshold. Relative degradation T_C and Γ superconducting microbridges was studied as a function of width of bridges at room temperature and at 77 K. The T_C value was found to be independent on width of bridge and Γ was decreased with width d (bridges created at room temperature in open atmosphere) From the experiments follows that the patterning of films using lasers (preferably pulsed lasers), is very effective method for study of different kinds of films and substrates.

6. References

1. Mannhart, J., Scheuermann, M. (1989) Micropatterning of high T_C films with eximer laser, Appl. Phys. Lett. **15**, 1271
2. Mossavati, R. at all (1991) Thinck film YBCO microstrip rezonators, Supercond. Sci. Technol. **4**, 145
3. Gallagher, W.J. (1989) High-T_C superconductivity in digital electronics, Solid State Technol. **11**, 151
4. Friemel, S. and Scilling, M. (1994) Input coils for YBaCuO flux transformers, Supercomd. Sci. Technol. **7**, 787
5. Pravew, S., Kalish, R. and Adel, M. (1986) Pulsed laser treatment of diamondlike carbon films, Appl. Phys. Lett. **48**, 1585
6. McEntee, J. (1995) Eximers etch diamond microstructures, Solid State Technol., **3**, 37
7. Trtík, V., Jelínek, M.and Kluenkov, E.B. (1994) Study of Laser Deposited PZT, PLZT, PMN and YBCO Thin Films, Journal of Physics D : Applied Physics **27**, 1-4
8. Bulíř, J., Jelínek, M., Vorlíček, V., Chvostová, D., Soukup, L. (1995) Laser Deposited Hard a-C Films. Journal of Non- Crystalline Solids **188**, 118
9. Jelínek, M., Jastrabík, L., Trtík, V., Studnicka, V. at all (1994) Excimer laser ablation and properties of chromium doped stroncium titanate thin films, Ferroelectrics, **152**, 73
10. Inam, A., Wu, X.D. and Venkatasen, T. at all (1987) Pulsed laser etching of high T_C superconducting films, Appl. Phys. Lett. **54**, 1112
11. Peak, U.C. and Kestenbaum, A. (1973) Thermal analysis of thin-film micromatching with lasers, J. Appl. Phys., **44**, 2260
12. Akoh, H., Sato, H. and Takada, S. (1993) Damage-less dry etching of YBaCuO films under liquid nitrogen cooling, IEEE Appl. Supercond. **3**, 2990
13. Nivele, M.J.M.E., Gerritsma, G.J and Rogalla, H. (1994) Coherent vortex motion in YBaCuO nanobridges prepared by a substrate-etching technique, Physica C, **233** , 185
14. Vase, P.,Yueqiang, S. and Freltoft, T. (1990) Deposition, characterization, and laser ablation patterning of YBCO thin films, Applied Surface Science **46**, 61

APPLICATIONS OF Nd AND Er:YAG LASERS IN OPHTHALMOLOGY AND DENTISTRY

H.JELÍNKOVÁ, K. HAMAL, V.KUBEČEK
Czech Technical University in Prague
Faculty of Nuclear Science and Physical Engineering
Břehová 7, 115 19 Prague 1, Czech Republic

J.PAŠTA
Military Hospital
160 00 Prague 6, Czech Republic

T.DOSTÁLOVÁ
Institute of Dental Research
Vinohradská 48, 120 60 Prague 2, Czech Republic

J.KUBELKA,S.PROCHÁZKA
Preciosa-Crytur
Přepeřská, 511 19 Turnov, Czech Republic

Abstract: Solid state lasers make possible rapid technological advances in medical applications by virtue of their wavelength and temporal mode versatility, convenience, relative compactness, and portability. The possibility of using high power solid state laser radiation in ophthalmology and dentistry is discussed and analyzed.

1. Introduction

Medical applications of various type of lasers follow from the results of the interaction of their radiation with a tissue. This interaction is mainly dependent on the penetration depth of the radiation into the tissue (given by wavelength of the radiation) and then on the duration of that interaction (continuous versus pulsed regime), on the energy, length of pulse, radiation power, etc.

The interaction processes can be divided into primary and secondary effects. The primary processes include spectral reflection, spectral absorption and transmission of radiation. The secondary effects are temperature, photochemical and acoustic phenomena, multi-photon absorption, Raman and Brillouin scattering, etc. Among the primary processes, the spectral absorption has the main role in the biophysical interaction.

R. Kossowsky et al. (eds.), High Power Lasers – Science and Engineering, 575–582.
© 1996 *Kluwer Academic Publishers. Printed in the Netherlands.*

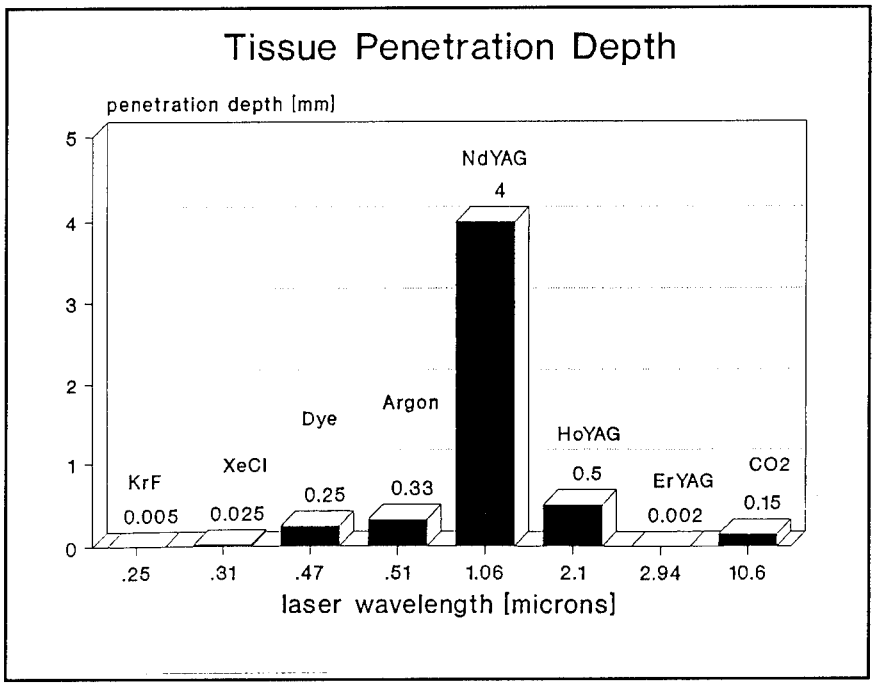


Fig.1. Dependence of tissue penetration depth on laser wavelength

As water is a prominent component of biological tissues, the interaction of radiation with tissue (tissue penetration depth) is mainly given by the absorption of radiation in water. Fig.1 shows an example of dependence of the tissue penetration depth on laser wavelength. A summary of the dependencies of medical applications on parameters of a given type of lasers has been made by Boulnois in [1]. From Fig.1 it follows that a wavelength of 1.06 μm (Nd:YAG laser)-due to its deep penetration into the tissue-is more suitable for cutting or destroying internal layers of tissue. On the other hand, the radiation of 2.94 μm (Er:YAG), 0.25 μm or 0.31 μm (excimer laser KrF and XeCl resp.) should be used for treating upper layers of tissue.

2. Ophthalmology

Laser applications in ophthalmology date 30 years back, but in the pioneering years laser radiation was used mainly for retina coagulation (ruby laser, argon laser). With the discovery of other types of lasers, radiations with different wavelengths have been tested for ophthalmology treatment.

Ophthalmic microsurgery (secondary cataract) uses a high power laser with the shortest pulses to generate plasma breakdown for removing the secondary lens capsule

tissue. From the radiation penetration curve into the eye it follows that it is possible to use the radiation of visible or near infrared region. Among the solid state lasers, the Nd:YAG or ruby lasers are suitable for this purpose, and therefore a simple laser unit which can generate either nanosecond or picosecond pulses is needed. The nanosecond pulse is usually obtained [2] by using an active or passive Q-switch, the train of picosecond pulses being generated by either an active or passive mode-locker and several combinations of those may be considered. However, there is still no laser unit capable to switch from the nanosecond to picosecond regime (both regimes are useful for ophthalmology treatments).

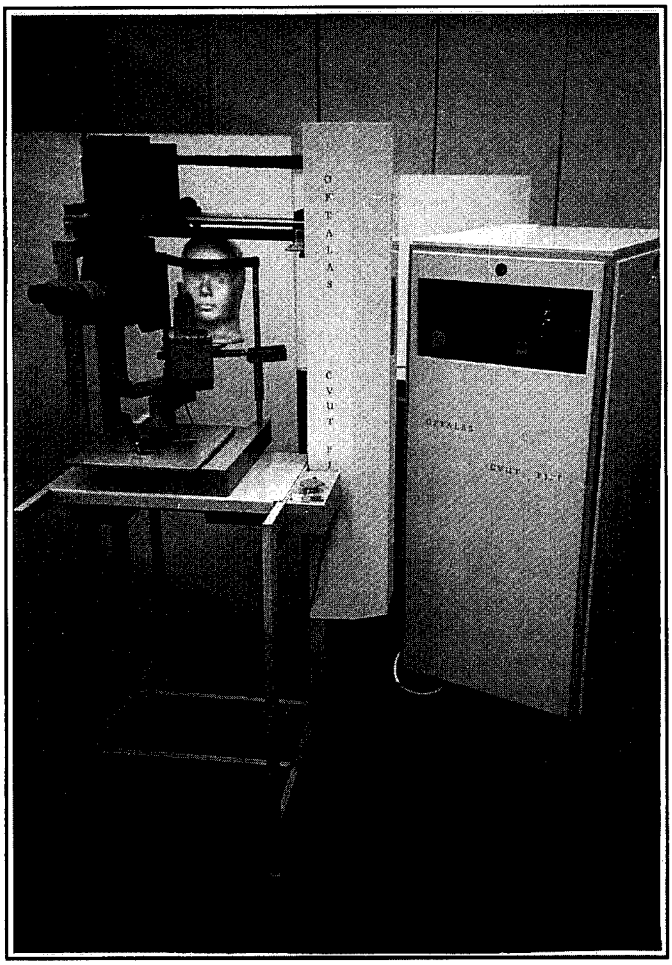


Fig.2. Nd:YAG photodisruptor for micro-surgery of the eye

2.1. FJFI Nd:YAG OPHTHALMIC LASER SYSTEM

The paper reports on a Nd:YAG laser allowing to select either a Q-switched or mode-locked regime of operation. The optical resonator is formed by a 5 meter concave 100% reflectivity mirror and a mirror with an 8% reflectivity which serves as an output coupler. To accomplish the single transversal mode of operation, a 1.2 mm diaphragm iris is inserted. To mode-lock the laser, a highly stable saturable dye (ML-51 in dichlorethane) was developed [3]. A flowing dye cell (5 mm thick, with the initial transmission of 35%) is inserted between the rear mirror and the crystal. To obtain nanosecond pulses, the BDN foil with the optimum initial transmission 45% [4] was inserted into the resonator. The

pulse duration in the picosecond regime was measured by Hamamatsu C979 streak camera and statistically processed. The result of measurements was 25 ps with RMS 15%. The nanosecond pulse, detected by a high speed photodiode was measured by the Tektronix transient digitizer and the pulse duration in this regime was measured to be 4 ns. The beam structure was monitored with a CCD camera. It was ascertained that the pulse shape was smooth and the output beam was close to Gaussian profile. The output energy monitored by the Gentec Joule meter was 7 mJ for both the picosecond and nanosecond regimes. Inserting an amplifier (to build a compact stable oscillator/amplifier system), we increased the output energy in both regimes by a factor of 10-15 (up to 70 mJ), allowing thus to compensate for any long term instabilities of the equipment, by just adjusting the output attenuator to obtain the desirable energy. The system characteristics are summarized in Tab.1 and the photograph of the system in Fig. 2. Besides the novel system design, we also turned considerable attention to the equipment reliability in the clinical practice.

TABLE 1. OFTALAS FJFI system characteristics

Type of laser	Nd:YAG
Wavelength	1.06 μm
Regime	Q-switch/mode-locked
Pulse duration	4 ns (Q-switch)
	25 ps (train) (mode-locked)
Output energy	1-70 mJ
Repetition rate	1 pps
Spot diameter in the focus	50 μm
Angle of acceptance	16^0
Guiding beam	He-Ne laser 0.6328 μm
Beam transmission	via mirrors
System of cooling	distilled water (closed)

2.2. FJFI Er:YAG OPHTHALMIC LASER SYSTEM

Recent studies have indicated that it is possible to use laser radiation for the surgery of the anterior segment of the eye. For this purpose it is necessary to reach the ablation effect. From Fig.1 follows that the required radiation is generated by an Er:YAG laser or excimer laser. Let us concentrate on a solid state Er:YAG laser. It is a very special feature of this laser that its emission wavelength matches exactly the main water absorption peak in the IR range (λ_{peak}=2.94 μm) [1]. Therefore, the photothermic ablation threshold for the irradiated tissue is lower than for radiations of other wavelengths.

For the experiment of cutting cornea tissue (in vitro), in our study an Er:YAG (2.94 μm) - ophthalmic laser system delivering 800 mJ of maximum energy in 200 μs long pulses was designed and constructed. The laser radiation was transported via delivery arms and focused on the tested surface of the tissue with a CaF_2 lens (f=55 mm) so as to increase the radiation energy density. Cadaverous human eyes were placed into a special stand and then tissues of the anterior eye segment were irradiated by the Er:YAG laser.

Direct external interventions were realized and a photoablation was initiated in a sealed anterior chamber. The treated tissue was then prepared for further investigation by scanning electron microscopy.

3. Dentistry

The applications of lasers in soft and hard dental tissue preparation have been under investigation for more than twenty years but until recently have been very limited. Ruby lasers (first used for this purpose) were found to be unsuitable for caries removal and tooth preparation due to the thermal damage of the tooth tissues they cause. But, convectional drilling machines are also not ideal because they produce a pain based on thermal effect and mechanical stress of dental tissues. Therefore new techniques in dental research which initiate the ablation effect of mineralized tissues are of significant interest.

In our study, a comparison has been made of the interaction of various solid state laser radiations with soft and hard dental tissues. Parameters of the lasers used in this experiment are summarized in Tab.2. The hard dental tissues, i.e. enamel and dentin, were irradiated in vitro by these radiations and thus the dental cavity could be prepared.

It was found that the real ablation effect was observed only with the Er:YAG irradiation of the tissue (Fig.3c). With shorter wavelengths (Tu:Cr:Ho:YAG-2.1 μm) the effect of "drilling" the tissue is either small (Fig.3b) or insignificant (Fig.3a) (for wavelengths Nd:YAG-1.06 μm or 1.44 μm, respectively).

3.1. Er:YAG DRILLING LASER SYSTEM

For the experiment, a Er:YAG laser drilling machine was designed. The system has a laser head with an articulated arm, water cooler, and power supply with automatic control. The laser head consists of an Er:YAG crystal with a diameter of 4 mm and length of 100 mm placed along with a xenon flashlamp into the pumping cavity (LMI 1620). A special design of the resonator enables to generate the output energy up to 700 mJ in a free running - long pulse mode - regime. The length of the generated pulses was measured to be 200 μsec. By the articulated arm the radiation is incited on the investigated place and focused by the CaF_2 lens (f=55 mm) on the tested samples. From measuring the temperature of the heated tissue irradiated by Er:YAG laser radiation it follows that cooling the tooth tissue is necessary [5,6,7,8]. For this reason - along with the articulated arm - the water and air are carried so as to be focused on the same place, it means that the irradiated tissue is under water spray.

The power supply consists of a controller and a high voltage charging unit. The controller allows the operator to check the generation of the laser energy and the high voltage charging unit supplies voltage to the laser head where the laser radiation is generated.

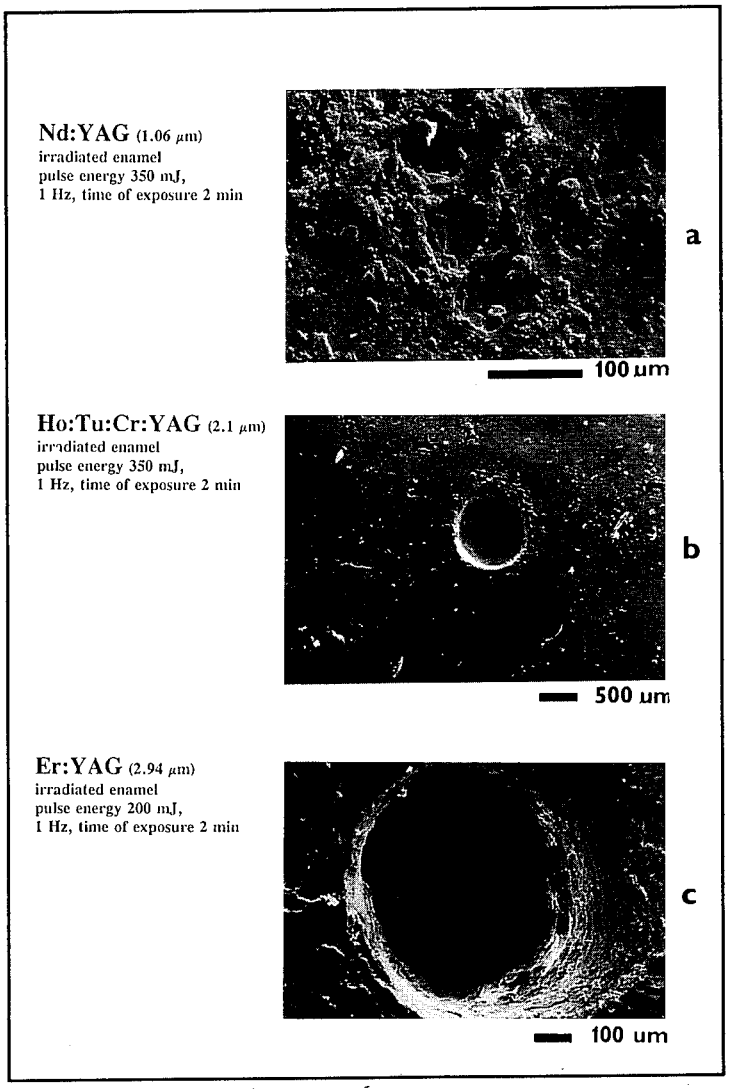


Fig.3. The effects of different radiation interactions with hard tissue

The water cooler is a self-contained system that provides water to the pumping cavity. The control system includes a microprocessor ensure that all parts of the system are working properly.

During the cooled pulsed Er:YAG laser preparation no carbonization in the dentin zone was observed. The pulsed Er:YAG laser radiation applied simultaneously with appropriate water cooling removes enamel and dentin efficiently without causing dangerous pulp temperature changes.

Table 2.: Parameters of used solid state lasers

Laser system	Nd:YAG	Nd:YAG	Ho:Tu:Cr:YAG	Er:YAG
Wavelength [μm]	1.06	1.44	2.1	2.94
Output energy [mJ]	350	300	800	600
Rep.rate up to[Hz]	6	6	1	3
Pulse duration [μs]	200	200	250	200
Delivery system:				
Quartz fiber Ø [μm]	600	600	500	-
Mir.arm+lens f [mm]	-	-	-	55
Output energy [mJ]	200	200	200	450

4. Conclusion

For eye microsurgery a special Nd:YAG laser system was prepared, allowing to choose the regime of operation and thus to compare immediately the effect of microsurgery treatments with nanosecond or picosecond pulses. The Nd:YAG system OFTALAS FJFI is used in clinical practice mainly for eye microsurgery (for iridectomy and capsulotomy).

From the first results with the eye tissue treated by an Er:YAG laser it follows that this mid-infrared radiation will be applicable in the eye surgery: for sclerostomy, where a permanently opened space is created, and for paracentesis.

Also for applications in dentistry, the studies have demonstrated that Er:YAG laser radiation might drill very well defined holes into the enamel and dentin [9]. With proper cooling, the prepared cavity is clean without considerable damage to the adjacent hard substances and without dentin carbonization.

It seems that among the many laser candidates investigated for the hard tissue removal, it only the Er:YAG mid-infrared radiation that could be probably used in practice at present, the main reason being very high absorption of this radiation in water and hydroxyapatite contained in tooth tissue [10,11,12]. The strong local thermal effect on the water leads to microexplosions in the liquid phase and therefore, the Er:YAG radiation has the ability to remove tissue particles during microexplosions and vaporize them.

The obtained results have demonstrated the applicability of the solid state Nd:YAG and Er:YAG radiations in ophthalmology and dentistry.

5. Acknowledgment

This research has been supported by the Grant Agency of the Czech Republic in the form of a research grant No. 308/94/1189 and No. 102/93/074.

6. References

1. Boulnois, J,L. (1986) *Photophysical Process in Recent Medical Laser Developments:A Review*, Lasers in Medical Science, 1.
2. Koechner, W. (1986) *Solid-State Laser Engineering*, Springer-Verlag, New York.
3. Hamal, K., Hrušková, V. and Jelínková, H. (1985) *Saturable dye for 1.06 μm*, Technical Digest Conference on Lasers and Electro-Optics, Optical Society of America, CLEO'85, Baltimore,WE4.
4. Kubelka, J. (1989) BDN in diacetobutyrate cellulose (private communication)
5. Dostálová,T., Krejsa,O., Jelínková,H., Hamal,K., Procházka,I. and Bakule,P. (1993) *Computer monitoring of the thermal effects induced by Erbium:YAG laser radiation during preparation of the hard tooth tissue*, Dental Applications in Lasers, Grigori B.Altshuler, Raimund Hibst, Editors, Proc. SPIE 2080, 51-54.
6. Burkes,E.J., Hoke,J., Gomes,E. and Wolbarsht,M (1992) *Wet versus dry enamel ablation by Er:YAG laser*, J. Prosthet. Dent., 67, 847-51.
7. Hibst,R. and Keller,U. (1990) *Heat effect of pulsed Er:YAG laser radiation*,SPIE vol.1200, Laser Surgery,pp.379-386.
8. Paghdiwala,A.,F., Vaidyanathan,T.K. and Paghdiwala,M.F. (1993) *Evaluation of Erbium:YAG laser radiation of hard dental tissues:analysis of temperature changes, depth of cuts and structural effects*, Scanning Microscopy International,7,3,989-997.
9. Dostálová,T.,Jelínková,H.,Hamal,K.,Krejsa,O.,Kubelka,J.,Procházka,S.(1995) *The evaluation of depth and profile cavity after laser ablation with different energy of Er:YAG laser radiation*, Proceeding of BIOS,95, Barcelona, Spain.
10. Koort,H,J. and Frentzen,M. (1992) *YAG-Lasers in Restorative Dentistry.A histological Investigation*, SPIE Vol.1643 Laser Surgery, 403-410.
11. Jelínková, H., Hamal,K., Kubeček,V., Dostálová,T.,Krejsa,O., Kubelka, J., Kvapil,Ji. and Procházka, S. (1994) *Irradiation of human dental tissues using 5 laser wavelengths*, Proceeding of CLEO/EUROPE-EQEC, Medical & Biological Applications, 62.
12. Hibst, R. and Keller,U. (1989) *Experimental Studies of the Application of the Er:YAG Laser on Dental Hard Substances:I.Measurement of the Ablation Rate*, Lasers in Surgery and Medicine 9,338-344.

LATE SUBMISSIONS

HISTORY, CURRENT STATUS AND OUTLOOK TO THE FUTURE OF HIGH POWER SOLID STATE LASERS

A.M.Prokhorov and A.A.Manenkov
General Physics Institute of Russian Academy of Sciences,
Vavilov Str., 38, Moscow, 117942, Russia

1. Introduction

The first laser operation has been demonstrated 35 years ago (Maiman, 1960 [1]). It was the solid state laser in which Cr^{3+}-doped supphire crystal (Cr^{3+}:Al_2O_3-ruby) was used as an active medium. Since that time many other types of lasers have been proposed and developed using various active media: atomic and molecular gases, liquid molecular solutions (dyes and salts), plasmas, semiconductors, free electrons, etc. However, a solid state laser family remains leading and the most important class of lasers up-to-now.

The aim of this lecture is to present a brief historical overview of principal milestones in quantum electronics on the way from masers to lasers, to describe main concepts in developments of high power solid state lasers and to present a current status and outlook to the future of such lasers.

Before starting a realization of this our plan it is reasonable to give some definitions related to the title "High power solid state lasers." The term "Solid-state lasers" (SSL) is commonly refered to a class of lasers based on iron group or rear earth ions doped crystals and glasses as the active media. Typical examples are ruby, Nd^{3+}:YAG, Nd^{3+}: silicate/phosphate glasses. However, SSL is a more wide class of lasers: it includes dye-impregnated polymer lasers, semiconductor diode lasers, and optical parametric oscillators (OPO).

The term "High power lasers" is usually refered to lasers radiation of which is capable to produce a strong action on a matter, like ablation, melting or stress-induced damage in solids, plasma formation in gases, liquids and solids. An average power of such lasers is typically exceeds 1W, whereas a peak power of lasers operating in pulsed modes can be varied from 1 kW to 10 pW (1 pW =1 petawatt=10^{15} W) depending on a pulse duration varied from milliseconds to femtoseconds. The corresponding term "High energy lasers" is usually refered to the pulsed lasers with output radiation energy varying in the range of 1-10^6 Joules. It is obvious that physics and engineering of high power/high energy lasers with such very wide variation of output power and energy, as well as physics of their laser-matter interaction, are quite different.

R. Kossowsky et al. (eds.), High Power Lasers – Science and Engineering, 585–601.
© 1996 *Kluwer Academic Publishers. Printed in the Netherlands.*

2. Basic milestones in quantum electronics

The new principal of amplification and generation of electromagnetic radiation based on stimulation emission of atoms was proposed and grounded in 1952-1954 (Basov, Prokhorov, and Townes [2-5]). The key idea of this principal consists of creation of thermodynamically nonequilibrium states in atomic or molecular systems when population, of some upper energy levels is higher than that of lower levels j (in thermodynamically equilibrium states the opposite relation takes place: $N_i<N_j$).

In such population - inverted systems stimulated emission at transition $i\rightarrow j$ exceeds stimulation absorption, and, hence, external electromagnetic radiation passing through the system can be amplified. Also, generation of electromagnetic radiation can be obtained in such atomic systems if they are placed into some electromagnetic structure with a positive feedback.

Thus, three main things are required to obtain amplification of electromagnetic radiation using this stimulated emission principle: an atomic medium with appropriate energy levels (i.e. satisfying some requirements for energy separations $E = E_i-E_j = \hbar\omega$ and stimulated emission probability A_{ij} to get an efficient amplification at the frequency ω), an external source for excitation of the atomic system to invert the energy levels population, and some electronic structure (a resonant cavity, etc.) in which the atomic system interacts with the electromagnetic field.

In accordance with this some basic ideas have to be pointed out which played the most important role in realization of quantum electronics principals and in development of a new class of amplifiers and oscillators of electromagnetic radiation-masers and lasers.

The first quantum electronics device was the ammonia maser operating at 1.25 cm wavelength (Gorton, Zeiger, and Townes, 1954 [4]). In this device the ammonia molecular beam was used as the active medium in which energy levels population inversion was achieved by applying to the beam an inhomogeneous electric field, and the electromagnetic structure was a cavity resonator of a type ordinary used in microwave electronics.

The next milestone on a way of quantum electronics was a proposal for the new method of the energy levels population inversion: it is so called three-level method based on application of external electromagnetic radiation at some appropriate frequency ω_p (Basov and Prokhorov, 1955 [5]). This method, called usually as electromagnetic pumping, turned out the universal and most efficient one for energy levels population inverting in different atomic and molecular systems, especially in solids and liquids, allowing to create quantum amplifiers and oscillators in a very wide spectral domain of electromagnetic radiation from microwaves to UV.

A proposal for a three-level solid state maser (Bloembergen, 1956 [6]) was the first application of pumping method. The energy levels of paramagnetic ions in crystals were suggested in this proposal as a proper system for creation of practically efficient low-noise microwave quantum amplifiers.

The first three-level solid state masers have been successfully demonstrated in 1957 and 1958 in gadolinium ethylsulphate [7], and ruby [8] crystals. Further investigations have shown that ruby is the most effective active material for solid-state masers at different wave lengths from decimeters to millimeters: a majority of practically used masers are based on

this material (particularly, in radioastronomy and long-distance space communication [9]. Note that a proposal of ruby for masers (Manenkov and Prokhorov, 1956 [10]) was based on comprehensive studies of microwave EPR spectra of this crystal carried out at the Lebedev Physical Institute in 1954-1955 [11, 12].

Successful development of microwave solid state masers in 1957-1959 stimulated an advance of quantum electronics principals to an optical region.

The first optical maser, called then as a laser, was demonstrated by Maiman in 1960 [1] who used a flashlamp pumped ruby rod as the active medium. The choice of ruby as the active material, was of course, not accidental for two reasons: first, the microwave ruby maser has been successfully developed, as we just mentioned above, by that time, second, optical spectra of ruby have been investigated in detail (Shugano and Tanabe, 1958 [13]). It is appropriate to note here similarities of microwave and optical spectra of ruby, in particular, a nature and characteristics of the ground ($^4A_2$) and excited (^2E) energy states of Cr^{+3} ions in ruby [14] used in microwave and optical masers ,respectively. In particular, both EPR ($^4A_2$ transitions) and fluorescence ($^2E \rightarrow {}^4A_2$ transitions) lines broadening are due to crystal electric field inhomogeneity of ruby samples [14].

Being engaged in studies of microwave EPR spectra of ruby and the microwave ruby masers in 1955-1958, as it has been mentioned above, we considered a possibility of optical maser action in ruby (Manenkov and Prokhorov, 1958 [15]), but unfortunately, have not find an appropriate optical pumping source. T.Maiman was lucky to use a flashlamp for this purpose and successfully demonstrated the optical maser action in ruby [1].

Besides the happy choice of the active material and the pumping source, one more component played a decisive role in the creation of the optical maser (laser) - proposal an open cavity resonator (Prokhorov, 1958 [16]). This type of resonators formed with two parallel flat mirrors became a basic model for other type optical resonators. Now many variations of the open resonator concept are very developed (see, for example [17]).

3. Main concepts of generation of high power laser pulses

Even at the beginning stage of laser development it became clear that solid state lasers are capable to generate high power radiation, especially in a pulsed regime, that opened wide perspectives for many important scientific and practical applications. Here we present some main concepts of generation of high power pulses.

A first very fruitful idea was a proposal for Q-switching of a laser resonator (Hellwarth, 1961 [18]).

The Q-switching concept consists of a single or periodic switch of the resonator losses at an operating spectral mode. The losses are maintained during an active medium pumping at some high level enough to prevent a self-oscillation of the laser (i.e. below oscillation threshold). At some instant when a population of an upper energy level of an atomic transition to be lased become high enough the losses are switched off allowing to the laser to generate the stimulated emission.

The first theoretical analysis of the Q-switching process (Prokhorov, 1963 [19]) has shown that a peak power of the laser pulse, generated in this regime, is much higher and a pulse duration is much shorter than those generated in a free-running (constant Q) regime.

Many experimental studies of the Q-switched laser operation have shown that the giant laser pulses can be generated in this regime with the output peak power and pulsewidth ranging, typically, from 1 to 100 mW and from 1 to 100 ns of power and time domains.

The principal optical scheme of the Q-switched laser is shown in Fig.1. Different type Q-switching elements are used in such scheme: electromechanical devices (rotating prisms, etc.) saturable absorbers (liquid or solid-state dye solutions [20], F-center contained crystals [21], transition ions doped crystals [22],etc.), electrooptic elements (Pockels sells, etc.) [23], nonlinear optical elements based on selffocusing and small-particle scattering [24].

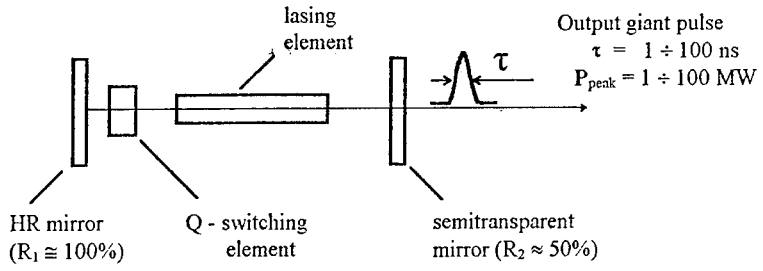


Fig. 1. Principal optical scheme of Q - switched laser

An optical switching response time and a transparency contrast ratio along with a damage threshold are main characteristics of these elements determining the efficiency of the Q-switching action and laser output characteristics. All type Q-switching elements, mentioned above, are used in practical laser divices depending on particular requirements and applications.

A mode-locking concept (Mocker and Collins, 1965 [25], De Maria et al, 1966 [26]) was the next step in the progress of short pulse high power lasers. Basically the mode-locking is further development of Q-switching concept. A theoretical analysis [27] has shown that in the mode-locking regime it is possible to generate laser pulses in CW or pulse train modes of the duration in the 100 fs-100 ps time domain region with the peak power in the region of 1-10 GW. The optical scheme of the mode-locked laser is shown in Fig. 2.

Various mode-locking elements similar to Q-switchers are used in practical laser devices: saturable absorbers, Kerr lenses, electrooptic elements, etc. (see [35] and references therein).

Amplification of laser pulses generated by a master laser oscillator in an external laser amplifier element was the next important concept to achieve a very high output power and energy of the pulses. This concept is a natural way to increase the output power and on

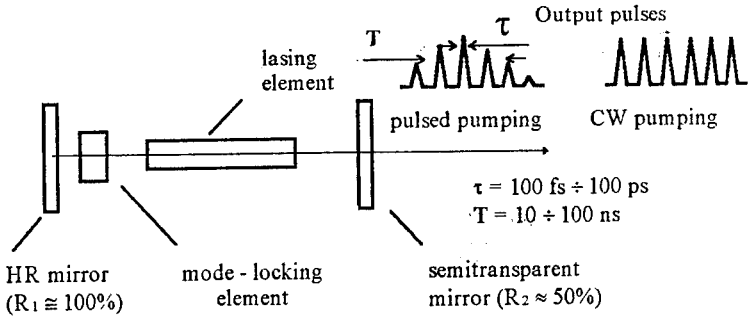


Fig. 2. Principal optical scheme of mode locked laser

the face of it is very simple one. However detailed analysis and experimental studies have shown that some fundamental processes, including nonlinear destortions, both amplitude and phase, and an optical damage are extremely important processes limiting energetic, spatial and temporal characteristics of the laser beam propagating through an amplifier system.

Such distortion are due to saturation of a laser transition of an active medium, its refractive index nonlinearity, and to various laser induced damage processes in the optical components of the amplifier system.

The oscillator-amplifier system and its principal elements are schematically shown in Fig.3. It consists of a single transverse mode laser oscillator (SMO) and several laser amplifiers (A_i) separated by spatial filters (F_i).

A single-mode operation of the maser laser oscillator and spatial filtering of the propagating laser beam are principally important to have a spatially homogeneous intensity distribution at any cross-section along the system to avoid (or reduce) a small-scale selffocusing which can initiate the damage of the system optical elements.

The single-mode operation of the master oscillator is achieved by different methods. One of these simply consists of inserting into an optical resonator of the laser a small-size pinhole allowing to oscillate only the lowest TE_{oo} mode with the Gaussian intensity profile.

A similar approach is used in a spatial filter: it consists (see Fig.3) of two lenses and a pinhole placed in their focal plane. The spatial intensity profile, $I_{out}(r)$ at the filter output is close to the Gaussian.

A geometrical shape of the laser amplifiers is also very important to reduce the selffocusing and damage danger. In this respect a proposal for the disc amplifier concept (Manenkov, 1966 [28], Swain et al, 1969 [29]; Mc Mahon et al, 1973 [30]) turned out the most effective approach to construction of high power solid state laser systems. At present time all the most powerful HPSSL systems used, in particular, in the inertial confinement

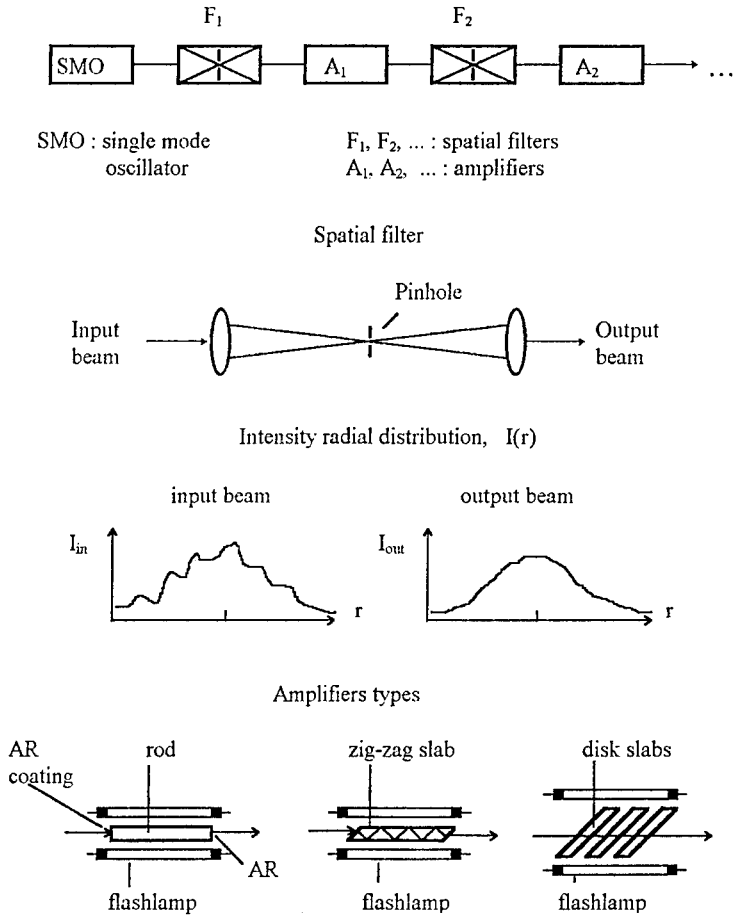


Fig. 3. Schematic of laser oscillator - amplifier system and its optical components

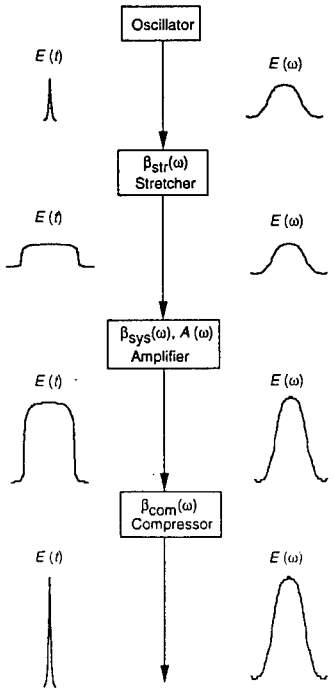
fusion experiments (see below for more details) are based on the disk amplifier concept. This concept looks basically as follows. A series of the flat disks of an active laser material (typically, Nd-doped glass) is placed into flashlamp pump box and set at Brewster's angle to an incident laser beam to be amplified (to avoid Frehnel's reflection losses). A thickness of the disks, their number and separation from each other are chosen from an analysis of the selffocusing effect and amplification efficiency desired. A diameter of the disks are chosen from a consideration of power/energy requirements for the laser system taking into account a laser induced surface and bulk damage thresholds of the disks.

The disk amplifiers have principal advantages over other laser amplifier configurations (rod, zig-zag slabs, etc.) allowing to reduce selffocusing and damage problems. Perhaps, the only disadvantage of the disk configuration is a non-compact

design. For this reason the rod and zig-zag slab amplifiers are often used in practical laser systems of a moderate output power/energy, whereas the multidisk amplifiers are definitely preferable when very high laser intensities are desired.*

Recently, a chirped-pulse amplification (CPA) concept (Strickland and Mourou, 1958 [33]) began to be applied for construction of ultrahigh power (of terawatts to petawatts levels) ultrashort pulse (of picoseconds to femtoseconds duration) laser systems [34].

Such systems basically consist of (see Fig. 4) a low-power ultrashort mode-locked laser oscillator, a pulse stretcher, a power amplifier, and output pulse compressor.



Stretching of the pulse before its amplification is required to avoid (or)significantly reduce) nonlinear phase distortions of the pulse in a amplifier medium which are due to an intensity-dependent medium refractive index change and to very wide Fourie-transformed spectra of the ultrashort pulses(especially, of femtosecond duration). For efficient amplification of femtosecond pulses a stretching factor has to be typically as high as 10^3-10^4. A recompression factor of the stretched pulse after amplification has to be of hear the same value taking into account some temporal change of a pulse shape during the amplification process. A simple consideration shows [34] that the Fourie transform-limited

* Note that a double pass one-disk amplifier in an active-mirror configuration [31, 32] can be designed in a rather compact construction but it has a limited gain.

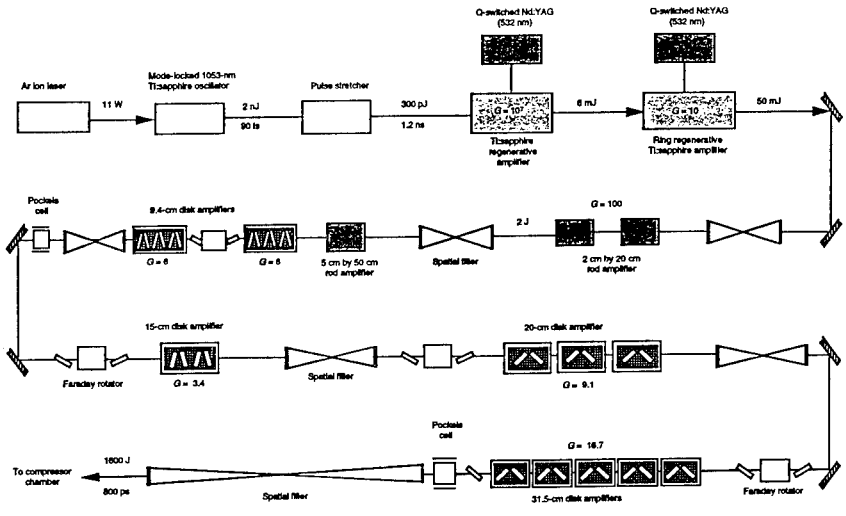
ultrashort pulse can be obtained after compression if the following condition is satisfied for phase characteristics of the compressor, stretcher and amplifier system:

$$\beta_{com}(\omega) = -[\beta_{str}(\omega)+\beta_{sys}(\omega)].$$

For stretching and compression of the laser pulses different optical elements possessing a positive and negative group velocity dispersion are used: fiber waveguides and metallic or dielectric diffraction gratings. The efficiency of the stretcher and composer elements is controlled not only by their dispersion characteristics but also by the laser included damage resistance which is extremely important characteristic of high power laser systems (below we will consider the damage problem in detail).

A practical realization of the CPA concept in ultrahigh power laser systems is, obviously, very complex problem including generation and manipulation of ultrashort pulses, efficient amplification, etc., to obtain at the end a spatially and temporally perfect laser beam with the high power and energy. It combines all the pulse generation and manipulation principles and component concepts described above, including mode-locking, pulse stretching and compression, pulse amplification with various type of laser amplifiers, spatial filtering.

Fig. 5 illustrates the complicity of the petawatt laser system developed recently at Lawrence Livermore National Laboratory [34].



4. Optical materials for HPSSLs

Optical elements for high power solid state lasers are divided in two main types: "active" (lasing) and "passive" (laser controlling). Both types elements are made from a wide variety of materials of different classes. Ion doped inorganic crystals and glasses, and dye-impregnated polymeric materials constitute the main families of active laser materials. Similar materials, but with different functional properties, and some other materials are

used to make various elements of conventional ("classic") and specific laser optics: mirrors, light deflectors and splitters, lenses, spatial filters, frequency converters, pulse stretchers and compressors, Q-switchers, mode-lockers, pump sources (flashlamps, laser diodes), etc.

Main requirements for "active" and "passive" type materials can be summarized as follows. Laser materials have to posses appropriate energy states of lasing atoms with high absorption and emission cross sections, and appropriate relaxation rates of transitions involved in pumping and lasing processes. Also, good thermal, mechanical and optical properties (thermal conductance, hardness, laser induced damage resistance, optical homogeneity, etc.) are very important characteristics of the HPSSL materials.

For "passive" materials used for controlling of operation modes and laser radiation characteristics the most important properties are: good functional characteristics (a high photosaturation contrast ratio and a short relaxation time for Q-switchers and mode-lockers, a high conversion efficiency for frequency converters, etc.), a high laser damage resistance, and high thermooptical properties.

A very wide search and extensive studies done during past 35 years, since the first successful demonstration of the solid-state laser, resulted in finding many effective optical materials for HPSSLs. Some typical examples are listed below and in section "Trends in HPSSLs". More extended list of the laser materials and their properties can be found in review papers, monographs and proceedings of conferences (see, for example [36-40]).

Laser crystals: Cr:Al_2O_3 (ruby), Cr:LiSAF, Nd:YAG,Nd:GSGG, Yb:c-FAP, Ti:Al_2O_3.

Laser glasses: Nd:silicate glass, Nd:phosphate glass.

Laser polymers: dye-impregnated modified PMMA.

Frequency converters (harmonic and parametric generation):KDP, KTP, ADP.

Passive Q-switchers: F-center crystals, dye-impregnated polymers, Cr-doped crystals.

5. Ultrahigh power solid-state laser systems

Shortly thereafter the first demonstration of the ruby laser and especially after development of Nd-glass lasers, it became clear that solid-state lasers can potentially generate very high power radiation which can be used in many applications including fundamental physics, industrial technology, and military purposes. In particular, attractive ideas have been proposed in the mid-1960's to use high power laser radiation to create high-temperature plasma, X rays, and neutrons (see, for example [41] and references therein). These ideas have been advanced significantly during last 30 years and now studies in these directions constitute a very broad research field having promising applications to thermonuclear fusion energetic and other technologies.

Ultrahigh power/energy systems operating at the fundamental Nd-laser frequency (wavelength λ= 1.06 μm or 1.05 μm) and its harmonics (mostly, 3-rd harmonic) with a pulsewidth in a nanosecond region, typically 1-3 ns) have been constructed for laser produced inertial confinement fusion (ICF) experiments in several laboratories: the Nova laser at Lawrence Livermore National Laboratory (LLNL), USA; the Omega laser at the Laboratory for Laser Energetics, University of Rochester, USA; the Gekko X11 laser at the Institute of Laser Engineering, University of Osaca, Japan; the Phebus laser at the Commissariat a l'Energi Atomique, Central d'Etude de Limeil-Valenton, France; the Helen

laser at the Atomic Weapons Research Establishment, England (see [42] and references therein); Delphin laser at the Lebedev Physical Institute [43]; and the UMI-35 and Micron lasers at General Physics Institute, Russian Academy of Sciences, Russia [44,45]; the Progress laser at the Vaviliv State Optical Institute, Russia [46]). All these systems are based on the oscillator-amplifier concept with Nd-glass power amplifiers of various types and architectures. The Nova system at LLNL, for example, designed as the single-pass multibeam system with an increasing aperture of Nd-glass disk amplifiers toward ends of the system. It is capable to produce the laser power as high as 100 kJ in the 1 ns pulse at the fundamental frequency (λ =1.05 μm) with a high (70%) conversion efficiency into the 3-rd harmonic.

Using such nanosecond multikilojoule Nd-laser systems many valuable results have been obtained in National ICF programs on high power laser-matter interaction (hot plasma properties, X-ray generation physics, laser induced damage in optical materials, etc.) allowing to formulate, in particular, realistic requirements for future laser systems for a practically efficient ICF operation.

Basing on these requirements new ICF laser systems are developed with improved laser characteristics. In particular, at LLNL a new concept has been recently proposed which is under technical realization and tests now (see [42] and references therein). This concept (National Ignition Facility-Beamlet Laser Project) is based on a large aperture, multipass Nd-glass laser which is more compact and expected to be more reliable system capable of irradiating fusion targets at the energy and power of 1.8 MJ and 500 TW in the 3-4 ns pulse duration at the third harmonic of the fundamental Nd-glass laser frequency. The laser system will have 192 independent "beamlets" each having a final squire clean aperture of 40x40 cm^2 [42].

Continuing interests in the ICF laser research and in high power laser physics, in general, have lead recently to a development of ultrashort pulse ultrahigh power laser systems capable to produce output laser peak power as high as several petawatts in the pulselength of hundreds of femtoseconds. Such systems based on the CPA concept described above, are developed in several Laboratories in France, Great Britain, Japan, and USA (see [34] and references therein). In particular a laser system with planned 1 kJ output energy at 100-500 fs (2 PW peak power) is under construction and tests now at LLNL in USA [34]. The system includes (see Fig.5) a mode-locked 1053 nm Ti: sapphire master oscillator, a pulse stretcher, Ti: sapphire regenerative amplifiers, several rod and disk Nd-glass amplifiers, and a pulse compressor. This laser is planned to be used in high-power laser-matter interaction studies, including atomic physics at ultra high optical fields (at intensities $I>10^{21}$ W/cm^2), hard X-ray emission, solid-density plasma physics and in the ICF research to study, in particular, a new "fast ignition concept". There is no doubt that a fulfillment of this plan will give principally new results important for both fundamental physics and potential practical applications.

In a conclusion of this section it is reasonable to note that a development and construction of ultrahigh power/energy laser systems, such as described briefly above, is, obviously, a very complex hard work, in both technical and financial aspects, which only limited number of world's laboratories is able to fulfill. For this reason, an international cooperation in the development and construction, and in use as well, of such systems are seemed to be an effective way to overcome the problems and to increase their scientific and practical efficiency.

6. Ultimate power and energy of HPSSLs

The question of what processes or factors limit a maximum power and energy of lasers of any type is one of fundamental problems of high power laser physics and laser technology. This problem was investigated during many years and it has been understood that the major process limiting the power and energy of solid-state lasers is a laser induced damage (LID) of surfaces, coatings and a bulk of optical components occurring at high laser intensities.

For this reason fundamental mechanisms of LID and technological factors affecting a damage resistance of optical materials and components were extensively studied during past 25 years. These studies have resulted in a reveal of main LID mechanisms of the surface, coating and bulk damage, and finding effective technological methods to increase the damage resistance of many optical materials and elements. These results can be summarized as follows (for more details see review papers [47, 49] and Boulder Damage Symposia Proceedings [40]).

1. Main LID mechanisms are associated with laser produced heating of absorbing inclusions ("extrinsic" mechanisms) and with impact ionization (election avalanche) and multiphoton absorption ("intrinsic" mechanisms). 2. Theoretical models for extrinsic and intrinsic damage mechanisms have been developed and main features of LID thresholds have been revealed.

Among extrinsic mechanisms the most effective ones are the mechanisms of thermal explosion of absorbing inclusions and photoionization by thermal UV black-body radiation of laser-heated inclusions [50].

A most adequate and well-grounded model for the electron avalanche LID mechanism based on a solution of kinetic equations for laser-ionized electrons and a material lattice temperature has been developed in [52, 53]. A role of multiphoton absorption was theoretically studied in [53].

3. It has been established that the LID thresholds for both extrinsic and intrinsic mechanisms depend on many material parameters and laser radiation characteristics.

Since material parameters are not usually well-known it is difficult to estimate damage thresholds for optical materials and elements used in high-power lasers. In this situation some theoretically predicted dependencies of the LID thresholds on laser radiation parameters are very valuable for elucidation of damage mechanisms and estimation of damage thresholds in concrete experimental conditions. Among these the most important dependencies of the LID threshold are its dependencies on a pulsewidth, a radiation frequency, an interaction volume/surface, and on a number of pulses. Two latter dependencies are connected with a statistical behavior of LID which is due to random distribution of absorbing inclusions in the materials.

4. An analysis of experimental data on LID, based on theoretical predictions, has shown that in a majority of optical materials and elements, used in HPSSLs, absorbing inclusion initiated damage mechanisms were dominating whereas the intrinsic mechanisms could be observed only in a very pure (inclusion-free) selected materials in specially arranged experimental conditions (in tightly focused laser beams, in particular), avoiding an influence of absorbing inclusions [47]. Domination of extrinsic damage mechanisms is especially expected for large-size optical components and wide-aperture laser beams used

in ultra-high power/energy laser systems where presence of absorbing inclusions is very probable.

5. The injurious effect of absorbing inclusions and structural defects on laser damage resistance (LDR)motivated a basic research and development of optical material technology. These efforts resulted in an improvement of material technology and a development of effective methods of significant increase of LDR of various type optical materials and elements (bulk materials, surfaces, and coatings). In particular, technology of optically pure(almost inclusion-free) glasses and polymeric materials, fine polishing technique, improved dielectric coatings technology, various treatment techniques (thermal and laser conditioning, etc.) have been developed [40, 47].

6. However, further investigations of the laser damage problem (both fundamental and technological aspects) are required. They are very important, in particular, for understanding of LID mechanisms at ultrashort (picosecond-femtosecond duration) laser pulses and for improvement of technology of dielectric coatings and diffraction gratings (most "weak" optical elements). In this respect, some recent theoretical results on a LID mechanism in coatings and pulse-width and pulseshape dependencies of the LID threshold to optical materials in ns-ps time domain [55] have to be mentioned. These results explain well experimentally observed data on LID in coatings and bulk materials and predict some features indicating ways for technological works aimed to increase the laser resistance of optical materials and elements used in high power lasers.

7. Trends in HPSSLs

Many practical applications of HPSSLs desire high efficiency, repetition rate and reliability with reasonable compactness and low cost of laser systems. In this respect, the HPSSLs based on flashlamp pumping do not completely satisfy this desire. It is especially related to large-scale HPSSL systems similar to that described above in Section 5.

Recently laser diodes began to be investigated as an appropriate pumping source for the HPSSLs promising to solve above problems. Main advantages of diode pumping over flashlamp pumping are a higher efficiency, less thermooptical distortions of laser elements, a higher spatial pumping homogeneity, a higher reprate, compactness of a laser system, etc. (for more details see [56]).

This approach become realistic one owing to recent technical advances in both laser diodes and crystals appropriate for diode pumping. Indeed, many high power diodes and diode arrays emitting in spectral ranges of laser crystal absorption bands, effective for pumping, are available now: AlGaAs(750-870 nm), InGaAlP(630-690 nm), InGaAs(890-1100 nm), InGaAsP (1300-1500 nm), InGaSb (1900-2300 nm) (see [56] and references therein). Also, laser crystals suitable for diode pumping are available: Yb:S-FAP, Yb:C-FAP, Cr:LiCAF, Nd:YVO_4, Nd:$GdVO_4$, Nd:$Ca_5(PO_4)_3F$, Nd:$Sr_5(VO_4)_3F$, Nd:$KGd(WO_4)_2$, Nd:$LaSe_3(BO_3)_4$ (see [56, 57] and references therein).

Progress in diode-pumped solid-state lasers (DPSSL) promises revolution in lasers and applications: in many cases DPSSL can replace traditional flashlamp-pumped lasers, including ultrahigh power/energy laser systems, such as systems intended for Inertial Fusion Energy Programs [56]. This "laser revolution" will be analogous to the revolution in radio and microwave electronics happened in 50-th - 60-th years of this century when vacuum tubes were replaced by semiconductor devices (diode oscillators, transistors, etc.).

8. Conclusions

The brief overview of high power solid-state lasers and overlook to the future development is this field can be summarized as follows.

1. The HPSSLs, started in 1960 with the ruby laser, have been well-developed during past 35 years:

- Concepts of generation of high power/energy laser pulses, including ultrashort pulses, have been developed and realized.
- Effective optical materials, both active (lasing) and passive (controlling radiation parameters),for the HPSSLs and their technology have been found and developed.
- The ultrahigh power/energy laser systems have been constructed and used in a number of laboratories in the world.
- Main features of laser induced damage in optical materials and elements, as the limiting factor of the ultimate laser power/energy in HPSSLs, have been understood and effective methods of the damage resistance increase have been proposed and realized. However, further researches, both fundamental and technological, have to be continued, especially for understanding of damage mechanisms and development of optical materials and elements for ultrahigh power lasers of ultrashort pulse (ps-fs) duration.
- Diode-pumped SSLs is challenge for future developments of HPSSLs.

References

1. T.Maiman (1960) Stimulated optical radiation in ruby, Nature, **187**, 493-494

2. N.G.Basov and A.M.Prokhorov (1954) JETP (Russian), **27**, 431

3. C.H.Townes (1953) J. Inst.Elec.Commun.Eng.(Japan), **36**, 650

4. J.P.Gordon, H.J.Zeiger, and C.H.Townes (1954) Phys.Rev. **95**, 282

5. N.G.Basov and A.M.Prokhorov (1955) JETP (Russian), **28**, 249

6. N.Bloembergen (1956) Phys.Rev. **104**, 324

7. H.E.Scoril, G.Feher, and Seidel (1957) "Operation of a solid-state maser" Phys.Rev. **105**, 762

8. G.M.Zverev, L.S.Kornienko, A.A.Manenkov, and A.M.Prokhorov (1958) JETP (Russian) **34**, 1660

9. A.A.Manenkov and V.B.Shteinshleiger (1977) Quantum amplifiers and their application, in radio reception systems of far-space communication and radioastronomy, in 1977 Annual of Comprehensive Soviet Encyclopedia (Russian), Moscow, A.M.Prokhorov (Editor), number 21, pp. 566-569

10. A proposal of ruby as a suitable maser material was made by A.A.Manenkov and A.M.Prokhorov at the end of 1956 when a research program on "Paramagnetic Masers" started at Lebedev Physical Institute, USSR Academy of Sciences jointly with Lomonosov Moscow State University (see A.M.Prokhorov, A.A.Manenkov, G.M.Zverev, and L.S.Kornienko (1958) Research Report to USSR Academy of Sciences on Paramagnetic Amplifiers at 15 cm and 21 cm wavelengths (Project Code "Rezeda"), Lebedev Physical Institute, Moscow.

11. A.A.Manenkov (1955) "Paramagnetic Resonance in Some Compounds of Iron and Rare Earth Elements" (Russian), PhD Dissertation (Degree of Candidate of Sciences), A.M.Prokhorov - Research Supervisor, Lebedev Physical Institute of USSR Academy of Sciences, Moscow.

12. A.A.Manenkov and A.M.Prokhorov (1955) Fine Structure of Paramagnetic Resonance Spectrum of $Cr^{3+}9$ Ion in Chromium Corundum, JETP, **28**, 762 (Russian)

13. S.Sugano and I.Tanabe (1958) J.Phys. Soc. Japan, **13**, 880.

14. A.A.Manenkov, A.A.Popova, and V.Ya.Khaimov-Mal'kov (1963) Investigation of crystalline field inhomogeneity in ruby, FTT (Solid State Phys.) (Russian) **5**, 1643.

15. A.A.Manenkov and A.M.Prokhorov (1958) Analysis of Optical pumping of ruby maser. Unpublished.

16. A.M.Prokhorov (1958) JETP (Russian) **34**, 1658.

17. S.Anikichev (1995) Laser Resonator Concepts, NATO ASI Proceedings, this Volume.

18. R.W.Hellwarth (1961) Control of fluorescent pulsations, in Advances in Quantum Electronics, R.Singer, Ed., New York: Columbia University Press, pp. 334-341. F.J.McClung and, R.W.Hellwarth (1961) Bull.Amer.Phys.Soc. **6**, 414, (1962); -- Giant optical pulsations from ruby, J. Appl. Phys. **33**, p.828-829.

19. A.M.Prokhorov (1963) Operation of quantum optical oscillator at instantaneous Q-switching on, Radiotechnika i Electronica (Russian), **8**, p.1073.

20. A.A.Manenkov and V.S.Nechitailo (1992) Polymer Laser Optics, Izvestia Acad.Nauk, seria fizicheskaia, **56**, N.8.

21. N.N.Il'ichev et al (1991) Kvant.Electron. (Russian) **18**, N 4, p.433-436.

22. S.V.Garnov, A.S.Epifanov, S.M.Klimentov, A.A.Manenkov, M.Yu.Nikol'sky, I.A.Shcherbanov (1991)"Generation of short nanosecond pulses in YAG:Nd laser with GSGG:Cr, Nd Q-switch, Kvant. Electron. (Russian), **19**, 653.

23. Yu.Lybarsky and V.Ovchinnikiv (1975) Solid-State Laser Technology, A.M.Prokhorov, Ed., MIR Publishers, Moscow (English translation).

24. G.B. Al'tshuler, V.S.Ermolayev, and K.I.Krylov (1984) Nonlinear light scattering effects in inhomogeneous media and their possible applications in lasers, Izvestia Acad. Nauk SSSR, seria fizich. (Russian), **18**, 1534-1544.

25. H.W.Mocker, R.J.Collins (1965) Appl.Phys.Lett., **7**, 270.

26. A.J.De Maria, D.A.Stetser, and H.Heynan (1966) J.Appl. Phys.Lett., **8**, 174.

27. See, for example, D.I.Bredley (1977) Generation Technique,in Ultrashort Light Pulses, S.L.Shapiro, Ed., Springer-Verlag, Berlin, Heidelberg, New York.

28. A.A.Manenkov (1966) Ruby Lasers, in A.M.Prokhorov (supervisor) and A.A.Manenkov (assistant supervisor) Investigation of Ways to Increase Efficiency of Solid-State Lasers, Report to the USSR Academy of Sciences on a First Stage of Research Project (Code "Landysh"), Lebedev Physical Institute, Academy of Sciences of the USSR, Moscow.

29. J.E.Swain, R.E.Kidder, K.Pettipiece, F.Rainer, E.D.Baird and B.Loth (1969) Large-Aperture Glass Disk Laser System, J.Appl. Phys. **40**, N 60, 3943.

30. J.M.Mc Mahon, J.L.Emmett, J.F.Holzrichter, and J.B.Trenholm (1973) A Glass-Disk-Laser Amplifier, IEEE J.Quant.Electr., **QE-9**, N 10, 992.

31. J.C.Almasi, J.P.Chernoch, K.F.Tittel, and K.Tomiyasu (1965) Faced Pumped Laser, Semi-Annual Tech.Summary Report for Office of Naval Research, Washington, DC (Note: A copy of this report became available to us recently from Dr.Richard Solarz of LLNL, Livermore, whose efforts are acknowledged).

32. J.C.Almasi, I.P.Chernoch, W.S.Martin, and K.Tomiyasu (1966) Face Pumped Laser, G.E.Report to the Office of Navel Research, May 1966 (Note: this reference is reproduced from [30]).

33. D.Strickland and G.Mouron (1985) Opt.Commun. **56**, 219-221. P.Maine, D.Strickland, P.Bodo, M.Passot, and G.Mourou (1988) IEEE J.Quant.Electr., **24**, 398-403.

34. M.D.Perry and G.Mourou (1994) Terawatt to Petawatt Subpicosecond Lasers, Science, **264**, 919-924.

35. D.E.Spence, P.N.Kean, and W.Silbett (1991) 60-fs pulse generation from a self-mode-locking Ti:sapphire laser, Opt. Lett.**16**, N 1, 42.

36. A.A.Kaminskii (1990) Laser Crystals, Their Physics and Properties, Shpringer-Verlag, Berlin, Heidenberg, New York, London, Paris, Tokio, Hong Kong: Second Edition.

37. A.A.Kominskii (1996) Crystalline Lasers: Physical Processes and Operating Schemes, CRC Press, Boca Raton, Ann Arbor, Boston (in press).

38. K.M.Dyumaev, A,A.Manenkov, A.P.Maslyukov, G.A.Matyushin, V.S.Nechitailo, and A.M.Prokhorov (1991) Interaction of laser radiation with optical

polymers, A.M.Prokhorov (Chef-Editor), A.A.Manenkov (Editor), Proceedings of General Physics Institute of USSR Acad.Sci., vol.33, "Nauka", Moscow (Russian).

39. Advanced Solid-State Lasers (1989-1995) OSA Proceedings, vol.5-24, Optical Society of America, Washington, DC

40. Laser Induced Damage in Optical Materials: 25-Year Index, 1969-1993, Arthur H. Guenther (Ed.) (1994) SPIE vol.2162, Bellingham, Washington.

41. J.L.Emmett, W.F.Krupke, and J.I.Davis (1984) Laser R&D at the Lawrence Livermore National Laboratory for Fusion and Isotop Separation Applications, IEEE J.Quant.Electr. QE-20, N 6, pp.591-602.

42. Inertial Confinement Fusion(1994) The ICF Quartely Report, v.5, N 1, J.Campbell (Scientific Editor) LLNL, Livermore, California.

43. The "Delfin" Laser Thermonuclear Instellation: Operation Complex and Future Directions (1988) Proceedings of the Lebedev Physical Institute of the USSR Acad.Sci., N.G.Basov (Series Editor),vol.178, edited by G.V.Sklizkov, Nova Science Publishers, Commack, USA.

44. V.V.Korobkin, V.M.Ovchinnikov, P.P.Pashinin, Yu.A.Pirogov, A.M.Prokhorov, and R.V.Serov (1976) The UMI-35 Laser Installation for Investigations in a Field of Thermonuclear Fusion, V111 All-Union Conference on Coherent and Nonlinear Optics, Summaries Digest, vol. 2, p.235, Tbilisi, USSR.

45. V.A.Batanov, V.A.Bogatyrev, I.A.Bufetov, S.B.Gusev, B.V.Erschov, P.I.Kolesnichenko, A.N.Malkov, A.M.Prokhorov, V.A. Spiridonov, V.B.Fedorov, V.K.Fomin (1978) Generation of high power giant laser pulses in multichanel installation "Micron" with application of large-size neodymium glass slabs, Izvestia Acad.Nauk, ser. fiz., 42, N 12, pp. 2504-2506 (Russian).

46. V.N.Alekseyev et al (1984) The 6-Channel Phosphate Neodymium Glass Laser Installation, Izvestia Akad. Nauk, ser.fiz.,v.48, N 8, pp. 1477-1484 (Russian).

47. A.A.Manenkov and A.M.Prokhorov (1986) Laser Induced Damage in Transparent Solids, Sov.Phys.Usp. 29, 104-122.

48. A.A.Manenkov (1988) Fundamental Mechanisms of Laser Induced Damage in Transparent Solids: up-to-dare status of research and understanding, Proceedings of Boulder Damage Symposium, H.E.Bennett, A.H.Guenther, D.Milam, B.E.Newnam, M.J.Soilean (Editors),NIST Spec.publ.775, pp. 486-501, Boulder, Colorado.

49. S.C.Jones, P.Braunlich, R.T.Caspar, X.-A.Shen, and P.Kelly (1989) Recent progress on laser-induced Modification and Intrinsic bulk damage of wide-gap optical materials, Opt. Eng. 28, 1039.

50. M.F.Koldunov, A.A.Manenkov, and I.L.Pokotilo (1990) Thermal explosion of absorbing inclusions as laser induced damage mechanism of dielectric surface, Kvant. Electronika, 17, 523-527 (Russian).

51. M.F.Koldunov, A.A.Manenkov, and I.L.Pokotilo (1988) Theoretical analysis of thermal explosion and photoionization instability of transparent dielectrics containing absorbing inclusions, Kvantovaja Electronika, 15, 554 (Russian).

52. A.S.Epifanov, A.A.Manenkov and A.M.Prokhorov (1976) Theory of avalanche ionization in transparent dielectrics under action of electromagnetic filed. JETF, 70, 728 (Russia).A.S.Epifanov, A.A.Manenkov and A.M.Prokorov (1978) Theory of

avalanche ionization in solids under action of electromagnetic field. Proceedings of FIAN, vol. **101**, 87-129, "Nauka", Moscow (Russian)

53. B.G.Gorshkov, A.S.Epifanov, and A.A.Manenkov (1979) Avalanche ionization in solids at large radiation quanta and relative role of multiphoton ionization in laser damage. JETF, vol. **76**, 617-629 (Russian).

54. M.F.Kuldunov, A.A.Manenkov and I.L.Pokotilo (1993) Theory of laser induced damage to optical coatings: inclusion-. ionization thermal explosion mechanism. in Laser induced damage in optical materials: SPIE Vol. **2114**, p. 469.

55. M.F.Koldunov, A.A.Manenkov and I.L.Pokotilo (1959) Pulsewidth and pulseshape dependence of laser induced damage threshold to transparent optical materials. Izvestia Acad. Nauk, ser. fiz. (Russian) (in press)

56. C.D.Orth, S.A.Payne, and W.F.Krupke. A Diode Pumped Solid-State Laser Driver For Inertial Fusion Energy (1994) Reprint (submitted to Nuclear Fusion) Lawrence Livermore Nat. Lab., Livermore, California.

57. B.H.Chai, J.Lefancher, X.X.Zhang, P.Hong, M.Bass, I.A.Scherbakov, and A.I.Zagumennyi (1994) Comparison of Laser Performance of Nd-doped YV_4, $GdVO_4$,$Ca_5(PO_4)_3F$, Sr_5PO_4F and $Sr_5(VO_4)_3F$ OSA Proceeding on Advanced Solid State Lasers, vol.**20**, p.41-51.

INDUSTRIAL FAST -AXIAL FLOW CARBON DIOXIDE LASERS IN RUSSIA.

V.V. DEMBOVETSKY , YU.N. ZAVALOV
Russian Academy of Sciences,
Scientific Research Center for Industrial Lasers
Shatura, Moscow Region, 140700 Russia,
Tel/Fax +07-(095)-135-54-30

Abstracts

The paper introduces to some problem of elaboration of fast-axial flow CO_2 lasers in Russia. The pilot model of FAF CO_2 laser TLA-600 with output power of above 600 Wt and electrooptical efficiency near 20% was designed. Specific operation modes of the FAF CO_2 laser were under investigation, included passive Q- switched mode.

. The model of stationary lasing for this type of laser was worked out. Based on well known active-medium kinetics, the model takes into account nonuniformity of saturation degree of active medium caused by both nonuniform pumping and inhomogeneities of active medium filling by resonant radiation and includes the phenomenon of transverse turbulent fluxes under conditions stated previously.

Data, calculated from kinetic model, are in accordance with experimental data, which were obtained on our setup and were processed with the procedures discussed in paper, in wide area of TLA-600 operations parameters.

1. Introduction

Industrial CO_2 lasers with fast-axial flow are known well. Their putting on the market is accompanied by corresponding commercial success in many countries. Storm growth of that market is a peculiarity of last years of 80s [1].

First fast-axial-flow (FAF) CO_2 laser was worked out in Russia at the end of 70s [2]. That was 1 kWt output power laser with DC sustained discharge pumping. A turbo blower was used in laser as tool that forced gas into discharge

R. Kossowsky et al. (eds.), High Power Lasers – Science and Engineering, 603–618.
© 1996 *Kluwer Academic Publishers. Printed in the Netherlands.*

tubes upto velocity of 100m/sec. Under that design conditions the optical resonator had Fresnel' number above eight. The elaboration of FAF CO_2 laser with gaussian transverse mode was begun in Russia only in the late 80s [3]. In particular, the Scientific Research Center for Industrial Lasers began R&D activities in this line of inquiry from study as well DC longitudinal discharge as RF (13.56 MHz) transverse discharge. After some experimental efforts, when stable discharge was realized with specific volume power over 10 Wt/cm^3 both to one above and to other, the DC discharge laser was chosen for practice realization. In last case, when gas discharge is stabilized by output resistance of the vacuum lamp individually for each gas discharge tube, the industrial tool contrasts with simple service, high level reliability and rich multitude of working mode: cw, high repeatition rate mode, superpulsing, combined pulsing.

2. Setup

Nowadays representative laser TLA-600, first of presumed series of lasers with correspond output power 600, 1200, 1800 Wt, has been designed. Root's pump with volume capacity near 190 l/sec is used for TLA-600, that determinates output power level. Three generation blocks were work out with different mode structure of radiation. FAF CO_2 laser have a distinctive feature to use directly the module conception. We use this conception both for design lasers with different output radiation paramaters and for design of some laser's assemblies. Yet some experimental activities are necessary to work out gas discharge tubes and optical resonator.In our experiments different types of axial or lateral injection were used, when gas flow was turbulized by various means.

Output cw power as a function of GDT current for two design versions of resonator block presents on Fig.1 and Fig.2 corresponding. Gaussian mode output power is up to 650 Wt, but for predominantly TEM^*_{01} mode maximum output power is 750 Wt with 18% efficiency (for 600 Wt output power efficiency is up to 22%) with 60 l*atm/hour gas mixture consumption . (Industrial purity gases were used.) Temporary stability was measured, and results are presented in Table. 1

TABLE 1.

Gas filling rate	l*atm/hour	50	85	140
Output power level	Watt	468	507	522
Long-term root-mean-square deviation, Δ_L	Watt	6	5.2	3.6
	%	0.64	0.51	0.35
Short-term root-mean-square deviation, Δ_S	Watt	10	7	2.6
	%	1.07	0.69	0.25

Enhanced pulse mode was realized. Peak power exceeding amounted to 8 times of average output in the range of frequencies 800...2200 Hz, when input

power exceeds as factor 5 over average input power. The pulse energy exceeds 300 mJ in frequency range up to 2500 Hz for 0.25msec pulse duration of load power [4].

We had studied different HRP mode technique [5]. In particular passive Q-switched technique was realized in 10 kHz frequency range. Combined this technique and current modulation, the HRP mode was received. Peak power exceeded over average more than 20-50 times when pulse repetition frequency is of some kHz order of magnitude.

Devoting enhanced attention to laser HRP mode, we had took into account non-traditional sphere of application, for example, in selective laser molecular technology, or as lidar source or as for some material processing.

3. Experimental Results

Transverse distribution of output radiation was measured by laser beam analyzer LBA-2/A (Germany) that was set on distance 12m from laser. One of results examplifies at Fig.3 for the version of 4-folded optical resonator (total length 5.25 m) with iris of about 17 mm. Quoted measurements show insignificant dependence of deviation from gaussian function over a wide range of laser operation parameters. It is supposed below, based on our measurements, that beam transverse distribution near single gauss mode.

Output power was measured as a function on number of simultaneously connected GDTs and as a function on reflective index of output mirror verified beam transverse structure for some values of discharge parameters: gas mixture pressure and GDT's current. Static pressure was measured downstream from GDT's orifice plate. Parameters of used mirrors are presented in Table. 2.

Experimental data are presented on Fig. 4 for GDT's current about 48 mA, and on Fig. 5 for GDT's current about 36 mA as GDT number's function on internal power near output mirror defined as:

$$P_{in} = P_{out} \frac{1+\sqrt{R}}{1-\sqrt{R}} \cdot 2 \qquad (1)$$

The goal of experiments is to vary internal intensity both by altering active medium length and by change of resonator Q -factor so fluid characteristics (pressure, current, gas components' ratio, flow parameters) are unaltered as possible due to presented procedure. Structure of beam distribution is thought to unaffected under power level alterations. Variation of fluid parameters, listed above, and variation of GDT's dimensions are assumed to be negligible.

As resonator losses were varied, so in-resonator losses and both small signal (below -SS) gain and saturation intensity might be defined. These parameters were determined from experimental data (Fig.4,5). The procedure of data treatment is explained from Fig.6. All data for current I=const, pressure p=const were extrapolated along line: R=const, when discharge length is varied to threshold. At Fig.6a there are threshold length (L_{thres}) functions on radiation losses defined from extrapolated data for current 48 mA in assumption of next [6]:

$$g_0^{exp}(p) \cdot L_{thres}^{exp}(p) = \Lambda - \ln(R)/2,$$

where -ln(*R*)/2 is the output lasing losses [6], Λ -intracavity losses. Fig.6b is the same, but for current 36 mA. The estimation of diffractive losses obtained does not far from Fahlen' results [7]. Average SS gain dependence represents at Fig.7 as pressure function.

Equivalent saturation intensity was defined in two-level approaching of GDT active medium by L-slope of function P^{in}(I,p,L,R) for I=const, p=const, R=const:

$$P^{in}(L,R) = J_S^{exp} \frac{\pi w^2}{2} \left(\frac{g_0^{exp} L}{\Lambda - 0.5 \cdot \ln(R)} - 1 \right),$$

where *w* is spot size of gauss beam. Equivalent saturation intensity is shown at Fig.8.

This technique is similar [8], but we approached data to threshold for gain determination that more reliable. Moreover we varied as output mirrors as GDT numbers so the task of SS gain and saturation intensity separation from experimental data set is desided more exactly.

TABLE 2.

Mirror	**indoor curvature R_1,m**	**Reflect. index R, %**	**outdoor curvature R_2,,m**	**Absorption %/cm**
blind (Cu)	+30 m	99	--	---
A (ZnSe)	27 m	73	16 m	< 0.08
B (ZnSe)	27 m	69	16 m	< 0.08
C (ZnSe)	25 m	55	>60 m	< 0.08
D (ZnSe)	24 m	45	16 m	< 0.08

4. Theoretical Background

4.1. Active Medium Kinetics

The case of one-dimension flow in isobaric approach was considered with homogeneous filling by resonance radiation. Discharge was taken into account to occupy only upstream region of GDT. Downstream there is a area where gas relaxes under radiation presence. It was taken into account also that the cross section of the relaxation region is more large than discharge cross section. The set of linearized differential equations of kinetics of the CO_2 laser active medium under 4 temperature approach was carried out for case stated above[9-12].

The gain, averaged along GDT's length, was calculated as resonant radiation function in urgent range of pressure and GDT's current under that conditions. CO_2:N_2:He mixture ratio is certain the same from experiments. Sample of gain distribution along GDT length represents at Fig.9a, but at Fig.9b some calculation result examplifies. As it follows from Fig.9b equivalent saturation parameter might be defined.

Calculation results are presented at Fig.10 as lines. These results are in accordance with experimental data of [13,14], where active medium of the FAF amplifier was under investigations.

4.2. Diffusive processes

As orifice turbulizer was used in our experiments, so there is a movement, either whirlwind or screw movement, but there is rotational movement in transverse direction from periphery region, where there is no radiation, into central area, where inverse media is too saturated by resonance radiation, and there is one back. We considered this phenomenon as turbulent diffusion [15] so diffuse equation was written:

$$\tau_2 \upsilon \frac{\partial \alpha}{\partial z} - \tau_2 D_\perp \Delta_\perp \alpha + \alpha\left(1 + \frac{J(r)}{J_s}\right) = \begin{cases} \eta_q \eta_d W / J_s, & z \in [0,\ \ell_d] \\ 0, & z \in [\ell_d, \ell_t] \end{cases}, \quad (2)$$

where $\alpha=\alpha(z,r)$ is SS gain, τ_2 is the efficient time of nonradiative relaxation of the upper laser level, υ is the gas flow velocity along the laser beam axis z, $D_\perp$ -is the turbulent diffusion index, $J_S=h\nu/\sigma\tau_2$- is the saturation intensity, σ -is the cross-section of light-induced transition, W -is the specific discharge power, η_d -is the efficiency of CO_2 molecules excitation to the

upper laser level, η_q -is the quantum efficiency, l_d -is the discharge area length, l_t is the tube length.

This equation was calculated for some laser parameters after averaging along axes z (gas flow direction), and results are presented in [15]. Physical understanding might exhibited after deciding (2) under some assumption for case of homogeneous filling by radiation only central part of gas tube. So there is a solution for gain parameter averaged along z:

$$\bar{\alpha} = \bar{\alpha}_0 \cdot \left(1 + \frac{J}{J_S \cdot (1 + \sqrt{\tau_2 / \tau_D})} \right)^{-1} \qquad (3), \text{ where } \tau_D = \frac{w^2}{D_\perp} \text{ is}$$

a time of active- particles removal from the area filled with radiation.

It should be noted that equation (3) does not include the explicit dependence upon the transit time of gas convective removal. That's, if the influence of convective gas removal upon the gas discharge stability is not considered, then the role of gas pumping in FAF lasers reduces to heat removal. Thus that distinguishes this laser type from transverse gas- flow laser where the convective transfer of excited particles into the radiation filled area dominates over the diffusive one [16].

To determine turbulent diffusion index, we refer to results of papers [17-18] as applied to conditions of our fast-axial-flow realization. In the case when a turbulizer in form of 12mm diameter hole is set into GDT (that is possible by off-axis gas injection), then the relationship is valid: $D_\perp / v = 0.025$, where $[D_\perp]$= cm^2/sec, $[v]$= cm/sec [17]. So for $v = 10^4$ cm/sec, $D \approx D_\perp$ =250 cm^2/sec.

So equivalent saturation intensity has increased as factor 2 due to additional channel of molecular leaving of upper lasing level in case: $\tau_D \approx \tau_2$..

5. Discussion

In order to connect calculated parameters of the active medium and lasing power level, it should to define function of saturation degree on gain-to-threshold ratio under stationary generation condition.

In case of homogeneous filling of plane resonator by active medium in pressure range, listed above, there is the following:

$$\frac{J}{J_s} = \frac{\alpha_0}{\alpha_{thres}} - 1, \qquad (4),$$

where α_0 is the SS gain included broaden line factor; α_{thres} is the threshold gain; J is the internal intensity.

It is easy to demonstrate for that case [19]:

$$\frac{\langle J^+ + J^- \rangle_{max}}{\langle J^+ + J^- \rangle_{min}} = \frac{1+R}{2\sqrt{R}} \qquad (5)$$

Therefore it is assumed in this paper that: $\langle J^+ + J^- \rangle \approx 2 * J = const(z)$

Casperson had considered case of nonuniform saturation of homogeneous active medium under lasing of transverse gauss mode [19]. In this case lasing condition differs from (4):

$$\frac{4J / J_s}{ln(1 + 4J / J_s)} = \alpha_0 / \alpha_{thres} \qquad (6)$$

Similar deduction concluded after Witteman's work [20], where peculiarities of gauss-beam amplification in lenselike medium of gas discharge laser had been considered. So there is an equation for case of gauss beam with axes intensity J_0 that lased through output mirror (reflective index R) of optical cavity, filled by lenselike active medium with axes SS gain α_0 and saturation intensity J_S in approach of paraxial beams:

$$\frac{\alpha_0 \cdot L}{1+2 \cdot J_0/J_S} \cdot \left(1 - 0.72 \cdot \left(\frac{\omega}{R_{tube}}\right)^2 + \frac{2 \cdot J_0/J_S}{1+2 \cdot J_0/J_S}\right) = \Lambda + \ln\frac{1}{\sqrt{R}}, \qquad (7)$$

Let us use procedure after [19] under lasing condition with active medium nonuniformity too so transverse distribution of average along flow SS gain is:

$$\alpha_0(r) \cong q_0 + q_2 r^2 + q_4 r^4, \ if\ r<R, \quad or: \alpha_0(r) \equiv 0, \ if\ r \geq R, \qquad (8)$$

and follow assumptions are:

-optical axes coincides with GDT axes in axes -symmetrical case;

-influence of biquadratic term on gauss beam structure is negligible: $q_2 > q_4 R^2$;

-for gaussian mode: $J(r,z)=P(z)f(r)$, where $P(z)$ -internal power and:

$$f(r)=2\exp(-2r^2/\omega^2)/(\pi\omega^2) \qquad (9).$$

Then we took (8-9) into account under stationary lasing condition when mode volume gain compensates all -resonant losses and output lasing losses. So there is a next equation:

$$q_0 L\frac{P_s}{2P}\left[ln\left(1+\frac{2P}{P_s}\right)-\frac{\gamma}{4}\frac{\omega^2}{2}\int_0^1\frac{ln\,y\,dy}{P_s/2P+y}+\frac{\varepsilon}{48}\frac{\omega^4}{4}\int_0^1\frac{ln^2\,y\,dy}{P_s/2P+y}\right], \qquad (10)$$
$$=\Lambda+ln\frac{1}{\sqrt{R}}$$

where $P_s=\pi\omega^2 J_s/2$, and γ, ε are corresponding second derivation $q(r)$ on r or fourth one to q_0 ratios.

The function of q_0 to threshold ratio on axes saturation degree, calculated from (10), is at Fig.11 under the distribution of average SS gain of:

$$q(r)=q_0\times J_0(2.405r/R), \text{ where } R \text{ is the radius of GDT.} \qquad (11).$$

For comparision curves (4), (6) and (7) are presented too. Line, approached curve (10) near zero, has a good agreement with (7) when $J/J_S>1$.

Two functions follow from linear approximation of (10) and relate experimental g_0^{exp} and J_s^{exp} with active medium parameters: SS gain α_0 and saturation intensity J_S:

$$\begin{cases} g_0^{exp}=\alpha_0\cdot 1.33\cdot\left(1-0.72\left(w/R\right)^2\right) \\ J_S^{exp}=J_S\cdot\left(1+\sqrt{\tau_2/\tau_D}\right)\cdot 2.05 \end{cases}, \qquad (12)$$

with assumption $J_S(r)\approx const$ and (11).

Taken into account: $\tau_2\approx p^{-1}$, $\tau_D\approx const(p)$, experimental data have been processed based on (12) and have been presented at Fig. 10 as dots. Obtained data are found to coincide with computational curves.

Thus the transverse distribution of average SS gain, caused by nonuniform distribution of as discharge current as gas temperature, was taken into account to provide for real beam distribution. As for transverse nonuniformity of saturation intensity, that it is primary determined by temperature gradient. Last one is not so important in FAF laser as for diffused- cooled laser. Heat flux in last laser type is determined by temperature gradients that distinguishes from convective cooled lasers. Thus our assumption that $J_S(r)\approx const$ is not so far from actuality.

6. Conclusions

The pilot model of FAF CO_2 laser with output power of above 600Wt and electrooptical efficiency near 20% TLA-600 was designed. Specific operation modes of the FAF CO_2 laser were under investigation included passive Q-switched mode.

The technique of determing of active medium parameters is modified. The output radiation power was measured at wide region of TLA-600 operational parameters such as current and pressure and for some values of reflective index of output mirror and under variation of discharge length. The experimental data of both small signal (below -SS) gain α_0 and saturation intensity J_S were obtained in wide range of variation of gas discharge parameters.

The stationary model of FAF CO_2 laser was worked out. The model takes into account nonuniformity of saturation degree of active medium caused by both nonuniform pumping and inhomogeneities of active medium filling by resonant radiation and includes the phenomenon of transverse turbulent fluxes under conditions stated previously.

7. Acknowledgment

This work has been partially supported by the Russian Foundation for Fundamental Research (grant number 95-02-05919).

8. References

1. Laser market review, (1989) *Lasers and Optronics, Buying Guide*, **7**, N13, 164-181.
2. Aleinikov, V.S., Bibikov, V.V., Lysogorov, O.S., *et al.* (1981) Compact carbon dioxide generator based on cloced-circuit with active medium convective cooling, *Electronnaya promyshlennost,* **5(101)-6(102),** 71-75.
3. Goikhman, V.Kh., Dembovetsky, V.V., Zavalov, Yu.N., *et al.* (1988) Research and optimization of parameters of the gas- discharge- elements of CO_2 laser with fast- axial gas flow, SRC IL Preprint N 45, Shatura, Moscow Region, (in Russian).
4. Averbukh, B.B., Dembovetsky, V.V., and Zavalov, Yu.N. (1993) High-repetition-rate regimes of CO_2 laser with fast- axial gas flowing, *Izvestia AH, ser.fiz.* **57**, 112-118.
5. Dembovetsky, V.V., Zavalov, Yu.N. and Sudutovich, G.I. (1988) Hysteresis and passive Q-switching of high-gain CO_2 laser, SRC IL Preprint N 67, Shatura, Moscow Region, (in Rus./Engl.).
6. Rigrod, W.W. (1978) Homogeneously broadened cw lasers with uniform distributed loss, *IEEE J. of Quantum Electron.* **14**, 377-381.

7. Fahlen, T.S. (1973) CO_2 laser design procedure, *Applied Optics* **12**, 2381-2390.
8. Freisinger, B., Shafer, J.H., Uhlenbush, J., Zhang Z.B., (1989) Microwave Excited CO_2 Lasers, *in: SPIE Proceed. on* "High Power Lasers and Laser Machining Technology," Ed.: M.L. Gaillard, A.Quenzer, **1132**, 22-28,.
9. Beverly III, R.E. (1982) Kinetic modeling of a fast axial flow CO_2 laser, *Opt. & Quantum Electron.* **14**, 25-40.
10. Losev, S.A. (1981) *Gasdynamic Lasers,* Springer, Berlin.
11. Smith, K. and Thomson, R.M. (1978) *Computer Modeling of Gas Lasers*, Plenum, N.-York.
12. Tychinsky, V.P. (1967) High-power gas lasers, *Uspekhi Fisicheskikh Nauk* **91**, N3, 389-424(in Russian).
13. Tsuchida, E. and Sato, H. (1988) Effect of gas-flow velocity on transient behavior of gain constant in a fast -axial flow CO_2 laser amplifier, *Jap.J.of Appl.Phys.* **27**, 1445-1453.
14. Tsuchida, E. and Sato, H. (1989) Enhancement of small-signal gain and mode-volume in a FAF CO_2 laser amplifier due to cooling of wall temperature, *Jap.J.of Appl.Phys.* **28**, 1606-1614.
15. Galushkin, M.G., Golubev, V.S., Dembovetsky, V.V., *et al.* (in SPIE press) Influence of excited molecules turbulent diffusion on energy parameters of fast-axial-flow CO_2 laser radiation, Thesises of the V Intern. Conf. 'Industial Lasers & Laser Applications'95, June 24-26, Shatura, Moscow Region, 20.
16. Galushkin, M.G., Golubev, V.S., Zabelin, A.M., *et al.* (1993) Influence of excited molecules turbulent diffusion on energy performances of industrial cw CO_2 lasers, in V.Ya. Panchenko and V.S. Golubev (eds.), *Proceed. of Russ. Conf. 'Industr. Lasers and Laser Material Processing',* SPIE **2257**, 148-155.
17. Bondarenko, A.V., Golubev, V.S., *et al.* (1979) About influence of the turbulence on self-stained discharge stability in air stream, *Fizika Plazmy* **5**, 687-692(in Russian).
18. Akishev, Yu.S., Napartovitch, A.P. (1978) Influence of gasdynamic turbulence on discharge stability in gas flow, *Fizika Plazmy* **4**, 1146-1149 (in Russian).
19. Casperson , L.W. (1980) Laser power calculations: sources of error, *Applied Optics* **19**, 422-434.
20. Ernst, G.E., and Witteman, W.J. (1973) Mode structure of active resonators, *IEEE J. of Quantum Electron.* **9**, 911-918.

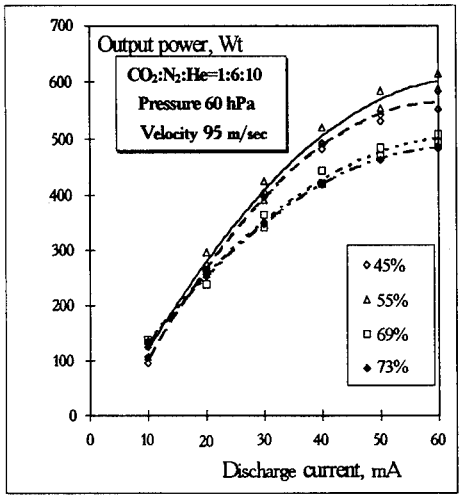


Figure 1. Output power on GDT current for some reflection index (Four-folded resonator and TEM_{00} mode).

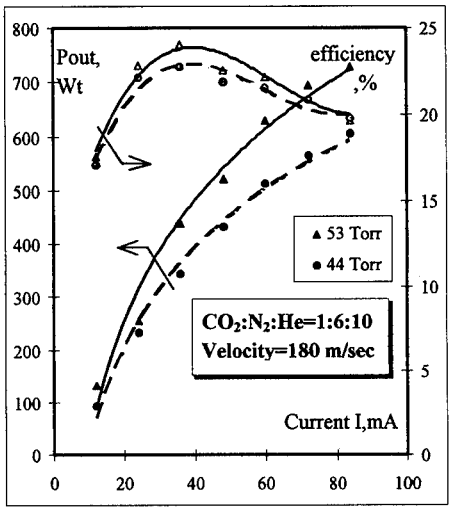
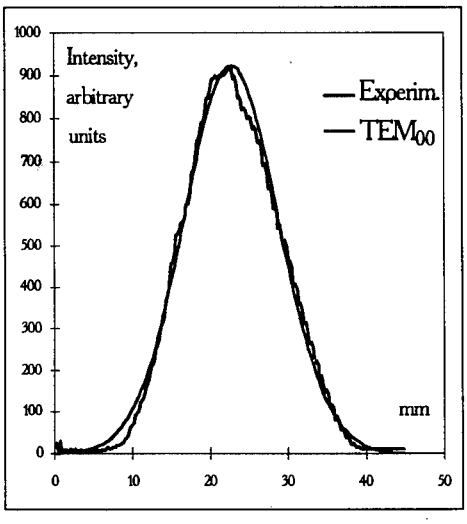


Figure 2. Output power and efficiency on GDT current for two gas pressure values (Two- folded resonator and TEM_{01}^{*} mode).



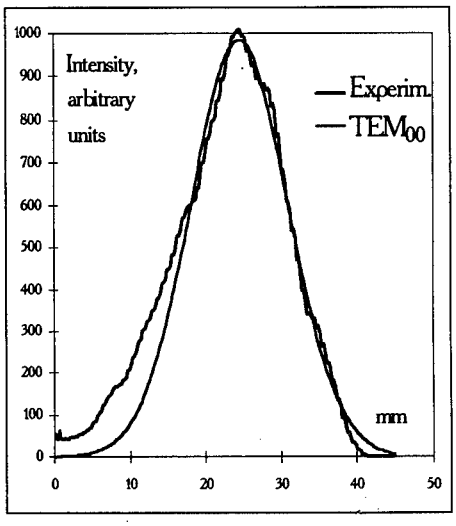


Figure 3. Output beam power distribution at two planes: horizontal(a) and vertical(b), on transverse coordinates at 12m from laser.

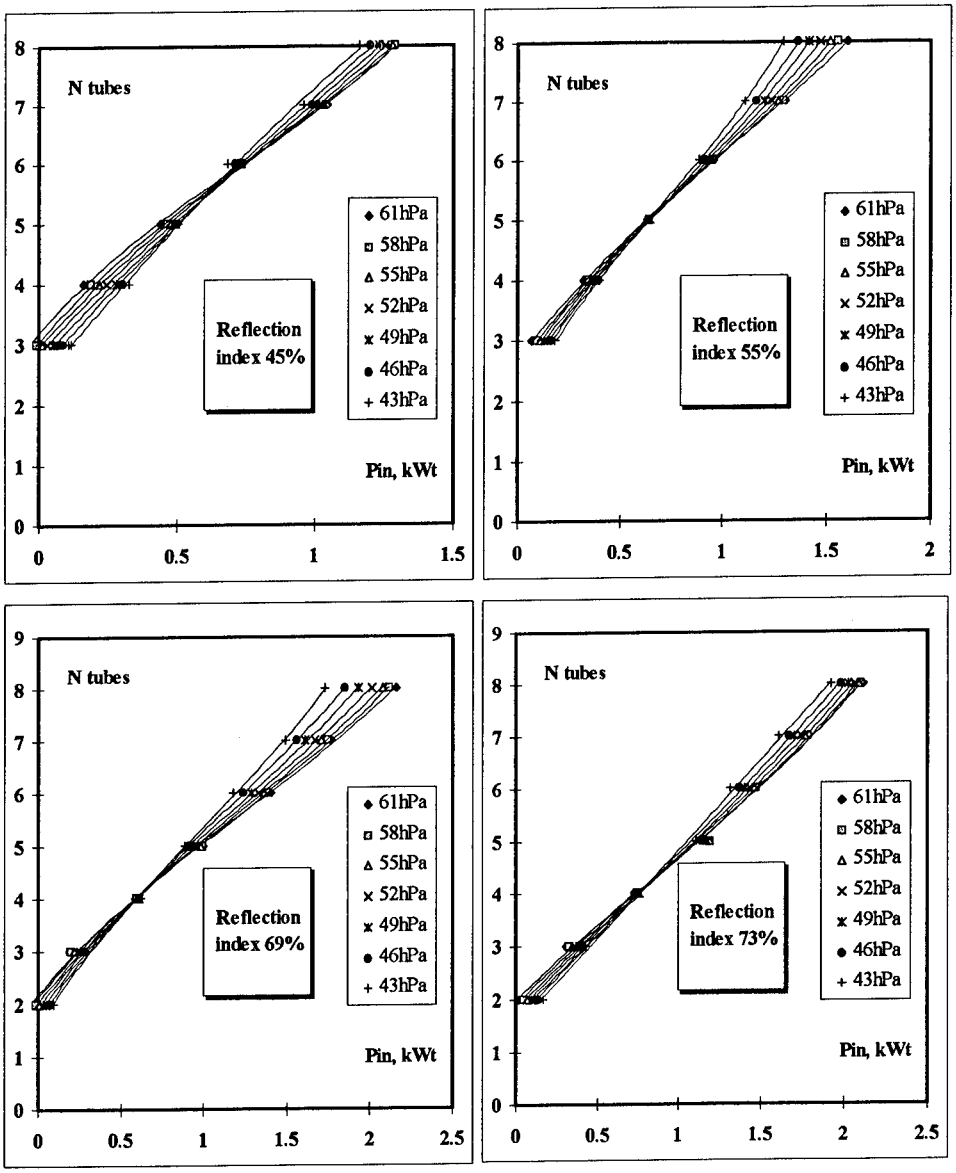


Figure 4. Number of GDT on internal power for some reflection index R and gas pressure. GDT current is 48 mA. CO_2:N_2:He= 1:6:10, upstream gas velocity 95 m/sec.

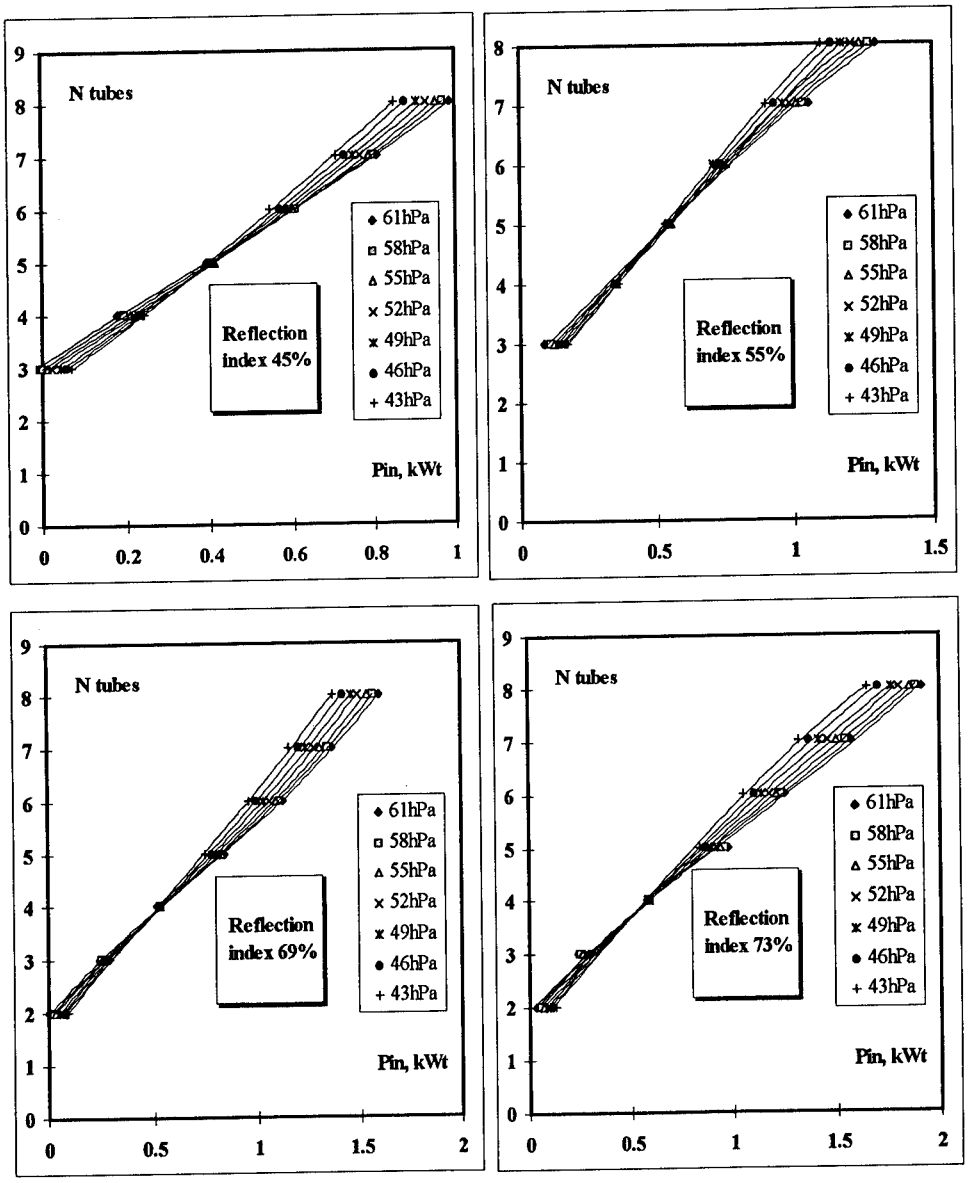


Figure 5. Number of GDT on internal power for some reflection index R and gas pressure. GDT current is 36 mA. CO_2:N_2:He= 1:6:10, upstream gas velocity 95 m/sec.

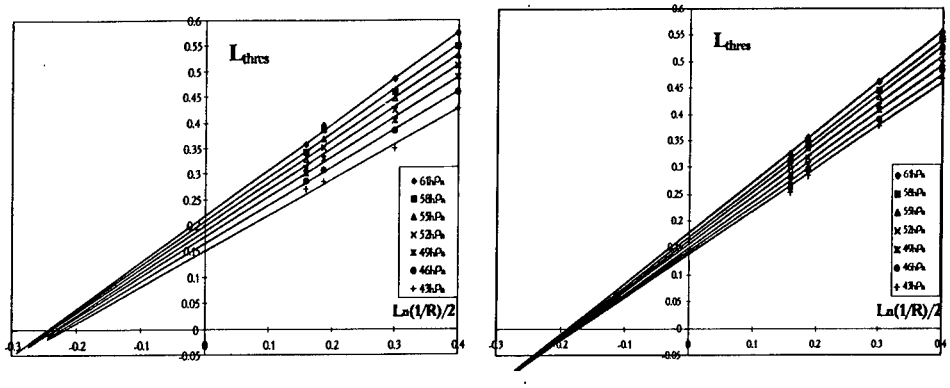


Figure 6a. Figure 6b.

Figure 6. Threshold of discharge length on radiation losses for some gas pressure values and GDT current 48 mA (a) and 36 mA (b).

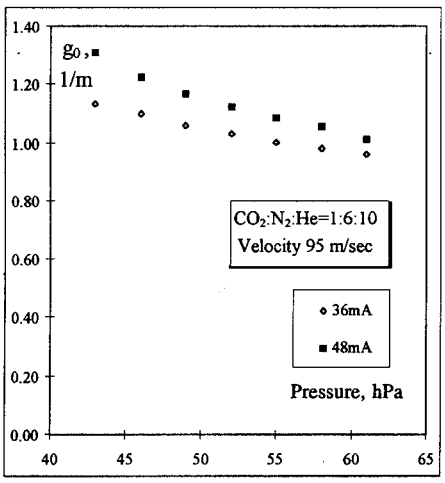


Figure 7.

Figure 7. Experimental function of average SS gain on gas pressure.

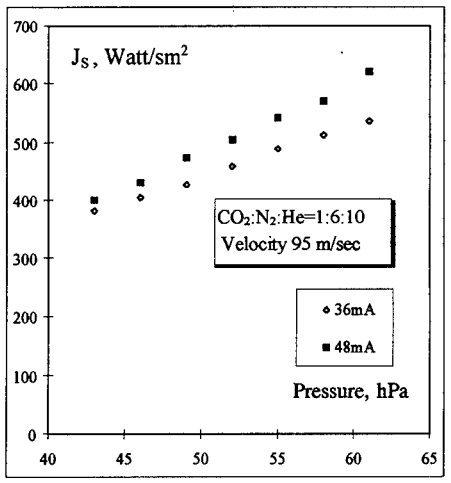


Figure 8.

Figure 8. Experimental function of equivalent saturation intensity on gas pressure.

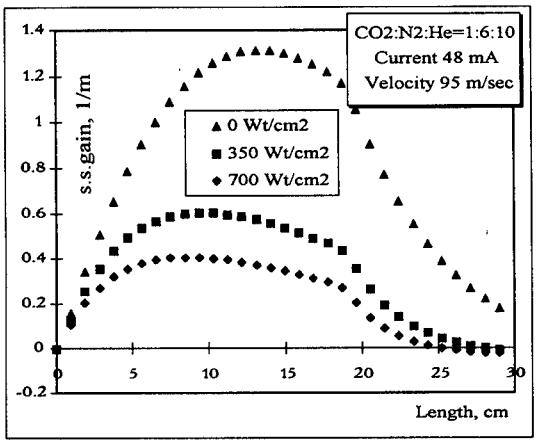


Figure 9a.

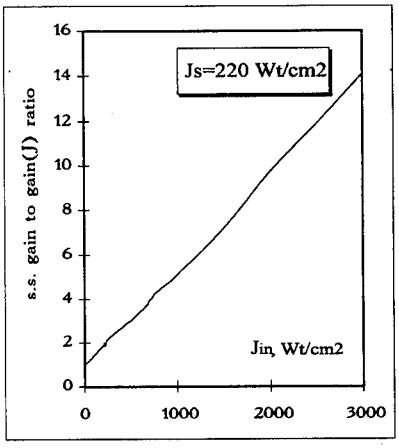


Figure 9b.

Figure 9.(a)-Calculated distribution of axial gain along gas flow for some internal radiation intensity. (b)-Ratio of SS gain to saturated gain on internal intensity (calculation for input power 10 Watt/sm^3 and gas pressure 60 hPa). As result: saturation intensity is 220 Watt/sm^2.

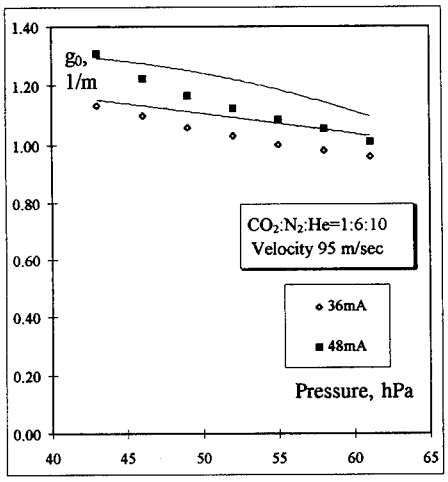


Figure 10a.

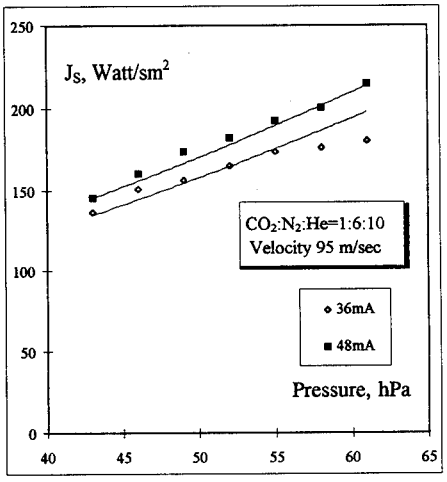


Figure 10b.

Figure 10. Calculated (lines) and experimental (dots) functions: (a)-averaged axial SS gain; (b)-saturation intensity of active medium, on gas pressure.

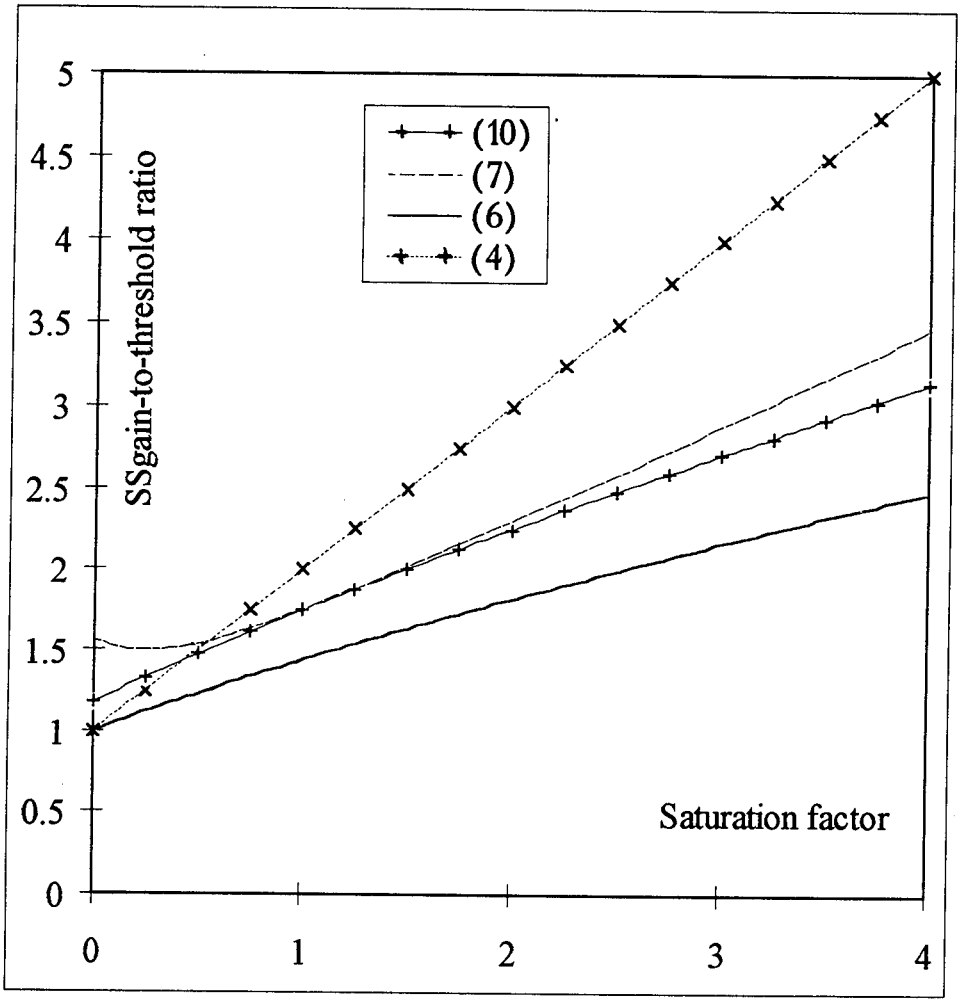


Figure 11. Ratio of axial SS gain to threshold on active medium saturation degree.

Fundamentals and Current Status of Excimer Lasers

B.LACOUR
CILAS
Route de Nozay, 91460, Marcoussis, FRANCE

Introduction

The Excimer Molecule.

The word "Excimer" has been proposed in 1960 by Houtermans [1] for diatomic homonuclear molecules having a stable bound state when one of the atoms is electronically excited. This word is a contraction of "excited dimer". Ten years later, the first experimental evidence of an excimer based laser was done by Basov [2] using an electron beam to excite liquid Xe.

1. Fundamentals

1.1. VARIOUS EXCIMERS

1.1.1 *Rare gas excimers*

In Fig. 1 are shown the typical potential energy curves of a rare gas excimer. It can easily be understood that the upper levels corresponds to a strongly bound molecule, but the lowest curve indicates that the fundamental level is repulsive. The laser transition takes place between the first excited level and the fundamental one.

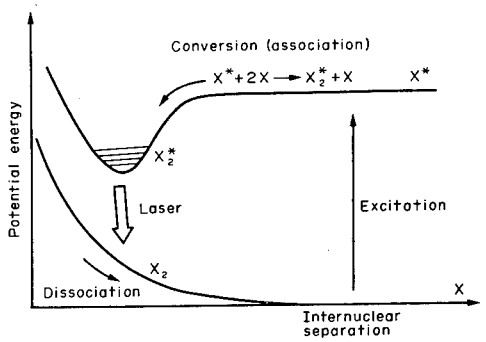


Figure 1. Basic molecular structure for excimers

R. Kossowsky et al. (eds.), High Power Lasers – Science and Engineering, 619–660.
© 1996 *Kluwer Academic Publishers. Printed in the Netherlands.*

Greats hopes were placed on this system at the beginning because of the ease to create the population inversion (the lowest, repulsive state as a very short lifetime) and of the good quantum efficiency. The reality has been found different. Figure 2 shows a more complete energy level diagram. It can be seen that absorption mechanisms exist. The most effective is ionization from the upper laser level which automatically puts a limit to the achievable population inversion. Other practical problems are the sensitivity of the gas to impurities and the exclusive E-beam pumping.

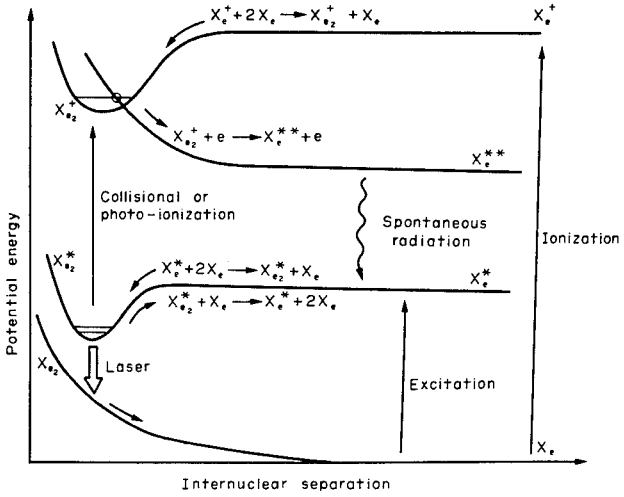


Figure 2. Energy level structure for the Xe system and important kinetic processes

1.1.2. *Rare gas halides*

In 1975 a new class of excimers was proposed [3]. If we consider an excited rare gas atom with one electron on the outer shell, it looks from the outside, like an alkaline atom. Thus it can be expected to form with a halogen atom a stable molecule similar to a rare gas excimer. This molecule was initially named exciplex, contracted form of excited complex. The word excimer is now commonly used for all types of exciplexes also. First experimental results were obtained during the same year on electron beam pumped XeBr [4], KrF, XeCl and XeF [5,6]. Discharge excitation of XeF and KrF was first demonstrated in 1976 [7,8]. Rare gas halides were found to be very efficient molecules and great efforts were done to improve the performances of the discharge excitation system with X-ray preionization [9], phototriggering [10] and/or spiker-sustainer circuits [11]. More recently R/D programs have been conducted in Europe and Japan, in order to promote the development of industrial, high average power, *discharge excited, rare gas halides lasers*. The main part of this topic will be devoted to this type of lasers.

1.1.3. *Other excimers*

Many "Excimer like" molecules have been proposed;their properties are summarized in table 1.

TABLE 1. The great excimer family

Rare gas - **Xe_2 : 172 nm**,Kr_2 : 146 nm, Ar_2 : 126 nm
Radiative lifetime : 5ns, Amplification cross section : 10^{-17} to10^{-18}cm^2
Rare gas halides- **XeF : 350nm, XeCl : 308nm**, XeBr : 282nm, **KrF : 248nm, KrCl : 222nm, ArF : 193nm.**
Radiative lifetimes : 4 to15 ns, Amplification cross section : $4x10^{-16}$ cm^2
Mercury halides - HgCl : 558nm, **HgBr : 500nm**, HgI : 444nm
Radiative lifetimes : 25ns, Amplification cross section : $3x10^{-16}$ cm^2.
R.G.H. blue green and trimers - **XeF C-->A : 485nm**, Xe_2Cl : 510nm, Kr_2F : 420nm
Radiative lifetimes : 100ns, Amplification cross section : 10^{-17} to 10^{-18}cm^2
Halogens and interhalogens - I_2 : 342nm, Br_2 : 292nm, Cl_2 : 258nm, **F_2 : 158nm**, IF : 491nm, BrF : 354nm, **ClF : 284nm**
Radiative lifetimes : 5ns, Amplification cross section :?

Mercury halides. HgBr laser emission can be obtained in the same experimental conditions than XeCl and with similar efficiency and output energy. A marked difference is the temperature of the laser head which has to be increased to 200°C to achieve a sufficiently high pressure of the $HgBr_2$ compound used in this laser. In spite of the corrosive and toxic properties of mercury compounds, mercury halides excimers are certainly the more energetic and efficient blue green gas lasers.

Great hopes were put also on the *bound to free, large bandwidth, blue green emission* of several excimers. The XeF C → A transition has been widely studied and laser emission has been obtained by electron beam pumping [12] or by photolytic dissociation of the stable compound XeF_2 [13]. Figure 3 shows the energy level diagram of XeF. Using electron beam excitation there is a strong competition between the C→ A and the high gain B→ X transitions worsened by a transient absorption at the C→ A transition wavelength. Thus the blue green laser emission appears after the electron beam pump pulse as can be seen in Fig. 3. C→ A discharge excitation has been tried with poor results.

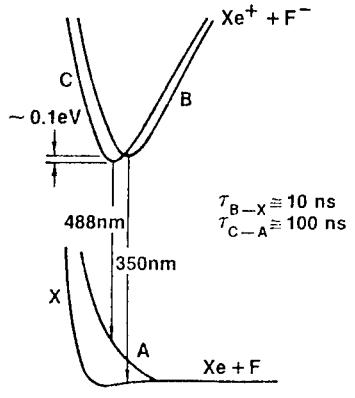


Figure 3. Schematic XeF energy level diagram

Xe_2Cl C → A was studied with the same experimental set up than XeF but gave lower results [14]. Figure 4 shows its energy level diagram as compared to XeCl.

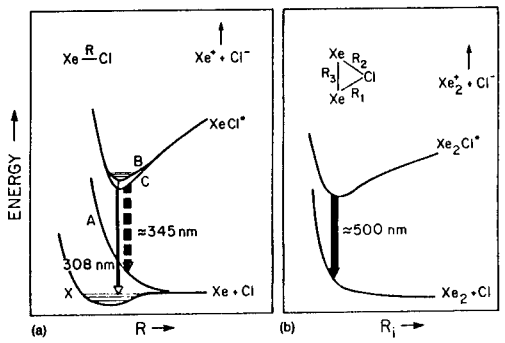


Figure 4. Simplified potential-energy diagram of the diatomic excimer XeCl and triatomic excimer Xe_2Cl

Going towards deep U.V., discharge excitation of *halogen and inter-halogen* molecules gave good results. F_2 laser emission, for instance, can be obtained from a modified excimer laser head with enhanced pumping power density. Output energy can reach 100mJ at 185nm[15].

Vacuum U.V. excimer emission can be expected from alcali-halides compounds. Table 2 summarizes their wavelength. So far, laser emission has not been obtained. Experimental conditions are however delicate, combining electron beam excitation and high temperature.

TABLE 2. Fluorescence emission wavelength of rare gas-alkaline mixture

	Li	Na	K	Rb	Cs
Xe	190 nm	182.7 nm	167.1 nm	164.1 nm	160 nm
Kr	149.5 nm	145.3 nm	135.5 nm	133.8 nm	131.6 nm
Ar	125 nm	121.3 nm	114.8 nm	114.1 nm	113.7 nm
Ne	81.2 nm	79.8 nm	77.2 nm	71.6 nm	
He	66.8 nm	65.8 nm			

1.2. PUMPING MEANS

Taking into account the short radiative lifetime of all the upper laser levels of excimers (see table 1), it is clear that they always need a high pumping power density to maintain a population inversion high enough to get a positive net gain. The typical value is 1 GW/l for XeCl but higher densities may be necessary when transient absorption and various loss mechanism become important for instance for deep U.V. or

large bandwidth lasers. Thus, the choice of the most effective pumping means is particularly important. Three systems have been widely used.

1.2.1. *Electron beam excitation*
It uses the high kinetic energy electrons produced by a pulsed, high voltage (> 100KeV) electron gun. These electrons are produced and accelerated in vacuum and have to go through a thin foil before entering the active medium. Part of the electron energy is always deposited in the foil which has also to remain tight while being chemically resistant to the gas and to withstand the pressure difference. The life time of such a foil is usually short and high repetition rate operation very difficult. Electron beam excitation allows however to pump any excimer molecule, to produce short or long pulses, and is the only pumping mean for very large gas volumes (several m^3 !).

1.2.2. *Photolytic pumping*
was first proposed for XeF. The availability of the stable fluorinated xenon compound XeF_2 which can be dissociated by U.V. light allows to produce directly the upper states of the laser transitions. By improving the incoherent U.V. sources it became possible to achieve high output energy on both transitions B → X and C → A [16]. The efficiency is however low and, due to the properties of the incoherent U.V. source used here (surface discharge), the maximum repetition rate will remain low.

1.2.3. *Discharge excitation*
Early at the beginning of rare gas halides , discharge excitation was found to be a very convenient pumping method. The first experiments used either a N_2 laser set up [7,8] or a CO_2 TEA system [17]. In fact it was found very quickly that the operating conditions for an excimer discharge, although more critical ,are somewhat similar to those encountered in a TEA laser. Most of the commercial excimer lasers use this type of excitation which is simple, reliable, efficient, not too much expensive and can be operated at high repetition rate. Due to the great possibilities of *discharge excited rare gas halides lasers*, the rest of this topic will be only concerned with them.

1.3. RARE GAS HALIDES DISCHARGE PHYSICS

The production of the upper laser level in a rare gas halide laser can be summarized by a two steps process.

-Excitation (or ionisation) of the rare gas atoms. It is the energy deposition step, and corresponds to the typical reactions (for XeCl)

$$e^- + Xe \rightarrow Xe^* + e^-, \qquad \text{or} \qquad e^- + Xe \rightarrow Xe^+ + 2e^-.$$

-Creation of the excimer molecule through a reaction between an excited or ionised rare gas atom and a halogen donor

$$Xe^* + HCl \rightarrow XeCl^* + H, \qquad \text{or} \qquad Xe^+ + Cl^- \rightarrow XeCl^*.$$

Of course the production reaction have to be faster than the loss mechanisms

(collisional quenching of the upper laser level, spontaneous or stimulated emission). The energy deposition is directly connected to the electron density and energy distribution. Hence it depends mainly on the current density and on the reduced electric field.

TABLE 3. Reactions forming excited rare gas halides [J.E. Velazco et al.: J. Chem. Phys. 65, 3468 (1976)]

Reaction	Rate [$cm^3 s^{-1}$]	Branching ratio for forming excited rare gas halide
$Xe^* + F_2 \rightarrow XeF^* + F$	7.5×10^{-10}	1.0
$Xe^* + OF_2 \rightarrow XeF^* + (?)$	5.7×10^{-10}	0.92
$Xe^* + NF_3 \rightarrow XeF^* + (?)$	9×10^{-11}	1.06
$Xe^* + NOF \rightarrow XeF^* + (?)$	3.9×10^{-10}	0.77
$Xe^* + Cl_2 \rightarrow XeCl^* + Cl$	7.2×10^{-10}	1.0
$Xe^* + HCl \rightarrow XeCl^* + H$	5.6×10^{-10}	
$Xe^* + Br_2 \rightarrow XeBr^* + Br$	6.0×10^{-10}	1[a]
$Kr^* + F_2 \rightarrow KrF^* + F$	7.2×10^{-10}	1.0
	5.2×10^{-10}[e]	
$Kr^* + OF_2 \rightarrow KrF^* + (?)$	5.3×10^{-10}	1.06
$Kr^* + NF_3 \rightarrow KrF^* + (?)$	8.9×10^{-11}	0.57
	1.1×10^{-10}[f]	
$Kr^* + NOF \rightarrow KrF^* + (?)$	4.7×10^{-10}	< 0.09
$Kr^* + Cl_2 \rightarrow KrCl^* + Cl$	7.3×10^{-10}	0.90
$Ar^* + F_2 \rightarrow ArF^* + F$	7.5×10^{-10}	
	9×10^{-10}	$\leqq 0.6$[e]
$Ar^* + Cl_2 \rightarrow ArCl^* + Cl$	7.1×10^{-10}	~ 0.5[b]
$Ar_2^* + F_2 \rightarrow ArF^* + Ar + F$	3×10^{-10}[c]	
	5.2×10^{-10}	< 0.3[c]
$Kr_2^* + F_2 \rightarrow KrF^* + Kr + F$	2.1×10^{-10}[d]	
	4.0×10^{-10}[e]	

[a] J. Velasco, D.W. Setser: J. Chem. Phys. **62**, 1990 (1975)
[b] L.A. Gundel et al.: J. Chem. Phys. **64**, 4390 (1976)
[c] H.H. Nakano et al.: SRI Rpt. MP 76-99, Stanford Res. Inst. Menlo Park, Calif. (1976) (unpublished)
[d] G.P. Quigley, W.M. Hughes: Appl. Phys. Lett. **32**, 649 (1978)
[e] C.-H. Chen, M.G. Payne, J.P. Judish: Private communication
[f] M.J. Shaw, J.D.C. Jones: Appl. Phys. **14**, 393 (1977)

The second reactions set has happily a very good branching ratio as can be seen in Table 3 [18] for several rare gases and halogen donors. By adjusting the gas mixture it is possible to set this second process as fast as the first one.

In conclusion, it is necessary, for optimum laser efficiency, to create *a Homogeneous Discharge with enough input Power Density.*

1.4. ENOUGH POWER DENSITY

1.4.1. *The Townsend model*

The mechanism of grow of a discharge in a gas has been described long time ago by

Townsend [19]. When a free electron appears in a gas (or a gas mixture) subjected to an electric field, it is accelerated towards the anode and undergoes elastic and inelastic collisions with gas molecules . If it can have a sufficiently high energy, it will be able to ionise a molecule thus releasing a new free electron. Townsend defined α as the number of electrons produced by each electron for a length unit (Fig. 5). Thus the number of electrons created will be $e^{\alpha d}$ at the distance d of the first electron location. Simultaneously, $e^{\alpha d}$ positive ions are created which are accelerated towards the cathode. Each ion can create on the cathode, through secondary emission, γ electrons. Thus the condition to make the electron number to increase with time and to create a continuous discharge is

$$\gamma(e^{\alpha d}-1)>1, \qquad (1)$$

where d is now the distance between the electrodes.

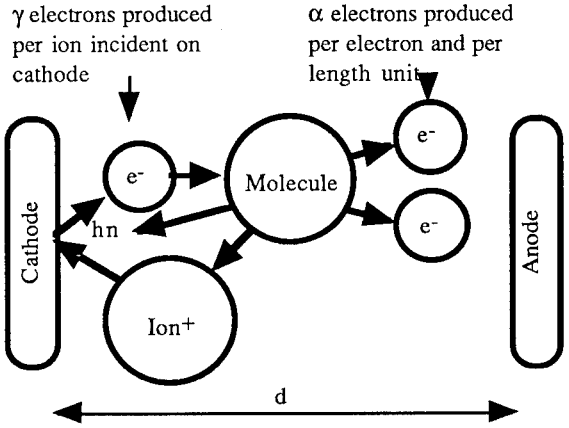


Figure 5. The Townsend model

A more complete calculation must take into account the mobility difference between ions and electrons and the electron diffusion. Practically , on the time scale of interest, ions may be supposed to stay still, and electrons to have a drift velocity Vd and a diffusion coefficient D (Fig. 6). The temporal evolution of the electronic density n_e can be written

$$\partial n_e/\partial t + \nabla (n_e.\vec{v}) = \alpha .V_d.n_e = K_T.n_e.n , \qquad (2)$$

where K_T is defined as the total ionisation rate coefficient , n is the neutral density and $\vec{v}$ is the electron velocity

$$\vec{v} = \vec{v}_d + D.\nabla n_e/n_e , \qquad (3)$$

We can then write

$$\partial n_e/\partial t = \alpha.V_d.n_e - \nabla(n_e.\vec{v}_d) - D.\nabla^2 n_e . \qquad (4)$$

In the second part of this equation, the first term corresponds to the ionization, the second one to the drift of the electrons and the third to the decrease of the electron density due to the diffusion process. This equation can be solved in a reference system

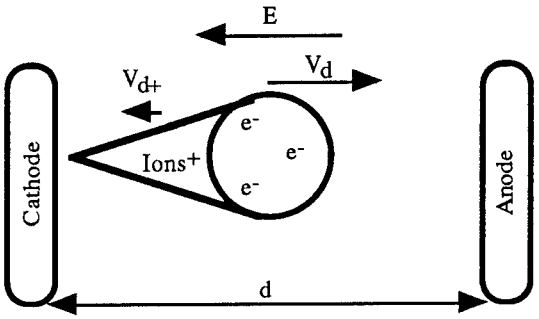


Figure 6. The Townsend model and the particule motion

moving with the electrons if Vd and D are supposed to be constant, at least for a given E/n value. One obtain

$$n_e(x,t) = n_{e0}.\exp(\alpha V_d t).\exp(-x^2/4Dt)/\sqrt{4\pi Dt}\ . \qquad (5)$$

V_d is usually supposed to be proportional to E

$$\vec{v}_d = \mu\vec{E}.$$

As can be seen in Fig. 7 for typical XeCl conditions this is an approximate assumption!

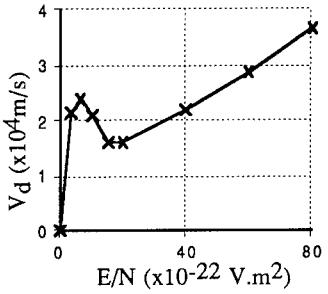


Figure 7. Electrons drift velocity as a function of the reduced electric field E/n for typical XeCl conditions

In a discharge excited rare gas halide laser, a great number of reactions are possible and seem to play an important role in the kinetics of the discharge and of the populations. Table 4 lists the reactions and reaction rates proposed by Riva [20] for a so called "simplified model". With more than 100 reactions, a physical understanding of the discharge is not straightforward. In fact numerous reactions have a negligible effect, at least during the most important phase of the discharge history i.e. *the beginning* . During this phase, the species populations are those of the initial gas mixture.Taking into account the the thresholds of all the cross-sections and the real gas composition, only a limited number of processes have to be taken into account as shown in Fig. 8.

-Momentum transfer for instance occurs only on Neon . Thus, for a given electric field, Neon pressure will determine a great part of the electron energy distribution. Increasing its pressure allows to increase the voltage across the discharge and hence the energy deposit without changing the efficiency of the excitation process.

-Because it has the lowest ionisation threshold of all the gas mixture components, Xenon will be the main supplier of free electrons, at least as long as the excited Xenon population is negligible.Then Xe* ionisation will take over(=step ionization).

-The only attaching molecule is the halogen donor, here HCl. Attachment cross-sections have a very low threshold, close to 0.1 eV for HCl and practically 0 for F_2. As a consequence, within a wide range of electron energy, attachment rate is practically constant. Concerning HCl, it has be shown that it depends strongly on the vibrational excitation of the molecule, increasing with it. Since the attachment reaction destroys the HCl molecule one would expect that this process will be less efficient at the end of the discharge if HCl burning has been significative.

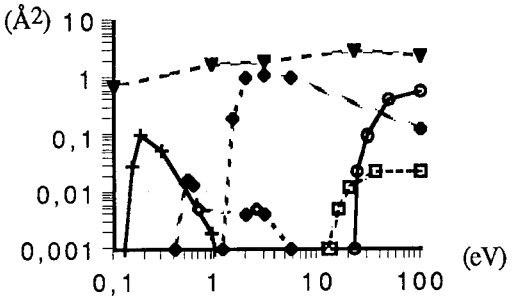


Figure 8. Electron cross-sections referred to density v.s. energy. Attachment on HCl(+), excitation of HCl vibrational states(◇), elastic collision on Ne(▼), ionisation of Xe(□), Xe*(●), Ne(○). Values calculated for a classical XeCl mixture.

The electron creation and loss rates can be easier and more practically understood by looking in Fig. 9 which shows these rates, K_i and K_a, as a function of the reduced electric field value and for the neutral gas mixture.n_e is given by the equation

$$dn_e/dt = (K_i - K_a).n.n_e \quad , \qquad (6)$$

where n is the gas density. These curves are very important to understand what happens during the beginning of the discharge (i.e. from the preionization to the voltage fall). The crossing of K_i and K_a gives the critical (or breakdown) reduced field value for the chosen gas mixture.

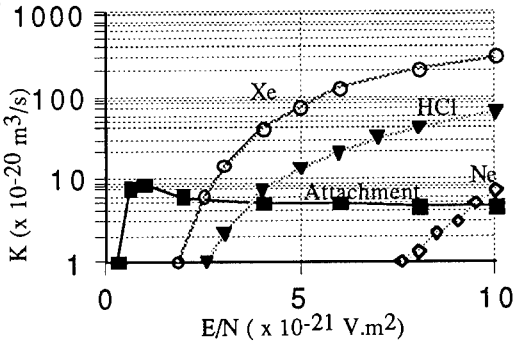


Figure 9. Reaction rates K_a (HCl),Ki (Xe, HCl, Ne) as a function of reduced electric field for a XeCl gas mixture : HCl : 0.07%, Xe : 0.2%, balance : Ne, total pressure : 5 bar absolute.

TABLE 4. Kinetic reactions taken into account in the minimum model and their rate constants. The number in parentheses corresponds to the power of 10. The rate constants given for the processes involving the laser photon correspond to the product of the cross section with the light velocity.

Process	Rate constant
Elastic collisions for momentum tranfer	
1 $e^- + Ne \Longrightarrow e^- + Ne$	Boltzmann
2 $e^- + Xe \Longrightarrow e^- + Xe$	Boltzmann
3 $e^- + HCl(v = 0) \Longrightarrow e^- + HCl(v = 0)$	Boltzmann
Excitations and ionizations by electronic collisions	
4 $e^- + Xe \Longleftrightarrow e^- + Xe^*$	Boltzmann
5 $e^- + Xe \Longleftrightarrow e^- + Xe^{**}$	Boltzmann
6 $e^- + Xe \Longleftrightarrow e^- + Xe^{***}$	Boltzmann
7 $e^- + Xe \Longrightarrow 2e^- + Xe^+$	Boltzmann
8 $e^- + Xe^* \Longleftrightarrow e^- + Xe^{**}$	Boltzmann
9 $e^- + Xe^* \Longleftrightarrow e^- + Xe^{***}$	Boltzmann
10 $e^- + Xe^{**} \Longleftrightarrow e^- + Xe^{***}$	Boltzmann
11 $e^- + Xe^* \Longrightarrow 2e^- + Xe^+$	Boltzmann
12 $e^- + Xe^{**} \Longrightarrow 2e^- + Xe^+$	Boltzmann
13 $e^- + Xe^{***} \Longrightarrow 2e^- + Xe^+$	Boltzmann
14 $e^- + Xe_2^* \Longrightarrow 2e^- + Xe_2^+$	Boltzmann
15 $e^- + HCl(v = 0) \Longleftrightarrow e^- + HCl(v = 1)$	Boltzmann
16 $e^- + HCl(v = 0) \Longleftrightarrow e^- + HCl(v = 2)$	Boltzmann
17 $e^- + HCl(v = 0) \Longleftrightarrow e^- + HCl(A)$	Boltzmann
18 $e^- + HCl(v = 0) \Longleftrightarrow e^- + HCl(B + C)$	Boltzmann
19 $e^- + HCl(v = 0) \Longrightarrow 2e^- + HCl^+$	Boltzmann
20 $e^- + HCl(v = 1) \Longleftrightarrow e^- + HCl(v = 2)$	Boltzmann
21 $e^- + HCl(v = 1) \Longleftrightarrow e^- + HCl(A)$	Boltzmann
22 $e^- + HCl(v = 1) \Longleftrightarrow e^- + HCl(B + C)$	Boltzmann
23 $e^- + HCl(v = 1) \Longrightarrow 2e^- + HCl^+$	Boltzmann
24 $e^- + HCl(v = 2) \Longleftrightarrow e^- + HCl(A)$	Boltzmann
25 $e^- + HCl(v = 2) \Longleftrightarrow e^- + HCl(B + C)$	Boltzmann
26 $e^- + HCl(v = 2) \Longrightarrow 2e^- + HCl^+$	Boltzmann
Penning collisions	
27 $Xe^* + Xe^* \Longrightarrow Xe^+ + e^- + Xe$	2.5 (−10) $cm^3\ s^{-1}$
Dissociative attachment	
28 $e^- + HCl(v = 0) \Longrightarrow H + Cl^-$	Boltzmann
29 $e^- + HCl(v = 1) \Longrightarrow H + Cl^-$	Boltzmann
30 $e^- + HCl(v = 2) \Longrightarrow H + Cl^-$	Boltzmann
Detachment reaction	
31 $Cl^- + Cl \Longrightarrow Cl + Cl + e^-$	5.0 (−10) $cm^3\ s^{-1}$
Recombinations	
32 $Xe_2^+ + e^- \Longrightarrow Xe^{***} + Xe$	2.3 (−7) $u^{-0.5}$ $cm^3\ s^{-1}$
33 $NeXe^+ + e^- \Longrightarrow Xe^{***} + Ne$	8.0 (−8) $u^{-0.5}$ $cm^3\ s^{-1}$
34 $HCl^+ + e^- \Longrightarrow H + Cl^*$	2.0 (−8) $u^{-0.5}$ $cm^3\ s^{-1}$
where u is in electron-volts	
Formation of ionic and neutral molecules	
35 $Xe^+ + 2Xe \Longrightarrow Xe_2^+ + Xe$	3.6 (−31) $cm^6\ s^{-1}$
36 $Xe^+ + Xe + Ne \Longrightarrow Xe_2^+ + Ne$	1.0 (−31) $cm^6\ s^{-1}$
37 $Xe^+ + 2Ne \Longrightarrow NeXe^+ + Ne$	5.0 (−32) $cm^6\ s^{-1}$
38 $Xe^* + Xe + Ne \Longrightarrow Xe_2^* + Ne$	1.6 (−32) $cm^6\ s^{-1}$
39 $H + Cl^- \Longrightarrow HCl(v = 0) + e^-$	9.6 (−10) $cm^3\ s^{-1}$
Charge transfers	
40 $NeXe^+ + Xe \Longrightarrow Xe^+ + Ne + Xe$	5.0 (−10) $cm^3\ s^{-1}$
41 $NeXe^+ + Xe \Longrightarrow Xe_2^+ + Ne$	5.0 (−12) $cm^3\ s^{-1}$
42 $HCl^+ + Xe \Longrightarrow Xe^+ + HCl(v = 0)$	3.4 (−10) $cm^3\ s^{-1}$

TABLE 4. (Continued)

De-excitations and quenchings (other than of XeCl)	
43 $Xe^{**} \Longrightarrow Xe^{*} + photon$	3.0 (7) s^{-1}
44 $Xe^{**} + Ne \Longrightarrow Xe^{*} + Ne$	3.0 (−12) $cm^3\ s^{-1}$
45 $Xe^{**} + Xe \Longrightarrow Xe^{*} + Xe$	3.0 (−12) $cm^3\ s^{-1}$
De-excitations and quenchings (other than of XeCl)	
46 $Xe^{***} + Ne \Longrightarrow Xe^{**} + Ne$	5.0 (−12) $cm^3\ s^{-1}$
47 $Xe^{***} + Xe \Longrightarrow Xe^{**} + Xe$	2.5 (−11) $cm^3\ s^{-1}$
48 $Xe_2^* \Longrightarrow 2Xe + photon$	6.0 (7) s^{-1}
49 $Xe^{*} + HCl(v = 0) \Longrightarrow Xe + H + Cl$	5.6 (−10) $cm^3\ s^{-1}$
50 $Xe^{*} + HCl(v = 1) \Longrightarrow Xe + H + Cl$	5.6 (−10) $cm^3\ s^{-1}$
51 $Xe^{*} + HCl(v = 2) \Longrightarrow Xe + H + Cl$	5.6 (−10) $cm^3\ s^{-1}$
52 $Xe^{**} + HCl(v = 0) \Longrightarrow Xe + H + Cl$	1.6 (−10) $cm^3\ s^{-1}$
53 $Xe_2Cl^{*} \Longrightarrow 2Xe + Cl + photon$	5.0 (6) s^{-1} [23]
54 $Xe_2Cl^{*} + Ne \Longrightarrow 2Xe + Cl + Ne$	3.0 (−14) $cm^3\ s^{-1}$
55 $Xe_2Cl^{*} + Xe \Longrightarrow 3Xe + Cl$	5.0 (−13) $cm^3\ s^{-1}$
56 $Xe_2Cl^{*} + HCl(v = 0) \Longrightarrow 2Xe + Cl + HCl(v = 0)$	6.0 (−10) $cm^3\ s^{-1}$
57 $Xe_2Cl^{*} + HCl(v = 1) \Longrightarrow 2Xe + Cl + HCl(v = 1)$	6.0 (−10) $cm^3\ s^{-1}$
58 $Xe_2Cl^{*} + HCl(v = 2) \Longrightarrow 2Xe + Cl + HCl(v = 2)$	6.0 (−10) $cm^3\ s^{-1}$
59 $Xe_2^{*} + HCl(v = 0) \Longrightarrow 2Xe + H + Cl$	8.2 (−10) $cm^3\ s^{-1}$
60 $Xe_2^{*} + HCl(v = 1) \Longrightarrow 2Xe + H + Cl$	8.2 (−10) $cm^3\ s^{-1}$
61 $Xe_2^{*} + HCl(v = 2) \Longrightarrow 2Xe + H + Cl$	8.2 (−10) $cm^3\ s^{-1}$
62 $HCl(B + C) \Longrightarrow H + Cl$	1.0 (10) s^{-1}
63 $HCl(A) \Longrightarrow H + Cl$	1.0 (10) s^{-1}
Vibrational kinetics of the HCl molecule	
64 $HCl(v = 0) + H \Longrightarrow H_2 + Cl$	3.8 (−11) $cm^3\ s^{-1}$
65 $HCl(v = 1) + H \Longrightarrow H_2 + Cl$	3.8 (−11) $cm^3\ s^{-1}$
66 $HCl(v = 2) + H \Longrightarrow H_2 + Cl$	3.8 (−11) $cm^3\ s^{-1}$
67 $HCl(v = 1) + H \Longrightarrow HCl(v = 0) + H$	5.1 (−11) $cm^3\ s^{-1}$
68 $HCl(v = 2) + H \Longrightarrow HCl(v = 0) + H$	4.6 (−11) $cm^3\ s^{-1}$
69 $HCl(v = 2) + H \Longrightarrow HCl(v = 1) + H$	3.2 (−11) $cm^3\ s^{-1}$
70 $HCl(v = 1) + Cl \Longrightarrow HCl(v = 0) + Cl$	1.0 (−11) $cm^3\ s^{-1}$
71 $HCl(v = 2) + Cl \Longrightarrow HCl(v = 0) + Cl$	3.5 (−12) $cm^3\ s^{-1}$
72 $HCl(v = 2) + Cl \Longrightarrow HCl(v = 1) + Cl$	1.0 (−11) $cm^3\ s^{-1}$
Formation of the XeCl molecule via neutral collisions	
73 $Xe^{**} + HCl(v = 0) \Longrightarrow XeCl^{**} + H$	6.6 (−10) $cm^3\ s^{-1}$
74 $Xe^{***} + HCl(v = 0) \Longrightarrow XeCl^{**} + H$	5.6 (−10) $cm^3\ s^{-1}$
75 $Xe^{*} + HCl(v = 1) \Longrightarrow XeCl^{**} + H$	2.0 (−10) $cm^3\ s^{-1}$
76 $Xe^{**} + HCl(v = 1) \Longrightarrow XeCl^{**} + H$	8.2 (−10) $cm^3\ s^{-1}$
77 $Xe^{***} + HCl(v = 1) \Longrightarrow XeCl^{**} + H$	5.6 (−10) $cm^3\ s^{-1}$
78 $Xe^{*} + HCl(v = 2) \Longrightarrow XeCl^{**} + H$	2.0 (−10) $cm^3\ s^{-1}$
79 $Xe^{**} + HCl(v = 2) \Longrightarrow XeCl^{**} + H$	8.2 (−10) $cm^3\ s^{-1}$
80 $Xe^{***} + HCl(v = 2) \Longrightarrow XeCl^{**} + H$	5.6 (−10) $cm^3\ s^{-1}$
81 $Xe + Cl + Ne \Longrightarrow XeCl + Ne$	1.25 (−33) $cm^6\ s^{-1}$
Ion–ion neutralizations	
82 $Xe^{+} + Cl^{-} \Longrightarrow XeCl^{**}$	7.2 (−7) $cm^3\ s^{-1}$
83 $Xe_2^{+} + Cl^{-} \Longrightarrow XeCl^{**} + Xe$	7.2 (−7) $cm^3\ s^{-1}$
84 $NeXe^{+} + Cl^{-} \Longrightarrow XeCl^{**} + Ne$	7.3 (−7) $cm^3\ s^{-1}$
85 $HCl^{+} + Cl^{-} \Longrightarrow H + Cl_2$	1.0 (−6) $cm^3\ s^{-1}$
Vibrationnal kinetics of the XeCl molecule	
86 $XeCl^{**} + Ne \Longrightarrow XeCl(B, v > 1) + Ne$	7.7 (−11) $cm^3\ s^{-1}$
87 $XeCl^{**} + Ne \Longrightarrow XeCl(C, v > 2) + Ne$	2.3 (−11) $cm^3\ s^{-1}$
88 $XeCl(B, v > 1) + Ne \Longleftrightarrow XeCl(B, v = 0) + Ne$	3.0 (−11) $cm^3\ s^{-1}$
89 $XeCl(B, v > 1) + Xe \Longleftrightarrow XeCl(B, v = 0) + Xe$	2.0 (−10) $cm^3\ s^{-1}$
90 $XeCl(C, v > 2) + Ne \Longleftrightarrow XeCl(C, v = 0, 1) + Ne$	3.0 (−11) $cm^3\ s^{-1}$
91 $XeCl(C, v > 2) + Xe \Longleftrightarrow XeCl(C, v = 0, 1) + Xe$	2.0 (−10) $cm^3\ s^{-1}$
92 $XeCl(B, v > 1) + Ne \Longleftrightarrow XeCl(C, v > 2) + Ne$	3.0 (−11) $cm^3\ s^{-1}$
93 $XeCl(B, v > 1) + Xe \Longleftrightarrow XeCl(C, v > 2) + Xe$	1.1 (−10) $cm^3\ s^{-1}$
94 $XeCl(B, v = 0) + Ne \Longleftrightarrow XeCl(C, v = 0, 1) + Ne$	3.0 (−11) $cm^3\ s^{-1}$
95 $XeCl(B, v = 0) + Xe \Longleftrightarrow XeCl(C, v = 0, 1) + Xe$	1.1 (−10) $cm^3\ s^{-1}$

For reactions 88–95 the direct coefficient is given

TABLE 4. (Continued)

Quenching of the XeCl molecule	
where (i) = (B, $v = 0$), (B, $v > 1$), (C, $v = 0, 1$) or (C, $v > 2$)	
96 $XeCl(i) + Ne \Longrightarrow Xe + Cl + Ne$	3.3 (−13) $cm^3\ s^{-1}$
97 $XeCl(i) + Xe \Longrightarrow 2Xe + Cl$	2.3 (−11) $cm^3\ s^{-1}$
98 $XeCl(i) + HCl(v = 0) \Longrightarrow Xe + Cl + HCl(v = 0)$	6.3 (−10) $cm^3\ s^{-1}$
99 $XeCl(i) + HCl(v = 1) \Longrightarrow Xe + Cl + HCl(v = 1)$	6.3 (−10) $cm^3\ s^{-1}$
100 $XeCl(i) + HCl(v = 2) \Longrightarrow Xe + Cl + HCl(v = 2)$	6.3 (−10) $cm^3\ s^{-1}$
Quenching of the XeCl molecule	
101 $XeCl(i) + HCl(A) \Longrightarrow Xe + Cl + HCl(A)$	6.3 (−10) $cm^3\ s^{-1}$
102 $XeCl(i) + Cl \Longrightarrow Xe + 2Cl$	6.3 (−10) $cm^3\ s^{-1}$
103 $XeCl(i) + H \Longrightarrow Xe + Cl + H$	6.3 (−10) $cm^3\ s^{-1}$
104 $XeCl(i) + 2Ne \Longrightarrow Xe + Cl + 2Ne$	1.0 (−33) $cm^6\ s^{-1}$
105 $XeCl(i) + 2Xe \Longrightarrow Xe_2Cl^* + Xe$	4.0 (−31) $cm^6\ s^{-1}$
106 $XeCl(i) + Xe + Ne \Longrightarrow Xe_2Cl^* + Ne$	5.0 (−32) $cm^6\ s^{-1}$
107 $XeCl(i) + e^- \Longrightarrow Xe + Cl + e^-$	1.2 (−7) $cm^3\ s^{-1}$
108 $XeCl + Ne \Longrightarrow Xe + Cl + Ne$	1.7 (−10) $cm^3\ s^{-1}$
Rate constant values for reaction 108 are given at 300 K	
Laser photon kinetics	
109 $XeCl(B, v = 0) + h\nu \Longrightarrow XeCl + 2h\nu$	2.4 (−5) $cm^3\ s^{-1}$
110 $XeCl + h\nu \Longrightarrow XeCl(B, v = 0)$	2.7 (−6) $cm^3\ s^{-1}$
111 $XeCl(B, v > 1) \Longrightarrow XeCl + h\nu$	9.1 (7) s^{-1}
112 $XeCl(B, v = 0) \Longrightarrow XeCl + h\nu$	9.1 (7) s^{-1}
113 $XeCl(C, v > 2) \Longrightarrow Xe + Cl + h\nu$	7.7 (6) s^{-1}
114 $XeCl(C, v = 0) \Longrightarrow Xe + Cl + h\nu$	7.7 (6) s^{-1}
115 $Xe_2Cl^* + h\nu \Longrightarrow XeCl + Xe$	3.6 (−7) $cm^3\ s^{-1}$
116 $Xe^* + h\nu \Longrightarrow Xe^+ + e^-$	1.8 (−9) $cm^3\ s^{-1}$
117 $Xe^{**} + h\nu \Longrightarrow Xe^+ + e^-$	2.3 (−7) $cm^3\ s^{-1}$
118 $Xe^{***} + h\nu \Longrightarrow Xe^+ + e^-$	2.8 (−7) $cm^3\ s^{-1}$
119 $Xe_2^* + h\nu \Longrightarrow Xe_2^+ + e^-$	4.2 (−7) $cm^3\ s^{-1}$
120 $Xe_2^+ + h\nu \Longrightarrow Xe^+ + Xe$	7.5 (−7) $cm^3\ s^{-1}$
121 $NeXe^+ + h\nu \Longrightarrow Xe^+ + Ne$	3.0 (−9) $cm^3\ s^{-1}$
122 $Cl^- + h\nu \Longrightarrow Cl + e^-$	3.6 (−7) $cm^3\ s^{-1}$
Rate constant values for reactions 109 and 110 are given at 300 K	

Breakdown voltage is a very important and, however sometimes confused notion. There are two breakdown voltages.

-The physical breakdown voltage, which depend only on the reduced electric field value and gas composition. Once the total electron multiplication rate becomes positive, then the breakdown voltage is reached.

-The practical breakdown voltage depends on the experimental conditions, ionising events, field strength,rise time and duration, because breakdown occurs only if the voltage is sufficient and lasts sufficiently long to allow an avalanche to take place and if initial electrons (at least one!), can be found in the future discharge volume.

$K_t = K_i - K_a$ is strongly dependent on the gas mixture composition; and impurities at a very low level may change considerably its value. As an example, Fig. 21a [21] shows how the avalanche time of a photo-switched high pressure discharge changes with the Xe content of a Neon-Xenon mixture. In this type of experiment a constant electric field is applied on the gas. A U.V. or X-ray preionization pulse seeds the gas with a determined initial electronic density ($n_{ei}=10^8 e/cm^3$ for instance) and the time to obtain the fall down of the voltage across the electrodes (corresponding to

$n_{ef} = 10^{15}$ e/cm^3 typically) is measured. This time can be correlated to K_t by solving the equation

$$\Delta t = (1/K_t.n).Ln(n_{ef}/n_{ei}). \quad (7)$$

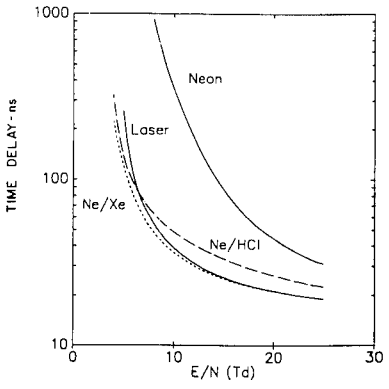


Figure 10. Avalanche time as a function of the reduced electric field and for several gas mixtures.

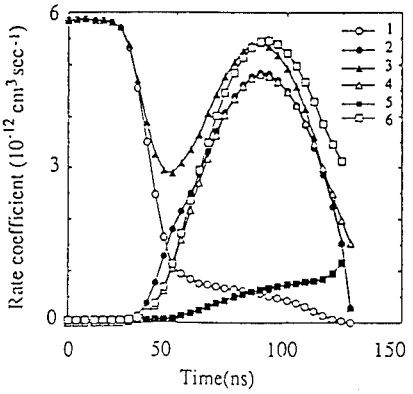


Figure 11. Electrons creation and loss rates v.s. time.1: direct ionization of Xe, 2: ionization of Xe*, 3: total ionization, 4: recombination, 5: attachment, 6: total loss rate.

In Fig. 10 [22] can be observed the behaviour difference between a pure gas and a gas mixture. Notice that curves for Ne/Xe, Ne/HCl, and Ne/Xe/HCl are close together!

As we explained before, the increase of excited states populations with time changes also significantly the K_i and K_a values in the discharge. In Fig. 11 can be seen the time dependency of electrons creation and loss rates as calculated by A.Belasri [23]. Following this figure, once the voltage drops across the discharge, Xe* ionization becomes the dominant electrons creating process and recombination the dominant loss process. This latest point is probably exaggerated as was shown by V.Puech [24].

1.4.2. *Modelling*

Using all the reaction rates listed in table 4, and solving the Boltzmann equation, it becomes possible to calculate the time behaviour of all the parameters of the discharge and the laser output . In most cases, this is done only in a spatially 0 dimension, time dependent way using a reference system moving with the electrons (V_d). Generally these models are able to predict the temporal evolution of electric parameters, and the laser output, at least the beginning. In many cases the end of the discharge is not well predicted because this type of calculation never takes into account the spatial quality of the discharge. Figure 12 shows a typical example taken from reference 20. Even though there is a good accordance between experiment and model at low field, at high field the predicted laser output is very different from the measured value although there is always a good accordance concerning the current. The author has shown that this discrepancy is

correlated with the appearance of Ne lines indicating that the discharge moves to an arc at this time.

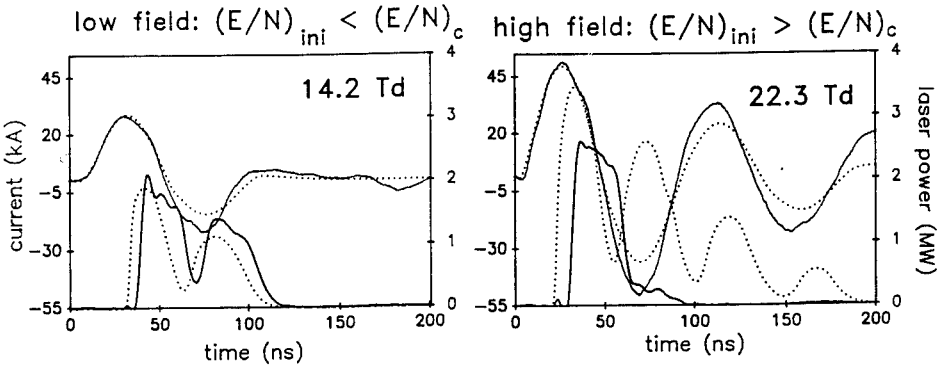


Figure 12. A comparison between model (dotted lines) and experiment (full lines). Upper curves: discharge current, lower curves: laser output. XeCl, P = 4 bars, C = 36 nF.

Another example of modelling result is shown in Fig. 13 [25],now concerning ArF. Here, if we only look to this figure, we would expect that the laser output to follow the ArF* density and hence be higher for the lowest value of the initial preionization density, namely : 10^2 e/cm^3. In fact, every excimer specialist knows that the best laser results will be obtained for $n_{e0} = 10^8$ e/cm^3, because this preionization density is needed to achieve a homogeneous discharge. *Excimer lasers need always a homogeneous discharge* and this (most!) type of modelling does only suppose that the discharge is homogeneous and can't give any information on its homogeneity.

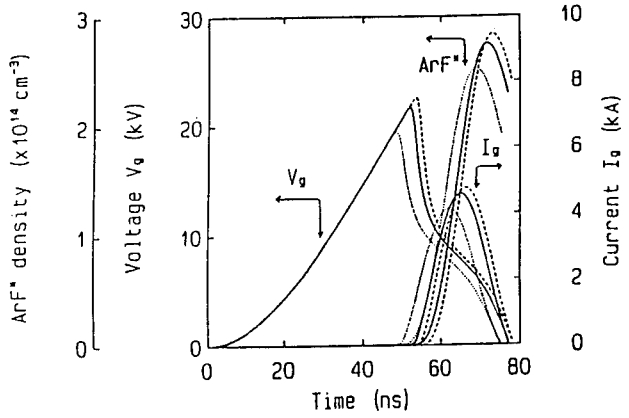


Figure 13. Waveforms of the discharge voltage V_g, current I_g and ArF* number density n_{ArF*} for n_{e0} values of:—10^2 cm^{-3};—10^4 cm^{-3}; $\cdots 10^8$ cm^{-3}.

1.5. A HOMOGENEOUS DISCHARGE

Very early after the beginning of the rare gas halides discharge excited lasers, it became evident that a homogeneous discharge was a necessary condition to have good laser efficiency, good laser output and to operate these lasers at high repetition rate. It became also clear that a powerful preionization system could help and, more was indispensable.

1.5.1. *Raether's streamer model*

At high pressure actually, the Townsend model is unable to predict the onset time of a discharge and its instability. A new model has been proposed by Raether [26] and Palmer [27] and is explained in Fig. 14. When an avalanche starts from a single initial electron, secondary electrons are moving towards the anode while positive ions practically stay still. Thus it appears a *space charge field* which, at high pressure (i.e. at high density and low electron mean free path) can become *comparable to the external field* and hence completely modify the field value all around the avalanche head. Thereby the head radius does not increase further and the avalanche becomes a streamer which propagates up to the anode. Due to enhanced ionisation rates, photo ionisation and field effects in front of the avalanche head, this propagation can be much faster than predicted by the Townsend model. Assuming a spherical avalanche head the critical length for the streamer transition may be calculated. If D_e is the electron diffusion coefficient, we can derive the Z_c and R_c values

$$R_c=(2.D_e.Z_c/V_d)^{1/2}, \tag{8}$$

$$D_e=1/3.\lambda.V_{th}\,, \tag{9}$$

$$\alpha.Z_c = \ln(4\pi\varepsilon_0 E\lambda/e)+\ln(Z_c)\,, \tag{10}$$

$$\alpha.Z_c \cong 20 + \ln(Z_c)\,, \tag{11}$$

with λ=electron mean free path, V_{th}=electron thermal velocity.

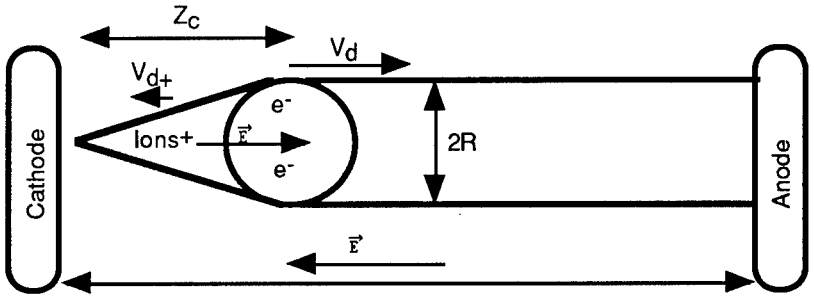


Figure 14. Schematics of a streamer avalanche.

1.5.2. *The minimum preionization density*

If we consider a sheet of initial electrons produced close to the cathode by some

preionization device, we can suppose that the discharge starting from these electrons will be homogeneous if all the avalanches collapse together before reaching their streamer dimension, as shown in Fig. 15. This condition, proposed by Levatter [28] can be written

$$n_{e0} > 1/(2R)^3, \tag{12}$$

On the other hand we can consider that most preionization systems put free electrons in the whole future discharge volume. In the field direction, superposition of avalanches will suppress any space charge effect (and hence any streamer formation) if

$$n_{e0} > 1/Zc^3, \tag{13}$$

Since, in excimer conditions, $Zc \approx 20$ R, this second condition is 1000 lower than the first one!

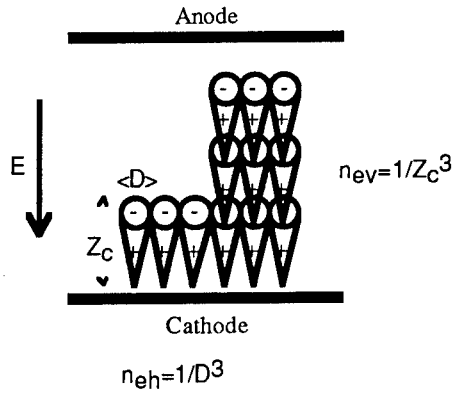


Figure 15. (One of the) Conditions for an homogeneous discharge.

In both cases we would expect the output energy of an excimer laser to be saturated when the preionization density is above some threshold value. This behaviour can be observed, for instance in Fig. 16 [29]. Here a KrF laser beam as been used to preionize a XeCl laser. It was sent into the XeCl laser through its rear mirror along its optical axis. It as been shown by Taylor ([30], see Fig. 23) that the electron density produced by a KrF beam in a XeCl gas mixture is proportional to its energy density and depends only on the exact gas composition included impurities. Thus a KrF beam is a very practical tool to study the effect of the preionization intensity and time dependency. The saturation of the XeCl output when the preionization is increased appears clearly in Fig. 16. As a proof of the proportionality between the preionization density and the KrF fluence, we have also represented on this figure the measured avalanche time as a function of the KrF input. Its variation follows the logarithmic relation (7). The XeCl laser used in this experiment had a built in Corona preionization device which was not used when the KrF preionization was used. A comparison is made on Fig. 16. A negatively driven Corona gives the maximum possible output energy while the positively driven Corona is less efficient. This comparison shows only that, in this particular case, a Corona preionization device can give the best possible results.

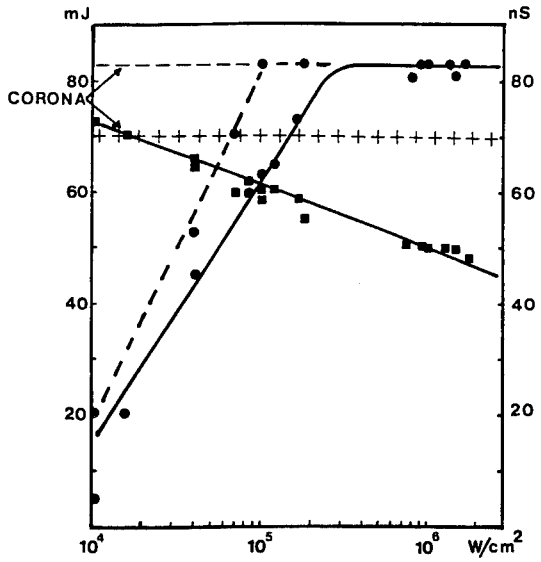


Figure 16. XeCl output (●) and avalanche time (■) (E/n = 0.7 10^{-20} V.m^2) v.s. KrF peak intensity. Full line: old gas mixture, dashed line: fresh gas mixture. Output energy of the same laser, but with negative (- -) or positive (++) corona preionization.

The remaining question is " What is the correct value for the minimum preionization density ?", and "Is it the same value in the whole discharge volume and/or close to the cathode ?" By inserting a mask in the KrF path it is possible in this experiment to modify the spatial distribution of the preionization density. This work was done by R.S.Taylor and he showed several things.

-It is possible to have a noticeable electronic density gradient in the field direction with little decrease of the laser output. This result seems to be in good accordance with equations (12) and (13) for the cathode layer and the volume respectively.

-If the preionization spatial width is reduced, the laser beam width is reduced to the same size but the output energy remains unchanged. This results seems to indicate that in this case the current flows entirely in the preionized region.

-If a stop is inserted in order to have, between the electrodes, and for instance in the middle, a non preionized region, strange things are observed. Laser effect occurs only in the preionized regions and the laser output energy density remains approximately constant (energy proportionnal to the "useful" section). This surprising result is not in accordance with streamer theory and condition (12).It shows that there is some local effect of the preionization on the discharge homogeneity, more compatible with condition (13).

The most beautiful result was obtained by Taylor when he put a mask with the letters NRC (for National Research Council) in front of the KrF laser and obtained a XeCl laser burn showing the same letters.

1.5.3. *Preionization v.s. time*

The pulse width of the necessary preionization depends whether an electric field is present or not.

With no E-field and for XeCl mixture, electron attachment is low, there is no collisional ionisation, preionization pulse duration can be long without any loss of efficiency.

With Fluorine based mixture,attachment is strong even in the absence of E-field. A short pulse is preferable.

Most commercial lasers are operated in this way. The slow preionization is triggered just before or at the beginning of the laser voltage rise. In this case a very steep and high voltage pulse is needed on the laser itself for three reasons.

-To avoid loss of electrons through attachment on Fluorine

-During the rise of the voltage, electrons drift towards the anode thus leaving a depleted zone behind them which is a source of instabilities.

-Depending on the gas mixture the multiplication rate can be quickly very high and provoke the gas breakdown before the desired voltage (and the desired energy) is reached.It is for instance the case of KrF or ArF.

When the preionization is applied in presence of the electric field (Photo- triggering [10]), things are different. Ionization begins from the first electron. An efficient preionization needs to be fast enough to put electrons in the gas faster than avalanche does in order to control the discharge and to make the streamers to join together. For a given U.V. or X-ray pulse shape and a given reduced field strength, the electron density history has two phases (Fig. 17). First the electron density increases like the integral of the U.V. (or X-ray) pulse, then, when this curve becomes too slow, the total ionisation rate of the gas takes over. We call the density achieved at the end of the first phase "The effective preionization density". Figure 18 [31] shows how the output energy of a XeCl laser depends on the electrodes voltage at the preionization time (Corona preionization in this case). By assuming a 10ns preionization pulse width the calculated effective preionization density presents(follows) the same behaviour than the output energy.

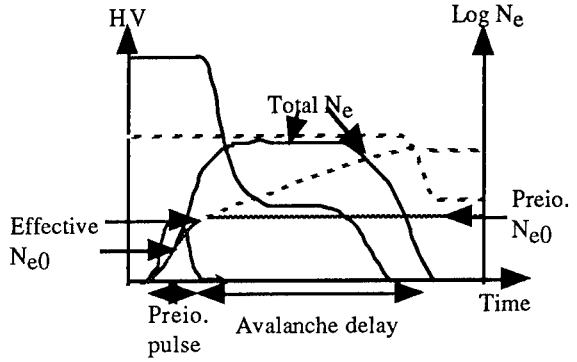


Figure 17. Voltage and electron density v.s. time in a photo triggered discharge for two initial voltage values: ---- high, ... low. N_{e0eff} is lower when this voltage is higher.

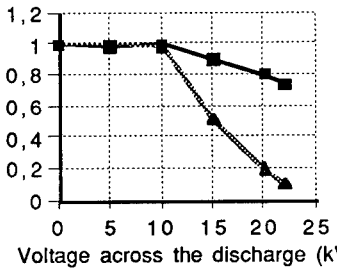


Figure 18. Laser output energy (■) and calculated effective preionization density (Δ) (normalized values) as a function of the voltage across the discharge when the preionization pulse is applied. Laser 530 U.V.: electrode spacing: 3cm, gas pressure: 5bar, total discharge voltage rise time: 400ns, preionization pulse width: 10ns.

Time stability of the discharge . It has been observed that all excimer discharges degenerate to arcs more or less rapidly. This is particularly true when these discharges are, from their beginning, not homogeneous. Amongst the processes playing a role in the discharge, most tends do decrease the homogeneity (Table 5). It has been shown for instance that HCl burning has a direct effect on the laser pulse duration [30]. Since HCl consumption is directly connected to its initial concentration, one would expect a correlation. Experimental results partially confirm this hypothesis (Fig. 20). Other deleterious effects are due to cathode materials, repetition rates, gas pollution.

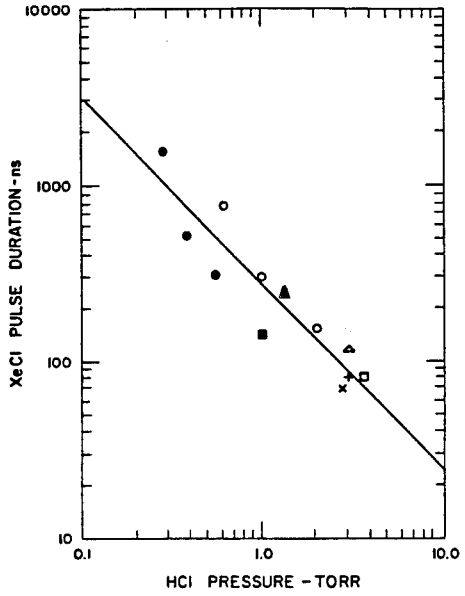


Figure 19. XeCl pulse duration (FWHM) as a function of HCl partial pressure. The data denoted by (O) represents the time for filaments to close the discharge gap. See [30] for other details.

Table 5. Reactions effect on discharge stability

Positive effect:
direct ionization : n_e ↗ V ↘ E/N ↘ Ki ↘
recombination : n_e ↗ rec ↗ Kt ↘
Negative effect:
step ionization : n_e ↗ Xe* ↗ Ki ↗
halogen depletion : n_e ↗ HCl ↘ Ka ↘ (Ki - Ka) ↗
gas local heating : T ↗ N ↘ E/N ↗ Ki ↗

1.6. PREIONIZATION DEVICES

The role of preionization devices is to create in the future discharge volume the minimum free electron density necessary to achieve a uniform discharge.

Two classes of preionizer may be distinguished depending on whether they act on gas majority components (X-rays, electrons) or on gas impurities (U.V. photons). We can also distinguish between in situ sources (incoherent U.V. photons) and outside sources (X-rays, electron beam, KrF laser).

Incoherent deep U.V. sources are widely used in commercial lasers : Arcs, corona or flash board devices are efficient ionizing sources (Fig. 20). These devices can preionize moderate gaps (up to 10cm), be operated at high repetition rate and are simple and inexpensive. On the other hand they contaminate more or less the gas mixture and produce a non uniform and badly known density. U.V. absorption at the ionization wavelength of major gas components is very strong. Hence the volume ionization can only be due to low concentration impurities having longer ionization wavelength.

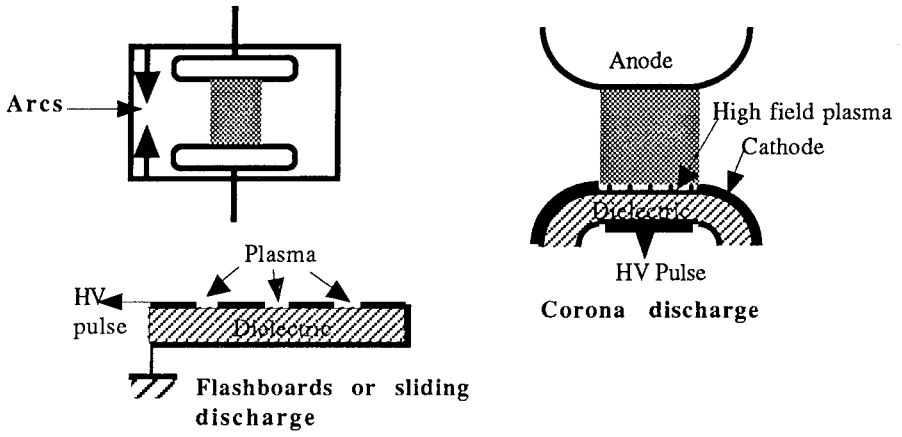
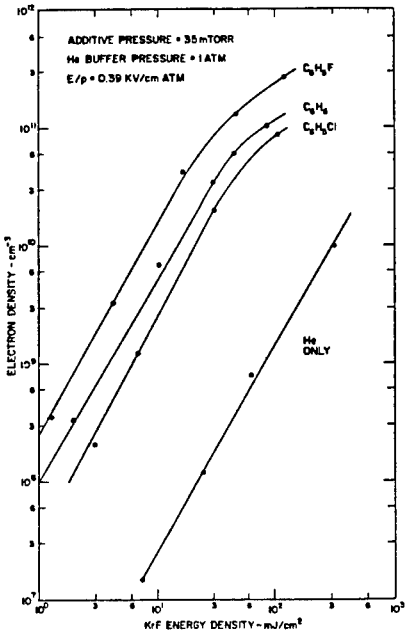


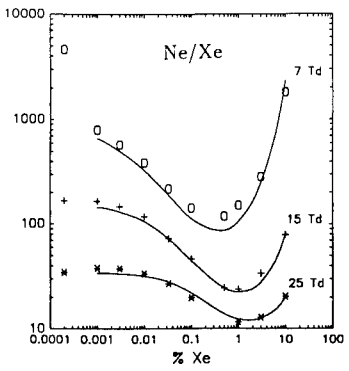
Figure 20. U.V. preionization devices.

From a more general point of view, Excimers discharges are very sensitive to impurities, and many incomprehensible features could, probably, be attributed to them. As an example is shown in Fig. 21a how the avalanche depends on the gas composition of a Ne-Xe mixture. Xe concentrations as low as 10^{-5} modify strongly the ionisation rate of the gas.

The same feature is expected from a KrF laser used as a preionizer (Fig. 21b) In spite of a non measurable absorption in a standard XeCl gas mixture, a low energy KrF beam can preionize it very efficiently. More, it allows to know precisely the time and space distribution of the produced electronic density.



b



a

Figure 21. a- Avalanche time (ns) of a Ne-Xe mixture as a function of the Xe content for 3 E/N values.
b- Electron density produced by the KrF beam as a function of its fluence.

X ray preionization presents the great advantage of being able to ionise all the gas mixture components. Knowing the X ray beam temporal, spatial and energy properties allows to evaluate precisely the electronic density. In usual excimers gas mixture the X ray absorption is moderate and great volumes may be preionized very uniformly, the only limitation being due to the beam divergence.

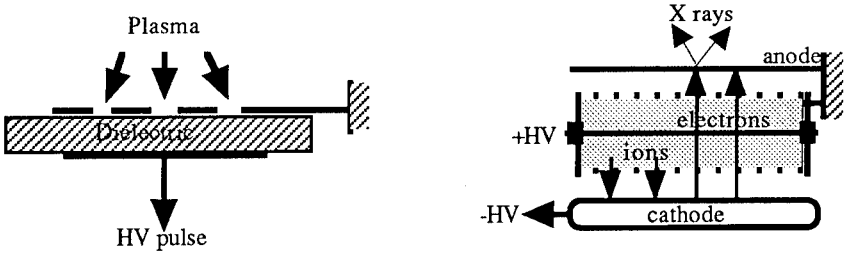
Technical limitation are however severe. A X-ray preionizer needs a high current density cathode, electrons fast acceleration to high voltages (in high vacuum, of course), X ray conversion on a thin, high Z and refractory material and finally, X rays injection in the gas through a thin, low Z, sheet of pressure and chemically resistant material.

The main difficulty concerns the cathodes. They have to emit high current

densities in short pulses. Heated cathodes cannot easily do that and are very sensitive to "Laboratory operating conditions" air inlets for example. Field effect cathodes, made of razor blades or carbon felt have been widely used. They are simple, cheap but their lifetime and repetition rate are very limited.

Recently [32] plasma cathodes have been proposed (Fig. 22). Like the preceding cathodes they are limited by the space charge effect (Child Langmuir law) but they seem to be rugged and able to provide short pulses at high repetition rate with a good reliability.

Secondary emission guns are used also [33]. They work at low pressure. Field ionization of the gas on the left branch of the Townsend curve acts as the primary ion source. These ions are accelerated towards the cathode and electrons are emitted through secondary emission. Due to the plasma, space charge effects are probably lowered. This gun has been operated reliably at high repetition rate
(> 1kHz), but cannot provide short (< 100ns) pulses.



a- Plasma cathode

b- Secondary emission X-ray gun

Figure 22. Elaborate systems for X-ray preionization.

2. Current Status

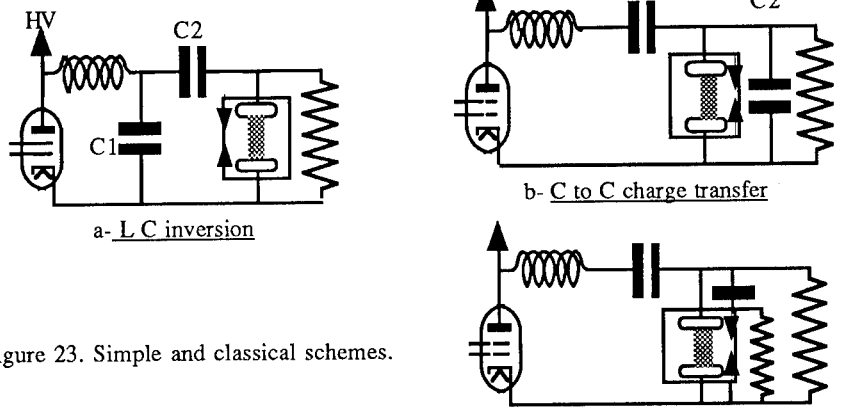
2.1. ELECTRICAL SCHEMES

We have seen before that the main difficulty for excimer lasers is to provide to the discharge enough power density in an homogeneous way. For that purpose, the electrical circuit must be able to furnish, typically, 10's of KV and 10's of KA within a short time, 100ns for example. Concerning the homogeneity, preionization is of course needed but also a low impedance circuit must be used to avoid voltage fall-of before a sufficiently high electronic density is obtained. This is frequently done by connecting small ceramic capacitors close to the electrodes and all along them. These capacitors are usually called "peaking capacitors".

2.1.1. *Simple circuits*

Typical main circuit inductances for an excimer laser are about 20nH or less. It is inconceivable to obtain such a low inductance with a single gas switch like a thyratron or a spark gap. More, the switch current in this case would be very high. Thereby in most cases, the discharge current is taken from capacitors directly connected to the electrodes. Figure 23a shows the first circuits which have been proposed for excimer lasers. In both cases two capacitors banks C1 and C2 (C1=C2) are used. In the LC inversion circuit the ringing of the "thyratron, inductance, C1" circuit inverts the voltage across C1 after a half period. The discharge is then fed by C1 and C2 in series with a total voltage equals to two times the DC high voltage (theoretically). The advantage of this scheme is the "low" voltage of the power supply, the drawback being the reduced life time of most capacitors used for C1 due to the strong and fast voltage inversion.

For this reason most commercial lasers use the charge transfer scheme (Fig. 23b) which is found to be less stressful. In this case the first ringing circuit is comprised with the thyratron, the inductance and C1 and C2 in series. At the beginning, C1 is charged to the DC high voltage and C2 to zero. When the thyratron is fired, the circuit rings and the charge of C1 is transferred to C2 after a half period. Then the discharge breaks down and the C2 energy goes into the discharge.



a- L C inversion

b- C to C charge transfer

c- C to C with automatic preionization

Figure 23. Simple and classical schemes.

These are very simplified explanations; things are in fact somewhat more complicated.

- The transfer or inversion efficiency is actually much lower than one because of losses in the wires and in the thyratron. Usual energy efficiencies are only about 50%.

-The difficulty is to fire the discharge homogeneously just on time to get the maximum efficiency and output energy. Preionization is produced generally at the beginning of the voltage rise. A popular automatic preionization circuit is presented also in Fig. 23c. With such a simple circuit, the only way to provoke the discharge when the

voltage reaches its peak value is to adjust the voltage rise time. But this will depend also on the gas mixture composition because ionization rates can be very different from one excimer gas mixture to another.

-These simple circuits although widely used in commercial lasers, have been found to have three drawbacks.

1 - Because of impedance mismatch between circuit and discharge the overall efficiency cannot be, in principle, very good.

2 - Because of the short voltage rise time needed for the discharge spatial quality the main switch is severely stressed and its life time is short.

3 - Such a simple scheme does not allow to obtain long pulses.

To overcome these drawbacks, elaborate circuits have been proposed.

2.1.2. *The spiker-sustainer circuit*

The idea [11] (Fig. 24a) is to separate the two functions of the electrical circuit. A first high voltage circuit, the spiker, is used to create a homogeneous discharge, whilst using little energy. A second, lower voltage circuit, the sustainer, feeds then the discharge with all the required energy. The impedance of this second circuit is adjusted to be as much as possible matched to the "discharge impedance". For the first demonstration, spark gaps have been used to separate the two circuits (Fig. 24b). Later, the use of a saturable inductance to isolate the energy storage line has been proposed. A simple circuit is shown in Fig.24c. Depending on whether the spiker and the sustainer have the same or the opposite polarities, the performances and ease of manufacturing can be different. To summarize, with the same polarity, the spiker is operated at lower voltage and the saturable inductance is smaller. On the other hand, in this case, the operation of the saturable inductance is not fully satisfactory because the saturation of the inductance by the spiker is followed by a reverse current from the sustainer towards the discharge which desaturates the inductance before resaturating it in the opposite sense.

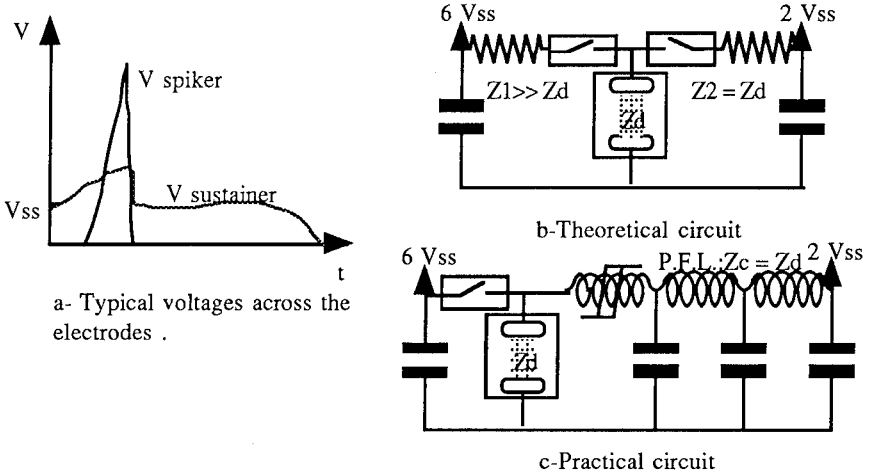


Figure 24. Spiker-sustainer principle and circuits.

Hence there is a delay between the spiker discharge and the sustainer discharge which is

not favourable to a good homogeneity. With opposite polarities, the sustainer current flows in the same direction than the saturating current from the spiker. In this case the switching of the saturable inductance is improved and the main discharge follows immediately the spiker discharge.

Spiker-sustainer circuits have allowed to obtain homogeneous and stable XeCl discharges. Pulses length as long as 1µs [30] and efficiencies close to 4% for shorter pulses (100 to 200 ns) have been reported.

This scheme is partially based on the impedance matching between the sustainer circuit and the discharge. It should be noted that the discharge impedance is not really a constant. It depends for example on the spiker voltage and rise time. However it is observed usually, and for XeCl, that once the discharge is fired, its voltage drops to a so called steady state voltage which corresponds to an equilibrium in the discharge between the electron creation and losses processes. This steady state voltage remains approximately constant as long as the HCl concentration does not change too much. Hence charging the sustainer to twice this steady state value corresponds to a kind of impedance matching.

The problem of main switch lifetime is only partially solved by the spiker sustainer circuit and at the expense of some complication. In fact the electrical stresses on the spiker switch remains severe. In order to radically improve the power switches life time, another alternative scheme has been proposed.

2.1.3. *The phototriggering or switchless circuit*

It uses the discharge as its own switch being triggered by the preionization pulse[10]. This operating way relaxes strongly the stresses on the switches, as shown in Fig.25, because the main voltage rise time can be much longer than in the classical circuits : 10µs for example.

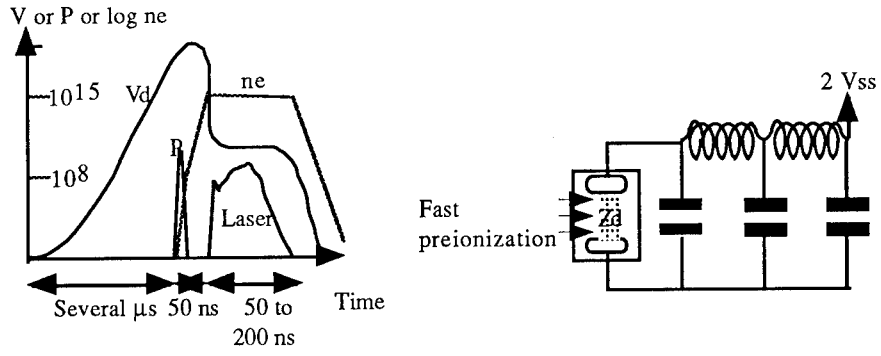


Figure 25. Principle (Discharge voltage, preionization pulse, electron density and laser power v.s. time.) and scheme of the phototriggered circuit.

Photo-triggering has been tried with Corona, X-ray or KrF preionization. High efficiency (> 4% [34,35]), high energy (up to 15J [36,37]) and high repetition rates

(700Hz [34,38]) have been obtained.

The only drawbacks of this scheme are the need of a very short preionization rise time (see Fig. 17) (but we are concerned in this case with a small energy, less than 1J) and the possibility of spontaneous breakdown before the preionization input.

A short preionization pulse is not, generally, so difficult to do. A Corona device is for instance well suited. More difficult is the manufacturing of a short pulse,high repetition rate, X-ray gun the more if it has to be reliable!

Spontaneous breakdown can be avoided by a careful design of the laser head. Field uniformity along the the insulating pieces is particularly critical. However at high repetition rate, spontaneous breakdown is generally observed, the critical time constant being near 10ms. Several mechanism can explain this behaviour of the discharge [31]. Probably the dominant mechanism is the ionization of the gas surrounding the discharge by its U.V. emission. Hence the gas coming between the electrodes has been preionized by the preceding discharge. It his very hard to prevent the coming gas to see the discharge because there is an unavoidable gas volume between the current returns and the discharge itself and because these current returns are generally not opaque. In practice, the gas volume concerned is of the order of 5 to 10 times the discharge volume at least and a time constant equal to 10 times the delay between one pulse and the follower can easily be explained!

2.2. LASER HEAD DESIGN

An excimer laser head is always a compromise . Simultaneously, it is necessary to have a good field homogeneity between the electrodes, a good insulation and no flashover along the insulators, a low discharge circuit inductance and a good aerodynamic profile to insure a uniform and speedy gas flow. The choice of the materials is restricted by chemistry considerations to a few metals and a very limited number of dielectrics. Though a good design of the internal set up can allow to have a dielectric field path equals to 150% of the electrode gap, with a bad design, even with 300% dielectric length, surface flashovers are observed. In Fig.26 is shown the half cross section of a modern laser head taken in ref. [34]. It can be seen that the fields along the insulator surface and between the electrodes are very uniform though there is no restriction to the gas flow. The discharge circuit inductance of this laser head is close to 10 nH for a 50 cm length discharge. The geometry of this head can probably be improved but it is already a very good compromise of all the parameters. In particular the capacitor bank position has been carefully chosen to lead to the best electric field uniformity. Older lasers having worse geometry will be described further.

2.3. ABOUT THE REPETITION RATE

Early at the beginning of rare gas halides lasers it was found difficult to increase the repetition rate above a few Hertz, depending on the discharge operating pressure and volume. It was demonstrated that the first reason for that was optical. After the

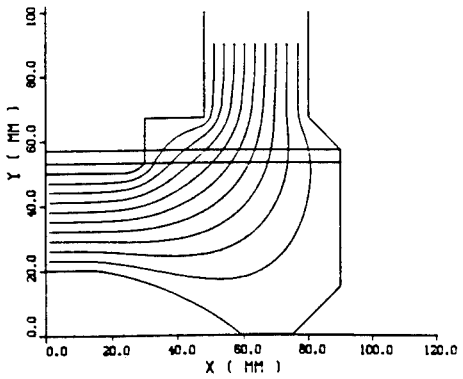


Figure 26. Voltage equipotential lines inside the 530 laser head.

discharge, the gas density becomes completely non uniform, due to the nonuniform nature of the energy deposit. The refractive index is completely disturbed and the coherent optical transmission is close to zero until the gas has recovered its homogeneity. This is a relatively slow process. Therefore it has been proposed to move the gas away from the interelectrode space and to replace it with fresh, homogeneous and cool gas. Hence the first repetition rate limit corresponds to the time needed to do that (Fig.27).

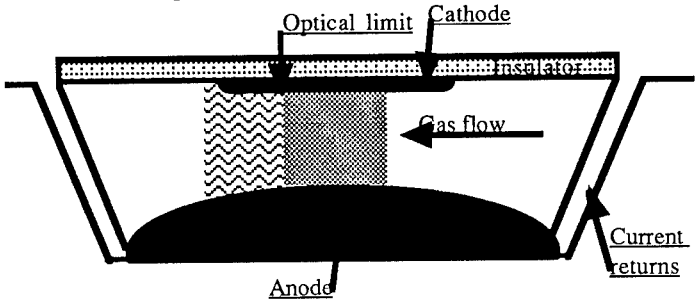


Figure 27. The simple optical limit to the repetition rate.

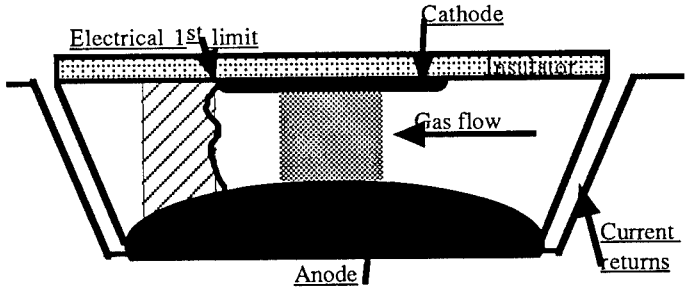


Figure 28. The1st backstream arcing limit to the repetition rate.

But, for several reasons, this delay is not enough. Because electrodes are always wider than the discharge, a conductive plasma can be still in contact with both electrodes (Fig.28) when the voltage is applied on them and will shorten the main discharge even if the amplifying medium is optically clear.

With a longer delay, insulator flashover can be observed because the plasma is in contact with the insulator thus reducing the practical insulator length (Fig.29).

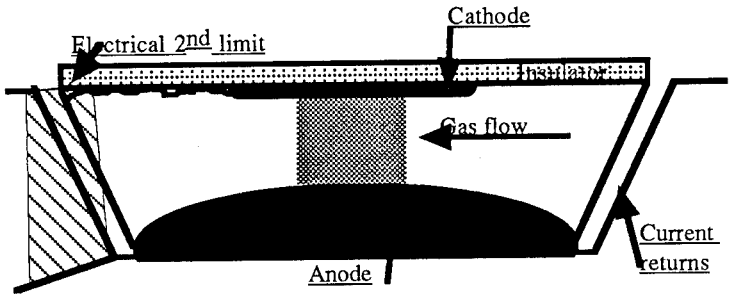


Figure 29. The insulator flashover limit to the repetition rate.

Finally the density and pressure perturbations produced by the discharge propagate in the laser vessel and are reflected by the walls. After a time of the order of 2 ms, a reverberation regime is established inside the whole laser, with a steady state random perturbation intensity which depends on the discharge quality and on the walls acoustical reflectivity [39]. This phenomenon is described in details in the paper of Bernard FORESTIER.

To summarize the problems related to the high repetition rate operation, it can be said that

-Below 300 Hz the limit is given by the time needed to evacuate the plasma from the whole electric field volume.

-This delay is much greater than the time needed to restore the gas homogeneity in the amplifying volume.

-Above 300 Hz acoustic waves reverberation plays an important role that increases very strongly with the repetition rate frequency.

-Pressure perturbations are essentially produced by post discharge arcs [39].

-The more the discharge is homogeneous, the better will be the high repetition rate operation.

More generally, for excimer lasers, the more the discharge is homogeneous, the better every thing.

2.4. CHEMISTRY CONSIDERATIONS

Due to its low concentration of halogen, the reactivity of an excimer gas mixture is moderate and the degradation of the laser head can be easily avoided. But any change in the gas composition as a very strong effect on the discharge quality and on the laser efficiency. The simple rules written below may help in the choice of laser materials and operating procedures.

-HCl and HF are acids when dissolved in water--> avoid water vapour input (remember that air contains water vapour).

-Metallic chlorides are highly soluble but fluorides aren't -->
Practically any metal can be used with fluorine and passivation with fluorine is more efficient and durable than passivation with chlorine.

-Fluorine reacts strongly with practically all plastic materials, excepted Teflon, Kelef, or Kynar but these materials may contain organic impurities or/and water.

- The more you go to the deep U.V., the more you'll find absorbing species.

-Chlorides or/and fluorides are insulating materials -->There is no durable passivation on the electrodes -->metal of electrodes must be carefully chosen.

-The goal is not to avoid corrosion but to keep the gas composition stable.

It is clear that HCl and F_2 does not behave in the same way . HCl is dissociated in the discharge, and, normally, recombines with the help of the U.V. emission of the neighbouring discharge. In case of hydrogen loss (leaks or OH radicals), the gas composition cannot be recovered. Figure 30 [40] shows how a small hydrogen concentration can extend the life time of HCl based gas mixtures.

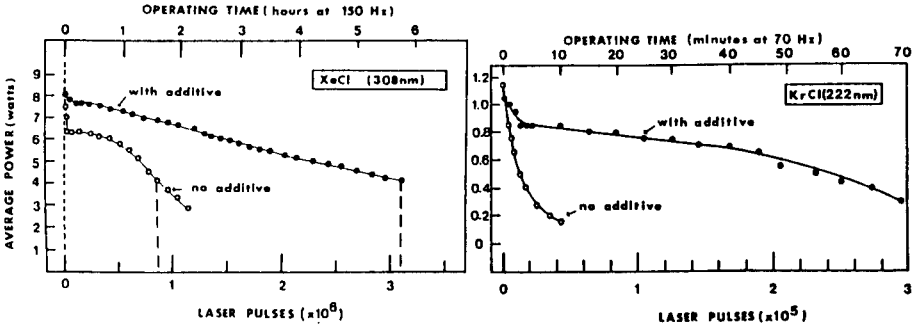


Figure 30. XeCl and KrCl average power output as a function of number of laser pulses at 150 Hz (XeCl) or 70 Hz (KrCl) with and without 1 Torr hydrogen additive.

Concerning F_2, there is a direct correlation between CF_4 concentration and laser efficiency decrease. Of course, CF_4 appearance depends on the insulators used for the laser head construction (Fig.31 [41]).

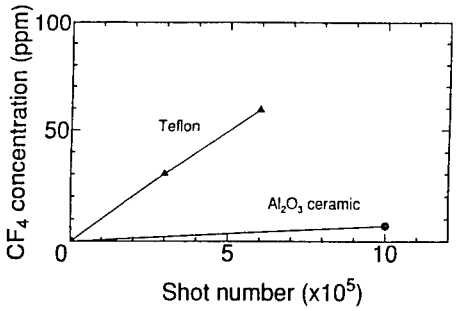


Figure 31. CF4 evolution with Teflon or alumina insulator.

The difference between HCl and F_2 based gas mixture (or between long and short wave length excimers) can be summarized as follows :

-HCl and long wave length are sensitive to the HCl losses,

-F_2 and short wave length are sensitive to gas contamination by absorbing species.

In this case, gas cleaning can improve very efficiently the gas mixture life time. An example is the popular cryogenic gas cleaning system from the Oxford Lasers Company. As shown in Fig.32 , most gas impurities are liquid or solid below 100°K , and hence can be removed from the gas mixture by a cold trap working at this temperature. This is the principle of the GP 2000. Note that, for best results, the cold trap temperature can be adjusted to avoid any interference with the gas mixture theoretical composition.

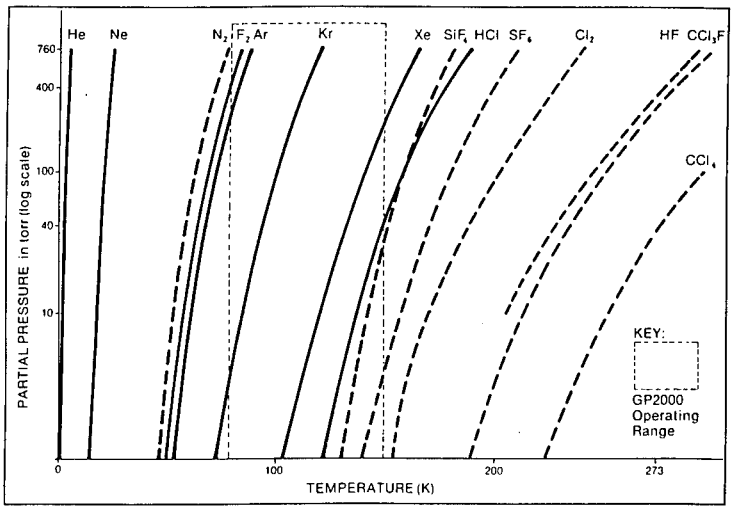


Figure 32. Principles of a commercial excimer gas purifier: Partial pressures of excimer laser gases and common impurities as a function of temperature.

A more elaborate and expensive system has been studied by T.Saito [42], and is shown in Fig.33.

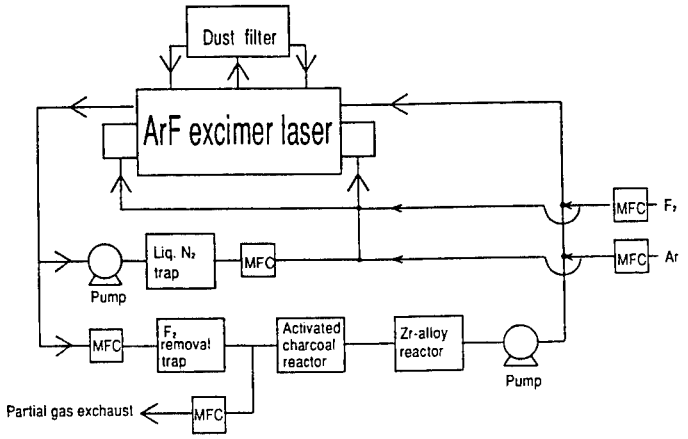


Figure 33. Diagram of an elaborate gas purifier for a long lifetime ArF laser.

2.5. LASER EXAMPLES

Although it is not a discharge excited rare gas halide laser, Aurora is the biggest excimer laser ever built [43]. It has been designed as a multi pass, high volume, E-beam pumped amplifier. Main characteristics are listed below.

AURORA CHARACTERISTICS

-Amplifying medium volume - aperture : 1mx1m, active length : 2m.
-Maximum input energy - 120 kJ
-Maximum repetition rate - 0.00....1 Hz ?
-Gas - mixture/pressure : F_2, Kr, Ar, 1.5Bar
-Size - total length : 25 m
-Output - Oscillator pulse energy : 5kJ (KrF), pulse duration : 300 ns.

In Fig.34 is shown the experimental set up.

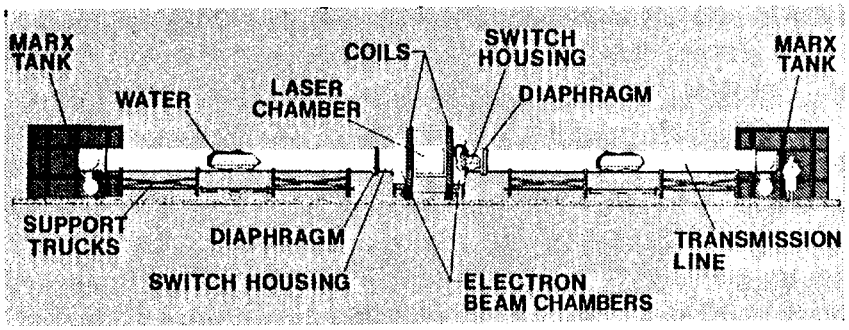


Figure 34. General view of the Aurora laser.

Concerning, this time, a discharge excited excimer laser, the biggest one remains probably the laser built at N.R.L. [44]. Water lines were used to store the energy and to transfer it to the discharge (Fig.35). Electrode spacing could reach 22cm. The laser head design (Fig.36) gave to N.R.L. researchers the opportunity to experience flashover problems related to a very bad electric field profile [45]. Figure 37 taken from this reference, shows the equipotential lines inside the laser head and Fig.38 a typical insulator flashover example. Nevertheless, this laser was able to deliver up to 66J at 308nm in a 180ns pulse.

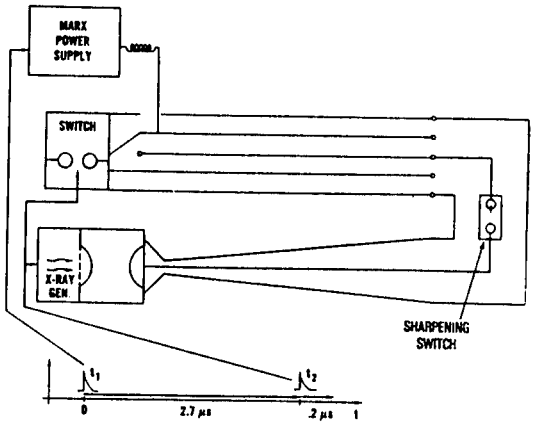


Figure 35. Schematic drawing of the N.R.L.laser system including the timing sequence for its firing. The Blumlein charging starts with a trigger pulse (t_1). The Blumlein discharge is commanded by a trigger pulse (t_2) 2.7μs later. The voltage pulse will arrive at the laser chamber 0.2μs after t_2 is fired.

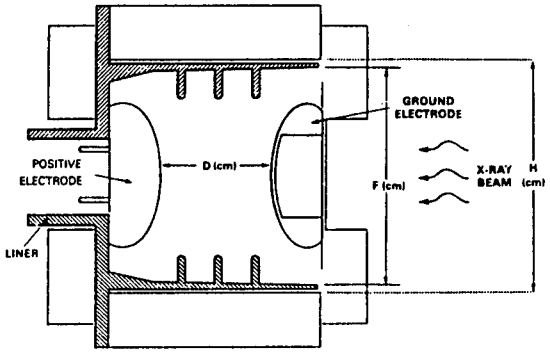


Figure 36. N.R.L. laser chamber and dielectric insulator is shown in cross section. A well-behaved discharge occurs only when D is less than three times the distance along the insulator surface between the electrodes.

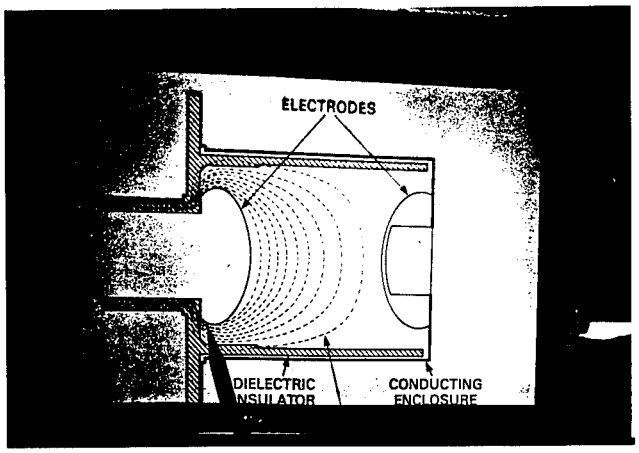


Figure 37. Equipotential lines in the N.R.L. laser chamber.

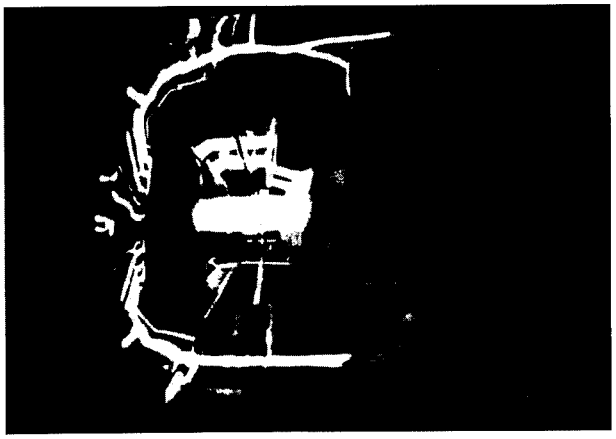


Figure 38. Example of insulator flashover in the N.R.L. laser chamber.

Many studies have been done to improve the high repetition rate performances of excimer lasers. The recent work of S.Takagi and his coworkers [46] at Toshiba gave impressive results, up to 5000 Hz repetition rate, with an average power as high as 500W. The complete laser is represented in Fig.39. It is characterised by a very high gas speed which insures a clearing ratio of 3 at 5000 Hz. (The clearing ratio is defined as the ratio of the gas velocity to the discharge width multiplied by the repetition rate frequency. Simply speaking, a clearing ratio of 3 means that there is theoretically two cold discharge volumes after each discharge. As shown in Fig.40, this laser was operated successfully either with a classical charge transfer thyratrons circuit or with a circuit combining thyratrons and MOS Assisted Gate-triggered Thyristors (MAGT). The power consumption of the blower as to be emphasized. It is at least of the same order of magnitude than the average power input in the discharge!

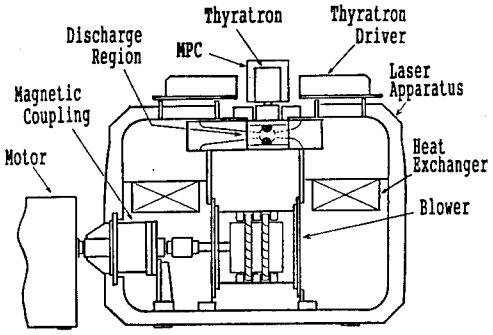


Figure 39. Schematic cross section of the Toshiba laser.

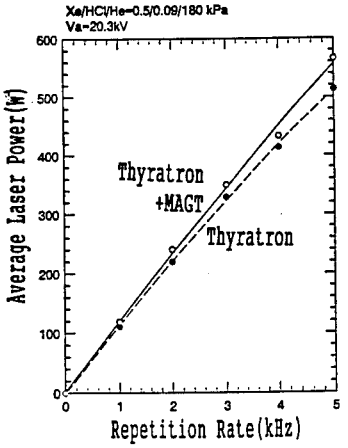


Figure 40. Average power of the Toshiba laser versus repetition rate.

The highest average power, 2KW, has been achieved by M.Inoue at Mitsubishi Electric Corporation [47] with a corona preionized laser operated at 800Hz. A spiker sustainer circuit was used (Fig.41). Single shot efficiency was 4.3%.It is noteworthy that the total pulse duration was very long, 400ns, even at the highest repetition rate. In Fig.42 is shown the average output power as a function of the repetition rate. This curve was obtained with a two modules oscillator having a total gain length of 3m and a cavity length of 5.2m!

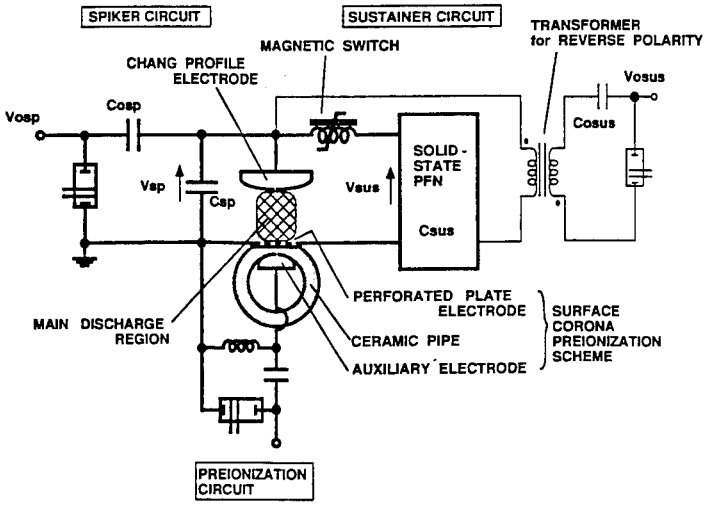


Figure 41. Schematic diagram of excitation system of the Mitsubishi laser.

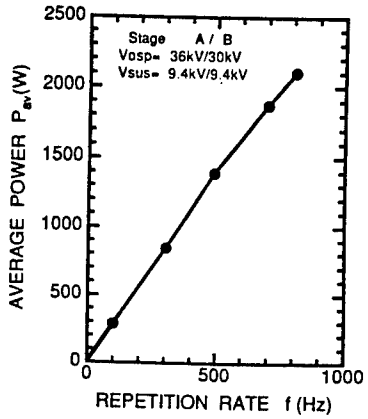


Figure 42. Average power of the Mitsubishi laser as a function of repetition rate.

A high discharge volume (10 liters) X ray preionized laser has been built at ENEA (Italy)[37].The energy output has reached 11 J per shot with a beam cross section of 7 x 10 cm2. Attempt to operate this laser in the switchless mode was partially successful. An energy of 4.8J has been obtained with 0.9% efficiency. In this mode, the laser was found very sensitive to self breakdown, probably because of corona discharges or, even, insulator flashover inside the laser head. In Fig. 43 is represented a cross section of the laser head. Such a geometry produces a very strong field enhancement along the edges of the high voltage electrode and on the insulator near it.

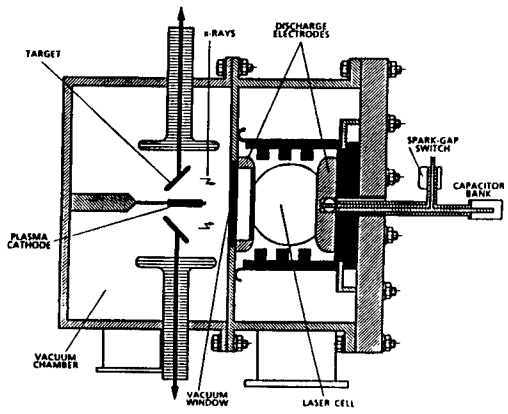


Figure 43. Cross section of the ENEA laser.

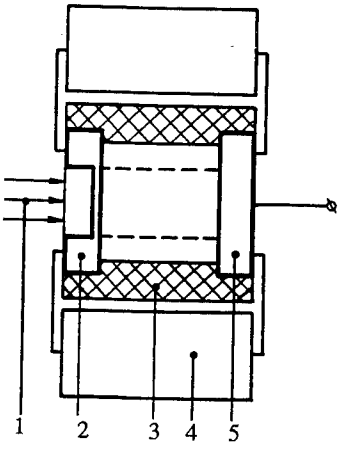


Figure 44. Cross section of Makarov laser. 1-X-ray preionization, 2- cathode, 3- insulator, 4- storage capacitors, 5- anode.

The geometry of the laser built by M.Makarov and his coworkers [36] was much well adapted to switch less operation (Fig.44) and, consequently an energy of 15J with an efficiency of 2.4% was achieved for an active volume of only 4.3 liters.

In France, studies within the framework of the Eureka EU 205 Project lead to the realisation of two 1KW average power lasers, the VEL at SOPRA and the 635 at LASERDOT.

The VEL is a high volume, low repetition rate, laser. Its characteristics are listed below.

SOPRA VEL CHARACTERISTICS

Discharge - gap : 9 cm, width : 6cm, length :135cm, volume : 7500cm^3
Maximum stored energy - 1kJ
X ray preionization -
Maximum repetition rate - 100Hz
Gas - mixture/pressure: HCl,Xe,Ne; 4, 30, 4500 mBar
flow speed : 18 m/s, total volume : 1500 l
blowers power : 3 kW
Size - height:2.5 m,length: 4 m,width: 2.4 m
Output - maximum pulse energy(V.E.L.15) : 20 J,
maximum pulse duration(V.E.L.15) : 260 ns
average power(V.E.L.1K) : 1 kW at 100 Hz

The 635 laser has been initially designed to deliver 500W at 500Hz. Its characteristics are also listed below.

LASERDOT/CILAS 635 LASER CHARACTERISTICS

Discharge - gap :3.5 cm, width : 3.5cm, length : 60cm, volume : 735cm^3
Maximum stored energy - 114J (C1=254nF,V1=30kV)
Corona preionization energy - 0.5 J
Maximum repetition rate - 500 Hz
Gas - mixture/pressure: HCl,Xe,Ne; 3.5, 10, 4500 mBar
flow speed: 35 m/s, total volume: 500 l
blowers power: 21 kW
Size - height:2 m,length: 1.83 m,width: 1.35 m

Output- pulse energy: 3 j, pulse duration: 75 ns
average power: 1 kW at 400 Hz

The 635 laser uses what we could call : a "fast phototrigerring principle". We have explain before that phototriggering is a very efficient scheme, but supposes that self breakdown is avoided. This condition can be achieved at low repetition rate by a proper choice of the laser head internal geometry and a clean gas. At high repetition rate, it is probably possible,(but very difficult!) to avoid these self breakdown while keeping the voltage rise time in the µs range. We have found it easier to reduced the voltage rise time up to the value were an electron will never produce a breakdown before the discharge. This time remains sufficiently long (0.5µs) to keep to the phototrigerring its interest from the main thyratron reliability point of view.

Figure 45 shows the laser. The design includes in the same stainless steel cylindrical vessel the complete gas circulation system, the discharge and the complete

high current and high voltage circuitry. The overall volume, including gas bottles, vacuum pump, blowers motors and high voltage supplies is less than $5m^3$.

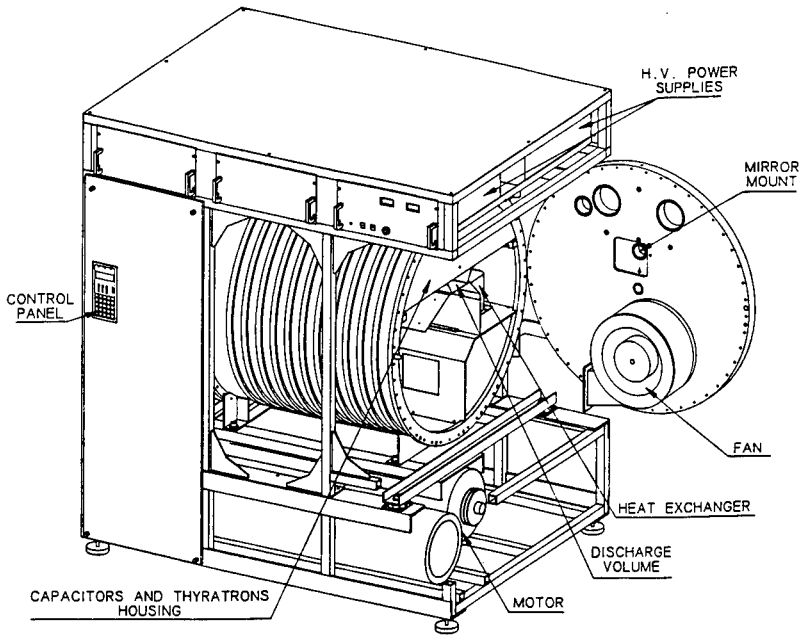


Figure 45. Details of the 635 LASERDOT / CILAS laser (panels removed and high pressure vessel open).

The geometry of the discharge current loop has been improved with respect to our preceding prototype (Fig.26). A very uniform field is achieved between the electrodes and along the insulators surfaces while keeping the inductance very low. This allows a good beam quality and a very good efficiency even at high repetition rate. As shown in Fig.46, the intrinsic efficiency is higher than 4%. In this figure we call "intrinsic efficiency" the ratio of the output energy to the energy stored in the discharge capacitors at the moment of the breakdown. The electric scheme is of the charge transfer type (see Fig.23) but with a separately controlled corona preionization device. The discharge loop inductance is only 8 nH, while the thyratron (or primary!) circuit inductance is much higher, 280 nH. Therefore no additional energy can be transferred directly from the primary capacitors to the discharge. In Fig.46 is also presented the "wall plug efficiency" which compares the laser output to the energy input (Blowers are not taken into account). It is always higher than 3%.

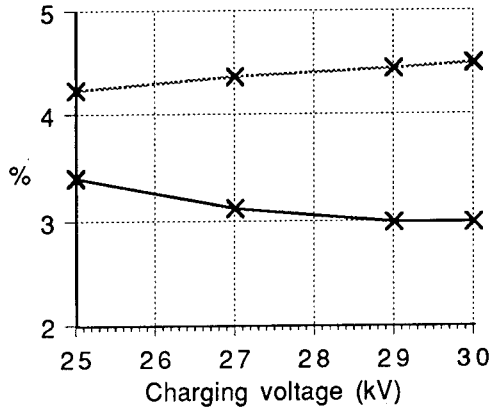


Figure 46. Wall plug (full line) and intrinsic (dotted line) efficiency of the LASERDOT / CILAS 635-2 laser as a function of the charging voltage. XeCl gas mixture pressure 4.5bar, capacitances: C1=254 nF, C2=242nF.

High repetition rate results are presented in Fig.47. The energy per pulse is constant up to 300Hz, then decreases slightly, due to the beginning of the acoustic waves reverberation regime. As a result, when a burst is fired, the energy decreases from pulse to pulse for the 5 to 10 first pulses and then remains practically constant. The use of acoustical dampers can reduce the stationary perturbation level in the laser cavity and hence help to reduce this phenomenon.

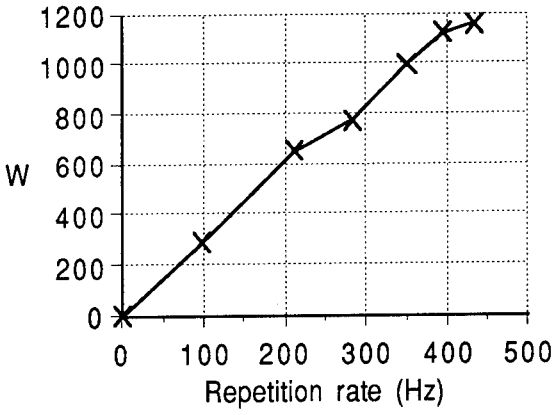


Figure 47. LASERDOT / CILAS 635 -2 laser . Average power v.s. rep.rate frequency.XeCl,pressure:4.5 bar,charging voltage:30 kV,stored energy:114J

3. Excimer lasers from users point of view

3.1. OPTICAL CHARACTERISTICS

3.1.1. *Beam homogeneity*
is of interest for many users. Former excimer lasers had inhomogeneous, narrow beams. Modern lasers are able to deliver square beams with a much better homogeneity. In Fig.48 are shown the beam cross sections of the 635 laser along the x and the y direction. When a better beam quality is required beam homogeniser are proposed by many excimer lasers manufacturers. With these devices a flat (within a few percent) pattern can be obtained on the target.

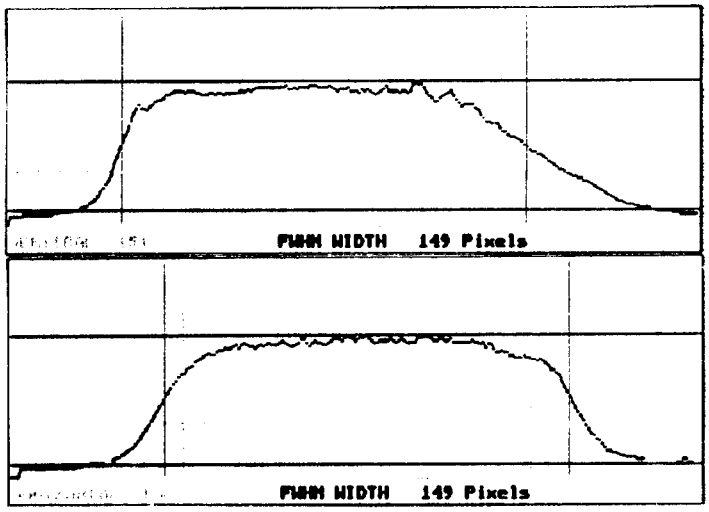


Figure 48. Near field beam cross section of the LASERDOT / CILAS 635 laser. Top: vertical, bottom: horizontal.

3.1.2. *Divergence*
is also of interest for fine work or for long distance use. An unstable cavity with a magnification of about 3 to 6 gives usually a very good result. In Fig.49 are compared the far field beam profiles obtained with a classical (flat-flat) or an unstable cavity. The brightness gain is over 10. In Fig.50 we show the average power as a function of repetition rate for both cavities. The energy decrease is only of the order of 15% with the unstable cavity (magnification 4).

3.1.3. *Pulse duration*
can be adjusted in a wide range : From µs to 10th of ps. Long pulses require a very good discharge quality and high reflectivity mirrors, ultra short pulses usually are done by a combination of excimer and dye lasers.

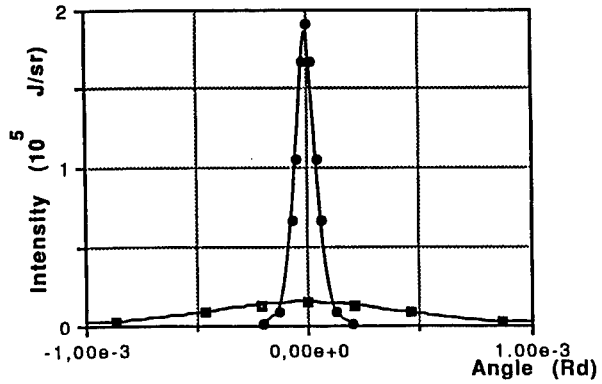


Figure 49. Far field intensity profile of the LASERDOT / CILAS 530 XeCl laser with stable (■) or unstable (●) cavity.

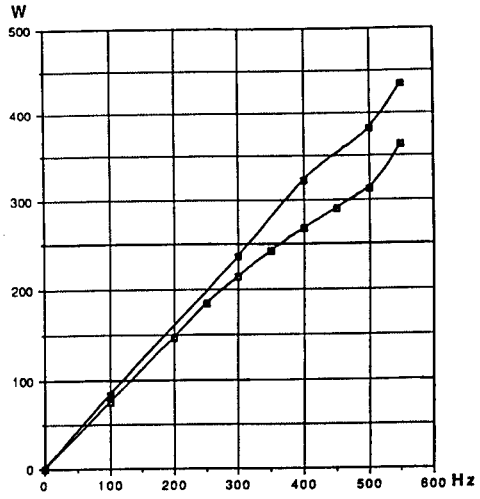


Figure 50. Output average power of the LASERDOT / CILAS 530 XeCl laser with stable (■) or unstable (□) cavity.Figure 50 and 51 are obtained in the same experimental conditions.

3.1.4. *The wide natural spectral width*
of excimer lasers is, sometimes, found useful to avoid speckle. In other case it is found desirable to have a narrow bandwidth. Several optical set ups have been proposed and the KrF problem is different from the XeCl problem because KrF emits on a single wide line and XeCl on several (4 or 5) narrower lines. Generally a narrow line width oscillator is done with little output energy. The main difficulty is to amplify *only* this narrow line width emission . For instance it can be observed that the amplification in XeCl shifts

with time from the injected line to the high gain lines [48].

3.2. RELIABILITY

Excimer lasers were said to have poor reliability in the past. Manufacturer have made big efforts to improve this situation. Now commercial excimer lasers are used for several industrial applications. Their reliability has been proven to be very good [49]. Number of shots higher than 10^9 and up times > 80% have been observed.

TABLE 6: Best performances

Energy - 66 J (N.R.L.)
Repetition rate frequency - 5kHz (Toshiba, Japan1994), 8kHz (mwave discharge : C.P.Christensen, 1987)
Beam cross section - 20 cm x 11cm (N.R.L.)
Divergence - 5 x diffraction limit
Narrower bandwidth - 0.1 cm^{-1}
Pulse duration -:Longer:1μs (R.S. Taylor)
Shorter : 280 fs (S.Watanabe et al. 1991)
Average power- > 1kW,MITSUBISHI, SOPRA, LASERDOT / CILAS.

As a conclusion,
table 6 shows the best values obtained in laboratory or commercial (industrial) equipments. It's time now for excimer lasers to find their niche in the industrial applications. Lasers are ready and reliable.

4. References

1. Houtermans F. G. (1960) Helv. Phys. Acta. **33**, 933.
2. Basov N. G. et al. (1970) ZhEFT Pis. Red. **12**, 473-474.
3. Velazco J. E. and Setser D. W. (1975) J. Chem. Phys. **62**, 1990-1991.
4. Searles S. K. and Hart G. A. (1975) Appl. Phys. Lett. **27**, 243-245.
5. Brau C. A. and Ewing J. J. (1975) Appl. Phys. Lett. **27**, 350-352.
6. Brau C. A. and Ewing J. J. (1975) Appl. Phys. Lett. **27**, 435-437.
7. Wang C. P. et al. (1976) Appl. Phys. Lett. **28**, 326-328.
8. Wang C. P. et al. (1976) Appl. Phys. Lett. **28**, 522-523.
9. Lin S. C. and Levatter J. I. (1979) Appl. Phys. Lett. **34**, 505-508.
10. De Witte O. Lacour B. and Vannier C. (1982) Proc. CLEO'82,THQ2.
11. Long W. H. et al. (1983) Appl. Phys. Lett. **43**, 735-737.

12. Ernst W. E. and Tittel F. K. (1979) Appl. Phys. Lett. **35**, 36-37.
13. Basov N. G. et al. (1979) Kvantov. Electron. **6**, 1074.
14. Tittel F. K. et al. (1980) Appl. Phys. Lett. **36**, 405-407.
15. Yamada K. et al. (1989) Appl. Phys. Lett. **54**, 597-599.
16. Zuev V. S. et al. (1989) Kvantov. Electron. **16**, 1154-1157.
17. Burnham R. and Djeu N. (1976) Appl. Phys. Lett. **29**, 707-709.
18. Velazco J. E. et al. (1976) J. Chem. Phys. 65, 3468.
19. Townsend (1902) Phil. Mag. **3**, 557.
20. Riva R. et al. (1995) J. Phys. D: Appl. Phys. **28**, 856-872.
21. Mizzi S. (1990) Thesis, Orsay, France.
22. Lacour B. (1990) SPIE Proceeding 1278.
23. Belasri A. Boeuf J. P. and Pitchford L. C. (1993) J. Appl. Phys. **74**, 1553-1567.
24. Puech V. (1995) Private communication.
25. Akashi H. et al.(1994) J. Phys. D: Appl. Phys. **27**, 1097-1106.
26. Raether H. (1964) Electron avalanche and breakdown in gases(Butterworth, London).
27. Palmer A. J. (1974) Appl. Phys. Lett. **25**, 138-140.
28. Levatter J. I. and Lin S. C. (1980) J. Appl. Phys. **51**, 210-222.
29. Beaupere D. et al. (1988) Proc. CLEO'88 TuH6.
30. Taylor R. S. (1986) Appl. Phys. B **41**, 1-24.
31. Besaucele H. (1994) Thesis, Strasbourg I, France.
32. Humphries S. et al. (1985) Appl. Phys. Lett. **47**, 468-470.
33. Pigache D. et al. (1983) XVI Internat. Conf. on "Phenomena in Ionized gases", Dusseldorf, Germany.
34. Lacour B. et al. (1988) Conf. LASER 88, HI 4, Lake Tahoe, Nevada, USA.
35. Lacour B. et al.(1995) "Operation of a compact industrial XeCl laser at high average power" to be published.
36. Bychkov Y. I.,Vinnik M. L. and Makarov M. K. (1992) Sov. J. of Quant. Electr. **19** , 542-543.
37. Bollanti S. et al. (1990) Appl. Phys. B 50, 415-423.
38. Lacour B. et al. (1994) SPIE Vol. 2206,41-45.
39. Truong J. P. (1993) Thesis, Marseille II, France.
40. McKee T. J. et al. (1980) Appl. Phys. Lett. **36**, 943-945.
41. Oxford Lasers Limited (1985) England.
42. Saito T. et al. (1994) AMMTRA Overseas Technology Exchange, 6-15.
43. York G. W. et al. (1985) Proc. CLEO'85 THL3.
44. Champagne L.F. et al. (1987) J. Appl. Phys. **62**, 1576-1584.
45. Champagne L.F. et al. (1985) Conf. LASER 85, HB 1, New Orleans.
46. Takagi S. et al. (1994) AMMTRA Overseas Technology Exchange, 48-57.
47. Inoue M. et al. (1994) AMMTRA Overseas Technology Exchange, 28-37.
48. Bourne O. L. and Alcock A. J. (1983) Appl. Phys. Lett. **42**, 777-779.
49. Lankard Sr J. R. and Wolbold G. (1992) Appl. Phys. A **54**, 355-359.

INDEX

Aberration
  Coefficients 59
  Wave Front 76
Ablation 527,549, 567
Absorber 126
Absorption 178,226
  Excited State 177
  Nonlinear 179
  Non Saturable 7
Acoustic Damping 409
Active Medium 255
Adaptive Optics 172
Aero-Acoustic Waves 392
Aerodynamics 401
Aluminium 505
  Growth Rate 510
Amplification 101,181
  Input Energy 13
  Pulse 21,20
Amplifier 246
  Multipass 182
  Terawatt 23
Angular Divergence 60,113
Applications 461
  Automotive 463
Ar+ Ion Laser 573
Asterix IV Laser 217
Astigmatic Telescope 270,279
Atomic Force Microscopy (AFM) 566
AVLIS - See Isotope Separation

Beam
  Characterization 308
  Delivery 469
  Divergence 60,449
  Intensity 381
  Modes 450
  Quality 241,291
  Propagation Factor 365
  Properties 449,467
  Transport 303,305,311
Bipyridyl 456
Bouguer's Law 54
Br_2: Ar 103
Brillouin Scattering 242

C_3F_7I 217
Cadillac DeVille 490
Carbon Film Deposition 527
Ce_3 : $LiSrAlF_3$ 177
Characterization 308
  Beam 527,529
  Carbon Films 527, 529
  Molybdenum Films 549
Chemical Lasers 66,73
Circuits 157,332
Cl_2 : Ar 102
Cladding 479
Clays 455
CO Lasers 35,40
CO_2 Lasers 3,125,272,466,499,603
  Amplifier, Terawatt 23
  High Pressure 18
  Transversely Excited 32
Coatings 549
Coherent Light 533
Coherence
  Index 47
  Radius 47
Compact Aperture 113
Copper 161,165
Copper Vapour Laser 505
Correlation Function 47
Coupling Coefficient 470
Cutting 465,495

Damage Threshold 221
Dentistry 575
Deposition 513,527
Design 1,177,284
  Laser Head 156,159
Diagnostics 164,166
  Stress in Metals 413
Diffraction Limit 196
Discharge 139,334,393
  Circuits 158
  Electric 27
  Homogeneous 627
  Longitudinal 342
  Physics, Rare Gas Halides 617
  Sliding 185
Divergence 60,113,449

Efficiency 28
Eigen Modes 257
Electric Circuit 146,151,634
Electron Density 47,207
Emission 178,226,347
Environmental Effects 316
Er : YAG 575
Excimer Lasers 35,191,459,613
  Operating Lasers, Examples 643
Excitation 14,98,155,161,186,
    200,393
  DC 42

Fe X-Ray Laser 205
Feedback Loop 352
Fiber Transport 314
FJFI Laser System 578
Fox and Lee Method 258
Fresnel Number 279
Fuel Injection 79

Gain 13,17,95,208
Gas Dynamic Laser 47,62,65,
    69,83,95
  Pulsed 69
GOLEM facility 376
Grotrian Diagram 201
Guide-Star Laser 322

HF Lasers 189
History, High Power Lasers 585
Halides 615
  Rare gas 617

Incoherent Light 533
Inductance
  Time Dependence 140,145,151
Inhomogeneities
  Active Medium 47
  Optical 56
Injection 163
Intensity 128,194,375,386
Interferance Patterns 439
Interferograms 51,77,212,393,443
Interferometry
  Shear 65
Intrinsic Stress 531

Iodine Lasers 217
IR Lasers 414,416
Isotope Separation 171,325

Joining Configurations 483

Kerf 251,494
Kerr-Lens Mode 177
Kinetics 154,622
KrF Lasers 552
Kurtosis 365

Laser Characteristics (Table) 9
Laser Head 638
Laser Technology 499
Laser Chemical Vapour Deposition
(LCVD) 505
  Aluminium 510
  Silicon 520
Lasers
  ArF^+ 30
  Chemical 66
  CO 35
  CO_2 3,125,272,466,499,603
  Copper Vapour 505
  Excimer 9,191,153,613,643
  Gas Dynamic 47,66,95
  Gyro 135
  HF 189
  Iodine 217
  KrF_2 30,552
  Mercury Dihalide 86
  Metal HyBrID 168
  Metal Vapour 153
  Nd : Glass 376
  Solid State 33,241,347,585
  UV 56,177,185
  X-Ray 89,373
  XeF 89
Lick Observatory 321
Line Broadening 6
Line Shape 6
Liquid Metal Targets 423
Losses
  Mirror 8
  Modulated 132
LUX III Laser 410

Manufacturing Technology 501
Mass Spectrometry 173,520
Materials Processing 170,463
Measurements 389
Melting 533
Mercury Dihalide 86
Metal HyBrID Lasers 168
Metal Sulfides 561
Metal Vapour Lasers 153
MgF_2 162
Mirror 8,243,283
  Concave 384
  Deformable 283,293
  Losses 8
Modeling 374
  Wave Evolution 405
  Thermal Distribution 522
Modulation 131,359
  Active 125
  Passive 125

National Ignition Facility 323
Nd : Glass Laser 376
Nd : YAG Laser 174,182,248,284,
    293,416,463,567,575
Ne-Kr-HCl 339
Neodymium Laser 423
Neon-Like 203,233
Ni_3S_4 563

Opacity 231
Ophthalmology 575
Optical
  Cavity 162
  Components 318
  Fibers 549,568
  Materials 592
  Path 32,47
Optics 239,303,373
Optimization 7
Oscillator Amplifier 246
Oscillogram 354
Output 187,287,297

Patterning 567
Perspectives 107
Phase Conjugation 241,433
Picosecond Pulse 22
Plasma 208
Power Density 29,475
Preionizer 38
Pressure Fluctuations 407
Pressure History 398,402
Process Technology 501
Pulse Generation 178,352,587
Pumping 27,83,100,180,202,220,
    248,251,287,332,343,616

Q Switching 349, 567
Quality
  Beam 241,291
  Control 391
  Optical 62,191
Quantum Electronics 255,586

Radiation
  Amplification 4
  Density 118
Raman Spectroscopy 455,530
Resistance
  Time Dependence 140,141,151
Resonators 243
  Compact Beam 115
  Computer Simulation 381
  High Effective Length 271
  Linear 382
  Open 255
  Spatial Filtering 268
  Stable 260
  Stable Plano-Concave 449
  Stigmatic Telescope 271
  Two Dimensional 276
  Two Rod 294
  Unstable 113,192,264,283,293

S_2 : Ar 102
Scanning Electron Microscopy
505,563
Schlieren Photography 395
Semiconductors 533
SF_6 : N_2 185
Shear Interferogram 433
Sheet Metal 486
Shock waves 229,561

Silane 520
Silicon 536,542
Simulation 381
Solid State Lasers 33,241,347,585
  Ultra High Power 593
Spatial Distribution 357
Spectral Reflection Factor 428
$SrTiO_3$ 570
Strehl Coefficient 55,75,122
Superconductor 571
Surface Treatment 476

Thermal Effects 471
Thermal Management 313
Thermal Waves 413
Thin Films 567
Ti : S 225
Time Diffraction Limit (TDL) 191
Transformation Hardening 476
Trimethylaluminium 505
Turbine Blade 419

UV Exilamps 331
UV Lasers 56,177,185
UV Plasma Sources 83,85
Variable Reflectivity Mirror 283,293

Wave Front 139
  Reconstruction 433
Wave Forms 336
Wave Function 47
Waveguide 272
  Coaxial 277
  Plane 274
  Resonator 255
  RF Excited 16
  Systems 16
Welding 479

X-Ray Diffraction 563,567
X-Ray Lasers 199,222,229,373
XeF Lasers 89

YBaCuO 569

LIST OF PARTICIPANTS

Amarande S.
Institute of Atomic Physics
Lasers Department
P.O.Box MG 6
R-76900 Bucharest Romania
T:+40.1.780.4290 F:
amarande%ro.ifa.bitnet@pucc

Anikichev Sergei
3000 Bathurst St, 1205
North York Ontario M6B 3B4 Canada
T:+1.416.256.4157 F:
rubisov@ecf.toronto.edu

Baumhacker Horst
Max Planck Institute
Quantum Optics
Garching Germany
T:+49.89.3290050 F:+49.89.32.905.200

Bollanti Sarah
ENEA
INN-FIS-LAC
P.O.Box c5
00044 Frascati (Rome) Italy
T:+39.6.94.00.57.16 F:+39.6.94.00.53.34
bollanti@efr419.frascati.enea.it

Bulat Taner
Istanbul University
Physics Department
Vezneciler
34459 Istanbul Turkey
T:+90.212.511.8480 F:+90.212.519.0834

Bulir Jiri
Czech Academy of Science
Institute of Physics
Na Slovance, 2
18040 Prague 8 Czech Republic
T:+42.2.66.05.2733 F:+42.2.82.12.27
bulir@fzu.cz

Chitica Nicolae
Institute of Atomic Physics
Laser Department
P.O.Box MG-6
RO-76900 Bucharest Romania
T:+40.1780.70.40 F:+40.1.312.22.47
lita@ifa.ro

Datsyuk Vitaly
Kiev T. Shevchenko Univ.
Physics Department
64 Vladimirskaya Street
Kiev 252017 Ukraine
T:+7.044.266.4477 F:+7.044.268.2395
alexey@ipu.univ.kiev.ua

Dimakov Sergei
Vavilov State Optical Institute
12 Birzhevaya
St. Petersburg, 199034 Russia
T:+7.812.218.9982 F:+7.812.218.1093

Eichler Hans
Technische Universitaet Berlin
Optisches Institut
Str. des 17. Juni 135
D-10623 Berlin Germany
T:+49.30.314.22498 F:+49.30.314.26888
eichler@physik.tu-berlin.de

Enescu Mihaela
Institute of Atomic Physics
Lasers Department
P.O.Box MG-06, Magurele
76900 Bucharest 5 Romania
T:+40.1.780.7040 F:+40.1.780.4290
menescu@ifa.ro

Farooq Aslam
Nat'nl Inst. of Silicon Technology
H. No 942 St 29, G-9/1
Islamabad Pakistan
T:+92.51.452.487 F:

Fattakhov Yakh'ya
Kazan Physical Technical Inst.
Radiation Physics Laboratory
Sibirski Trakt 10/7
Kazan Tatarst 420029 Russia
T:+7.8432.761241 F:+7.8432.765075
fattakhov@ksc.iasnet.com

Forestier Bernard
Universite d'Aix-Marseille II
Institute of Fluid Mechanics
1 Rue Honnorat
13003 Marseilles, France
T:33.91.10.78.00 F:33.91.08.58.91

Grivas Christos
FORTH - Hellas
Inst. Electronic Struct. & Physics
P.O.Box 1527, Vassilicka Voutou
71110 Heraklion Greece
T:+30.81.391315 F:+30.81.391318
drig@iesl.forth.gr

Grozdanov Krassimir
Institute of Electronics
72 Czarigradsko Shose Blvd.
1784 Sofia Bulgaria
T: F:+359.2.75.70.53

Gyorgy Eniko
Institute of Atomic Physics
Lasers
P.O.Box MG-6
RO-76900 Bucharest Romania
T:+40.1780.70.40 F:+40.1.312.22.47
lita@ifa.ro

Hackenberg Wolfgang
für Extraterrestische Physik
Max Plank Institute
Giessenbachstrasse
D-85740 Garching Germany
T:+49.89.3299.3276 F:+49.89.3299.3569
hacki@sharph.mpa-garching.mpg.de

Hening Alexandru
Institute of Atomic Physics
Lasers Div.
P.O.Box MG-21
RO-76900 Bucharest Romania
T:+40.1.780.4677 F:+40.1.312.22.45
hening@ifa.ro

Hogan Geoffrey
Oxford University
Laser Group
Clarendon Lab., Parks Road
Oxford, OX1 3PU UK
T:+44.1856.272259 F:+44.1865.272400
g.hogan@physics.ox.ac.uk

Ivanov Borislav
Higher Inst. Chemical Technol.
Dept. of Semiconductors
8 Kl. Ohridski Street
1756 Sofia Bulgaria
T:+359.2.6254.649 F:+359.2.522.006
blivanov@cserv.mgu.bg

Jelinekova Helena
Czech Technical U.
Nuclear Sci. & Physics Dept.
Brehova 7
115 19 Prague 1 Czech Republic
T:+42.2.8576.2243 F:+42.2.5876.2252
hjelin@troja.fjfi.cvut.cz

Knutsen Per
The Alpine Group, Inc.
Business Development
1790 Broadway
New York NY 10019-1412 USA
T:+1.212.757.3333 F:+1.212.757.3423

Kossowsky Ram
Emerging Technologies, Inc.
6327 Burchfield Avenue
Pittsburgh PA 15217 USA
T:+1.412.421.4408 F:+1.412.421.4342
ramkoss@ix.netcom.com

Kozlova Ariadna
Moscow Aviation Institute
Physics Department
Volokolamskoye Shosse, 4
Moscow 125871 Russia
T:+7.095.158.4594 F:+7.095.158.2977
spirin@k804.mainet.msk.su

Jelinek Miroslav
Czech Academy of Science
Physics Institute
2 Na Slovance
18040 Prague 8 Czech Republic
T:+42.2.66.05.2733 F:+42.2.82.1227
jelinek@fzu.cz

Kakkouras Andronikos
University of Strathclyde
EEE Optoelectronics Div.
204 George Street
Glasgow G1 1XW UK
T:+44.41.552.4400 F:+44.41.552.2487
cubv71@ccsun.strath.ac.uk

Komarov Konstantin
Inst. Autom. and Electrometry
Solid State Lasers
Universitetskii Pr. 1
Novosibirsk 630090 Russia
T:+7.383.2.35.02.08 F:+7.383.235.48.51
komarov@iae.nsk.su

Kotomtseva Lyudmila
Belarus Academy of Science
Institute of Physics
70 F. Skarina Ave.
220072 Minsk 1 Belarus
T:+7.0172.395521 F:+7.0172.393131
ifanbel%bas03.basnet.belpak.minsk.by

Kubishkin Alexander
Scientific Res. Cntr., Lasers
NICTL RAN
Svyatoozerskaya 1
Shatura, Moscow Reg. 140700 Russia
T:+7.095.135.0254 F:+7.095.135.5430
center@laser.nictl.msk.su

Kuz'min Victor
Troitsk Institute
Moscow Region
142092 Troitsk Russia
T:+7.095.334.0518 F:+7.095.334.5776
kochet@anet.sovam.com

Lacour Bernard
Laserdot Corporation
Lasers Department
Rue de Nozay
91460 Marcoussis France
T:33.1.64.54.4800 F:33.1.69.80.6283

Lavi Shimon
DDR&D - MAFAT
Lasers Department
Hakirya
Tel Aviv Israel
T:+972.3.697.5404 F:+972.3.697.5897

Lavrov Alexander
Russ. Scien. Ctr. Appl. Chem.
Deputy Laboratory Chief
14 Dobrolubov Ave.
St. Petersburg 197198 Russia
T:+7.812.238.9406 F:+7.812.271.3488
lavrov@cheminfo.spb.su

Lovoi Paul
Internat. Tech. Associates
2281 Calle de Luna
Santa Clara, CA 95054 USA
T:+1.408.748.9955 F:+1.408.727.3027

Lucianetti Antonio
European Laser Engineering
Faculty of Physics
Via Borgo Palazzo 90
24100 Bergamo Italy
T:+39.35.233.938 F:
lauricf@vaxmi.mi.infn.it

Manenkov Alexander
General Physics Institute
38 Vavilova Street
Moscow, 117942 B-333 Russia
T:+7.095.135.1331 F:+7.095.135.0270
manenkov@lftt.gpi.msk.su

Manukyan Genrikh
Efremov Research Institute
Min. Atom
Sovetski Avenue 1
St. Petersburgh 189631 Russia
T:+7.812.265.8995 F:+7.812.314.3360

Markevich Maria
Belarus Institute of Electronics
Physics of Thin Films Dept.
22 Logoiskij Tract
220841 Minsk Belarus
T:+7.2.65.33.32 F:+7.2.65.25.41

Moshkov Vladislav
Baltic State Technical Univ.
1 First Krasnoarmeyskaya St.
St. Petersburg, 198005 Russia
T:+7.812.251.2162 F:+7.812.251.2257
kaflt@sovam.com

Mraz Peter
Avantek, s.r.o.
Mierove nam. 11
915 01 Trencin Slovakia
T:+42.834.5726 F:+42.834.5520

Naumov Vadim
Institute of Physics
Photoactivity Department
46 Prospect Nauki
Kiev 252650 Ukraine
T:+7.044.265.7778 F:+7.044.265.8342
class@semicond.kiev.ua

Nelson Thomas
University of Illinoise
Physics Department
M/C 373, 845 W. Taylor, Rm 2136 SES
Chicago IL 60607-7059 USA
T:+1.312.413.2109 F:+1.312.996.8824
nelson@uicwspphy.uic.edu

Novgorodov Maxim
Lebedev Physical Institute
Optics Department
Leninsky Prospect, 53
Moscow 117924 Russia
T:+7.095.135.2240 F:+7.095.938.2251
rubin@sci.fian.msk.su

Okada Yasuhiro
Sumitomo Heavy Industries, Ltd
R&D Center, Optronic Group
63-30 Yuuhigaoka,
Hiratsuka Kanagawa Japan
T:+81.46.321.8980 F:+81.46.321.8464
kye03346@niftyserve.or.jp

Pavel Nicolaie
Institute of Atomic Physics
IFTAR-MALIRM
P.O.Box MG-6
76900 Bucharest Romania
T:+40.1.780.7040 F:+40.1.780.4290
npavel@roifa.bitnet

Persephonis Peter
University of Patras
Physics Department
26500 Patras Greece
T:+30.61.997.470 F:+30.61.991.980
pet-per@physics.upatras.gr

Pina Ladislav
Czech Technical University
Physical Electronic Department
V Holesovickach 2
CZ-18000 Prague, 8 Czech Republic
T: F:
pina@troja.ejfi.cvut.cz

Polyakova Galina
Efremov Research Institute
Min. Atom
Sovetski Avenue 1
St. Petersburgh 189631 Russia
T:+7.812.265.8995 F:+7.812.314.3360

Prokhorov Kirill
General Physics Institute
VKIV
Vavilov Street, 38
Moscow 117942 Russia
T:+7.095.135 3448 F:+7.095.135 3448
cyr@ewm.gpi.msk.su

Protasov Yuri
Bauman State University
2 Bauman Street
Moscow 107005 Russia
T:+7.095.263.6024 F:+7.095.267.9893
postmaster@interd.bmgtu.msk.su

Rabczuk Grazyna
Institute of Fluid Mechanics
Fiszera 14
Gdansk Poland
T:+48.58.41.12.71 F:+48.58.416.144

Rodionov A
Vavilov State Optical Institute
12 Birzhevaya
St. Petersburg, 199034 Russia
T:+7.812.218.9982 F:+7.812.218.1093
mak@ilph.spb.su

Rodrigues A.
New University of Lisbon
Department of Electrical Engineering
DEE-FCT/UNL
2825 Monte de Caparica Portugal
T:+351.1.295.4464 F:+351.1.295.7810

Roessler David
General Motors
Research & Development Cntr.
30500 Mound Road, Bldg. 1-6
Warren, MI 48090-9055 USA
T:+1.313.986.0660 F:+1.313.986.3091

Rus Bedrich
Institute of Physics
Department of Gas lasers
CZ-18040 Prague, 8 Czeck Republic
T:+42.2.6605.2619 F:+42.2.821.227
rus@fzu.cz

Saraev Denis
Tomsk State University
Russian Materials Science Cntr.
2/1 Akademicheskii Av.
Tomsk 634055 Russia
T:+7.3822.25.8881 F:+7.3822.25.9576
denis@monster.tomsk.su

Shashkov Vladimir
Troitsk Institute
Moscow Region
142092 Troitsk Russia
T:+7.095.334.0518 F:+7.095.334.5776
kochet@anet.sovam.com

Shekhtman Valentin
Engineer. Physical Laboratory
Director
Pushkin 8, Box 260
St. Petersburg 189620 Russia
T:+7.812.476.2059 F:+7.812.293.2778
eflekst@sovam.com

Shentsev Nikolay
Insti., Physics & Technology
Ozernay 10-12, Sergiev Posad 7
Moscow 141300 Russia
T:+7.095.584.9958 F:
trc@meyer.msk.su

Spalding Ian
AEA Technology
FS/141
Oxfordshire Culham, Abington OX14 3DB
T:+44.235.464206 F:+44.235.464138

Tarasenko Viktor
High Currents Electronic Inst.
Siberian Division
4 Akademichesky Ave.
Tomsk 634055 Russia
T:+7.8.382.2.25.86.85 F:+7.8.382.2.25.94.10
tarasenko@loi.hcei.tomsk.su

Taylor John
Lawrence Livermore N.L.
Optical Systems Group
P.O.Box 5508, L-462
Livermore, CA 94550 USA
T:1.510.423.4438 F:1.510.423.3143

Teodorescu Octav
University of Bucharest
Department of Physics
C.P. 22-90
Bucharest Romania
T:+40.1.673.6603 F:+40.1.312.4591

Trtik Vitezslav
Czech Academy of Science
Institute of Physics
Na Slovance, 2
18040 Prague 8 Czech Republic
T:+42.2.66.05.2733 F:+42.2.82.12.27
trtik@fzu.cz

Tumanov Igor
Efremov Research Institute
Min. Atom
Sovetski Avenue 1
St. Petersburgh 189631 Russia
T:+7.812.265.8995 F:+7.812.314.3360

Vrbova Miroslava
Czech Technical U.
Physical Engineering
Brehova 7
115 19 Prague 1 Czech Republic
T:+42.2.311.1296 F:+42.2.2431.0783
vrbova@vc.cvut.cz

Walter Robert
W.J. Schafer Associates, Inc.
2000 Randolph Road, SE
Albuquerque NM 87106 USA
T:+1.505.242.9992 F:+1.505.242.9975

Witteman W.
University of Twente
P.O.Box 217
7500 AE Enschede, The Netherlands
T:+31.53.899.111 F:+31.053.338.065

Zaripov Shamil
Inst. Mathematic & Mechanics
Department of Gas Dynamics
Kazan State U,, Universitetskaya 17
Kazan Tartars 420008 Russia
T:+7.8432.387525 F:+7.8432.380.994
zapirov@niimm.kazan.su

Zavalov Yuri
Scientific Research Cntr., Lasers
NICTL
Svyatoozerskaya 1
Shatura, Moscow Reg. 140700 Russia
T:+7.096.45.20681 F:+7.096.45.24651
center@laser.nictl.msk.su